Magneto-structural correlations in $[Mn_3O]^{7+}$ core SMMs and selected 4d, 5d and 4f SMMs

Marc Sigrist

PhD Thesis

2014

Supervised by:

Prof. Jesper Bendix

Department of Chemistry
University of Copenhagen

Dr. Hannu Mutka

Institut Laue-Langevin

This thesis has been submitted to the PhD School of The Faculty of Science, University of Copenhagen

Table of Contents

Resume på dansk

Denne afhandling beskriver de resultater der er opnået ved studier af en række molekyl-basererede magnetiske systemer. Særlig vægt er lagt på studiet af en klasse af tre-kernede mangan(III) komplekser.

I kapitel 2 beskrives undersøgelserne af en række Mn_3 enkelt-molekyl magneter med forskellige ekvatoriale R-sao^{2-} (oximat) ligander. Disse tre-kernede mangankomplekser udmærker sig ved at have meget restriktive ligandomgivelser på Jahn-Teller akserne for mangan(III) centrene hvilket fører til molekyler med meget lidt geometrisk frihed. Samtidig fører substitution på oximatliganderne (sao^{2-}) med grupper af forskellig rumlig beskaffenhed (fra H over Me og Et til Ph) til symmetribrud hvorved den lokale trigonale symmetri ophæves. Således udviser molekylerne med ligander af varierende størrelse også afvigelser fra C_3 symmetri i varierende grad. Ved at anvende uelastisk neutronspredning (INS) er indflydelsen af symmetry og geometri på den energetiske opsplitning af grundtilstands spinmultipletten og relaxationsbarrieren blevet undersøgt.

Kapitel 3 udgør en fortsættelse af forfatterens kandidatarbejde [1]. I dette kapitel undersøges mulighederne for at optimere den effektive barriere for ralaxation af magnetiseringen, U_{eff}, ved at ensrette anisotropi-akserne for de individuelle magnetiske centre. Den strukturelle variation, der fører til ensretningen af de enkelte ioners anisotripiretninger, blev opnået ved at udskifte en brodannende tripodal ligand ClO_4^- med den større analog ReO_4^-. Dette mål har været efterstræbt før, med de tidligere forsøg ver ikke frugtbare fordi det ikke var muligt at opnå isostrukturelle systemer. Eftersom kun ændringer af begrænset størrelse kan forventes i de magnetiske egenskaber, ved små geometriske ændringer så er det af afgørende betydning at minimere komplikationer der følger af utilsigtede strukturelle variationer. Derfor blev den eksperimentelle tilgang forbedret ved at finde og anvende et andet system hvori den perfekte trigonale symmetri er bevaret og hvori, ydermere, de intermolekylære vekselvirkninger er undertrykt pga. større afstande mellem molekylerne.

I kapitel 4 beskrives undersøgelser vha. INS af en række af forskellige systemer, der udviser inter-molekylære exchange-vekselvirkninger så som dem nævnt ovenfor. De undersøgte systemer har usædvanligt store relaxationsbarrierer, som ikke kan forklares udelukkende baseret på kombination af enkelt-center anisotripier.

Kapitel 5 beskriver resultater for en ganske anden type af tre-kernede forbindelser. I stedet for de trekantede Mn_3 enkelt-molekyl magneter undersøges heterometalliske systemer med en lineær topologi: Mn(III)-M(III)-Mn(III) (M = Ir, Ru, Os). Forbindelserne har sammensætningen $(NEt_4)[Mn_2(5\text{-Brsalen})_2(MeOH)_2M(CN)_6]$ med en Schiff-base ligand på hvert Mn(III) center. Begge Mn centre er desuden bundet til et central hexacyanidometallat(III) (4d/5d) ion gennem cyanido

liganderne. Indledningsvis er undersøgelserne af systemet med det diamagnetiske Ir(III) center beskrevet, dels for at bestemme anisotropien af mangancentrene D_{Mn} and E_{Mn} og dels for at bestemme størrelsen af den magnetiske kobling mellem de terminale mangancentre gennem iridium. Disse undersøgelser er gennemført vha. EPR- og INS-spektroskopi samt magnetiseringsmålinger. Den opnåede værdi for den aksiale anisotropi på mangancentrene, D_{Mn}, er så efterfølgende anvendt som rettesnor i parametertilpasningerne til de eksperimentelle data for osmium og ruthenium systemerne. De sidstnævnte systemer udviser anisotrop exchange-vekselvirkning mellem Mn-centrene og den centrale metalion. I stedet for at anvende cyanokomplekser som byggesten til magnetiske materialer baserede på de tungere overgangsmetaller en ny, lovende byggesten i form af $[ReF_6]^{2-}$ blev fundet og undersøgt. $(PPh_4)_2[ReF_6]\cdot 2\ H_2O$ blev syntetiseret og denne forbindelses magnetiske egenskaber blev studeret vha. magnetiseringsmålinger suppleret med INS, høj-felt-EPR og X-bånd EPR spektroskopi. Det viste sig, overraskende, at selvom denne en-kernede forbindelse har en positiv nulfeltsplitningsparameter, så udviser den langsom relaxation af magnetiseringen karakteriseret ved udtalte maksima i ud-af-fase komponenten af ac susceptibiliteten, χ'' , hvis målingerne blev foretaget med et lille statisk felt påtrykt. Desuden er en-dimensionale kæder med det gennemgående motiv $M(viz)_4[ReF_6]$ (M = Zn, Ni) fermstillet og undersøgt. Vekselvirkningen indenfor kæden i $Ni(viz)_4[ReF_6]$ er blevet bestemt og fundet at være meget kraftig ved parametrisering af dc susceptibilitetsdata på to forskellige måder. En yderligere vekselvirkning mellem nabo-kæderkan observeres at føre til stabilisering af en antiferromagnetisk ordnet grundtilstand ved lave temperaturer. Studiet af exchange-vekselvirkninger gennem fluoridligander blev udvidet ved en sammenligning af fire forskellige Gd(III)-Cr(III) komplekser med fluorid som broligand mellem gadolinium og chrom. Strukturerne varierer fra et simpelt to-kernet system over firkanter med alternerende Cr og Gd centre til en trekant af Gd_3, der er holdt sammen af et Cr(III) kompleks over og et under trekantens plan. Magnetiseringsmålinger og tæthedsfunktionalberegninger (DFT) viste en korrelation mellem exchange-vekselvirkningens størrelse og bro-vinklen ved fluorid. Slutteligt er en række en-kernede, trigonale Er(trensal) komplekser med små forskelle i trensal-ligandsystemet blevet syntetiseret og karakteriseret ved INS-spektroskopi og magnetiseringsmålinger.

Abstract in English

This thesis describes the insight sought and gained for a range of molecule-based magnetic systems with special emphasis on a class of trinuclear manganese(III) complexes.

In chapter 2 a series of Mn_3 SMMs with different equatorial R-sao^{2-} oximate ligands are studied. The unique structural property of these Mn trinuclear complexes is that due to the restrictive ligand surrounding along the JT-axes of the Mn(III) ions, the molecule becomes very rigid and the addition of a bulkier group on the sao^{2-} ligand (from H, over Me and Et to Ph) leads a breaking of the trigonal symmetry. The molecules with the different sized ligands therefore show deviation from C_3 symmetry

to different degrees. Using INS the influence of the symmetry on the ground spin state multiplet splitting and the relaxation barrier was studied.

Chapter 3 represents a continuation of the authors master thesis[1]. Here, the possibilities of enhancing the effective barrier height U_{eff} by alignment of the single center anisotropy axes were studied. The alignment was achieved by exchanging a bridging tripodal ligand ClO_4^- with the larger analogue ReO_4^-. This has already been attempted once [2], but the effect could not be observed due to a lack of isostructural systems. As the changes in the magnetic behavior are expected to be small for such a small structural change, it is crucial to minimize such complications. Therefore the experiment was improved by employing a different system where the trigonal symmetry was maintained and inter-molecular interactions were inhibited by larger distances between the molecules.

In chapter 4 several systems showing inter-molecular exchange interactions, such as the ones mentioned above, were studied using INS. The studied systems show unusually large relaxation barriers, which cannot solely be explained by a combination of the single center anisotropies.

Chapter 5 shows the results of other trinuclear compounds. Instead of the triangular Mn_3 SMMs, the molecules are linear, heterometallic Mn(III)-M(III)-Mn(III) (M = Ir, Ru, Os). The SMMs of the form $(NEt_4)[Mn_2(5\text{-Brsalen})_2(MeOH)_2M(CN)_6]$ has a Schiff-base ligand on each Mn center, that both are linked to a central hexacyanidometallates(III) (4d/5d) ion by cyanide bridges. First the molecule containing the diamagnetic Ir(III) was measured using EPR and INS as well as magnetic measurements, to determine the anisotropy on the Mn sites D_{Mn} and E_{Mn} and to obtain a maximum value for the exchange coupling between the two Mn through Ir. The D_{Mn} is then used as a guiding value for the fitting of the experimental data of the analogous compounds with Os and Ru. These compounds show anisotropic exchange between Mn and the central metal ion. Instead of using $M(CN)_6^{3-}$ as a building block for larger SMMs a new module was found with $[ReF_6]^{2-}$. $(PPh_4)_2[ReF_6]\cdot 2H_2O$ was synthesized and its magnetic properties characterized by magnetic measurements as well as INS and High-Field and X-band EPR spectroscopy. Interestingly the mononuclear compound has a positive ZFS value, but shows in spite of that, peaks in the out-of-phase components of the Ac susceptibility χ'' can be observed if a small magnetic field is applied. Furthermore, chains with reoccurring motif $M(viz)_4[ReF_6]$ (M = Zn, Ni) have been synthesized and the intra-chain exchange coupling parameter for the $Ni(viz)_4[ReF_6]$ chain has been determined and found to be large by fitting of dc susceptibility data using two different approaches. An additional exchange interaction between neighboring chains can be observed leading to stabilization of an antiferromagnetic ground state at low temperatures. The exchange interactions through fluoride bridges were further investigated by comparing four different fluoride bridged Gd(III)-Cr(III) compounds, from a simple dinuclear complex over squares with alternating Gd and Cr to a triangle of Gd_3 that is “capped” by one Cr(III) above and one below the Gd_3-plane each. Magnetic measurements and DFT calculations showed a

correlation between the exchange coupling interactions and the bending of the F^- bridges. Lastly a series of trigonal Er(trensal) compounds with slightly varying ligand field surroundings has been synthesized and characterized by INS spectroscopy and magnetic measurements.

1. Introduction

1.1 Single molecule magnets

Paramagnets consist of freely rotatable spins that align with an applied field and relax to a random orientation when the field is removed. Ordered magnets on the other hand consist of regions with aligned spins. In a magnetic field these regions align and hinder each other from relaxing when the field is removed, this leads to a remnant magnetic moment in the absence of a polarizing magnetic field. In the intermediate situation, the so-called super-paramagnet, the ferromagnetic regions are, in principle, shrunk to the size of a single molecule. Super-paramagnets still show remnant magnetic moments but so far only at very low temperatures and with relatively short relaxation times.

The first representative of this class of systems is $[Mn_{12}O_{12}(CH_3CO_2)_{16}(H_2O)_4]$-·$4H_2O$·$2CH_3CO_2H$ (commonly referred to as Mn_{12}OAc or Mn_{12}). Interestingly while the molecules existence was predicted in 1921[3] and its structure was presented in 1980[4], it was not before 1993 that its extraordinary magnetic properties were unveiled[5, 6].

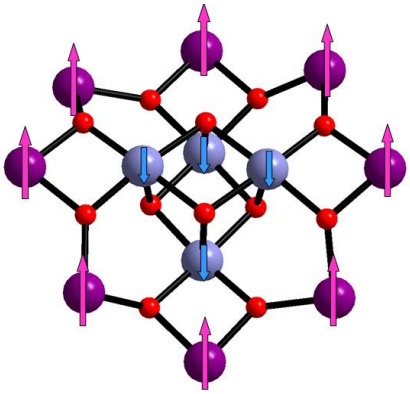

Fig. 1.1: coupling scheme of Mn_{12} the pink arrows symbolize the 8 spins S = 2 of the Mn(III) (violet) that are antiferromagnetically coupled to the 4 Spins S = 3/2 of Mn(IV) (blue)

SMMs consist of a paramagnetic metal center with spin S or several metal centers that are exchange coupled to have a spin ground state $S \neq 0$. The M_s levels of this spin ground state are split by axial anisotropy. This anisotropy is called zero-field splitting (ZFS). If the ground state is well separated from higher states, in the so-called strong exchange limit, the magnetic behavior at low temperatures can be described with a Hamiltonian that only includes the ground state spin multiplet. In Mn_{12}, 8 Mn(III) ions are antiferromagnetically coupled to 4 Mn(IV) (see fig. 1.1), resulting in a well isolated S = 10 ground state. The ZFS splits the M_s levels into Kramers doublets M_S = ±10, M_S = ±9, M_S = ±8 and so forth see figure 1.2. At very low temperatures, only the M_S = ±10 states are populated. The Hamiltonian describing the axial asnisotropy and the splitting of the M_S states at zero field is $\widehat{H}_{ZFS} = D * (\hat{S}_z^2 \quad -\frac{1}{3}S(S+1))$ and will be further discussed in section 1.3.

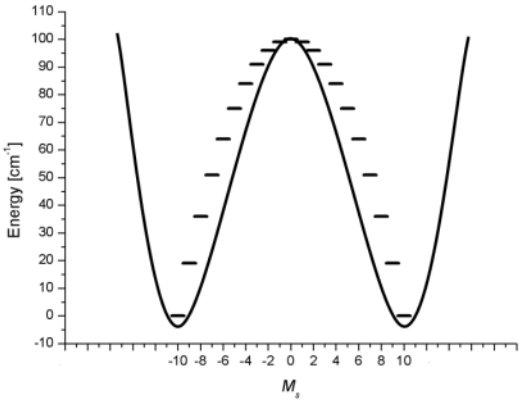

Fig. 1.2: Energy level splitting in of an S =10 in zero magnetic field with D = -1 cm^{-1}.

If a field along the z axis is applied the M_S states change energy according to:

$$\Delta E_{M_S}(B) = \mu_B M_S g B \qquad (1.1)$$

where B is the magnetic field, μ_B is the Bohr magneton with a value of $0.9274 \cdot 10^{-23}$ JT^{-1} and g generally taking a value close to 2 for Mn(III) complexes.

In a magnetic field only one M_S state is therefore lowest in energy which means at sufficiently low temperatures only this M_S state is populated.

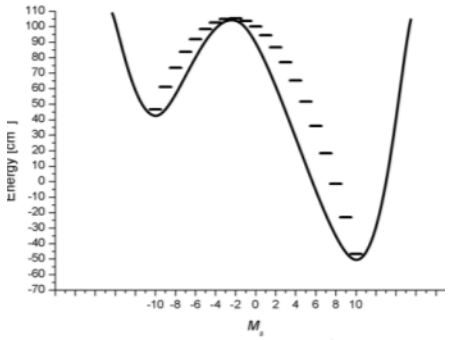

Fig. 1.3: Energy level diagram at an applied field B_z = 5 T

After removal of the field the system can, in a first treatment, relax in two ways. The first way is by absorbing or emitting phonons to change between M_S states. It thus relaxes from M_S = 10 to M_S = 9 to M_S = 8 etc. by absorbing phonons until it reaches the M_S = 0 state, from which it can excite phonons to "fall" to M_S = -1, m_s = -2 and so forth until the M_S = 10 and M_S = -10 state are again equally populated and the magnetic moment is again zero. As the system has to relax from M_S = -10 to M_S =10 over M_S = 0, the energy difference between M_S = ±10 and M_S = 0 is called the barrier height U and is calculated after eq. 1.2.

$$U = |D|S^2 \qquad (1.2)$$

A second way of relaxation of the magnetization consists of tunneling between degenerate M_S states. At very low temperatures, that means a tunneling from M_S = 10 to M_S = -10. If only the axial ZFS (*D*) is considered then the two states are orthogonal to each other and have therefore no overlap of the wave functions, thus the tunneling probability is zero. A perturbation has to be included which mixes the two states. Such a perturbation is, to second order, the rhombic ZFS which is expressed as *E* (with the operator $(\hat{S}_x^2 - \hat{S}_y^2)$). The tunnel splitting of the two states, which occurs as the overlapping states are interacting with each other[7], is very small in respect to the barrier height and therefore a first tunneling from M_S = 10 to M_S = -10 is very improbable. The *E* term however mixes M_S states whose quantum numbers differ by 2. The mixing of M_S = 10 with M_S = 8 to M_S = 6 and so forth to M_S = -10 represents a higher order tunneling pathway. At higher temperatures the system can tunnel through higher lying M_S states. As the system has thermally populated higher lying M_S states by absorbing phonons just as discussed in the first relaxation way. This is called phonon assisted tunneling relaxation. A major factor is that the tunnel splitting (and therefore the probability that the system will tunnel) is larger for smaller M_S values[7]. Furthermore there is no tunneling for half integer spins and M_S values due to the Kramers theorem. The measured relaxation barrier is called effective barrier U_{eff} .

In general it can be said that a "good" SMM i.e. an SMM that shows slow relaxation at high temperature, needs a well isolated ground state with a maximized *S* value and a large ZFS. The ZFS of the whole cluster is a sum of the single center ZFS tensors. Due to the fact that the projection coefficients of the single center tensors on the global easy axis of the molecule are inverse quadratic dependent on the *S* value, as it will be further discussed in section 1.3[8], the synthesis of molecules with larger spin ground state will not augment U_{eff}. For possible applications (e.g. spintronics [9] and quantum computing[10]) molecular magnets with high blocking temperatures (the temperature at which the relaxation of the magnetization is slow compared to the time scale of the technique of investigation[11]), well separated ground stated with large anisotropies have to be developed. For the future design of such SMMs it is fundamental to achieve a better understanding of the relations between the structure and the magnetic properties of a compound.

Due to certain traits of manganese, it has been a well-used source of paramagnetic moment in molecular magnetism. As Mn is able to exist in several different oxidation states leads to the possibility of mixed valance complexes where the spin ground state differs from zero even in the case of antiferromagnetic interactions between the metal centers. Furthermore Mn(III) generally shows large magnetic anisotropy. Therefore it does not surprise that a large quantity of manganese molecules and building blocks have been published. They span a huge range of nuclearity from mononuclear to nanoscopic systems as Mn_{84}[12-14]. As U_{eff} does not necessarily increase with higher nuclearity[8], it was decided to concentrate the efforts in this study on simpler molecules (i.e. molecules with lower nuclearity and as far as possible high symmetry).

A simple building block for many Mn based SMMs is the $[Mn_3O]^{7+}$ core. Many of those systems have been published and analyzed as there are countless possibilities to chemically alter the complexes to observe how changes in the magnetic behavior correspond to changes in the structure. [2, 15-23] The parameters describing the systems are discussed here.

1.2 Exchange coupling

The exchange coupling of general, i.e. non-symmetrical, $[Mn_3O]^{7+}$ core SMMs is described by the exchange coupling Hamiltonian in equation 1.3

$$\hat{H}_{ex} = -2J_1\hat{S}_1\hat{S}_2 - 2J_2\hat{S}_2\hat{S}_3 - 2J_3\hat{S}_3\hat{S}_1 \quad (1.3)$$

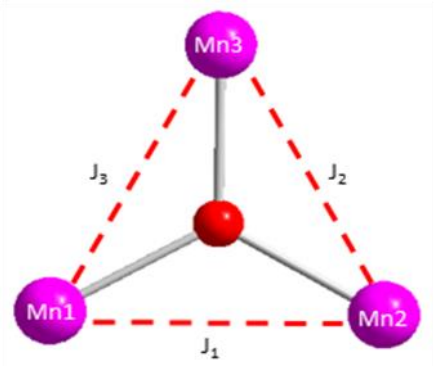

Fig 1.4: Exchange coupling

Where $\hat{S}_1$ stand for the spin operator of the Mn1 ion, $\hat{S}_2$ for the spin operator of Mn2 and so forth. In the magnetism community there are several notations in use, apart from the Hamiltonian in eq. 1.3 a $-J$ (instead of $-2J$) form as well as a J form are also widely in use. The $-2J$ form has been chosen for the data treatment in this work as it is most common in the magneto-chemistry community.

If the molecule possesses three-fold symmetry the all three exchange parameters J_1, J_2 and J_3 have to be equal. Therefore the Hamiltonian can be simplified to eq 1.4.

$$\hat{H}_{ex} = -2J(\hat{S}_1\hat{S}_2 + \hat{S}_2\hat{S}_3 + \hat{S}_3\hat{S}_1) \quad (1.4)$$

Over the last 35 years many $[Mn_3O]^{7+}$ based compounds have been synthesized and their magnetic properties investigated. Here a small introduction to the different kinds of $[Mn_3O]^{7+}$ based molecules and the important structural factors determining the nature and magnitude of the exchange coupling are given. The mentioned compounds and their parameters are listed in table 1.1. The structure of one representative of each kind of system is pictured in figure 1.6.

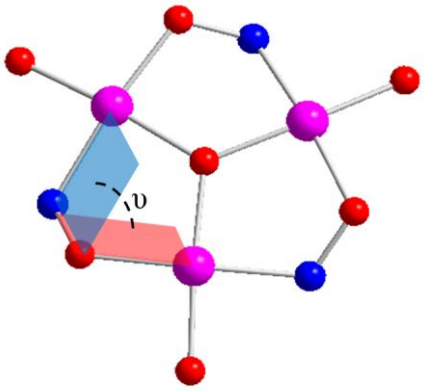

Fig. 1.5: Oximate twisting angle υ color code: Mn (pink), O (red), N (blue).

In 1978 a series of $[Mn_3O]^{7+}$ core molecules of the general formula $[Mn_3O(O_2CR)_6L_3]^{0,+}$ [24-26], was published. All but one of the presented compounds are mixed valence complexes and all of the complexes are antiferromagnetically coupled. $[Mn_3O(O_2CMe)_6py_3](ClO_4)$, the one complex containing only trivalent Mn was used as precursor for the synthesis of $[Mn_3O(O_2CMe)_3(mpko)_3]ClO_4$ (mpko = methylpyridylketoneoximate)[27], a ferromagnetic coupled complex with an $S = 6$ ground state with relatively small zero field splitting, $D = -0.34$ cm^{-1}, and a consequently small effective relaxation barrier ($U_{eff} = 10.9$ K). The fact that the exchange coupling changed from antiferromagnetic in the former compounds to ferromagnetic in the latter complex was first attributed to the position of the central μ_3-O in respect to the Mn_3 plane[27]. It was noted that it the μ_3-O lies within the Mn_3 plane anti-ferromagnetic exchange is dominant due to the $Mn_{d\pi}$-$O_{p\pi}$-$Mn_{d\pi}$ orbital overlap. Another important factor determining the exchange coupling was determined by comparing the $mpko^-$ complexes with later discovered sao^{2-} (salicylaldoximate) linked compounds[28]. In this theoretical study $[Mn_3O(O_2CMe)_3(mpko)_3]ClO_4$ was compared with $[Mn_3O(sao)_3(O_2CMe)H_2O(py)_3]$. The oximate twisting angle υ (see figure 1.5) showed to have an enormous influence on the exchange coupling parameter. Ferromagnetic exchange is promoted for large oximate twisting angles υ, while small υ angles promote antiferromagnetic exchange.

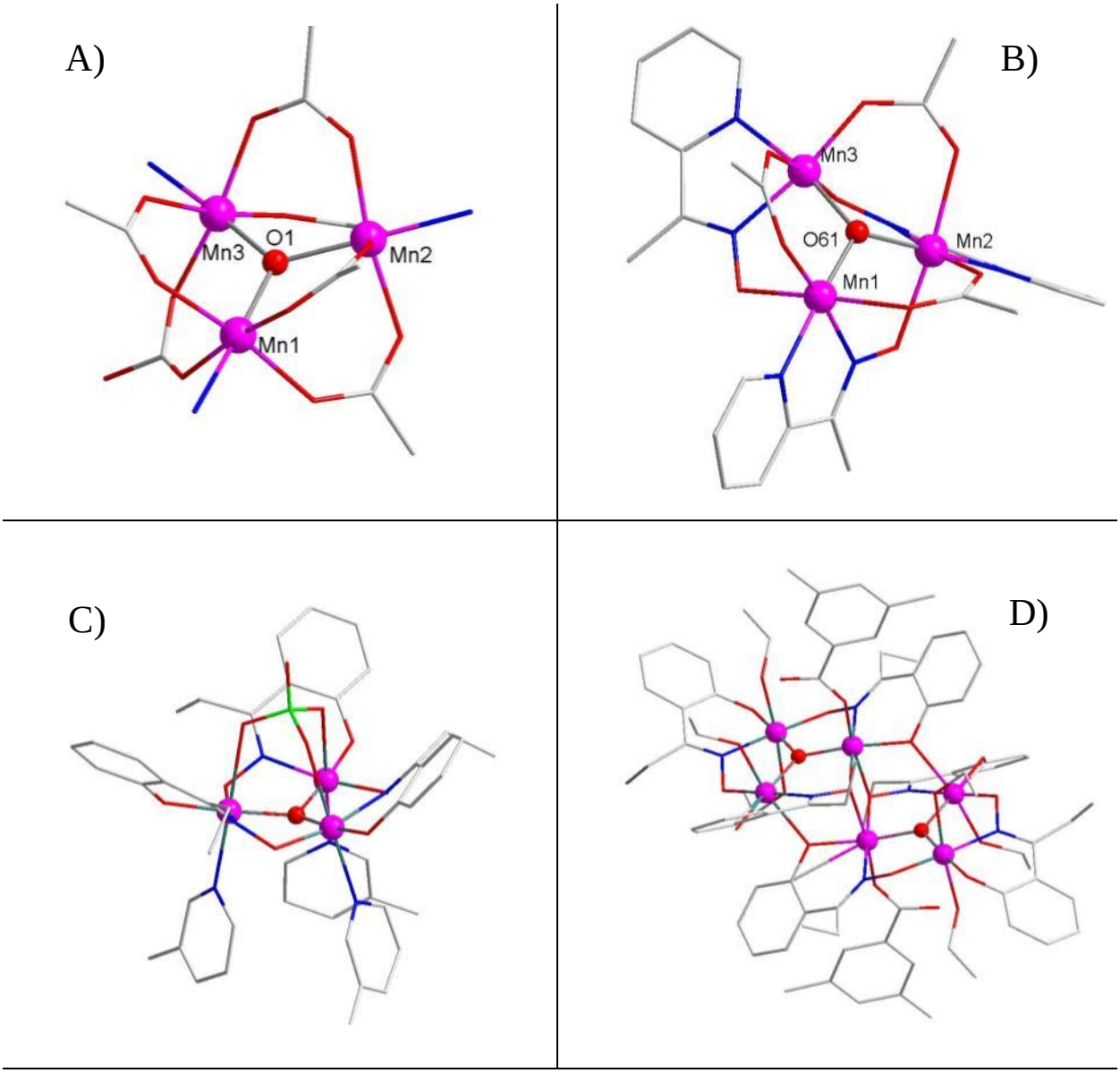

Fig. 1.6: structures of representative examples of the compound classes discussed in the text for clarity reasons all but the Mn ions and the μ_3-O are represented in wireframe mode. A) $[Mn_3O(O_2CMe)_6py_3](ClO_4)$, the counter ClO_4^- counter ion and the pyridine ligands (apart from the coordinating N have been omitted. B) $[Mn_3O(O_2CMe)_3(mpko)_3]ClO_4$, ClO_4^- was omitted. C) $[Mn_3O(Et\text{-}sao)_3(\beta\text{-}pic)_3]ClO_4$ (β-pic = β-picoline, Et-sao = Ethyl-salicylicaldoximate) D) $[Mn_6O_2(Et\text{-}sao)_6(O_2CPh(Me)_2)_2(EtOH)_6]$

While the crystallographic structure file of the latter compound, $[Mn_3O(sao)_3(O_2CMe)H_2O(py)_3]$, was never published there is a vast amount of $Mn_3O(R\text{-}sao)_3$ analogs that show the above mentioned correlation[18, 23]. Even more numerous are molecules with sao^{2-} coupled Mn_6O_2 cores, which consist of two off-set stacked $Mn_3O(R\text{-}sao)_3$ subunits. This series contains $[Mn_6O_2(Et\text{-}sao)_6(O_2CPh(Me)_2)_2(EtOH)_6]$, ferromagnetically coupled SMM with a ground state spin of S = 12 and a former record holding effective barrier height of U_{eff} = 86.4 K [29], as well as compounds that also

have antiferromagnetic interactions such as $[Mn_6O_2(sao)_6(O_2CH)_2(MeOH)_4]$, with a spin ground state of $S = 4$ [19, 21, 23, 30, 31].

Table 1.1 structural parameters vs. exchange coupling parameters for selected compounds

	υ[°]	μ_3-O shift [Å]	*J, J'*	
$[Mn_3O(O_2CMe)_6py_3](ClO_4)$	n. appl.	0.001	-10.2	[24]
$[Mn_3O(O_2CMe)_3(mpko)_3]ClO_4$	9.0, 11.6, 13.0	0.295	20 (14.1, 3.8)[a]	[27, 32]
$[Mn_3O(sao)_3(Et\text{-}py)_3ClO_4]$	13.11	0.294	-3.02	[18]
$[Mn_3O(Et\text{-}sao)_3(\beta\text{-}pic)_3ClO_4]$	44.96	0.2754	3.4	[18]
$[Mn_3O(Ph\text{-}sao)_3(\beta\text{-}pic)_3ClO_4]$	46.2, 39.3, 40.8	0.2565	1.2	[18]
$[Mn_6O_2(Et\text{-}sao)_6(O_2CPh(Me)_2)_2(EtOH)_6]$	42.6, 36.7, 34.1	0.034	1.63[b]	[21, 29]
$[Mn_6O_2(Et\text{-}sao)_6(O_2CPh(C{\equiv}CH))_2(EtOH)_4(H_2O)_2]$	38.9, 38.7, 32.1	0.074	0.79[b]	[21]
$[Mn_6O_2(sao)_6(O_2CH)_2(MeOH)_4]$	25.6, 10.4, 18.0	0.226	+1.25, -4.6,-1.8	[21]

[a] The magnetic data was initially fitted with a model containing two *J* parameters (values in bracket), later $J_1 = J_2 = J_3$ was assumed. For the chosen examples of Mn_6O_2 molecules all exchange parameters are the same the Hamiltonian is $\hat{H} = -2J(\hat{S}_1\hat{S}_2 + \hat{S}_2\hat{S}_3 + \hat{S}_3\hat{S}_1 + \hat{S}_{1'}\hat{S}_{2'} + \hat{S}_{2'}\hat{S}_{3'} + \hat{S}_{3'}\hat{S}_{1'} + \hat{S}_2\hat{S}_{3'} + \hat{S}_{2'}\hat{S}_3 + \hat{S}_2\hat{S}_{2'})$ where $S_{1,2,3}$ are spins on one Mn_3 subunit and $S_{1',2',3'}$ are spins on the other Mn_3 subunit

Several theoretical studies are supporting the experimentally found correlation.[28, 33, 34]. Both parameters, the oximate twisting and the influence of the out-of-plane shift of the μ_3-O on the exchange coupling interaction. In general it can be stated that the exchange interaction will be more strongly ferromagnetic with bigger twisting angles υ and smaller μ_3-O out-of-plane shifts. If υ is close to zero, the interaction is antiferromagnetic. A large μ_3-O shift weakens the interaction (less ferromagnetic for large υ, less antiferromagnetic for small υ)[34].

The exchange coupling parameter is commonly determined by modeling magnetic susceptibility data of powdered samples in the form of χT vs. T over a wide temperature region. Special experimental care has to be taken to avoid orientation of the strongly anisotropic crystallites in the field. This effect can generally be avoided by fixing the crystallites in e.g. eicosane or hexadecane. Furthermore, the crystallites can be very sensitive to solvent loss, leading to deterioration. In addition, from the modeling perspective, the presence of small intermolecular interactions altering the susceptibility curve may give rise to inaccuracies in the determination of intra-complex exchange coupling constants. In literature when faced with such problems a common solution is to only fit high

temperature data [18]. As SQUID measurements can only be performed with an applied field Zeeman terms have to be included in the model and the fact that the susceptibility is not an absolute value makes it very prone to even the smallest weighting errors. If the energy difference between the lowest lying spin multiplet and the next higher one is in an energy range that is suitable for inelastic neutron scattering (INS), the exchange coupling parameter could be directly accessed (i.e. in the absence of a field).

1.3 Zero field splitting (ZFS)

In a molecule with an isolated spin ground state (GS) with the spin, *S*, the ZFS Hamiltonian $\widehat{H}_{ZFS}$ to second order is defined by eq. 1.5.

$$\widehat{H}_{ZFS} = D(\hat{S}_z^2 \quad -\frac{1}{3}S(S+1)) + E(\hat{S}_x^2 - \hat{S}_y^2) \tag{1.5}$$

Where *D* is the ZFS parameter and *E* is the rhombic anisotropy term, as mentioned above. In the perfect trigonal symmetry that is often present in $[Mn_3O]^{7+}$ core SMMs $E = 0$ has to be fulfilled. In an uncoupled basis with three ions, $\widehat{H}_{ZFS}$ is a sum of the single ion ZFS with the single center ZFS parameter D_n.

$$\widehat{H}_{ZFS} = \sum_{n=1}^{3} D_n(\hat{S}_{nz}^2 - \frac{1}{3}S_n(S_n+1)) \tag{1.6}$$

This means that in a SMM with *N* symmetry equivalent ions and aligned anisotropy axes the D_n and *D* are connected by:

$$D = N \cdot d_n \cdot D_n \tag{1.7}$$

d_n is called a projection coefficient and can be calculated for each complex by a simple formula[8]:

$$d_i = \frac{S_i(2S_i-1)}{S(2S-1)} \tag{1.8}$$

In the case of $[Mn_3O]^{7+}$ core systems $N \cdot d_i$ is therefore $\frac{3}{11}$. As the anisotropy axes of each ion are very seldom mutually aligned but rather tilted with respect to each other and the global anisotropy axes, eq 1.6 and1.7 often overestimates *D* for given D_i. In the case of such local JT axes tilting or if the molecule is not trigonal following Hamiltonian can be used instead of 1.6[16]:

$$\widehat{H}_{ZFS} = \sum_{n=1}^{3} D_n \left[\left(\frac{\sin\delta_n}{2} e^{-i\varphi_n}\hat{S}_n^+ + \frac{\sin\delta_n}{2} e^{i\varphi_n}\hat{S}_n^- + \hat{S}_n^z \cos\delta_z\right)^2 - \frac{1}{3}S_n(S_n+1)\right] \tag{1.9}$$

Here δ is the tilting angle of the single center anisotropy axes (see fig. 1.6) that in this work was determined from the crystal structures. Where $\cos^2\delta$ projects the single center anisotropy tensors onto the easy axis of the molecule $\sin^2\delta$ projects them onto the Mn_3 plane (i.e. the hard plane), φ_n is the angle between two of those projections of D_i

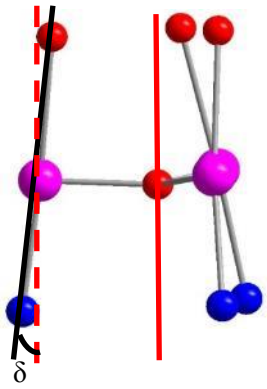

Fig 1.6 Tilting angle δ of the local JT axes (black line along N-Mn-O) in respect to the global anisotropy axis of the molecule (the three fold axis, red solid line and its projection on the Mn(III)ion)

onto the hard plane of the molecule. In case of a trigonal symmetry φ_n values are 0°, 120° and 240° and the parts of eq. 1.9 containing φ_n cancel each other out, the remaining terms can be simplified to:

$$\hat{H}_{ZFS} = \sum_{n=1}^{3} D_n \left[\left(\hat{S}_n^z \cos\delta_z \right)^2 - \frac{1}{3} S_n (S_n + 1) \right] \qquad (1.10)$$

The ZFS can be determined by fitting of magnetization SQUID data as well as single crystal hysteresis curves. This has the same difficulties as the determination of *J* mentioned above. The ZFS can also be probed spectroscopically by INS and High Field, High-Frequency (HF-) EPR. While there is a vast amount of work already presented on the structural origins of the exchange coupling parameter measured by magnetic measurement, the same thorough examination was not performed for the ZFS of Mn_3 compounds. Although several Mn_6O_2 compounds have been measured by INS and HF-EPR [35-37], only few HF-EPR studies[16] and to the authors knowledge, no INS has been performed on the $Mn_3O(R\text{-}sao)_3$ subunits. The simpler trinuclear systems with possible trigonal symmetry represent excellent model systems to study structural influences on the ZFS, because of a reduced number of parameters. For such a study high quality INS data is paramount over the so far measured EPR data[38], because of the independence of Zeeman terms.

1.4 Higher order Terms

In an $S = 6$ system, apart from the second order parameters *D* and *E*, ZFS terms up to the 6th order are possible. These higher order terms are only included in the model if they improve the fit the experimental data significantly. This is quite common for 4th order terms and very rare for 6th order terms. In table 1.2 the higher order operators and their parameters are listed. As the only 6th order

parameter used in the discussion of the $[Mn_3O]^{7+}$ core SMMS in this thesis is B_6^6, this operator is the only 6th order operator listed.

Table 1.2: Higher order spin operators [39].

Parameter	Operator
B_4^0	$35\hat{S}_z^4 - (30S(S+1) - 25)\hat{S}_z^2 - 6S(S+1) + 3S^2(S+1)^2$
B_4^2	$\frac{1}{4}\{(7\hat{S}_z^2 - S(S+1) - 5)(\hat{S}_+^2 + \hat{S}_-^2) + (\hat{S}_+^2 + \hat{S}_-^2)(7\hat{S}_z^2 - S(S+1) - 5)\}$
B_4^3	$\frac{1}{4}\{\hat{S}_z(\hat{S}_+^3 + \hat{S}_-^3) + (\hat{S}_+^3 + \hat{S}_-^3)\hat{S}_z\}$
B_4^4	$\frac{1}{2}(\hat{S}_+^4 + \hat{S}_-^4)$
B_6^6	$\frac{1}{2}(\hat{S}_+^6 + \hat{S}_-^6)$

In strict trigonal symmetry the spin operators corresponding to the parameters B_4^2 and B_4^4 are not allowed. While is B_4^3 operator mixes M_S states for which $\Delta M_S = \pm 3$, B_4^0 acts only along the z-axis, and therefore only changes the energy of the M_S without mixing them. It acts on states with the same absolute M_S values exactly the same way, it does not remove degeneracy. It also shifts the energy of the $M_S = 6$ and $M_S = 0$ state in the same direction and with similar ΔE, which means that the barrier U (the spectroscopic barrier, not the effective barrier, as this discounts tunneling processes) is not greatly influenced by B_4^0. However the spacing of the energy levels between the $M_s = \pm 6$ and $M_s = 0$ states are greatly influenced by B_4^0. A possible origin of the B_4^0 term is the interactions of higher states with the ground state multiplet [16, 40-42]. Therefore, a large exchange coupling interaction will give rise to a small B_4^0 term and vice versa. This means that after a full characterization of the ground state multiplet and the modeling to a giant spin Hamiltonian up to 4th order, conclusions on the value of the exchange coupling parameter can be drawn from the value of the B_4^0 term[16].

1.5 Introduction to Neutron Scattering

In the years since the first neutron scattering experiments in the 1930s and the consequent development of high power neutron sources, neutrons have become a widely applied probe for a vast array of properties in many different research fields. There are two different kinds of large scale neutron sources. In spallation sources, a proton beam produced by an accelerator is captured by a target (e.g. mercury or tantalum), which then expels neutrons. As all neutron experiments in this thesis were performed in reactor sources, these will be discussed in further details. In nuclear reactors the neutrons are produced as a product of the fission of highly enriched uranium-235. The neutron flux from the reactor will show a Maxwellian distribution characteristic to the reactor coolant but can be shifted with a hot and a cold moderator, so called sources, to achieve the needed energies[43]. The neutron flux at different energies $\phi(E)$ can be calculated by eq. 1.11.

$$\phi(E) = \frac{E}{(kT)^2} e^{-E/kT} \qquad 1.11$$

Where T is the temperature of the moderator, k is the Boltzmann constant and the energy E is in eV. In the high flux reactor at ILL the main moderator is heavy water (D_2O). The hot source consists of a graphite block that attains temperatures up to 2000 Kelvin due to heating by gamma radiation from the fission reaction. The cold source is a liquid deuterium chamber at ~23 K. Due to the lower energy of cold neutrons the critical scattering angle for total reflection becomes sufficiently large so that the neutrons can be guided in neutron mirror coated guides with negligible loss. These guides allow cold neutron instruments to be placed relatively far from the reactor as opposed to thermal neutron instruments that are more optimally placed in the close vicinity, using beam tubes starting from the main moderator. The use of guides does not only provide space for more instruments per neutron source, it also helps to reduce the background radiation from the reactor by introducing a curvature of the guide, so that high energy neutrons and gammas are not reflected and do not reach the instrument.

A couple of unique properties make neutrons a very successful probe. First and foremost the charge neutrality ensures that neutrons can penetrate samples deeply, providing users with a bulk probe. It will also not be perturbed if the experiment requires the presence of an electrical field. The wavelength range 0.1 Å < λ < 1000 Å allows unraveling of structures with a wide range of lattice parameters from small inorganic molecules to large biological superstructures. The energy of these wavelengths spans spectroscopic needs from lattice and molecular vibrations to magnetic excitations and the analysis of diffusion processes. In contrast to x-rays the scattering lengths of neutrons do not depend on the electron density but vary with an apparent randomness from element to element and isotope to isotope. This means for instance that the crystallographic position of even very light atoms with heavy neighbors can be accurately determined. Furthermore sample containers and cryogenic

equipment can be made from "neutron transparent" material like aluminum, while "x-rays transparent" materials are not suitable for such applications. The feature most interesting for this thesis is certainly the neutron spin, s = ½, as this allows for the observation of magnetic excitations. Such magnetic excitations can be measured by inelastic neutron scattering INS which will be briefly explained here. More thorough treatments can be found in references [44-47]. In INS a neutron beam with an initial wave vector $\vec{k}_i$ leaves the sample after a scattering process with a final wave vector $\vec{k}_f$ and energy E_f.

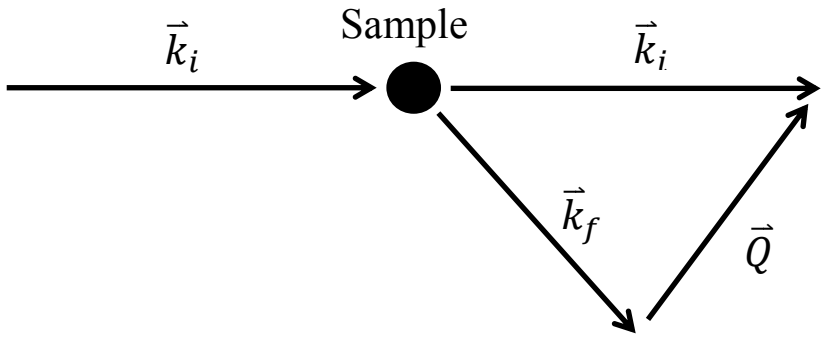

Figure 1.7 Schematic neutron scattering process.

The difference of the two wave vectors is called scattering vector $\vec{Q}$.

$$\hbar\vec{Q} = \hbar(\vec{k}_i - \vec{k}_f) \tag{1.12}$$

If this scattering process is inelastic the neutrons loose or gain energy in the sample $\Delta E \neq 0$. The change in energy is calculated by

$$\Delta E = \omega\hbar = \frac{\hbar^2}{2m}(k_i^2 - k_f^2) \tag{1.13}$$

with m being the neutron mass. The probability of magnetic scattering S, proportional to the measured intensity, is correlated to the energy difference between two states(i.e. the energy transfer ω) and the scattering vector Q and is measured as the double differential cross section $d^2\sigma/d\Omega dE_f$ with dΩ representing a fixed angle around the detector angle Ω and σ is the total number of neutrons scattered by the sample. The double differential neutron cross section for magnetic scattering with non-polarized neutrons is presented, for the case of a mononuclear spin-only system:

$$\frac{d^2\sigma}{d\Omega dE_f} = (\gamma r_0)^2 \frac{k_f}{k_i}\left[\frac{g}{2}F(Q)\right]^2 e^{(-2W(Q))} \sum_{\alpha,\beta}\left(\delta_{\alpha,\beta} - \frac{(Q_\alpha * Q_\beta)}{Q^2}\right) S^{\alpha\beta}(Q,\omega) \tag{1.14}$$

With the gyrometric ratio γ = -1.913, the classical electron radius r_0 = 2.818·10^{-15} m, $\alpha,\beta = x, y, z$, $\delta_{\alpha,\beta}$ the Kronecker delta and the Debye-Weller factor exp(-2W(Q)). F(Q)is the magnetic form factor. The term describing the studied system and energy level transitions from an initial state |i> with energy E_i

to a final state $|f\rangle$ with energy E_f, and therefore the interesting quantity is the scattering function $S^{\alpha,\beta}(Q,\omega)$:

$$S^{\alpha,\beta}(Q,\omega) = \sum_{jj'} e^{\left(iQ\left(r_j - r_{j'}\right)\right)} \sum_{i,f} p_i \langle i|\hat{S}_{j',\alpha}|f\rangle\langle f|\hat{S}_{j,\beta}|i\rangle\, \delta(E_i - E_f + \hbar\omega) \qquad (1.15)$$

Where rj is the position of the metal ions that carry spins and p_i is the population of the initial state. The energy levels E_i and E_f are described by the magnetic Hamiltonian of the molecule.

For the case of several scatterers, i.e. in Mn_3, the matrix elements get added and for a polycrystalline sample the expressions have to be powder averaged, which means that the intensities over all orientations have to be added up. The intensity of a transition is dependent of the magnetic form factor $F(Q)$, the ratio k_f/k_i and the matrix elements $\langle f|\hat{S}_{j,\beta}|i\rangle$. The magnetic form factors are tabulated for every paramagnetic ion[48] .

During the last years, INS has been a very useful tool for the magnetochemistry community. First and foremost INS has been used for the determination of exchange coupling interactions, whether from dimers [49] or bigger molecules [50]but it was also used to probe zero field splitting interactions [51, 52]. The technique is so powerful as one can obtain information at zero field over a high energy range (6 $cm^{-1} < E_i <$ 200 cm^{-1} for IN5) and at very low temperatures.

From the distribution of neutron wavelengths arriving at the instrument different ones will be needed according to the experiment that is being performed. There are several ways to select the wavelength. One way is by using a monochromator crystal where the needed wavelength diffracts at a known angle. The benefit of the technique is that the instrument does not have to be placed at the end of the beam line which means that it is possible to place more than one instrument on one line. The fact that the detector does not have a direct line of sight to the reactor reduces the gamma background immensely in a similar way like the kink in the neutron guides mentioned above. Furthermore for applications where the neutrons do not need to be pulsed the possible continuous neutron stream possible with this technique provides a higher flux on the sample. Alternatively choppers can be used. These may be disk choppers, several spinning disks of neutron absorbing material with holes that let neutron pass or so called Fermi choppers, alternating straight or curved parabolic layers of absorbing and neutron transparent material[53]. When spinned at the right frequency, neutrons with the wanted speed will travel through the chopper in the transparent material while too fast or too slow neutrons will get absorbed.

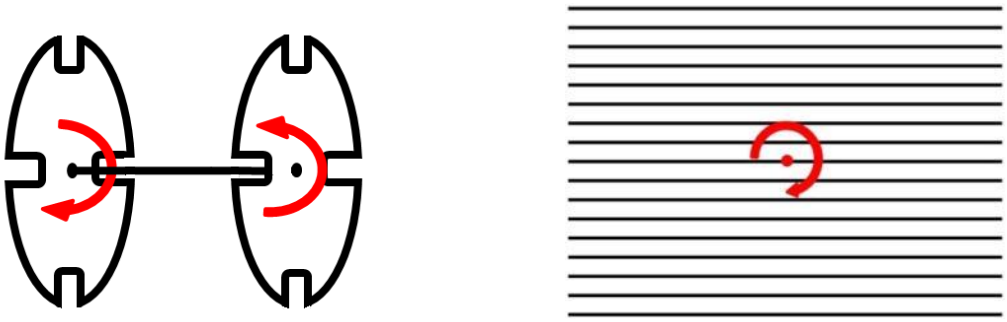

Fig 1.8 Scheme of a two disc choppers (left) and a Fermi chopper with straight channels, the black lines symbolize neutron absorbing layers (right). The neutrons travelling direction is from left to right.

If spectroscopy is performed on a Time-of-Flight spectrometer as opposed to a triple-axis spectrometer the neutron beam has to be pulsed, as a reference time, t_0, has to be known. Often the Fermi choppers and disc choppers are combined or choppers are combined with monochromators to get pulsed beams with the right wavelength. The typical set-up of a Time-of-Flight spectrometer is shown in Figure 1.9 exemplified by IN5b.

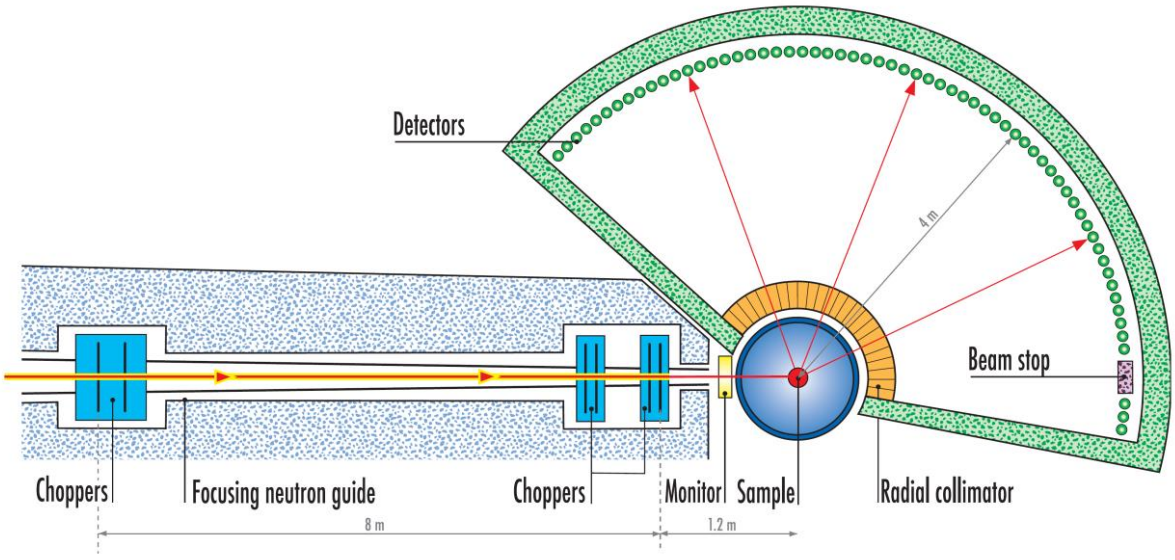

Figure 1.9 Instrument Layout of IN5b obtained from [54]

The neutron beam enters the instrument from the left in Figure and passes through two pulsing choppers. Then the beam passes through a contaminant chopper and a frame overlap chopper that absorbs all but the needed neutron pulses. This has to be done so that the slowest neutrons going out of the sample (i.e. the neutrons that transfer the most energy to the sample) of the first neutron pulse do not overlap with the fastest neutrons of the next pulse in the detector. The fraction of pulses that get absorbed to the total number pulses is smaller for shorter wavelengths. The last two choppers are called monochromator choppers. They can select the wavelength by only letting neutrons pass that passed the distance from the pulse choppers to the monochromator choppers in a specific time.

The selected wavelength determines the maximal energy transfer from the neutron to the sample. Therefore the temptation would be big to use short wavelengths to maximize the incoming energy E_i of the neutron beam and maximize the neutron flux at the sample because more pulses can be used. This has the drawback that the energy resolution at shorter wavelengths is much smaller than for longer ones. This leads not only to broader and therefore less well defined peaks but also means that the broader elastic line can hide low energy transitions in the quasi-elastic background. For a certain experiment one therefore uses several different wavelength, short ones that have a high enough E_i to allow for the transitions with the largest energy transfer ΔE to be observed and long ones that have high enough resolution to resolve transitions with the smallest $|\Delta E|$. The instrument resolution for a given wavelength is also not constant over the whole energy spectrum. Figure 1.10 shows the calculated resolutions at different peak positions (ΔE) for IN5b and for the different wavelengths used in this work.

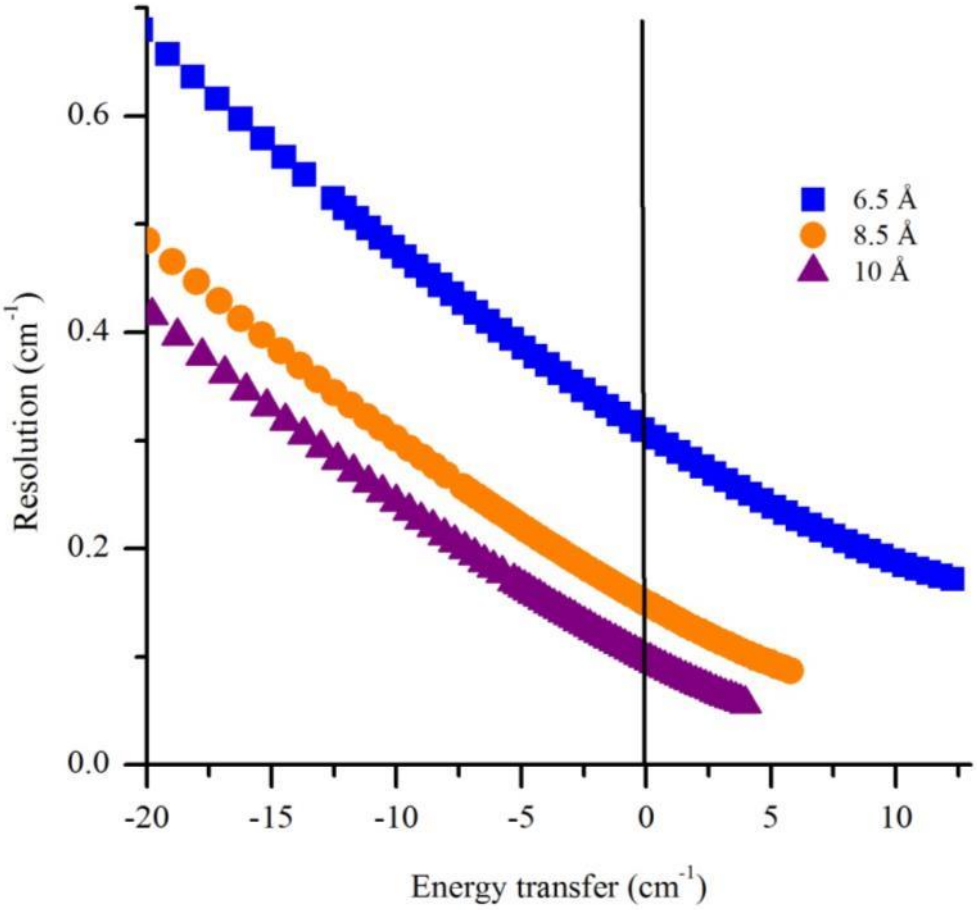

Fig. 1.10: Theoretical energy resolution of IN5b calculated for incident beam wavelengths between 6.5 Å and 10 Å.

Even though a similar energy range can be probed with INS and HF-EPR there are unique advantages to both techniques. EPR has a superior energy resolution and sensitivity. This means that measurements on even small sample quantities can yield spectra with high signal to noise ratios. While there exist techniques to measure EPR at zero field, most EPR spectra are still recorded with an

applied field, which means that Zeeman terms have to be included in the model, like when modeling SQUID magnetometer data. This raises the number of parameters by one or up to three more. INS on the other hand uses large sample quantities (~1 g) and needs long recording times. The absence of an external field enables INS to probe energy level differences without interference of sample orientation and Zeeman terms. The *Q* dependence of the intensity, which is a property that can be measured uniquely with INS, is different for each transition and can therefore help to distinguish transitions. More explanations on the *Q* dependence will be given in the next section.

1.6 Theoretical example of a GS multiplet characterization by INS

As an theoretical example of a spectroscopic analysis of a compound by INS a perfectly trigonal $[Mn_3O]^{7+}$ core SMM with J = 3.5 cm^{-1} and D_i = -3 cm^{-1} is examined. For further simplification the single center anisotropy axes are perfectly aligned, δ = 0°. In this case the GS multplet would be well separated from the excited spin multiplets as it can be seen in the energy level diagram in Figure 1.11. The GS levels can be described with the giant spin Hamiltonian parameters D = -0.80 cm^{-1} and B_4^0 = -1.7·10^{-5} cm^{-1} (these parameters have been obtained by fitting the lowest 13 energy levels to a GS Hamiltonian). The figure also illustrates the nomenclature for the energy levels as it is used in many simulation and fitting software. The levels are hereby numbered from lowest energy to highest in ascending order.

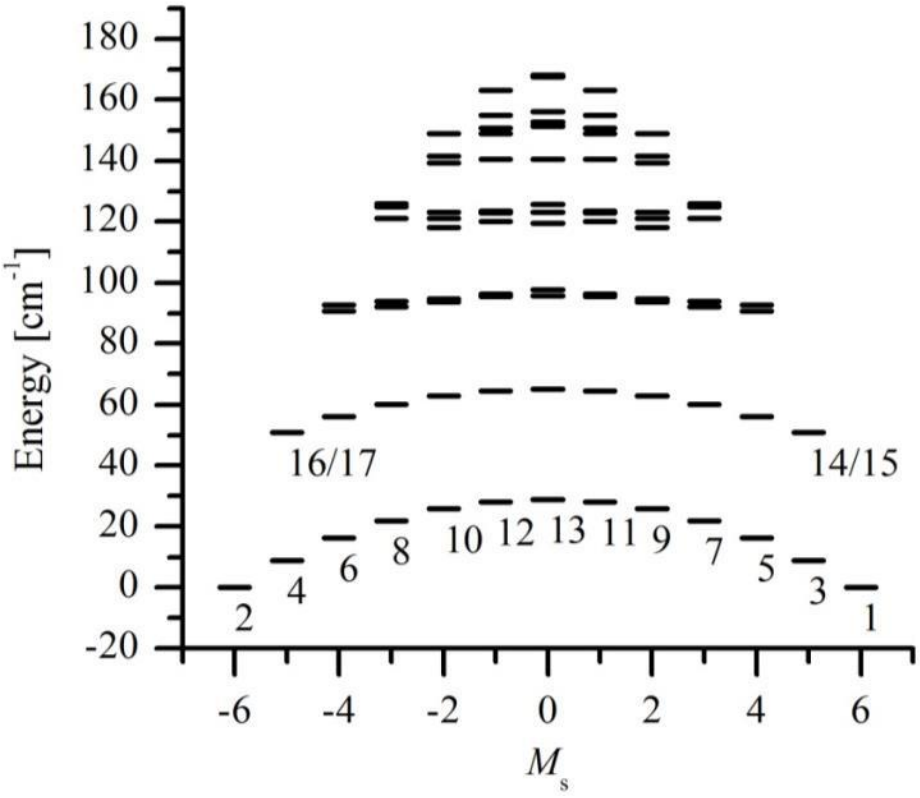

Fig. 1.11 energy level diagram of the exemplary compound described in the text. All M_S states of the S = 6 ground state as well as the four lowest M_S states of the two degenerate S = 5 are labeled according to comment convention in software.

A in a neutron experimenton this compound, only the lowest states would be populated at the lowest practical temperature of 1.5 K. As the conditions for INS are ΔS = 0, ±1 and M_S=± 1, 0 transitions are therefore only possible from state 1 to states 3, 14 and 15 and from state 2 to states 4, 16 and 17. A representation of those transitions can be seen in figure 1.12. At higher temperatures the lowest states 1 and 2 get depopulated in favor of higher states. At 6 K, according to Maxwell-Bolzmann statistics, 10 % of the molecules are in states 3 or 4 and even 5 and 6 are together 2 % populated. The population of the states 1 and 2 decreased from nearly 100 % at 1.5 K to 87 %. This means that additional transitions are now possible from states 3 to 5, 18, 19 and to 1 as well as from 4 to 6, 20, 21 and 2 respectively. At higher temperatures all M_S states of the GS multiplet are nearly equally populated and all transitions originating from the GS multiplet following the selection rules are possible

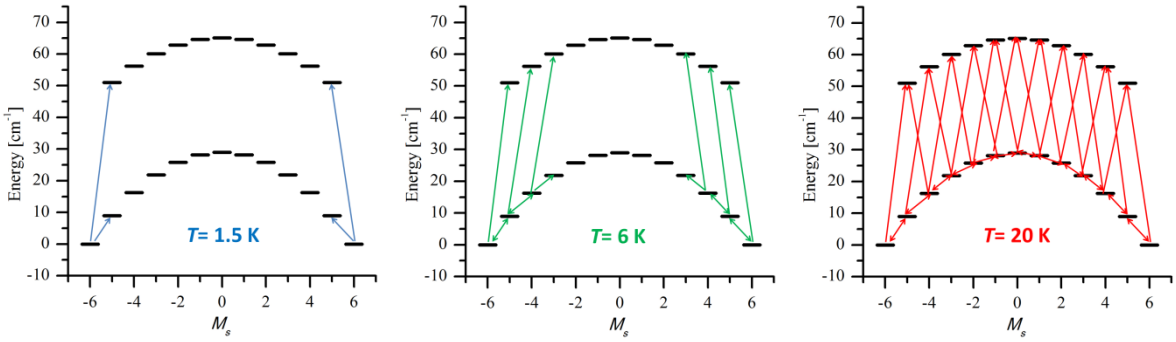

Fig 1.12. Prominent transitions at different temperatures from 1.5 K (left) to 6 K (middle) and 20 K (right)

As the allowed transitions differ in the energy transferred to or from the neutron, each transition corresponds to a characteristic neutron time-of-flight/energy transfer. The energy difference between the initial state 1 (i. e. S = 6, M_S = 6) to the final state 3 (S = 6, M_S = 5) for example is 9 cm^{-1} and therefore the transition can be observed at this transition energy. The transition between the states 1 and 14 (i. e. S = 5, M_S = 5) can be observed at 51 cm^{-1}.

At a constant energy, the intensity of a transition can show a distinct dependence on the scattering vector. In figure 1.13 this so called Q-dependence is presented for selected transitions. As the Q-dependence is measured as the scattering angle with a fixed and constant angle range (determined bydetector geometry), the probed $\vec{Q}$-window will be very different for different initial neutron energies.

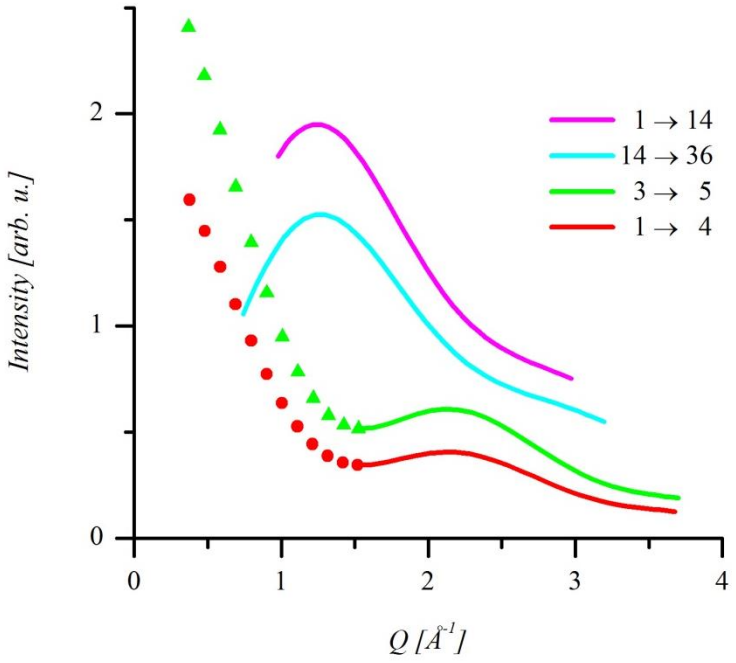

Fig. 1.13 Q-dependence of selected transitions, the circles and triangles represent the area visible at 6.5 Å incident wavelength.

A real example of the *Q*-dependence measured on a $[Mn_3O]^{7+}$ core SMM at 6.5 Å incident wavelength is presented in Fig 1.14, showing all transitions within the $S = 6$ GS multiplet. The presented $S(Q,\omega)$ plot shows lines at distinct energies as described above. The lines are more intense at lower *Q* values and are decreasing with increasing *Q*. This is consistent with the theoretical behavior in fig 1.13. Several factors will mask the *Q*-dependence of the sample. Phonons are more intense at higher *Q*-values and decrease in intensity at lower *Q*. Furthermore hydrogen scatters incoherently and therefore adds to the background of the $S(Q,\omega)$ plot.

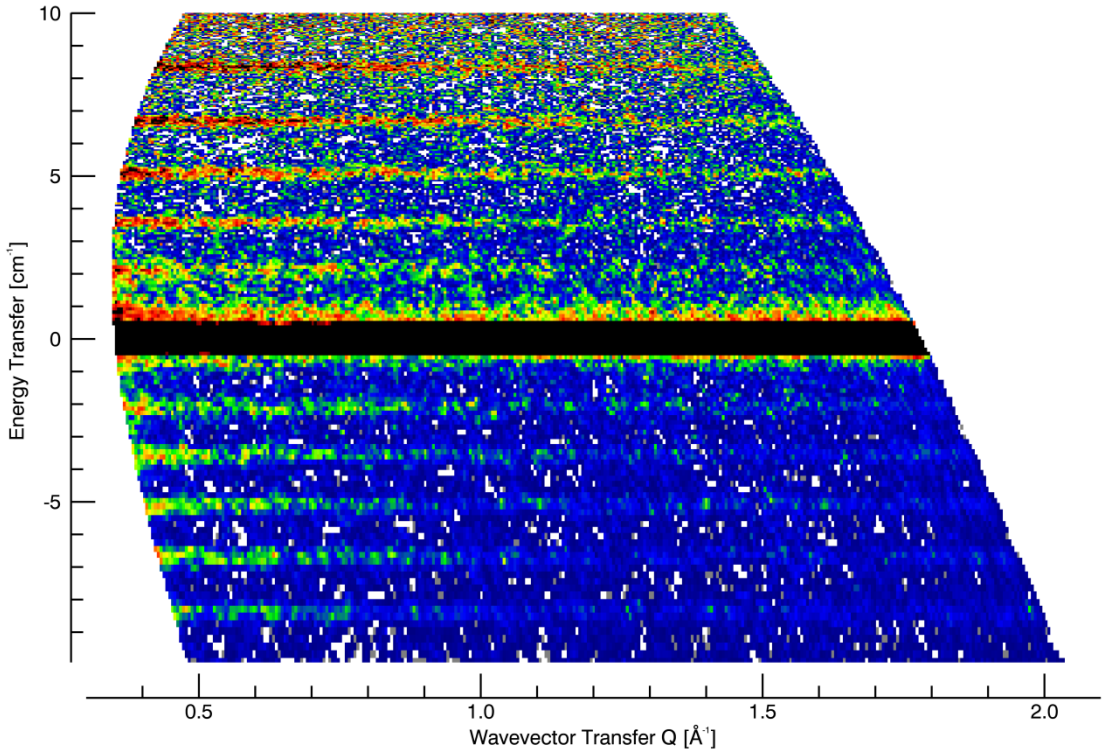

Fig. 1.14: $S(Q,\omega)$ map of a $[Mn_3O]^{7+}$ core SMM at 6.5 Å incident wavelength.

If the model describing the system is a Giant Spin Hamiltonian, there is no accurate magnetic form factor, as the model assumes a theoretical single scatterer with a spin $S = 6$ standing in for the three Mn(III) ions. Therefore the *Q*-dependence and the intensity can in most cases not be reproduced very well. In the case of the spectra recorded in the course of this work, the *Q*-dependence in the measured *Q*-range is rather flat, which means that the magnetic form factor becomes less critical.

For the present work the characteristic energy transfer is more important than the *Q*-dependence. Therefore the data for all presented compounds is summed over the complete available *Q* range unless otherwise noted. Which would, for the theoretical example above, lead to the spectra presented in figure 1.15.

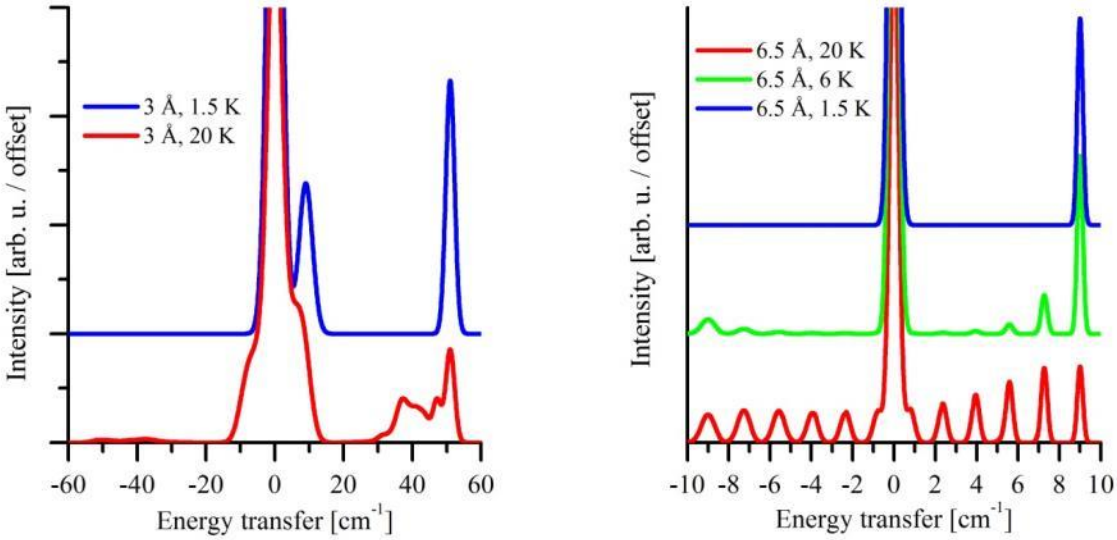

Fig. 1.15: Simulation of the temperature dependence at different incident wavelengths. 3 Å (left) showing the transitions to the S =5 states and 6.5 Å (right) with the resolved transitions within the S = 6 multiplet.

The prominent central peak in both graphs does not represent the complete elastic line but only the magnetic contribution to the elastic line. This means that in a real experiment the transitions close to $\Delta E = 0$ are often masked by the elastic line. A further complication of the spectroscopic analysis of the compound discussed in this work is the small deviance from perfect symmetry and therefore the breakdown of the condition $J_1 = J_2 = J_3$. Even small differences between the J parameters broaden the peaks originating from the 1 to 14 transition. In combination with background from phonons and high ^{1}H background at high energies complicate the observation of this peak even further. The focus of the present work was therefore on INS transition within the GS multiplet.

1.7 Experimental Procedures

Magnetic measurements were performed on Quantum Design MPMS-5XL SQUID magnetometers with either a dc or an rso sample transport. The polycrystalline samples were mounted in gelatine capsules and possible sample orientation was prevented by embedding the crystals in eicosane or hexadecane. Dc susceptibility measurements were performed with static fields of 1000 Oe. AC susceptibility was measured with no static field and oscillating fields with driving amplitudes of 3.5 Oe or 3.8 Oe. The experimental data were treated using the program MagProp which is a component of the "Data Analysis and Visualization Environment" package (DAVE) [55].

The INS measurements have been performed on the disk chopper time-of-flight spectrometer IN5b at the Institut Laue-Langevin, with the exception of several compounds in chapter 5 that were measured with thermal neutron time of flight spectrometer IN4c also located at Institut Laue-Langevin. Approximately 1g (up to 2 g for IN4c) of each sample was filled in double wall cylinders or in aluminum bags and cooled to temperatures between 1.5 K and 50 K in the standard ILL "orange" cryostat or a cryofurnace. The obtained data were treated using the ILL Large Array Manipulation Program (LAMP)[56, 57]. A standard macro was used to transform the data into the intensity format $I(2\theta,\text{ToF})$ (2θ = scattering angle; ToF = time-of-flight)[58]. Another macro, see Apendix, was used to extract other information such as $I(2\theta,\omega)$, $I(Q,\omega)$ as well as $I(\omega)$ summed over all Q. The measured energy transfers were fitted by diagonalization of the giant spin Hamiltonian using the program package MagProp[55] and the obtained parameters were used to simulate the spectra with the "ins" programme provided by H. Weihe (University of Copenhagen) [59]

2. Lowering the symmetry of trinuclear manganese(III) complexes - breakdown of the Giant Spin approximation

2.1 Abstract

In this chapter a series of compounds of the type $[NEt_4]_3[Mn_3Zn_2O(R\text{-}5X\text{-}sao)(N3)_6Cl_2]$ (R= H, Me, Et, Ph; X=H, Me) have been analyzed using magnetic measurements as well as spectroscopy. The goal is a deeper study of the correlation between the sao^{2-} ligand and the exchange coupling parameter. The series also shows a deviation from three-fold symmetry to different degrees. If the deviation is big it results in the breakdown of the giant spin model and in greatly reduced U_{eff}

2.2 Introduction

In 2008 P. L. Feng *et al.* published a series of $[Mn_3O]^{7+}$ core molecules [16]. In this publication 6 molecules of similar structure have been presented. The formulas of the six compounds are listed in table 2.1 as an overview for this introduction.

Table 2.1: overview of complexes studied in [16]

Complex	Molecular formula	Space grp.	U_{eff}[K]
A	$[NEt_4]_3[Mn_3Zn_2(sao)_3O(N_3)_6Cl_2]$	$R3c$	44
B	$[NEt_4]_3[Mn_3Zn_2(sao)_3O(N_3)_6Br_2]$	$R3c$	43.7
C	$[NEt_4]_3[Mn_3Zn_2(Me\text{-}sao)_3O(N_3)_6Cl_2]$	$R3c$	45.6
D	$[AsPh_4]_3[Mn_3Zn_2(sao)_3O(N_3)_6Cl_2]$	$R\text{-}3c$	-
E	$[NEt_4]_3[Mn_3Zn_2(sao)_3O(N_3)_6I_2]\cdot 2MeOH$	$P2_1/c$	-
F	$[NEt_4]_3[Mn_3Zn_2(sao)_3O(N_3)_8]\cdot MeOH$	$P2_1/n$	-

Only complexes **A** to **D** have trigonal symmetry, complexes **E** and **F** will not be discussed here for reasons of brevity. All complexes consist of three manganese(III) ions that are linked by a central μ_3-oxide and three peripheral salicylaldoximate ligands ($R\text{-}sao^{2-}$). Above and below the manganese plane are six azido-ligands connecting the Mn ions to two tetrahedral, diamagnetic zinc(II) ions in an $\eta_1{:}\eta_1{:}\eta_1{:}\mu_3$ mode (see Fig 2.1). Each Zn is therefore coordinated to three N_3 groups with the last coordination site (along the threefold axis of the molecule) occupied by Cl^- for **A**, **C** and **D** and Br^- for **B**. See figure 2.1 and 2.4.

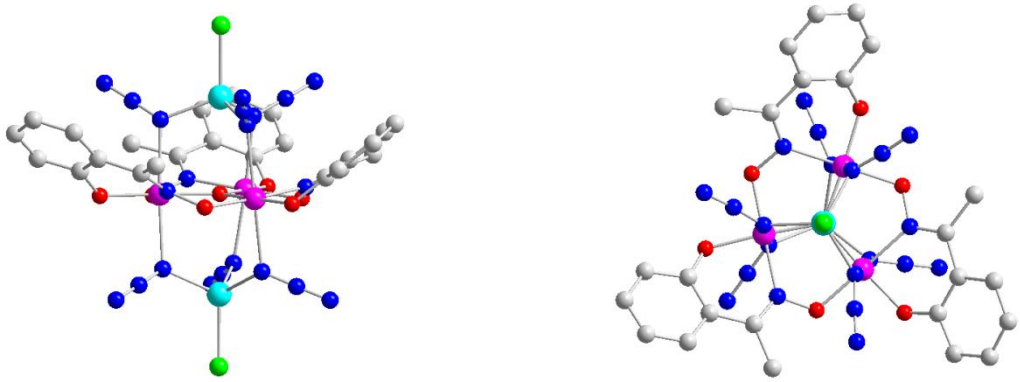

Fig 2.1: structure of molecule C viewed along the c axis (right) and perpendicular to it (left). The three NEt_4^+ counter ions as well as the hydrogen atoms have been omitted for clarity. Colour code: Mn (pink), Zn (turquoise), Cl (green), C (gray), O (red) and N (blue). Reproduced after [16].

In complexes **A**-**C** the sao^{2-} and Me-sao^{2-} respectively are tilted outside of the Mn_3 plane considerably and the Mn-N-O-Mn oximate bridge has a torsion angle, defined in section 1.3, of υ = 32.05° for **A**, υ = 32.08° for **B** and υ = 36.1° for **C**. Without a doubt the additional methyl group in Me-sao^{2-} of **C** and the consequential steric effect are responsible for the bigger torsion angle in this molecule. In molecule **D**, as an effect of the much bulkier $AsPh_4^+$ counter ions (compared to the NEt_4 in **A** to **C**) the sao^{2-} ligands lie in the Mn_3 plane with a much smaller torsion angle of υ =11.93°. The presented DC susceptibility and reduced magnetization data deliver further proof for the connection between the exchange coupling and the oximate torsion angle. The reported exchange coupling parameters *J* for the complexes are:

$J_{\mathbf{A}}$ = 2.4 K, $J_{\mathbf{B}}$ = 2.3 K, $J_{\mathbf{C}}$ = 4.7 K and $J_{\mathbf{D}}$= -4.1 K[16]. The ferromagnetically coupled molecules **A** to **C** show single molecule magnet behavior with very similar effective barrier heights for magnetization relaxation (see table 2.2). By single crystal HF-EPR measurements, the parameters of the Giant Spin Hamiltonian have been determined[16]. As previously discussed (see e.g. eq 1.7), the global ZFS *D* is linked to the single center ZFS D_i through the projection coefficient $d = \frac{3}{11}$ and a JT axes tilting δ. These parameters are listed in table 2.2.

Table 2.2: Fitting parameters of complexes **A** to **C**

Complex	g	D_i [cm^{-1}]	δ from structure	D [cm^{-1}]	B_0^4 [cm^{-1}]
A	1.93	-3.13	8.43	-0.804	$-5.28 \cdot 10^{-5}$
B	1.94	-3.18	8.09	-0.818	$-5.07 \cdot 10^{-5}$
C	2.01	-3.05	8.44	-0.808	$-2.50 \cdot 10^{-5}$

During his master thesis the author studied complex **A** and **B** by inelastic neutron scattering[1].

Figure 2.2 shows a temperature dependence of the ground state transitions of molecule **A** measured on IN5 at 6.5 Å incident wavelength. At the time when these spectra were recorded the beam-stop of the instrument leaked, which is responsible for the shoulder at ΔE = 1 cm^{-1}. This can be seen from the Q-dependence and the temperature dependence. The peak positions were simulated with the Giant-Spin Hamiltonian parameters D = -0.814 cm^{-1} and B_0^4 = $-4.85 \cdot 10^{-5}$ cm^{-1}.

These parameters are similar if not exactly the same as the ones reported by [16]. It has to be noted that while HF-EPR possesses a superior resolution, the treatment of INS data can be done without including the Zeeman terms, as it is measured at zero field. As a result the g factors, which play a crucial role in reproducing EPR spectra, do not enter INS data treatment.

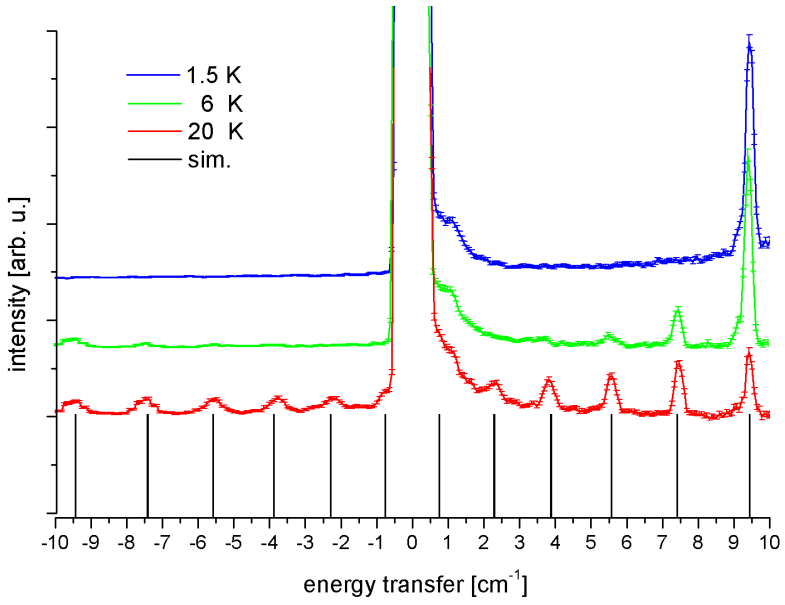

Fig 2.2: Temperature dependence of magnetic GS transitions in molecule **A** measured at 6.5 Å incident wavelength.

For **B** inelastic neutron scattering data have been collected at 6.5 Å as well as 8.5 Å incident wavelength (see fig. 2.3). Both wavelengths have their advantages and provide complementary

information. The spectrum measured at the shorter wavelength shows the M_S = ±6 to M_S = ±5 excitation with a much higher resolution as the M_S = ±5 to M_S = ±6 deexciation observed with both wavelength. At 8.5 Å however, the incident neutron energy is not high enough to enable this excitation. The longer wavelength with its higher resolution around the elastic line is able to resolve the M_S = ±1 to M_S = 0 transition.

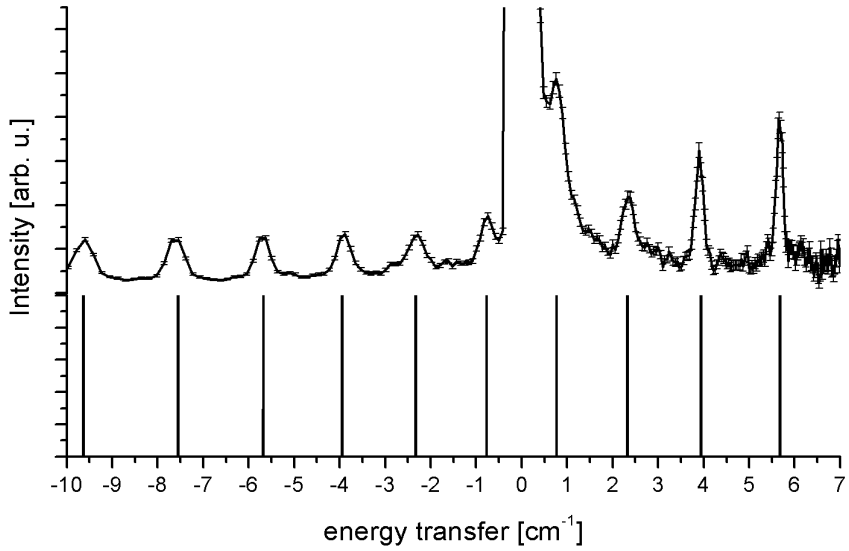

Fig 2.3: INS spectrum of **B** measured at 20 K and 7.5 Å incident wavelength.

The following giant-spin Hamiltonian parameters have been determined for complex **B**:
D = -0.829 cm^{-1}, B_0^4 = 5.12· 10^{-5} cm^{-1}.

Due to the great success in determining the ground state splitting parameters and previously [16] demonstrated possibilities of minute modifications the author decided to study this class of $[Mn_3O]^{7+}$ core SMMs further. Three additional analogs are studied in this work. A pictorial representation of the molecules can be seen in figure 2.4. Special attention was given to further modifications of the salicylaldoximate ligands, to further study the dependence of the exchange coupling to the oximate twisting, and to attain further proof for its correlation to the B_0^4 term. Due to the fact that the complexes with bulkier sao^{2-} substitutes did not retain the 3-fold symmetry the data could only be modelled with additional rhombic anisotropy.

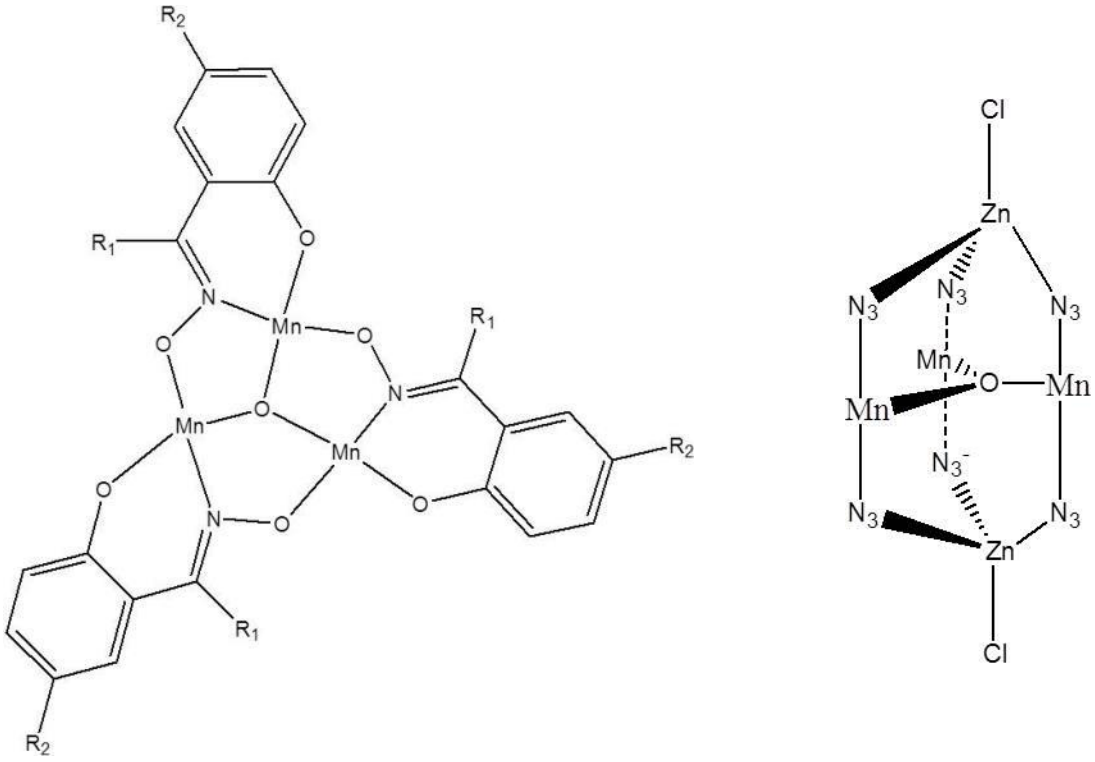

Fig. 2.4: Pictorial representation of the molecules studied in this chapter (left) viewing direction orthogonal to the Mn_3 plane with R_1 =Me(**1**), Et(**2**), Ph(**3**), R_2 = H(**1**,**2**), Me(**3**), (right) viewing direction from within the Mn_3 plane.

2.2 Synthesis:

Me-saoH_2 and Et-saoH_2 have been prepared after [60] by the addition of an excess amount of hydroxylamine (50% in H_2O) to an aqueous suspension of *o*-hydroxyacetophenone and 2-hydroxypropiophenone, respectively. After heating to 90 °C for 30 minutes the solution was cooled and the white compounds crystallized. Benzo-5-Me-saoH_2 (see figure 2.2) was prepared by addition of 2-hydroxy-5-methylbenzophenone to a hydroxylamine solution in water. The suspension is stirred and refluxed for several hours. After decanting the solution from the residual 2-OH-5-Me-benzophenone, Benzo-5-Me-saoH_2 crystallized upon cooling.

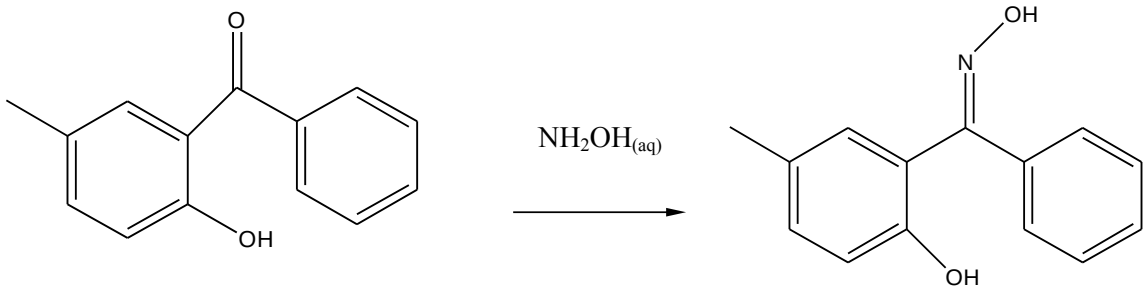

2-OH-5-Me-benzophenone Benzo-5-Me-saoH_2

Fig 2.5: Scheme of Benzo-5-Me-saoH_2 synthesis.

$[NEt_4]_3[Mn_3Zn_2(Me\text{-}sao)_3O(N_3)_6Cl_2]$, in the following called **1,** was synthesized according to ref. [16]. The sample was characterized by elemental analysis: found C, 39.02%; H, 5.38%; N, 22.8%; (calc. C, 39.14; H, 5.54%; N, 22.82%) and x-ray powder diffraction (see fig S1).

$[NEt_4]_3[Mn_3Zn_2(Et\text{-}sao)_3O(N_3)_6Cl_2]$ **(2)** was synthesized after a modified procedure of compound **1**:

To a stirred solution of 250 mg anhydrous $MnCl_2$ (2.05 mmol) and 181 mg anhydrous $ZnCl_2$ in 50 ml MeOH, 260 mg NaN_3 and 330 mg Et-saoH_2 were added. The solution was stirred for 2 h during which it turned black/green. After addition of 0.7 ml NEt_4OH (20% in H_2O) the solution was stirred for 5 additional minutes and filtered. After 5 days, crystals suitable for X-ray diffraction were obtained.

$[NEt_4]_3[Mn_3Zn_2(Ph\text{-}5\text{-}Me\text{-}sao)_3O(N_3)_6Cl_2]$ **3** was synthesized stirring 63.5 mg anhydrous $MnCl_2$ (0.505 mmol), 55.5 mg anhydrous $ZnCl_2$, 109.5 mg Benz-5-Me-saoH_2 and 65.5 mg NaN_3 in 25 ml MeOH for 2h. After addition of 0.175 ml NEt_4OH (20% in H_2O) and 5 minutes of additional stirring the solution was filtered left undisturbed for 5 days. Single crystal X-ray-diffraction suited crystals appeared in 25 % yield based on Mn. Elemental analysis found: C: 46.68%, H: 5.4%, N: 19.99% (calc: C: 46.59%, H: 5.51%, N: 19.76%)

2.3 X-ray crystallography

$[NEt_3]_4[Mn_3Zn_2O(Et\text{-}sao)_3(N_3)_6Cl_2]$ (**2**) crystallizes in the space-group *C*1*c*1 with cell parameters *a* = 23.15 Å, *b* = 13.45 Å, *c* = 22.39 Å, $\alpha = \gamma = 90°$ and $\beta = 101.2°$. The unit cell contains four molecules.

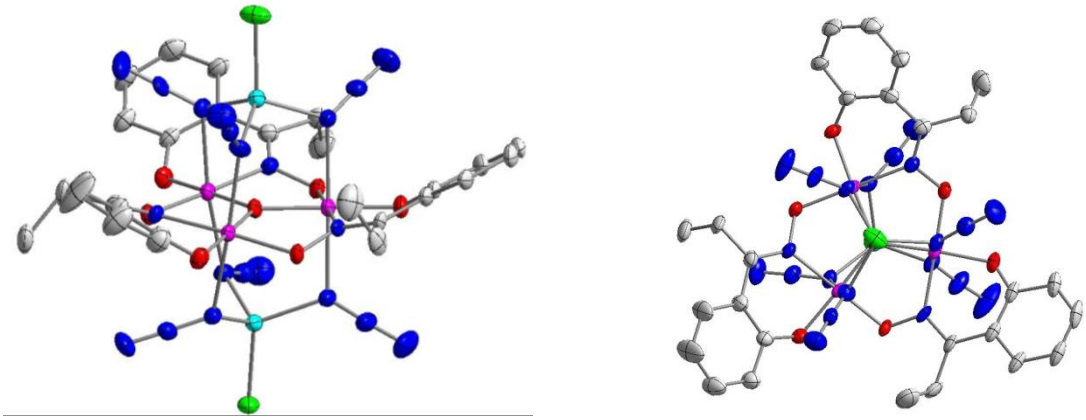

Fig 2.6: Structure of **2** viewed from within the Mn_3 plane (left) and orthogonal to it. The hydrogen atoms as well as the three NEt_4^+ counter ions have been omitted for clarity.

The main difference between the molecular structure of compound **2** and the structures of **1** and **A**, is the bulkier ethyl group on the sao^{2-} ligand that leads to sterical stress. Instead of twisting the oximate bridge further, as it is the case when changing from sao^{2-} in **A** to Me-sao^{2-} in **1**, the symmetry of this rigid molecule can no longer be maintained. This means that on the molecular level one of the ethyl groups is not oriented in the same way as the other two. While two oximate twisting angles are similar two each other with υ_1 =33.12° and υ_2 = 33.82° the third one υ_3 = 36.35°, is considerably larger.

Table 2.3: magneto-structural parameters

Compound	υ [°]	δ [°]	φ [°]
1	36.1	8.5	trigonal
2	33.82(45), 35.12(41), 36.35(45)	8.76, 8.96, 7.07	0, 118.79, 239.32
3	27.82(3), 31.17(3), 40.12(3)	7.31, 5.97, 8.88	0, 115.6, 234.2

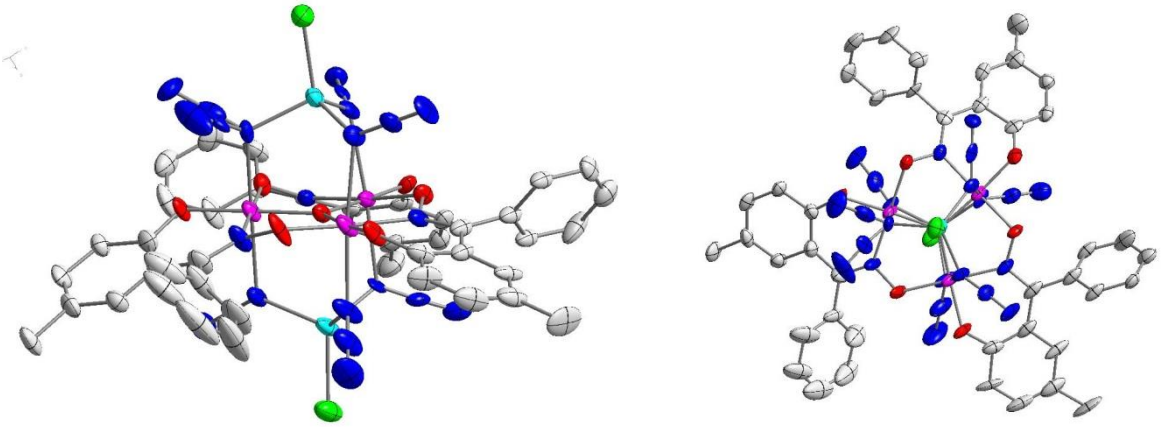

Fig 2.7: structure of **3** viewed from within the Mn_3 plane (left) and orthogonal to it. The hydrogen atoms as well as the three NEt_3 counter ions have been omitted for clarity.

Compound **3** crystallizes in the $P2_1/c$ space group with four molecules in a unit cell with the following lattice parameters: a = 22.4620(15) Å, b = 14.202(3) Å, c = 28.407(4) Å and $\alpha = \gamma$ = 90.000(14)°, β =116.633(9)°. The data of the measured crystal was of relatively poor quality. Therefore several conflicts could not be investigated further. One of the Cl^- is partially (estimated 15%) with N_3^-, furthermore one azide ligand is disordered. Like in compound **2** the bulky oximate ligand breaks the symmetry but to a much greater degree than compound **2**. Two of the oximate twisting angles are very similar to each other υ_1 = 27.820(31)° and υ_2 = 31.168(30)°, while the third is considerably larger υ_3 = 40.120(29)°. The single center anisotropy axis tilting angles δ are 7.31°, 5.97° and 8.88°. Some important distances and angles of compounds **2** and **3**, are listed in table 2.4.

Table 2.4: Important structural parameters for compounds **2** and **3**. All lengths are given in units of Å.

	2	**3**
μ_3-O-out-of-plane shift	0.062(4)	0.0313(3)
∡Mn-O-Mn [°]	119.7(2), 119.7(2), 120.4(24)	120.13(2), 118.79(2), 121.00 (1)
$Mn\text{-}N_{azide1}$	2.387(5), 2.333(4), 2.341(4)	2.4060(5), 2.4275(5), 2.2870(5)
$Mn\text{-}N_{azide2}$	2.312(4), 2.323(4), 2.337(4)	2.3117(5), 2.3280(5), 2.4012(5)
μ_3-O-Mn	1.886(4), 1.881(4), 1.886(4)	1.8677(3), 1.9046(1), 1.8870(3)
$Mn\text{-}O_{phenolate}$	1.875(4), 1.863(4), 1.861(4)	1.8848(3), 1.8691(1), 1.8675(3)
$Mn\text{-}O_{oximate}$	1.903(4), 1.933(4), 1.915(4)	1.9210(2), 1.9135(3), 1.9040(2)
$Mn\text{-}N_{oximate}$	2.003(45), 2.001(5), 2.018(5)	2.0485(2), 2.0261(4), 2.0013(3)
Mn-Mn	3.256(1), 3.256(1), 3.272(1)	3.2691(4), 3.2634(3), 3.2680(6)

2.4 Direct-current susceptibility

The temperature dependence of the susceptibility measured at 0.100 T is presented as a $\chi_M T$ (T) plot in fig. 2.8. At 300K the $\chi_M T$ value is, with ~10 cm^3 K mol^{-1}, well above the theoretical value of 9 cm^3 K mol^{-1} for three uncoupled Mn(III) ions. When cooling from room temperature $\chi_M T$ increases reaching a maximum of 19.8 at 13 K before sharply decreasing to 17.4 cm^3 K mol^{-1} at 2.55 K. The field dependence has been measured in the region of 5 mT to 5 T at 6 temperatures between 2 and 8 K. The magnetization data as well as the $\chi_M T$ data have been simultaneously fitted to the asymmetric Hamiltonian defined in eq 1.3 and 1.9 with the angles $\delta_{1,2,3}$= 8.76°, 8.96°, 7.07° and $\varphi_{1,2,3}$ = 0°, 118.79°, 239.32° determined from the crystal structure. The resulting parameters are: J_1 = 2.03 cm^{-1}, J_2 = 2.05 cm^{-1}, J_3 = 4.76 cm^{-1}, $D_{1=2=3}$ = -3.08 cm^{-1}, g = 1.95 cm^{-1}. Furthermore a model scaling factor of 1.013 has been introduced to account for small errors during the sample weighting or the instrument calibration and a fitted diamagnetic correction of $6.7 \cdot 10^{-4}$ emu/mol that can account for overcorrection during the data workup.

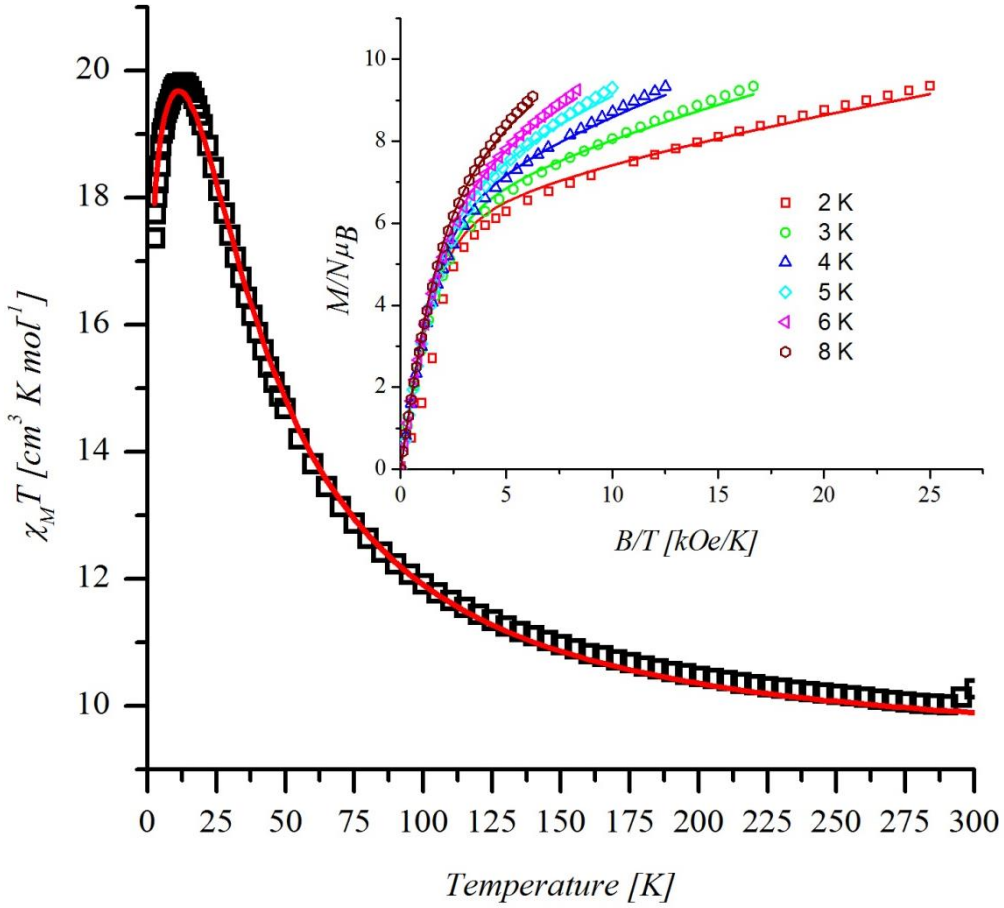

Fig 2.8 susceptibility data of **2** measured at 0.1 T in the temperature range 1.9-300 K (left). Reduced magnetization data grouped according to temperature for clarity (top right). The solid lines represents the best possible fit for both data sets simultaneously obtaining the parameters described in the text.

The magnetic data of **3** was fitted to a Hamiltonian with $J_1 = J_2$, as these two parameters were not converging during the fitting process, unlike for compound **2.** The number of parameters was reduced to avoid an overparameterisazion of the system. The resulting parameters were

$J_1 = J_2 = 0.494$ cm^{-1}, $J_3 = 3.004$ cm^{-1}, $D_i = -3.11$ cm^{-1}, $g = 1.93$ with a model scaling factor of 1.007 and a diamagnetic correction of $-500 \cdot 10^{-6}$ cm^3 K mol^{-1} to account for the hexadecane that was used to prevent the crystallites from orienting in high fields and the diamagnetic contribution of the molecule itself.

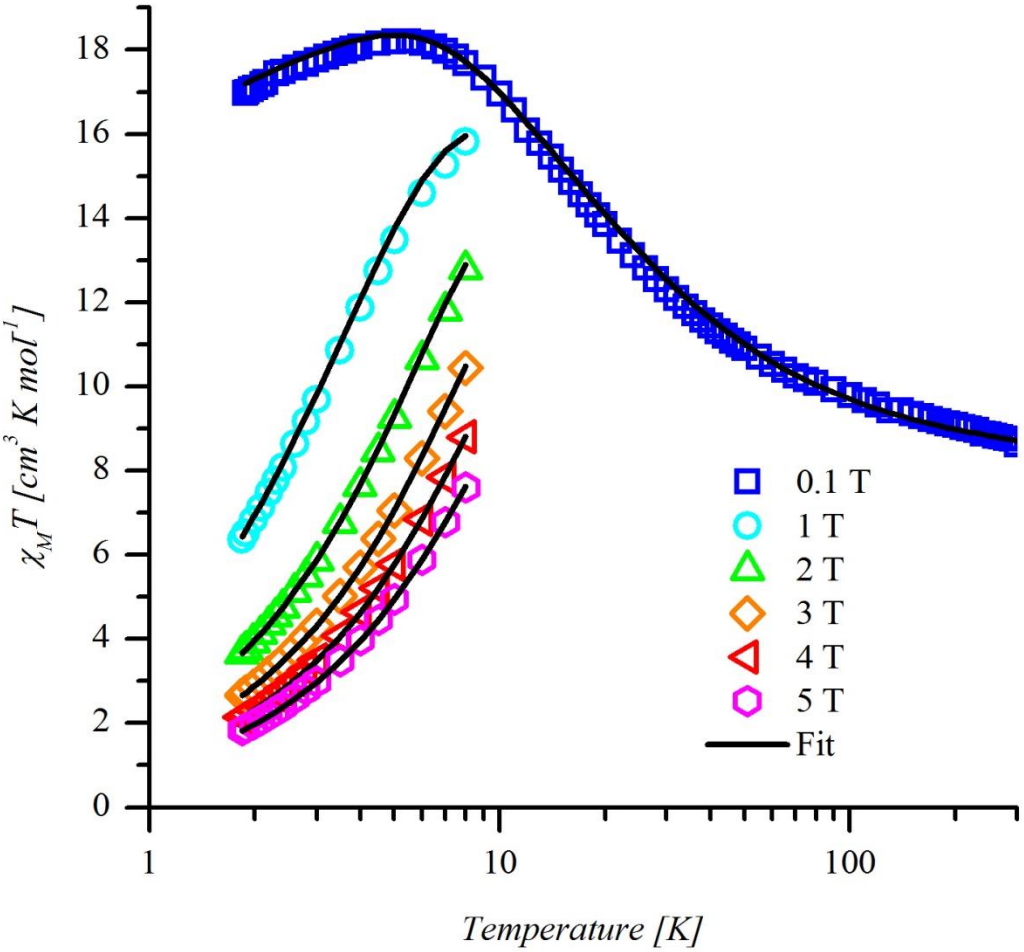

Fig 2.9: susceptibility and reduced magnetization data of **3** represented as a $\chi_M T$ vs. T plot. The solid lines represent the best possible fit with parameters described in the text.

2.5 AC-susceptibility

AC susceptibility data has been collected on polycrystalline samples of **2** and **3** in the absence of a static field and a driving amplitude of 3.5 Oe for compound **2** and 3.8 Oe for compound **3** respectively. The in-phase and out-of-phase susceptibility data are shown in Figures 2.10 and 2.11

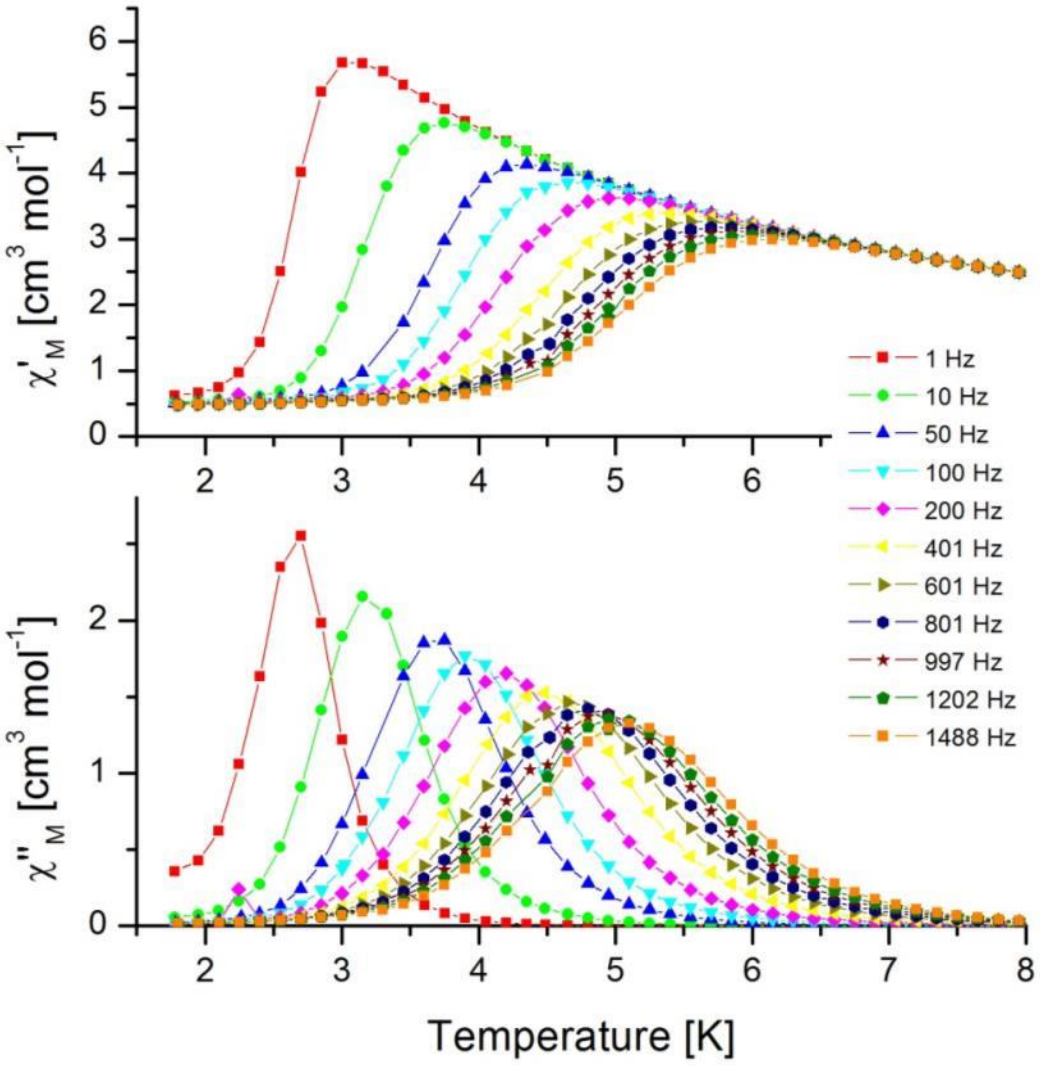

Fig 2.10: in-phase (top) and out-of-phase (bottom) AC-susceptibility data of compound 2 in the frequency range 1 Hz-1488 Hz.

Compound **2** shows clear peaks in the out-of-phase component of the susceptibility. The temperature shift of the peak maxima between the different frequencies is very similar to that observed for the literature compounds **A**, **B** and **1**.

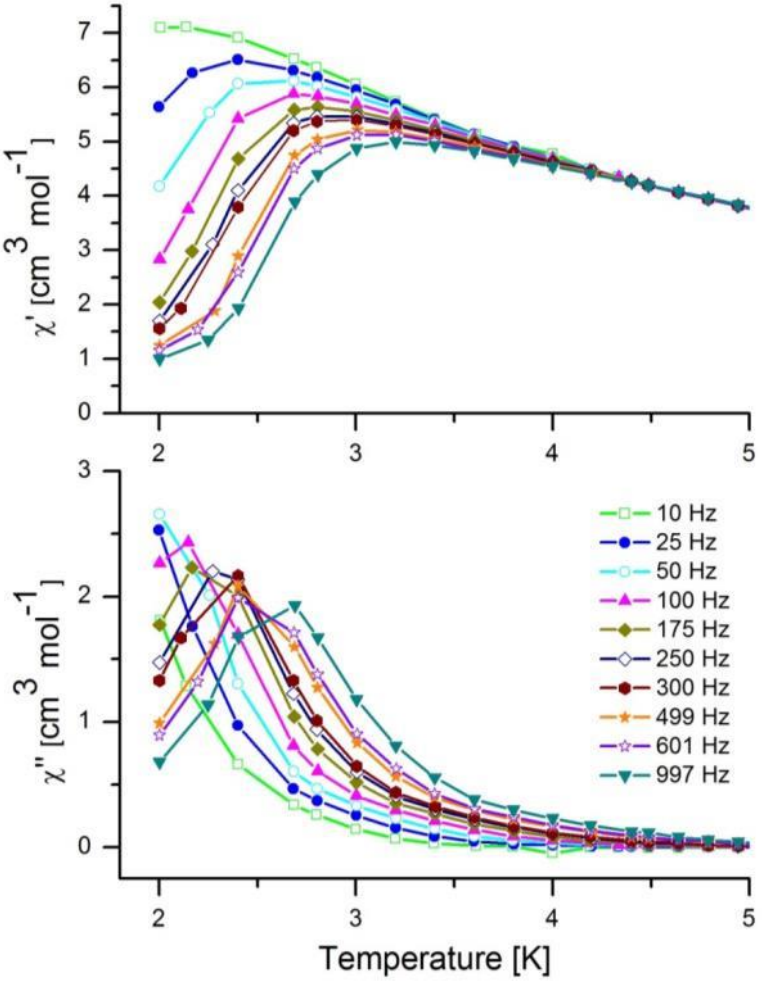

Fig 2.11: in-phase (top) and out-of-phase (bottom) AC-susceptibility data of **3**

Compound **3** also shows a peak in the out-of-phase component of the susceptibility. At lower frequencies the peaks shift to temperatures that are too low to be measured with the employed set-up, therefore only frequencies between 100 Hz and 997 Hz were used for the Arrhenius plot.

In figure 2.11 the Arrhenius plots for compounds **2** and **3** are presented. The comparison reveals that compound **3** has a much smaller relaxation barrier U_{eff} than compound **2**.

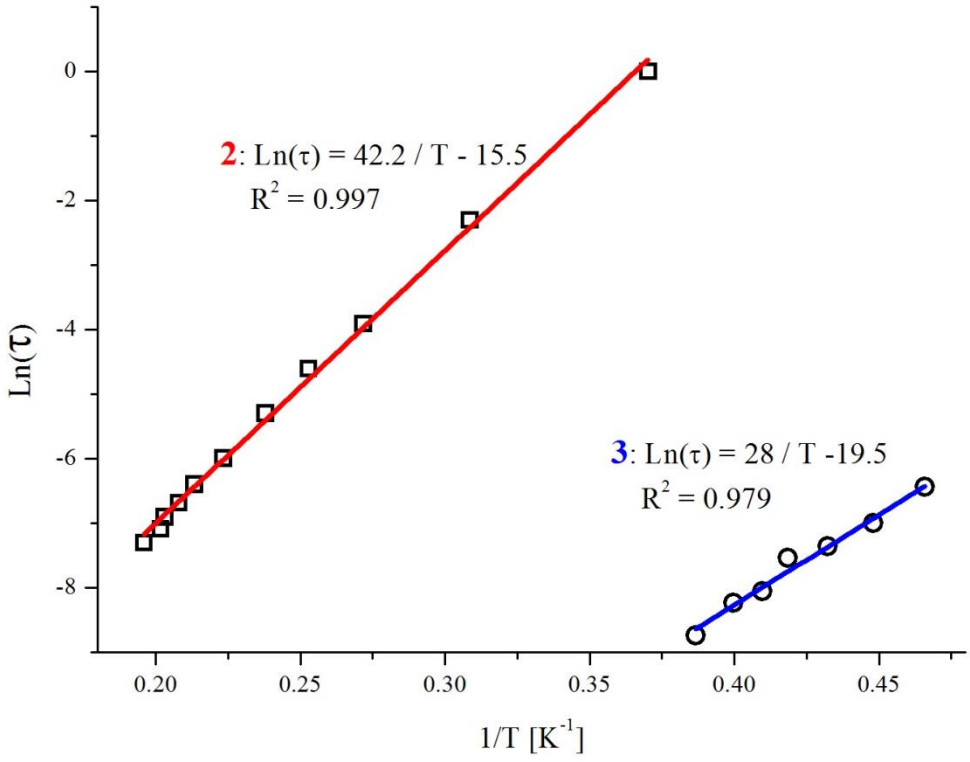

Fig. 2.12 Arrhenius plot of the out-of-phase peak positions of coumpund **2** for frequencies between 1 Hz and 1488 Hz and compound **2** between 100 and 997 Hz.

The energy level diagrams at zero field in fig 2.13 illustrate the differences in U_{eff} of compounds **2** and **3**. In compound **2** the ground state multiplet is well separated from the higher states. Therefore only the S = 6 multiplet is involved in the relaxation process at low temperatures. In compound **3** the S = 6 ground state multiplet is not well separated from the higher multiplets. There are therefore different relaxation pathways in this compound, which leads to the lower barrier U_{eff}.

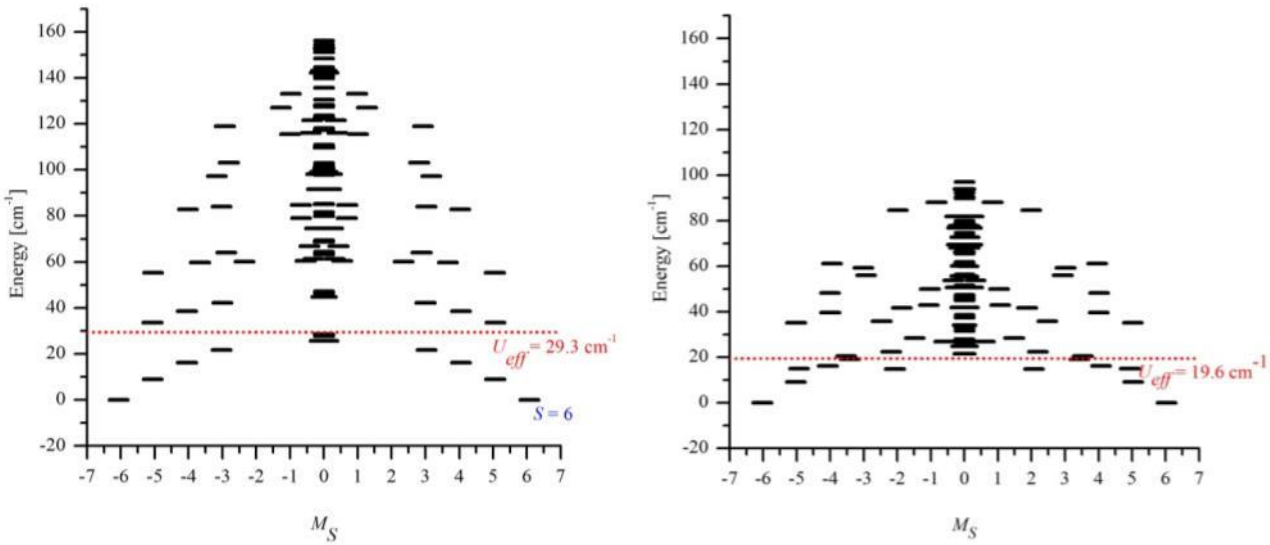

Fig. 2.13. Zero field energy level diagram of compound **2** (left) and compound **3** (right)

2.6 Inelastic neutron scattering

INS spectra of compound **1**, **2** and **3** have been collected as described in the previous chapter. The only difference is that for compound **3** a cryo-furnace (CF) has been used instead of the more common orange cryostat (OC). The fact that the base temperature of the CF (1.8 K) is slightly higher than the OC and other problems associated with the CF (see below) were outweighed by the long waiting time a change to a OC would have caused. A change of the sample environment requires a pressurization and evacuation of the detector chamber. Furthermore a warm cryostat may need several hours to cool down.

The spectrum of complex **1** measured at 6.5 Å incident wavelength shows a cold transition at 9.22 cm^{-1}. At 6 K transitions at 7.41 and 5.66 cm^{-1} can be observed. At this temperature they are of low intensity but become more intense as the temperature is raised to 20 K. “warm transitions can be observed at 7.41, 5.66, 4.00 and 2.35. A temperature independent artifact is observed at 8.86 cm^{-1} and temperature dependent features at 8.17 and 6.06 cm^{-1}. These features have a very low intensity and their FWHMs are much smaller than the theoretical resolution of the instrument at these peak positions, which suggests that they are not a physical property of the sample. Therefore these artifacts are not further discussed. The transition at 2.35 cm^{-1} is considerably wider than the resolution of the instrument at this energy.

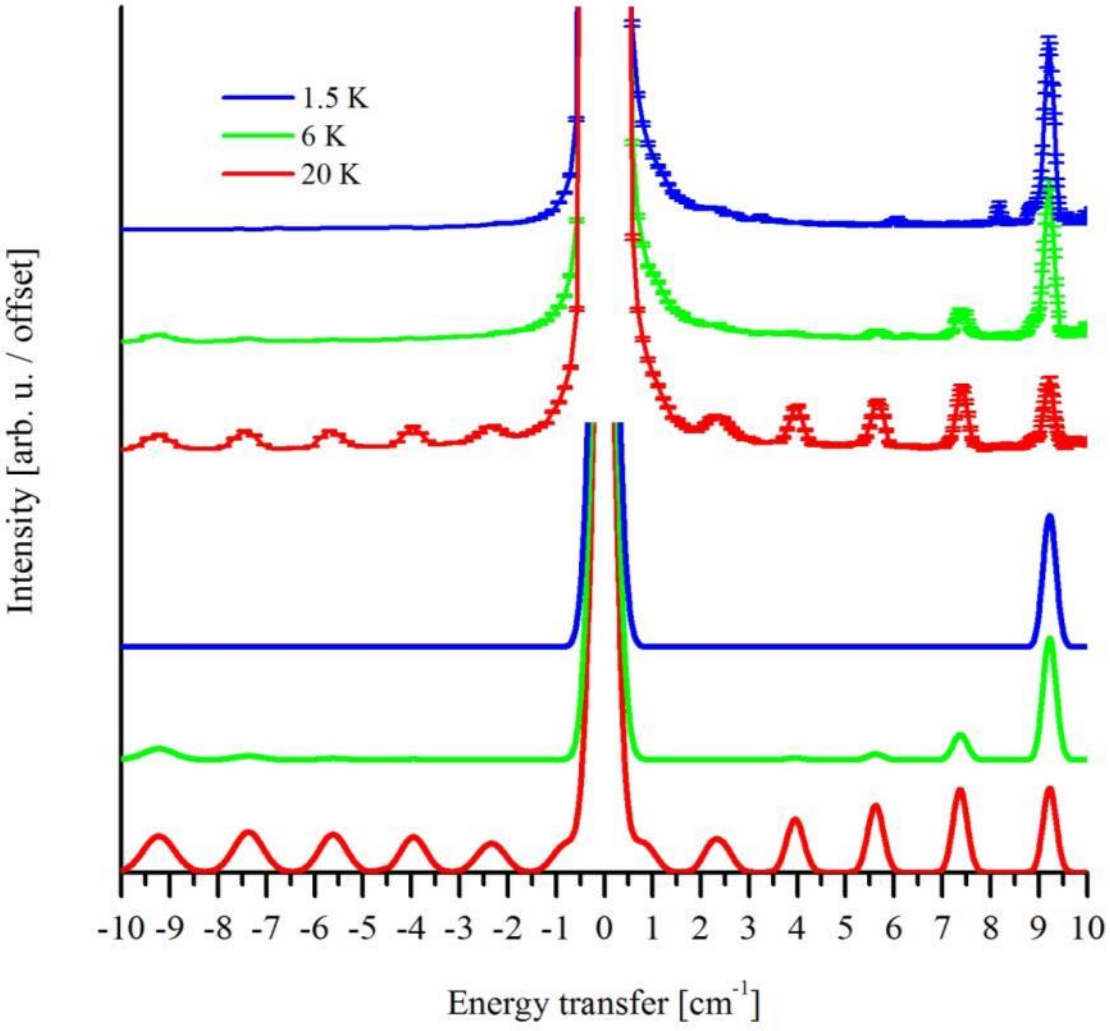

Fig 2.14: top: temperature dependence of INS of **1** spectra measured on IN5 at 6.5 Å incident wavelength. The spectra at 6 K and 1.5 K have been shifted in intensity for clarity. Bottom: simulation of the spectrum with GS model parameters described in the text.

The higher resolution spectra measured at 8.5 Å and 10 Å incident wavelength and 20 K are presented in Figure 2.15. At higher resolution the mixing of the higher M_S states that was only visible as a widening of the peaks at 6.5 Å is visible as a splitting of said peaks at 8.5 and 10Å. The transition $M_S = \pm 1$ to $M_S = 0$ can only scarcely be resolved from the elastic line at 10 Å incident wavelength.

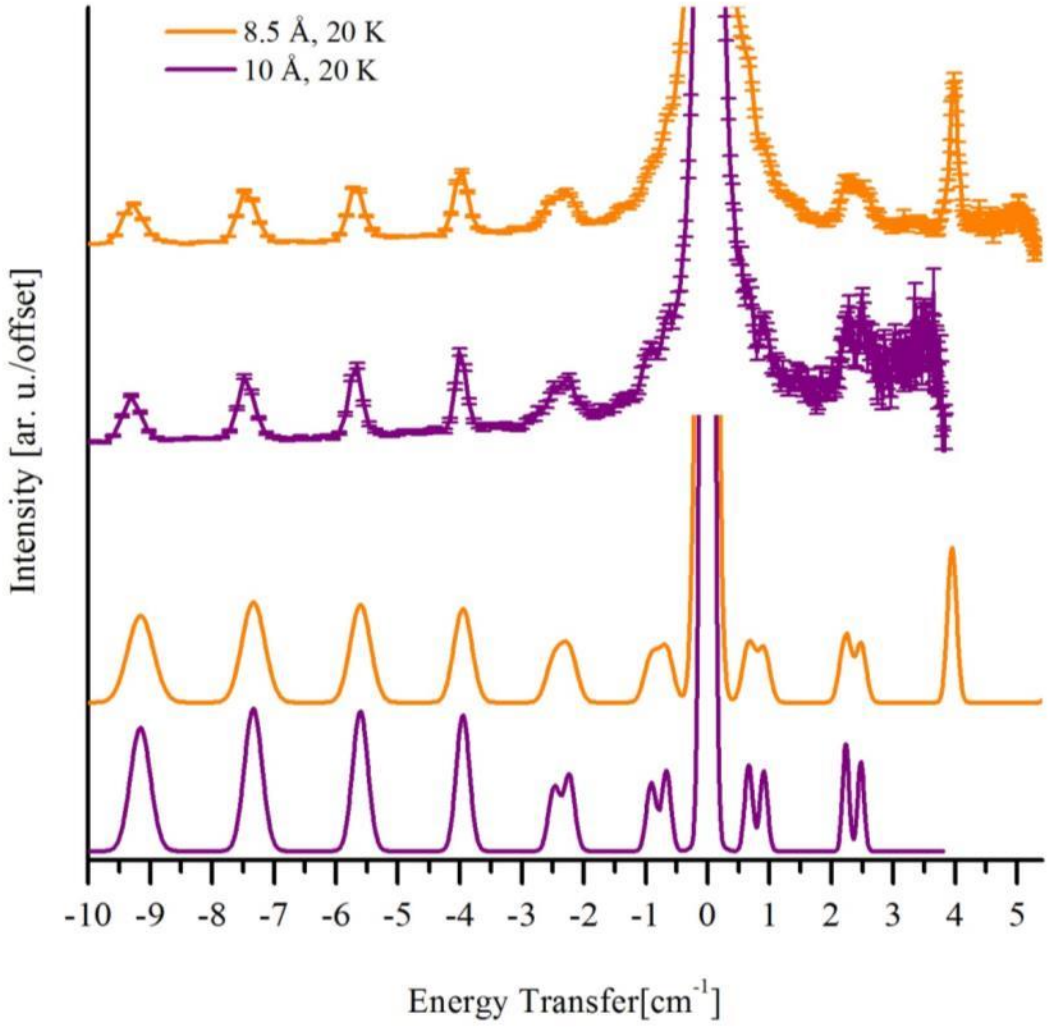

Fig. 2.15 INS spectra of compound **1** measured 20 K with 8.5 and 10 Å incident wavelengths.

The original publication measured single crystal HF-EPR along the *z* axis and one orientation in the hard plane[16]. As EPR has a higher resolution than INS and there was no rhombic anisotropy needed to fit the data in the original publication, it has been attempted to fit the published EPR data with the new INS data simultaneously. The resulting GS Hamiltonian parameters are: D = -0.810 cm^{-1}, E = 0.0058 cm^{-1}, B_0^4 = -2.51 · 10^{-5}, g =2.00. The importance of the small rhombic anisotropy E is illustrated in fig. 2.16. The simulated peaks close to the elastic line are clearly not split, unlike the simulations with E = 0.0058 cm^{-1} in Fig 2.15 and the measured spectra. These parameters can also reproduce the

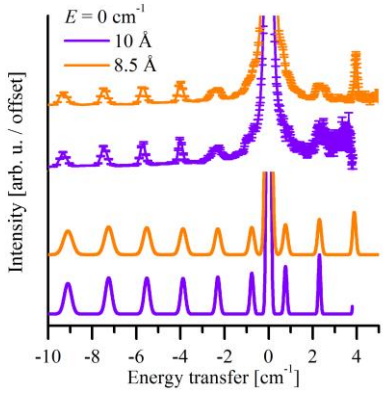

Fig. 2.16 simulation of the neutron data with rhombic anisotropy limited to E = 0 cm^{-1}.

reduced magnetization data presented, with a model scaling factor of 1.056 (see fig. S2). The model scaling factor used to reproduce the results from the publication was 1.07.

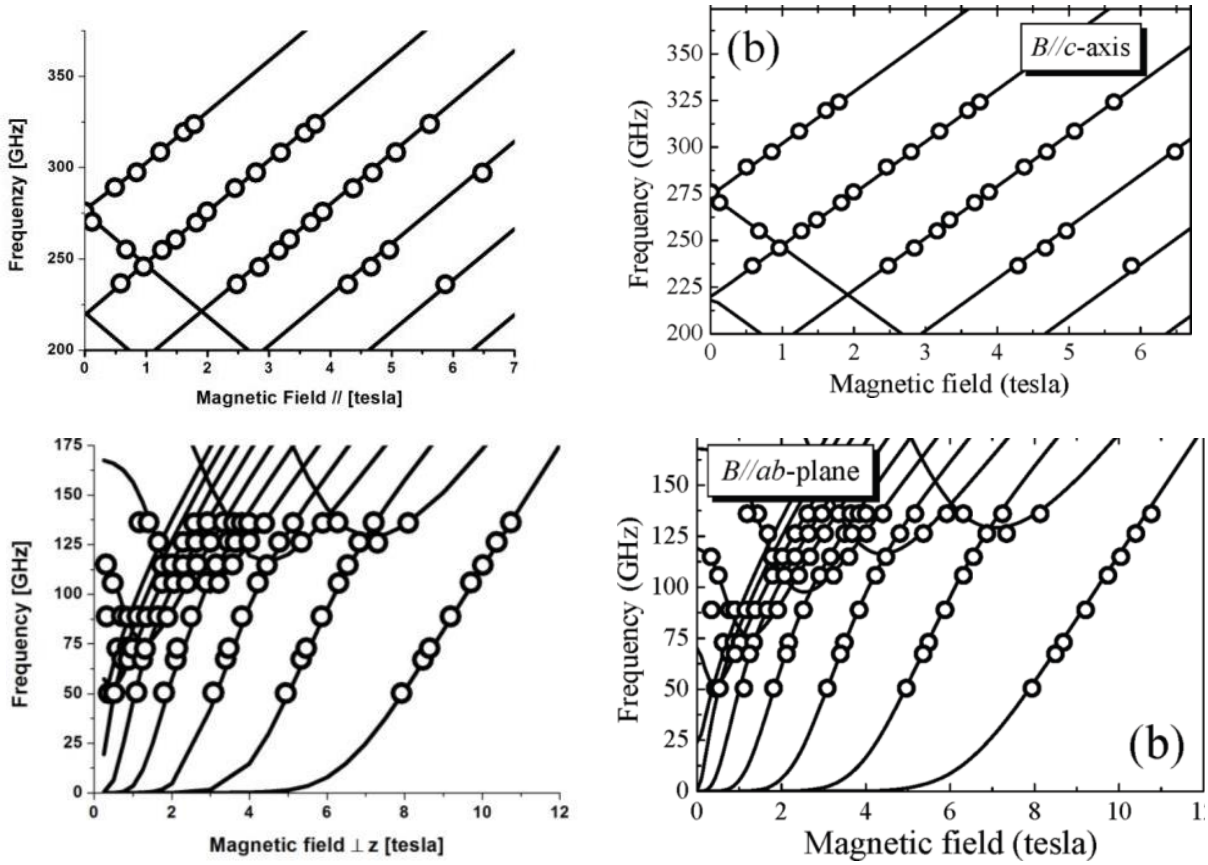

Fig. 2.17. A simultaneous fit of the HF-EPR data from [16] and the new INS data to a Giant-Spin Hamiltonian produced the following parameters: D = -0.810 cm^{-1}, E = 0.0058 cm^{-1}, B_0^4 = -2.51·10^{-5}, g = 2.00. The parameters g_x and g_y were restrained to be equal to g_z during the fit, g_z was left unrestrained. The two plots on the left side show how well the new model can reproduce the HF-EPR data compared with the plots from [16]on the right side

The INS spectra of **2** measured at 6.5 Å incident wavelength and 1.5 K to 20K show a cold transition at 9.06 cm^{-1} (cf. Fig. 2.18). At higher temperatures other transitions are visible at 7.24, 5.50

and 3.83 cm^{-1}. At 20 K a doublet at around 2.3 cm^{-1} can be observed as well as another transition that is not resolved at this wavelength. Therefore a spectum at 8.5 Å incident wavelength was measured to resolve these transitions (cf. Fig 2.19)

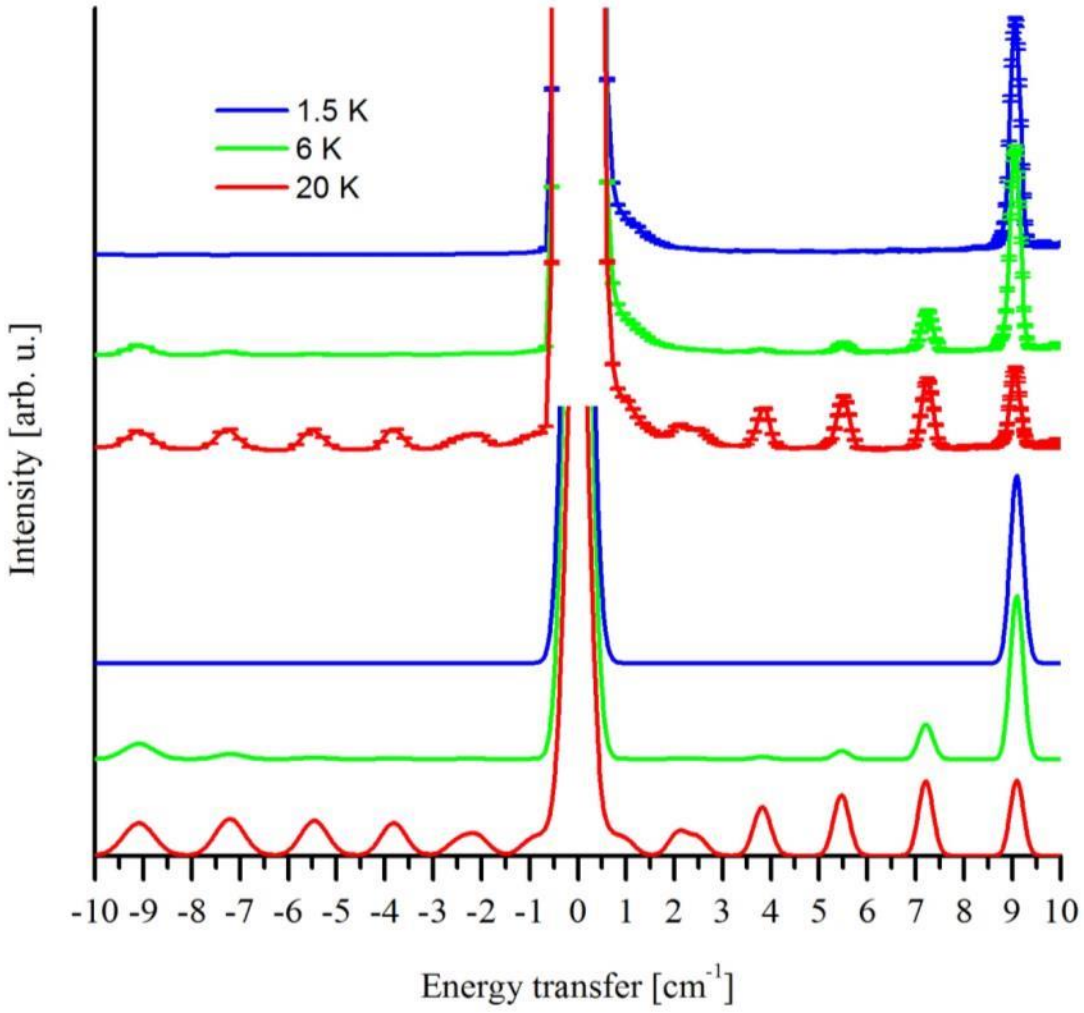

Fig 2.18: above temperature dependence of INS of **2** spectra measured on IN5 at 6.5 Å incident wavelength. Below: simulation of the same spectra. The spectra and simulations at 6 K and 1.5 K have been shifted along the ordinate for clarity

The high resolution data shows four clearly resolved peaks at 2.49, 2.09, 0.99 and 0.57 cm^{-1} and at their corresponding positions on the energy gain side.

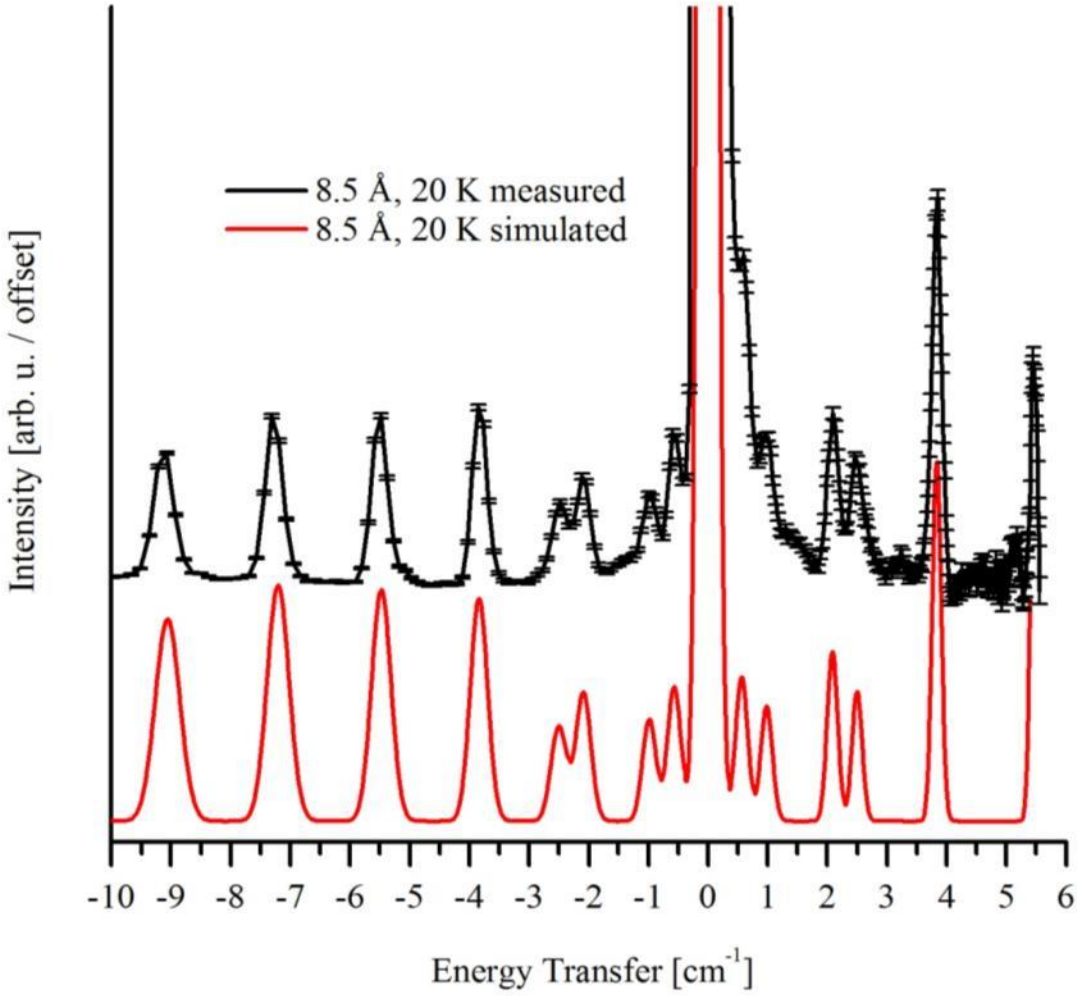

Fig 2.19: high resolution spectrum of **2** measured at 8.5 Å incident wavelength and 20 K

The position of the "cold" transition $M_S = \pm 6$ to $M_S = \pm 5$ at 9.09 cm^{-1} indicates that compound **2** has a slightly smaller ZFS parameter *D* than compound **1**. The clear splitting of the lower M_S number transitions indicates a considerably larger rhombic ZFS parameter *E*. A fit of the peak positions to a giant spin model afforded the parameters: $D = 0.794$ cm^{-1}, $E = 0.0099$ cm^{-1}, $B_0^4 = -3.27 \cdot 10^{-5}$ cm^{-1}.

The INS spectra of compound **3** (Figure 2.20) at 6.5 Å show one transition at 9.21 cm^{-1} and several transitions at higher temperatures at 7.25 cm^{-1} and 5.35 cm^{-1}. A temperature independent shoulder at 2.1 Å was determined to be due to multiple scattering from the cryofurnace. The peak shifts position according to the incident wavelength which is a fingerprint of multiple scattering. The additional path length travelled by the neutrons due to the multiple scattering was determined from the time-of-flight data and matched the diameter of the outer cryofurnace wall. The transition at 5.35 cm^{-1} is twice as broad as the theoretical resolution of the instrument. From these three transitions and the broadening of the mentioned transition the parameters of the GS model can be determined. They are:

D = 0.796 cm^{-1}, E = 0.0190 cm^{-1}, B_0^4 = -4.73·10^{-5} cm^{-1}. Transitions closer to the elastic line could not be fitted by this Hamiltonian for several reasons. Firstly, the spectra have a high background close to the elastic line due to the sample itself and the cryofurnace. Secondly, the GS model does not describe this system accurately as it was determined not to have a well separated ground state multiplet (see Fig. 2.13)

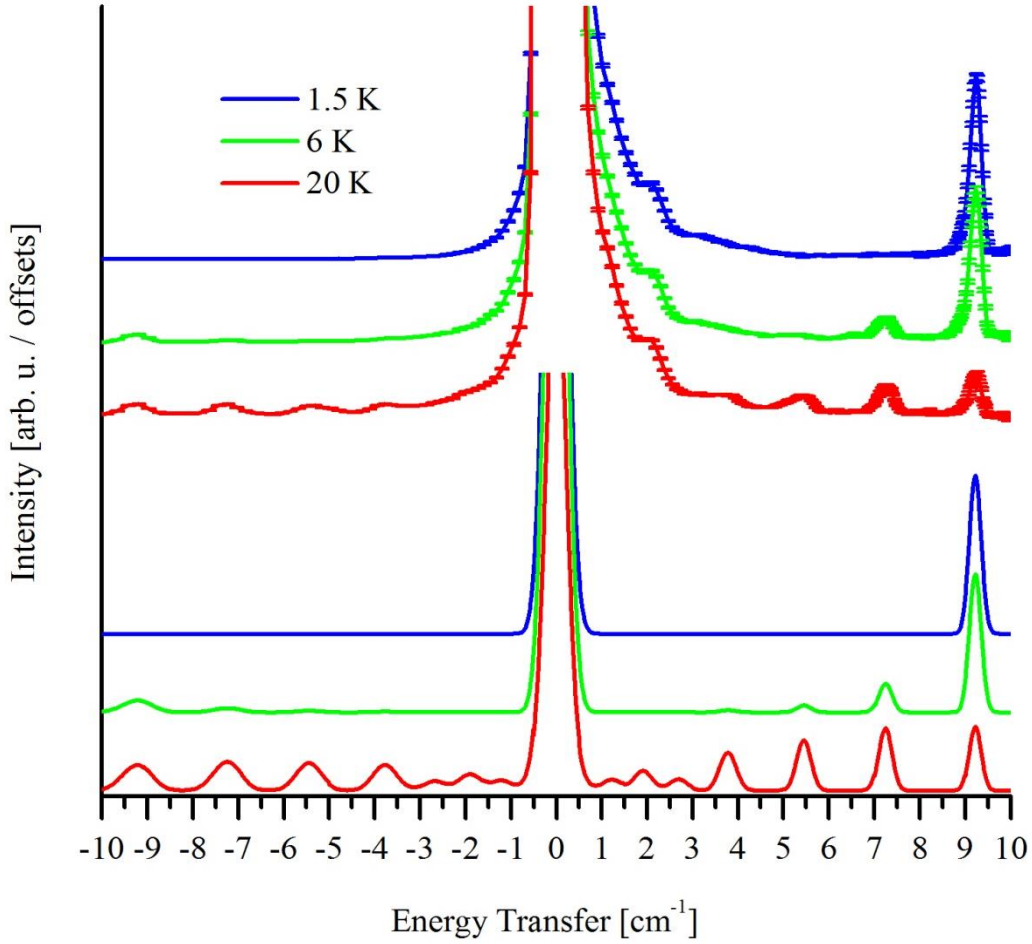

Fig 2.20: above temperature dependence of INS of **3** spectra measured on IN5 at 6.5 Å incident wavelength. Below: simulation of the same spectra. The spectra and simulations at 6 K and 1.5 K have been shifted in intensity for clarity

2.7 Discussion/Summary

As basis for the discussion, a summary of the parameter values describing the electronic structure of compounds **1**-**3** has been made in Table 2.5 below.

Table 2.5 Parameter values determined for compounds **1** to **3**

	1	**2**	**3**
Name	$[NEt_4]_3[Mn_3Zn_2(Me\text{-}sao)_3O(N_3)_6Cl_2]$	$[NEt_4]_3[Mn_3Zn_2(Et\text{-}sao)_3O(N_3)_6Cl_2]$	$[NEt_4]_3[Mn_3Zn_2(Ph\text{-}sao)_3O(N_3)_6Cl_2]$
U_{eff} [K]	45.6[16]	42.2	28
J [cm^{-1}]	3.26[16]	2.04, 2.05, 4.76	0.5, 3
D_i [cm^{-1}]		-3.08	-3.11
g		1.95	1.93
D[cm^{-1}]	0.81	0.79	-0.796
E[cm^{-1}]	0.0058	0.01	0.019
B_0^4 [cm^{-1}]	$-2.51*10^{-5}$	$-3.27*10^{-5}$	$-4.73*10^{-5}$

In this chapter it was shown how inelastic neutron scattering can be essential for the accurate description of the ground state of $[Mn_3O]^{7+}$ SMMs. While INS does not provide equally high resolution as EPR, the absence of a magnetic field reduces the amount of parameters needed to describe the experimental findings. Therefore the problem becomes simpler and the solution more stable and reliable.

The chapter presents a series of SMMs with a deviation from three-fold symmetry to different extents. Due to the fact that the axial ligands are linked both above and below the Mn_3-plane, these complexes have a high rigidity. When a bulkier group on the sao^{2-} ligand is introduced, the oxiate bridges tend to twist [16, 18, 23], this tends to be accompanied by a tilting of JT axes on the Mn(III) centers in respect to each other. The fact that the tilting of the JT axes are restricted by the $Zn(N_3)_3$ groups above and below the Mn_3 plane might lead to the breaking of the symmetry observed in this series. While previously presented INS results for $[NEt_4]_3[Mn_3Zn_2O(sao)_3(N_3)_6Cl_2]$ and $[NEt_4]_3[Mn_3Zn_2O(sao)_3(N_3)_6Br_2]$[1] were consistent with the EPR and crystallographic data in literature[16], the INS spectrum of **1** clearly shows a small rhombic anisotropy which mandates that the trigonal symmetry of the complex is broken. As the crystal structure does not contain solvent molecules, solvent lost can be excluded as the origin of the symmetry breaking. Previously published HF-EPR data for **1** was modeled without E term[16]. This data could be reproduced with an GS parameters obtained from INS by slightly varying the g values. It was shown Complexes **2** and **3** crystallize in crystal systems with lower symmetry, with **2** deviating from trigonal symmetry to a lesser degree than compound **3** as it is illustrated by oximate twisting angles υ that have a smaller range. The combined steric effects of the phenyl and methyl groups on the sao^{2-} ligand in **3** are significantly bigger than the steric effect of the smaller ethyl group in **2**. This results in a bigger

distortion, a bigger deviation from trigonal symmetry for **3** than for **2**. This results in very different oximate twisting angles. The magnetic data of **3** has been fitted to a Hamiltonian containing only two *J* parameters instead of the three possible ones for broken symmetry in order to avoid overparameterization. In compound **2** two of the exchange parameters converge "naturally". This convergence as well as the reduction of parameters in **3** is rationalized, as both molecules have two angles υ that are similar and one that is considerably larger. The obtained exchange coupling parameters are consistent with theoretical results [1, 34] taking not only υ but also the out-of-plane shift of the μ_3-O from the Mn_3 plane into account.

As a series, these compounds represent a beautiful example of how a deviation from symmetry, if sizable enough, can lead to a breakdown of the Giant Spin Model as well as to a sizable reduction of the effective relaxation barrier U_{eff}. Compound **2** is at low temperatures well described with a GS model and has a similar U_{eff} as the symmetrical members of the series, whereas the ground state multiplet of **3** cannot be completely described with a GS model and the U_{eff} is reduced significantly.

3. Enhancing the effective barrier height by axial alignment, small deviations from perfect symmetry

3.1 Abstract

In this chapter we focus on three $Mn_3O(R\text{-sao})_3(2,4'\text{-bipyridine})_3XO_4$ -type complexes (where R = Me, Et and X = Cl or Re). These molecules possess crystallographic trigonal symmetry which simplifies the analysis due to the reduced amount of fitting parameters. Furthermore they represent a system that is susceptible to small changes due to its small rigidity compared to the systems presented in the previous chapter and there are no intermolecular interactions observed. These factors make these systems the ideal candidates to study the alignment of local Jahn-Teller (JT) axes with respect to the global anisotropy axis.

3.2 Introduction

$Mn_3O(Me\text{-sao})_3(2,4'\text{-bipyridine})_3ClO_4$ (**4**) was first published by Yang *et. al.* [61] in 2008. The reported molecule consists of three manganese (III) ions that are linked by a μ_3-oxide. Each Mn(III) ion is coordinated to one of three 2,4′-bipyridine at the 4′ nitrogen position and to one perchlorate group topping the molecule in a $\eta_1{:}\eta_1{:}\eta_1{:}\eta_3$-mode (see Fig 3.1). One of three Me-sao^{2-} ligands completes the octahedral coordination sites on each Mn in a $\eta_1{:}\eta_1{:}\eta_2$ -mode by binding the deprotonated phenolate and the oximate nitrogen with the same Mn and linking to the neighboring Mn with the oximate oxygen. For symmetry reaons, the easy axis of the molecule goes through the μ_3-oxygen as well as through the chlorine atom. Due to the relatively small size of perchlorate ion the local JT axes, following the bipyridine-Mn-ClO_4^--oxygen directions, are tilted with respect to the global anisotropy axis and the μ_3-oxygen is located 0.27 Å below the Mn_3 plane. The oximate twisting angle, υ = 44.15°, is relatively large.

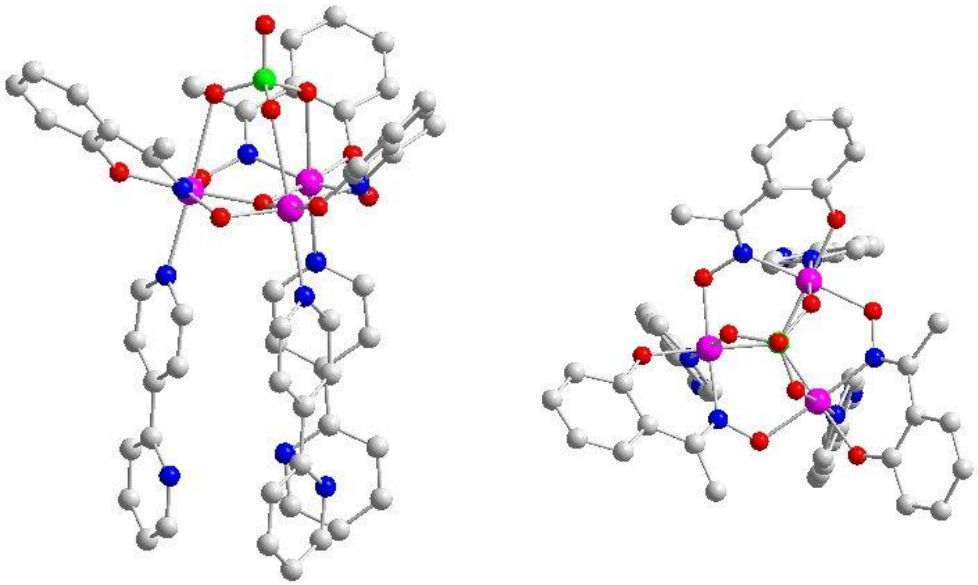

Figure 3.1: structure of **4** reproduced after [61] viewed orthogonal to the crystallographic *c* axis (left) and along the *c* axis (right)

The communication [61] presented DC susceptibility as well as AC susceptibility and magnetization hysteresis data. From this data the parameters for the single center Hamiltonian have been determined to be g = 1.95 and J = 3.58 cm^{-1}. The measured effective relaxation barrier was reported as U_{eff} = 37.5 K with $\tau_0 = 1.0 \cdot 10^{-7}$ s. The global ZFS value was estimated to be D = -1.3 cm^{-1}, which could not be reproduced by the author with the same data set. From the presented data [61] it is believed that a factor of two was forgotten in the calculation of the parameter. It should therefore be D = -0.65 cm^{-1}, which is more in the expected region for such systems [18, 20].

During his master thesis the author measured complex **4** and Mn_3O(Me-sao)$_3$(2,4′-bipyridine)$_3ReO_4$ (**5)** by INS and HF-EPR. This INS data was only measured at 6.5 Å incident wavelengths and therefore does not show all possible GS multiplet transitions. As the $M_S = \pm 1$ to $M_S = 0$ was not resolved, it could not be determined with certainty whether these molecules show a small rhombic anisotropy even though the EPR data for **5** suggested such a splitting. In this chapter we present the structure of compound **5** and high resolution INS spectra of **4** and **5**. Furthermore, Mn_3O(Et-sao)$_3$(2,4'-bipyridine)$_3ClO_4$ (**6**) a new analogous compound is introduced and its electronic ground state multiplet characterized by INS.

3.3 Synthesis

Me-saoH_2 and Et-saoH_2 have been prepared as described in ref. [60] by the addition of an excess amount of hydroxylamine to an aqueous suspension of *o*-hydroxyacetophenone and 2′-hydroxypropiophenone, respectively. After heating to 90 °C for 30 minutes the solution was cooled to room temperature and the white or yellow-white compounds crystallized.

Mn_3(Me-sao)$_3$(2,4′-bipyridine)$_3ClO_4$ (**4**) was synthesized according to ref. [61]. Mn_3(Me-sao)$_3$(2,4′-bipyridine)$_3ReO_4$ (**5**) was synthesized by a modified procedure of the one described in ref. [1] for the perchlorate analog:

277 mg of $Mn(ReO_4)_2$ (0.5 mmol, prepared from freshly precipitated $MnCO_3$ and perrhenic acid) was dissolved together with 75 mg of Me-saoH_2 (0.5 mmol) in 40 ml of MeCN. After addition of 0.1 ml NEt_3 (0.72 mmol) the colorless solution turned very dark. After 5 minutes of stirring 78 mg of 2,4′-bipyridine (0.5 mmol) was added and the solution was stirred for additional 30 minutes. After filtering the solution was left undisturbed for 3 days until **5** precipitated. The precipitated polycrystalline material formed, was washed with a mixture of MeCN:Et_2O (1:5). The yield was 42.1% based on Mn. Analytical composition for [Mn_3(Me-sao)$_3$(2,4′-bipyridine)$_3ReO_4$]·0.5MeCN calculated (found): C: 48.15 (48.51) %, H: 3.37 (3.26) %, N: 9.36 (9.65)%.

Mn_3(Et-sao)$_3$(2,4′-bipyridine)$_3ClO_4$ (**6**)was synthesized by a modified procedure of ref. [1]:

180 mg of $Mn(ClO_4)_2 \cdot 6\ H_2O$ (0.5 mmol) was dissolved together with 83 mg of Et-saoH_2 (0.5 mmol) in 30 ml of MeCN. After addition of 0.04 ml NEt_3 (0.288 mmol) the slightly yellow solution turned dark green. After 5 minutes of stirring 78 mg of 2,4′-bipyridine (0.5 mmol) was added and the solution was stirred for additional 30 minutes. After filtering the Et_2O was slowly diffused into the solution. After 3 days, compound **6** was obtained as polycrystalline material. Single crystals were obtained by slowly evaporating the solvent after the filtration, over a course of 2 weeks.

3.4 X-ray crystallography

X-ray diffraction analysis has been performed on single crystals of compounds **5** and **6**. Table 3.1 summarizes the structural parameters suspected of particular importance to the magnetic behaviour of compounds **4** to **6**, as well as different selected bond lengths and angles.

Compound **5** crystallizes in the trigonal space group *P*-3 with two molecules in the unit cell. Like compound **4** the three Mn(III) ions are linked by a μ_3-oxygen. Furthermore three Me-sao^{2-} ligands each coordinate to one metal center with the deprotonated phenolate group as well as the oximate N whilst bridging to the next Mn(III) with the oximate O in a μ_1:μ_1:μ_2 mode. The main difference to **4** is that the ClO_4^- group has been exchanged with ReO_4^-. The Mn-O4 distance is slightly smaller (2.461 Å)

than in compound **4** but the anisotropy axis can still be assumed to be approximately along this bond. The size difference between ClO_4^- and the considerably larger ReO_4^- (the O-Re distance is approximately 1.2 times as big as the OCl distance) leads to an alignment of the JT axes of the individual Mn centers relative to the structure of **4**. The tilting angle in this compound is δ = 12.9°. Other structural differences are a smaller μ_3-O out-of-plane shift and a bigger oximate twisting angle: The μ_3-oxygen lies 0.161 Å below the Mn_3 plane and the oximate twisting angle is υ = -46.4(1)°. The 2,4′-bipyridine ligands are disordered to the extent that 25% of them are rotated 160° around the axis approximately defined by N11, C14 and C17 (cf. Fig. 3.2).

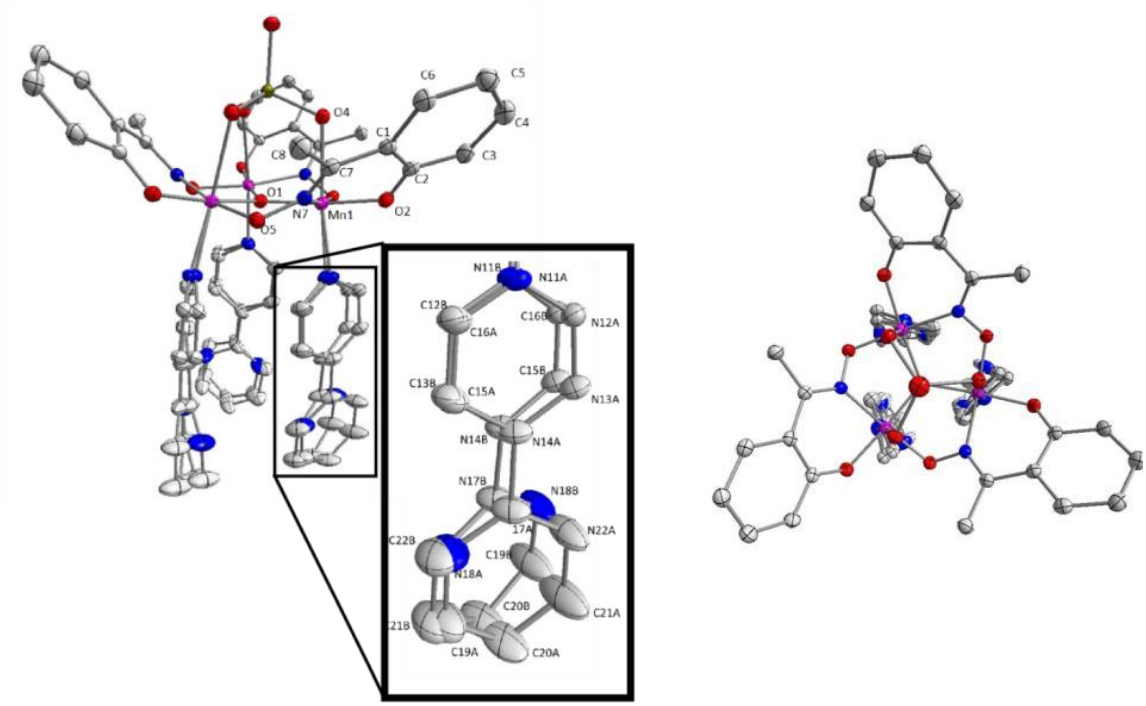

Fig. 3.2: structure of **5** along the three-fold axis (right), and perpendicular to it (right) the insert shows an amplification of the 2,4′-bipyridine ligands, showing their disorder. For reasons of clarity the solvent molecules as well as the hydrogen atoms have been omitted.

Compound **6** crystallizes in hexagonal, chiral space group *P*6_3, with four molecules in the unit cell. There are two different species (A and B) present in the crystal structure. In one species the oximate bridges Mn-N-O-Mn are oriented in a right handed way from the point of view of the ClO_4^-, while it is left handed for the other. The fact that these two chiral molecules are not centrosymmetric and therefore are not racemates, like in **4** and **5**, explains the chiral space group. The two species show very similar absolute values for the oximate twisting angle. With υ_A = -46.5(5)° and υ_B = 47.2(6)° the twisting angle is also similar to that observed for **2** and considerably bigger than that found in **4,** which is expected for the larger Et-sao^{2-} ligand compared to the Me-sao^{2-}. The two JT tilting angles of both

systems δ_A = 14.64°and δ_B = 14.64° are very similar to each other and to complex **4.** The same is true for the μ_3-O out-of-plane shifts which are 0.22 Å for one molecule and 0.28Å for the other.

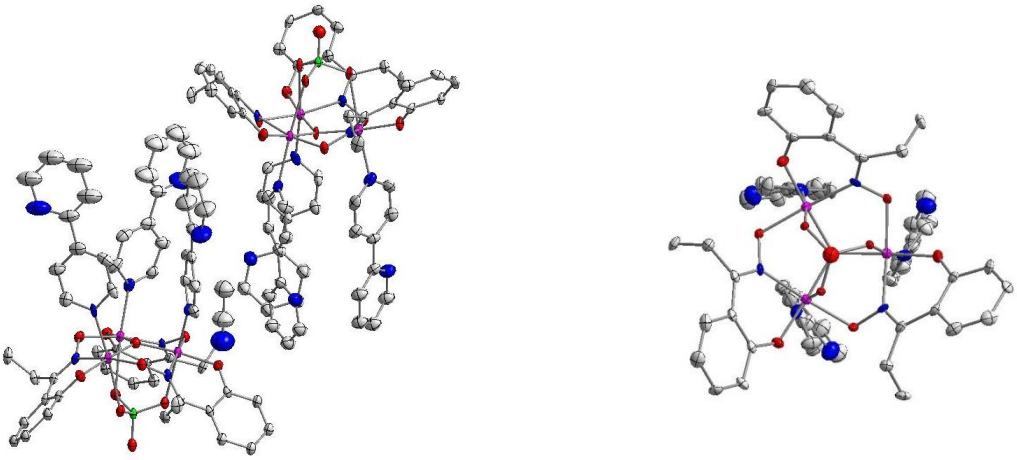

Fig 3.3: structure of compound **6** (left) head to tail arrangement of the two species A and B. (right) top view of species A along its anisotropy axis. Hydrogen atoms and solvent molecules were omitted for clarity.

To conclude, the structures of the here presented compounds are very similar, but show some interesting differences. The fact that two of the molecules (**5** and **6**) have a similar oximate twisting angle υ, while **4** and **6** show very similar tilting angles δ, means that this selection of compounds is very promising to study the isolated effects of those angles on the electronic structure.

Table 3.1: selected structural parameters for compounds **4**-**6**

	4	**5**	**6a/b**
υ[°]	-44.2(4)	-46.4(1)	-46.5(5), 47.2(6)
μ_3-O shift [Å]	0.269(6)	0.160(2)	0.288(8), 0.280(8)
δ	14.62	12.9	14.64,14.76
Mn-OX [Å][a]	2.556(3)	2.461(1)	2.544(6), 2.542(6)
Mn-N(bipyridine) [Å]	2.263(3)	2.29(1)/2.23(5)[b]	2.271(8), 2.272(8)
Mn-μ_3O [Å]	1.8989(9)	1.9100(3)	1.900(2), 1.890(2)
Mn-O(phenolate) [Å]	1.857(3)	1.866(6)	1.862(8), 1.858(5)
Mn-N(oximate) [Å]	1.984(6)	1.991(2)	1.982(5), 1.986(5)
Mn-O(oximate) [Å]	1.908(4)	1.920(2)	1.920(4), 1.902(7)
Mn-Mn [Å]	3.255(1)	3.2962(4)	3.252(2),3.247(2)
∠Mn-O-Mn [°]	118.05(3)	119.33(1)	117.74(5), 117.84(5)

a) X = Cl, Re; b) the two values originate from the disordered bipyridine

3.5 AC susceptibility:

The AC susceptibility of compound **6** has been measured and that of compound **5** has been re-measured since the presence of a small impurity was been suspected in the previously reported dataset [1]. All measurements were done in the absence of a static field and with an applied oscillating field with frequencies between 1 Hz and 1488 Hz and amplitudes of 3.5 Oe.

A plot of the in-phase as well as the out-of-phase susceptibility of compound **5** is presented in figure 3.4 while figure 3.5 contains the data of compound **6**. In Figure 3.6 the Arrhenius plots of both compounds are presented.

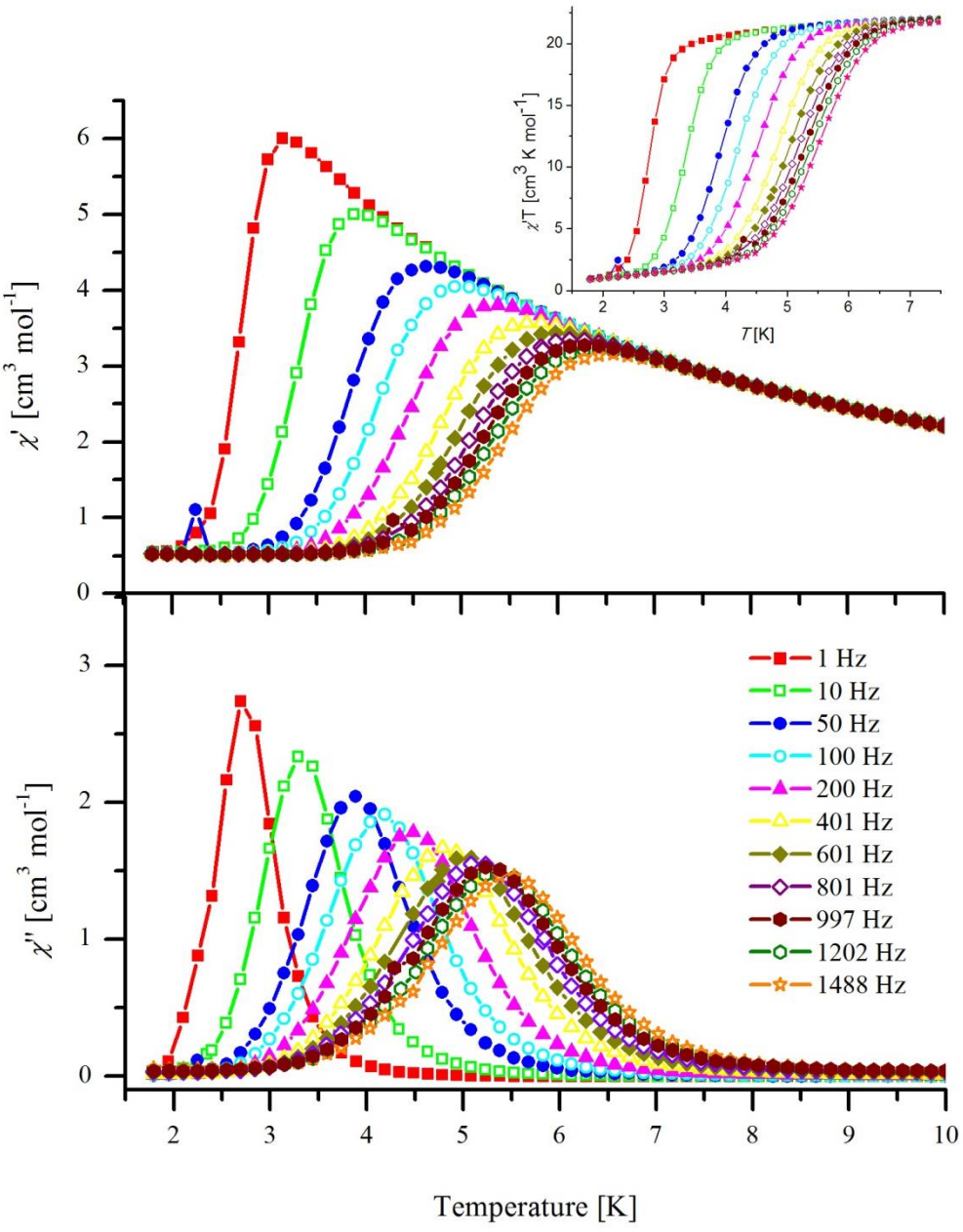

Fig 3.4: AC susceptibility of **5** in-phase signal (above) out-of-phase signal (below) and the $\chi'T$ vs T plot (insert).

The AC susceptibility data of both compounds **5** and **6** show expected similarities to the observed behavior of **4** [61]. The in-phase susceptibility of **5** and also **6** start to show frequency dependence below ca. 6.5 K. The susceptibility starts to reduce for higher frequencies while it still increases for low frequencies until it reaches a maximum at lower temperatures. At temperatures above 6.5 K $\chi' T$ is constant and independent of the frequency (see Fig 3.4, insert). This is concurrent with a similar frequency dependence of the out-of phase component of the susceptibility. For both compounds the out-of-phase signals show near-symmetrical peaks that go to zero at low temperatures for **5** and very close to zero for **6**.

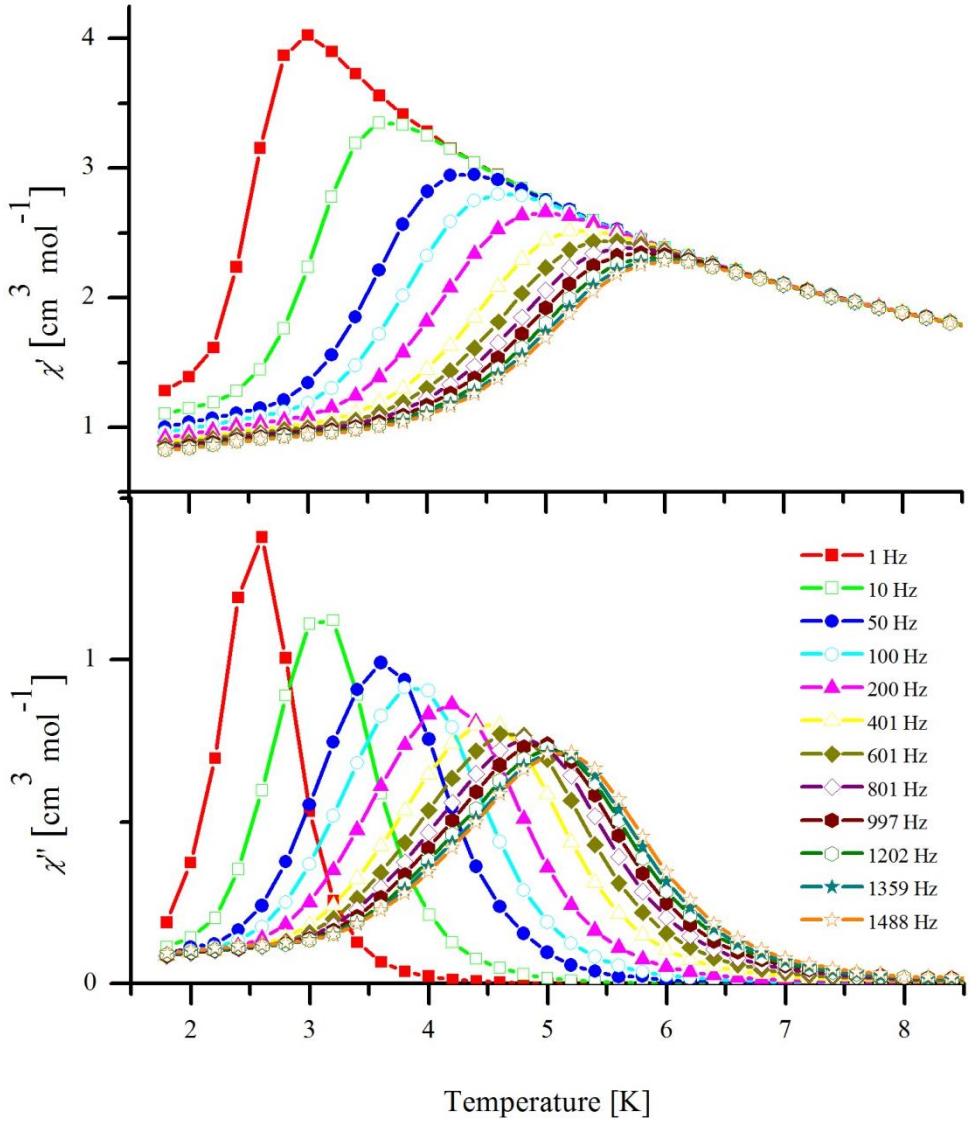

Figure 3.5: In-phase and out-of-phase AC susceptibility of compound **6**.

The frequency dependent peak positions of the out-of-phase signal were fitted to an Arrhenius equation. The effective barrier height of compound **5** was determined to be U_{eff} = 40.6 ± 0.9 K with τ_0 = $8.0 \cdot 10^{-8}$ s. The barrier for **6** U_{eff} = 38.1 ± 0.6 K with τ_0 = $7.5 \cdot 10^{-8}$ s.

The barrier height of compounds **4** and **6** are similar as expected due to the similar tilting angles δ, of the JT axes according to eq. 1.9 and 1.10 and 1.7 as well as references [8, 16]. Even though not many (but comparable with other studies[16, 23]) data points have been measured U_{eff} of **5** is significantly bigger than the values of **4** and **6.**

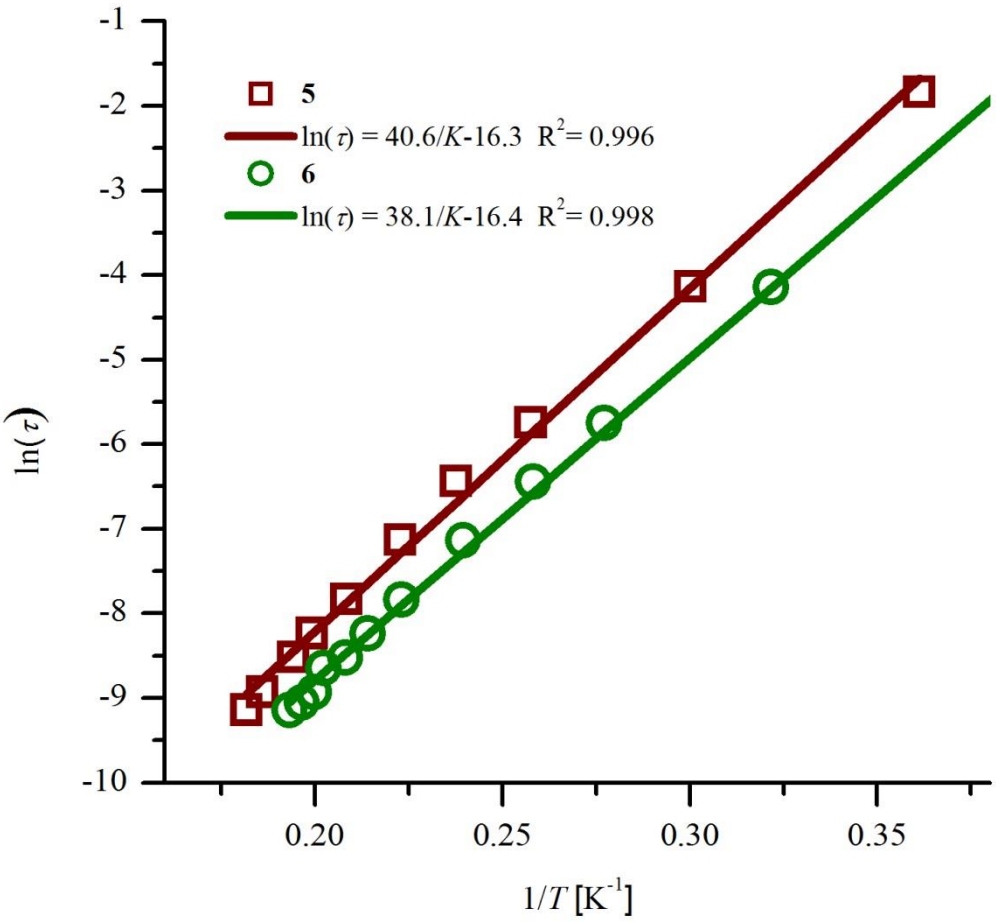

Fig 3.6: Arrhenius plot of compounds **5** and **6** for frequencies 1-1488 Hz.

3.6 Spectroscopy

The neutron spectra of compound **4** measured at 8.5 Å and 10 Å incident wavelengths at temperatures 15 K and 20 K respectively are presented in Fig 3.7 as neutron intensity vs. energy transfer plot summed over the whole *Q*-range. The peaks are labelled I to VI with additions of "a" for the neutron energy loss transitions and "b" for the energy gain transitions. The *Q*-ranges are 0.08 $Å^{-1}$< Q < 1.28 $Å^{-1}$ for λ_I = 8.5 Å and 0.08 $Å^{-1}$ < Q < 1.08 $Å^{-1}$ for λ_I =10 Å. Due to the noisy spectra obtainable at 10 Å the data was energy binned with ΔE = 0.01 meV. Apart from the already well ascertained transitions Ia, IIa, IIIa and IVa at 7.93, 6.28, 4.73 and 3.29 cm^{-1} respectively, the high resolution spectra enable a more accurate determination of the position of transition labeled V as well as the newly observed transitions labeled VI at 1.95 and 0.69 cm^{-1}, respectively. Transition V has FWHM 0.28 and 0.32 on the neutron gain and loss side of the spectrum measured at 8.5 Å. These values are considerably higher that the theoretical resolution of IN5 at these peak positions and the used chopper settings. The theoretical values are 0.13 cm^{-1} at ΔE = 1.95 cm^{-1} and 0.18 cm^{-1} at ΔE = -1.95 cm^{-1}. The same applies to VI where, at 8.5 Å incident wavelength, FWHM(gain) = 0.27cm^{-1} and FWHM(loss) = 0.304 cm^{-1} with theoretical resolutions of 0.16 cm^{-1} and 0.14 cm^{-1}. This is a clear indication of a mixing of the $M_S = \pm 1$ states as the mixed states split the transition in a doublet. Such a mixing can be explained by introducing a small rhombic anisotropy E into the GS Hamiltonian. A measurement at 10 Å incident beam wavelength, could not further resolve the widened transitions. The higher resolution of the 10 Å setting was countered by the low flux, which lead to such a noisy spectrum, that an energy binning of ΔE = 0.01meV had to be applied to see the transitions on the gain side. These results nevertheless show the importance of higher resolution measurements and this information could not have been extracted from 6.5 Å data as the resolution of the instrument is similar to the FWHM at this setting.

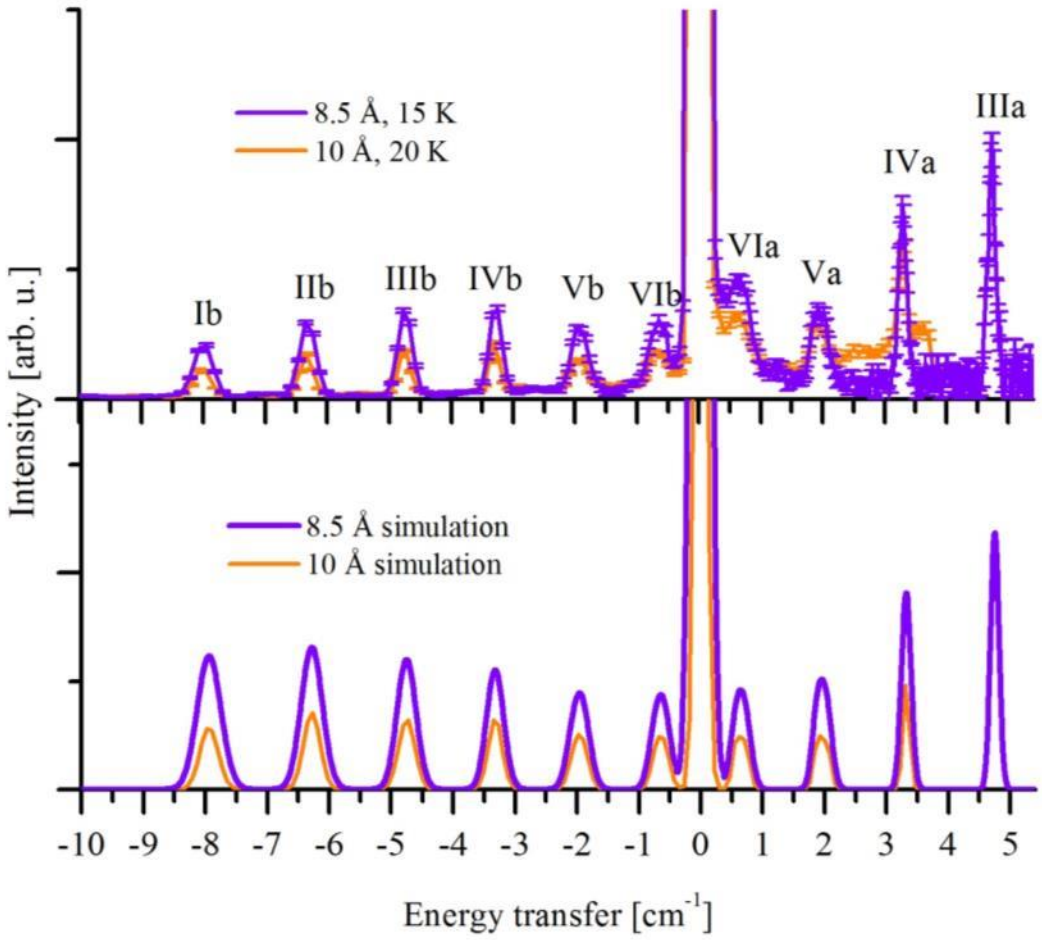

Fig 3.7: high resolution spectrum of **4** measured with 8.5 Å incident wavelength at 15 K and with 10 Å at 20 K. The 10 Å data have been energy-binned with ΔE = 0.01 meV (above). Simulation of the two spectra with the Giant Spin Hamiltonian parameters given in the text (below)

The INS data, together with the previously reported HF-EPR data [1] recorded at 285 GHz and 345 GHz and temperatures of T = 5 K, 10 K and 20 K each, were fitted to a GS Hamiltonian. The HF-EPR spectra recorded with 285 GHz radiation and their simulations are presented in Fig. 3.8. The angle dependence of the transitions show that the transitions at higher fields are mainly due to field that are applied orthogonal to the easy axis of the molecule (θ = 90°) while the much wider spaced transitions at low fields arise from field orientations parallel to the easy axis.

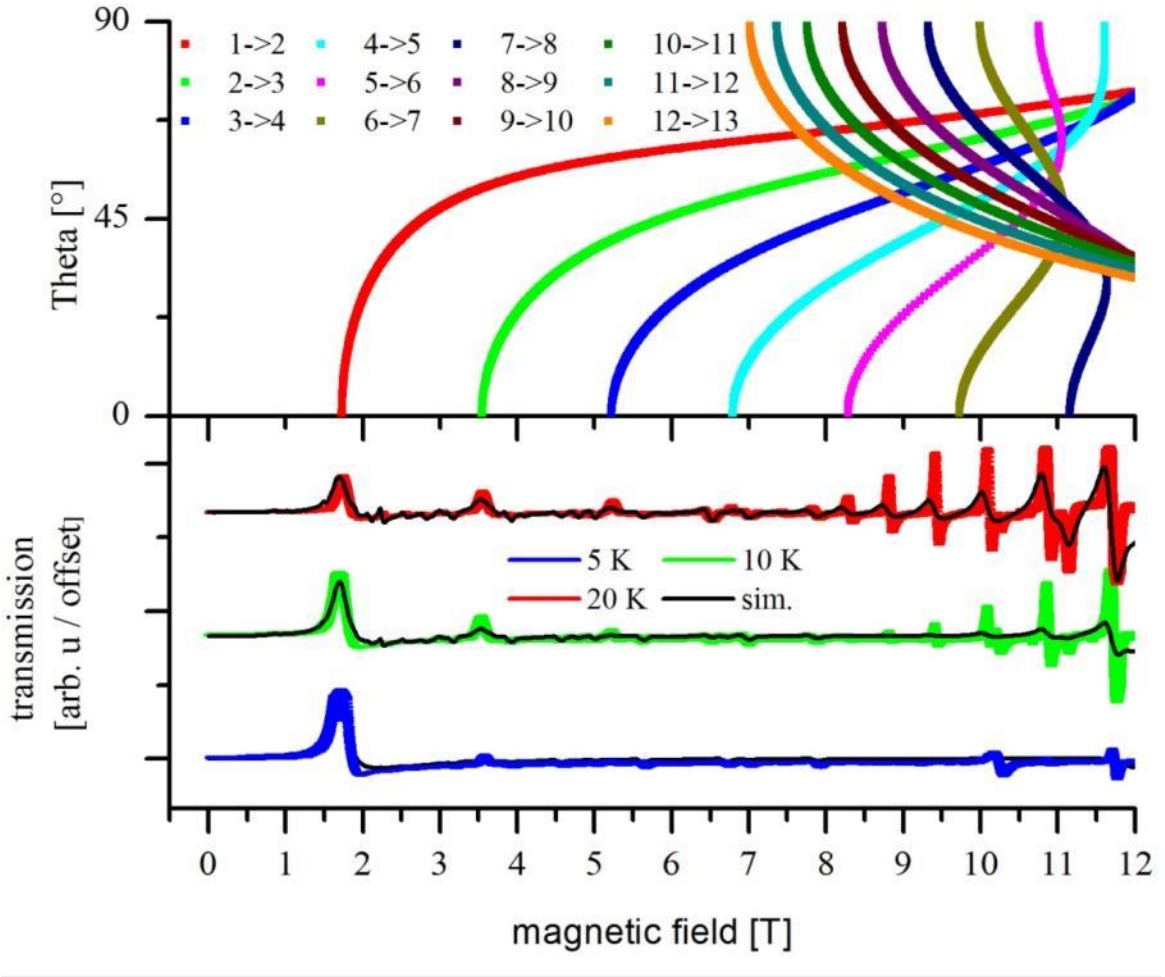

Fig 3.8: Below: EPR spectra and simulations of **4** measured at 285 GHz at 5 K, 10 K, 20 K and simulations. Top: Calculated angular dependence of transitions.

The GS Hamiltonian Parameters obtained from the fit of both the EPR and INS data are:

D = -0.69 cm^{-1}, E = -0.0036 cm^{-1}, B_4^0 = -3.43·10^{-5} cm^{-1}, $g_x = g_y$ = 1.99 and g_z =1.96

In Figure 3.9 a calculation of the field dependence of the GS multiplet transitions with two field orientations (parallel and orthogonal to the easy axis) is presented together with the measured INS and EPR transitions.

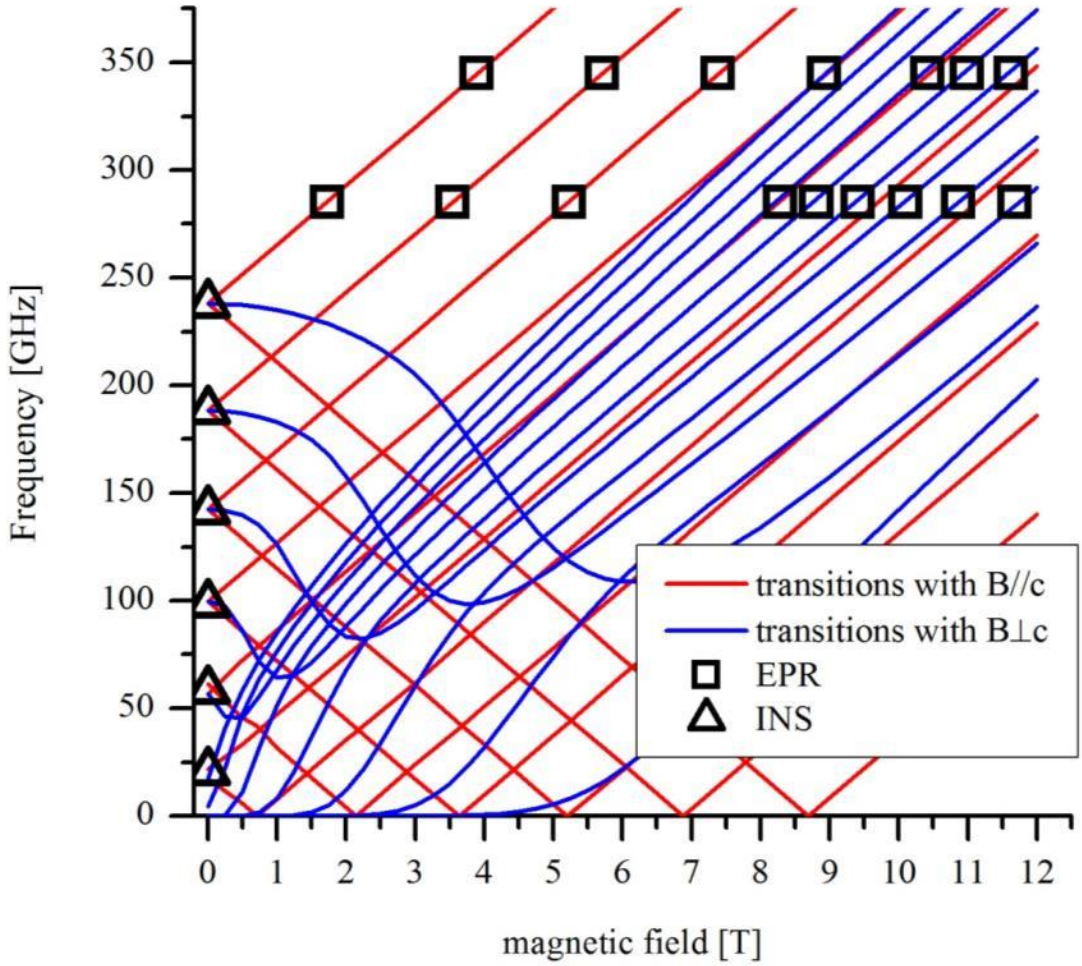

Fig. 3.9: field dependence of allowed transitions within the GS multiplet in **4**, with the field along the easy axis (red lines) and within the easy plane (blue lines). Observed EPR and INS transitions have been indicated.

Compound **5** has been measured at 8.5 Å incident wavelength and at 20 K. The observed transitions at -8.34 cm^{-1}, -6.67 cm^{-1}, ±5.08 cm^{-1} and ±3.58 cm^{-1} were in agreement with the previously presented data measured at 6.5 Å. Like for compound **4**, the higher resolution spectrum of **5** also shows that the peak corresponding to the M_s=±2 to M_s=±1 transition at ΔE = 2.1 cm^{-1} (FWHM=0.3 cm^{-1}) is significantly wider than the instrumental resolution at this position (0.12 cm^{-1}). In addition the lowest energy transitions, between M_s±1 and M_s=0 has been resolved. It lies at ΔE=0.7 cm-1 and is also widened by a mixing of the M_s=±1 levels. A fit of the observed peaks to Gaussian model distributions showed small differences between the energy gain and energy loss side for the M_s= ±6 to M_s = ±5 transition while all other transitions positions match. The energy loss transition is measured at a far higher resolution and is defined by more experimental points (the ΔE spacing between data points becomes smaller the bigger the energy transfer gets), therefore only the energy loss transition was used for the fit.

A direct comparison between the data sets of compounds **4** and **5** shows two noteworthy observations. While the lowest energy transition M_s=±1 to M_s=0 is nearly at the same position for both compounds, the M_s= ±6 to M_s = ±5 transition for compound **5** is shifted to higher energies. The latter clearly shows that compound **5** has a bigger ZFS than **4** and the former fact indicates that **4** must be described with a larger B_4^0 term than **5**.

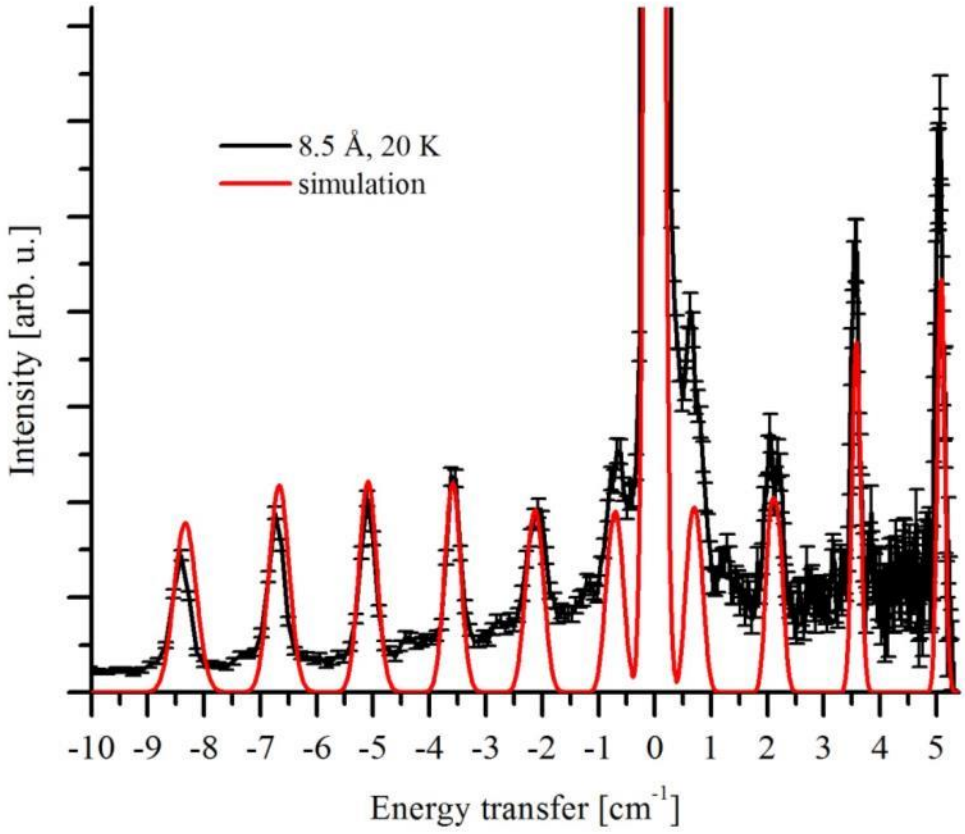

Fig 3.10 high resolution spectrum of **5** measured at 20K and 8.5Å.

For compound 5 previously reported EPR data included 190 GHz at T = 5 K and 20 K, 285 GHz at T = 5 K and T = 10 K and 345 GHz T = 5 K and T = 15 K. All the EPR data was fitted together with the INS data to a GS Hamiltonian Fig. 3.11 shows the data obtained at 190 GHz and the simulation of the spetra as well as the dependence of the individual transitions from the angle θ.

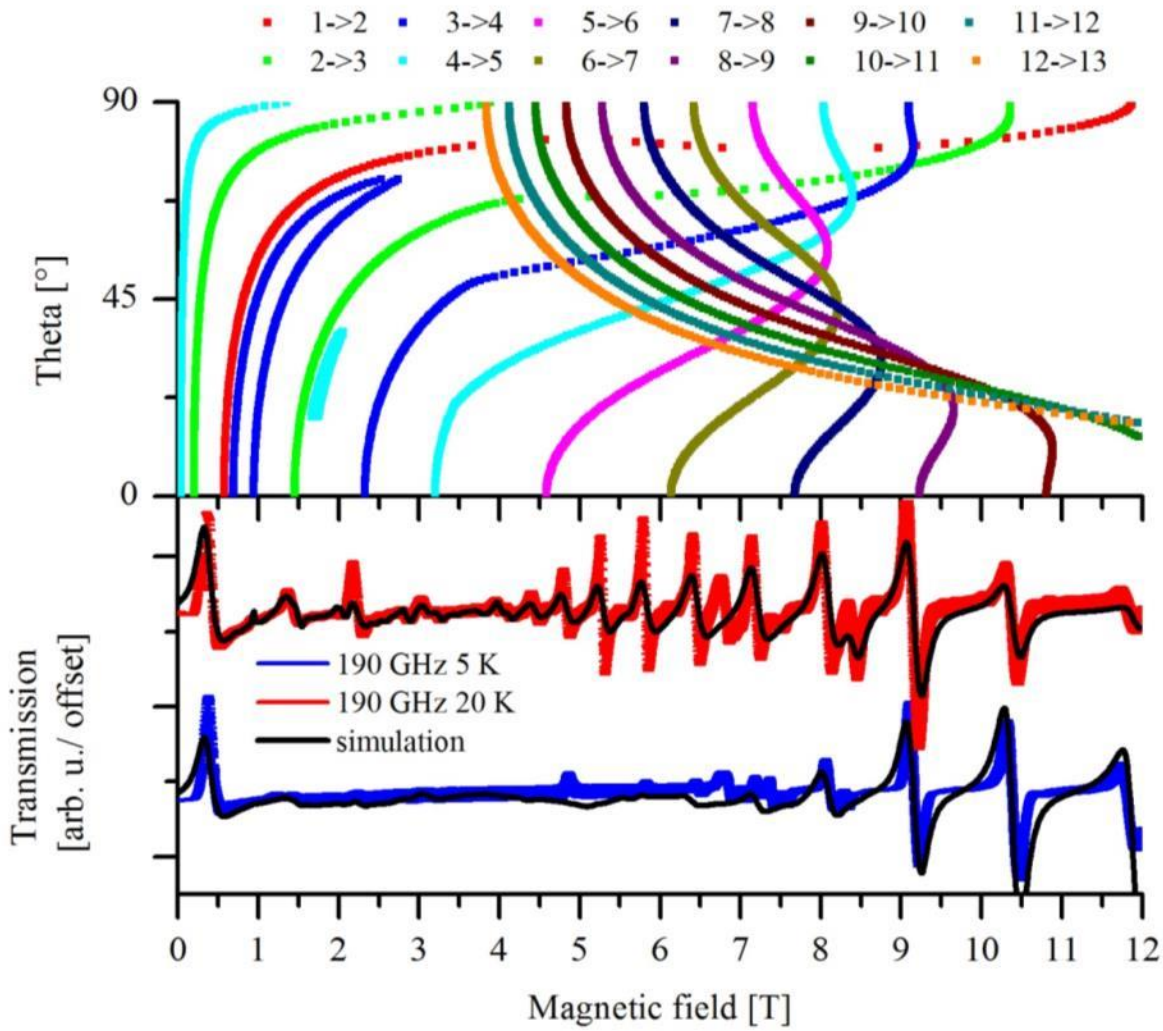

Fig 3.11: below: EPR spectra and simulations of compound **5** measured at 190 GHz at 5 K and 20 K and simulations. Above: angular dependence of transitions.

The GS Hamiltonian parameters obtained for **5** are:

D = -0.736 cm^{-1}, E = 0.0039 cm^{-1} B_4^0 = -2.43·10^{-5} cm^{-1}, $g_x = g_y$ =1.98 and g_z = 1.97

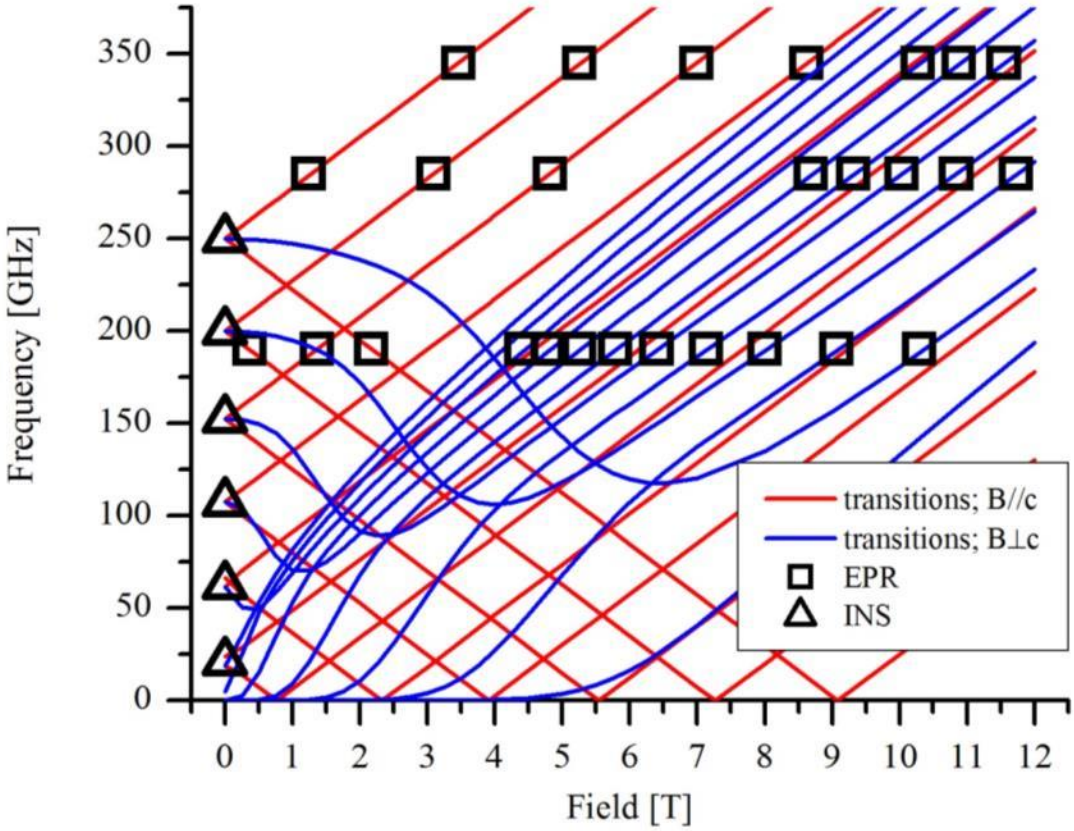

Fig. 3.12: field dependence of allowed transitions within the GS multiplet in **5**, with the field along the easy axis (red lines) and within the easy plane (blue lines). With observed EPR and INS transitions.

The INS spectra of compound **6** at 6.5 Å incident wavelength shows the typical temperature dependence already observed for **4** and **5**. At 20 K five transitions at energy transfers ΔE = 7.88 cm^{-1}, 6.24 cm^{-1}, 4.70 cm^{-1}, 3.27 cm^{-1} and 1.94 cm^{-1} can be observed on the energy loss side. With the higher resolution wavelength 8.5 Å one more transition on the energy loss side at ΔE = 0.65 cm^{-1} is resolved. Due to the fact that none of the observed peaks are split or broadened, it can be assumed that there is no rhombic anisotropy in this compound and that these peaks represent all possible transitions within the ground state multiplet of this compound. The peaks spacing on the energy gain side of the spectrum differ slightly from the loss side of the loss side, as previously observed. The peak positions at 6.5 Å are -7.91 cm^{-1}, -6.24 cm^{-1}, -4.69 cm^{-1}, -3.24 $cm^{-1}$and -1.91 cm^{-1}. For reasons mentioned above only the transitions on the energy loss sides of the spectra were fitted to a giant spin Hamiltonian. It yielded the parameters D = -0.683 cm^{-1} and B_4^0 = -3.77*10^{-5}. Figure 3.13 shows the temperature dependence of **6** measured at 6.5 Å incident wavelengths and simulated. Figure 3.14 shows the higher resolution spectrum measured at 8.5 Å and 20 K and the simulation.

Interestingly the two species **6a** and **6b** cannot be distinguished by the INS spectra. The reason is that they are structurally so similar that their magnetic behavior is identical to techniques with the resolution of the employed INS spectrometers.

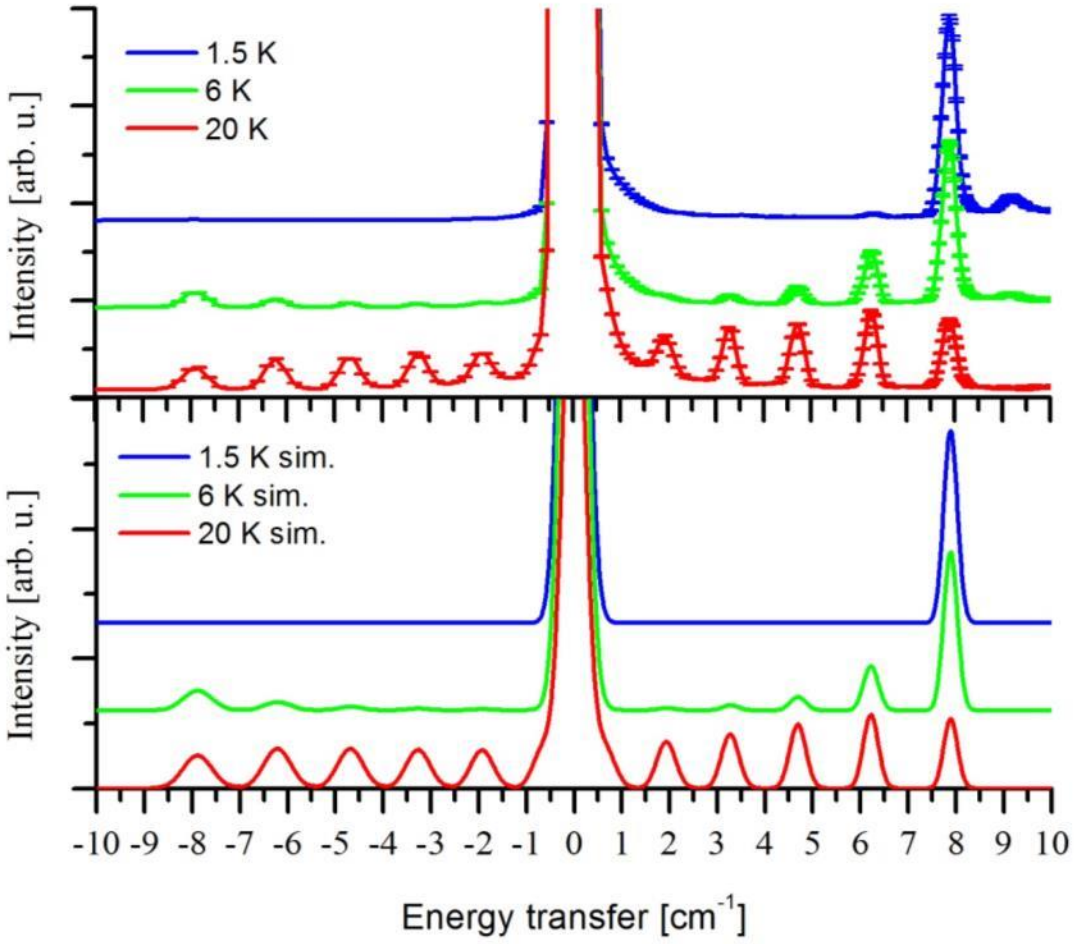

Fig 3.13: temperature dependence of **6** measured at 6.5 Å.

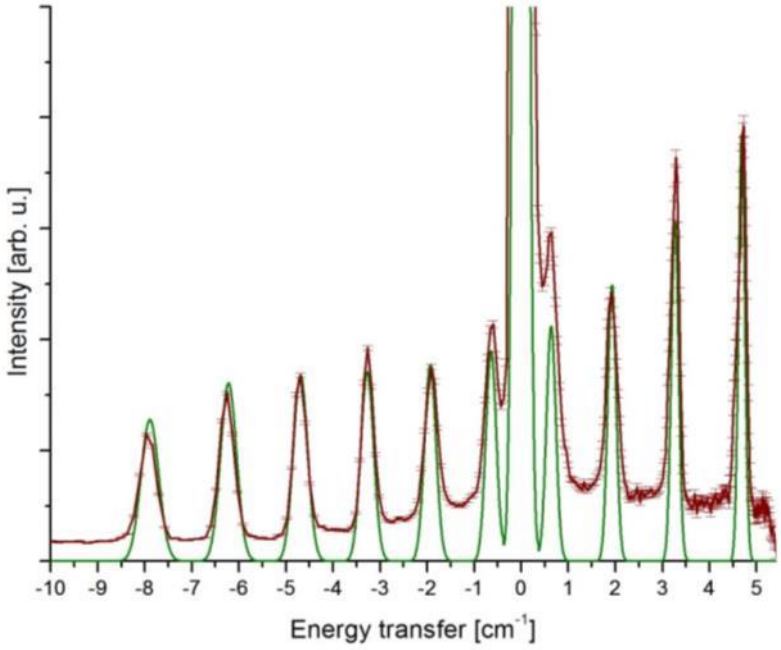

Fig 3.14: high resolution spectrum of **6** measured at T = 20K and 8.5Å.

3.7 Discussion/Summary

If all possible transitions within the GS multiplet are resolved and the rhombic anisotropy is small (i.e. no peak is split into two), the sum of all transitions on either side of the elastic line represents the energy difference between the lowest and the highest state in the Ground state multiplet[46]. These so called spectroscopic barrier heights were obtained for the three compounds measured in this chapter. For **4** it is U_{spec}=35.8 K, for **5** U_{spec}=38.1 K and for **6** U_{spec}=35.5 K. The spectroscopic barriers show the same trend as the effective barrier determined by AC susceptibility measurements. The barrier of **5** is higher than the barriers of the two other compounds, which can be attributed to a bigger ZFS and ultimately to the smaller ZFS tilting angle δ. All values for U_{eff} are smaller than the corresponding U_{spec}, which is intrinsically impossible. The spectroscopical barrier is the energy difference between m_s = 6 and m_s = 0 while the effective barrier allows for alternative relaxation pathways due to tunneling. Therefore $U_{eff} \leq U_{spec}$ applies. The small difference between the two barriers is attributed to the relatively inexact method determination of U_{eff} compared to spectroscopic methods. While INS provides a direct method to determine the U_{spec}, U_{eff} is determined by a linear regression and results vary significantly for different ranges of used frequencies. It can therefore be concluded that $U_{eff} \approx U_{spec}$, which means that the relaxation of magnetization in these compounds is only happening by absorption and emission of phonons and not by (thermally assisted) tunneling.

In Table 3.1 the measured parameters describing the systems are listed as a basis for discussion.

Table 3.1 Deduced parameters for compounds **4**-**6**

	4 $Mn_3O(Me\text{-}sao)_3(2,4'\text{-}Bipy)_3ClO_4$	**5** $Mn_3O(Me\text{-}sao)_3(2,4'\text{-}Bipy)_3ReO_4$	**6** $Mn_3O(Et\text{-}sao)_3(2,4'\text{-}Bipy)_3ClO_4$
υ [°]	-44.2(4)	-46.4(1)	-46.5(6), 47.2(6)
δ [°]	14.62	12.9	14.64,14.76
D [cm^{-1}]	-0.69	-0.74	-0.68
E [cm^{-1}]	0.0036	0.004	0
B_4^0 [cm^{-1}]	$-3.43\cdot10^{-5}$	$-2.43\cdot10^{-5}$	$-3.77\cdot10^{-5}$
g_x,g_y,g_z	1.99, 1.99,1.96	1.98, 1.98, 1.97	not obtained
D_i [cm^{-1}]	-2.70	-2.86	-2.66
U_{eff}[K]	37.5	40.6	38.1
U_{spec} [K]	35.8	38.1	35.5

The structures and high resolution INS spectra presented in this chapter together with previously reported EPR data represent a model experiment to show how the global anisotropy of a polynuclear complex of paramagnetic centers can be optimized by aligning the local anisotropy axes of those centers. The high resolution spectra of compounds **4** and **5**, as additions to the previously reported spectra, proved to be crucial for the detailed characterization of their ground state multiplets as they revealed small rhombic anisotropies present. This can be explained by defects in the crystals, such as missing solvent molecules that reduce the symmetry without being observable by X-ray diffraction, which demands that the distortions to be very small. It was shown how the exchange of the small tridentate capping ligand ClO_4^- with the bigger ReO_4^- aligns the local ZFS axes by 1.72° and therefore increases the global ZFS. As a counterintuitive side effect of the alignment, the oximate twisting angle, υ, of compound **5** increased as well. Compound **6** shows similar twisting angles as **5** as a result of steric effects from the larger Et-group on the aldoximate ligand. As the oximate twisting angles υ are determining the exchange coupling interaction [34, 62], compound **5** and **6** have a larger exchange coupling parameter than compound **4.** As it is not always possible to obtain reliable exchange coupling parameters from DC susceptibility data in these systems, it can only be observed in the higher order terms. Forth order terms result from S-mixing of the GS multiplet with higher states, and scale therefore with J/D [42, 63]. The larger J in **5** compared to **4** leads to a larger separation of the GS multiplet from higher-lying multiplets, which can be observed in the reduction of the B_0^4 parameter. The same dependence should lead to a small 4^{th} order parameter in **6,** which is not the case. This has to

be further investigated by INS on a completely deuterated sample of **6**, in hope of directly determining the exchange coupling parameter and by HF-EPR spectroscopy, in order to confirm the 4^{th} order term.

4. Effects of intermolecular interactions in extended 2D networks of trimeric Mn(III) core SMMs

4.1 Abstract

Commonly, intermolecular interactions are ignored in the analysis of the magnetic properties of SMM's. Whether this is justifiable is not a question which is very simple to answer. The effects of intermolecular interactions can be disguised in the parametrization of the individual molecules and hence the data does not necessarily allow for distinguishing the effects of intermolecular interactions. The trinuclear systems studied in this thesis carry the benefit of being extremely well characterized and could therefore furnish a possible test-case for evaluating the importance of intermolecular interactions in determining barriers for SMM's. In this chapter we focus on three $Mn_3O(R\text{-}sao)_3(MeOH)_3XO_4$ -type complexes (where R=Me, Et and X = Cl or Re). These molecules possess relaxation barriers U_{eff} that are higher than would be expected from experience with the similar complexes in the previous chapters. This could be an effect of intermolecular coupling. Two literature compound and one new member of this family of compounds have been synthesized and the intermolecular exchange interaction of the new compound has been estimated by fitting the magnetic data with a correction utilizing molecular field approximation. A previous study using EPR suggested a Giant spin Hamiltonian with parameters up to 6^{th} order but excluding intermolecular exchange interactions to describe the electronic structure at low temperatures [18]. INS measurements show that this model does describe the reality well.

4.2 Introduction

A new class of $[Mn_3O]^{7+}$ core SMMs with unusually large relaxation barriers have been discovered in 2008 [2]. The first examples were $Mn_3O(Et\text{-}sao)_3(MeOH)_3ClO_4$ (**7**) and $Mn_3O(Et\text{-}sao)_3MeOH(H_2O)_2ReO_4$. While the latter is not trigonal and will for that reason not be discussed further, compound **7** crystallizes in the trigonal space group $R\bar{3}$ with the unit cell parameters a = b =13.4 Å, c= 34.1Å, α = β = 90° and γ = 120°. A depiction of the molecular structure of **7** is given in Figure 4.1.

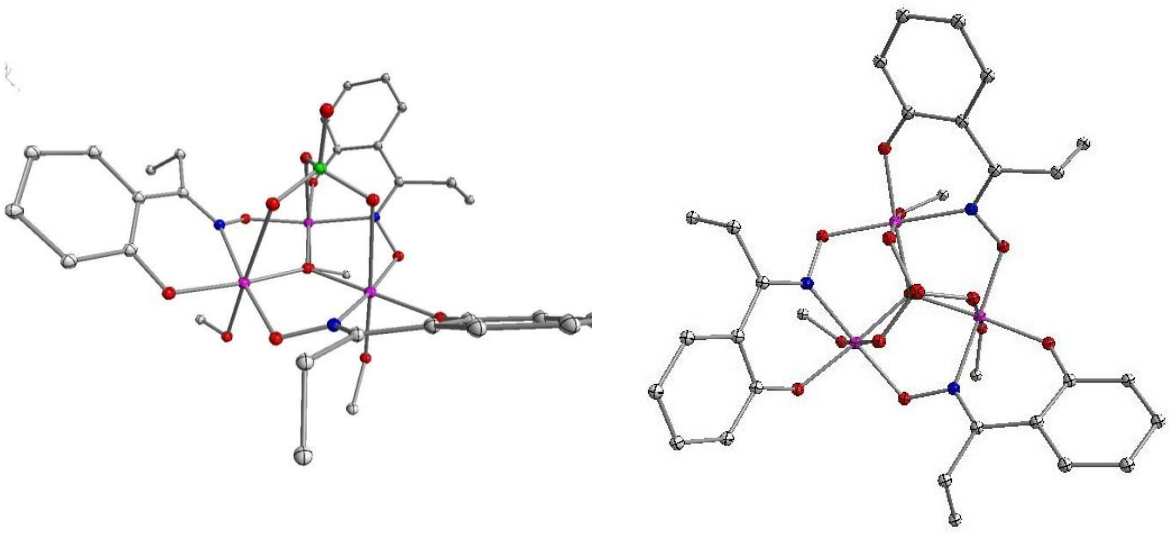

Figure 4.1 Structure of $Mn_3O(Et\text{-}sao)_3(MeOH)_3ClO_4$ **7** reproduced after [2] along the c axis (right) and perpendicular to it (left) Hydrogen atoms have been omitted for clarity

The methanol enables hydrogen bonding between each molecule and its three next neighbors. Each MeOH-hydrogen bonds to the sao^{2-} phenolate of the closest neighboring molecule, with a bond distance of *d*=1.946(1) Å. This leads two layers of head to head arranged molecules, with a distance of 3.67 Å between the two nearest Mn planes. The distance to the next Mn_3 double layer is 8.32 Å. One molecule from one layer is therefore hydrogen bonded to its three next nearest neighbors in the next Mn_3 layer, which leads to a hexagonal superstructure shown in Fig.4.2.

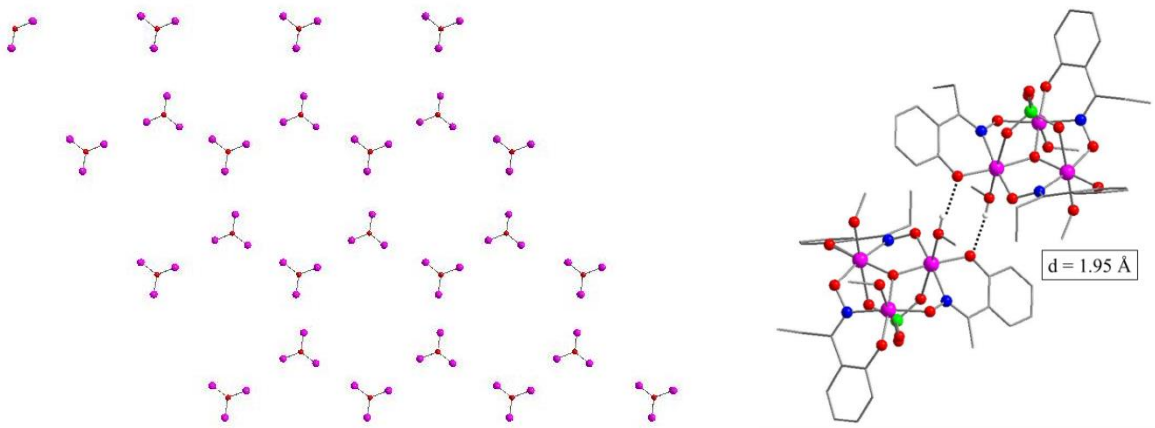

Figure 4.2: (left) Network of compound **7** viewed along the c-axis. All atoms apart from the $[Mn_3O]^{7+}$ core have been omitted for clarity. (right) H-bridges between two neighboring molecules, all H-atoms apart from the ones taking part in the bond are omitted.

The magnetic behavior of the non-trigonal $Mn_3O(Et\text{-}sao)_3MeOH(H_2O)_3ReO_4$ was not presented in the original publication but it was reported to be very similar to that of **7.**

Compound **7** has an effective barrier of U_{eff} of 57.8 K. The best possible fit of the DC data afforded an exchange coupling parameter J= 2.8 cm^{-1} in the temperature range 75K-300K. The problems encountered with modelling of the DC data at lower temperatures were rationalized by the effects of inter-molecular interactions, due to the hydrogen bonding. The effect of the intermolecular interactions can also been observed in single crystal magnetism hysteresis measurements. As it can be seen in Figure 4.3 there is no step at 0T which is an indication for antiferromagnetic interactions between the Mn_3 units. Furthermore apart from the dominant resonance at H ≈ 0.9 T there are several smaller features that are qualitatively rationalized by a bias field originating from the antiferromagnetically coupled neighbouring molecules. The reduced magnetization data was only fitted at low temperatures and high fields. A Giant spin model with parameters S=6 and D=-0.9 cm^{-1} was reported to reproduce the data best but with a "still rather poor"[2] agreement. The ZFS parameter is overestimated, as the fit does not include intermolecular exchange interactions. To achieve such a big global anisotropy D with the single centre tilting angles θ = 12.96°, the single centre anisotropies would have to amount to for these complexes rather unrealistically high values of D_i= 3.5 cm^{-1}.

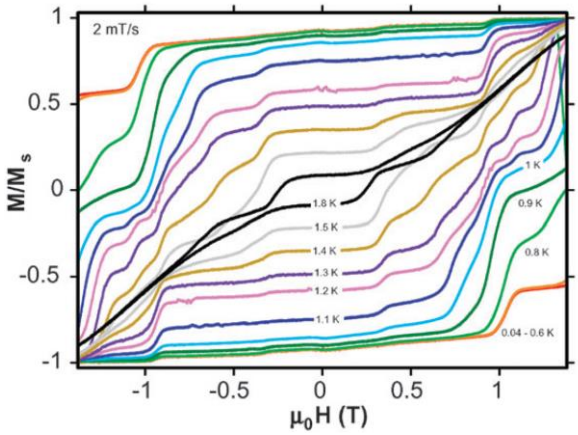

Figure 4.3: *M* vs, B single crystal hysteresis measurement of compound 7 **[2]**

In a 2009 publication high field, high frequency EPR data of **7** measured with 91 GHz radiation and fields in the hard plane were presented and fitted to a GS Hamiltonian giving the following parameter values [18]:

D=-0.686 cm^{-1}, B_0^4 = -5.04*10^{-5} cm^{-1}, B_3^4 = -7.42*10^{-5} cm^{-1}, B_6^6 = -1.1*10^{-5} cm^{-1}.

With $Mn_3O(Me\text{-}sao)_3(MeOH)_3ClO_4$ (**8**) and $Mn_3O(Ph\text{-}sao)_3(MeOH)_3ClO_4$, two analogous compounds have recently been presented by Yang et. al. [64]. Both complexes differ from **7** by the organic part of the salicylic aldoximate ligand R-sao^{2-}. The change from Et-sao^{2-} to Me-sao^{2-} from **7** to **8** is rather small and structurally these compounds are very similar. Contrarily to that, $Mn_3O(Ph\text{-}sao)_3(MeOH)_3ClO_4$, does not form the 2D networks like **7** and **8**. Instead of each MeOH group forming hydrogen bonds to a different neighboring molecule, all three MeOH ligands form bridges to the ClO_4^- group of the same neighbor (see Figure 4.4).

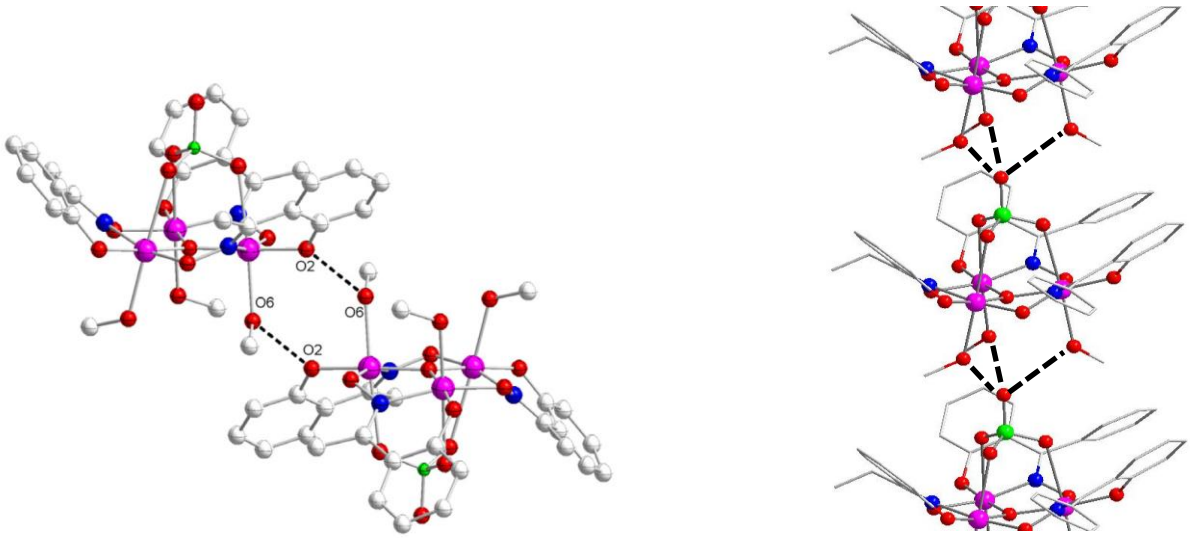

Figure 4.4: Structure and intermolecular interaction of $Mn_3(Me\text{-}sao)_3(MeOH)_3ClO_4$ **8** (left) and $Mn_3(Ph\text{-}sao)_3(MeOH)_3ClO_4$

The DC susceptibility of both complexes was measured and the data were modeled to a Hamiltonian containing only the exchange coupling term $J=J_1=J_2=J_3$, the Zeeman terms plus a correction for the intermolecular exchange interaction using the molecular field approximation. In this correction the magnetic moments of neighboring spins act as an external field on a given spin. The susceptibility in this model is obtained with the expression given in eq. 4.1[56, 65, 66]:

$$\chi = \frac{\chi_0}{1-\frac{zJ'}{g^2\beta^2}\chi_0} \qquad 4.1$$

Where z is the number of nearest neighbors, J' is the intermolecular exchange coupling parameter and χ_0 is the susceptibility without intermolecular exchange. The obtained parameters were g=1.99 J=2.71 cm^{-1}, J'= -0.12 cm^{-1} for compound **8** with z=3 and g=2.01 J=3.13 cm^{-1}, J'= -0.01 cm^{-1} for $Mn_3(Ph\text{-}sao)_3(MeOH)_3ClO_4$ with z=2. The much smaller intermolecular exchange coupling in $Mn_3(Ph\text{-}sao)_3(MeOH)_3ClO_4$ as compared to that of compound 8, can be explained by the different exchange pathways. Unsurprisingly the MeOH-phenolate H-bridge in **8** promotes stronger interaction, as it is a much shorter exchange pathway. Furthermore the higher number of neighbors in for compound **8** enhances the influence of intermolecular exchange in this complex even further. The effect of this can be seen in the $\chi_M T$ vs T plots where the maximum value of $\chi_M T$ of compound **8** (17.3 cm^3 K mol^{-1}) is reduced in respect to the one for $Mn_3(Ph\text{-}sao)_3(MeOH)$ (20.7 cm^3 K mol^{-1}) which with its small J' is very close to theoretical value for isolated ferromagnetically coupled Mn_3 complexes (21 cm^3 K mol^{-1}). The influence of the intermolecular interactions (zJ') can additionally be observed in singe-crystal hysteresis measurements. In Figure 4.5 a direct comparison between the single crystal hysteresis measurements of the two compounds are reprinted from [64] for illustration purposes. The hysteresis curves of $Mn_3(Ph\text{-}sao)_3(MeOH)_3ClO_4$ are very similar to the curves recorded for isolated Mn_3 SMMs such as compound **4 (**Chapter 3) [61], and shows only steps in the magnetization attributed to

tunneling due to interferences between M_S states. For compound **8** however many more weaker steps have been found.

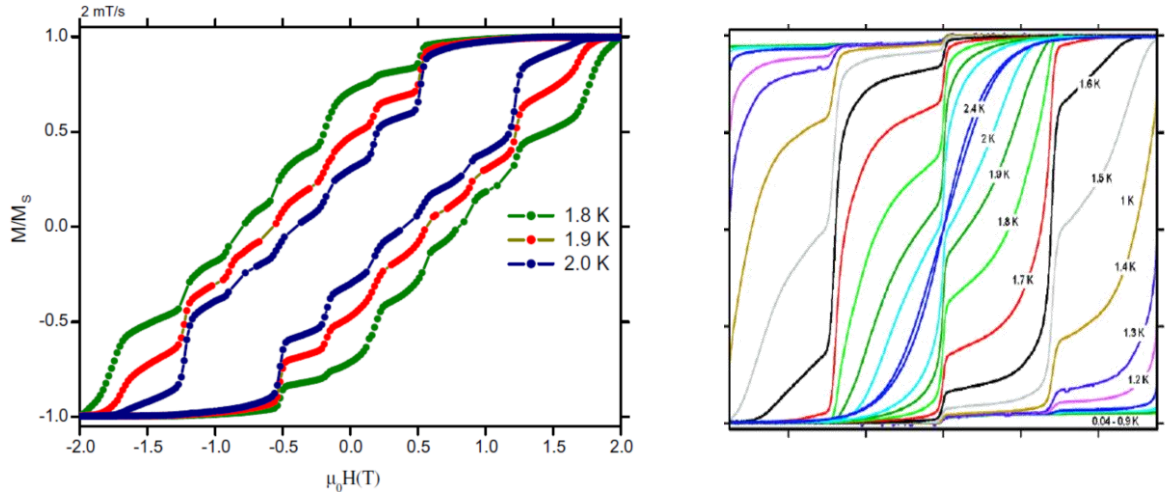

Figure 4.5: Single crystal hysteresis of **8** (left) and $Mn_3(Ph\text{-}sao)_3(MeOH)_3ClO_4$ (right) obtained from [64]

The original study [64] of **8** and $Mn_3(Ph\text{-}sao)_3(MeOH)_3ClO_4$was focused on the effect of the crystal packing on the intermolecular exchange, therefore no analysis of the ZFS of the ground state has been performed. Furthermore neither of the reported values of the ZFS parameter (for magnetization and EPR data) of compound **7** alone offer an explanation for the very big relaxation barriers in these compounds as the theoretical barrier in this case is $U = U_{spec} = DS^2 < U_{eff}$ [20]. As this is not possible, the intermolecular coupling has to be included as a factor hindering the relaxation. The analysis of these intermolecular interactions is therefore crucial for the understanding of relaxation behavior in these kinds of complexes. There have been synthetic efforts to create new extended networks comprised of Mn_3O core SMMs [17, 20, 67] but there still lacks a method to quantify the intermolecular interaction and its effects. In this chapter INS data of **7** and **8** have been recorded with the goal to see the effect of *J*' in the ground state splitting at zero field, (opposed to the EPR measurements performed on compound **7** mentioned above), as the removal of the Zeeman terms from the model constitutes an important simplification of the problem. Furthermore with $Mn_3O(Me\text{-}sao)_3(MeOD)_3ReO_4$ **9** a new compound has been synthesized and its magnetic properties characterized. The exchange from ClO_4^- in **8** to ReO_4^- in **9** was an attempt of aligning the single center anisotropy axes following the examples of Chapter 3 and ref [2].

4.3 Synthesis

The ligands Me-saoH_2 and Et-saoH_2 were synthesized after [60] as described in the previous chapters. $Mn(ReO_4)_2$ was synthesized by reacting $HReO_4$ (which was obtained from NH_4ReO_4 by ion-exchange) with freshly precipitated $MnCO_3$ All other chemicals have been commercially obtained.

Mn_3(Et-sao)$_3$(MeOH)$_3ClO_4$ (**7**) was synthesized after [2]

Mn_3(Me-sao)$_3$(MeOH)$_3ClO_4$ (**8**)was synthesized after [64]

Mn_3(Me-sao)$_3$(MeOH)$_3ReO_4$ (**9**) was synthesized after a modified procedure of [64]:

563 mg (1.01mmol) of $Mn(ReO_4)_2$ was dissolved in 20 ml MeOH with 151 mg (1 mmol) Me-saoH_2 and 110 mg (1.09 mmol) NEt_3. After stirring for 2 h, 60 ml of Et_2O were added. The solution was filtered and left undisturbed. After one to three days, small cubic-shaped dark crystals of **9** formed. The yield was 64% based on Mn. Elemental analysis found (calc.): C: 33.11(33.27), H: 3.05 (3.41), N: 4.08 (4.31). The result of the x-ray diffraction and IR measurement are in the appendix A.

The samples for INS were produced by using crystals of **9** as seeds, in order to obtain smaller and highly pure crystallites. Furthermore, a mono deuterated analog of the compound Mn_3(Me-sao)$_3$(MeOD)$_3ClO_4$ was synthesized by use of mono deuterated methanol instead of the standard one as solvent. The in this way deuterated crystals form faster and to bigger sizes. This is probably contingent on the lower water content of MeOD compared to MeOH.

4.4 Crystallography

In addition to a single crystal diffraction experiment where the MeOH ligands were very disordered, a neutron diffraction experiment on the "Very Intense Vertical Axis Laue Diffractometer" VIVALDI was performed.

A black single crystal of $Mn_3O(Me\text{-}sao)_3(MeOD)_3ReO_4$ (size: 3 x 3 x 1 mm) was wrapped in Al foil, mounted to a Al/V pin and placed in a standard ILL orange cryostat. Data was collected at 295 K and 2 K. the sample was rotated around the axis of the cryostat 14 steps at 295K and 15 at 2 K respectively.

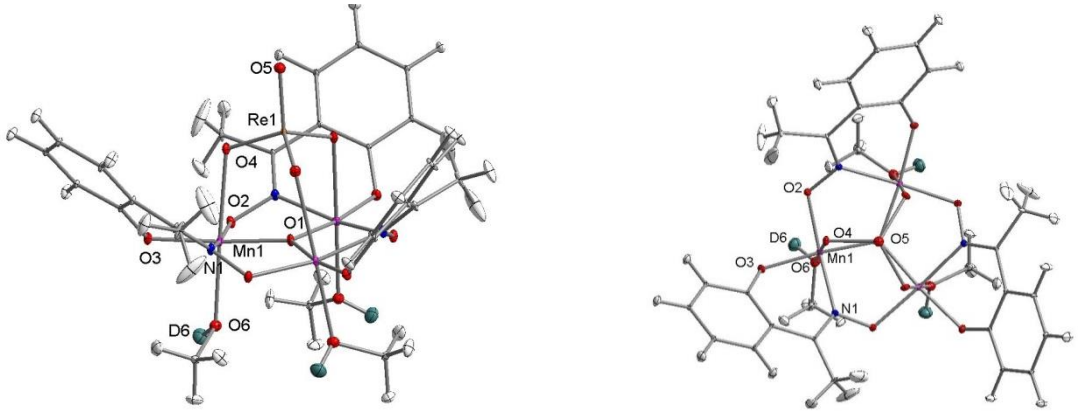

Figure 4.6 Structure of **9** at 2 K determined by single-crystal neutron diffraction on VIVALDI

Like **8**, compound **9** crystallizes in the trigonal space group $R\bar{3}$. With parameters $a = b = 12.76$, $c = 35.68$, $\alpha = \beta = 90°$, $\gamma = 120°$ V=5034.47 the unit cell contains six molecules and is only is slightly smaller than the one of **8.** The resulting structure is shown in Figire 4.6 and the most important distances and angles of this compound are listed and compared with compounds **7** and **8** in Table 4.1. There is no phase transition between the low and high temperature data. There is a small elongation of all coordinate bonds when cooling as well as a bigger oximate twisting angle υ and a smaller JT tilting angle δ. The exchange from ClO_4^- in **7** and **8** to ReO_4^- **9** reduces the JT tilting angle δ by over 3°. The oximate twisting angle υ of **7** and **9** are very similar, while it is smaller for **8.** O1 is furthermore nearly lying in the Mn_3 plane in **9** and considerably shifted out of the plane in the other compounds.

Table 4.1 Selected distances and angles

	7	**8**	**9 2K/295K**
υ	-42.12(14)	-39.25(12)	-42.94 / -42.72
δ	12.96	12.44	9.12 / 9.61
H-bond distance	1.946(1)	2.069(1)	1.731 / 1.777
*Mn-O4	2.550(1)	2.579(1)	2.451 / 2.447
*Mn-O6	2.192(1)	2.192(1)	2.221 / 2.209
*Mn-O1	1.8794(4)	1.879(1)	1.859 / 1.838
*Mn-O3	1.882(2)	1.908(1)	1.855 / 1.823
*Mn-O2	1.903(1)	1.8767(3)	1.881 / 1.851
*Mn-N1	1.990(1)	1.994(1)	1.989 / 1.951
*∡Mn-O-Mn	119.02(9)	119.42(9)	119.98 / 119.95
*O1-Mn_3-plane	-0.1792(17)	-0.1485(18)	-0.029 / -0.041

*The labeling differs from structure to structure, the labels used in this table are the ones of compound **9** shown in Fig 4.6.

4.5 magnetic measurements

Susceptibility and magnetization measurements have been performed on **9**. The susceptibility data measured with B = 1000 Oe over the Temperature range of 1.9-300 K is represented in figure 4.7 as a $\chi_M T$ vs. T plot. The magnetization data was collected at 2, 3, 4 and 5 K with magnetic fields between B = 50-50000 Oe (figure 4.8). Contrary to the above mentioned studies these data sets were both modeled to a Hamiltonian containing the exchange coupling term $\widehat{H}_{ex}$ (eq. 1.4) and ZFS terms $\widehat{H}_{ZFS}$ (eq. 1.6). In the fit of the susceptibility data the intermolecular exchange parameters J' enters as a correction of χ using MFT as it has been applied for **8** [64], see eq. 4.1.

To fit the magnetization data, the same Hamiltonian as for the susceptibility data was used but for the intermolecular exchange interaction a solution for two self-consistent equations was searched for[68]. The crystal was in the modeling divided into two sublattices where the magnetic moment on each sublattice act as bias fields onto the other sublattice. The two magnetic moments M_A, M_B of sublattices A and B as a function of the field B, the temperature and the coupling to the neighboring moment J' are therefore:

$$M_A = f\left(B + \frac{zJ'}{g^2\beta^2} M_B, T\right) \quad 4.2$$

$$M_B = f\left(B + \frac{zJ'}{g^2\beta^2} M_A, T\right) \quad 4.3$$

The best fit parameters for both data sets are: g= 2, J = 4.86 cm^{-1}, D_i = -2.3 cm^{-1} J'= -0.5 cm^{-1}, z=3

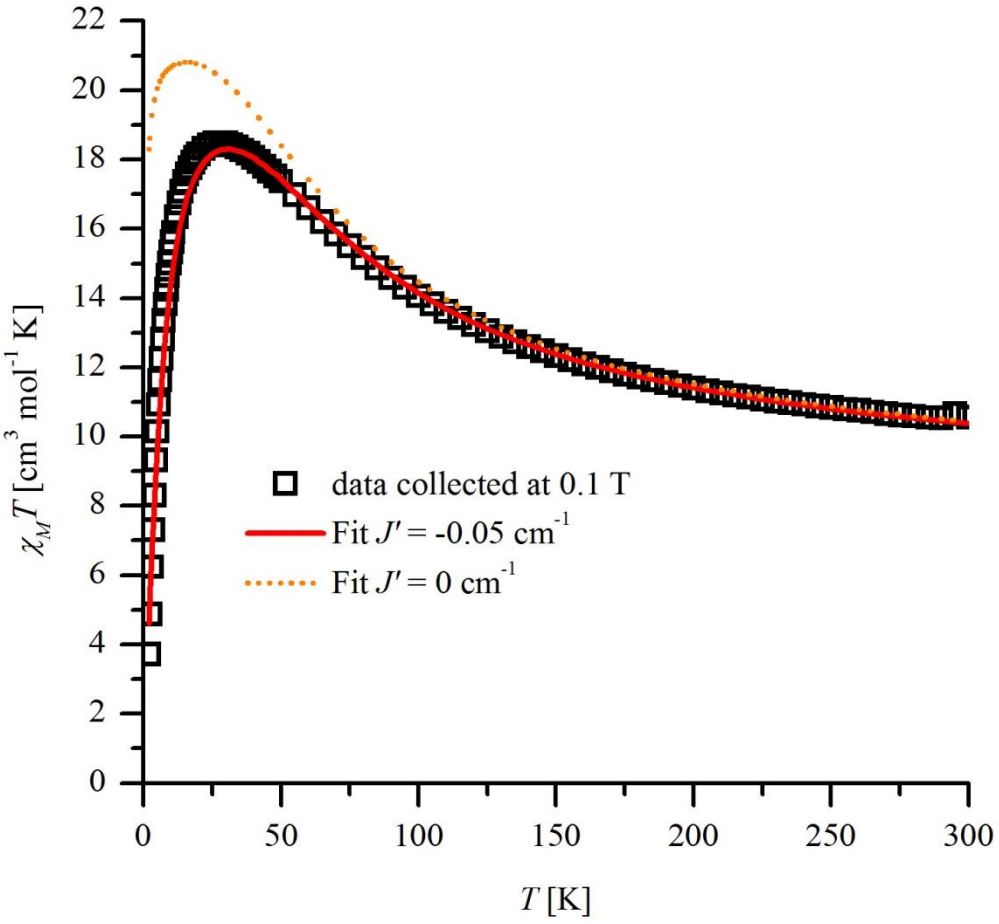

Figure 4.7: susceptibility data of compound **9** collected with 1000 Oe over the temperature range 2 K-300 K the red solid line represents the best fit including the intermolecular exchange coupling, the dotted orange line is a model without this interaction

The measured $\chi_M T$ values at 300 K are still well above the theoretical value for 3 uncoupled Mn(III) ions: 9 cm^3 mol^{-1} K. Below 300 K, $\chi_M T$ rises with lowering temperatures as it expected for ferromagnetically coupled Mn(III) trimers, reaching a maximum value of 18.5 cm^3 mol^{-1} K at 27.8 K. Below this temperature, $\chi_M T$ declines steeply towards 0, which can attributed to both the ZFS and the intermolecular exchange. Figure 4.8 illustrates that the same set of parameter values also reproduce the magnetization data very well.

This consistent modeling can only be achieved by fitting all data to the same model unlike it has been done for the cited studies [2, 64]. Fitting only the high temperature data to a model with purely intra-molecular exchange interactions and Zeeman terms, and fitting only the very low temperature and high field data to a giant Spin Hamiltonian as it was done for **7** [2], is a frequently used and reasonable way of extracting the intra-molecular exchange coupling. However it neglects the intermolecular exchange, which in this case has a notable effect on the relaxation barrier height. Furthermore as the effects of the intermolecular exchange interactions are most prominent at low temperatures, in the MFT when neighboring spins have the biggest moment to act as a bias on the magnetic field, an omission of these interactions from the fitting process leads to an overestimation of the ZFS parameter.

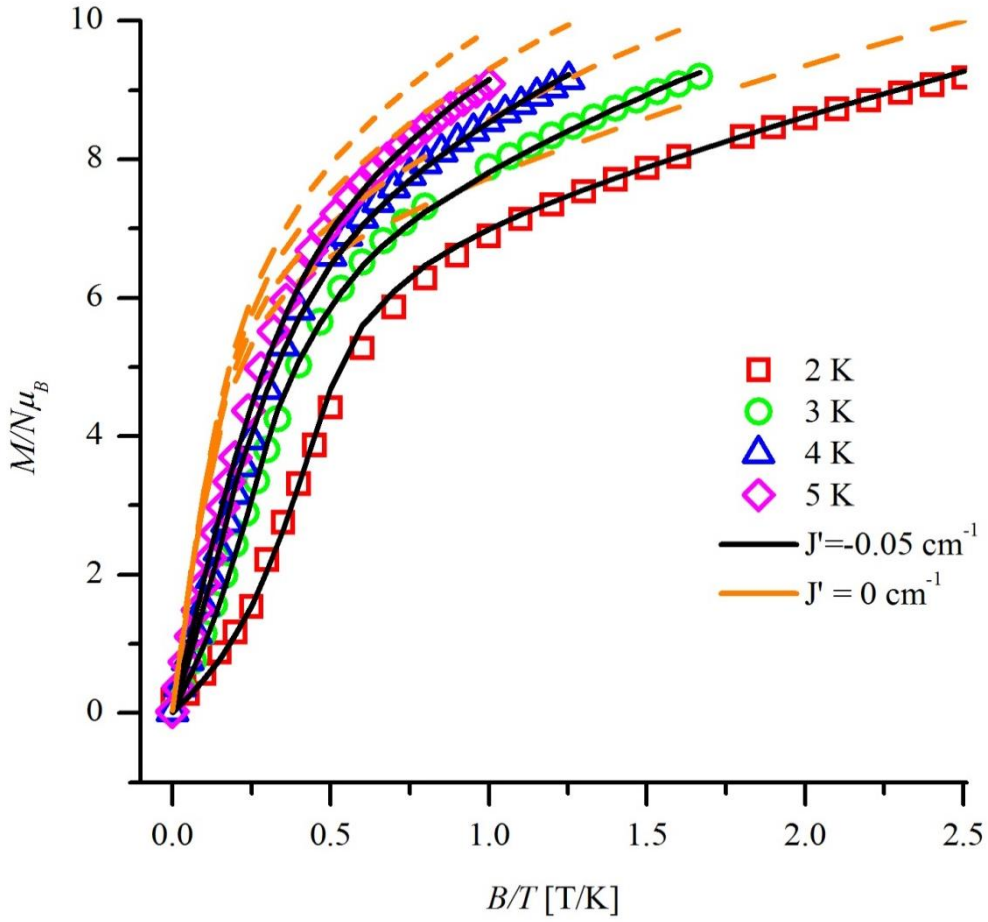

Figure 4.8 magnetization data for compound **9**. The data was grouped in four temperature groups. Fits with and without intermolecular exchange, with other parameters described in the text

AC susceptibility data have been collected over the temperature range of 2.2 K - 10 K with no applied static field and oscillating fields with amplitude of 3.5 Oe and frequencies between 50 Hz and 1488 Hz. The in-phase and out-of-phase susceptibility data are presented in Figure 4.9 and are very similar to the data sets published for compounds **7** and **8.** The peak positions of the very symmetric

out-of-phase peaks were used to construct the Arrhenius plot provided in Figure 4.10. The effective barrier determined in this way has a height of U_{eff} = 60.6 K. This is slightly higher than the U_{eff} of **7** and **8**. This is the same effect as observed in Chapter 3, where an alignment of the anisotropy axes on each metal center result in a larger global ZFS and therefore according to eq.1.2 a larger U_{eff}.

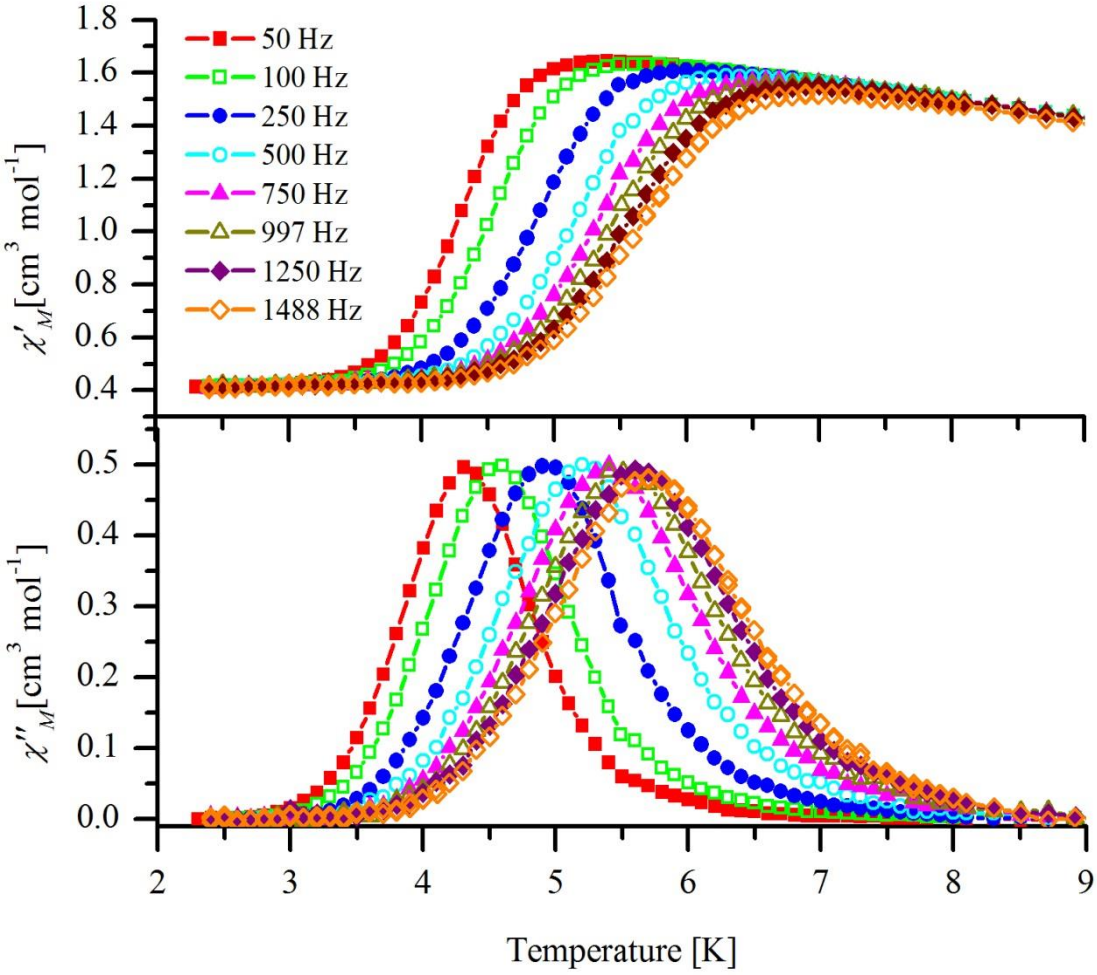

Fig 4.9 in-phase (top) and out-of-phase(bottom) AC susceptibility of compound **9** for frequencies between 50 Hz and 1488 Hz.

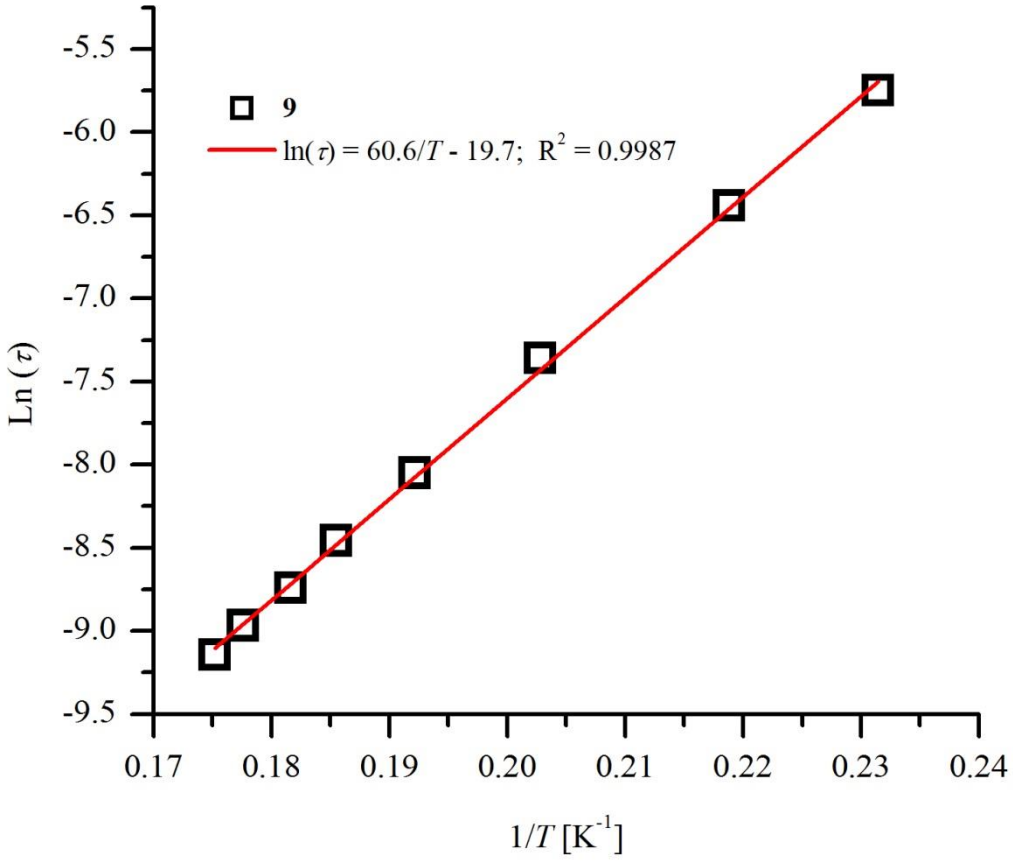

Figure 4.10 Arrhenius plot for compound **9** taken for frequencies between 50 Hz and 1488 Hz

4.6 Inelastic Neutron Scattering

The INS data of compound **7** shows a very feature rich spectrum. The cold transition at 8.5 cm^{-1} shows a shoulder at 8.0 cm^{-1}. A further peak at 2.1 cm^{-1} is temperature independent and shifts to lower energy transfer values when measured with a longer wavelength. The origin of this peak is multiple scattering on the cryo-furnace that was used for this compound. The part of the elastic line that experiences multiple scattering arrives at the detector later, which makes it appear like energy was transferred. The exact same peak was also observed for compound **3** in chapter 2, as this compound was measured in the same sample environment. At higher temperatures the cold transition Ia lowers in intensity and shifts to lower to energy transfer. At 20 K the slightly asymmetric transition (Ia in Figure 4.11 is a dubett at 8.27 and 7.93 cm^{-1} Furthermore several warm transitions, IIa-VIa, with energy transfers of 6.5 cm^{-1}, 5.0 cm^{-1}, 3.4 cm^{-1} can be observed. Further transitions on the energy loss side of the spectrum could not be resolved from the elastic line because of the large background due to quasi-elastic scattering and the masking due to the above mentioned multiple scattering. On the gain side

however, new energy transfers Vb and VIb at positions -2.03 $cm^{-1}$and -0.95 cm^{-1} could be observed. These peak positions were verified by a measurement with longer incident beam wavelength. All peaks are significantly broader than the resolution of the instrument, which indicates that they are all doublets or multiplets. This interpretation is supported by measurements with longer wavelengths and also by the data recorded at 6 K where two peaks are clearly visible for transition IIa.

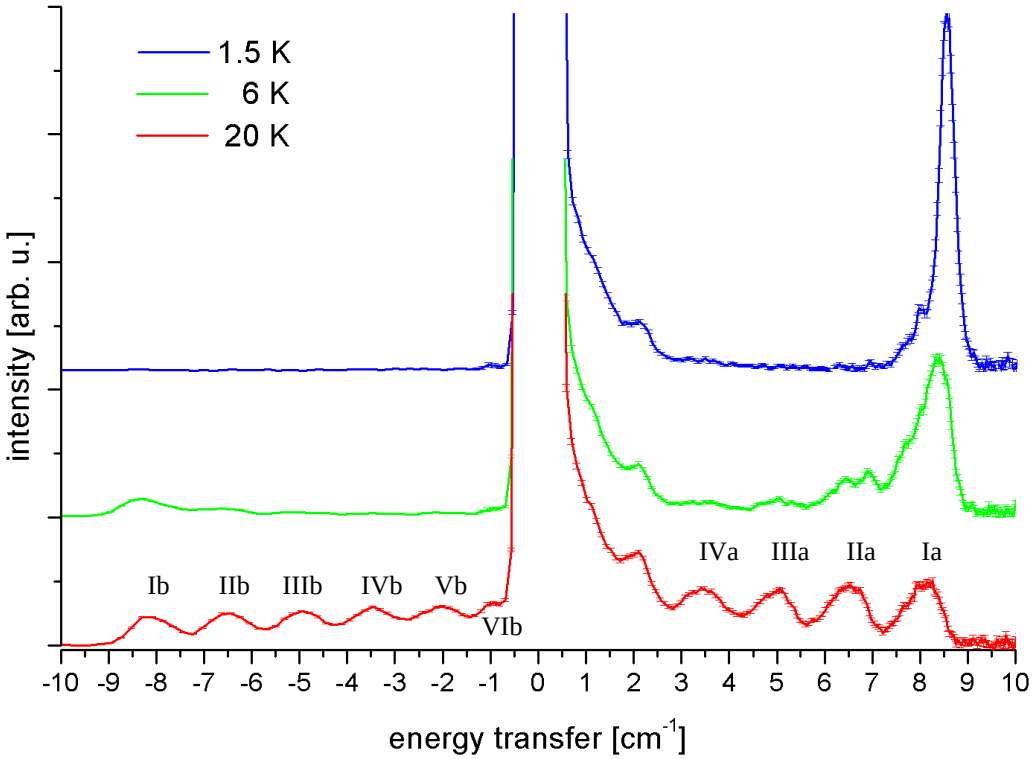

Figure 4.11 INS spectrum of **7** measured at 6.5Å incident wavelength. The three temperatures 20 K, 6 K and 1.5 K are presented with an off-set for clarity.

It was attempted to reproduce the INS spectrum with the GS Hamiltonian parameters obtained from EPR measurements. Figure 4.12 shows a comparison of the spectrum at 6.5 Å incident wavelength with the simulation. From the comparison it is clear that this set of parameters does not reproduce the INS spectrum. The peak positions of the simulation are at too low absolute energy transfer values. This is particularly pronounced for peaks Ia, Ib, IIa and IIb. This means that the parameters D and/or B_0^4 are too small. The model predicts the splitting of the transition IIIa and IVa with a value that is slightly too large, but does not account for splitting of the other transitions.

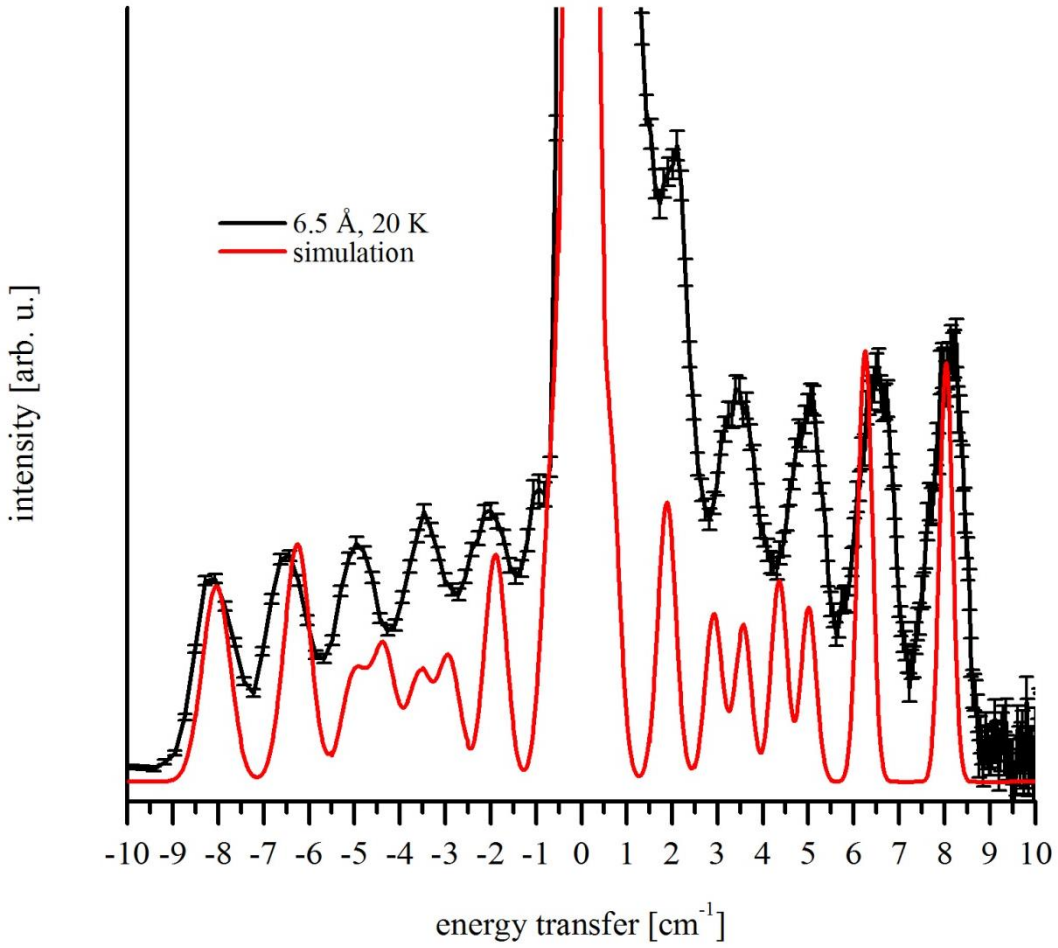

Figure 4.12: comparison of the measured data at 6.5Å and 20K with the simulation with $\widehat{H}_{GS}$ parameters: D = -0.686 cm^{-1}, B_0^4 = -5.04*10^{-5} cm^{-1}, B_3^4 = -7.42*10^{-5} cm^{-1}, B_6^6 = -1.1*10^{-5} cm^{-1}

The temperature dependence of the spectrum of compound **8** (fig.4.13) measured at 6.5 Å incident wavelength is nearly identical (at temperatures 1.5 K, 6 K, and 20 K) with the one for compound **7**. The main difference is that the transition of IIIa of compound **7** is at a slightly lower energy transfer ΔE=4.9 cm^{-1}. Furthermore the intensity of the right peak of transition IIa at 6 K in compound **7** is slightly higher than the left peak. In compound **8**, the proportions are reversed.

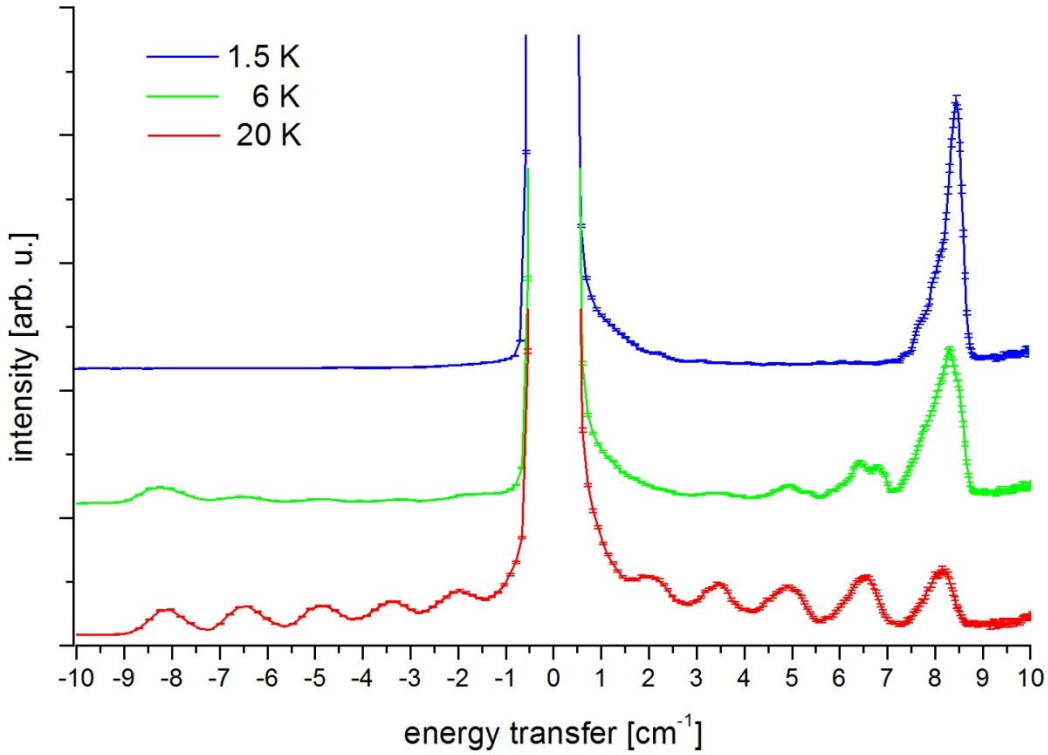

Figure 4.13 INS spectrum of compound **8** measured at 6.5Å incident wavelength. The three temperatures 20K, 6K and 1.5 K are presented with an off-set for clarity

The spectrum of compound **9** given in Figure 4.14 shows the shift to higher absolute energy transfer values expected for the exchange of ClO_4^- with $ReO_4^-$and the resulting alignment of JT axes. Apart from the shift the spectrum shows the same general features as the spectra for **7** and **8**. The cold transition has two visible shoulders at 8.3 cm^{-1} and 8.6 cm^{-1} on the main peak at 9.1 cm^{-1}. Like in the previous examples all transitions at 20 K are split as it is suggested by the peak FWHMs that are far bigger than the theoretical resolution of the instrument.

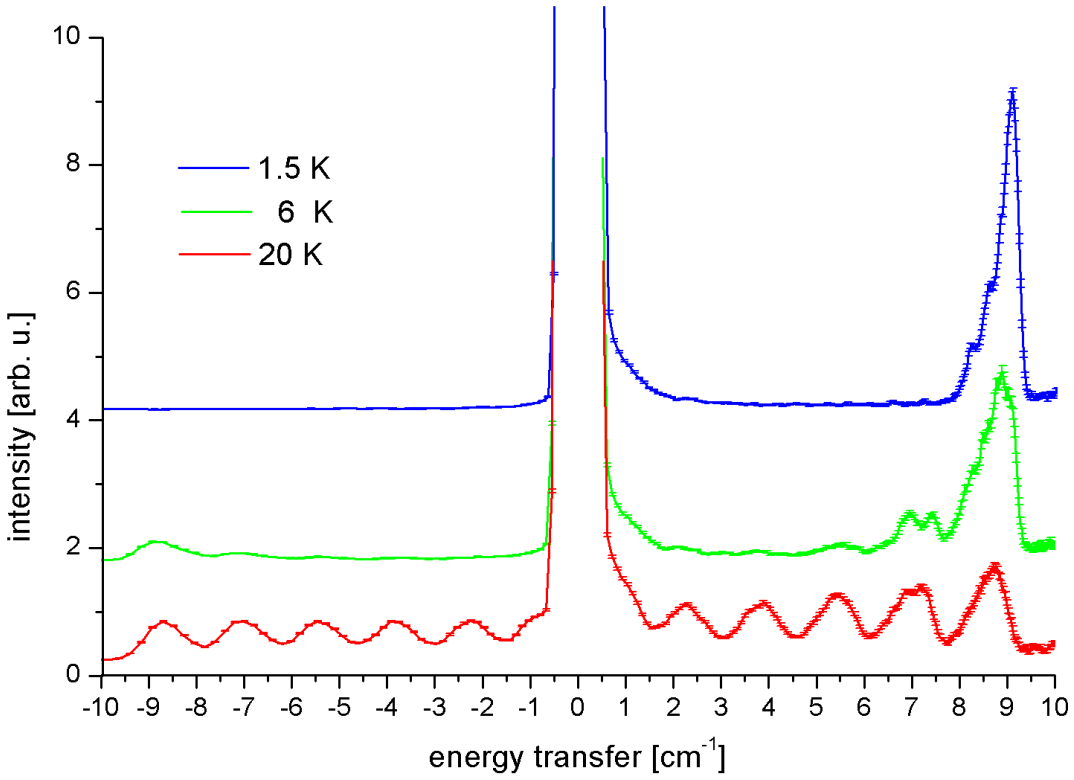

Figure 4.14. Temperature dependant INS spectrum of **9** measured at 6.5Å incident wavelength

Fits for all the data-sets were attempted with giant Spin but no successful model for the intermolecular exchange was found due to the immense complexity and the large dimensionality of the problem as the Hilbert space is growing with the power of metal centers in the spin clusters involved. Thus, the dimension of the matrices describing the exchange interactions between *n* *S*=6 molecules is 13^n. A feasible modeling can thus only encompass a few interacting complexes.

In order to exclude an influence of a possible coupling interaction of the spins of the metal center with the nuclear spin of the H atom H6, measurements of **9** were done for the non-deuterated species as well as the species where H6 was exchanged for D6. No difference was observed between the spectra for the protic v.s. deuterated sample

4.7 Conclusions

The systems discussed in this chapter show highly interesting barrier heights, which cannot be explained by simple spitting of the ground state multiplet due to the ZFS parameter. As those parameters are generally not large as it is shown for the very similar systems in chapter 3. It was shown that it is necessary to include a small antiferromagnetic intermolecular exchange parameter to fit susceptibility curves in these complexes [2, 64]. Later, a study appeared in the literature where EPR data of compound **7** were modeled to a Giant Spin Hamiltonian with parameters up to sixth order, without taking intermolecular interactions into account. The INS data presented here show that the Giant Spin Hamiltonian parameters arrived at from alternative studies cannot reproduce the electronic structure of these systems. It is suggested that the splitting of the INS transitions could be explained by intermolecular antiferromagnetic interaction between $S = 6$ multiplets. It was shown by mono-deuteration of the methanol groups that are responsible for the hydrogen bonds between the complexes, that coupling to these nuclear spins does not play a role. Furthermore, no phase transitions occur as function of temperature and the systems retain their structure in the complete temperature interval (2 K – 295 K) as it was shown by the neutron diffraction experiments. Accordingly, structural changes can be excluded as a possible source for behavior. Although some improved understanding has been gained, the complexity and high dimensionality of the problem requires further investigations with techniques such as polarized neutron scattering to provide a complete picture.

5. SMMs based on 4d, 4f and 5d metal ions, bridging ligands and ligand field variations

5.1 Introduction

A lot of the 3d metal based SMMs like the Mn(III) systems discussed in the previous chapters have quenched orbital momenta. This simplifies the analysis and is therefore ideal for the magneto-structural correlation that represents the main topic of this thesis. On the other hand it means that the anisotropy only arises due to second order perturbation effects, which limit the anisotropies to small values compared to metal ions with unquenched orbital contributions. For this reason it is sensible to use 4d, 4f or 5d metal ions rather than 3d metal ions when designing a SMM. Another important factor is that the exchange interactions are stronger in 4d and 5d metal compounds than 3d metal compounds due to the more diffuse orbitals. 4f metal ions show generally weaker interactions as the 4f electrons are shielded by the 5s and 5p shells.

This chapter discusses some of the results obtained in collaboration with colleagues that lead to several publications. In section 5.2, which is based on references [69, 70], the exchange interactions within cyanide bridged trimeric SMMs containing two Mn(III) and one 4d or 5d ion respectively are investigated. Section 5.3 highlights some examples of exchange mediated by fluoride bridges [71, 72]. The Fluride Ion as bridging ligand is not well studied so far in respect to its magnetic properties and only one example of $[MF_6]^{x-}$ as building block for a magnetic material is known.[73] The chapter concludes with study of mono-ionic, trigonal Er(III) SMMs with slight differences in the coordinating ligands[74]. SMMs based on lanthanides are very promising due to the above mentioned higher anisotropy. The sensitivity towards the Ligand Field (LF) makes theoretical predictions of the direction and sign of the anisotropy much less feasible for 4f than for 3d metals. Therefore an exact analysis of the magnetic structure of the most simple 4f SMM a single ion Magnet SIM with a trigonal symmetry is a crucial study that furthers the entire field of Molecular magnetism.

Common to all these systems is that INS has played a central role in providing coherent pictures of their electronic structures. In each studied case spectroscopic information at zero fields was crucial. In several cases transitions between different *S* states were observed by INS which would not have been possible by EPR.

5.2 cyanide bridged systems

The complexes in the previous chapters all had the ligands in the easy plane of the molecule in common. Another ligand that like $saoH_2$ is synthesized from salicylic aldehyde or related compound like o-hydroxyacetophenoen [60] is diphenolH_2salen (more commonly: salen)[75]. Salen is a widely used ligand for Mn(III) complexes [76-78]. In this section we focus on the a group these Mn(III)salen based compounds: a trimeric complex that, in contrast to the Mn trimers discussed in the previous chapters, only consist of two Mn(III) ions, bridged in a near linear arrangement by a hexacyano-M(III). In literature there are several examples, where the central metal center in Mn(III)-M(III)-Mn(III) is a transition metal such as M=Cr or Fe[68, 79-83]. Additionally very recent examples with 4d (M=Ru)[84] and 5d (M=Os) [83] metals have been presented by collaborators. In these previous publications the synthesis, the structures and magnetic data for both, the Ru and the Os compound were presented. Furthermore INS data was presented for the Os compound as well as Thz-EPR data for the Ru compound. As the proposed model, of an isotropic (i.e. Ising type) exchange interaction between Mn and Os could not be supported by later recorded Thz-EPR measurments, further investigation was needed. The new compound $NEt_4[Mn^{III}_2(5\text{-Brsalen})_2MeOH_2Ir^{III}(CN)_6]$ **10** was synthesized and studied by INS, EPR and magnetic measurements, the results of which are presented in this section. The diamagnetic central ion enables the measurement of the anisotropy on the Mn(III) centers as well as the weak exchange interaction between the Mn ions without the presence of additional momenta. Furthermore additional INS data of $NEt_4[Mn^{III}_2(5\text{-Brsalen})_2MeOH_2Os^{III}(CN)_6]$ **11** was recorded and the model was adapted to explain all data the previously reported [83] as well as the new INS and Thz-EPR data. New INS spectra of $NEt_4[Mn^{III}_2(5\text{-Brsalen})_2MeOH_2Ru^{III}(CN)_6]$ (**12**) complete the characterization of this compound. The importance of anisotropic exchange was unequivocally established by use of this broad spectrum of techniques including INS.

The molecular structure of **10** (see fig. 5.1) like those of **11** [83] and **12** [84] consists of a central hexacyanometallate, in this case $[Ir(CN)_6]^{3-}$, that is bridging to two Mn(III) in trans configuration. Each Mn(III) ion is coordinated to one Brsalen ligand and one terminal MeOH. The MeOH Ligands enable intermolecular H-bridges. It is noteworthy that the Mn-Ir-Mn just like the Mn-Os-Mn and Mn-Ru-Mn directions are not linear but slightly bent.

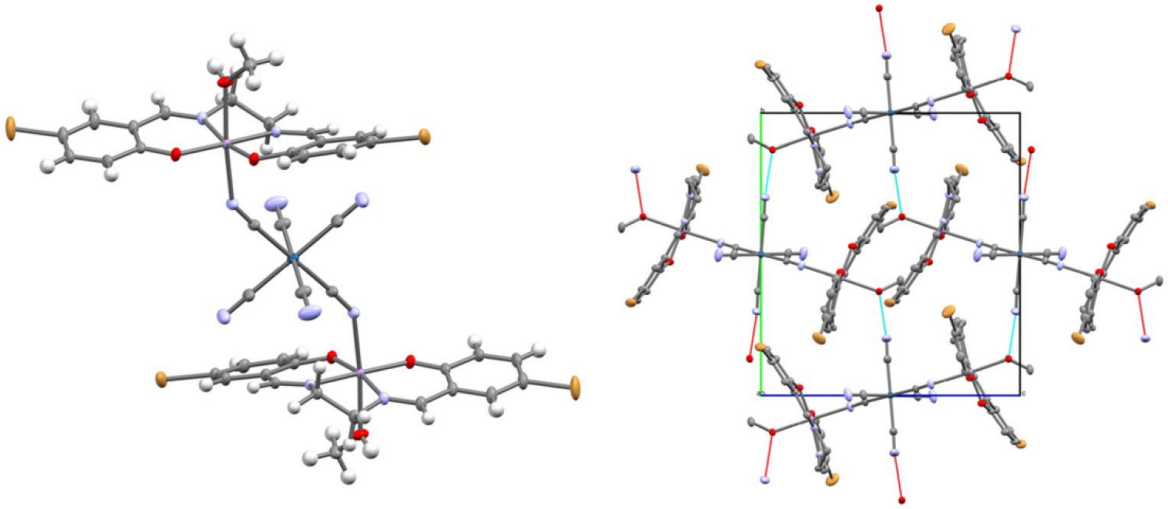

Figure 5.1 structure of **10** (left) and crystal packing with illustrated H-bonds as blue and red lines (right) The counter ions have been omitted for clarity. Color code: C (gray), H (white), Br (orange), N (light blue), O (red), Mn (violet) and Ir (blue).

The following models were used to describe the systems. The Hamiltonian for compound **10** is given in equation 5.1

$$\hat{H} = \mu_B g_{Mn} B \sum_{1,3} \hat{S}_i + \sum_{1,3} (D_{Mn}(\hat{S}_{iz}^2 - \frac{1}{3} S_i(S_i + 1)) + E_{Mn}(\hat{S}_{i,x}^2 - \hat{S}_{i,y}^2))$$

$$+ J_{Mn-Mn}(\hat{S}_1 * \hat{S}_3) \qquad (5.1)$$

The diamagnetic Ir(III) is not included in the Hamiltonian.

For compound **11** and **12** additional terms for the central ions have to be included. In Os and Ru the cubic ligand filed leads to a $^2T_{2g}$ (O_h) ground term, which in turn is then split by the spin orbit splitting into $G'_{g(3/2)}$ and the lower laying $E'_{1g(1/2)}$. The orbital momentum of Os and Ru can be simplified as a $\hat{\varsigma} = \frac{1}{2}$ pseudospin, considering only the lowest lying states as the spin orbit couplings are big for both hexacyanides $\zeta_{Os} \approx 3000$ cm^{-1} $\zeta_{Ru} \approx 880$ cm^{-1}[83-87]. The additional terms in the Hamiltonian are:

$$\mu_B g_{eff,M} B + \hat{\varsigma} * J * (\hat{S}_1 + \hat{S}_3) \qquad (5.2)$$

Where J is a diagonal matrix with the elements J_{xx}, J_{yy} and J_{zz}. The g factors of the Os and Ru $\hat{\varsigma} = \frac{1}{2}$ pseudospin Kramers doublets can be estimated by $g_{eff}=(g_e+4\kappa)/3$ with the so called orbitalreduction factor κ [88, 89]. This yields estimates of $g_{eff,Os}$ = 1.8 and $g_{eff,Ru}$ = 1.9 [83, 84]. The exchange interaction between the two Mn(III) ions $J_{Mn\text{-}Mn}$ is not taken into account for **11** and **12**.

Furthermore a small inter-molecular interaction was taken into account, as it has been done previously[59, 82-84], using the mean-field approach[90] when analyzing powder susceptibility data. The mean-field corrected susceptibility was calculated using equation 5.3.

$$\chi_{MF} = \frac{1}{3}\sum_{a=x,y,z}\left[\frac{1}{\chi_{calc,a}} - \xi\right]^{-1} \qquad (5.3)$$

Where ξ stands for the molecular field constant.

The INS spectra of **10** (fig. 5.2) measured with the incident wavelengths λ_i = 5 Å (Figure 5.1a) shows two transitions at the base temperature 1.5 K at the energy positions 10.6 cm^{-1} (peak I) and 11.8 cm^{-1} (peak II). Furthermore there are visible "hot" transitions at temperatures of 6 K and more intense ones at 15 K. These transitions are at energy transfer values 3.1 cm^{-1} (III) and 4.2 cm^{-1} (IV). The longer wavelength spectra recorded at λ = 6.5 Å reveals an addition transition at 1.2 cm^{-1}.

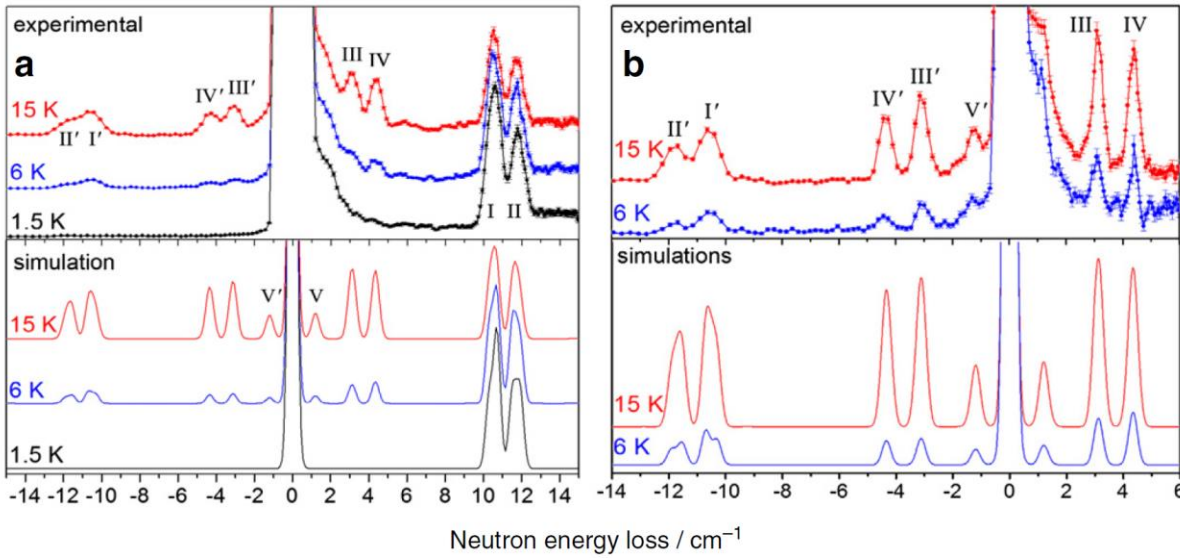

Fig. 5.2: measured and simulated INS spectra of **10** measured at different temperatures and two different incident wavelength a) 5 Å, 1.5 K, 6 K and 15 K b) 6.5 Å 6 K and 15 K

A least square fit of the neutron transitions awarded the following parameters. D = -3.72(5) cm^{-1} and E = 0.21(1) cm^{-1}. The S = 2 states on each metal center are split by the axial ZFS to M_S=±2, M_S=±1 and M_S=0. The rhombic ZFS then lifts the degeneracy of the Kramers doublets. This leads to the splitting of transition I and II which would only one peak without the rhombic anisotropy. HF-EPR data of **10** was collected at a frequency 285GHz at 5 K, 15 K and 25 K is presented in figure 5.3. The data can be reproduced with the same parameters as the INS data with an additional small exchange coupling parameter $J_{Mn\text{-}Mn}$ ~ 0.05 cm^{-1}. There is no exchange interaction observable in the neutron spectrum, which means that $|J_{Mn\text{-}Mn}|$ value cannot be bigger than 0.05 cm^{-1}.If the exchange coupling

would be bigger the FWHM of the observed peaks would wider. The presented peaks in fig 5.2 have FWHMs that correspond to the resolution of IN5.

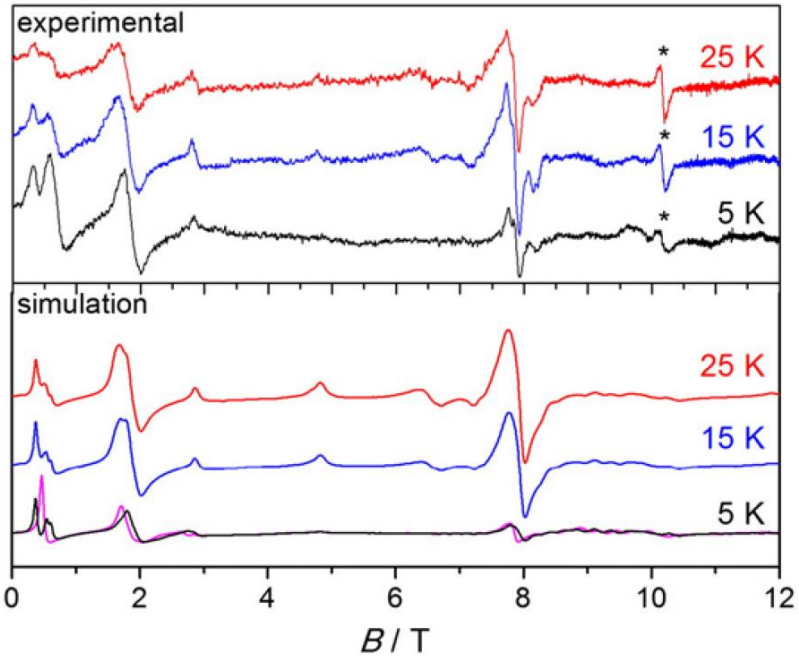

Fig. 5.3 experimental and simulated High-Field High-Frequency EPR spectra of **10**. The purple line represents a simulation without the $J_{Mn\text{-}Mn}$ exchange coupling parameter. The features at B = 10.18 T marked by the asterisk correspond to Mn(II) (g=2) impurities.

The magnetic data presented in Fig. 5.4 were reproduced with the parameters obtained from INS data. D = -3.7 cm^{-1} and E = 0.2 cm^{-1} plus g =1.98 cm^{-1} and exchange parameter J = 0.05 cm^{-1}.

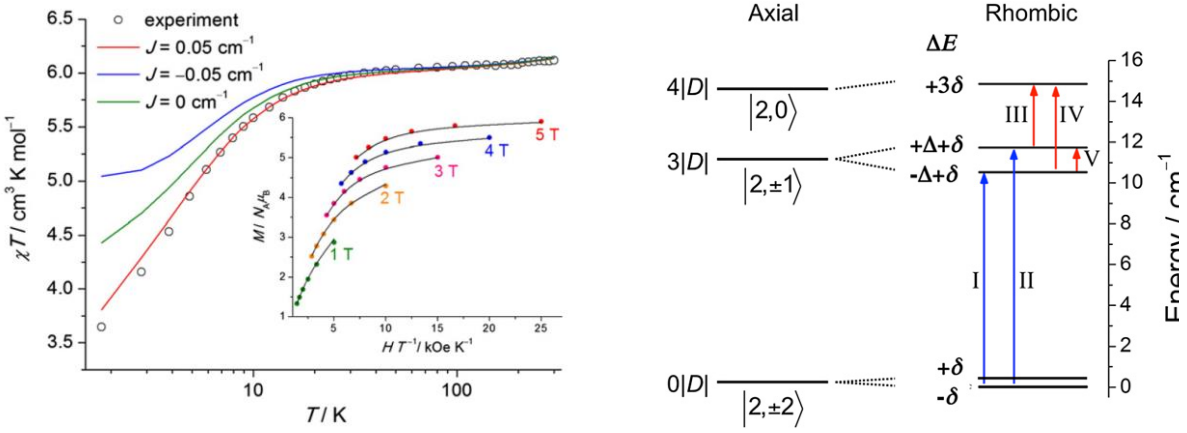

Figure 5.4 Magnetic susceptibility data measured at 0.1 T and reduced magnetization (insert) of **10**, (right) influence of the rhombic anisotropy E illustrated in an energy level diagram

A powdered sample of **11** was measured by Thz-EPR spectroscopy. The so obtained absorption spectra show three main features M1, p1 and p2. M1 which at zero field (fig. 5.5a) is at the energy of 14.95(20) shows a strong temperature dependence of intensity, while p1 and p2 only show slight temperature dependence. The fact that M1 is most intense at low temperatures means that transition originates from a low energy state that gets depopulated at higher temperatures. In fig. 2b it can be seen that M1 shifts to higher energy and broadens when a field is applied. This behavior originates from the Zeeman splitting of the ground and first excited states. The features p1 and p2 excitations corresponding to vibrational and twisting modes of the molecules[82].

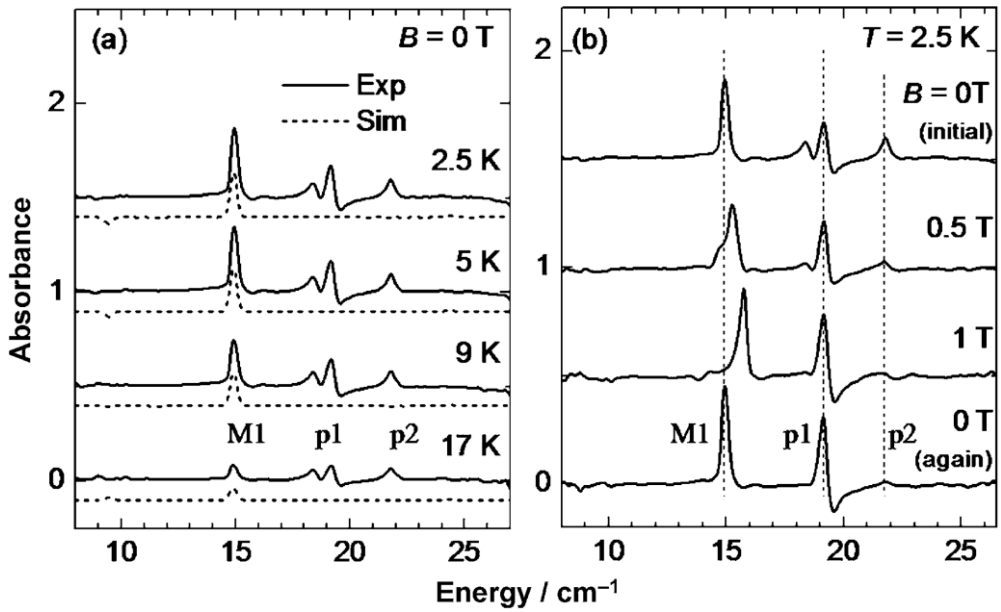

Fig. 5.5. Thz-EPR absorption spectra of compound **11**. Measured at different Temperatures (a) and fields (b). the curves have been off-set for clarity.

INS of a polycrystalline sample of **11** was measured at different temperatures and with two different incident neutron wavelengths λ = 5 Å and 3.8 Å. At low temperatures the same "cold" transition M1 that was observed in the Thz-EPR experiment can be observed at 15.0(3) cm^{-1}. A further strong transition at low temperature can be observed with λ = 3.8 Å at 28.2(4) cm^{-1}. Additional features at cold temperatures are A, p3 and p4 at energies 11.0(3) cm^{-1}, 28.2(4) and 20.0(5) cm^{-1}. At higher temperatures M1 and M2 lose intensity while p3 and p4 are temperature independent. The hot transitions labeled m1, m2, m3 are found at energies 6.6(3), 9.1(3) and 13.2(3) cm^{-1}. Additional analysis of the INS sample after the experiment was able to trace the origins of the feature A to a small impurity of the isostructural $NEt_4[Mn^{III}_2(5\text{-}Brsalen)_2MeOH_2Fe^{III}(CN)_6]$. The synthetic procedure was

changed as a result of this observation to ensure pure samples for Thz-EPR and magnetic measurements. Feature A was neglected in the analysis of the data.

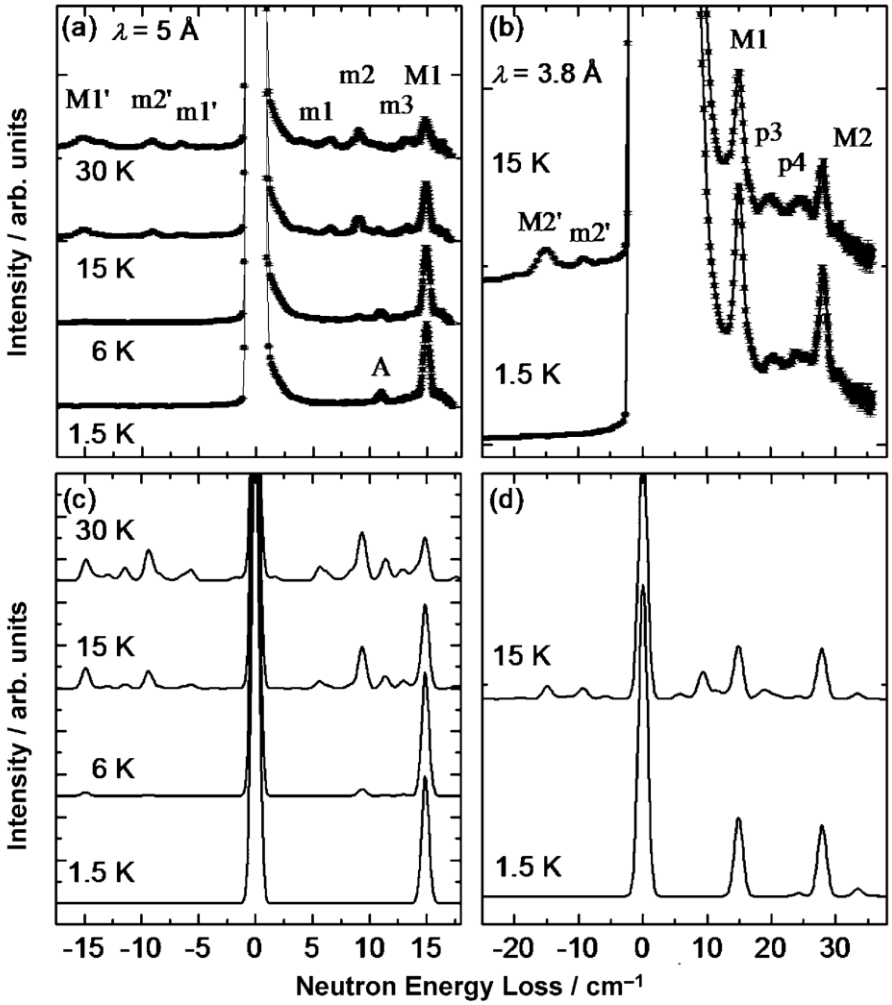

Fig. 5.6: inelastic neutron spectra of **11** measured different temperatures and at the two incident wavelength λ_i a) 5Å, b) 3.8 Å and c,d) the simulated spectra for the respective λ_i and temperatures.

A polycrystalline sample of **12** was measured with Thz-EPR at zero field and different temperatures (fig 5.7 a) and at a constant temperature of 5 K with an applied magnetic field varying between 0 T and 0.9 T (fig.5.7 b). At zero field and low temperatures (3K) three features can be observed. At 12.8(1) cm^{-1} the very intense transition M1 (FWHM = 0.26 cm^{-1}) can be found. This feature decreases in intensity with increasing temperatures analogue to the identically labeled feature in the Thz-EPR spectrum of **11**. Furthermore, the temperature independent features p1 and p2 can be found at energies 18.4(2) and 19.3(2) cm^{-1}. These energy values are very similar to the ones observed in compound **11** as it is expected for vibrational and twisting modes of such similar molecules. M1 splits into two peaks with an applied magnetic field

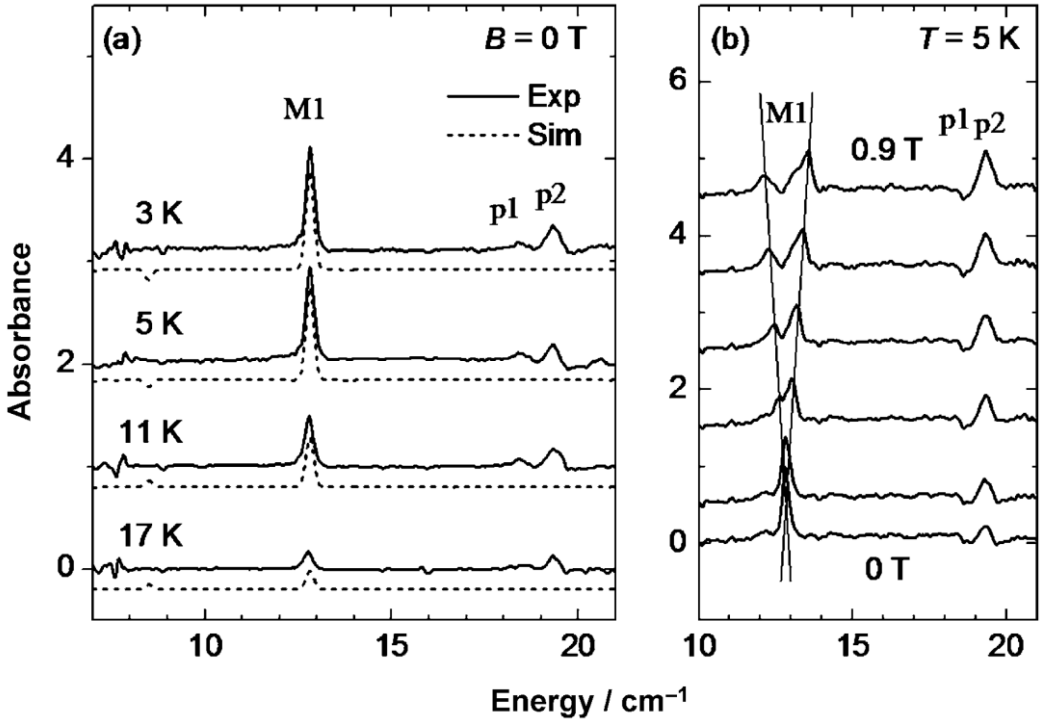

Figure 5.7. Thz-EPR absorption spectra of compound **12**. Measured at different Temperatures (a) and fields (b). the curves have been off-set for clarity.

A polycrystalline sample of **12** was measured by INS at different temperatures and with two different incident wavelengths (λ= 4.8 Å and 4 Å). The position (12.9(3) cm^{-1}) and temperature dependence of transition M1 measured by INS confirmed the results obtained by Thz-EPR. A second cold transition M2 not observable by Thz-EPR can be seen in fig. 5.8 b at 24.0(5) cm^{-1}. A "hot" transition m1 can be observed at 7.3(4) cm^{-1}. Several peaks p3, p4 and x at energies 16.6(4), 20.0(5) and 3.8(4) cm^{-1} are not of magnetic origin based on the temperature dependence and Q-dependence.

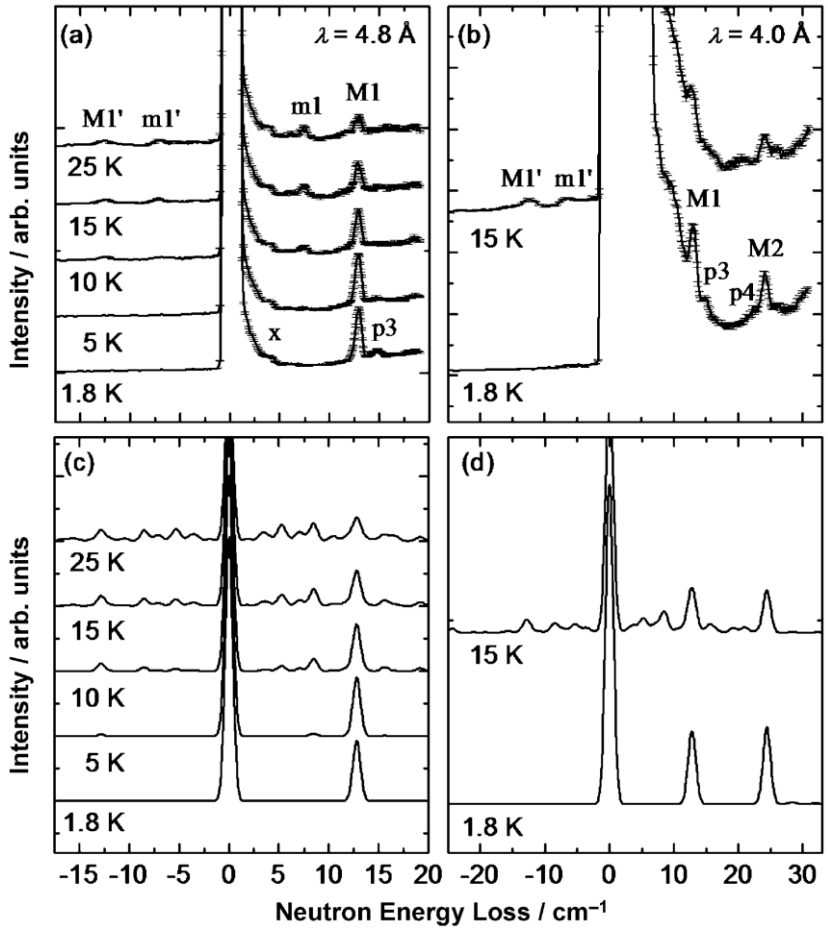

Fig. 5.8: inelastic neutron spectra of **12** measured different temperatures and at the two incident wavelength λ_i a) 4.8 Å, b) 4 Å and c,d) the simulated spectra for the respective λ_i and temperatures.

The temperature dependence of **11** was measured again after an aging process was discovered in **11.** Due to this aging process, the data looks slightly different form reference [83]. Both the data presented here and the reference data can be reproduced with the same values for the fit parameters by only slightly varying the intermolecular exchange ξ. It is suspected that the loss of the methanol ligands is responsible for these variances. The room temperature χT value of **11** was 6.13 cm^3 K mol^{-1}. Upon cooling below 100 K the χT product rises slowly to a maximum value of 8.1 cm^3 K mol^{-1}at 16 K after which it drops steeply. The high temperature data is consistent with the expected value for the three uncorrelated spins, the two Mn(III) S = 2 with g_{Mn} = 2 and the pseudospin τ =1/2with g_{Os} = 1.8. The χT data of **12** is very similar to the one of **11**.The high temperature value of of **12**, 6.2 cm^3 K mol^{-1} is only slightly bigger than **11** as it is expected with the slightly bigger g value for Ru g_{Ru} =1.9. The maximum χT value of 7.4 cm^3 K mol^{-1} reached at 14 K is slightly lower.

The *M(H)* data of **11** and **12** are very similar and both do not saturate at high field of 5 T. This is due to high anisotropy and/or low lying excited states.

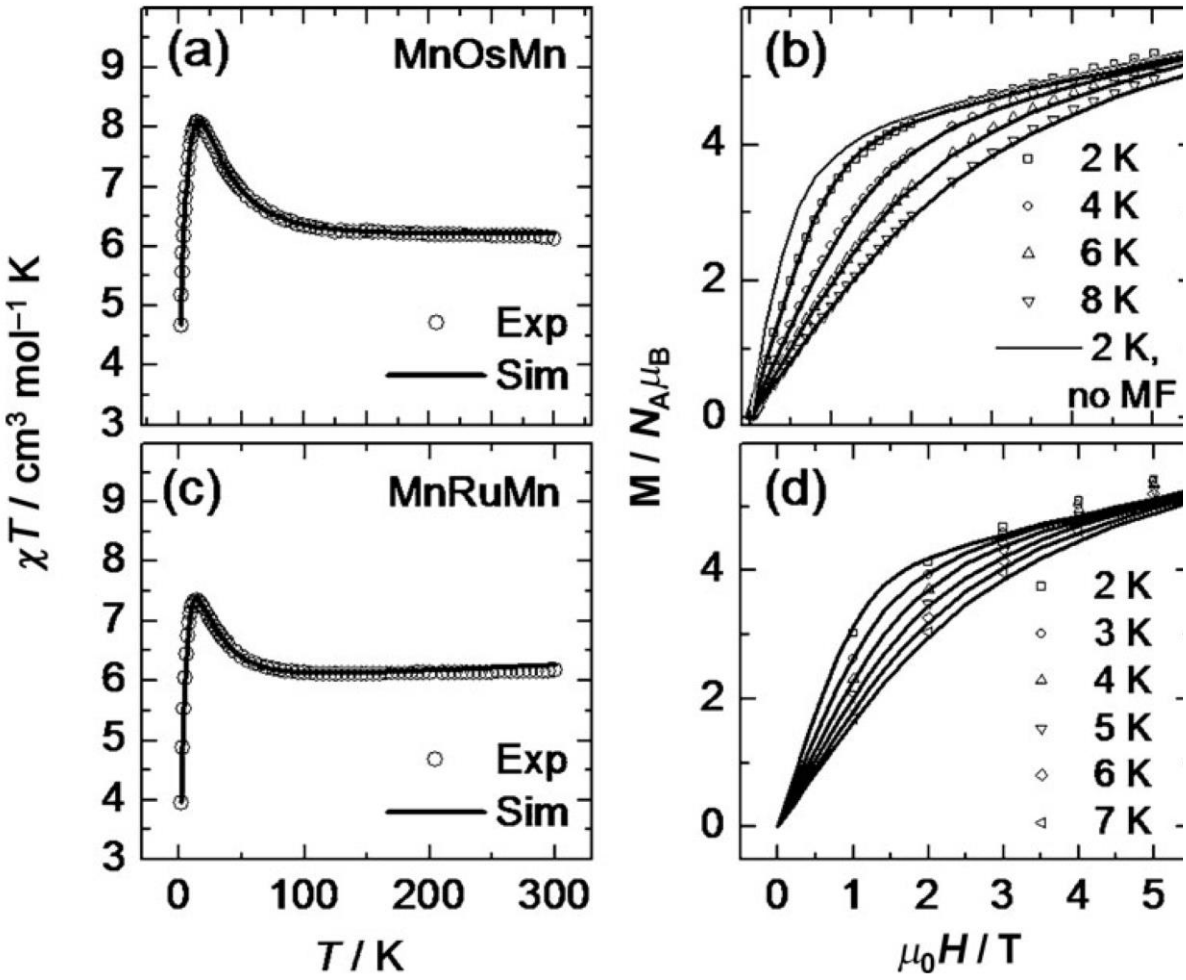

Fig 5.9: temperature dependent χT product of a) **11** and c) **12** and field dependence of magnetisazion for b) **11** in the temperature range 2-8 K and d) **12** with temperatures between 2 and 7 K. The solid lines represent simulations using the obtained best-fit parameters described in the text. The thin line in b) represents a calculated *M(H)* curve at T = 2 K without intermolecular interactions. The experimental data in c and d was already presented in [84]

The magnetic data was fitted together with the spectroscopic data by diagonalisation of the Hamiltonians described in eq 5.1 (without $J_{Mn\text{-}Mn}$) and 5.2. Temperature independent paramagnetic contributions, $1.85 \cdot 10^{-4}$ cm^3 mol^{-1} for **11**[86] and $7.94 \cdot 10^{-4}$ cm^3 mol^{-1} for **12**[87] were taken into account. The D parameter for **11** was fixed to D_{Mn}=-4.0 cm^{-1}, a value that is close to the one found for **10**. In both the treatment for **11** and **12**, the E term was neglected due to it being very small. The D_{Mn} tensor was rotated for both compounds from the z axis into the xy plane by θ=38°, in order to account for the bent geometry. This is described by a rotated ZFS tensor:

$$D_{Mn} = R_x^{-1}(\theta) D' R_x\ (\theta) \qquad 5.4$$

Where R_x is a rotation about the x axis by θ degrees and D'= diag(-1/3D, -1/3D, 2/3D). The fitted parameters for both compounds are collected in Table 5.1.

Table 5.1 Fitted spin-Hamiltonian parameters for compounds **11** and **12**

	11	**12**
J_{xx} [cm^{-1}]	18(2)	20(3)
J_{yy} [cm^{-1}]	-35(2)	-25(3)
J_{zz} [cm^{-1}]	33(2)	26(3)
ξ [mol cm^{-3}]	-0.118(4)	-0.15(3)
g_{Mn}	1.98 (fixed)	1.96 (fixed)
D [cm^{-1}]	-4.0 (fixed	-3.9(3)

It can be noted that both compounds show anisotropic exchange interactions, opposed to what has been found for **11** previously [83]. This show the importance of both spectroscopic techniques INS and Thz-EPR for the characterization of such compounds. The average of the absolute values of the exchange coupling parameters $J_{av}=(|J_{xx}|+|J_{yy}|+|J_{zz}|)/3$ increases by a factor of 1.2 from **12** to **11** (from Ru to Os). This is expected as the 5d orbitals have higher overlap as they are more diffuse than 4d orbitals.

5.3 Fluoride bridged systems

In this chapter we discuss two different fluoride bridged systems. In a first step the angular dependence of the exchange coupling interaction in F bridged Gd(III)-Cr(III) complexes is investigated by explaining the magnetic data obtained for a series of such complexes by DFT calculations. The second part of the chapter hexafluoro Re(IV) is investigated both as a single ion magnet and as a building block for molecular chains with constituent magnetic centers. Whereas cyanide which is exceedingly well explored as bridging ligand in molecule-based magnetism, fluoride-

bridged systems have received very little attention. As it will be shown here, this is undeserved as fluoride can dwarf cyanide with respect to the strength of magnetic interaction.

5.3.1 Angular dependence of the exchange coupling interactions

Recently a series of F bridged Ln-Cr complexes has been presented [91, 92]. Among these publications are the structures and magnetic behavior of the three Gd(III)-F-Cr(III) compounds **14-16** [93, 94]. These types of compounds are interesting as they can show a magnetocaloric effect and could therefore have possible applications as molecular coolers. Especially the pentanuclear version, **16** has shown good magnetic refrigeration properties[93]. For future design of such systems it is crucial to identify the structural parameters that determine the magnetic behavior. In the Cr-Gd series **14-16** the Gd(III)-F and F-Cr(III) distances are very similar, while the exchange coupling parameter vary. This suggest that the Gd(III)-F-Cr(III) bond angle is one of the structural parameters determining the exchange coupling interaction. As the series consists of polynuclear compounds with several Gd-Cr bridges, a simpler dinuclear Gd(III)Cr(III) model compound **13** was synthesized and its magnetic properties has been characterized by SQUID measurements and INS. INS on samples containing Gd in natural isotopic composition is very uncommon as

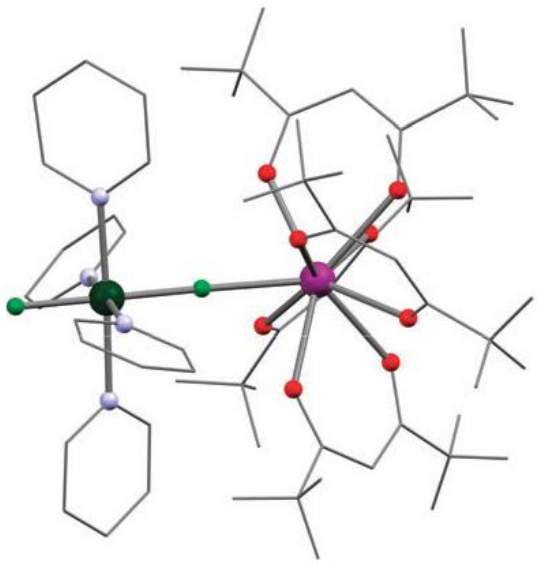

13: *trans*-$[CrF_2(py)_4]Gd(hfac)_4$

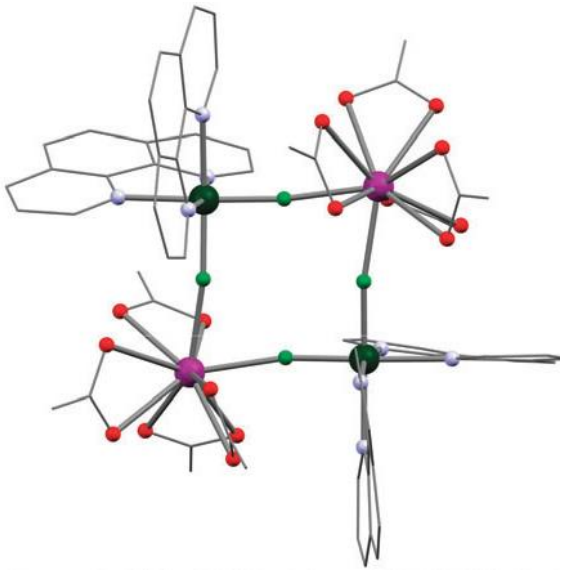

14: cyclo-{*cis*-$[CrF_2(phen)_2]Gd(NO_3)_4\}_2$

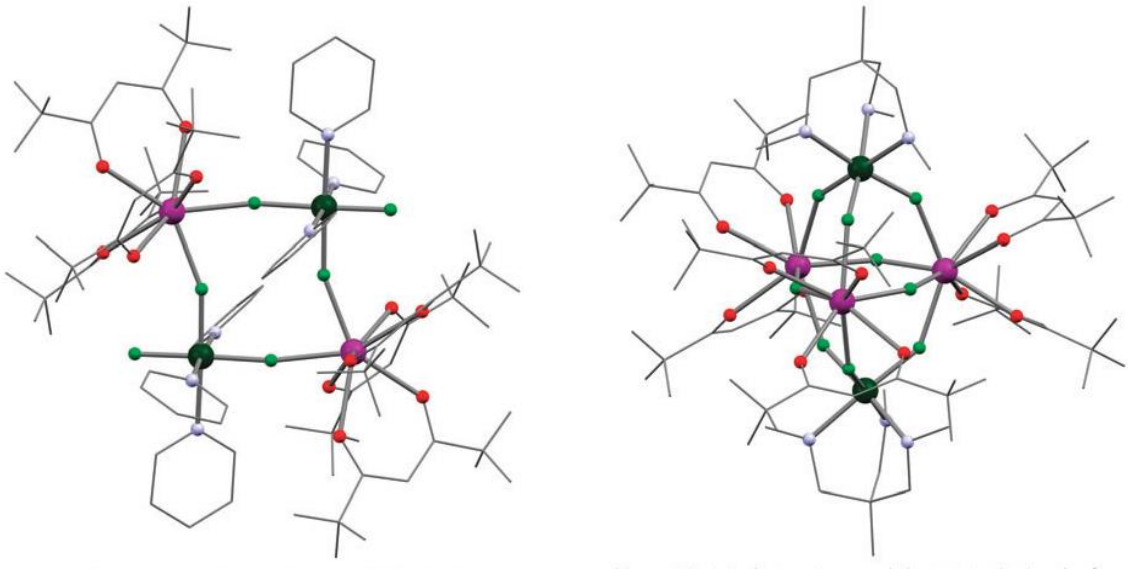

15: cyclo-{*mer*-$[CrF_3(py)_3]Gd(hfac)_3\}_2$ **16**: $\{fac\text{-}[CrF_3(Me_3tame)]\}_2Gd_3(hfac)_6\}_2$

Fig 5.10: Molecular structures of compounds **14** – **16**. Color scheme: Gd, purple, Cr dark green, F, light green, O red, N, blue, C atoms and bonds are represented as wireframe , H atoms are omitted

In Figure 5.11 a recapitulation of the previously published χT curves for compounds **14-16** and the new curve of compound **13** are presented. The χT values at high temperatures, T-> 300 K, of all compounds are in good agreement with the theoretical values for uncorrelated Cr(III) (S_{Cr} = 3/2 and Gd(III) (S_{Gd} = 7/2) ions with g = 2. At lower temperatures all compounds show decreasing χT values indicating antiferromagnetic interactions within the clusters. The susceptibility data were fitted to the isotropic Hamiltonian described in eq. 5.5 using the Levenberg-Marquardt algorithm [95] and numerical diagonalisation of the matrices using a program by S. Piligkos:

$$\hat{H}_{iso} = \mu_B B \sum_i g_i \hat{S}_i + J_{ij} \sum_{i,j>i} \hat{S}_i \hat{S}_j \qquad (5.5)$$

The parameters obtained from the independent fitting of χT data and the low temperature magnetization data of **13** are:

J_{GdCr}= 0.84(4) $cm^{-1}$and J_{GdCr}=0.82(4) cm^{-1} with g factors fixed to g_{Cr}=1.97 g_{Gd}=1.99, respectively.

The previously reported parameters are J_{GdCr}= 0.71 cm^{-1} and fixed $g_{Cr} = g_{Gd}$ = 2for **14** [93], J_{GdCr}= 0.57(7) cm^{-1} with fixed g_{Cr}=1.98 and g_{Gd}= 2 for **15** [94] and J_{GdCr}= 0.14(7) cm^{-1} with fixed $g_{Cr} = g_{Gd}$ = 2 and an additional J_{GdGd}= 0.06(7) cm^{-1} for **16** [93].

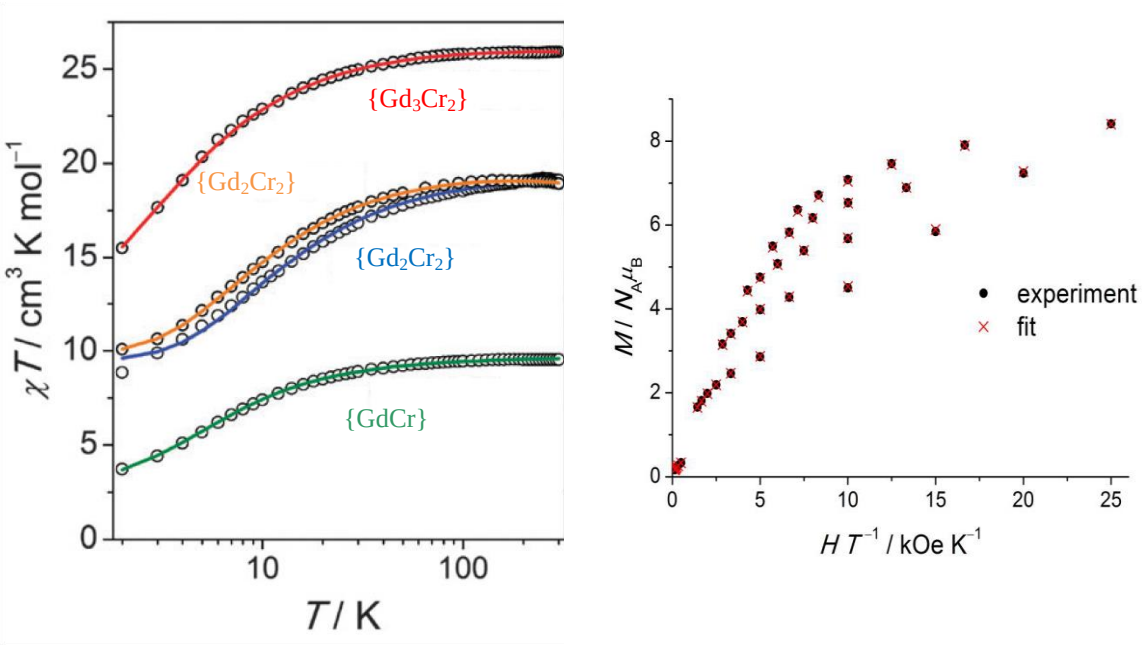

Fig 5.11 (left) χT data of **13-16** measured (circles) and the fits described in the text (solid lines), (right) reduced magnetization data of **13** with fit.

INS data of **13** was collected on IN5 at different temperatures and two different incident wavelengths λ_i = 6.5 and 4.8 Å. The spectra are presented in Fig. 5.12. In defiance of the difficulties arising from the very high neutron absorption cross-section of ^{157}Gd, σ_{abs}=650(4)b, which is naturally abundant (15.7%) a clear doublet can be seen with λ_i = 6.5 Å and T= 1.5 K at 2.2 cm^{-1} A and 3.0 cm^{-1} B. Due to the high noise levels the transitions cannot with certainty be ascribed to a magnetic origin as there is not a clear Q-dependence. The temperature dependence however matches a magnetic transition. A hot transition can be observed at 3.3 cm^{-1} at T = 15 K. The spectroscopic data was analyzed using the anisotropic Hamiltonian in eq. 5.6.

$$\hat{H}_{aniso} = \hat{H}_{iso} + D_{Cr}(\hat{S}^2_{z,Cr} - \frac{1}{3}S_{Cr}(S_{Cr}+1)) \qquad (5.6)$$

Affording parameters J = 0.87 cm^{-1} and D_{Cr} = 0.5cm^{-1}. The influence of D_{Cr} can clearly been seen in the splitting of the doublet in the neutron spectrum.

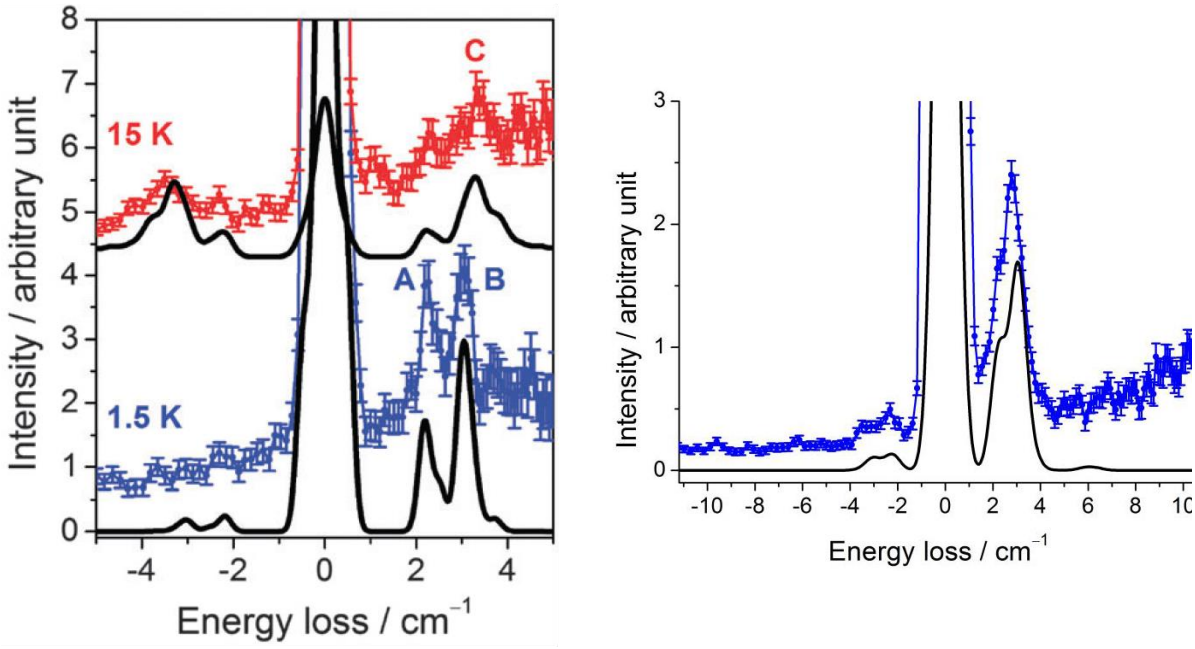

Fig 5.12 INS data and simulation of **13** with (left) λ_i = 6.5 Å at T = 1.5 and 15 K and (right) with λ_i =4.8 Å at T=1.5 K.

The obtained exchange coupling parameters of all four compounds are plotted as a function of the Gd-F-Cr angle in figure 5.12. The exchange for all compounds is antiferromagnetic and is clearly correlating with the bridge angle. The solid line in 5.12 represents DFT computational data (B3LYP/TZV) that has been obtained using the Gaussian 09 program suite. The DFT calculation shows excellent agreement with the experimental parameters and corroborates the correlation of J with fluoride bridging angle. It suggests that with angles smaller than ca. 138° exchange interactions become ferromagnetic. The mechanism behind it is that the orthogonal 3d and 4d orbitals lead to ferromagnetic interactions, while for orbitals with overlap, antiferromagnetic interactions dominate. Another factor is the charge transfer from the 3d orbital of Cr(III) to the 5d orbital of Gd(III) which strengthens the ferromagnetic interactions. A spin delocalization, as it can be deduced from the calculated spin densities on Gd, Cr and μ-F, reduces the charge transfer component. More information about these mechanisms can be found in [96-101] as well as the publication that this chapter is founded on [72]. The orbital overlap integrals (S_{ab}) have been calculated for different angles. The overlap is maximal at bridging an angle of 180° which leads to the antiferromagnetic interaction. The overlap decreases with decreasing angle. The analysis of the spin density is shown in fig. 5.13 (right). It reveals that at low angles the density on Cr(III) increases while the density on Gd(III) and μ-F decrease. This means a lower delocalization which facilitates the CT mechanism leading to ferromagnetic interactions.

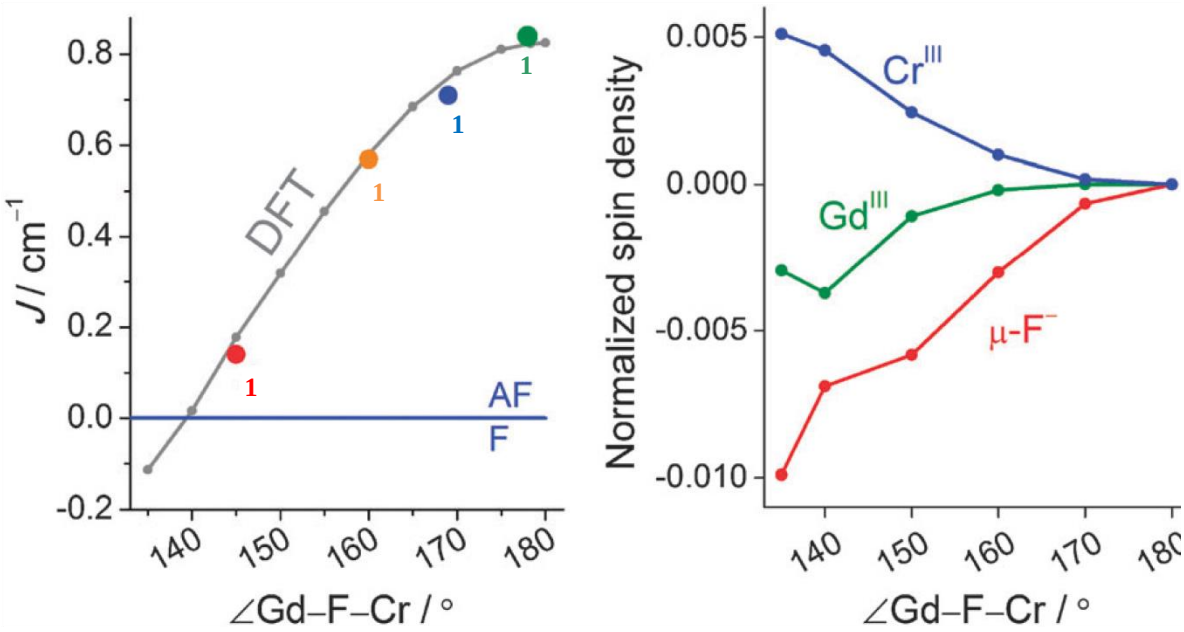

Fig 5.13 (left) DFT calculated angular dependency of the exchange coupling parameter (gray line) with experimentally determined J parameters for compounds **13-16** (dots), (right) normalized spin density as a function of the angular distortion in compound **13**

In summery the strong angular dependence of the exchange interactions in a family of F-bridged Gd(III)-Cr(III) compounds has been analyzed and rationalized by DFT calculations.

5.3.2 hexafluoro Re(IV) as building block

In contrast to the $M(CN)_6^{x-}$ in section 5.2, homoleptic fluoride complexes are not commonly used as building blocks for molecular based magnetic materials. So far only one example is known [73]. The absence of further examples could be founded in the fact that the synthetic conditions are very harsh. A homoleptic fluoride complex with a Re(IV) central ion $(PPh_4)_2[ReF_6] \cdot 2H_2O$ **17** (Fig 5.14) is introduced in this chapter. The magnetic properties are studied and compared to the properties of the chain compound $[Zn(viz)_4(ReF_6)]_\infty$ **18** (Fig 5.14). In this compound the Re(IV) ions are interspaced with diamagnetic Zn(II) ions. Therefore the Spins in **18** behave like the isolated spins in **17**. While **17** crystalizes in the triclinic spacegroup $P\bar{1}$, **18** crystallizes in the tetragonal space group $P4_2/n$ with the 4-fold axis along the Re(IV)-Zn(II)-Re(IV) axis. Furthermore with $[Ni(viz)_4(ReF_6)]_\infty$ **19** an isostructural compound to **18** has been synthesized with a paramagnetic Ni(II) in place of the Zn(II), in order to have an insight into the F-mediated exchange interaction in this type of compounds.

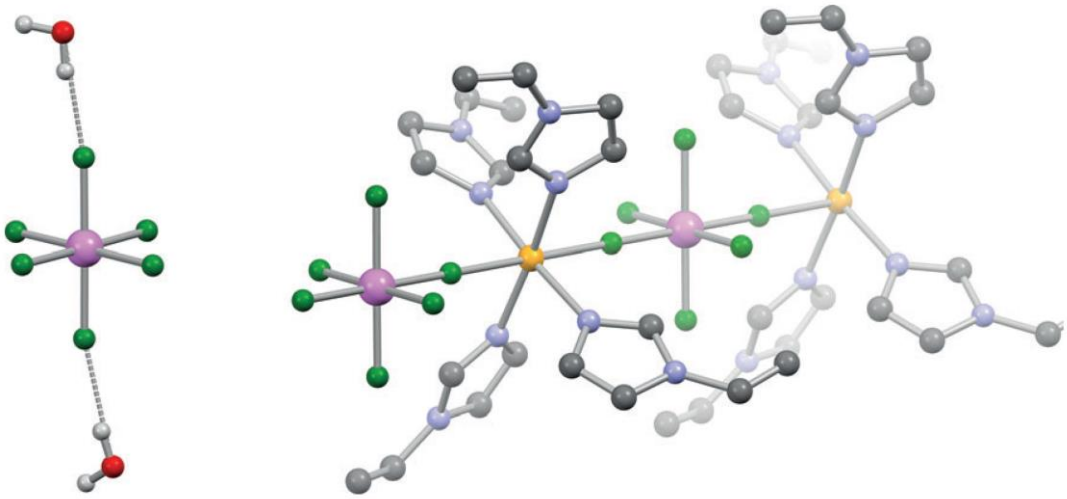

Fig. 5.14: molecular structure of **17** with omitted $P(Ph_4)^+$ counter ions (left), two repetitive motifs in the chains **18** and **19** (left).

The temperature dependence of χT for **17** and **18** were measured with a field of 0.1 T is presented together with the field dependence of the magnetization between 1.8 and 10 K in fig. 5.15. The χT product lowers from 1.43 cm^3 K mol^{-1} at 300 K to 0.88 cm^3 K mol^{-1} at 1.8 K. As intermolecular exchange interactions can be excluded due to the large Re-Re distances of 11 Å in **17**, this reduction of χT at low temperatures is an effect of ZFS. The data of both compouds is nearly identical. The magnetic data as well as spectroscopic data below was fitted to the following Hamiltonian (eq 5.7) describing the S =3/2 system,

$$\hat{H} = \mu_B g H \hat{S} + D\hat{S}_z^2 - \frac{1}{3}S(S+1)) + E(\hat{S}_x^2 - \hat{S}_y^2) \quad (5.7)$$

which is eq. 1.5 with the additional field dependent terms. From the magnetic data the ZFS *D* was estimated to be around 28 cm^{-1}.

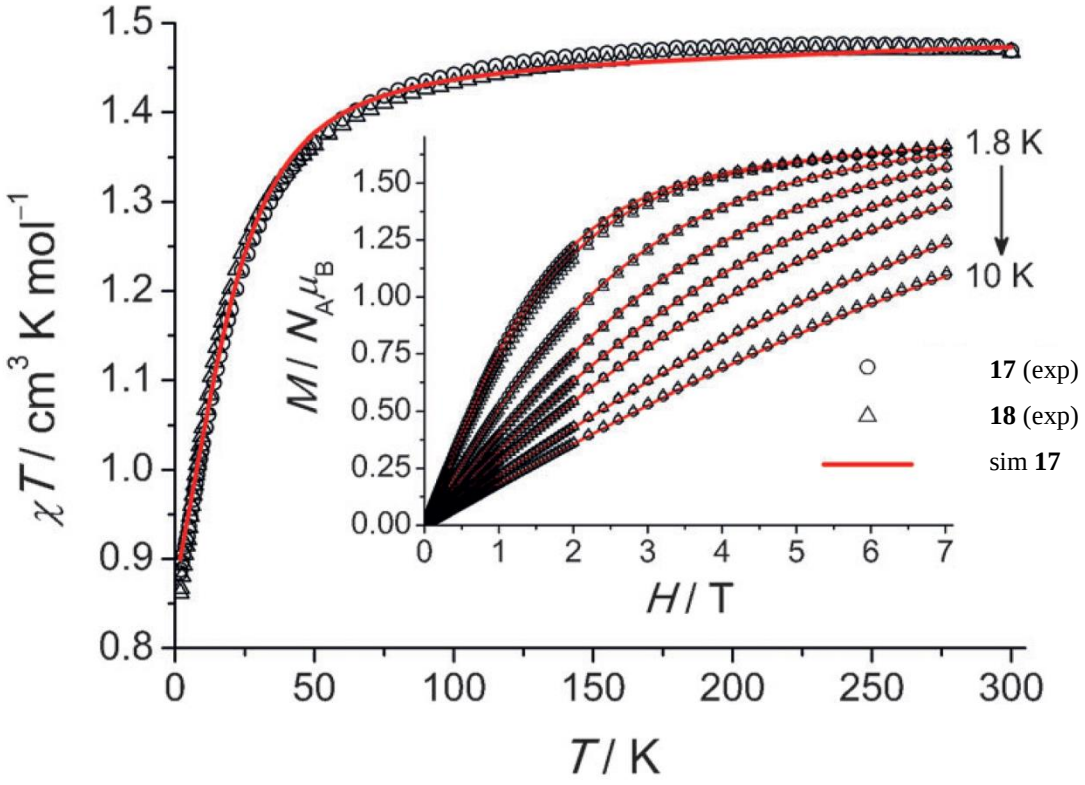

Fig. 5.15: susceptibility data measured at a constant field 0.1 T of **17** (circles) and **18** (triangles). Insert: reduced magnetization data measured at temperatures between 1.8 and 10 K. The red fit lines are for **17**

To study these systems by INS, 2 g of fully deuterated powdered **17** was wrapped with aluminum foil and measured on the time-of-flight spectrometer IN4c. The only prominent peak was found at 48 cm^{-1}. The temperature dependence of the peak (Fig 5.16a) and its *Q*-dependence (Fig 5.16c) strongly indicate a magnetic origin. The energy transfer corresponds to the energy difference between the two doublets $\Delta E = 2\sqrt{D^2 + 3E^2}$.

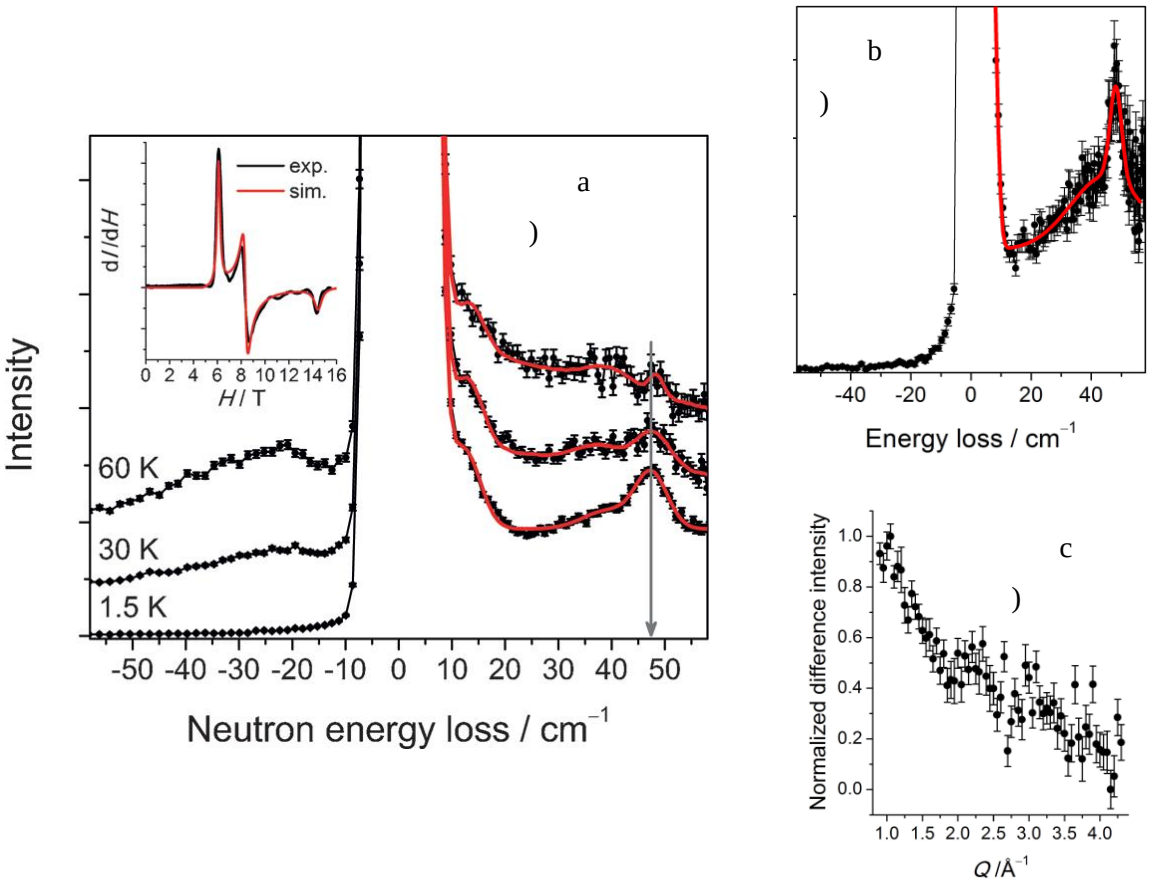

Fig. 5.16: INS data of **17** a) measured at λ_i=2.2 Å at three temperatures between 1.5 and 60 K the data has been added over the *Q* range 0.8 to 1.65 Å^{-1} at the magnetic peak position b) measured at λ_i=2.8 Å and 1.6 K summed over all *Q*. c) *Q* -dependence of the magnetic transition at 48 cm^{-1} (in b) for a clearer view of the dependence the q-dependence of the background next to the peak (at 35cm^{-1}) has been subtracted. The red lines are a sum of four Gaussians, insert a) HF-EPR spectrum of **17** at 5.4 K with 331.2 GHz radiation.

The simultaneous fit of the INS and HF-EPR data yielded parameters D = 23.6 cm^{-1} and $|E|$=2.6 cm^{-1} for **17**. The magnetic data was fitted with these values for D and E fixed, which yielded the following g factors g = 1.69 for the dc data and g =1.76 for the reduce magnetization data. The slightly lower latter g value is in agreement with the HF-EPR data. INS measurements of **18** were not successful, but from the nearly identical magnetic data it can be assumed that the splitting between the two Kramers doublets is very similar for both compounds. Angular Orbital Model (AOM) calculations with the values $e_\sigma^{average}$ =13'000cm^{-1} and $e_\pi^{average}$ =2000cm^{-1} ($\Delta_0 = 3e_\sigma - 4e_\pi$) with a small anisotropy $e_{\sigma,ax} < e_{\sigma,eq}$, $e_{\pi,ax} < e_{\pi,eq}$ reproduced the value and sign of D.

Ac susceptibility measurements were performed on both compounds **17** and **18**. In zero static field no slow relaxation of magnetization was observed. With a small dc field, however, both compounds show clear peaks in χ'' vs. T despite the positive ZFS. The out-of-phase components at optimum dc field H = 0.25 T is presented in Figure 5.17. The fitting of the maximum χ'' values at H = 0.5 T to the Arrhenius law ($\tau(T)=\tau_0 \exp[U_{eff}/(k_BT)]$) resulted in U_{eff} =28.3 K and $\tau_0 = 9.6 \cdot 10^{-9}$ s for **17** and U_{eff} =29.6 K and $\tau_0 = 4.7 \cdot 10^{-10}$ s for **18**. These two compound are new menmbers of a small class of Single Ion Magnets with a positive ZFS[102-105], with only one other example of mononuclear 5d compound[106]. The magnetisazion dynamics is apparently not only a property of the crystal lattice and its phonon spectrum/heat capacity [107], otherwise the magnetic data of **17** and **18** would hardly be so similar.

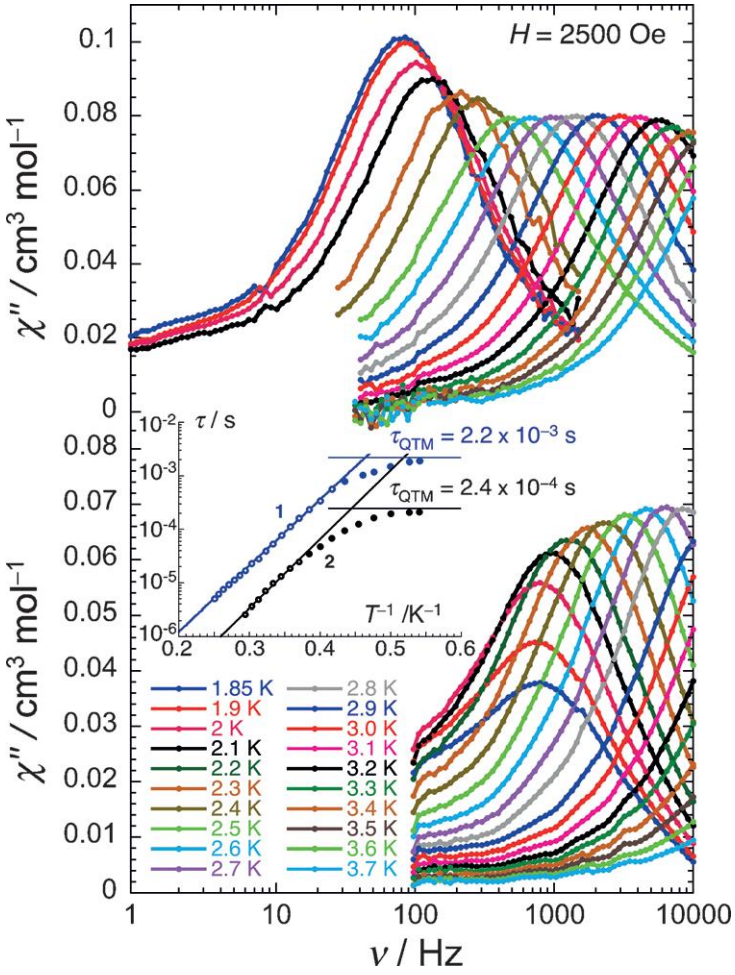

Fig. 5.17: out-of-phase component of the AC suszeptibility of **17** and **18** at optimum dc field H 0.25 T Insert: Arrhenius plot of the peak maxima of the χ'' peaks

Rhombicity as a possible origin for slow relaxation of magnetization can be excluded because of the strict 4-fold symmetry of **18**. X-band EPR of $[Zn(viz)_4(ZrF_6)]_\infty$ with ca. 5% Re(IV) doped is presented in fig. 5.17.

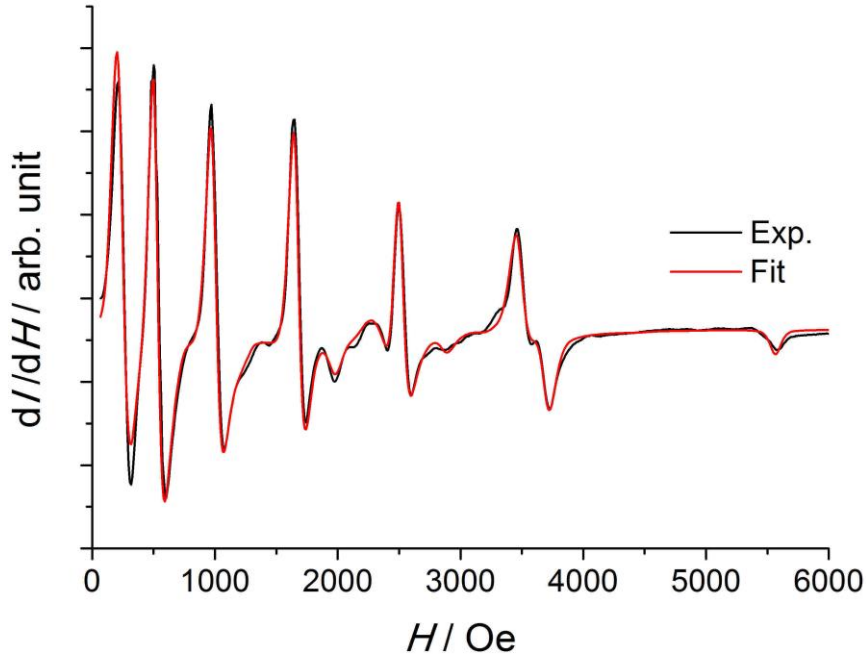

Fig. 5.17: X-band EPR of $[Zn(viz)_4(ZrF_6)]_\infty$ doped with 5% Re(IV)

The hyperfine couplings for **18** were determined to be A_z =0.06179(7) cm^{-1} and A_{xy} = 0.04953(1) cm^{-1}. The associated energy $A_z S_{Re} I_{Re} \approx 0.23$ cm^{-1} is very similar to the magnetic energy in the AC measurments $g_{Re}\mu_B H \cdot S_{Re}$ = 0.3 cm^{-1} at H = 0.25 T. This observation together with the similarity of the magnetic data for **17** and **18** suggests, that the magnetic dynamics could be influenced by the interaction of nuclear with electronic spins, rather than the conventionally considered spin-phonon coupling.

The susceptibility data collected for **19** are presented in Fig. 5.18. The value of the χT product of **19** at room temperature is 3.3 cm^3 K mol^{-1} and increases upon cooling until reaching a maximum of 25.8 cm^3 K mol^{-1} at 6.5 K. This increase is probably due to ferromagnetic interactions between Re(IV) and Ni(II), which can be rationalized by the orthogonality of the respective configurations of Re(IV) (t_{2g}^3) and Ni(II) ($t_{2g}^6 e_g^2$). The data has been modeled employing the Hamiltonian in eq.5.8.

$$\hat{H} = \mu_B H \sum_i g_i \hat{S}_i - 2J \sum_i \hat{S}_i \hat{S}_{i+1} \qquad (5.8)$$

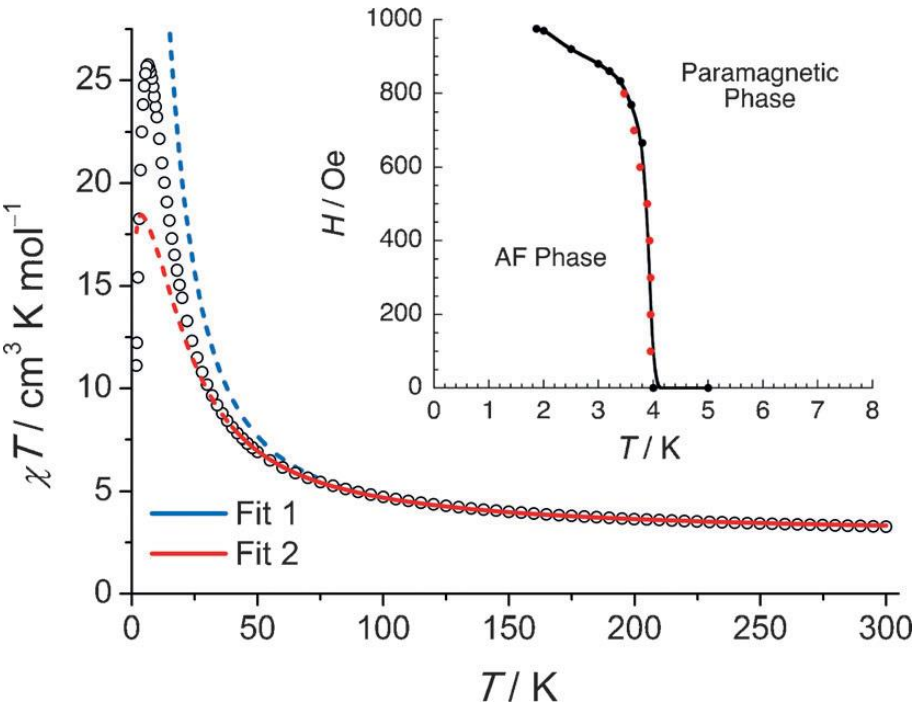

Fig 5.18: temperature dependence of χT of **19** measured with H = 0.1 T, with the two different fits. The dashed lines are extrapolation of the fits. Insert: H vs T magnetic phase diagram for **19** extracted from (black points) dM/dH vs. H maxima and (red points) χ vs.T at low fields

The χT data at high temperatures was fitted in two ways. Fit 1 represents a modeled approach suggested by Drillon et al. [108] for classical spins in the temperature range T = 80-300 K. Fit 2 is an exact diagonalisazion of a $[Ni(II)Re(IV)]_6$ model ring in the temperature range T = 40-300K. The exchange interaction parameters extracted from both fits are similar J(fit1) = 10.8(8)cm^{-1} and J(fit2) = 11.8(5) cm^{-1}. The values are also in agreement with DFT calculations J(DFT) =12.7 cm^{-1}. These values are very large and exceed interactions between Re(IV) and Ni(II) through other bridges such as CN^- (3.7 cm^{-1})[109]. No slow relaxation of magnetization could be observed from AC measurements without and with field in **19**. However below approximately 4 K, the M vs. H curves show S shapes that indicate an antiferromagnetic ground state. From the points of infection of the S shaped curves and from the χ vs T data at low fields, the temperature dependence of H_c (the critical field) was extracted in order to create the magnetic phase diagram presented in fig. 5.18 (insert).

In summery compounds **17** and **18** have been presented and their magnetic properties have been investigated by magnetic measurements and EPR- and INS spectroscopy. Both compounds consist of magnetically isolated Re(IV) ions with S = 3/2 and a positive ZFS parameter. Despite the positive D both compounds show slow magnetic relaxation. Compound **19** shows very strong ferromagnetic interactions between the Ni(II) and Re(IV) ions but no slow relaxation of magnetization.

5.4 influence of small variations of the periferical Ligands on 4f SIM properties

Magnetic molecular materials based on 4f metal ions recently have shown interesting advances as SIM components in spintronics devices [110, 111]. 4f SIMs are promising for such applications because of their high anisotropy. Upon depositing a SIM on a device the molecule will undergo small variations. These changes will change the ligand field (LF), and therefore the magnetic properties. Sessoli *et. al.* demonstrated the hypersensitivity of the anisotropy of 4f metal complexes towards the LF using single-crystal SQUID measurements and *ab initio* calculations, while also showing that magneto-structural correlation methods that are common for 3d [112] metal complexes fail for 4f metals[113, 114].

(H_3trensal=2,2',2''-tris(salicylideneimino)triethylamine) and two more analogs with slightly differing trensal ligands. Compound **20** has been presented as part of an isostructural series [115, 116] which has been studied by optical spectroscopy [117, 118] but its magnetic properties has never been reported.

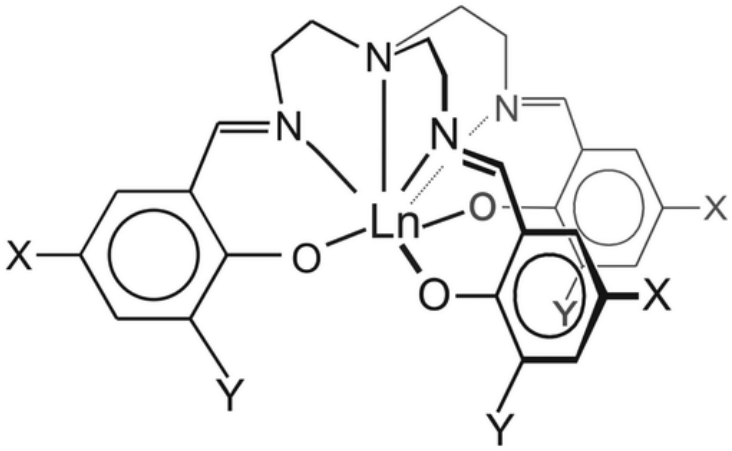

Fig. 5.19 : schematic representation of **20**-**23**, **20:** X=Y=H, **21:** X=CH_3, Y=I, **22:** X=Cl, Y=H

The trensal ligand has been changed to 2,2',2''-tris(3-iodo-5-methyl-salicylideneimino)triethylamine = (5-Me,3-I-trensalH_3) for **21** 2,2',2''-tris(5-chlorosalicylideneimino)triethylamine = 5-Cltrensal for **22** in order to create small distortions of the first and second coordination sphere (see fig 5.20) and in order to study the effects based on electron donating and with drawing substituents. While compounds **20** and **21** both have trigonal symmetry, which reduces the Ligand field parameters from 27 to only 9, **22** belongs, with the $P2_1/c$ space group, to a monoclinic crystal class. Magnetic measurements on a single crystal of **20** and polycrystalline powders of all three samples have been performed but are not presented here. The results of these

magnetic measurements can be studied in reference [74]. This sections focuses on the INS that was obtained for the three compounds. The spectroscopic and the magnetic data are together fitted to a Hamiltonian of the sixth order, describing the $^4I_{15/2}$ ground multiplet. Higher states are neglected in the treatment as the energy difference to the next higher multiplet is much larger (~6000 cm^{-1}) than the splitting of the $^4I_{15/2}$ ground multiplet (~600 cm^{-1}) and the studied temperature range. The results were compared with state of the art *ab initio* calculation using the Molcas 7.8 package program[119] using the Complete Active Space Self-Consistent Field (CASSCF) method [120] or the calculation of the spin-free wave function(more details in ref [74]). *Ab* initio calculations were conducted for the structure of **20** measured at T = 122 K and 293 T with very similar results for both structures. For **21** the crystal structure was measured at T = 122 K was used for the calculations and for **22** the structure of a Gd analog of **22** where Er is replaced with Gd was used[121]. The label CASSCF(2) which is used here corresponds to the notation in the publication [74] and for the calculation of one molecule embedded in 5 layers of point charges.

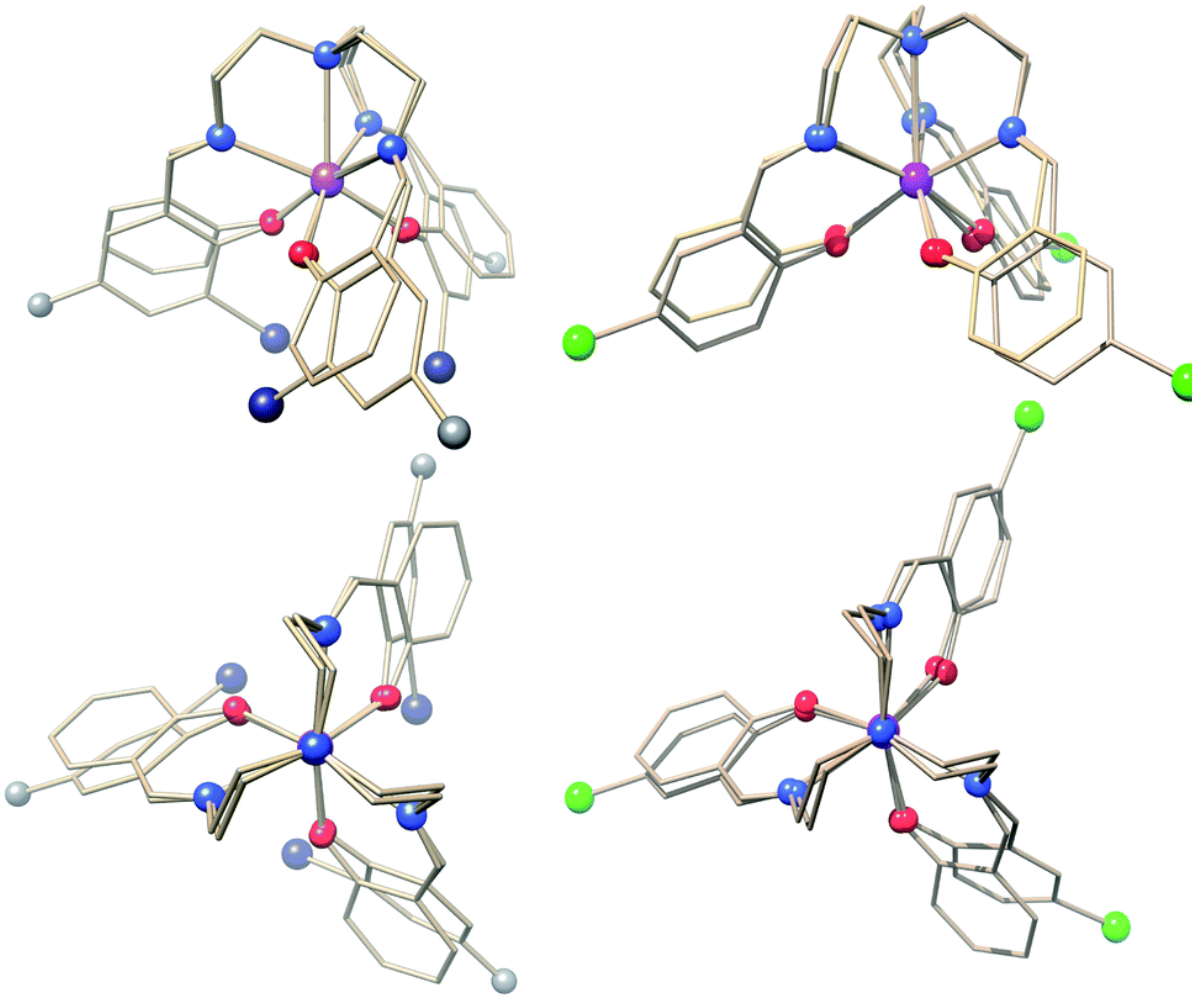

Fig 5.20: structural overlays of **20** with **21** (left side) and **22** (powder phase,right side) along the three-fold axis of **20** (below) and near orthogonal to it (above) for clarity reasons everything apart from the central ion, the coordinating atoms and the trensal substituents are shown as wireframes.

Inelastic neutron scattering data was for compounds **20** and **20´** was collected with the incident neutron wavelength λ_i = 2.2 Å at T= 1.5 K, the spectra are presented in Fig5.21. The high temperature data measured at T = 50 K was downscaled using the Bose Factor $\left[1 - e^{(\hbar\varpi/k_BT)}\right]^{-1}$. Magnetic peaks M1, M2 and M3 were found ant energy positions 53, 102 and 111 cm^{-1}. The features P1, P2 and P3 were determined to be phonon transitions based on the temperature dependence and by comparing the spectra on **20** with **20´**. The difference between the positions of the phonon peak P1 of **20** and **20**' can be explained by the difference in mass of the central 4f ion. The observed magnetic transitions M1-M3 are in agreement with energies reported (54, 102 and 110 cm^{-1})[117].

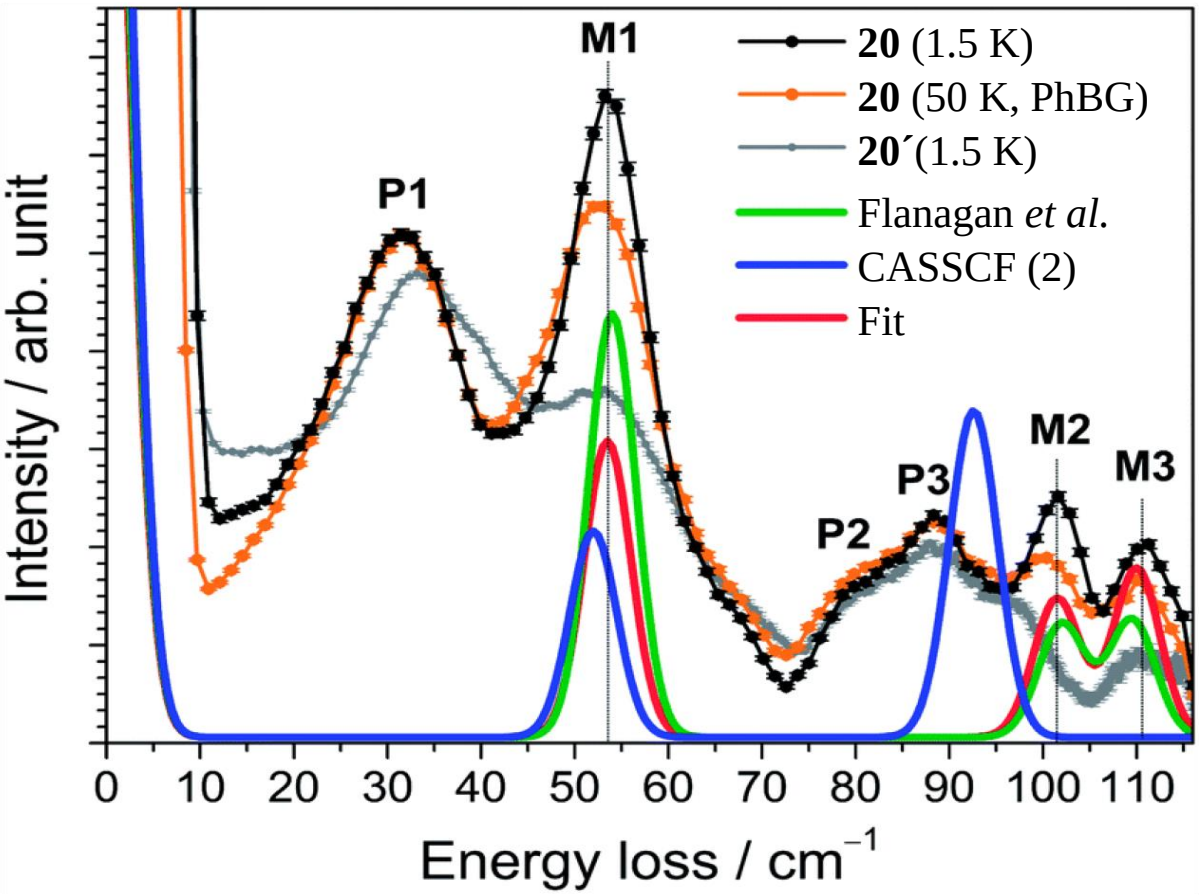

Fig 5.21 INS spectra of **20** at 1.5 K and 50 K and **20´**at 1.5 K measured with incident neutron wavelength λ_i=2.2 Å (the 50 K is downscaled using the Bose factor). The solid lines represent simulations using the different sets of parameters (see text)

Low temperature data of **21** recorded with λ_i = 1.4 Å and λ_i = 2.8 Å is presented in figure 5.22.Three cold transitions can be observed at 37 cm^{-1} (M1), 70 cm^{-1} (M2) and 140 cm^{-1} (M3). The magnetic origin of excitations M1-M3 can be seen by comparing the spectra of 21 with 21' and by analyzing the q-dependence as well as the temperature dependence of the observed peaks. The INS data was fitted together with, here not presented [74], magnetic data to a Hamiltonian containing all the Stevens parameters allowed for C_3 symmetry. The results are presented in table 5.2.

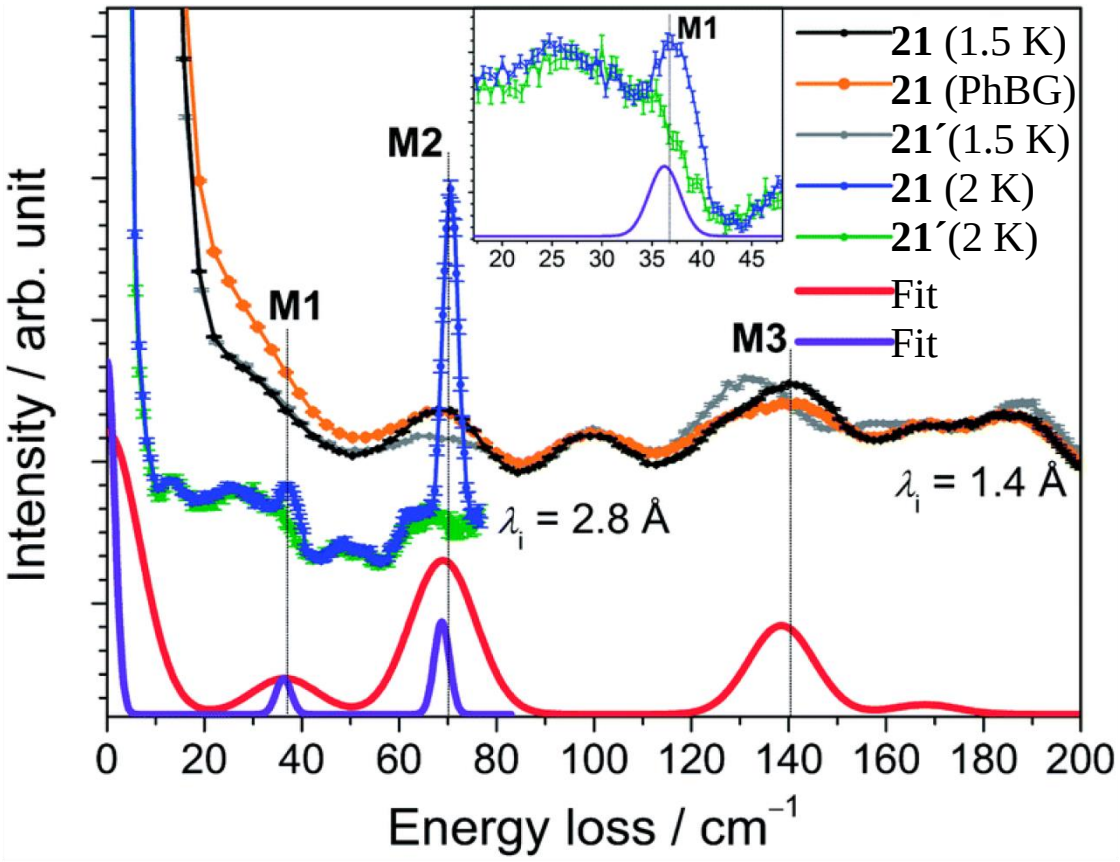

Fig 5.22 INS spectra of **21** and **21´**at low temperatures measured with incident neutron wavelengths λ_i=2.8 Å and λ_i=1.4 Å. The solid lines represent simulations with resolutions comparable to the resolutions with λ_i=2.8 Å (purple) and λ_i=1.4 Å (red).

The INS spectrum (figure 5.23) for compound **22** measured at T =1.5 K and λ_i=2.2 Å shows three transitions at 29 cm^{-1} (M1), 76 cm^{-1} (M2) and 106 cm^{-1} (M3). All three transitions were determined to be of magnetic origins, by comparison with the spectrum of the diamagnetic **22'**. An additional measurement with the shorter wavelength λ_i=1.1 Å did not reveal any additional transition in the higher energy range (up to 500 cm^{-1}). A "hot" transition (m4) can be observed with λ_i=2.8 Å and T = 20 as well as T=40 K at 48 cm^{-1}. The INS data was fitted together with, here not presented [74], magnetic data. The results are presented in table 5.2. Only Stevens parameters allowed for C_3 symmetry were included in the fit. This is an approximation, as the compound possesses lower symmetry, but no better fit was achieved by the inclusion of further parameters. While there are several parameter sets can reproduce the magnetic data, only one (see table 5.2) can reproduce the "hot" transition m4. This shows the power INS. The *ab initio* calculations based on the Gd analog [121] did not reproduce the experimental spectrum. The most probable reasons for this are structural changes due to the exchange of the Gd with Er, that cannot be detected by powder XRD.

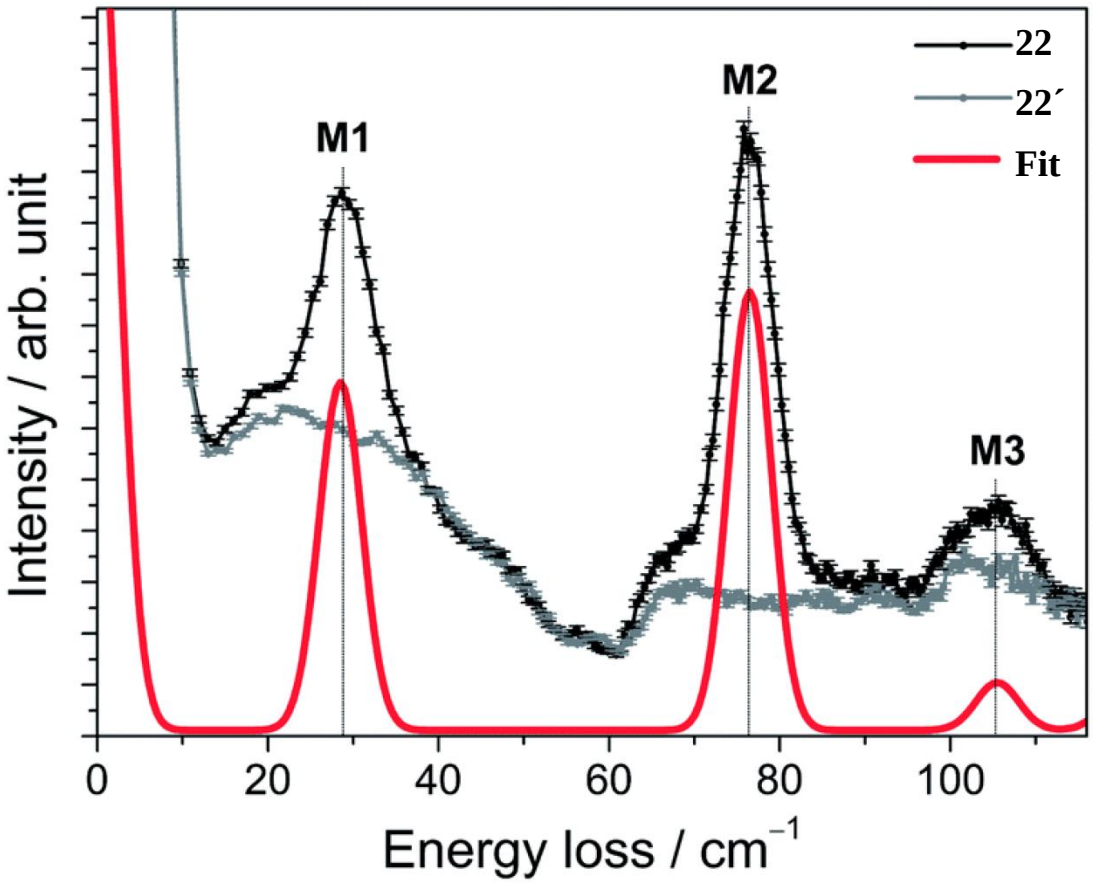

Fig 5.23 INS spectra of **22** and **22'** measured with an incident wavelength λ_i = 2.2 Å at temperature T = 1.5 K The solid line corresponds to the best fit.

As base for a short discussion of the results the obtained Stevens parameters are listed in table 5.2 together with the parameters obtained from *ab initio* calculations for **20** and **21**. Furthermore the results of Flanagan *et*. al [117] were converted to Stevens parameters in order to be able to compare them. Calculated Stevens parameters, forbidden in trigonal symmetry, are non-zero in table 5.2. This is due to the use of the Cholesky decomposition of the bioelectronics integrals, which has limited numerical accuracy.[119]

The parameter sets of **20** are in good agreement, but the new spectroscopic and magnetic data suggests a slightly bigger ZFS parameter. The differences between ab initio calculation and experimental results are slightly bigger for **21** than **20**. This discrepancy can be explained by structural variations between the measurement temperatures for the INS (1.5 to 40 K) and the structure (122K).

Table 5.2: Stevens coefficients (B_k^q) in units cm^{-1} for compounds **20**-**22**.

	Compound **20**			Compound **21**		Compound **22**
k, q	CASSCF (2)	Flanagan *et. al* ref [117]	Best fit	CASSCF (2)	Best fit	Best fit
2, -2	$3.780 \cdot 10^{-3}$			$3.244 \cdot 10^{-3}$		
2, -1	-5.321 • 10-3			$6.266 \cdot 10^{-3}$		
2, 0	-0.8776	-0.975	-1.07(2)	$-2.824 \cdot 10^{-1}$	$-1.9(6) \cdot 10^{-1}$	1.22(2)
2, 1	$5.058 \cdot 10^{-3}$			$-3.124 \cdot 10^{-3}$		
2, 2	$3.439 \cdot 10^{-4}$			$1.775 \cdot 10^{-3}$		
4, -4	1.274 • 10-4			$-1.964 \cdot 10^{-4}$		
4, -3	0	0	0	0	0	0
4, -2	$1.273 \cdot 10^{-4}$			$-1.894 \cdot 10^{-4}$		
4, -1	$-7.482 \cdot 10^{-5}$			$1.359 \cdot 10^{-4}$		
4, 0	$-1.010 \cdot 10^{-3}$	$-0.260 \cdot 10^{-3}$	$-0.2(2) \cdot 10^{-3}$	$1.461 \cdot 10^{-3}$	$-6.0(6) \cdot 10^{-3}$	$-3.9(5) \cdot 10^{-3}$
4, 1	6.359 • 10-5			$-2.101 \cdot 10^{-5}$		
4, 2	8.629 • 10-5			$-3.777 \cdot 10^{-5}$		
4, 3	0.1770	0.287	0.255(5)	$1.707 \cdot 10^{-1}$	$1.1(4) \cdot 10^{-1}$	1(1) • 10-2
4, 4	$-1.21 \cdot 10^{-4}$			$1.348 \cdot 10^{-5}$		
6, -6	$1.555 \cdot 10^{-5}$	$5.89 \cdot 10^{-4}$	$3.5(5) \cdot 10^{-4}$	$4.235 \cdot 10^{-5}$	$1.6(7) \cdot 10^{-4}$	$1.2(1) \cdot 10^{-4}$
6, -5	$1.335 \cdot 10^{-5}$			$-4.616 \cdot 10^{-6}$		
6, -4	$-4.404 \cdot 10^{-7}$			$5.479 \cdot 10^{-7}$		
6, -3	$-1.165 \cdot 10^{-4}$	$-2.45 \cdot 10^{-4}$	$-1(2) \cdot 10^{-4}$	$-2.341 \cdot 10^{-4}$	$1.3(2) \cdot 10^{-3}$	$7(7) \cdot 10^{-5}$
6, -2	$-2.360 \cdot 10^{-6}$			$1.853 \cdot 10^{-6}$		
6, -1	$3.101 \cdot 10^{-6}$			$-6.209 \cdot 10^{-6}$		
6, 0	$9.685 \cdot 10^{-5}$	$1.23 \cdot 10^{-4}$	$1.25(1) \cdot 10^{-4}$	$8.896 \cdot 10^{-5}$	$9.5(6) \cdot 10^{-5}$	$-1.07(3) \cdot 10^{-4}$
6, 1	$-2.971 \cdot 10^{-6}$			$1.485 \cdot 10^{-6}$		
6, 2	$-1.892 \cdot 10^{-6}$			$-1.123 \cdot 10^{-6}$		
6, 3	$-0.8741 \cdot 10^{-3}$	$-0.943 \cdot 10^{-3}$	$-1.27(2) \cdot 10^{-3}$	$-5.176 \cdot 10^{-4}$	$-1(5) \cdot 10^{-5}$	$3.13(8) \cdot 10^{-6}$
6, 4	$8.189 \cdot 10^{-7}$			$-8.547 \cdot 10^{-7}$		
6, 5	$7.960 \cdot 10^{-6}$			$4.747 \cdot 10^{-6}$		
6, 6	$0.8663 \cdot 10^{-3}$	$1.03 \cdot 10^{-3}$	$1.27(2) \cdot 10^{-3}$	$7.316 \cdot 10^{-4}$	$4.2(8) \cdot 10^{-4}$	$1.4(1) \cdot 10^{-5}$
g_{Er}	6/5	6/5	1.18(1)	6/5	1.18(1)	1.18(1)

In general it can be noted that the spectra and the parameters describing the ground state splitting of the three compounds vary greatly. This is also reflected in the *ab initio* calculations. As the three compounds have very similar first coordination spheres (see fig 5.20) the differences in the electronic structure are very likely based on two contributions. One is the difference between electron withdrawing and donating substituents on the trensal ligand, the other are changes in the π interactions mainly occurring due to changes in the orientation of the aromatic rings. Spectroscopic techniques and especially INS proved to be crucial tools for the exact determinations of such changes in properties due to peripheral ligand functionalization.

6. References

1. Sigrist, M., *Magneto-structural correlation in $[Mn_3O]^{7+}$ core SMMs.* master thesis, 2010.
2. Inglis, R., et al., *Enhancing SMM properties via axial distortion of MnIII3 clusters.* Chemical Communications, 2008(45): p. 5924-5926.
3. Weinland, R.F. and G. Fischer, *On manganese acetate and benzoate.* Zeitschrift Fur Anorganische Und Allgemeine Chemie, 1921. **120**(2): p. 161-180.
4. Lis, T., *Preparation, structure, and magnetic properties of a dodecanuclear mixed-valence manganese carboxylate.* Acta Crystallographica Section B, 1980. **36**(9): p. 2042-2046.
5. Sessoli, R., et al., *magnetic bistability in a metal-ion cluster.* Nature, 1993. **365**(6442): p. 141-143.
6. Sessoli, R., et al., *High-Spin molecules - $Mn_{12}O_{12}(O_2CR)_{16}(H_2O)_4$.* Journal of the American Chemical Society, 1993. **115**(5): p. 1804-1816.
7. Gatteschi, D. and R. Sessoli, *Quantum tunneling of magnetization and related phenomena in molecular materials.* Angewandte Chemie-International Edition, 2003. **42**(3): p. 268-297.
8. Waldmann, O., *A Criterion for the Anisotropy Barrier in Single-Molecule Magnets.* Inorganic Chemistry, 2007. **46**(24): p. 10035-10037.
9. Bogani, L. and W. Wernsdorfer, *Molecular spintronics using single-molecule magnets.* Nature Materials, 2008. **7**(3): p. 179-186.
10. Leuenberger, M.N. and D. Loss, *Quantum computing in molecular magnets.* Nature, 2001. **410**(6830): p. 789-793.
11. Gatteschi, D., R. Sessoli, and A. Cornia, *Single-molecule magnets based on iron(III) oxo clusters.* Chemical Communications, 2000(9): p. 725-732.
12. Arom, G., et al., *Manganese carboxylate clusters: from structuralaesthetics to single-molecule magnets.* Polyhedron, 1998. **17**(17): p. 3005-3020.
13. Soler, M., et al., *Synthesis, characterization and magnetic properties of $Mn_{30}O_{24}(OH)_8(O_2CCH_2C(CH_3)_3)_{32}(H_2O)_2(CH_3NO_2)_4$: the largest manganese carboxylate cluster.* Polyhedron, 2001. **20**(11-14): p. 1365-1369.
14. Soler, M., et al., *Single-molecule magnets: A large Mn-30 molecular nanomagnet exhibiting quantum tunneling of magnetization.* Journal of the American Chemical Society, 2004. **126**(7): p. 2156-2165.
15. Feng, P.L., et al., *Single-molecule-magnet behavior and spin changes affected by crystal packing effects.* Inorganic Chemistry, 2008. **47**(19): p. 8610-8612.
16. Feng, P.L., et al., *Nanomodulation of Molecular Nanomagnets.* Inorganic Chemistry, 2009. **48**(8): p. 3480-3492.
17. Inglis, R., et al., *Ground Spin State Changes and 3 D Networks of Exchange Coupled $[MnIII_3]$ Single-Molecule Magnets.* Chemistry – A European Journal, 2008. **14**(30): p. 9117-9121.
18. Inglis, R., et al., *Twisting, bending, stretching: strategies for making ferromagnetic [MnIII3] triangles.* Dalton Transactions, 2009(42): p. 9157-9168.
19. Datta, S., et al., *A comparative EPR study of high- and low-spin Mn6 single-molecule magnets.* Polyhedron, 2009. **28**(9–10): p. 1788-1791.
20. Inglis, R., et al., *Ferromagnetic Mn-3 Single-Molecule Magnets and Their Supramolecular Networks.* Australian Journal of Chemistry, 2009. **62**(9): p. 1108-1118.

21. Inglis, R., et al., *Attempting to understand (and control) the relationship between structure and magnetism in an extended family of Mn-6 single-molecule magnets.* Dalton Transactions, 2009(18): p. 3403-3412.
22. Inglis, R., S.J. Dalgarno, and E.K. Brechin, *A new family of Mn6 SMMs using phosphinate ligands.* Dalton Transactions, 2010. **39**(20): p. 4826-4831.
23. Inglis, R., et al., *Twisted molecular magnets.* Chemical Communications, 2012. **48**(2): p. 181-190.
24. Vincent, J.B., et al., *Preparation and physical properties of trinuclear oxo-centered manganese complexes of general formulation $[Mn_3O(O_2CR)_6L_3]^{0,+}$ (R = methyl or phenyl; L = a neutral donor group) and the crystal structures of $[Mn_3O(O_2CMe)_6(pyr)_3](pyr)$ and $[Mn_3O(O_2CPh)_6(pyr)_2(H_2O)]$ *0.5MeCN.* Journal of the American Chemical Society, 1987. **109**(19): p. 5703-5711.
25. Christou, G., *Manganese carboxylate chemistry and its biological relevance.* Accounts of Chemical Research, 1989. **22**(9): p. 328-335.
26. McCusker, J.K., et al., *Ground-state variability in mu-3-oxide trinuclear mixed-valence high-spin molecules-$Mn_{12}O_{12}(O_2CR)_{16}(H_2O)_4$.* Inorganic Chemistry, 1992. **31**(10): p. 1874-1880.
27. Stamatatos, T.C., et al., *Initial Example of a Triangular Single-Molecule Magnet from Ligand-Induced Structural Distortion of a [MnIII3O]7+ Complex.* Journal of the American Chemical Society, 2005. **127**(44): p. 15380-15381.
28. Cano, J., et al., *On the origin of ferromagnetism in oximato-based [Mn3O]7+ triangles.* Dalton Transactions, 2008(2): p. 234-240.
29. Milios, C.J., et al., *A Record Anisotropy Barrier for a Single-Molecule Magnet.* Journal of the American Chemical Society, 2007. **129**(10): p. 2754-2755.
30. Milios, C.J., et al., *A Single-Molecule Magnet with a "Twist".* Journal of the American Chemical Society, 2006. **129**(1): p. 8-9.
31. Milios, C.J., et al., *Toward a Magnetostructural Correlation for a Family of Mn6 SMMs.* Journal of the American Chemical Society, 2007. **129**(41): p. 12505-12511.
32. Stamatatos, T.C., et al., *New Mn3 structural motifs in manganese single-molecule magnetism from the use of 2-pyridyloximate ligands.* Polyhedron, 2007. **26**(9–11): p. 2165-2168.
33. Cremades, E., et al., *Theoretical Methods Enlighten Magnetic Properties of a Family of Mn6 Single-Molecule Magnets.* Inorganic Chemistry, 2009. **48**(16): p. 8012-8019.
34. Atanasov, M., et al., *Theoretical Insights into the Magnetostructural Correlations in Mn3-Based Single-Molecule Magnets.* Inorganic Chemistry, 2011. **50**(6): p. 2112-2124.
35. Carretta, S., et al., *Breakdown of the giant spin model in the magnetic relaxation of the Mn-6 nanomagnets.* Physical Review Letters, 2008. **100**(15).
36. Carretta, S., et al., *Neutron spectroscopy and magnetic relaxation of the Mn-6 nanomagnets.* Polyhedron, 2009. **28**(9-10): p. 1940-1944.
37. Pieper, O., et al., *Inelastic neutron scattering and frequency-domain magnetic resonance studies of S=4 and S=12 Mn_{6} single-molecule magnets.* Physical Review B, 2010. **81**(17): p. 174420.
38. Lee, S.C., et al., *High-frequency EPR characterization of a triangular Mn-3 single-molecule magnet.* Polyhedron, 2007. **26**(9-11): p. 2225-2229.
39. Gatteschi, D., R. Sessoli, and J. Villain, *Molecular Nanomagnets*. 2006, Oxford New York: Oxford University Press.
40. Wilson, A., et al., *Magnetization tunneling in high-symmetry single-molecule magnets: Limitations of the giant spin approximation.* Physical Review B, 2006. **74**(14): p. 4.

41. Accorsi, S., et al., *Tuning anisotropy barriers in a family of tetrairon(III) single-molecule magnets with an S=5 ground state.* Journal of the American Chemical Society, 2006. **128**(14): p. 4742-4755.
42. Liviotti, E., S. Carretta, and G. Amoretti, *S-mixing contributions to the high-order anisotropy terms in the effective spin Hamiltonian for magnetic clusters.* Journal of Chemical Physics, 2002. **117**(7): p. 3361-3368.
43. Carpenter, J.M., *Neutron Production, Moderation and Characterization of Sources*. 2004.
44. Furrer, A. and O. Waldmann, *Magnetic cluster excitations.* Reviews of Modern Physics, 2013. **85**(1): p. 367-420.
45. Furrer, A. and H.U. Güdel, *Neutron inelastic scattering from isolated clusters of magnetic ions.* Journal of Magnetism and Magnetic Materials, 1979. **14**(2–3): p. 256-264.
46. Basler, R., et al., *Molecular spin clusters: New synthetic approaches and neutron scattering studies.* Chemphyschem, 2003. **4**(9): p. 910-926.
47. Squires, G.L., *Introduction to the theory of thermal neutron scattering*. 1978, Cambridge, UK: Cambridge University Press.
48. Brown, P.J., *Magnetic Form Factors*, in *Neutron Data Booklet*, A.-J. Dianoux and G. Lander, Editors. 2003, OCP Science Imprint: Grenoble.
49. Gudel, H.U. and A. Furrer, *Neutron inelastic-scattering study of exchange interactions in a Chromium(III) dimer my-hydroxo-bisphentaaminechromium(III) chloride monohydrate.* Molecular Physics, 1977. **33**(5): p. 1335-1344.
50. Waldmann, O., et al., *Exchange-coupling constants, spin density map, and Q dependence of the inelastic neutron scattering intensity in single-molecule magnets.* Physical Review B, 2007. **75**(17): p. 11.
51. Andres, H., et al., *Inelastic neutron scattering and magnetic susceptibilities of the single-molecule magnets $Mn_4O_3X(OAc)_3(dbm)_3$ (X = Br, Cl, OAc, and F): Variation of the anisotropy along the series.* Journal of the American Chemical Society, 2000. **122**(50): p. 12469-12477.
52. Caciuffo, R., et al., *Neutron Spectroscopy for the Magnetic Anisotropy of Molecular Clusters.* Physical Review Letters, 1998. **81**(21): p. 4744-4747.
53. Peters, J., *Neutron transmission probability through a revolving slit for a continuous source and a divergent neutron beam.* Nuclear Instruments & Methods in Physics Research Section a-Accelerators Spectrometers Detectors and Associated Equipment, 2005. **540**(2-3): p. 419-429.
54. *The yellow book: Guide to Neutron Research Facilities* ed. G. Cicognani. 2008, Grenoble: Institut Laue-Langevin
55. Azuah, R.T., et al., *DAVE: A Comprehensive Software Suite for the Reduction, Visualization, and Analysis of Low Energy Neutron Spectroscopic Data.* Journal of Research of the National Institute of Standards and Technology, 2009. **114**(6): p. 341-358.
56. Cukiernik, F.D., et al., *Pyrazine-mediated antiferromagnetic intermolecular exchange in mixed-valent diruthenium tetracarboxylates.* Inorganica Chimica Acta, 1994. **215**(1–2): p. 203-207.
57. Richard, D., M. Ferrand, and G.J. Kearley, *Analysis and visualisation of neutron-scattering data.* Journal of Neutron Research, 1996. **4**(1-4): p. 33-39.
58. in5_reduce.prox. Available from: http://www.ill.eu/instruments-support/instruments-groups/instruments/in5/more/data-analysis/.
59. Tregenna-Piggott, P.L.W., et al., *Single-Ion Anisotropy and Exchange Interactions in the Cyano-Bridged Trimers (Mn_2MIII)-M-III$(CN)_6$ (M-III = Co, Cr, Fe) Species*

Incorporating Mn(5-Brsalen) (+) Units: An Inelastic Neutron Scattering and Magnetic Susceptibility Study. Inorganic Chemistry, 2009. **48**(1): p. 128-137.

60. Dunstan, W.R. and T.A. Henry, *VIII.-Occurrence of orthohydroxyacetophenone in the volatile oil of Chione glabra.* Journal of the Chemical Society, Transactions, 1899. **75**(0): p. 66-71.
61. Yang, C.-I., et al., *A $[MnIII_3O]^{7+}$ Single-Molecule Magnet: the Anisotropy Barrier Enhanced by Structural Distortion.* Inorganic Chemistry, 2008. **47**(22): p. 10184-10186.
62. Cremades, E., et al., *Theoretical Methods Enlighten Magnetic Properties of a Family of Mn-6 Single-Molecule Magnets.* Inorganic Chemistry, 2009. **48**(16): p. 8012-8019.
63. Barra, A.L., et al., *The origin of transverse Anisotropy in axially symmetric single molecule magnets.* Journal of the American Chemical Society, 2007. **129**(35): p. 10754-10762.
64. Yang, C.-I., et al., *Crystal packing effects within $[MnIII_3O]^{7+}$ single-molecule magnets: Controlling intermolecular antiferromagnetic interactions.* Polyhedron, 2011. **30**(18): p. 3272-3278.
65. O'Connor, C.J., Progress in Inorganic Chemistry, 1982. **29**: p. 203-283.
66. Lecren, L., et al., *Slow relaxation in a one-dimensional rational assembly of antiferromagnetically coupled Mn-4 single-molecule magnets.* Journal of the American Chemical Society, 2005. **127**(49): p. 17353-17363.
67. Inglis, R., et al., *Assembling molecular triangles into discrete and infinite architectures.* CrystEngComm, 2010. **12**(7): p. 2064-2072.
68. Tregenna-Piggott, P.L.W., et al., *Single-Ion Anisotropy and Exchange Interactions in the Cyano-Bridged Trimers $MnIII_2MIII(CN)_6$ (MIII = Co, Cr, Fe) Species Incorporating [Mn(5-Brsalen)]+ Units: An Inelastic Neutron Scattering and Magnetic Susceptibility Study.* Inorganic Chemistry, 2008. **48**(1): p. 128-137.
69. Pedersen, K.S., et al., *Mn-III zero-field splitting parameters and weak exchange interactions in a cyanide-bridged {Mn-III-Ir-III-Mn-III} cluster.* Inorganic Chemistry Communications, 2012. **24**: p. 24-28.
70. Dreiser, J., et al., *Three-Axis Anisotropic Exchange Coupling in the Single-Molecule Magnets NEt_4 $MnIII_2(5\text{-}Brsalen)_2(MeOH)_2MIII(CN)_6$ (M=Ru, Os).* Chemistry-a European Journal, 2013. **19**(11): p. 3693-3701.
71. Pedersen, K.S., et al., *$[ReF6]2-$: A Robust Module for the Design of Molecule-Based Magnetic Materials.* Angewandte Chemie International Edition, 2014. **53**(5): p. 1351-1354.
72. Singh, S.K., et al., *Angular dependence of the exchange interaction in fluoride-bridged Gd-III-Cr-III complexes.* Chemical Communications, 2013. **49**(49): p. 5583-5585.
73. Mahenthirarajah, T., Y. Li, and P. Lightfoot, *Hydrothermal synthesis of vanadium oxyfluoride chains incorporating covalently bound copper coordination complexes.* Inorganic Chemistry, 2008. **47**(19): p. 9097-9102.
74. Pedersen, K.S., et al., *Modifying the properties of 4f single-ion magnets by peripheral ligand functionalisation.* Chemical Science, 2014. **5**(4): p. 1650-1660.
75. Pfeiffer, P., et al., *Tricyclische orthokondensierte Nebenvalenzringe.* Justus Liebigs Annalen der Chemie, 1933. **503**(1): p. 84-130.
76. Miyasaka, H., A. Saitoh, and S. Abe, *Magnetic assemblies based on Mn(III) salen analogues.* Coordination Chemistry Reviews, 2007. **251**(21-24): p. 2622-2664.
77. Choi, H.J., J.J. Sokol, and J.R. Long, *High-spin metal-cyanide clusters: species incorporating $[Mn(salen)]^+$ complexes as a source of anisotropy.* Journal of Physics and Chemistry of Solids, 2004. **65**(4): p. 839-844.

78. Birk, T., et al., *Magnetic Properties of a Manganese(III) Chain with Monoatomic Bridges: catena-MnF(salen).* Inorganic Chemistry, 2011. **50**(12): p. 5312-5314.
79. Miyasaka, H., et al., *Complexes Derived from the Reaction of Manganese(III) Schiff Base Complexes and Hexacyanoferrate(III): Syntheses, Multidimensional Network Structures, and Magnetic Properties.* Journal of the American Chemical Society, 1996. **118**(5): p. 981-994.
80. Miyasaka, H., et al., *Assembling Bi-, Tri- and Pentanuclear Complexes into Extended Structures Using a Desolvation Reaction: Synthesis, Structure, and Magnetic Properties of Manganese(III)−Schiff-Base−Hexacyanoferrate Polymeric Compounds and Their Derived Extended Structures.* Inorganic Chemistry, 1998. **37**(2): p. 255-263.
81. Ferbinteanu, M., et al., *Single-Chain Magnet $(NEt_4)[Mn_2(5\text{-}MeOsalen)_2Fe(CN)_6]$ Made of MnIII−FeIII−MnIII Trinuclear Single-Molecule Magnet with an ST = 9/2 Spin Ground State.* Journal of the American Chemical Society, 2005. **127**(9): p. 3090-3099.
82. Dreiser, J., et al., *Frequency-Domain Fourier-Transform Terahertz Spectroscopy of the Single-Molecule Magnet (NEt_4) $Mn_2(5\text{-}Brsalen)_2(MeOH)_2Cr(CN)_6$.* Chemistry-a European Journal, 2011. **17**(27): p. 7492-7498.
83. Pedersen, K.S., et al., *Enhancing the Blocking Temperature in Single-Molecule Magnets by Incorporating 3d-5d Exchange Interactions.* Chemistry-a European Journal, 2010. **16**(45): p. 13458-13464.
84. Pedersen, K.S., et al., *A linear single-molecule magnet based on $Ru\text{-}III(CN)_6^{3-}$.* Chemical Communications, 2011. **47**(24): p. 6918-6920.
85. Albores, P., et al., *Crystal structure and electronic and magnetic properties of hexacyanoosmate(III).* Inorganic Chemistry, 2006. **45**(6): p. 2361-2363.
86. Van den Heuvel, W., M.F.A. Hendrickx, and A. Ceulemans, *A CASPT2 study of the electronic spectrum of hexacyanoosmate(III).* Inorganic Chemistry, 2007. **46**(19): p. 8032-8037.
87. Bendix, J., P. Steenberg, and I. Sotofte, *Isolation and molecular structure of hexacyanoruthenate(III).* Inorganic Chemistry, 2003. **42**(15): p. 4510-4512.
88. Gerloch, M. and J.R. Miller, *Covalence and the Orbital Reduction Factor, k, in Magnetochemistry*, in *Progress in Inorganic Chemistry*. 2007, John Wiley & Sons, Inc. p. 1-47.
89. Griffith, J.S., *The Theory of Transition-Metal Ions*. 1961, Cambridge: Cambridge University Press.
90. Ashcroft, N.W. and N.D. Mermin, *Solid State Physics*. 1976, Florida: Saunders College Publishing.
91. Dreiser, J., et al., *X-ray Magnetic Circular Dichroism (XMCD) Study of a Methoxide-Bridged DyIII–CrIII Cluster Obtained by Fluoride Abstraction from cis-$[CrIIIF_2(phen)_2]^+$*. The Journal of Physical Chemistry A, 2012. **116**(30): p. 7842-7847.
92. McRobbie, A., et al., *Chromium chains as polydentate fluoride ligands for lanthanides.* Chemical Communications, 2011. **47**(22): p. 6251-6253.
93. Birk, T., et al., *Fluoride Bridges as Structure-Directing Motifs in 3d-4f Cluster Chemistry.* Inorganic Chemistry, 2012. **51**(9): p. 5435-5443.
94. Thuesen, C.A., et al., *Fluoride-bridged $\{Ln_2Cr_2\}$ polynuclear complexes from semi-labile mer-$[CrF_3(py)_3]$ and $[Ln(hfac)_3(H_2O)_2]$*. Dalton Transactions, 2012. **41**(37): p. 11284-11292.
95. Press, W.H., et al., *Numerical Receipes in C: The Art of Scientific Computing*. 2nd ed. 1992, Cambridge, MA: Cambridge University Press.
96. Singh, S.K. and G. Rajaraman, *Decisive interactions that determine ferro/antiferromagnetic coupling in {3d-4f} pairs: a case study on dinuclear {V(IV)-Gd(III)} complexes.* Dalton Transactions, 2013. **42**(10): p. 3623-3630.

97. Singh, S.K., N.K. Tibrewal, and G. Rajaraman, *Density functional studies on dinuclear {(NiGdIII)-Gd-II} and trinuclear {(NiGdNiII)-Gd-II-Ni-III} complexes: magnetic exchange and magneto-structural maps.* Dalton Transactions, 2011. **40**(41): p. 10897-10906.
98. Rajaraman, G., et al., *Density functional studies on the exchange interaction of a dinuclear Gd(III)-Cu(II) complex: method assessment, magnetic coupling mechanism and magneto-structural correlations.* Dalton Transactions, 2009(17): p. 3153-3161.
99. Paulovic, J., et al., *Mechanism of ferromagnetic coupling in copper(II)-gadolinium(II) complexes.* Journal of the American Chemical Society, 2004. **126**(10): p. 3321-3331.
100. Rajeshkumar, T. and G. Rajaraman, *Is a radical bridge a route to strong exchange interactions in lanthanide complexes? A computational examination.* Chemical Communications, 2012. **48**(63): p. 7856-7858.
101. Singh, S.K., et al., *Theoretical studies on {3d-Gd} and {3d-Gd-3d} complexes: Effect of metal substitution on the effective exchange interaction.* Polyhedron, 2013. **66**: p. 81-86.
102. Zadrozny, J.M., et al., *Slow magnetic relaxation in a pseudotetrahedral cobalt(II) complex with easy-plane anisotropy.* Chemical Communications, 2012. **48**(33): p. 3927-3929.
103. Vallejo, J., et al., *Field-Induced Slow Magnetic Relaxation in a Six-Coordinate Mononuclear Cobalt(II) Complex with a Positive Anisotropy.* Journal of the American Chemical Society, 2012. **134**(38): p. 15704-15707.
104. Colacio, E., et al., *Slow Magnetic Relaxation in a Co-II-Y-III Single-Ion Magnet with Positive Axial Zero-Field Splitting.* Angewandte Chemie-International Edition, 2013. **52**(35): p. 9130-9134.
105. Huang, W., et al., *Field-induced slow relaxation of magnetization in a tetrahedral Co(II) complex with easy plane anisotropy.* Dalton Transactions, 2013. **42**(43): p. 15326-15331.
106. Martinez-Lillo, J., et al., *Highly Anisotropic Rhenium(IV) Complexes: New Examples of Mononuclear Single-Molecule Magnets.* Journal of the American Chemical Society, 2013. **135**(37): p. 13737-13748.
107. Casimir, H.B.G. and F.K. du Pré, *Note on the thermodynamic interpretation of paramagnetic relaxation phenomena.* Physica, 1938. **5**(6): p. 507-511.
108. Drillon, M., et al., *Classical Treatment of a Heisenber Linear-Chain with Spin Alteration - Appication to the MnNi(edta)*6H20 Complex.* Chemical Physics, 1983. **79**(3): p. 449-453.
109. Harris, T.D., et al., *$ReCl_4(CN)_2^{2-}$: A High Magnetic Anisotropy Building Unit Giving Rise to the Single-Chain Magnets $(DMF)_4MReCl_4(CN)_2$ (M = Mn, Fe, Co, Ni).* Journal of the American Chemical Society, 2010. **132**(11): p. 3980-3988.
110. Urdampilleta, M., et al., *Supramolecular spin valves.* Nature Materials, 2011. **10**(7): p. 502-506.
111. Ganzhorn, M., et al., *Strong spin-phonon coupling between a single-molecule magnet and a carbon nanotube nanoelectromechanical system.* Nature Nanotechnology, 2013. **8**(3): p. 165-169.
112. Petit, S., et al., *A dinuclear cobalt(II) complex of calix 8 arenes exibiting strong magnetic anisotropy.* Dalton Transactions, 2007(40): p. 4582-4588.
113. Cucinotta, G., et al., *Magnetic Anisotropy in a Dysprosium/DOTA Single-Molecule Magnet: Beyond Simple Magneto-Structural Correlations.* Angewandte Chemie-International Edition, 2012. **51**(7): p. 1606-1610.
114. Luzon, J. and R. Sessoli, *Lanthanides in molecular magnetism: so fascinating, so challenging.* Dalton Transactions, 2012. **41**(44): p. 13556-13567.

115. Bernhardt, P.V., B.M. Flanagan, and M.J. Riley, *Isomorphous lanthanide complexes of a tripodal N_4O_3 ligand.* Australian Journal of Chemistry, 2000. **53**(3): p. 229-231.
116. Bernhardt, P.V., B.M. Flanagan, and M.J. Riley, *Completion of the isomorphous Ln(trensal) series.* Australian Journal of Chemistry, 2001. **54**(4): p. 229-232.
117. Flanagan, B.M., et al., *Ligand-field analysis of an Er(III) complex with a heptadentate tripodal N4O3 ligand.* Inorganic Chemistry, 2001. **40**(21): p. 5401-5407.
118. Flanagan, B.M., et al., *A ligand-field analysis of the trensal (H_3trensal=2,2 ',2 ''-tris(salicylideneimino)triethylamine) ligand. An application of the angular overlap model to lanthanides.* Inorganic Chemistry, 2002. **41**(20): p. 5024-5033.
119. Aquilante, F., et al., *Software News and Update MOLCAS 7: The Next Generation.* Journal of Computational Chemistry, 2010. **31**(1): p. 224-247.
120. Roos, B.O., P.R. Taylor, and P.E.M. Siegbahn, *A complete active SCF Method (CASSCF) using a Density-Matrix formulated super-CI Approach.* Chemical Physics, 1980. **48**(2): p. 157-173.
121. Kanesato, M., F.N. Ngassapa, and T. Yokoyama, *Crystal structure of a gadolinium(III) complex of tripodal tris(((5-chlorosalicylidene)amino)ethyl)amine.* Analytical Sciences, 2001. **17**(11): p. 1359-1360.

Appendix A: additional figures

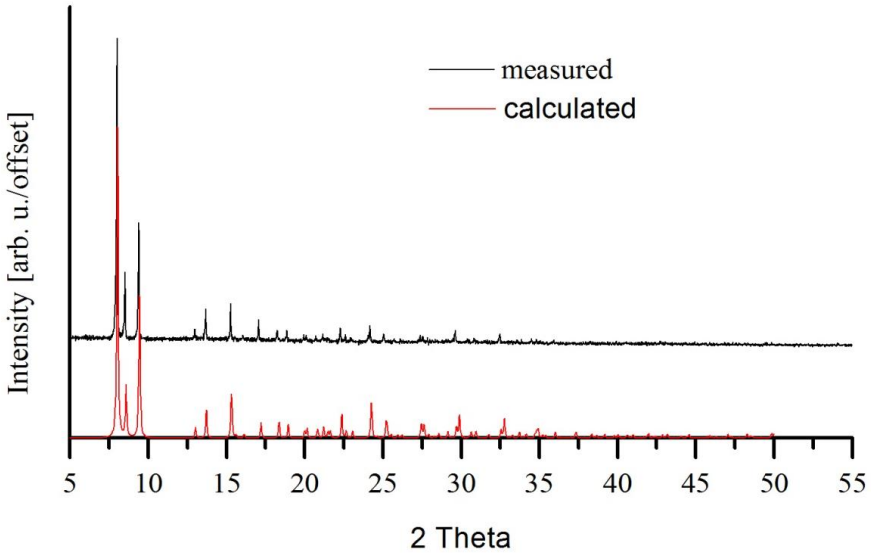

Figure A1: measured x-ray powder diffractogram of compound **1** and calculated from the published structure file.

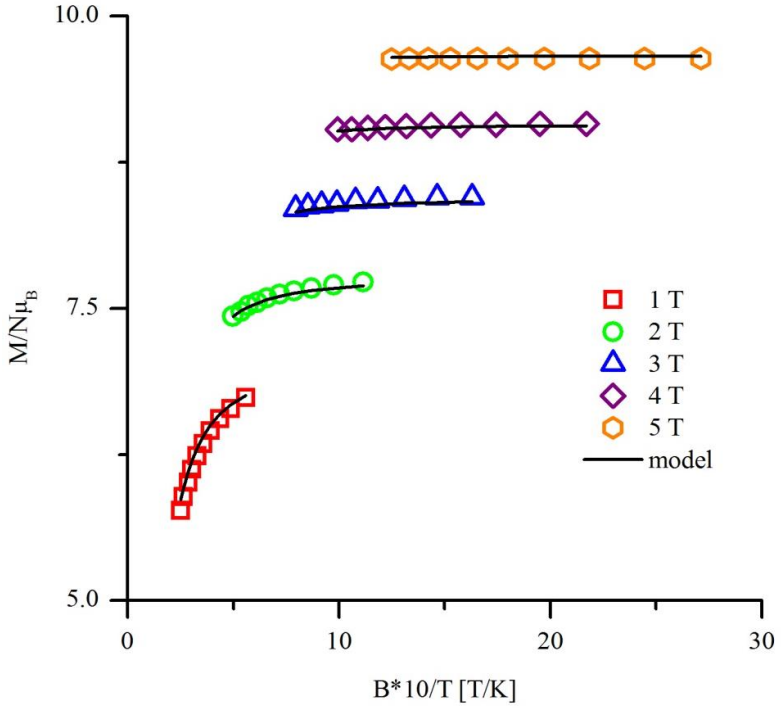

Figure A2: reduced magnetization data of compound **1** digitized from [16] and simulation with the Giant spin Hamiltonian parameters described in chapter 2

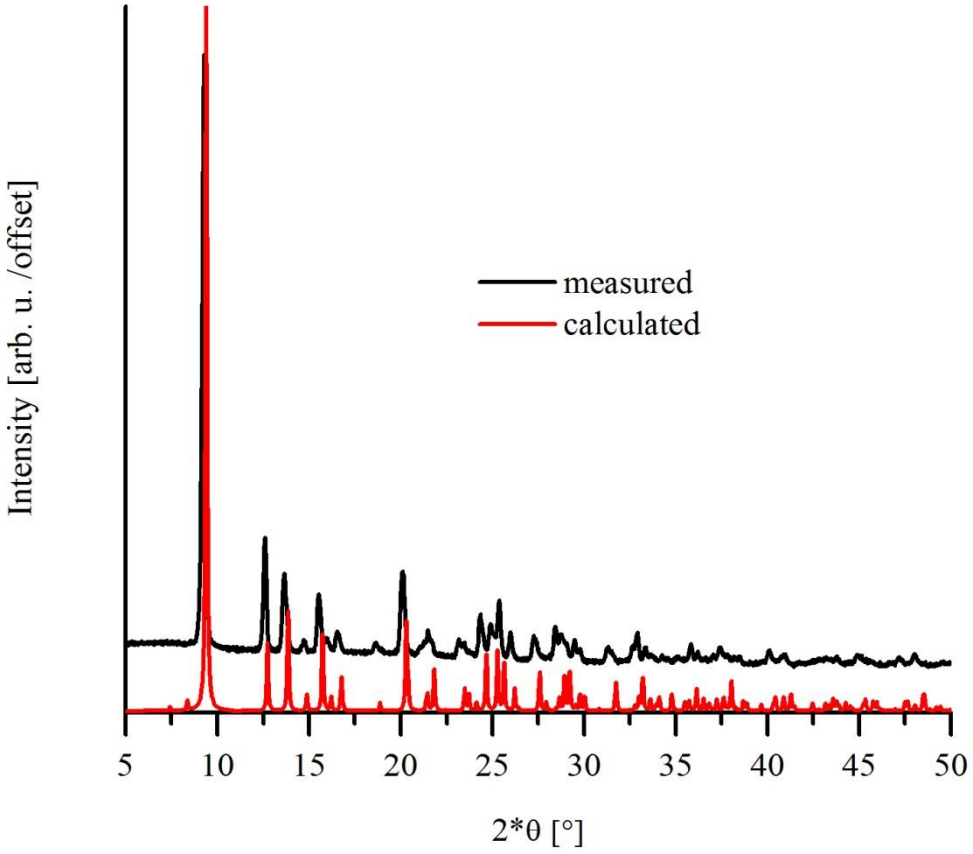

Fig.A3: powder x-ray diffraction data of compound **7** after the neutron experiment (black) and calculated from the crystalstructure (red)

Appendix B: publications

Publications that are part of the thesis

M. Sigrist, K.S. Pedersen, T.J. Morsing, J. Hauser, M. Atanasov, H. Mutka, S. Decurtins, P.L.W. Tregenna-Piggott, , J. Bendix, Effects of JT axis alignment in $[Mn_3O]^{7+}$ core SMMs, studied by Inelastic Neutron Scattering, in preparation for European Journal of Inorganic Chemistry

I: K. S. Pedersen, L. Ungur, **M. Sigrist**, A. Sundt, M. Schau-Magnussen, V. Vieru, H. Mutka, S. Rols, H. Weihe, O. Waldmann, L. F. Chibotaru, J. Bendix, J. Dreiser, Modifying the properties of 4f single-ion magnets by peripheral ligand functionalisation. *Chemical Science* **5**, 1650-1660 (2014)

II: K. S. Pedersen, **M. Sigrist**, M. A. Sørensen, A.-L. Barra, T. Weyhermüller, S. Piligkos, C. A. Thuesen, M. G. Vinum, H. Mutka, H. Weihe, R. Clérac, J. Bendix, [ReF6]2−: A Robust Module for the Design of Molecule-Based Magnetic Materials. *Angewandte Chemie International Edition* **53**, 1351-1354 (2014)

III: J. Dreiser, K. S. Pedersen, A. Schnegg, K. Holldack, J. Nehrkorn, **M. Sigrist**, P. Tregenna-Piggott, H. Mutka, H. Weihe, V. S. Mironov, J. Bendix, O. Waldmann, Three-Axis Anisotropic Exchange Coupling in the Single-Molecule Magnets NEt4 MnIII2(5-Brsalen)2(MeOH)2MIII(CN)6 (M=Ru, Os). *Chemistry-a European Journal* **19**, 3693-3701 (2013)

IV: S. K. Singh, K. S. Pedersen, **M. Sigrist**, C. A. Thuesen, M. Schau-Magnussen, H. Mutka, S. Piligkos, H. Weihe, G. Rajaraman, J. Bendix, Angular dependence of the exchange interaction in fluoride-bridged Gd-III-Cr-III complexes. *Chemical Communications* **49**, 5583-5585 (2013)

V: K. S. Pedersen, **M. Sigrist**, H. Weihe, P. L. W. Tregenna-Piggott, M. Schau-Magnussen, J. Dreiser, H. Mutka, A. L. Barra, J. Bendix, Mn-III zero-field splitting parameters and weak exchange interactions in a cyanide-bridged {Mn-III-Ir-III-Mn-III} cluster. *Inorganic Chemistry Communications* **24**, 24-28 (2012)

Further publications

K. S. Pedersen, **M. Sigrist**, H. Weihe, A. D. Bond, C. A. Thuesen, K. P. Simonsen, T. Birk, H. Mutka, A.-L. Barra, J. Bendix, Magnetic Interactions through Fluoride: Magnetic and Spectroscopic Characterization of Discrete, Linearly Bridged Mn(III)2(mu-F)F4(Me3tacn)2 (PF6). *Inorganic chemistry* **53**, 5013-5019 (2014)

Y.-F. Ran, M. Steinmann, **M. Sigrist**, S.-X. Liu, J. Hauser, S. Decurtins, Tetrathiafulvalene-based lanthanide coordination complexes: Synthesis, crystal structure, optical and electrochemical characterization. *Comptes Rendus Chimie* **15**, 838-844 (2012) (not discussed in the thesis)

M. Atanasov, B. Delley, F. Neese, P. L. Tregenna-Piggott, **M. Sigrist**, Theoretical Insights into the Magnetostructural Correlations in Mn3-Based Single-Molecule Magnets. *Inorganic Chemistry* **50**, 2112-2124 (2011)

0:

Anisotropy barriers in manganese(III)-oximate single-molecule magnets investigated by inelastic neutron scattering and HF-EPR spectroscopy.

Marc Sigrist, Philip L. W. Tregenna-Piggott, Kasper S. Pedersen, Mikkel A. Sørensen, Anne-Laure Barra, Hannu Mutka and Jesper Bendix

Manuscript draft

EurJIC European Journal of Inorganic Chemistry
ChemPubSoc Europe
FULL PAPER

DOI: 10.1002/ejic.201((will be filled in by the editorial staff))

Anisotropy barriers in manganese(III)-oximate single-molecule magnets investigated by inelastic neutron scattering and HF-EPR spectroscopy.

Marc Sigrist,[a,c] Philip L. W. Tregenna-Piggott,[d] Kasper S. Pedersen,[a] Mikkel A. Sørensen,[a] Anne-Laure Barra,[b] Hannu Mutka[c] and Jesper Bendix*[a]

Keywords: Molecular magnetism / neutron scattering / anisotropy architecture / mangansese / oximate

The ground state electronic structure of the *S*=6 ground states of three trinuclear, ferromagnetically coupled manganese(III) oximate complexes have been investigated in detail by use of INS and HF-EPR spectroscopy. The systems $Mn_3O(R\text{-}sao)_3(2,4'\text{-bipyridine})_3XO_4$ have been chosen to possess high crystallographic symmetry. A consistent parametrization of all experimental data was achieved and effective barriers determined from ac-susceptibility data were shown to be in good accordance with the barriers deduced from spectroscopic techniques.

Introduction

Polynuclear transition metal complexes have played a central role in the development of molecule-based magnetism.[1] In particular systems with multiple Mn(III) centers have yielded the most intensely studied and some of the best performing single molecule magnets (SMMs).[2] The pronounced Jahn-Teller (JT) distortions of high-spin manganese(III) systems provides for large single ion anisotropies, which contributes to the overall molecular ground state zero-field splitting. However, the JT distortions also provides for a spread of bond strengths for the individual Mn(III) centers. This in turn allows for some control over the assembly of polynuclear systems, which to some degree has been exploited in rational synthesis of larger systems from smaller polynuclear complexes. Among the polynuclear manganese(III) systems a class of tri-nuclear oximate complexes stand out as particularly well studied and versatile. Thus, Brechin, Inglis and co-workers have characterized the $Mn_3O(oximate)_3^+$ unit in detail and used the assembly of this motif to arrive at hexa-nuclear complexes which were found to be SMMs with record barrier heights.[3] Since systems based on the $Mn_3O(oximate)_3^+$ units constitutes one of the best characterized and best performing classes of polynuclear SMM building blocks, we set out to study some members of this class by the most sensitive and informative spectroscopic techniques: HF-EPR and inelastic neutron scattering (INS). For this nalysis three systems have been chosen: $Mn_3O(Me\text{-}sao)_3(2,4'\text{-bipyridine})_3XO_4{\cdot}0.5MeCN$ (X = Cl (**1**) or Re (**2**), Me-sao^{2-} = 2-hydroxyphenylethanone oximate) $Mn_3O(Et\text{-}sao)_3(2,4'\text{-bipyridine})_3ClO_4$ (**3**, Et-sao^{2-} = 2-hydroxyphenylpropione oximate). All three selected systems have the trinuclar complexes located at special position with crystallographic threefold symmetry which aids the data parametrization and analysis. Thus, for symmetry reasons, the unique (easy) axis of the molecule goes through the μ3-oxygen as well as through the chlorine/rhenium atom. Due to the relatively small size of perchlorate ion the local JT axes, following the $N_{(bipyridine)}$-Mn-$O_{(perchlorate/perrhenate)}$ directions, are tilted with respect to the global anisotropy axis and the μ_3-oxygen is out of the plane of the three manganese centers. For **1** dc susceptibility as well as ac susceptibility and magnetization data was reported by Tsai *et. al.* [4] From these data spin-Hamiltonian parameters have been determined g = 1.95 and J = 3.58 cm-1. The measured effective relaxation barrier was reported as U_{eff} = 37.5 K with $\tau_0 = 1.0{\cdot}10^{-7}$ s. The molecular ZFS value was estimated to be $D = -1.3$ cm^{-1}, however we were unable to arrive at a comparable value using the published. The discrepancy between our optimized value for D and the reported value amounts to a factor of two. We obtain D = -0.65 cm^{-1}, which is also more in the expected range for such systems [5].

Results and Discussion

X-ray structures

Synthesis and structural characterization of **1** was first reported by Tsai *et. al.* [4]. Compounds **2** and **3** were synthesized by similar routes as that used to obtain **1** employing aerial oxidation of manganese(II) salts of the capping anions. Compound **1** crystallizes in the trigonal space group *P*-3 and **2** is isomorphous to **1** (*vide infra* and cf. Figure 1): the complex consists of three manganese (III) ions that are linked by a μ_3-oxide. Each Mn(III) ion is coordinated to one of three 2,4′-bipyridine at the 4′ nitrogen position and to one oxygen from the perchlorate/perrhenate ion

[a] Department of Chemistry, University of Copenhagen, Universitetsparken 5, DK-2100 Copenhagen, Denmark. Fax: +45 35 32 02 14; Tel: +45 35 32 01 11; E-mail: bendix@kiku.dk
[b] Grenoble High Magnetic Field Laboratory, CNRS, BP 166, F-38042 Grenoble Cedex 9, France
[c] Institut Laue-Langevin, F-38042 Grenoble Cedex 9, France.
[d] Dr. P. Tregenna-Piggott, Laboratory for Neutron Scattering, Paul Scherrer Institut, 5232 Villigen PSI, Switzerland. (deceased)

Supporting information for this article is available on the WWW under http://www.eurjic.org/ or from the author.

topping the complex and acting as μ_3-κ^3 ligand. One of three Me-sao^{2-} ligands completes the octahedrally derived coordination around each Mn in a η_1:η_1:η_2 -mode by binding the deprotonated phenolate and the oximate nitrogen with the same Mn and linking to the neighboring Mn via the oximate oxygen.

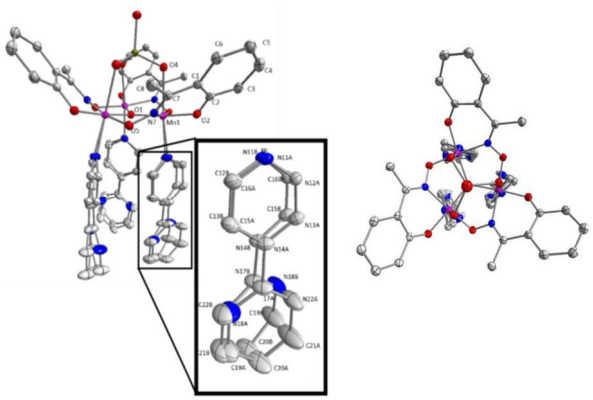

Figure 1. Structure of **2** along the three-fold axis (right), and perpendicular to it (right) the insert shows an amplification of the 2,4′-bipyridine ligands, showing their disorder. For reasons of clarity the solvent molecules as well as the hydrogen atoms have been omitted.

Conversely, **3** although exhibiting the same connectivity and symmetry of the trinuclear species crystallizes in the hexagonal, chiral space group $P6_3$, with four molecules in the unit cell, consisting of two pairs of symmetry unrelated molecules. (cf. Figure 2).

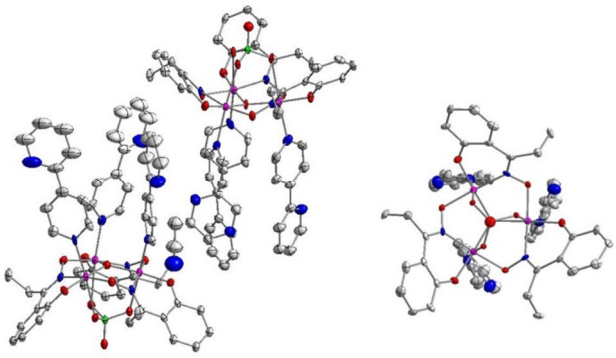

Figure 2. Structure of compound **3**. Left: head to tail arrangement of the two symmetry unrelated complexes. Right: top view of a single complex along the threefold axis. Hydrogen atoms and solvent molecules were omitted for clarity.

Metrical data for the two new systems **2** and **3** are collected together with those previously reported for **1** in Table 1. In Table 1, two important geometric parameters are defined: the oximate twist angle, υ, defined by the Mn-N-O-Mn dihedral angle (cf. SI Fig. S1a) and the tilting angle, δ, defined as the unique angle between the molecular threefold axis (cf. SI Fig. S1b) and the ligators (N,O) defining the JT axis of the individual Mn(III) centers. In addition the μ_3-O distance from the plane defined by the three Mn ions is reported.

Table 1. Selected structural metrics for **1**, **2** and **3**

	1	**2**	**3**
Mn-OX / Å[a]	2.556(3)	2.461(1)	2.544(6), 2.542(6)
Mn-N(bipyridine) /Å	2.263(3)	2.29(1)/2.23(5)[b]	2.271(8), 2.272(8)
Mn-μ_3O / Å	1.8989(9)	1.9100(3)	1.900(2), 1.890(2)
Mn-O(phenolate) / Å	1.857(3)	1.866(6)	1.862(8), 1.858(5)
Mn-N(oximate) / Å	1.984(6)	1.991(2)	1.982(5), 1.986(5)
Mn-O(oximate) / Å	1.908(4)	1.920(2)	1.920(4), 1.902(7)
Mn-Mn / Å	3.255(1)	3.2962(4)	3.252(2), 3.247(2)
Mn-O-Mn /°	118.05(3)	119.33(1)	117.74(5), 117.84(5)
υ / °	-44.2(4)	-46.4(1)	-46.5(5), 47.2(6)
δ / °	14.62	12.90	14.64, 14.76
μ_3-O shift / Å	0.269(6)	0.160(2)	0.288(8), 0.280(8)

[a] X = Cl, Re [b] the two values originate from the disordered bipyridine ligands.

The difference between **1** and **2** is the exchange of the ClO_4^- group with ReO_4^-. The Mn-O4 distance to the capping ligand is at 2.461(1) Å, though still long, noticably shorter in **2** than in **1**. This is in accordance with the generally accepted higher donor and base strength of perrhenate over perchlorate. The difference in size between ClO_4^- and ReO_4^- leads to a closer alignment of the JT axes of the individual Mn centers relative to the molecular threefold axis in **2** as compared to the ClO_4^- analogs **1** and **3**. The tilting angles, δ, quantifying this are 12.9° , 14.6° , and 14.6°/14.7° for **2**, **1**, and **3**, respectively. Other structural differences between the two systems **1** and **2** differing only in the nature of the capping ligand are a smaller μ_3-O out-of-plane shift and a larger oximate twisting angle in **2**. Noticably, the difference in twist angle is countered by the change of ethyl for methyl substituents and **2** and **3** have almost identical μ_3-O out-of-plane shift and oximate twisting angle. The larger oximate twist angle obtained by the Et-sao^{2-} ligand compared to the Me-sao^{2-} is expectable based on packing efficiency. The μ_3-O out-of-plane shifts, which are close in magnitude for **1** and **3** are probably a consequence of the capping ligand geometry and thus expected to correlate with the JT-axis tilt angle.

Magnetism

AC susceptibility:

To probe the SMM properties of **2** and **3**, the ac susceptibility data were recorded for these compounds. Plots of χ' and χ'' vs. temperature are provided in Figs. 3 and 4, respectively.

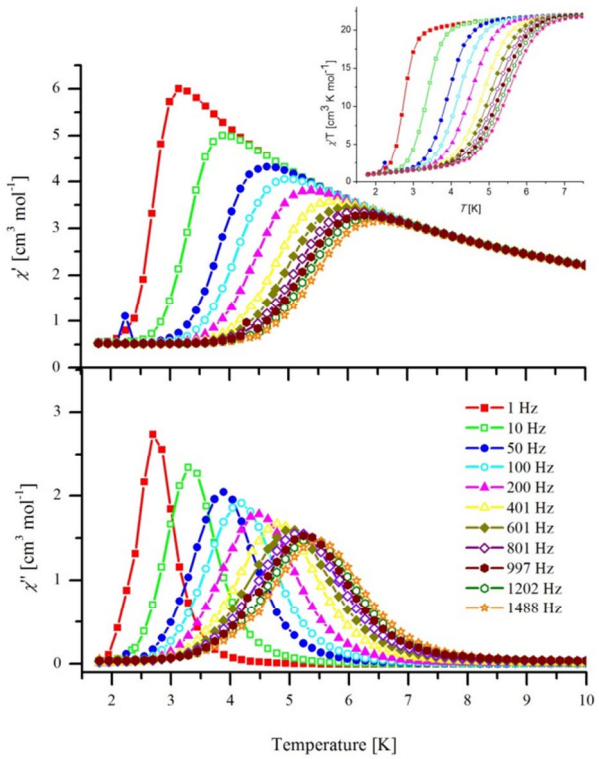

Figure 3. ac susceptibility of **2** in-phase signal (top) out-of-phase signal (bottom) and the $\chi'T$ vs T plot (insert).

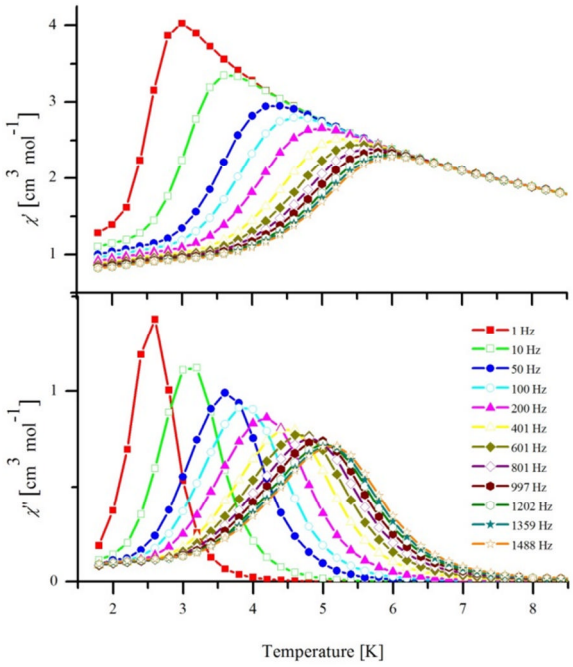

Figure 4. ac susceptibility of **3** in-phase signal (top) out-of-phase signal (bottom).

The AC susceptibility data of both compounds **2** and **3** show SMM behaviour like **1**.[4] The frequency dependence of the in-phase susceptibility of **2** and **3** commence below ca. 6.5 K. The susceptibility starts to reduce for higher frequencies while it still increases for low frequencies until it reaches a maximum at lower temperatures. At temperatures above 6.5 K $\chi'T$ is constant and independent of the frequency (see Figure 3, insert). A similar frequency dependence of the out-of phase component of the susceptibility is observed: for both compounds the out-of-phase signals show near-symmetrical peaks that reaches zero at low temperatures for **2** and almost does so for **3**. The frequency dependent peak positions of the out-of-phase signal were fitted to an Arrhenius equation. In Figure 5 activation-barrier plots of data for both compounds are presented. The effective barrier height of compound **2** was determined to be U_{eff} = 40.6 ± 0.9 K with τ_0 = $8.0 \cdot 10^{-8}$ s. The barrier for **3** U_{eff} = 38.1 ± 0.6 K with τ_0 = $7.5 \cdot 10^{-8}$ s.

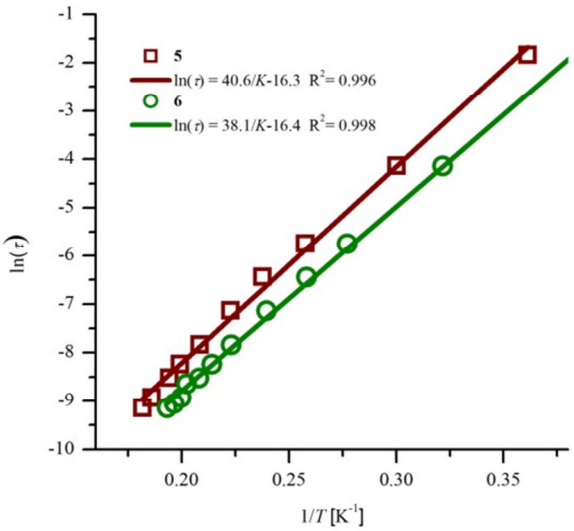

Figure 5. Arrhenius plot of compounds **2** and **3** for frequencies 1-1488 Hz.

The barrier height of compounds **1** and **3** are similar as expected due to the similar tilting angles δ, of the JT axes.[6] The barrier for **2** U_{eff} is larger than for the former systems in agreement with the improved alignment of the single center anisotropies.

INS spectroscopy

INS is a very powerful technique for investigating the energy spectrum pertinent to magnetic properties. The INS spectra of compound **1** measured at 8.5 Å and 10 Å incident wavelengths at temperatures 15 K and 20 K respectively are shown in Figure 6 as neutron intensity vs. energy transfer plot summed over the whole Q-range. For assignment consult the supporting information (Fig. S2).

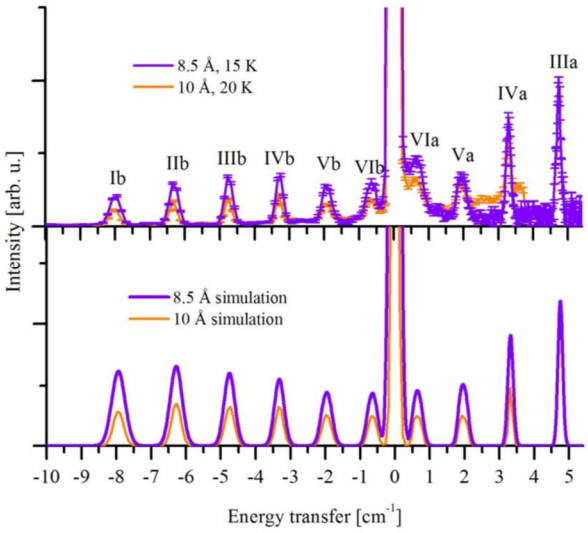

Figure 6. High resolution spectrum of **1** measured with 8.5 Å incident wavelength at 15 K and with 10 Å at 20 K. The 10 Å data have been energy-binned with ΔE = 0.01 meV. The Q-ranges are 0.08 Å^{-1}< Q < 1.28 Å^{-1} for λ_I = 8.5 Å and 0.08 Å^{-1} < Q < 1.08 Å^{-1} for λ_I =10 Å. Simulation of the two spectra with the Giant Spin Hamiltonian parameters given in the text (below)

Compound **2** has been measured at λ = 8.5 Å incident wavelength and at T = 20 K (cf. Figure 7). As for **1**, the spectrum of **2** also shows a peak corresponding to the M_s=±2 to M_s=±1 transition at ΔE = 2.1 cm^{-1} (FWHM=0.3 cm^{-1}) which is significantly wider than the instrumental resolution at this position (0.12 cm^{-1}). In addition the lowest energy transitions, between M_s±1 and M_s=0 has been resolved. It lies at ΔE=0.7 cm-1 and is also widened by a mixing of the M_s=±1 levels.

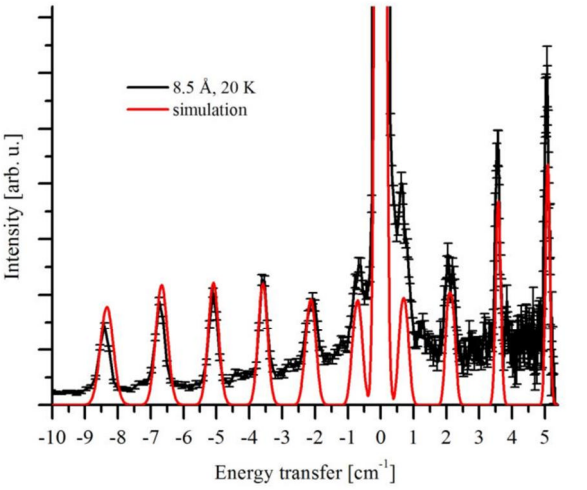

Figure 7. High resolution INS spectrum of **2** measured at T=20K and λ=8.5 Å

A fit of the observed peaks to Gaussian model distributions showed small differences between the energy gain and energy loss side for the M_s= ±6 to M_s = ±5 transition while all other transitions positions match. The energy loss transition is measured at a far higher resolution and is defined by more experimental points (the ΔE spacing between data points becomes smaller with increasing energy transfer), therefore only the energy loss transition was used for the fit. A direct comparison between the data sets of compounds **1** and **2** shows two noteworthy observations. While the lowest energy transition M_s=±1 to M_s=0 is nearly at the same position for both compounds, the M_s= ±6 to M_s = ±5 transition for compound **2** is shifted to higher energies. The latter clearly shows that compound **2** has a bigger ZFS than **1** and the former fact indicates that **1** must be described with a larger B_4^0 term than **2**.

The INS spectra of compound **3** shows the typical temperature dependence already observed for **1** and **2**: At a relatively high temperature of T = 20 K five transitions at energy transfers ΔE = 7.88 cm^{-1}, 6.24 cm^{-1}, 4.70 cm^{-1}, 3.27 cm^{-1} and 1.94 cm^{-1} can be observed on the energy loss side. With the higher resolution wavelength: λ = 8.5 Å one more transition on the energy loss side at ΔE = 0.65 cm^{-1} is resolved. Since none of the observed peaks are split or broadened, it can safely be assumed that there is no rhombic anisotropy and that the observed peaks represent all possible transitions within the ground state multiplet of this compound. The peaks spacing on the energy gain side of the spectrum differ slightly from the loss side of the loss side, as previously observed. The peak positions at 6.5 Å are −7.91 cm^{-1}, −6.24 cm^{-1}, −4.69 cm^{-1}, −3.24 cm^{-1}and −1.91 cm^{-1}. Figure 8 shows the temperature dependence of **3** measured at λ = 6.5 Å incident wavelengths and its simulation. Figure 9 shows the higher resolution spectrum measured at λ = 8.5 Å and T = 20 K and the simulation. Interestingly the two symmetry-independent molecules in **3** cannot be distinguished by the INS spectra due to their very similar metrics.

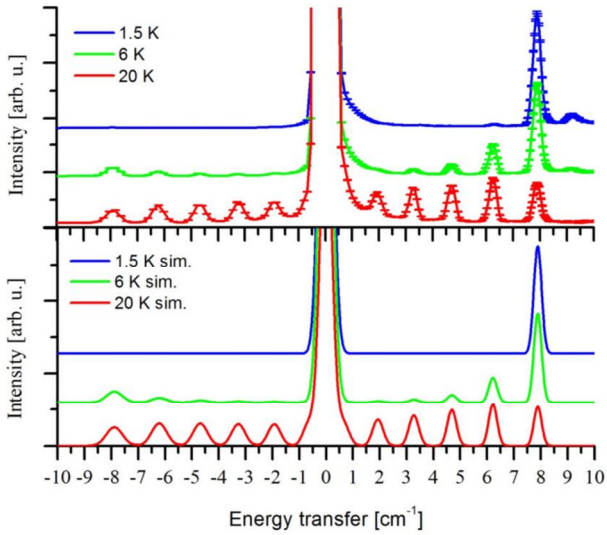

Figure 8. Temperature dependent INS spectra of **3** measured at λ = 6.5 Å.

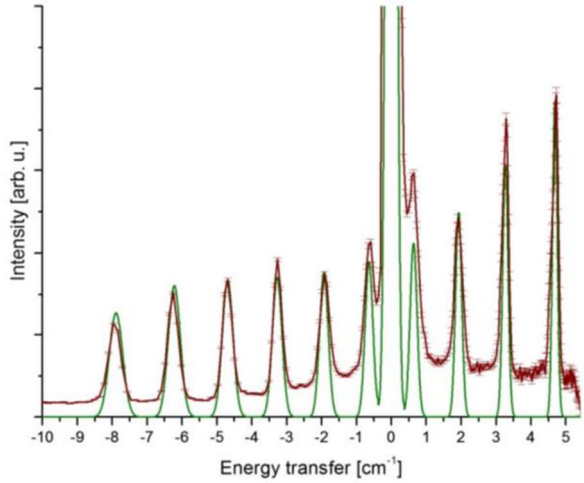

Figure 9. INS spectrum of **3** measured at λ = 8.5 Å and T = 20 K

HF-EPR spectroscopy

In order to supplement the INS data and independently corroborate the assignment made of all INS peaks belonging to the S=6 ground state of the trinuclear complexes, **1** was also investigated by HF-

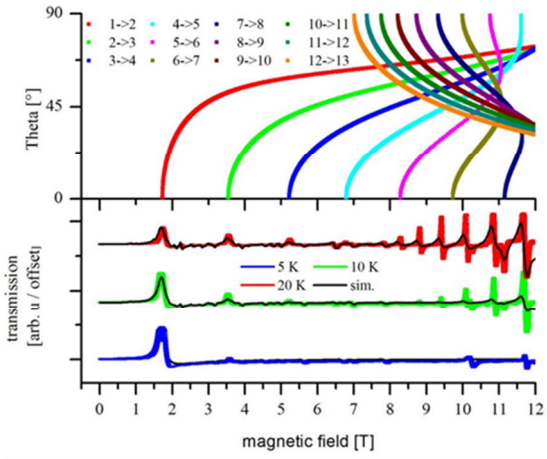

Figure 10. EPR spectra and simulations measured at 285 GHz at 5 K, 10 K, 20 K and simulations (Bottom). Calculated angular dependence of line positions (Top).

EPR spectroscopy. Spectra were recorded with frequencies of 285 GHz and 345 GHz and temperatures of T = 5 K, 10 K and 20 K. The temperature variation of the 285 GHz data and their simulation are shown in Figure 10. The angle dependence of the line positions in the simulations show that the transitions at higher fields are mainly due to field that are applied orthogonal to the easy axis of the molecule (θ = 90°) while the much wider spaced transitions at low fields arise from field orientations parallel to the easy axis.

The spectroscopic data were parametrized by the following spin-Hamiltonian:

$$\hat{H} = \mu_B \boldsymbol{gB} - 2J(\hat{S}_1\hat{S}_2 + \hat{S}_2\hat{S}_3 + \hat{S}_3\hat{S}_1)$$

$$+D(\hat{S}_z^2 - S(S+1)) + E(\hat{S}_x^2 - \hat{S}_y^2)$$

$$+B_4^0(35\hat{S}_z^4 - (30S(S+1) - 25)\hat{S}_z^2 - 6S(S+1) + 3S^2(S+1)^2)$$

The parameters obtained from the simultaneous fit of both the EPR and INS data are: D = -0.69 cm^{-1}, E = -0.0036 cm^{-1}, B_4^0 = -3.43·10^{-5} cm^{-1}, $g_x = g_y$ = 1.99 and g_z =1.96

Figure 11 illustrates the excellent simultaneous account of both INS and HF-EPR spectral data. Calculated field dependence of the transition energies (frequencies) within the ground state multiplet two field orientations (parallel and orthogonal to the easy axis) is presented together with the observed INS and EPR transitions.

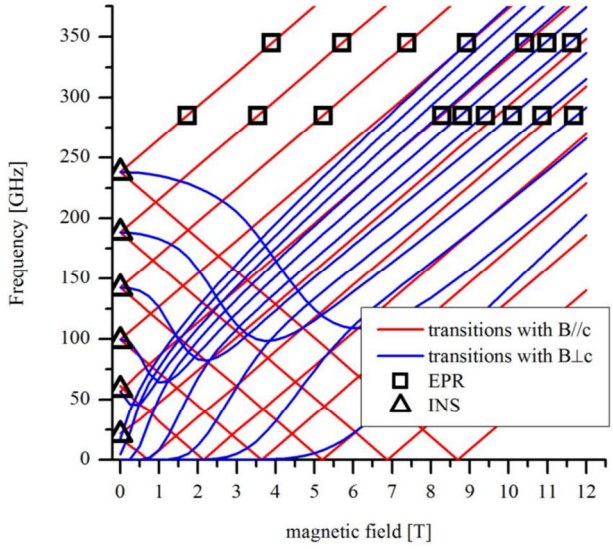

Figure 11. Field dependence of allowed transitions within the ground state multiplet in **1**, with the field along the easy axis (red lines) and within the easy plane (blue lines). Observed EPR and INS transitions have been indicated by squares and triangles.

For compound **2** HF- EPR data include ν = 190 GHz at T = 5 K and 20 K, ν = 285 GHz at T = 5 K and T = 10 K and ν = 345 GHz T = 5 K and T = 15 K. All the EPR data were as above fitted together with the INS data to a spin-Hamiltonian. Figure 12 shows the data obtained at ν = 190 GHz and the simulation of the spectra.

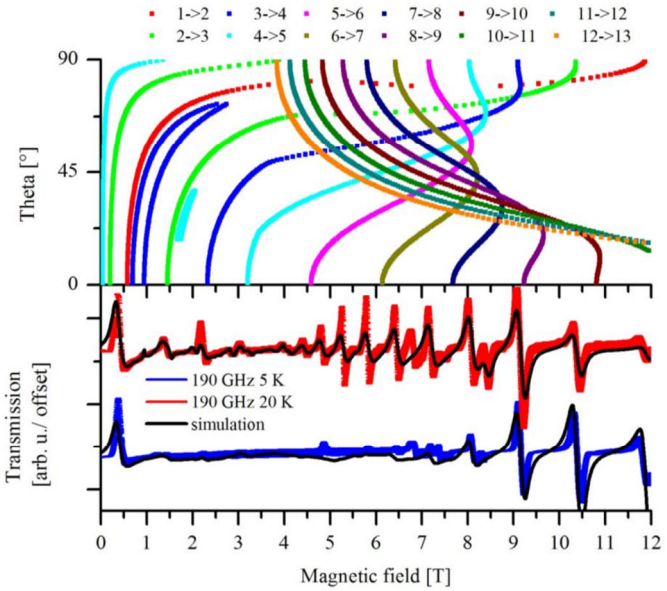

Figure 12. EPR spectra and simulations of compound **2** measured at ν = 190 GHz at T = 5 K and 20 K and simulations (Bottom). Calculated angular dependence of line positions (Top).

Again, the agreement with spectroscopic data from bojth HF-EPR and INS is illustrated by simultaneous plotting of field dependence the observed transitions and the computed energies as shown in Figure 13.

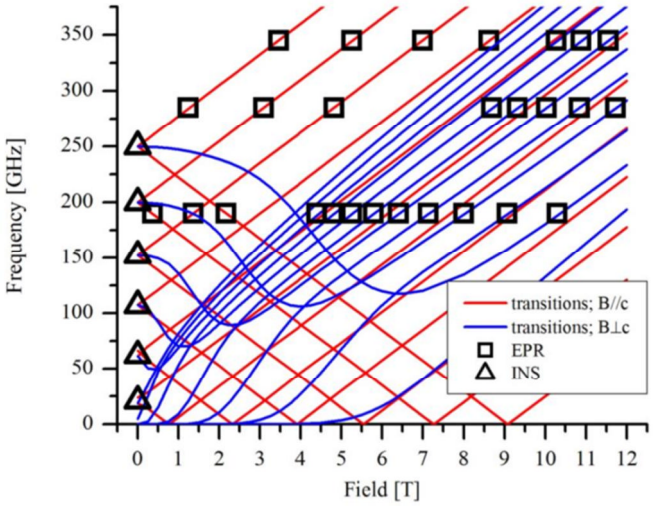

Figure 13: field dependence of allowed transitions within the GS multiplet in **2**, with the field along the easy axis (red lines) and within the easy plane (blue lines). Observed EPR and INS transitions are indicated by squares and triangles, respectively.

The GS Hamiltonian parameters obtained for **2** are D= − 0.736 cm^{-1}, E = 0.0039 cm^{-1} B_4^0 = − 2.43·10^{-5} cm^{-1}, g_x = g_y =1.98 and g_z = 1.97

Conclusions

A very direct connection exists between the conventional double well picture of the ground spin state components of an SMM and inelastic neutron spectroscopy. Hence, if all possible transitions within the GS multiplet are resolved and the rhombic anisotropy is small (i.e. no peak is split into two), the sum of the energies of all transitions on either side of the elastic line represents the energy difference between the lowest and the highest state in the ground state multiplet.[7] It was shown possible to directly obtain these spectroscopic barrier heights for compounds **1**-**3** with resulting values of U_{spec}=35.8K, U_{spec}=38.1K, and U_{spec}=35.5 K, respectively. All obtained spin-Hamiltonian parameters are collected in Table 2.

Table 2 Inferred spin-Hamiltonian parameters for compounds **1**-**3.**

	1	**2**	**3**
D /cm^{-1}	− 0.69	− 0.74	− 0.68
E /cm^{-1}	0.0036	0.004	0
B_4^0 /cm^{-1}	− 3.43·10^{-5}	− 2.43·10^{-5}	− 3.77·10^{-5}
g_x,g_y,g_z	1.99, 1.99,1.96	1.98, 1.98, 1.97	-
D_i /cm^{-1}/	− 2.70	− 2.86	− 2.66
U_{eff}/K	37.5	40.6	38.1
U_{spec} /K	35.8	38.1	35.5

The spectroscopic barriers show the same trend as the effective barrier determined by AC susceptibility measurements. The barrier of **2** is higher than the barriers of the two other compounds, which can be attributed to a bigger ZFS and ultimately to the smaller ZFS tilting angle δ imposed by the capping perrhenate ion. All values for U_{eff} are smaller than the corresponding U_{spec}, but only marginally. The small difference illustrates that quantum tunneling of the magnetization (QTM) is quite unimportant for these systems of high symmetry. It is noteworthy, that the quest for high-spin ground states in pursuit of SMM behavior has been somewhat lessened by the realization that the theoretical barriers scale with $(S_{total})^0$ rather than by $(S_{total})^2$. This study, however, emphasizes that suppression of (QTM) becomes easier for systems with large ground state spins, since matrix elements which mix M_s states many units apart, will necessarily be small if sufficiently high (approximate) symmetry is present.

Experimental Section

Synthesis

Me-saoH$_2$ and Et-saoH$_2$ have been prepared as described in ref. [60] by the addition of an excess amount of hydroxylamine to an aqueous suspension of *o*-hydroxyacetophenone and 2′-hydroxypropiophenone, respectively. After heating to 90 °C for 30 minutes the solution was cooled to room temperature and the white or yellow-white compounds crystallized.

Mn_3(Me-sao)$_3$(2,4′-bipyridine)$_3ClO_4$ (**1**) was synthesized according to ref. [61]. Mn_3(Me-sao)$_3$(2,4′-bipyridine)$_3ReO_4$ (**2**) was synthesized by a modified procedure of the one described in ref. [1] for the perchlorate analog:

277 mg of Mn(ReO$_4$)$_2$ (0.5 mmol, prepared from freshly precipitated $MnCO_3$ and perrhenic acid) was dissolved together with 75 mg of Me-saoH$_2$ (0.5 mmol) in 40 ml of MeCN. After addition of 0.1 ml NEt$_3$ (0.72 mmol) the colorless solution turned very dark. After 5 minutes of stirring 78 mg of 2,4′-bipyridine (0.5 mmol) was added and the solution was stirred for additional 30 minutes. After filtering the solution was left undisturbed for 3 days until **5** precipitated. The precipitated polycrystalline material formed, was washed with a mixture of MeCN:Et$_2$O (1:5). The yield was 42.1% based on Mn. Analytical composition for [Mn_3(Me-sao)$_3$(2,4′-bipyridine)$_3ReO_4$]·0.5MeCN calculated (found): C: 48.15 (48.51) %, H: 3.37 (3.26) %, N: 9.36 (9.65)%.

INS spectroscopy

INS: Spectra were collected on a time-of-flight spectrometer IN5 at the Institut Laue-Langevin, Grenoble, France. About 2 g of non-deuterated crystalline powder was loaded into a 10 mm diameter double-walled hollow aluminum cylinder. A standard ILL Orange cryostat and a cryo-furnace were used for temperature control of 1 and 2, respectively. The data were analyzed by using the LAMP program package.

HF-EPR spectroscopy

EPR data were acquired at the High Magnetic Field Laboratory (Grenoble, France). Detailed descriptions of the equipment can be found in a) Muller, F.; Hopkins, A.; Coron, N.; Grynberg, M.; Brunel, L.-C.; Martinez, G. Rev. Sci. Instrum. 60 (1989) 3681. b) A.-L. Barra, L.C. Brunel, J.B. Robert, Chem. Phys. Lett. 165 (1990) 107. The spectrawere simulated using home-written software.

X-ray Crystallography

Single-crystal X-ray diffraction data were acquired on a Nonius KappaCCD area-detector diffractometer equipped with an Oxford Cryostreams low-temperature device. All collections were performed with Mo Kα radiation (λ = 0.71073 Å, graphite monochromator) at T = 122(1) K. Crystal structures were solved by direct methods (SHELXS97) with subsequent refinement with the SHELXL97 software package. Non-hydrogens were refined anisotropically whereas hydrogens were localized in the Fourier difference map and constrained to riding their parent atom in a fixed geometry.

SQUID-measurements

Magnetic measurements: Magnetic measurements were performed usinga Quantum-Design MPMS-XL SQUID magnetometer. For dc susceptibility measurements, a field of 100 mT was applied. The polycrystalline samples directly obtained from the synthetic procedure were filtered off, washed with MeOH, and immediately transferred to a polycarbonate capsule and covered with 1-octadecene. The susceptibility was corrected for diamagnetic contributions by means of Pascal's constants.

References

[1] G. Aromí, E. K. Brechin, *Struct. Bonding (Berlin)* **2006**, *122*, 1–67. +++

[2] a) M. D. Godbole, O. Roubeau, R. Clérac, H. Kooijman, A. L. Spek, E. Bouwman, *Chem. Commun.* **2005**, 3715–3717; b) L. F. Jones, E. K. Brechin, D. Collison, J. Raftery, S. J. Teat, *Inorg. Chem.* **2003**, *42*, 6971–6973; c) A. J. Tasiopoulos, W. A Wernsdorfer, K. A. Abboud, G. Christou, *Angew. Chem. Int. Ed.* **2004**, *43*, 6338–6342; d) S. Maheswaran, G. Chastanet, S. J. Teat, T. Mallah, R. Sessoli,W. Wernsdorfer, R. E. P. Winpenny, *Angew. Chem. Int. Ed.* **2005**, *44*, 5044–5048; e) M. Soler, W. Wernsdorfer, K. Folting, M. Pink, G. Christou, *J. Am. Chem. Soc.* **2004**, *126*, 2156–2165; f) E. K. Brechin, E. C. Sañudo, W. Wernsdorfer, C. Boskovic, J. Yoo, D. N. Hendrickson, A. Yamaguchi, H. Ishimoto, T. E. Concolino, A. L. Rheingold, G. Christou, *Inorg. Chem.* **2005**, *44*, 502–511; g) H.-C. Yao, Y.-Z. Li, Y. Song, Y.-S. Ma, L.-M. Zheng, X.-Q. Xin, *Inorg. Chem.* **2006**, *45*, 59–65; h) R. W. Saalfrank, T. Nakajima, N. Mooren, A. Scheurer, H. Maid, F. Hampel, C. Trieflinger, J. Daub, *Eur. J. Inorg. Chem.* **2005**, 1149–1153; i) C. Papatriantafyllopoulou, C. P. Raptopoulou, A. Escuer, C. J. Milios, *Inorg. Chim. Acta* **2007**, *360*, 61–68; j) E. C. Sañudo, E. K. Brechin, C. Boskovic, W. Wernsdorfer, J. Yoo, A. Yamaguchi, T. R. Concolino, K. A. Abboud, A. L. Rheingold, H. Ishimoto, D. N. Hendrickson, G. Christou, *Polyhedron* **2003**, *22*, 2267–2271; k) C. Boskovic, E. K. Brechin, W. E. Streib, K. Folting, D. N. Hendrickson, G. Christou, *Chem. Commun.* **2001**, 467–468; l) N. C. Harden, M. A. Bolcar, W. Wernsdorfer, K. A. Abboud, W. E. Streib, G. Christou, *Inorg. Chem.* **2003**, *42*, 7067–7076; M. D. Godbole, O. Roubeau, A. M. Mills, H. Kooijman, A. L. Spek, E. Bouwman, *Inorg. Chem.* **2006**, *45*, 6713–6722.

[3] a) C. J. Milios, R. Inglis, A. Vinslava, R. Bagai, W. Wernsdorfer, S. Parsons, S. P. Perlepes, G. Christou, E. K. Brechin, *J. Am. Chem. Soc.* **2007**, *129*, 12505 –12511; b) R. Inglis, L. F. Jones, C. J. Milios, S. Datta, A. Collins, S. Parsons, W. Wernsdorfer, S. Hill, S. P. Perlepes, S. Piligkos, E. K. Brechin, *Dalton Trans.* **2009**, 3403–3412.

[4] C.-I. Yang, W. Wernsdorfer, K.-H. Cheng, M. Nakano, G.-H. Lee, H.-L. Tsai *Inorg. Chem.* **2008**, *47*, 10184-10186.

[5] a) R. Inglis, G S. Papaefstathiou, W. Wernsdorfer, E. K. Brechin *Aust. J. Chem.* **2009**, *62*, 1108–1118. b) R. Inglis, S. M. Taylor, L. F. Jones, G. S.. Papaefstathiou, S. P. Perlepes, S. Datta, S. Hill, W. Wernsdorfer, E. K. Brechin, *Dalton Trans.* **2009**, 9157-9168.

[6] a) P. L. Feng, C. Koo, J. J. Henderson, P. Manning, M. Nakano, E. del Barco, S. Hill and D. N. Hendrickson, *Inorg. Chem.*, **2009**, *48*, 3480–3492. b) O. Waldmann, *Inorg. Chem.*, **2007**, *46*, *10035–10037*.

[7] R. Basler, C. Boskovic , G. Chaboussant, H. U. Güdel, M. Murrie, S. T. Ochsenbein, A. Sieber *ChemPhysChem* **2003**, *4*, 910-926.

Received: ((will be filled in by the editorial staff))
Published online: ((will be filled in by the editorial staff))

Entry for the Table of Contents

Layout 1:

Key Topic

Highly resolved inelastic neutron scattering spectroscopy and HF-EPR spectroscopy yields a uniquely accurate picture of the ground state energetics of trinuclear Mn(III)-oximate complexes. The variation in the magnitude of anisotropy barriers leading to SMM-behavior of these systems are explicable in terms of molecular structures.

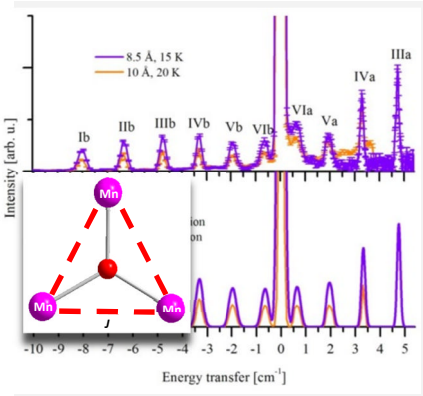

Marc Sigrist,[I] Philip L. W. Tregenna-Piggott, Kasper S. Pedersen, Mikkel A. Sørensen, Anne-Laure Barra, Hannu Mutka and Jesper Bendix*

…….. Page No. – Page No.

Anisotropy barriers in manganese(III)-oximate single-molecule magnets investigated by inelastic neutron scattering and HF-EPR spectroscopy.

Keywords: Molecular magnetism / neutron scattering / anisotropy architecture / mangansese / oximate

Supporting information for

Anisotropy barriers in manganese(III)-oximate single-molecule magnets investigated by inelastic neutron scattering and HF-EPR spectroscopy.

Marc Sigrist, Philip L. W. Tregenna-Piggott, Kasper S. Pedersen, Mikkel A. Sørensen, Anne-Laure Barra, Hannu Mutka and Jesper Bendix

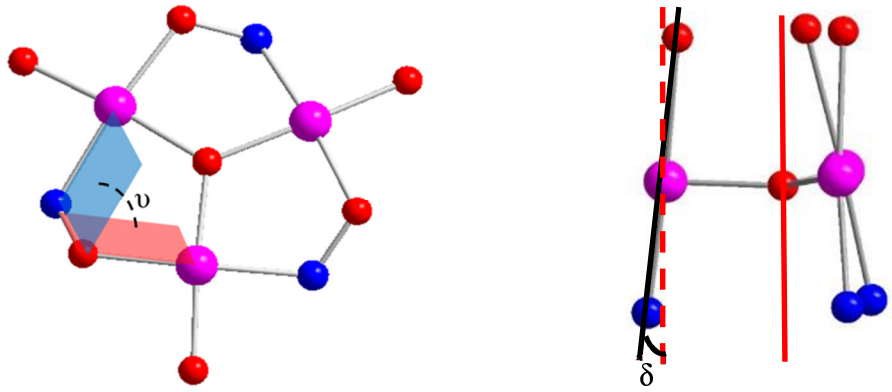

A B

Figure S1. A (left): Definition of the oximate twist angle (υ). B (right) definition of the JT-axis tilt angle (δ). Black line along N-(Mn)-O, red solid line along the global threefold axis and its projection on the Mn(III)ion (red dotted line).

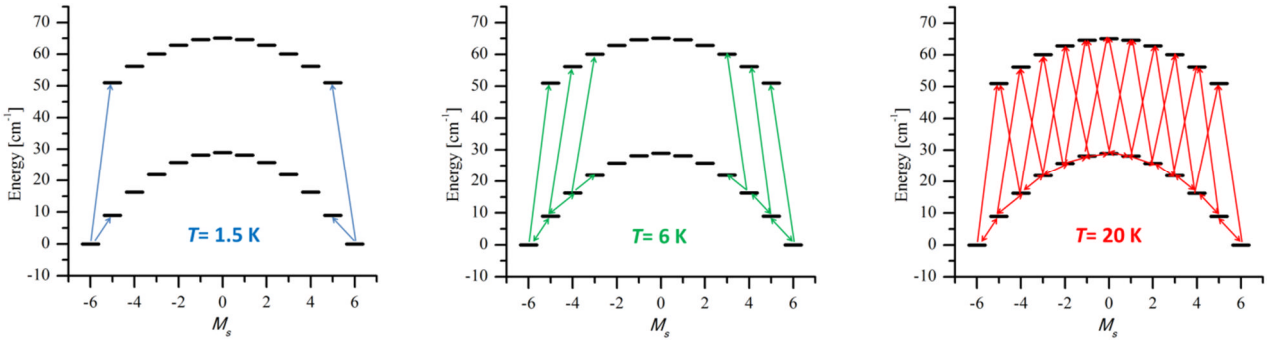

Figure S2. Prominent transitions at different temperatures from 1.5 K (left) to 6 K (middle) and 20 K (right) in all cases connecting the *S*=6 ground state with the excited *S*=5 state.

I:

Modifying the properties of 4f single-ion magnets by peripheral ligand functionalisation

K. S. Pedersen, L. Ungur, M. Sigrist, A. Sundt, M. Schau-Magnussen, V. Vieru, H. Mutka, S. Rols, H. Weihe, O. Waldmann, L. F. Chibotaru, J. Bendix, J. Dreiser

Chemical Science **5**, 1650-1660 (2014)

Chemical Science

EDGE ARTICLE

View Article Online
View Journal | View Issue

Cite this: *Chem. Sci.*, 2014, **5**, 1650

Modifying the properties of 4f single-ion magnets by peripheral ligand functionalisation†

Kasper S. Pedersen,[a] Liviu Ungur,[b] Marc Sigrist,[ac] Alexander Sundt,[d] Magnus Schau-Magnussen,[a] Veacheslav Vieru,[b] Hannu Mutka,[c] Stephane Rols,[c] Høgni Weihe,[a] Oliver Waldmann,[d] Liviu F. Chibotaru,[b] Jesper Bendix*[a] and Jan Dreiser*[e]

Received 4th November 2013
Accepted 3rd January 2014

DOI: 10.1039/c3sc53044b

www.rsc.org/chemicalscience

We study the ligand-field splittings and magnetic properties of three Er^{III} single-ion magnets which differ in the peripheral ligand sphere but exhibit similar first coordination spheres by inelastic neutron scattering (INS) and SQUID magnetometry. The INS spectra of the three compounds are profoundly different pointing at a strong response of the magnetic behavior to minor structural changes, as they are *e.g.* encountered when depositing molecules on surfaces. The observation of several magnetic excitations within the $J = 15/2$ ground multiplet together with single-crystal magnetic measurements allows for the extraction of the sign and magnitude of all symmetry-allowed Stevens parameters. The parameter values and the energy spectrum derived from INS are compared to the results of state-of-the-art *ab initio* CASSCF calculations. Temperature-dependent alternating current (ac) susceptibility measurements suggest that the magnetisation relaxation in the investigated temperature range of 1.9 K < T < 5 K is dominated by quantum tunnelling of magnetisation and two-phonon Raman processes. The possibility of observing electron paramagnetic resonance transitions between the ground-state doublet states, which can be suppressed in perfectly axial single-ion magnets, renders the studied systems interesting as representations of quantum bits.

Introduction

The strong magnetic anisotropy of 4f ions is an essential basis for the properties of technologically applied magnetic materials. Magnetic anisotropy is determined by the local ligand (or crystal) field and a detailed understanding is of paramount importance to achieve control over it. Within the field of molecular magnetism, *single* 4f ions shielded from adjacent magnetic centres, typically by organic ligands, have gained interest due to the observation of intrinsic slow relaxation of the magnetisation with energy barriers for magnetisation reversal of as much as 652 cm^{-1}.[1] Such molecular systems are commonly referred to as mononuclear single-molecule magnets (SMMs) or single-ion magnets (SIMs). Recently, promising results for the incorporation of 4f SIMs in spintronics devices[2] have opened up questions regarding the sensitivity of the magnetic properties towards small perturbations unavoidable in the anchoring or deposition of the molecules to *e.g.* a nanotube or a substrate. The strong response of the magnetic properties to the ligand field (LF) in traditional 4f magnets also holds true for lower-dimensional, molecular magnets like 4f SIMs.[3] This has initiated several approaches to estimate LF splittings by calculations from *e.g. ab initio*[4] or charge distributions.[5] *Ab initio* calculations on 3d clusters have shown the crucial role played by the second coordination sphere.[6a] Using single-crystal measurements, corroborated by *ab initio* calculations, Sessoli and co-workers demonstrated for 4f complexes exceedingly high sensitivity of the magnetic anisotropy towards the LF and that simple magneto–structural correlations used for transition element SMMs may fail completely for predicting *e.g.* the direction of the easy-axis of magnetisation in 4f SIMs.[1b,6] These results present a challenge for the design and control of nanostructured devices relying on 4f SIMs and point to the need for a detailed understanding of the sensitivity of the LF towards small changes of the first and second coordination sphere. Mimicking the environment experienced by a 4f SIM outside the native crystallographic environment is a complicated task. Because of the difficulties in acquiring structural information of metal ion complexes in solution or for surface-attached systems, such studies are best performed by structural modifications in the solid state. Nevertheless, even in the solid state the most detailed understanding of the magnetic properties of 4f systems is in most cases hampered by the lack of fundamental knowledge

[a]*Department of Chemistry, University of Copenhagen, DK-2100 Copenhagen, Denmark. E-mail: bendix@kiku.dk*

[b]*Theory of Nanomaterials Group, Katholieke Universiteit Leuven, Celestijnenlaan 200F, 3001 Leuven, Belgium*

[c]*Institut Laue-Langevin, 38042 Grenoble Cedex 9, France*

[d]*Physikalisches Institut, Universität Freiburg, 79104 Freiburg, Germany*

[e]*Ecole Polytechnique Fédérale de Lausanne, Institute of Condensed Matter Physics, 1015 Lausanne and Swiss Light Source, Paul Scherrer Institut, 5232 Villigen PSI, Switzerland. E-mail: jan.dreiser@epfl.ch*

† Electronic supplementary information (ESI) available: Crystallographic details, INS spectra, magnetic data, EPR spectra, computational details. CCDC 969146–969148. For ESI and crystallographic data in CIF or other electronic format see DOI: 10.1039/c3sc53044b

about the eigenvalues and eigenvectors of the single-centre ligand field operators. To obtain this information, the luminescence pertinent to most 4f ions has gained increasing popularity as a spectroscopic tool to estimate LF splittings in SIMs, but the successful parameter determination is significantly limited by the spectroscopic resolution, possible occurrence of "hot" transitions and non-radiative decay.[1b,7,8] Furthermore, the 4f–4f luminescence is not always accessible and can be screened by strong ligand-centred optical transitions as in the case of phthalocyaninate systems. In solid-state physics, information on the LF levels in 4f systems has traditionally been acquired by inelastic neutron scattering (INS) but, surprisingly, this technique has not been used to study any LF spectra of 4f SIMs.[9]

Here, a small class of structurally similar Er^{III} SIMs has been investigated by INS spectroscopy and magnetometry. The compounds differ by peripheral ligand modifications and the presence or lack of crystallographic trigonal symmetry of the 4f centre. The parent complex; Er(trensal) (**1**) (H_3trensal = 2,2′,2″-tris(salicylideneimino)triethylamine), which is part of an isostructural series,[10] was studied by Riley and co-workers who parameterised the ligand field based on optical spectroscopy, but never reported on the magnetic properties.[11]

The trensal^{3-} back-bone is relatively rigid when coordinating to lanthanide ions and can easily be functionalised.[12] An attractive feature of **1** is the presence of a crystallographic three-fold symmetry of the Er^{III} ion ($P\bar{3}c1$ space group) and the concomitant reduced number of symmetry-allowed LF parameters. Further, high-resolution optical spectra are available from which all possible LF parameters were unraveled.[11a] Additionally, using the slightly modified ligand system 2,2′,2″-tris(3-iodo-5-methylsalicylideneimino)triethylamine (3-I,5-Me-trensalH_3) gives Er(3-I,5-Me-trensal) (**2**, *cf.* Scheme 1) again being trigonal ($P\bar{3}$ space group). On the contrary, chlorine-substituted 2,2′,2″-tris(5-chlorosalicylideneimino)triethylamine) (5-Cl-trensalH_3) yields Er(5-Cl-trensal) (**3**), which crystallises in the monoclinic $P2_1/c$ space group with no axial, local symmetry. For these reasons, the presented compounds are ideal test beds for the systematic study of LF perturbations induced by minute modifications of the LF geometry and strength.

Experimental section

Synthesis

All starting materials were purchased from commercial sources and used without further purification. The large-scale synthesis of **1** was first performed by the procedure published by Bernhardt *et al.*[10a] However, this procedure often gave powder samples containing significant amounts of an unidentifiable phase. For this reason, we employed another, modified literature procedure of Kanesato and Yokoyama which also proved useful to obtain large single crystals suitable for single-crystal SQUID magnetometry.[13] In addition, all employed samples were rigorously characterised by single-crystal or powder X-ray diffraction and elemental analysis. $Er(CF_3SO_3)_3\cdot 9H_2O$ (0.50 g, 0.64 mmol) and tris(2-aminoethyl)amine ("tren", 0.19 g, 1.3 mmol) were refluxed in acetonitrile (15 ml) for 15 min. The solution was cooled and placed at the bottom of a 35 ml glass tube (∅ ≈ 8 mm) and layered with acetonitrile (*ca.* 20 ml) and salicylaldehyde (0.24 g, 2.1 mmol). Large pencil-shaped crystals developed over a week. For **2**, 3-iodo-5-methylsalicylaldehyde was synthesized as described in literature.[14] For 3-I,5-Me-trensal, to 3-iodo-5-methylsalicylaldehyde (7.5 g, 29 mmol) dissolved in boiling methanol (100 ml) was added tris(2-aminoethyl)amine (1.5 g, 10 mmol). After cooling to room temperature, the crystalline, yellow product was isolated by filtration and washed with methanol. Yield: 7.8 g (88%). Calc. (found) for $C_{30}H_{33}I_3N_4O_3$ (%): C, 41.02 (41.04); H, 3.79 (3.48); N, 6.38 (6.33). Subsequently, $Er(NO_3)_3\cdot 5H_2O$ (220 mg, 0.50 mmol) was dissolved in methanol (20 ml) and added to a boiling methanol (150 ml) solution of 3-I-5-Me-trensal (0.40 g, 0.46 mmol) and triethylamine (0.14 g, 1.4 mmol). The boiling was continued for 5 min, the mixture was cooled to RT and **2** was isolated by filtration and washed with methanol. Yield: 0.44 g (88%). Polycrystalline samples of **3** were synthesised as reported for the Gd analogue and proven to be isostructural from X-ray powder diffraction. The structural data for the Gd analogue with Gd replaced by Er was employed in the *ab initio* calculations for **3**.[15] Recrystallisation from boiling methanol afforded single crystals suitable for structure determination (*cf.* Table S1 and Fig. S3†). This phase is found to be different from the powdered sample used in the INS and magnetic measurements and no further studies were performed on this phase. The diamagnetic Y analogues (**1′**–**3′**) were synthesized similarly and shown by X-ray powder diffraction to be isostructural to the Er systems (*cf.* Fig. S4–6†). Er-doped **1′** samples were obtained similarly. Elemental analysis results (%): Calc. (found) for **1**: C, 52.07 (52.01); H, 4.37 (4.01); N, 9.00 (8.98). Calc. (found) for **2**: C, 34.56 (34.86); H, 2.90 (2.60); N, 5.37 (5.38). Calc. (found) for **3** ($C_{27}H_{24}Cl_3ErN_4O_3$): C, 44.66 (44.53); H, 3.33 (2.95); N, 7.72 (7.65). Calc. (found) for **1′** ($C_{27}H_{27}N_4O_3Y$): C, 59.56 (58.86); H, 5.00 (4.95); N, 10.29 (10.52). Calc. (found) for **2′**: C, 37.37 (37.47); H, 3.14 (2.79); N, 5.81 (5.77). Calc. (found) for **3′**: C, 50.06 (49.90); H, 3.73 (3.40); N, 8.64 (8.58).

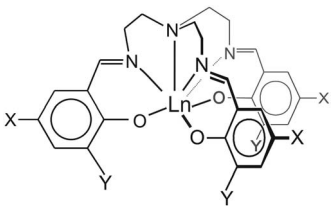

Scheme 1 Pictorial representation of **1**–**3**: **1** X = Y = H; **2**: X = CH_3, Y = I; **3**: X = Cl, Y = H. The three-fold rotation axis in **1** and **2** lies along the axial, tertiary amine N–Ln bond.

X-Ray crystallography

Single-crystal X-ray diffraction studies were performed at 122(1) K on a Nonius Kappa CCD area-detector diffractometer (equipped with an Oxford Cryostreams low-temperature device, using graphite-monochromated Mo-K_α radiation (λ = 0.71073 Å) or on a Bruker D8 VENTURE diffractometer equipped with Mo-K_α high-brilliance IμS (micro-source) radiation (λ = 0.71073 Å), a

multilayer X-ray mirror and a PHOTON 100 CMOS detector, and an Oxford Cryosystems low-temperature device. The instrument was controlled with the APEX2 software package. The structures were solved using direct methods (SHELXS97) and refined using the OLEX2 programme.[16] All non-hydrogen atoms were refined anisotropically, whereas H-atoms were isotropic and constrained. Crystal structure and refinement data for **1** (122 K), **2** (122 K) and **3** (122 K, recrystallised phase) are summarised in Table S1.† Powder X-ray crystallographic data were collected on a Ge Bruker D8 Advance Powder diffractometer operating in 2θ–θ configuration using Co-K_α ($\lambda = 1.7902$ Å) radiation.

Elemental analysis

Elemental analysis for C, H and N was performed with a CE Instrument: FLASH 1112 series EA, at the microanalysis laboratory, University of Copenhagen.

Magnetic measurements

SQUID magnetometer and PPMS. The magnetic data shown in all figures except S51 and S52 were acquired on a Quantum-Design MPMS-XL SQUID magnetometer and a Quantum Design physical property measurement system (PPMS). Magnetisation data were obtained with selected fields from 0 to 5 T and ac data obtained with frequencies 1–1500 Hz (MPMS) and up to 10 kHz (PPMS) with an ac field amplitude of 3.0–3.8 Oe (MPMS) and 10 Oe (PPMS) with or without applications of static field. Single crystals were checked by single-crystal X-ray diffraction for phase purity before each measurement. Single-crystal magnetic data were obtained with a horizontal rotator setup. Prior to all measurements the response of the rotator was determined and subtracted from the response in the real experiment. Polycrystalline samples were immobilised in hexadec-1-ene in polycarbonate capsules. The diamagnetic contribution to the sample moment from the sample holder and sample was corrected through background measurements and Pascal constants, respectively. Paramagnetic relaxation times were obtained from $\chi''(\nu_{ac})$ data as $\tau(T) = [2\pi\nu_{max}(T)]^{-1}$.

Hall magnetometer. The field dependence of the isothermal magnetisation of a single crystal of **1** of a mass of 0.26 mg was measured with a home-built micro-Hall magnetometer at temperatures between 1.4 and 8.4 K. The sweeping rate of the external magnetic field was varied in the range from 150 to 2300 mT s^{-1}.

Inelastic neutron scattering

INS spectra were obtained on the time-of-flight spectrometers IN4 and IN5 located at Institut Laue-Langevin, Grenoble, France. Several grams of non-deuterated samples were measured in double-wall Al/Mg sample cans or as wrapped in Al foil at selected temperatures and incoming neutron wavelengths. The Y^{III} analogues **1′**, **2′** and **3′** were systematically measured with the same settings to facilitate a precise assignment of the phonon spectra. The data were reduced and analysed using the Large Array Manipulation Program (LAMP).[17] Magnetic (de)excitations were localised by their characteristic $|\mathbf{Q}|$ (linear momentum transfer) dependence which follows the magnetic form factor, their temperature variation and the comparison with the spectra of the diamagnetic Y^{III} analogues.

Electron paramagnetic resonance

EPR spectra were acquired on a Bruker Elexsys E500 equipped with a Bruker ER 4116 DM dual mode cavity, an EIP 538B frequency counter and a ER035M NMR Gauss-meter. The spectra were simulated or fitted using home-written software.[18] Large single crystals of Er^{III} doped into **1′** were obtained as described for **1** but employing $Y(CF_3SO_3)_3\cdot 9H_2O$ with a 5 mol% presence of $Er(CF_3SO_3)_3\cdot 9H_2O$.

Modelling

In order to compare the LF obtained from the published optical spectra[11a] as well as that from *ab initio* calculations we will use sets of extended Stevens operator coefficients or, in short, Stevens parameters. This involves a reduction of the quantum-mechanical basis set to the states of the Er^{III} ground-state multiplet $^4I_{15/2}$. Such a procedure is justified because the temperature range used in our measurements lies far below the energies of the first excited $^4I_{13/2}$ multiplet ($\sim$6000 cm^{-1}).

Zero-field splitting Hamiltonian. In the following we will refer to the zero-field splitting (zfs) Hamiltonian as the extended Stevens operators parameterisation with only the ground-state multiplet as basis (*vide infra*). In contrast, the LF Hamiltonian operates on the full space of the $4f^{11}$ configuration with all possible multiplets of Er^{III}.

The following procedure was applied to convert the published LF parameterisation into Stevens parameters: The energy spectrum of **1** was calculated using the published LF model and best-fit parameters[11a] by using the same software written by M. F. Reid.[19] The eigenvalues and eigenvectors in the $|L,S,J,m\rangle$ basis using 284 states at energies of up to $\sim$50000 cm^{-1} were exported into a MATLAB program.[20] The LF Hamiltonian H_{LF} in matrix form was obtained by back transformation $H_{LF} = AH_{diag}A^\dagger$ with A the unitary matrix containing the eigenvectors as columns and H_{diag} the diagonal matrix of the corresponding eigenvalues. To obtain the zfs Hamiltonian only the coefficients in the eigenvectors v_i referring to the ground-state multiplet $^4I_{15/2}$ were considered and the resulting new eigenvectors were renormalized to $\mathrm{norm}(v_i) = 1$.

As mentioned later in the text least-squares fits were performed by minimising the sum of weighted and squared deviations $\kappa^2 = \sum_i (y_{obs,i} - y_{calc,i})^2 \times w_i$ with $y_{obs,i}$ and $y_{calc,i}$ the experimental and calculated values of the $\chi T(T)$ product, field-dependent magnetisation and of the energies of the INS transitions. The weight w_i results from the inverse square of the estimated experimental errors. In the case of **1** also the published energy spectrum was included as observations and a smaller weight ($w_i = 0.03$ *vs.* 0.1) was given to the high-energy part of the spectrum which could not be observed by INS.

Effective spin-1/2 Hamiltonian. In this common simplified formalism given by $\hat{H}_{eff} = \mu_0\mu_B(g_\parallel \hat{\tau}_z H_z + g_\perp \hat{\tau}_x H_x + g_\perp \hat{\tau}_y H_y)$ the zfs is omitted and the magnetic anisotropy is now present in the g-factor. $\hat{\tau}$ has the properties of a spin-1/2 angular momentum mapped on to the lowest Kramers doublet. The coordinate

frame is chosen to be identical with that of the zfs Hamiltonian eqn (1) (*vide infra*), *i.e.*, the *z*-axis coincides with the molecular C_3 axis.

All spin-Hamiltonian calculations shown in this work are based on full diagonalisation. The matrices of the extended Stevens operators were generated with the help of the *stev* function from the EasySpin package written by Stefan Stoll.[21] The powder average of the magnetisation for large fields was generated using a 110-point Lebedev–Laikov grid.[22]

***Ab initio* calculations.** The *ab initio* calculations were carried out using the Molcas 7.8 package program.[23] The calculations for **1** were performed using the measured crystal structures at 122 and 293 K. The differences in the results are negligible (see ESI†). For **2** the measured crystal structure at 122 K and for **3** the structure of the Gd analogue with Gd replaced by Er were used. All elements were described using standard basis sets from the ANO-RCC library available in Molcas. The TZP basis set was employed for Er and first coordination sphere atoms, DZP for the atoms involved in the aromatic rings around the central atom and DZ for the other atoms. Contractions of the employed basis sets are given in Table S2.† In order to save disk space, the Cholesky decomposition of bielectronic integrals was employed with a threshold of 0.5×10^{7}. The spin-free wave functions and corresponding energies were calculated within the Complete Active Space Self-Consistent Field (CASSCF) method.[24] The active space of the CASSCF method included 11 electrons of Er^{III} spanning seven 4f-type orbitals. The spin–orbit interaction was considered within the Douglas–Kroll–Hess Hamiltonian in the mean-field approximation. The spin–orbit coupling was taken into account within the restricted active space state interaction (RASSI) method,[25] by mixing all spin-quartet states (35) and all spin-doublet states (112). On the basis of the resulting spin–orbital multiplets, the SINGLE_ANISO[26] program was used to compute the magnetic properties and the LF parameters. Further, we tested the effect of the crystal environment (Madelung potential) on the low-lying energy states. To this end, the Madelung potential was approximated by five layers of point charges. Every point charge was placed at the Cartesian position of each atom belonging to the crystal environment. The charge value assigned to each atom was the calculated Mulliken charge of the corresponding atom in the ground state, taken from the previous CASSCF calculation on the individual molecule. The reason for describing the Madelung potential in this way is to give a realistic charge distribution in the crystal environment formed by neutral molecules.

Results and discussion

The condensation products of tris(2-aminoethyl)amine ("tren") with aromatic aromatic aldehydes have been extensively employed as ligands for single lanthanide ions[12] and bicompartmental systems.[27] However, only few of the systems possess the high symmetry that is beneficial for the present type of study. For the unsubstituted, pristine **1**, the crystal structure at room temperature was reported by Kanesato and Yokoyama and our redetermination of the structure at 122 K revealed only small differences with respect to the 300 K structure. The structure is shown in Scheme 1 and Fig. 1 (Fig. S1†). **1** crystallises in the $P\bar{3}c1$ space group and possesses crystallographic three-fold (C_3 point group) symmetry of the seven-coordinate Er^{III} ion. For the novel **2** and **3**, the space groups are $P\bar{3}$ and $P2_1/c$, respectively, and the Er sites have local C_3 and C_1 symmetries. The bond lengths and angles of the first coordination sphere are almost identical for **1–3** as visible in Fig. 1 (Fig. S1–3†). The root-mean-square deviations of the central Er^{III} ion and the first coordination sphere are 0.082 Å (**1** *vs.* **2**) and 0.17 Å (**1** *vs.* **3**), respectively, illustrating the strong similarity of the first coordination spheres. Importantly, the Er–N_{amine} distances of 2.67–2.70 Å the average Er–N_{imine} of 2.46–2.47 Å, and the Er–$O_{phenolate}$ of 2.18–2.19 Å are all in the typical range of Ln–N and Ln–O distances. Hence the results of the present study can be considered representative for these ligators.

The ground state of Er^{III} is well described by a $^4I_{15/2}$ Russell–Saunders term. In the absence of any symmetry the enormous number of 27 LF parameters is allowed to be nonzero and the precise determination of a unique parameter set is certainly impossible. In the presence of three-fold rotational symmetry (C_3), the number of symmetry-allowed terms drops dramatically to 9. However, magnetisation and susceptibility data on most 4f systems, especially on polycrystalline samples, are not very distinct, hence the unambiguous determination of 9 parameter values still remains a challenge. For compound **1**, high-resolution optical spectra are available from which all possible LF parameters were unraveled by Riley and co-workers.[11a] The LF parameters were fitted to several multiplets, however, here we are concerned with the magnetic properties which are largely determined by only the ground multiplet. Hence all excited multiplets can be safely neglected. This can be understood by considering that the first excited $^4I_{13/2}$ multiplet is separated by more than 6000 cm^{-1} from the ground state while the full span

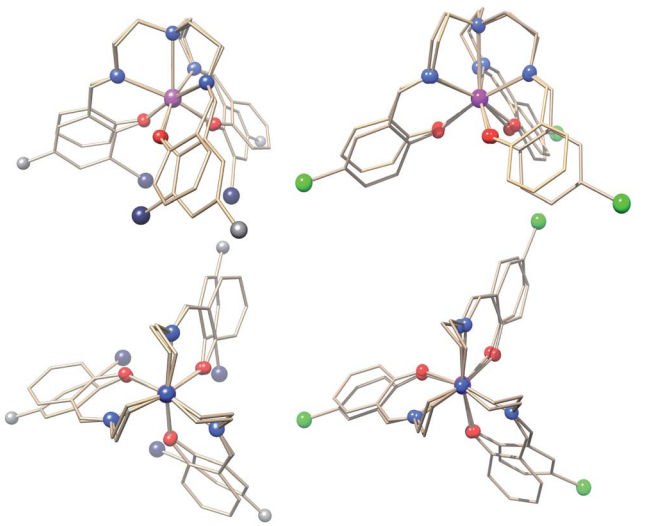

Fig. 1 Structural overlays of **1** with **2** (left figures) and **3** (powder phase, right figures). The projections at the bottom are along the three-fold rotation axis of **1**. Colour code: Er, purple; I, dark blue; Cl, green; O, red; N, blue; C, grey. With the exception of the substituents, the remaining parts of the trensal^{3-} ligands are shown as wireframe for clarity.

of the LF-split $^4I_{15/2}$ ground multiplet is around 600 cm^{-1}.[11a] The limited resolution of the optical spectroscopy and approximations that result from the translation of LF into zero-field splitting (zfs) parameters lead to only a rough prediction of the magnetic properties which are extremely sensitive to small changes in the LF. Therefore, an optimised set of zfs parameters for the ground-state multiplet of **1** is sought by fitting the zfs Hamiltonian simultaneously to the neutron and optical spectroscopic data as well as to the temperature and field dependence of the magnetisation.

In order to compare the *ab initio* calculated LF with that from optical spectroscopy both were translated into an extended Stevens operator description working on the $^4I_{15/2}$ ground multiplet

$$\hat{H}_{\mathrm{zfs}} = \sum_{k,-k\le q\le k} B_k^q \hat{O}_k^q \qquad (1)$$

Magnetic field was taken into account in the phenomenological LF model by the effective Zeeman Hamiltonian $\hat{H}_z = g_{\mathrm{Er}}\mu_0\mu_{\mathrm{B}}\hat{\mathbf{J}}\cdot\mathbf{H}$ while an exact microscopic expression has been used in *ab initio* calculations.[4] From $\hat{H} = \hat{H}_z + \hat{H}_{\mathrm{zfs}}$ the magnetic properties and the INS spectra were calculated. Further, least-squares fits to the magnetic data and the neutron spectra were performed to find optimised parameter sets. In the fits, the B_4^{-3} parameters were fixed to zero which corresponds to a fixing of the coordinate frame hence it can be done without loss of generality. To allow for a comparison, the *ab initio* calculated parameter sets and that obtained from optical spectroscopy were transformed by rotations of the coordinate frame in order to give $B_4^{-3} = 0$.

Static properties of 1

The INS excitation spectra for **1** and **1′** obtained at 1.5 K are shown in Fig. 2 and S7–12.† For **1**, the spectrum is dominated by two prominent transitions labelled as P1 and M1 and located at 31 and 53 cm^{-1}, respectively. The peaks are intense and nicely visible although the experiments were performed on non-deuterated samples. The phonon background can be estimated by downscaling a high-temperature spectrum according to the Bose factor[28] $[1 - \exp(-\hbar\omega/k_{\mathrm{B}}T)]^{-1}$ as shown in Fig. 2. Phononic and magnetic peaks are distinguished by studying the dependence of their intensity on temperature (Fig. S9–11†), on linear momentum transfer Q (Fig. S7 and 8†), and by comparison with the estimated phonon background and with the purely phononic spectrum of the nonmagnetic **1′**. Accordingly, phononic and magnetic features are labelled as P*n* and M*n*, respectively. The temperature dependence of M1-3 indicates that the associated transitions are excitations from the ground state to excited states ("*cold transitions*"). Depending on the nature of the phonon modes, their energy is a function of the mass of the involved 4f ion, thereby explaining the small difference between the spectra of **1** and **1′** around the feature P1. The positions of M1, M2 and M3 of 53, 102 and 111 cm^{-1} are in perfect agreement with the energies reported by Flanagan *et al.* of 54, 102 and 110 cm^{-1}.[11a] Given the precise knowledge of the energy spectrum it is interesting to perform a correlation with the magnetic properties. Also this provides one of the rare opportunities to further examine the performance of the LF

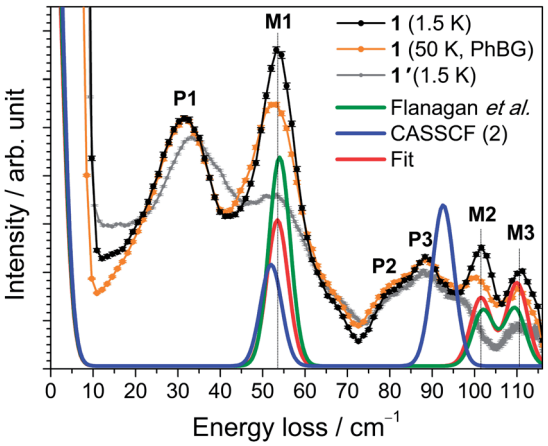

Fig. 2 INS spectra of **1** (black trace) and **1′** (grey) acquired with λ_i = 2.2 Å at T = 1.5 K. The intensity was summed over the complete available Q range. The calculated phonon background from the 50 K spectrum (see main text) is shown as an orange curve (PhBG). The lower red, blue and green traces are simulations employing different sets of Stevens parameters as described in the text.

parameters reported by Flanagan *et al.* as well as state-of-the-art CASSCF/RASSI-SO calculations. The *ab initio* calculated crystal field components of the J = 15/2 multiplet in **1** taking into account the structure obtained at T = 293 K are given in Table 1. The last column indicates the multiplet energies extracted from luminescence spectra. The agreement with *ab initio* calculated energies is remarkably good for the lowest four Kramers doublets (*cf.* Fig. 2). Also the calculated energies arising from higher multiplets (J = 13/2, 11/2) compare very well (*cf.* Table 1). Further we have employed the experimental structure determined at low temperature (T = 122 K) for similar *ab initio* calculations. The resulting energy spectrum (Table S3†) and extended Stevens parameters (Table S4†) are similar to those obtained for the room-temperature structure.

The magnetic properties of **1** measured as field-dependent magnetisation $M(H)$ and product of magnetic susceptibility and temperature (χT) on a polycrystalline sample and on a single crystal parallel and perpendicular to the crystallographic three-fold axis are shown in Fig. 3 and 4. The temperature dependence of the magnetisation and the corresponding fits using Hamiltonian eqn (1) are shown in Fig. S25.†

The single-crystal magnetisation data are clearly proving the presence of strong magnetic anisotropy. Further, at 300 K the χT exhibits still a distinct anisotropy confirming the overall span of the LF split ground multiplet being comparable to the thermal energy at room temperature. The X-band EPR spectra of an Er^{III}-doped **1′** (*ca.* 5 mol%) single-crystal provide $g_{||}$ = 11.8 and $g_{\perp}$ = 3.53 (*cf.* Fig. S28†) in excellent agreement with the low-temperature part of the χT data. Furthermore, the observation of an EPR signal from the ground-state doublet directly confirms that the ground-state Kramers doublet transforms like the $\Gamma_{4,5}$ irreducible representation[29] as stated in ref. 11*a*. The calculation of the magnetisations parallel and perpendicular to the three-fold axis using the effective spin-1/2 Hamiltonian with the g-values from EPR slightly underestimates the magnetisation compared to the experimental data (*cf.* Fig. S26†). This is particularly severe at

Table 1 *Ab initio* calculated and observed energies of low-lying Kramers doublets in **1** (293 K structure) in units of cm^{-1}

Free-ion multiplet	One molecule CASSCF (1)	One molecule embedded in 5 layers of point charges CASSCF (2)	Observed (ref. 11*a*)
$^4I_{15/2}$	0	0	0
	64	52	54
	99	91	102
	103	93	110
	198	203	299
	421	410	568
	459	448	610
	484	472	642
$^4I_{13/2}$	6652	6650	6594
	6687	6679	6612
	6692	6683	6621
	6705	6705	6690
	6903	6892	6909
	6904	6893	6928
	6917	6906	6939
$^4I_{11/2}$	10 716	10 711	10 291
	10 724	10 722	10 301
	10 738	10 732	10 316
	10 863	10 854	10 444
	10 869	10 859	10 449
	10 883	10 872	10 510

larger field due the admixture with excited states leading to a change in the wavefunctions (second-order effects). The fitted Stevens parameter set for **1** using the zfs Hamiltonian eqn (1) yields nearly perfect agreement with all magnetic and spectroscopic data. The effective *g*-factors of the lowest Kramers doublet derived from the fitted Stevens parameters are $g_{||} = 11.9$ and $g_{\perp} = 3.36$ which coincide almost perfectly with the values found from EPR. The *ab initio* calculated main values are $g_{||} = 13.68$ and $g_{\perp} = 2.28$. The *g*-factor anisotropy is somewhat overestimated, which can be due to the following reason: the first excited Kramers doublet possesses opposite magnetic anisotropy with respect to the ground one, being of easy plane type ($g_{||} = 2.87$ and $g_{\perp} = 7.62$). This means that small modifications of the LF will strongly influence the magnetic anisotropy of the ground multiplet given the proximity of the first excited Kramers doublet. The calculations employing the low-temperature structure show a similar trend (Table S5†).

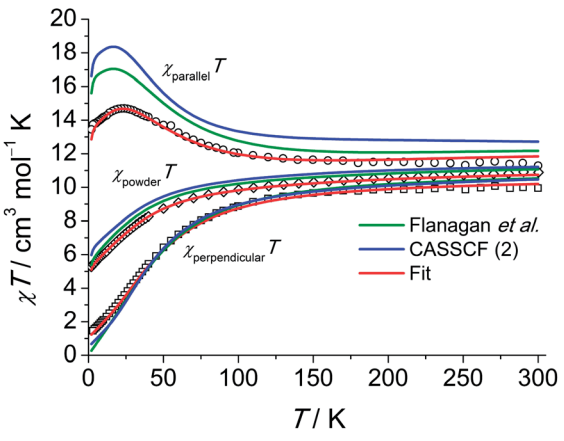

Fig. 3 Experimental χT ($\chi = M/H$, $H = 2000$ Oe) products for a single crystal of **1** along (○) and perpendicular (□) to the C_3 axis and for a polycrystalline sample of **1** (◇, $H = 1000$ Oe). For the polycrystalline sample the χT was calculated as $(\chi_{xx}T + \chi_{yy}T + \chi_{zz}T)/3$. Calculations using eqn (1) are shown as solid lines as indicated in the plot.

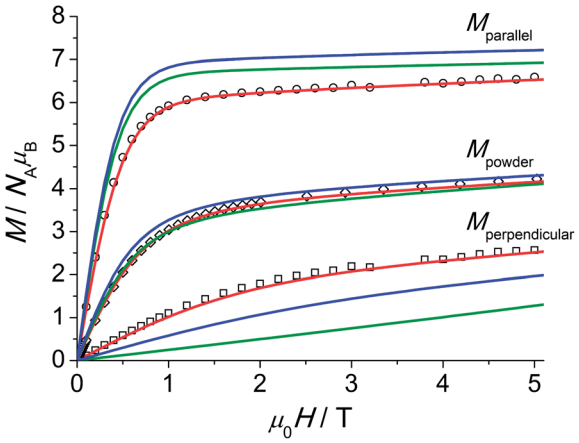

Fig. 4 Experimental magnetisation at $T = 2.0$ K for **1** along (○) and perpendicular (□) to the C_3 axis and for a polycrystalline sample (◇). The powder average of the magnetisation (*M*) was obtained by averaging over a spherical surface. The colour labelling of the simulations and fit is identical to that employed in Fig. 3.

An overview of the Stevens parameters obtained for **1** by *ab initio* calculations, from optical spectroscopy and from fits to the magnetic and INS data is given in Table 2. There is good agreement between the different parameter sets. Parameters forbidden in C_3 symmetry come out to be non-zero from *ab initio* calculations because of limited numerical accuracy due to employment of Cholesky decomposition of the bielectronic integrals,[23] however, they are small compared to most of the allowed parameters of the same rank *k*. Since the comparison of sets of Stevens parameters is rather abstract it is of great help to examine the performance of the *ab initio* calculations and LF parameters from optical spectroscopy in reproducing the magnetic and INS data. Notably, as visible from the magnetisation and susceptibility data, the parameter sets obtained from optical spectra and *ab initio* calculations suggest slightly stronger anisotropy than what is consistently obtained from single-crystal magnetic data and EPR measurements.

Static properties of 2

The INS spectra of **2** and the dc magnetic data are shown in Fig. 5 and 6, respectively. The detailed temperature dependence of the INS spectra of **2** and **2′** is given in Figs. S13–17.† The neutron spectra of **2** (Fig. 5) are remarkably different from those of **1**. The magnetic and phononic features were disentangled using the same criteria and procedures as for **1**. In the 2.8 Å spectra, a prominent peak, M2, is observed at 70 cm^{-1} and a weaker feature M1 at 37 cm^{-1}. In the 1.4 Å spectrum the magnetic features are not very strong. An additional magnetic feature M3 at an energy loss of 140 cm^{-1} can be identified (*cf.* Fig. S13†).

Least-squares fits of all C_3-allowed Stevens parameters to the magnetic data and the INS spectra of **2** were performed as described for compound **1**. The best–fit parameters and the corresponding simulated curves are shown in Table 2 and in Fig. 5 and 6. By using random initial values we were able to obtain three parameter sets only slightly differing in κ^2 (*cf.* Modelling Section) that reproduce all available data very well. A comparison of the three sets yields that the 'axial' parameters B_2^0, B_4^0 and B_6^0 are quite robust, while the 'non-axial' parameters are fluctuating. The *ab initio* calculated magnetic properties and INS spectra, which were based on the 122 K structural data, are presented in Figs. S32–34.† While the calculated magnetic properties are only slightly deviating from the experimental data, the INS spectra do not match well. Given that the *ab initio* predictions for the similar compounds **1** and **2** are expected to be of equal accuracy, the likely explanation for the larger discrepancy in **2** is that the employed 122 K structural data differs significantly from the geometry at 1.5 to 40 K, where the INS experiments were performed. In such a situation INS and optical spectroscopic data are indispensable for an accurate description of the electronic spectra of lanthanide SIMs.

Static properties of 3

For **3**, a representative INS spectrum at 2.2 Å is shown in Fig. 7. More INS data of **3** and **3′** are shown in Fig. S18–22.† The comparison of the spectra of **3** and **3′** reveals magnetic excitations at 29 cm^{-1} (M1), 76 cm^{-1} (M2) and 106 cm^{-1} (M3). An inspection of the temperature dependence indicates that M1-3 are cold transitions. Comparing the 1.1 Å spectra indicate no further magnetic excitations up to energy transfers of *ca.* 500 cm^{-1}. However, in the temperature dependence of the 2.8 Å spectra, a magnetic excitation (m4) starting out from an excited state ("hot" transition) was located at 48 cm^{-1}. The parameters derived from *ab initio* calculations, done for the room-temperature structure of Gd(5-Cl-trensal)[15] in which Gd has been replaced by Er, do not satisfactorily reproduce the experimental data (*cf.* Tables S9–11 and Fig. S35–37†). Structural changes due to the exchanged central ion, or changes not detectable in powder XRD and/or due to the low temperatures in the experiments are obvious reasons for this discrepancy. A fit to the magnetic data and INS spectra using the *ab initio* derived parameters as initial values stops in a local minimum. To extract LF parameters within our phenomenological model, fits using random initial values were performed. The best results are plotted as solid lines in Fig. 6 and 7. While there are several parameter sets which lead to an excellent reproduction of the $M(H)$ and χT, the INS plays a decisive role here. Only one of the parameter sets reproduces well also the warm INS transition m4 (*cf.* Fig. S20†). In these fits, only parameters allowed in C_3 symmetry were considered, which is certainly a strong approximation in view that this compound actually possesses lower symmetry. However the introduction of more fit parameters would not lead to a significant improvement of the fits since a

Table 2 Stevens coefficients B_k^q for compounds **1–3** in units of cm^{-1}. CASSCF calculations are based on 122 K structural data

	Compound **1**			Compound **2**		Compound **3**
k, q	*ab initio* CASSCF (2)	Flanagan *et al.*[11a]	Best fit	*ab initio* CASSCF (2)	Best fit	Best fit
2, −2	3.780×10^{-3}			3.244×10^{-3}		
2, −1	-5.321×10^{-3}			6.266×10^{-3}		
2, 0	−0.8776	−0.975	−1.07(2)	-2.824×10^{-1}	$-1.9(6) \times 10^{-1}$	1.22(2)
2, 1	5.058×10^{-3}			-3.124×10^{-3}		
2, 2	3.439×10^{-4}			1.775×10^{-3}		
4, −4	1.274×10^{-4}			-1.964×10^{-4}		
4, −3	0	0	0	0	0	0
4, −2	1.273×10^{-4}			-1.894×10^{-4}		
4, −1	-7.482×10^{-5}			1.359×10^{-4}		
4, 0	-1.010×10^{-3}	-0.260×10^{-3}	$-0.2(2) \times 10^{-3}$	-1.461×10^{-3}	$-6.0(6) \times 10^{-3}$	$-3.9(5) \times 10^{-3}$
4, 1	6.359×10^{-5}			-2.101×10^{-5}		
4, 2	8.629×10^{-5}			-3.777×10^{-5}		
4, 3	0.1770	0.287	0.255(5)	1.707×10^{-1}	$1.1(4) \times 10^{-1}$	$1(1) \times 10^{-2}$
4, 4	-1.121×10^{-4}			1.348×10^{-5}		
6, −6	1.555×10^{-5}	5.89×10^{-4}	$3.5(5) \times 10^{-4}$	4.235×10^{-5}	$1.6(7) \times 10^{-4}$	$1.2(1) \times 10^{-4}$
6, −5	1.335×10^{-5}			-4.616×10^{-6}		
6, −4	-4.404×10^{-7}			5.479×10^{-7}		
6, −3	-1.165×10^{-4}	-2.45×10^{-4}	$-1(2) \times 10^{-4}$	-2.341×10^{-4}	$1.3(2) \times 10^{-3}$	$7(7) \times 10^{-5}$
6, −2	-2.360×10^{-6}			1.853×10^{-6}		
6, −1	3.101×10^{-6}			-6.209×10^{-6}		
6, 0	9.685×10^{-5}	1.23×10^{-4}	$1.25(1) \times 10^{-4}$	8.896×10^{-5}	$9.5(6) \times 10^{-5}$	$-1.07(3) \times 10^{-4}$
6, 1	-2.971×10^{-6}			1.485×10^{-6}		
6, 2	-1.892×10^{-6}			-1.123×10^{-6}		
6, 3	-0.8741×10^{-3}	-0.943×10^{-3}	$-1.27(2) \times 10^{-3}$	-5.176×10^{-4}	$-1(5) \times 10^{-5}$	$3.13(8) \times 10^{-6}$
6, 4	8.189×10^{-7}			-8.547×10^{-7}		
6, 5	7.960×10^{-6}			4.747×10^{-6}		
6, 6	0.8663×10^{-3}	1.03×10^{-3}	$1.27(2) \times 10^{-3}$	7.316×10^{-4}	$4.2(8) \times 10^{-4}$	$1.4(1) \times 10^{-5}$
g_{Er}	6/5	6/5	1.18(1)	6/5	1.18(1)	1.18(1)

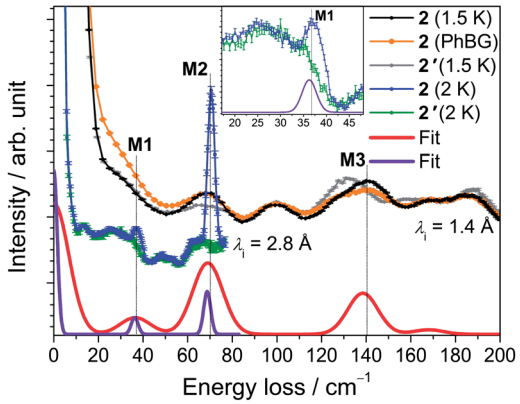

Fig. 5 INS spectra of **2** (black and blue traces) and **2′** (grey and green traces) obtained with incident neutron wavelengths of 1.4 Å (at T = 1.5 K) and 2.8 Å (at T = 2 K). The curves are offset to improve clarity. The calculated phonon background from the 40 K spectrum is shown as a solid orange line. The red and purple lines are simulations with resolutions comparable to the 1.4 and 2.8 Å data set, respectively, as described in the text. Inset: Zoom of the low-energy region of the 2.8 Å spectra around peak M1.

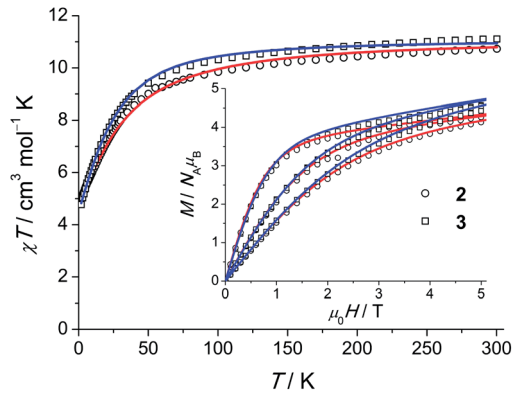

Fig. 6 χT ($\chi = M/H$, H = 1000 Oe) products for polycrystalline **2** and **3**. Open symbols correspond to the experimental data, solid lines are calculated curves obtained from the model of eqn (1). Field-dependent magnetisation $M(H)$ at 2, 4 and 6 K is shown in the inset.

good fit can already be achieved with the current parameter set. In such a situation, in order to find values of all 27 LF parameters *ab initio* calculations are indispensable. Our study shows that the ligand field spectrum of lanthanides is highly sensitive to the structural details. These may not be correctly captured by the structures of isostructural compounds as emphasized by the example of compound **3**.

Dynamic magnetic properties of 1–3

The temperature dependencies of the magnetisation relaxation times of **1** (polycrystalline and as oriented single-crystal), Er-doped **1′** and **3** measured by ac SQUID magnetometry are shown in Fig. 8. In the absence of a static field none of the compounds **1–3** showed a peak in the out-of-phase component (χ'') of the ac susceptibility (Fig. S42, S47 and 48†). In small dc fields, clear maxima in $\chi''(\nu_{ac})$ are observed for **1** and **3**, whereas

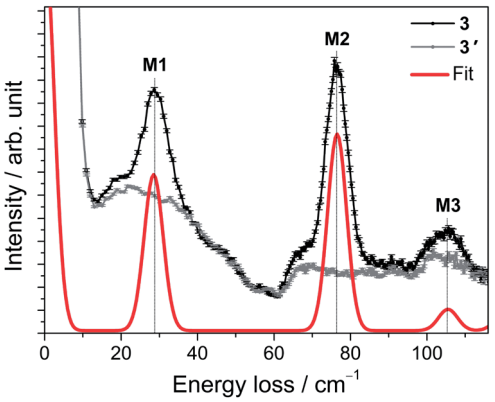

Fig. 7 INS spectra of **3** (black trace) and **3′** (grey trace) acquired with an incident neutron wavelength of 2.2 Å at T = 1.5 K. The red line is the simulation using the best-fit parameters as described in the text.

only onsets of peaks are observed in **2** with $\nu_{ac} \leq 1.5$ kHz at 1.8 K (*cf.* Fig. S47†). The magnetisation curves of an aligned (magnetic field applied parallel to the C_3 axis) single crystal were also measured using a micro-Hall sensor at temperatures down to 1.4 K and magnetic field sweep rates up to 2.3 T s^{-1}. However, magnetic hysteresis was not observed (*cf.* Fig. S51 and 52†). A polycrystalline sample of 10% Er^{III} doped into **1′** shows almost the same temperature dependence as pristine **1**. The field dependence (*cf.* Fig. S50†), however, hints at a weak effect of intermolecular interactions, which are suppressed in the diluted sample. For this reason we focus here on the latter compound, in order to investigate the mechanism that dominates the magnetisation relaxation.

With the frequently made assumption of an Orbach process and a temperature-independent quantum tunnelling of magnetisation (QTM) as dominant relaxation processes, a good fit can be obtained yielding a barrier for magnetisation reversal of Δ_{eff} = 20(1) cm^{-1}. The size of this barrier is, however, not compatible with the observed excited-state separation of 54 cm^{-1} and an Orbach process can be ruled out as a dominating

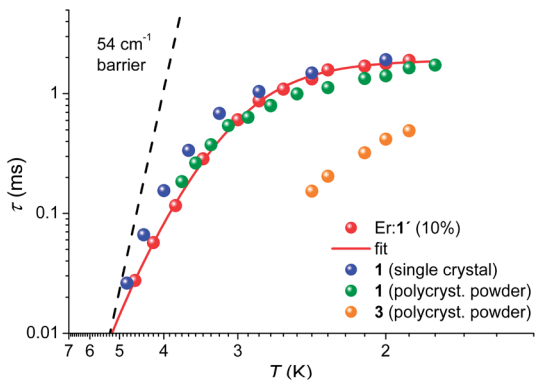

Fig. 8 Arrhenius plot for **1** as a single crystal measured with H_{dc} = 900 Oe applied along the C_3 axis, as polycrystalline material (H_{dc} = 900 Oe), and as Er doped into **1′** (Er:**1′**), H_{dc} = 1100 Oe. For **3**, the data were acquired on a polycrystalline sample only (H_{dc} = 700 Oe). The solid red line represents the best fit to the Er:**1′** data using the model of eqn (2). The dashed solid line is the Arrhenius prediction $\tau(T)$ = 9ps × exp[54 cm^{-1}/($k_B T$)].

relaxation mechanism in the studied temperature range of 1.9 K < T < 5 K. In view of this narrow temperature range and the gradually increasing slope towards higher temperatures it might however be possible that the Orbach process becomes the leading mechanism at elevated temperatures. It has been proposed theoretically and experimentally that first and second-order Raman processes may be significant.[30] Indeed we find that the relatively simple model for the temperature-dependent magnetisation relaxation times, eqn (2):

$$\tau^{-1} = {\tau_{QTM}}^{-1} + CT^{n} \quad (2)$$

gives an excellent fit to the experimental data on the Er-doped **1′**. The first term takes into account temperature-independent QTM while the second term represents a two-phonon Raman process. The best-fit parameters extracted using eqn (2) are $C = 0.17(3)\ s^{-1}\ K^{-n}$, $n = 8.0(1)$ and $\tau_{QTM} = 1.93(5)$ ms and the corresponding calculated curve is shown in Fig. 8. For a two-phonon Raman process an exponent of $n = 9$ was predicted for Kramers ions[30a] but n may vary depending on the exact energies of the lowest Kramers doublets.[30b] Experimentally the T^n power law was indeed found with an exponent deviating from $n = 9$ in most cases.[30c,d,g] From this viewpoint the value of the exponent found here is in reasonable agreement with the expectations for two-phonon Raman processes. Also, the values for C and τ_{QTM} are in reasonable ranges.[30d] Further confirmation for the importance of a two-phonon Raman process comes from fits for Er-doped **1′** using a complete model (*cf.* Fig. S50†).[30] Here, all four processes (QTM, Orbach with $\Delta_{eff} = 54\ cm^{-1}$, direct and Raman) were included and the fit took into account simultaneously both temperature and field dependent relaxation time data. A fit assuming only an Orbach mechanism, the direct process, and QTM fails to reproduce the data. For both compounds a more or less pronounced increase of the relaxation times with field is visible reaching a maximum at fields of *ca.* 1 kOe, followed by a strong decay upon further increase of the field. Modelling these data is challenging because of the complexity induced by the simultaneous presence of more than one relaxation process. Similar to other studies (*e.g.* ref. 30*e* and *f*) the data on Er-doped **1′** can be understood by the quenching of tunneling in the low-field regime and the direct process becoming dominant at high fields. The complete fits reproduce the data very well, and the derived parameters for the four relaxation mechanisms demonstrate that both the Orbach and direct processes are small as compared to the QTM and Raman processes (for details see ESI†). The hyperfine field of $B_{hyp,ac} = 17$ mT deduced from the B_2 parameter describing the field dependence at low fields is consistent with $B_{hyp,EPR} = 26$ mT extracted from EPR measurements. The observations hence illustrate nicely the presence of a non-Orbach process in a 4f SIM at low temperatures corroborated by the spectroscopic proof. Notably, this behavior parallels Na[Dy(DOTA)]·$4H_2O$ in which the first excited state was estimated from room-temperature luminescence spectra.[1b]

When comparing the magnetic and spectroscopic properties of compounds **1–3** studied in this work, it becomes clear that they are vastly different. This is also reflected in the results of the *ab initio* calculations. Interestingly, the introduction of substituent groups far from the first coordination sphere leads to drastic modifications of the low-lying energy spectrum, hence the changes are not at all just a small perturbation to the system. The strong effect of the second coordination sphere on the anisotropy of the metal ion in a Co^{II}_2(calix-8-arene)$_2$ complex was found by *ab initio* calculations to originate from the significantly stronger chemical bond within the ligand group than between the ligand atoms and the metal ion.[6a] Accordingly, in lanthanide complexes the sensitivity of the magnetic anisotropy to modifications in the second (and more distant) coordination sphere can be expected to be even higher. As depicted in Fig. 1 the first coordination sphere of the series **1–3** is largely similar. Therefore, the differences in the properties are likely to arise from two contributions. One comes from the difference in the electron withdrawing or donating effects imposed by the substituents and another from the subtle structural distortions of the first and second coordination sphere. The latter contributions are likely to be associated with changes in π interactions that are expected to be strongly dependent on the tilting of the aromatic rings. As an evidence for this picture, changes in the first coordination sphere have induced strong changes in the magnetic behaviour for Tb^{III}-phthalocyaninate systems, where a contraction of the ligand sphere lead to an increase of the barrier for magnetisation reversal.[31] A few recent studies further suggest that subtle changes in the far range can also have strong effects on lanthanide anisotropy.[32] A strong response of the ^{57}Fe Mössbauer spectra was detected in a Fe_2Dy_2 SMM upon peripheral ligand substitution suggesting a concomitant change of the lanthanide anisotropy and 3d–4f exchange coupling.[33] Moreover, similar effects were proposed on the basis of an *ab initio* study on the SIM Na[Dy(DOTA)]·$4H_2O$.[1b] These recent studies already shed some light onto this topic but it was so far difficult to imagine that the spectroscopic changes were so profound.

These results should have an impact on the current efforts of studying surface-deposited SMMs and SIMs and the grafting of such species on to carbon nanotubes and other nanostructured materials. It certainly cannot be taken for granted that the magnetic properties remain unchanged after the grafting or surface deposition process even if the molecular stoichiometry is retained and the molecules seem to be intact. Our study suggests that even if the first coordination sphere remains unchanged after the surface deposition, the interaction of the ligand with the surface may have similar effects as the ligand functionalisation studied here. However, it should also be noted that the present results can be seen as an opportunity to use the surface in order to modify the magnetic properties of the deposited SMMs or SIMs. Currently, this still seems to be out of reach mainly because the understanding of the observed effects is underdeveloped. Controlling and harnessing such interactions may open up paths to achieving unprecedented spintronic applications.

Conclusions

In summary, an extensive study of the magnetic and low-energy spectroscopic properties of a small family of Er^{III} SIMs has been

performed. The measured data are compared to results from previously published optical spectroscopy as well as to state-of-the-art *ab initio* CASSCF/RASSI-SO calculations. The peripheral ligand functionalisation leads to largely unexpected drastic changes in all properties. These results are important in view of the on-going grafting of SMMs and SIMs on to surfaces and nano-objects suggesting that changes far away from the first coordination sphere can lead to vastly different magnetic properties. If control over these effects can be achieved, it may open a path to obtaining superior magnetic properties by using advantageous combinations of SIMs and surfaces.

Moreover, strong evidence is delivered that the Orbach mechanism is of minor importance for the relaxation of magnetisation in these systems at temperatures 1.9 K < T < 5 K. In contrast, it appears that the relaxation is dominated by tunnelling of magnetisation at the lowest temperatures and that two-phonon Raman processes are dominating at temperatures close to 4 K.

Note added after submission

We became aware of an accepted manuscript by E. Lucaccini *et al.* about Er(trensal) and Dy(trensal) complexes.[34]

Acknowledgements

We thank Dr M. Medarde-Barragan for help with the PPMS measurements. J. D. acknowledges funding by the Ambizione program of the Swiss National Science Foundation. K. S. P. thanks the Danish Ministry of Science, Innovation and Higher Education for an EliteForsk travel scholarship. J. B. thanks the Carlsberg Foundation and the Villum Foundation for support for diffraction equipment. H. W. and J. B. acknowledge support from the Danish Research Council FNU (12-125226). L. U. is a postdoc of the FWO-Vlaanderen (Flemish Science Foundation). Methusalem and INPAC projects of the KU Leuven are also gratefully acknowledged.

References

1 (*a*) N. Ishikawa, M. Sugita, T. Ishikawa, S. Koshihara and Y. Kaizu, *J. Am. Chem. Soc.*, 2003, **125**, 8694; (*b*) G. Cucinotta, M. Perfetti, J. Luzon, M. Etienne, P. E. Car, A. Caneschi, G. Calvez, K. Bernot and R. Sessoli, *Angew. Chem., Int. Ed.*, 2012, **51**, 1606; (*c*) M. A. AlDamen, S. Cardona-Serra, J. M. Clemente-Juan, E. Coronado, A. Gaita-Ariño, C. Martí-Gastaldo, F. Luis and O. Montero, *Inorg. Chem.*, 2009, **48**, 3467; (*d*) S.-D. Jiang, B.-W. Wang, G. Su, Z.-M. Wang and S. Gao, *Angew. Chem., Int. Ed.*, 2010, **49**, 7448; (*e*) D. N. Woodruff, R. E. P. Winpenny and R. A. Layfield, *Chem. Rev.*, 2013, **113**, 5110; (*f*) S.-D. Jiang, B.-W. Wang, H.-L. Sun, Z.-M. Wang and S. Gao, *J. Am. Chem. Soc.*, 2011, **133**, 4730; (*g*) S. Cardona-Serra, J. M. Clemente-Juan, E. Coronado, A. Gaita-Ariño, A. Camón, M. Evangelisti, F. Luis, M. J. Martínez-Pérez and J. Sesé, *J. Am. Chem. Soc.*, 2012, **134**, 14982; (*h*) R. Westerström, J. Dreiser, C. Piamonteze, M. Muntwiler, S. Weyeneth, H. Brune, S. Rusponi, F. Nolting, A. Popov, S. Yang, L. Dunsch and T. Greber, *J. Am. Chem. Soc.*, 2012, **134**, 9840; (*i*) N. Ishikawa, M. Sugita, N. Tanaka, T. Ishikawa, S. Koshihara and Y. Kaizu, *Inorg. Chem.*, 2004, **43**, 5498; (*j*) P. E. Car, M. Perfetti, M. Mannini, A. Favre, A. Caneschi and R. Sessoli, *Chem. Commun.*, 2011, **47**, 3751; (*k*) S. Jiang, B. Wang, G. Su, Z. Wang and S. Gao, *Angew. Chem., Int. Ed.*, 2010, **49**, 7448; (*l*) G. Chen, C. Gao, J. Tian, J. Tang, W. Gu, X. Liu, S. Yan, D. Liao and P. Cheng, *Dalton Trans.*, 2011, **40**, 5579; (*m*) A. Watanabe, A. Yamashita, M. Nakano, T. Yamamura and T. Kajiwara, *Chem.–Eur. J.*, 2011, **17**, 7428; (*n*) H. L. C. Feltham, Y. Lan, F. Klöwer, L. Ungur, L. F. Chibotaru, A. K. Powell and S. Brooker, *Chem.–Eur. J.*, 2011, **17**, 4362; (*o*) K. R. Meihaus, J. D. Rinehart and J. R. Long, *Inorg. Chem.*, 2011, **50**, 8484; (*p*) M. Jeletic, P.-H. Lin, J. J. Le Roy, I. Korobkov, S. I. Gorelsky and M. Murugesu, *J. Am. Chem. Soc.*, 2011, **133**, 19286; (*q*) N. F. Chilton, S. K. Langley, B. Moubaraki, A. Soncini, S. R. Batten and K. S. Murray, *Chem. Sci.*, 2013, **4**, 1719; (*r*) C. R. Ganivet, B. Ballesteros, G. de la Torre, J. M. Clemente-Juan, E. Coronado and T. Torres, *Chem.–Eur. J.*, 2013, **19**, 1457; (*s*) R. J. Blagg, L. Ungur, F. Tuna, J. Speak, P. Comar, D. Collison, W. Wernsdorfer, E. J. L. McInnes, L. F. Chibotaru and R. E. P. Winpenny, *Nat. Chem.*, 2013, **5**, 673–678.

2 (*a*) M. Urdampilleta, S. Klyatskaya, J. P. Cleuziou, M. Ruben and W. Wernsdorfer, *Nat. Mater.*, 2011, **10**, 502; (*b*) R. Vincent, S. Klyatskaya, M. Ruben, W. Wernsdorfer and F. Balestro, *Nature*, 2012, **488**, 357; (*c*) M. Ganzhorn, S. Klyatskaya, M. Ruben and W. Wernsdorfer, *Nat. Nanotechnol.*, 2013, **8**, 165.

3 (*a*) L. Sorace, C. Benelli and D. Gatteschi, *Chem. Soc. Rev.*, 2011, **40**, 3092–3104; (*b*) J. D. Rinehart and J. R. Long, *Chem. Sci.*, 2011, **2**, 2078; (*c*) J.-L. Liu, Y.-C. Chen, Y.-Z. Zheng, W.-Q. Lin, L. Ungur, W. Wernsdorfer, L. F. Chibotaru and M.-L. Tong, *Chem. Sci.*, 2013, **4**, 3310–3316.

4 L. F. Chibotaru, in *Advances in Chemical Physics*, John Wiley & Sons, Inc., 2013, p. 397.

5 (*a*) J. J. Baldoví, S. Cardona-Serra, J. M. Clemente-Juan, E. Coronado, A. Gaita-Ariño and A. Palii, *Inorg. Chem.*, 2012, **51**, 12565; (*b*) N. F. Chilton, D. Collison, E. J. L. McInnes, R. E. P. Winpenny and A. Soncini, *Nat. Commun.*, 2013, **4**, 2551; (*c*) O. S. Reu, A. V. Palii, S. M. Ostrovsky, P. L. W. Tregenna-Piggott and S. I. Klokishner, *Inorg. Chem.*, 2012, **51**, 10955.

6 (*a*) S. Petit, G. Pillet, D. Luneau, L. F. Chibotaru and L. Ungur, *Dalton Trans.*, 2007, 4582–4588; (*b*) J. Luzon and R. Sessoli, *Dalton Trans.*, 2012, **41**, 13556.

7 (*a*) J.-C. G. Bünzli and C. Piguet, *Chem. Soc. Rev.*, 2005, **34**, 1048; (*b*) S. V. Eliseeva and J.-C. G. Bünzli, *Chem. Soc. Rev.*, 2010, **39**, 189.

8 (*a*) M.-E. Boulon, G. Cucinotta, J. Luzon, C. Degl'Innocenti, M. Perfetti, K. Bernot, G. Calvez, A. Caneschi and R. Sessoli, *Angew. Chem., Int. Ed.*, 2013, **52**, 350; (*b*) K. Yamashita, R. Miyazaki, Y. Kataoka, T. Nakanishi, Y. Hasegawa, M. Nakano, T. Yamamura and T. Kajiwara, *Dalton Trans.*, 2013, **42**, 1987.

9 (*a*) A. Furrer and O. Waldmann, *Rev. Mod. Phys.*, 2013, **85**, 367; (*b*) J. Dreiser, K. S. Pedersen, C. Piamonteze, S. Rusponi, Z. Salman, M. E. Ali, M. Schau-Magnussen, C. A. Thuesen, S. Piligkos, H. Weihe, H. Mutka, O. Waldmann, P. Oppeneer, J. Bendix, F. Nolting and H. Brune, *Chem. Sci.*, 2012, **3**, 1024; (*c*) M. Kofu, O. Yamamuro, T. Kajiwara, Y. Yoshimura, M. Nakano, K. Nakajima, S. Ohira-Kawamura, T. Kikuchi and Y. Inamura, *Phys. Rev. B: Condens. Matter Mater. Phys.*, 2013, **88**, 064405.

10 (*a*) P. V. Bernhardt, B. M. Flanagan and M. J. Riley, *Aust. J. Chem.*, 2000, **53**, 229; (*b*) P. V. Bernhardt, B. M. Flanagan and M. J. Riley, *Aust. J. Chem.*, 2001, **54**, 229.

11 (*a*) B. M. Flanagan, P. V. Bernhardt, E. R. Krausz, S. R. Lüthi and M. J. Riley, *Inorg. Chem.*, 2001, **40**, 5401; (*b*) B. M. Flanagan, P. V. Bernhardt, E. R. Krausz, S. R. Lüthi and M. J. Riley, *Inorg. Chem.*, 2002, **41**, 5024.

12 (*a*) W.-K. Wong, H. Liang, J. Guo, W.-Y. Wong, W.-K. Lo, K.-F. Li, K.-W. Cheah, Z. Zhou and W.-T. Wong, *Eur. J. Inorg. Chem.*, 2004, 829; (*b*) P. Dröse and J. Gottfriedsen, *Z. Anorg. Allg. Chem.*, 2008, **634**, 87; (*c*) S. Mizukami, H. Houjou, M. Kanesato and K. Hiratani, *Chem.–Eur. J.*, 2003, **9**, 1521; (*d*) S. J. Archibald, A. J. Blake, M. Schroder and R. E. P. Winpenny, *J. Chem. Soc., Chem. Commun.*, 1994, 1669; (*e*) P. Dröse, J. Gottfriedsen, C. G. Hrib, P. G. Jones, L. Hilfert and F. T. Edelmann, *Z. Anorg. Allg. Chem.*, 2011, **637**, 369; (*f*) M. Kanesato, S. Mizukami, H. Houjou, H. Tokuhisa, E. Koyama and Y. Nagawa, *J. Alloys Compd.*, 2004, **374**, 307; (*g*) M. Kanesato, T. Yokoyama, O. Itabashi, T. M. Suzuki and M. Shiro, *Bull. Chem. Soc. Jpn.*, 1996, **69**, 1297.

13 M. Kanesato and T. Yokoyama, *Chem. Lett.*, 1999, 137.

14 H. Voβ, K. J. Wannowius and H. Elias, *J. Inorg. Nucl. Chem.*, 1975, **37**, 79.

15 M. Kanesato, F. N. Ngassapa and T. Yokoyama, *Anal. Sci.*, 2001, **17**, 1359.

16 O. V. Dolomanov, L. J. Bourhis, R. J. Gildea, J. A. K. Howard and H. Puschmann, *J. Appl. Crystallogr.*, 2009, **42**, 339.

17 LAMP, the Large Array Manipulation Program; D. Richard, M. Ferrand and G. J. Kearley, *J. Neutron Res.*, 1996, **4**, 33.

18 Q. Scheifele, T. Birk, J. Bendix, P. L. W. Tregenna-Piggott and H. Weihe, *Angew. Chem., Int. Ed.*, 2008, **47**, 148.

19 J. J. Dallara, M. F. Reid and F. S. Richardson, *J. Phys. Chem.*, 1984, **88**, 3587.

20 *MATLAB R2010a*, The MathWorks Inc., Natick, MA, USA, 2010.

21 S. Stoll and A. Schweiger, *J. Magn. Reson.*, 2006, **178**, 42.

22 V. I. Lebedev and D. N. Laikov, *Dokl. Math.*, 1999, **59**, 477.

23 F. Aquilante, L. De Vico, N. Ferre, G. Ghigo, P.-A. Malmqvist, P. Neograd, T. B. Pedersen, M. Pitonak, M. Reiher, B. O. Roos, L. Serrano-Andres, M. Urban, V. Veryazov and R. Lindh, *J. Comput. Chem.*, 2010, **31**, 224.

24 B. O. Roos, P. R. Taylor and P. E. Siegbahn, *Chem. Phys.*, 1980, **48**, 157.

25 B. O. Roos and P.-A. Malmqvist, *Phys. Chem. Chem. Phys.*, 2004, **6**, 2919.

26 L. F. Chibotaru and L. Ungur, *J. Chem. Phys.*, 2012, **137**, 064112; SINGLE_ANISO module is described in the MOLCAS manual: http://molcas.org/documentation/manual/node95.html.

27 (*a*) R. Rodríguez-Cortiñas, F. Avecilla, C. Platas-Iglesias, D. Imbert, J.-C. G. Bünzli, A. de Blas and T. Rodríguez- Blas, *Inorg. Chem.*, 2002, **41**, 5336; (*b*) C. Platas, F. Avecilla, A. de Blas, C. F. G. C. Geraldes, T. Rodríguez-Blas, H. Adams and J. Mahía, *Inorg. Chem.*, 1999, **38**, 3190; (*c*) J.-P. Costes, F. Dahan and F. Nicodème, *Inorg. Chem.*, 2003, **42**, 6556; (*d*) F. Avecilla, A. de Blas, C. Platas, T. Rodriguez-Blas, R. Bastida, A. Macias, A. Rodriguez, D. E. Fenton and J. Mahia, *Chem. Commun.*, 1999, 125; (*e*) C. Platas, F. Avecilla, A. de Blas, T. Rodriguez-Blas, C. F. G. C. Geraldes, E. Toth, A. E. Merbach and J.-C. G. Bünzli, *J. Chem. Soc., Dalton Trans.*, 2000, 611; (*f*) Q.-Y. Chen, Q.-H. Luo and H.-k. Fun, *J. Chem. Crystallogr.*, 2002, **32**(10), 377.

28 (*a*) G. Shirane, S. M. Shapiro, and J. M. Tranquada, in *Neutron Scattering with a Triple-Axis Spectrometer*, Cambridge University Press, Cambridge, England, 2002; (*b*) J. Dreiser, O. Waldmann, C. Dobe, G. Carver, S. T. Ochsenbein, A. Sieber, H. U. Güdel, J. van Duijn, J. Taylor and A. Podlesnyak, *Phys. Rev. B: Condens. Matter Mater. Phys.*, 2010, **81**, 024408.

29 If the ground state doublet belonged to the other possible (Γ_6) irreducible representation, it would contain mixtures of only $m_J = \pm 15/2$, $\pm 9/2$ and $\pm 3/2$ states hence an intra-doublet transition would be forbidden by the EPR selection rule $\Delta m_J = \pm 1$ independent of the exact wavefunction.

30 (*a*) R. Orbach, *Proc. R. Soc. London, Ser. A*, 1961, **264**, 458; (*b*) R. Orbach and M. Blume, *Phys. Rev. Lett.*, 1962, **8**, 478; (*c*) R. W. Bierig, M. J. Weber and S. I. Warshaw, *Phys. Rev.*, 1964, **134**, A1504; (*d*) J. M. Zadrozny, M. Atanasov, A. M. Bryan, C.-Y. Lin, B. D. Rekken, P. P. Power, F. Neese and J. R. Long, *Chem. Sci.*, 2013, **4**, 125; (*e*) D. E. Freedman, W. H. Harman, T. D. Harris, G. J. Long, C. J. Chang and J. R. Long, *J. Am. Chem. Soc.*, 2010, **132**, 1224; (*f*) J. D. Rinehart and J. R. Long, *J. Am. Chem. Soc.*, 2009, **131**, 12558; (*g*) A. Kiel and W. B. Mims, *Phys. Rev.*, 1967, **161**, 386.

31 S. Takamatsu, T. Ishikawa, S.-y. Koshihara and N. Ishikawa, *Inorg. Chem.*, 2007, **46**, 7250.

32 F. Habib, G. Brunet, V. Vieru, I. Korobkov, L. F. Chibotaru and M. Murugesu, *J. Am. Chem. Soc.*, 2013, **135**, 13242.

33 V. Mereacre, A. Baniodeh, C. E. Anson and A. K. Powell, *J. Am. Chem. Soc.*, 2011, **133**, 15335.

34 E. Lucaccini, L. Sorace, M. Perfetti, J. Costes and R. Sessoli, *Chem. Commun.*, 2014, **50**, 1648.

II:

$[ReF_6]^{2-}$: A Robust Module for the Design of Molecule-Based Magnetic Materials

K. S. Pedersen, M. Sigrist, M. A. Sørensen, A.-L. Barra, T. Weyhermüller, S. Piligkos, C. A. Thuesen, M. G. Vinum, H. Mutka, H. Weihe, R. Clérac, J. Bendix

Angewandte Chemie International Edition **53**, 1351-1354 (2014)

Magnetic Modules

DOI: 10.1002/anie.201309981

$[ReF_6]^{2-}$: A Robust Module for the Design of Molecule-Based Magnetic Materials**

Kasper S. Pedersen, Marc Sigrist, Mikkel A. Sørensen, Anne-Laure Barra, Thomas Weyhermüller, Stergios Piligkos, Christian Aa. Thuesen, Morten G. Vinum, Hannu Mutka, Høgni Weihe, Rodolphe Clérac,* and Jesper Bendix**

Abstract: *A facile synthesis of the $[ReF_6]^{2-}$ ion and its use as a building block to synthesize magnetic systems are reported. Using dc and ac magnetic susceptibility measurements, INS and EPR spectroscopies, the magnetic properties of the isolated $[ReF_6]^{2-}$ unit in $(PPh_4)_2[ReF_6]\cdot 2H_2O$ (**1**) have been fully studied including the slow relaxation of the magnetization observed below ca. 4 K. This slow dynamic is preserved for the one-dimensional coordination polymer $[Zn(viz)_4(ReF_6)]_\infty$ (**2**, viz = 1-vinylimidazole), demonstrating the irrelevance of low symmetry for such magnetization dynamics in systems with easy-plane-type anisotropy. The ability of fluoride to mediate significant exchange interactions is exemplified by the isostructural $[Ni(viz)_4(ReF_6)]_\infty$ (**3**) analogue in which the ferromagnetic Ni^{II}–Re^{IV} interaction ($+10.8\ cm^{-1}$) dwarfs the coupling present in related cyanide-bridged systems. These results reveal $[ReF_6]^{2-}$ to be an unique new module for the design of molecule-based magnetic materials.*

Diffuse orbitals and large magnetic anisotropies resulting from strong spin-orbit coupling make complexes with central ions from the 4d and 5d series interesting modules for magnetic materials.[1] The preponderance of homo-[2] and heteroleptic[3] cyanide building units has been hard to challenge in the field of molecular magnetism and only few exceptions have been reported.[4] Although homoleptic fluoride complexes are well-described in the literature, they have been used only once[5] as modules to design molecule-based magnetic materials. The rarity of hexafluoridometalate-based magnetic materials may be due to the harsh synthetic conditions often required for the formation of fluoridometalates and to their common inherent lability, outside hydrofluoric acid solutions, towards, for example, hydrolysis. The combination of the kinetic inertness of octahedral d^3 complexes and the potential strong magnetic anisotropy of 5d systems, led us to explore the $[ReF_6]^{2-}$ ion as a possible module to build molecule-based magnetic materials. $[ReF_6]^{2-}$ can be generated by dissolving $[ReX_6]^{2-}$ (X = Cl, Br) salts in a KHF_2 melt.[6] The subsequent isolation of water-soluble $K_2[ReF_6]$ from mixtures with KF and KHF_2 is however problematic. Instead, we found that using molten NH_4HF_2 as a fluoride source, gave quantitatively the water-soluble $(NH_4)_2[ReF_6]$ salt that is easily converted into $(PPh_4)_2[ReF_6]\cdot 2H_2O$ (**1**) by metathesis. The molecular structure of the $[ReF_6]^{2-}$ unit in **1** (hydrogen bonded to two water molecules) is shown in Figure 1 (left) and Figure S1 of the Supporting Information.

When 1-vinylimidazole (viz) is added to a methanol solution of $[ReF_6]^{2-}$ and M^{2+} (M = Zn, Ni), chains with alternating metal centers, $[M(viz)_4(ReF_6)]_\infty$ (M = Zn (**2**), Ni

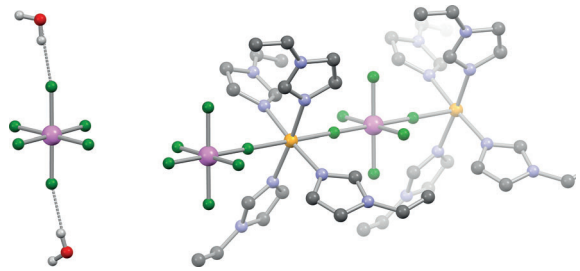

Figure 1. Structures of the $[ReF_6]^{2-}\cdot 2H_2O$ unit in **1** (left) and the chain motif of **2** and **3** (right). Re pink, Zn/Ni yellow, F green, O red, N blue, C gray; H small, light gray. $[PPh_4]^+$ ions and viz hydrogen atoms are omitted for clarity. Selected bond lengths [Å] and angles [°] for **1**: Re-F 1.9515(11)–1.9720(11), **2**: Re-F_{ax} 1.964(3), Re-F_{eq} 1.950(3), Re-F-Zn 180 **3**: Re-F_{ax} 1.9627(16), Re-F_{eq} 1.9496(13); Re-F-Ni 180.

[*] K. S. Pedersen, M. Sigrist, M. A. Sørensen, Dr. S. Piligkos, Dr. C. Aa. Thuesen, M. G. Vinum, Dr. H. Weihe, Prof. Dr. J. Bendix
Department of Chemistry, University of Copenhagen
Universitetsparken 5, 2100 Copenhagen (Denmark)
E-mail: ksp@kiku.dk
bendix@kiku.dk

K. S. Pedersen, Dr. R. Clérac
CNRS, CRPP, UPR 8641
33600 Pessac (France)
and
Univ. Bordeaux, CRPP, UPR 8641
33600 Pessac (France)
E-mail: clerac@crpp-bordeaux.cnrs.fr

M. Sigrist, H. Mutka
Institut Laue-Langevin
38042 Grenoble Cedex 9 (France)

Dr. A.-L. Barra
Laboratoire National des Champs Magnétiques Intenses, CNRS
38042 Grenoble Cedex 9 (France)

Dr. T. Weyhermüller
Max Planck Institute for Chemical Energy Conversion
Mülheim an der Ruhr (Germany)

[**] K.S.P. and S.P. thank the Danish Ministry of Science, Innovation and Higher Education for an EliteForsk travel scholarship and a Sapere Aude Fellowship (10-081659), respectively. This work was partially supported by the University of Bordeaux, the Région Aquitaine, the ANR and the CNRS. J.B. thanks the Danish Research Councils for Independent Research for support (12-125226).

Supporting information for this article is available on the WWW under http://dx.doi.org/10.1002/anie.201309981.

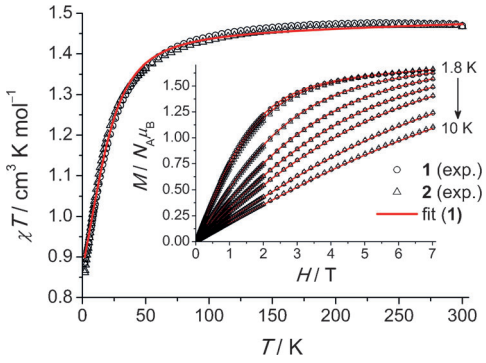

Figure 2. Temperature dependence of the χT product for **1** (circles) and **2** (triangles) at 1000 Oe. Inset: Field dependence of the magnetization between 1.8 and 10 K. The red lines are the best fit for **1** as described in the text.

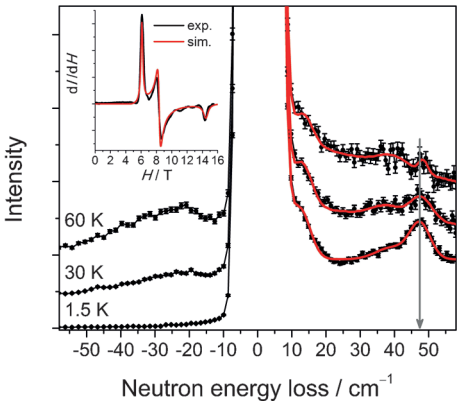

Figure 3. INS spectra of fully deuterated **1** ($\lambda_i = 2.2$ Å, linear momentum (Q) range of 0.80 Å$^{-1} \le Q \le$ 1.65 Å^{-1} at the magnetic peak position). The solid red line represents a sum of four Gaussians. Gray arrow highlights the peaks at 48 cm^{-1}. Inset: HF-EPR spectrum obtained at 5.4 K with 331.2 GHz microwave radiation and its simulation.

(**3**)), are formed. These compounds crystallize in the $P4_2/n$ space group with the Re^{IV} ion occupying a tetragonal position with a slight tetragonal elongation of the octahedron (Figure 1 (right), Figures S2, S3). Despite the different local environments, the magnetism of the isolated Re^{IV} site in the $[PPh_4]^+$ salt, **1**, and the Zn^{II} chain, **2**, are nearly perfectly overlapping as illustrated by the χT versus T ($\chi = M/H$) and M versus H data shown in Figure 2.

The χT product decreases steadily from the room temperature value of 1.43 cm^3 K mol^{-1} to 0.88 cm^3 K mol^{-1} at 1.8 K. As the $[ReF_6]^{2-}$ ions in **1** are separated by more than 11 Å, the main origin for the χT decrease is the single-ion anisotropy (zero-field splitting, ZFS). The magnetic and spectroscopic data for the $S = 3/2$ system were fitted or simulated, respectively, considering the following spin-Hamiltonian Equation (1):

$$\hat{H} = \mu_B g H \hat{S} + D\left(\hat{S}_z^2 - \frac{1}{3}S(S+1)\right) + E\left(\hat{S}_x^2 - \hat{S}_y^2\right) \quad (1)$$

where D and E are the axial and rhombic ZFS parameters, respectively, and the remaining symbols have their usual meaning. To unravel the magnetic anisotropy of **1**, high-field (HF) and X-band EPR spectroscopy and inelastic neutron scattering (INS) were employed. The rough estimation of D from the χT versus T data [Figure 2, Eq. (1)] leads to a value of around 28 cm^{-1} (40 K). The splitting between the two doublets of $2\sqrt{D^2 + 3E^2}$ can be directly probed in zero magnetic field by INS as shown in Figure 3 and Figures S8–S9 for a fully deuterated sample of **1**.

The magnetic origin of the prominent peak observed at 48 cm^{-1} was demonstrated on the basis of its temperature and Q dependence (Figure S9). The combined analysis of HF-EPR (Figure 3) which mainly probes the $|E|/D$ ratio, and INS spectroscopic data allows an accurate evaluation of $g = 1.69$, $D = 23.6$ cm^{-1} (34.0 K), and $|E| = 2.6$ cm^{-1} (3.7 K). Fixing D and E to these spectroscopically determined values, the fitting of the dc magnetic data with only an isotropic g factor leads to $g = 1.76$ and 1.72 for the χT versus T and M versus H data, respectively [red solid lines in Figure 2, Eq. (1)]. The slightly lower g factor for the low-temperature magnetization data is in agreement with the estimation from EPR (Figure 3, Figures S11–S12) and can be explained by different effective g factors of the two doublets resulting from the strong spin-orbit coupling (see Supporting Information). Attempts to spectroscopically measure the zero-field splitting in **2** by INS were unsuccessful, possibly due to the large incoherent cross section of the protons. However, the strong similarity of the magnetic data for **1** and **2** suggests a similar inter-Kramers doublet separation. Using the angular overlap model (AOM) with $e_\sigma^{average} = 13\,000$ cm^{-1} and $e_\pi^{average} = 2000$ cm^{-1} ($\Delta_O = 3e_\sigma - 4e_\pi$) and introducing a small anisotropy between the axial and equatorial fluoride ligands such that $e_{\sigma,ax.} < e_{\sigma,eq.}$ and $e_{\pi,ax.} < e_{\pi,eq.}$ readily accounts for the sign and magnitude of the observed D value (Figure S13–S16).[7]

Despite the positive sign of D, ac susceptibility measurements were performed for **1** and **2**. In zero-dc field, no slow relaxation of the magnetization was observed. However, application of a small dc field gives rise to clear peaks in the out-of-phase component, χ'', of the ac susceptibility (Figures 4 and S19–S26) characteristic of slow dynamics of the magnetization. The associated relaxation times, τ, at the optimum field, H^*, of 2500 Oe (Figures S21, S22, S25, and S26) follow an Arrhenius law, $\tau(T) = \tau_0 \exp\{\Delta_{eff}/(k_B T)\}$, with $\Delta_{eff} = 19.7$ cm^{-1} (28.3 K; $\tau_0 = 9.6 \times 10^{-9}$ s) and $\Delta_{eff} = 20.6$ cm^{-1} (29.6 K; $\tau_0 = 4.7 \times 10^{-10}$ s) for **1** and **2**, respectively (Figure 4). This dynamic behavior parallels that of a few other mononuclear complexes reported to exhibit single-molecule magnet (SMM) properties notwithstanding $D > 0$.[8] Moreover, note that the $[ReF_6]^{2-}$ module is only the second example of a mononuclear 5d complex for which slow relaxation of magnetization has been observed.[9] Intriguingly, the magnetization dynamics of **1** and **2** are strongly similar, indicating that the slow relaxation is not solely a property of the crystal lattice and its heat capacity.[10] Notably, the strictly axial symmetry of **2** precludes a rationalization of the relaxation barrier in terms of rhombicity. The hyperfine couplings in **2** were determined by X-band EPR at $A_z =$

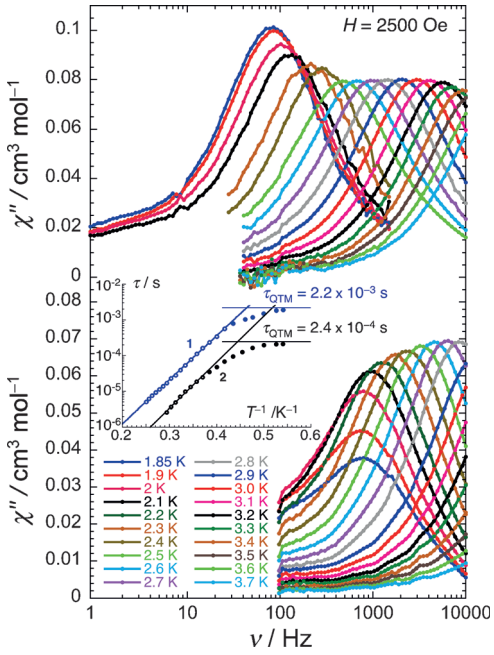

Figure 4. Frequency dependence of the out-of-phase component (χ'') of the ac susceptibility for **1** (top) and **2** (bottom) at selected temperatures between 1.85 and 3.7 K in an 2500 Oe dc field. Inset: τ versus $1/T$ plot for **1** and **2**. The data points were extracted from the $\chi''(\nu)$ maxima at 2500 Oe with $\tau = (2\pi\nu_{ac})^{-1}$.The solid lines corresponds to the fit of the data to an Arrhenius law (see text).

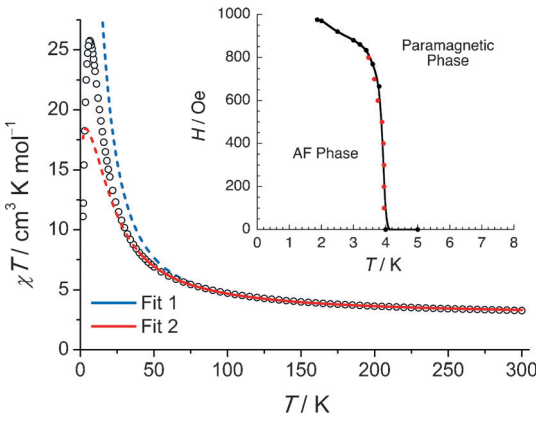

Figure 5. Temperature dependence of the χT product for **3** at 1000 Oe. The solid blue and red lines represent fit 1 and fit 2, respectively, as described in the text. The dashed lines are the extrapolation of the fits to 1.8 K. Inset: (T, H) magnetic phase diagram for **3** extracted from the dM/dH versus H maxima (black points) and χ versus T data at low fields (red points; Figures S28, S29).

0.06179(7) cm^{-1} and $A_{xy} = 0.04953(1)$ cm^{-1} studying the diamagnetic isomorphous $[Zn(viz)_4(ZrF_6)]_\infty$ analogue doped with Re^{IV} (ca. 5%; Figure S12). Interestingly, the associated energy of $A_z S_{Re} I_{Re} \approx 0.23$ cm^{-1} ($I(^{185,187}Re) = 5/2$) is close to the magnetic energy, 0.3 cm^{-1} ($g_{Re}\mu_B H^* S_{Re}$) at the optimum field (2500 Oe) in the ac measurements. In conjunction with the similarity of the magnetic properties of **1** and **2** (Figure 2), this observation could suggest that the magnetization dynamics is more influenced by the interaction between electronic and nuclear spins than by the spin-phonon coupling.

Lowering the temperature, the χT product of **3** (Figure 5) is increasing from 3.3 $cm^3 K mol^{-1}$ at 300 K until reaching a maximum of 25.8 $cm^3 K mol^{-1}$ at 6.5 K. This increase suggests intra-chain Re^{IV}–Ni^{II} ferromagnetic interactions, which are readily explained by the strict orthogonality of the respective t_{2g}^3 and $t_{2g}^6 e_g^2$ configurations resulting from the perfectly linear fluoride bridge. The modeling of the magnetic susceptibility was performed using the following Heisenberg chain Hamiltonian [Eq. (2)].

$$\hat{H} = \mu_B H \sum_i g_i \hat{S}_i - 2J \sum_i \hat{S}_i \hat{S}_{i+1} \qquad (2)$$

The high-temperature data, where quantum effects and magnetic anisotropy have less influence,[11] have been modeled by the approach suggested by Drillon et al. for classical spins in the zero-field limit (fit 1, see Supporting Information)[12] and by exact block diagonalization of the spin-Hamiltonian matrix for a twelve-membered $\{Ni^{II}Re^{IV}\}_6$ ring model (fit 2).[13] These magnetic models yield similar large J interactions evaluated at 10.8(8) cm^{-1} (15.5 K, fit 1) and 11.8(5) cm^{-1} (17.0 K, fit 2).

Using the X-ray structure and calculating J by DFT methods (see Supporting Information) yields $J = 12.7$ cm^{-1} (18.3 K) in good agreement with the above models. For Re^{IV}–Ni^{II} linkages, the fluoride-mediated interaction exceeds the strongest interactions observed through for example, cyanide (3.7 cm^{-1}).[3,14,15] In **3**, no slow relaxation of the magnetization was observed by ac technique (even under dc field), but the field-dependence of the low-temperature magnetization exhibits a characteristic S-shape (Figures S27, S28) indicative of an antiferromagnetic ground state below approximately 4 K (see Supporting Information). From the inflection points of M versus H plots and the χ versus T data at low fields, the temperature dependence of the critical field H_C was extracted and shown in the inset of Figure 5. The magnitude of the antiferromagnetic inter-chain interactions (zJ') is also estimated from $g_{av}\mu_B H_C^0 S_{eff} = 2\,|\,zJ'\,|\,S_{eff}^2$, where H_C^0 is the critical field extrapolated to $T = 0$ K and S_{eff} is the effective spin of 5/2, yielding $zJ' \approx -0.018$ cm^{-1} (−0.026 K). It is important to mention that **3** does not exhibit single-chain magnet properties for two main reasons: 1) the local planar anisotropy for rhenium ($D_{Re} > 0$) that is expected to dominate the chain properties, and 2) the strict tetragonal symmetry of the chains that prevents the canting of the anisotropy axes/planes and thus prevents single-chain magnet behavior.

In summary, a new high-yield synthesis of the $[ReF_6]^{2-}$ ion is described and a detailed study of its physical properties reported, revealing its pronounced magnetic anisotropy upon small structural distortions and its intrinsic slow magnetization dynamics. The chemical robustness allowed its use as a module to synthesize one-dimensional coordination polymer with 3d metal ions. Its ability to mediate significantly strong exchange interactions between magnetic metal ions makes $[ReF_6]^{2-}$ an interesting and unique module for the design of new molecule-based magnetic materials.

Experimental Section

$(NH_4)_2[ReCl_6]$ was prepared as described in literature and the synthesis of $(NH_4)_2[ReF_6]$ is described in the Supporting Information.[16] All other reagents were purchased from commercial sources and used as received.

1: A saturated aqueous solution of PPh_4Cl (0.75 g, 2.0 mmol) was added to a saturated aqueous solution of $(NH_4)_2[ReF_6]$ (0.25 g, 0.74 mmol). The mixture was left standing for 12 h to yield $(PPh_4)_2[ReF_6]\cdot 2H_2O$. Yield: 0.43 g (57%). Elemental Analysis (%) calcd for $C_{48}H_{44}F_6O_2P_2Re$: C 56.80, H 4.37, F 11.23; found: C 56.61, H 4.22, F 11.18. The deuterated analogue was synthesized similarly by using $[D_{20}]PPh_4Cl$ in D_2O (see the Supporting Information).

$[M(viz)_4(ReF_6)]_\infty$ (Zn (**2**), Ni (**3**)): $(PPh_4)_2[ReF_6]\cdot 2H_2O$ (100 mg, 0.099 mmol) and $NiCl_2\cdot 6H_2O$ (100 mg, 0.42 mmol) or $Zn(NO_3)_2\cdot 6H_2O$ (125 mg, 0.42 mmol) were dissolved in MeOH (40 mL) before adding 1-vinylimidazole (0.8 g, 8.5 mmol). The solution was left standing for 1 day to give **2** and **3**, respectively. Yields: **2**: 56 mg (76%), **3**: 52 mg (72%). Elemental Analysis (%) calcd for $C_{20}H_{24}F_6N_8ZnRe$ (**2**): C 32.37, H 3.26, N 15.10; found: C 32.65, H 3.13, N 15.05. Elemental Analysis (%) calcd for $C_{20}H_{24}F_6N_8NiRe$ (**3**): C 32.67, H 3.29, N 15.24, F 15.50; found: C 32.69, H 3.20, N 15.20, F 15.36.

Crystallographic data and additional experimental details of the characterization, spectroscopic data, magnetic properties and the DFT calculations can be found in the Supporting Information. CCDC 964856–964859, contain the supplementary crystallographic data for this paper. These data can be obtained free of charge from The Cambridge Crystallographic Data Centre via www.ccdc.cam.ac.uk/data_request/cif.

Received: October 24, 2013
Revised: November 17, 2013

Keywords: coordination polymers · fluoride · magnetic anisotropy · rhenium · single-molecule magnets

[1] X.-Y. Wang, C. Avendano, K. R. Dunbar, *Chem. Soc. Rev.* **2011**, *40*, 3213.
[2] a) D. E. Freedman, D. M. Jenkins, A. T. Iavarone, J. R. Long, *J. Am. Chem. Soc.* **2008**, *130*, 2884; b) K. S. Pedersen, M. Schau-Magnussen, J. Bendix, H. Weihe, A. V. Palii, S. I. Klokishner, S. Ostrovsky, O. S. Reu, H. Mutka, P. L. W. Tregenna-Piggott, *Chem. Eur. J.* **2010**, *16*, 13458; c) K. Qian, X.-C. Huang, C. Zhou, X.-Z. You, X.-Y. Wang, K. R. Dunbar, *J. Am. Chem. Soc.* **2013**, *135*, 13302.
[3] a) T. D. Harris, M. V. Bennett, R. Clérac, J. R. Long, *J. Am. Chem. Soc.* **2010**, *132*, 3980; b) I. Bhowmick, E. A. Hillard, P. Dechambenoit, C. Coulon, T. D. Harris, R. Clérac, *Chem. Commun.* **2012**, *48*, 9717; c) X. Feng, J. Liu, T. D. Harris, S. Hill, J. R. Long, *J. Am. Chem. Soc.* **2012**, *134*, 7521.
[4] J. Martínez-Lillo, D. Armentano, G. De Munno, W. Wernsdorfer, M. Julve, F. Lloret, J. Faus, *J. Am. Chem. Soc.* **2006**, *128*, 14218.
[5] T. Mahenthirarajah, Y. Li, P. Lightfoot, *Inorg. Chem.* **2008**, *47*, 9097.
[6] a) R. D. Peacock, *J. Chem. Soc.* **1956**, 1291; b) E. Weise, *Z. Anorg. Allg. Chem.* **1956**, *283*, 377.
[7] C. K. Jørgensen, K. Schwochau, *Z. Naturforsch. A* **1965**, *20*, 65.
[8] a) J. M. Zadrozny, J. Jui, N. A. Piro, C. J. Chang, S. Hill, J. R. Long, *Chem. Commun.* **2012**, *48*, 3927; b) J. Vallejo, I. Castro, R. Ruiz-García, J. Cano, M. Julve, F. Lloret, G. De Munno, W. Wernsdorfer, E. Pardo, *J. Am. Chem. Soc.* **2012**, *134*, 15704; c) E. Colacio, F. Ruiz, E. Ruiz, E. Cremades, J. Krzystek, S. Carretta, J. Cano, T. Guidi, W. Wernsdorfer, E. K. Brechin, *Angew. Chem. Int. Ed.* **2013**, *52*, 9130; d) W. Huang, T. Liu, D. Wu, J. Cheng, Z. W. Ouyang, C. Duan, *Dalton Trans.* **2013**, *42*, 15326.
[9] J. Martínez-Lillo, T. F. Mastropietro, E. Lhotel, C. Paulsen, J. Cano, G. De Munno, J. Faus, F. Lloret, M. Julve, S. Nellutla, J. Krzystek, *J. Am. Chem. Soc.* **2013**, *135*, 13737.
[10] H. B. G. Casimir, F. K. Du Pré, *Physica V* **1938**, *6*, 507.
[11] For fits 1 and 2, the experimental data were fitted in the 80–300 K and 40–300 K temperature ranges, respectively.
[12] M. Drillon, E. Coronado, D. Beltran, R. Georges, *Chem. Phys.* **1983**, *79*, 449.
[13] T. Birk, K. S. Pedersen, S. Piligkos, C. A. Thuesen, H. Weihe, J. Bendix, *Inorg. Chem.* **2011**, *50*, 5312.
[14] However, a stronger coupling through cyanide was found in a cyanide-based $Cu^{II}-Re^{IV}$ chain ($J=+29\ cm^{-1}$); T. D. Harris, C. Coulon, R. Clérac, J. R. Long, *J. Am. Chem. Soc.* **2011**, *133*, 123.
[15] I. Bhowmick, T. D. Harris, P. Dechambenoit, E. A. Hillard, C. Pichon, I.-R. Jeon, R. Clérac, *Sci. China Chem.* **2012**, *55*, 1004.
[16] G. W. Watt, R. J. Thompson, *Inorg. Synth.* **1963**, *7*, 189.

III:

Three-Axis Anisotropic Exchange Coupling in the Single-Molecule Magnets NEt_4 $MnIII_2$(5-Brsalen)$_2$(MeOH)$_2$MIII(CN)$_6$ (M=Ru, Os)

J. Dreiser, K. S. Pedersen, A. Schnegg, K. Holldack, J. Nehrkorn, M. Sigrist, P. Tregenna-Piggott, H. Mutka, H. Weihe, V. S. Mironov, J. Bendix, O. Waldmann

Chemistry-a European Journal **19**, 3693-3701 (2013)

CHEMISTRY
A EUROPEAN JOURNAL

FULL PAPER

DOI: 10.1002/chem.201203781

Three-Axis Anisotropic Exchange Coupling in the Single-Molecule Magnets $NEt_4[Mn^{III}_2(5\text{-Brsalen})_2(MeOH)_2M^{III}(CN)_6]$ (M = Ru, Os)

Jan Dreiser,*[a, b] Kasper S. Pedersen,[c] Alexander Schnegg,[d] Karsten Holldack,[e] Joscha Nehrkorn,[a] Marc Sigrist,[f] Philip Tregenna-Piggott†,[g] Hannu Mutka,[f] Høgni Weihe,[c] Vladimir S. Mironov,[h] Jesper Bendix,[c] and Oliver Waldmann*[a]

Abstract: We have investigated the single-molecule magnets $[Mn^{III}_2(5\text{-Brsalen})_2(MeOH)_2M^{III}(CN)_6]NEt_4$ (M = Os (**1**) and Ru (**2**); 5-Brsalen = *N*,*N*′-ethylenebis(5-bromosalicylidene)iminate) by frequency-domain Fourier-transform terahertz electron paramagnetic resonance (THz-EPR), inelastic neutron scattering, and superconducting quantum interference device (SQUID) magnetometry. The combination of all three techniques allows for the unambiguous experimental determination of the three-axis anisotropic magnetic exchange coupling between Mn^{III} and Ru^{III} or Os^{III} ions, respectively. Analysis by means of a spin-Hamiltonian parameterization yields excellent agreement with all experimental data. Furthermore, analytical calculations show that the observed exchange anisotropy is due to the bent geometry encountered in both **1** and **2**, whereas a linear geometry would lead to an Ising-type exchange coupling.

Keywords: magnetic properties · manganese · osmium · ruthenium · single-molecule studies

Introduction

After the seminal discovery of slow relaxation and quantum tunneling of magnetization in $Mn_{12}OAc$,[1] the field of molecular magnetism has received fast-growing attention. A particular focus lies in the design of single-molecule magnets[2] (SMMs) that are desired to possess ever longer magnetization relaxation times at ever higher blocking temperatures. Here, magnetic anisotropy plays a key role.[3] In 3d metal ions, single-ion anisotropies are typically small because the orbital momentum is often quenched by the ligand field, and thus, anisotropy only appears through second-order perturbation effects. In contrast, when the first-order contribution can be exploited, the anisotropy is strongly enhanced. In this sense 4d, 4f, or 5d metal ions are more appropriate for introducing anisotropy than most of their 3d congeners. Indeed, much effort has been devoted to the synthesis of 4f SMMs,[4] which currently possess the longest magnetization relaxation times among molecular clusters. However, the well-shielded 4f shell of the lanthanides mostly results in weak magnetic exchange interactions, and hence, the use of 4d and 5d ions to build exchange-coupled clusters and SMMs can be advantageous.[5] The 4d and 5d orbitals are more diffuse than the 3d orbitals, enabling stronger exchange coupling to neighboring ions. Notably, to date, the strongest ferromagnetic coupling observed through the cyanide ion is found in the Re^{IV}–Cu^{II} chain $(nBu_4N)[Cu^{II}(Tp)][Re^{IV}Cl_4(CN)_2]\cdot 1.33\,CH_3CN$ (Tp^- = hydrotris(pyrazol-1-yl)borate) with $-J = +29\ cm^{-1}$ (in the $-2\mathbf{J}\mathbf{S}_1\cdot\mathbf{S}_2$ Hamiltonian definition).[6]

The angular momentum of half-integer spin 4d, 4f, and 5d ions is often described by using a $\tau = 1/2$ pseudospin approach, only taking into account the lowest doublet. Then the magnetic anisotropy induced by a ligand field enters by anisotropic exchange interactions, but orbitally dependent exchange can also give rise to anisotropic interactions.[7] Despite the expected large anisotropies and possibly enhanced SMM properties, very few SMMs are based on 4d and 5d

[a] Dr. J. Dreiser, J. Nehrkorn, Prof. O. Waldmann
Physikalisches Institut, Universität Freiburg
79104 Freiburg (Germany)
E-mail: jan.dreiser@psi.ch
oliver.waldmann@physik.uni-freiburg.de

[b] Dr. J. Dreiser
Present address: Swiss Light Source
Paul Scherrer Institut, 5232 Villigen PSI (Switzerland)

[c] K. S. Pedersen, Dr. H. Weihe, Prof. J. Bendix
Department of Chemistry, University of Copenhagen
2100 Copenhagen (Denmark)

[d] Dr. A. Schnegg
Helmholtz-Zentrum für Materialien und Energie
Institut für Silizium-Photovoltaik
12489 Berlin (Germany)

[e] Dr. K. Holldack
Helmholtz-Zentrum für Materialien und Energie
Inst. f. Methoden und Instrumente der Forschung
mit Synchrotronstrahlung, 12489 Berlin (Germany)

[f] M. Sigrist, Dr. H. Mutka
Institut Laue-Langevin, 38042 Grenoble Cedex 9 (France)

[g] Dr. P. Tregenna-Piggott
Laboratory for Neutron Scattering, Paul Scherrer Institut
5232 Villigen PSI (Switzerland)

[h] Dr. V. S. Mironov
A. V. Schubnikov Institute of Crystallography
119333 Moscow (Russia)

[†] Deceased.

Supporting information for this article is available on the WWW under http://dx.doi.org/10.1002/chem.201203781.

transition-metal ions. In the synthesis of paramagnetic clusters, most efforts have been devoted to cyanide precursors, especially those of Nb,[8] Mo,[9] W,[10] and Re,[11] whereas clusters incorporating Ru[12] and Os[13] have received little attention. Recently, some of us have reported the synthesis and magnetic properties of two isostructural, trinuclear SMMs $NEt_4[Mn^{III}_2(5\text{-Brsalen})_2(MeOH)_2M^{III}(CN)_6]$ (M = Os (**1**, Figure 1)[14] and Ru (**2**);[15] 5-Brsalen = *N*,*N*′-ethylenebis(5-bromosalicylidene)iminate), which are part of a family

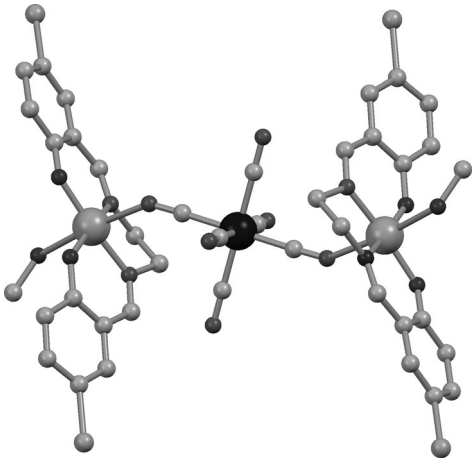

Figure 1. Molecular structure of **1** obtained from X-ray diffraction. For clarity, the NEt_4^+ counterion and H atoms have been omitted.

of cyanide-bridged trinuclear clusters[16] that incorporate different center ions and partly with different capping ligands. Spin-Hamiltonian models were proposed based on inelastic neutron scattering (INS) data in the case of **1**, frequency-domain Fourier-transform terahertz electron paramagnetic resonance[17] (THz-EPR) data in the case of **2**, and magnetization measurements for **1** and **2**. In reference [14], the exchange coupling between Mn^{III} and Os^{III} ions in **1** was found to be ferromagnetic and of Ising type.

After performing THz-EPR measurements on **1**, we found that the proposed model could not reproduce the observed magnetic feature. This motivated us to extend our data basis by recording additional INS data and to elaborate the modeling of **1** to encompass all experiments. For compound **2**, INS spectra were taken to complement the available THz-EPR results; this allowed for an improved description of the magnetic behavior of **2**. We present herein our detailed investigation of **1** and **2** using previous and newly recorded INS, THz-EPR, and superconducting quantum interference device (SQUID) magnetometry measurements that significantly go beyond the characterization data reported in references [14] and [15]. By comparing THz-EPR and INS spectra, both measured at zero magnetic field, we achieved experimental discrimination between different spin-Hamiltonian models. This was possible because the intensities of the transitions observed in INS and THz-EPR spectra depend sensitively and quite differently on the wave functions of the involved quantum states. In a spin-only situation this gives rise to different spin selection rules of $\Delta S = 0, \pm 1$ and $\Delta S = 0$ for INS and EPR, respectively. Hence, the combination of both techniques can resolve ambiguities present in analyses when using only one spectroscopic method, even if it is as powerful as INS. The case of **1** provides a striking example. In contrast to previous findings, we have to introduce maximally anisotropic exchange couplings J_{xx}, J_{yy}, and J_{zz} between Mn^{III} and Os^{III} or Ru^{III} ions, respectively, with antiferromagnetic J_{xx} and J_{zz}, and with ferromagnetic J_{yy} to reproduce all experimental data. Our improved model yields excellent agreement with all available data and the spin-Hamiltonian model is strongly supported by theoretical insight based on orbitally dependent exchange.

Results

The THz-EPR spectra of a powder sample of **1** at different temperatures and magnetic fields are shown in Figure 2. Three features are observed: M1, p1, and p2. An inspection

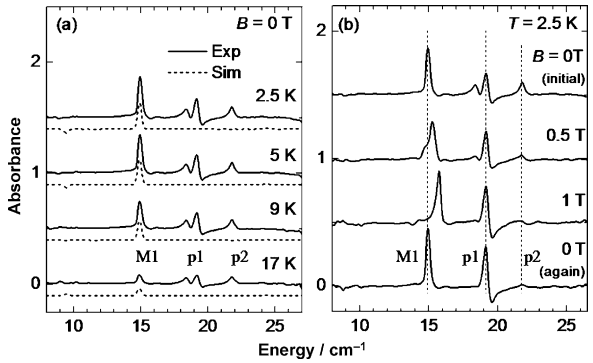

Figure 2. Absorbance spectra obtained by THz-EPR spectroscopy of a powder sample of **1** for different temperatures (a) and magnetic fields (b). The curves have been offset to improve visibility. The dashed lines are calculated curves obtained by using the best-fit parameters and model described in the text.

of Figure 2a reveals that the intensity of M1 at an energy of 14.95(20) cm^{-1} decreases strongly with increasing temperature, whereas the intensities of p1 and p2 show only weak temperature dependence. The spectra shown in Figure 2b demonstrate that upon application of a magnetic field M1 responds strongly, whereas features p1 and p2 do not shift. The spectra are shown in chronological order from top to bottom, revealing a crystallite orientation effect due to the magnetic field. Importantly, the dependence on temperature and magnetic field suggests that M1 originates from a "cold" magnetic transition, that is, a transition involving magnetic energy levels and originating from the ground state. The broadening and shift seen in Figure 2b can thus be attributed to Zeeman splitting of the ground and first excited states. Features p1 and p2 can be ascribed to vibration-

al or twisting modes of the molecules within the crystal.[16e] The width of the features (full-width at half maximum (FWHM) for M1 = 0.34 cm^{-1}) is limited by the sample, since the spectra were measured with the spectrometer resolution set to 0.2 cm^{-1}.

Experimental INS spectra of **1** at various temperatures and wavelengths are shown in Figure 3a and b. The energy-loss side is shown on the right side of the elastic peak. The spectra plotted in Figure 3a show five features on the energy gain side. Two of these features, M1 and A, at energies of 15.0(3) and 11.0(3) cm^{-1}, are strongest at the lowest temperature, whereas the other features, m1, m2, and m3 (energies 6.6(3), 9.1(3), and 13.2(3) cm^{-1}, respectively), appear only at elevated temperatures. The measurements at shorter wavelength, shown in Figure 3b, reveal three additional features, M2, p3, and p4, at energies of 28.2(4), 20.0(5), and 24.5(5) cm^{-1}. Similar to M1, M2 is strongest at the lowest temperature. Features p3 and p4 are essentially temperature independent. This temperature dependence suggests that peaks M1, M2, and A are cold magnetic transitions. The widths of features M1 and M2 for both wavelengths of 3.8 and 5.0 Å are comparable to those of the elastic lines of FWHM = 1.6 and 0.75 cm^{-1}, respectively. Careful analysis, following the recording of the INS spectra, revealed that feature "A" stems from a small amount of $NEt_4[Mn^{III}_2(5\text{-}Brsalen)_2(MeOH)_2Fe^{III}(CN)_6]$ ("Mn-Fe-Mn") impurity, which is isostructural with **1**, present in the sample. After a change to the synthetic procedure, this contamination could be avoided (see the Experimental Section) and was not present in the samples used to obtain the THz-EPR and the magnetic data shown herein. Feature A is, thus, neglected in subsequent analyses.

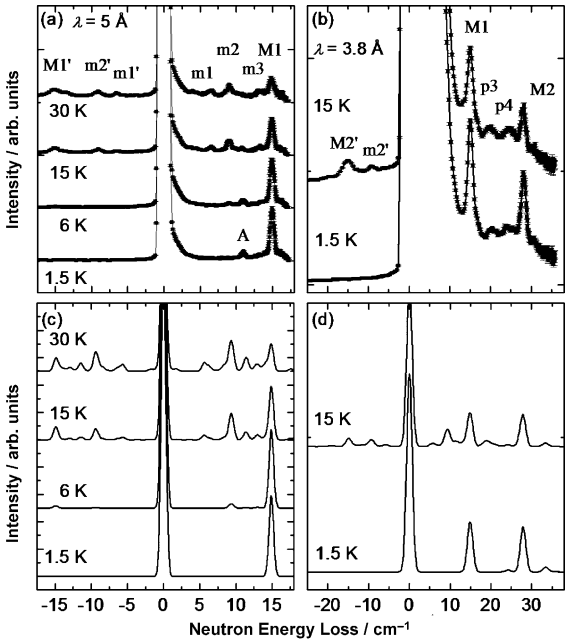

Figure 3. a) and b) INS spectra recorded on a powder sample of **1** at different temperatures and wavelengths. c) and d) Simulated INS spectra for the same experimental parameters as those used in parts a) and b) obtained by using the best-fit parameters and model described in the text. The curves have been offset for clarity.

The THz-EPR spectra recorded on a powder sample of **2** at different temperatures are shown in Figure 4a and the magnetic-field dependence is plotted in Figure 4b. Three features are identified: M1, p1, and p2 at energies of 12.8(1), 18.4(2), and 19.3(2) cm^{-1}. Feature M1 (FHWM = 0.26 cm^{-1}) shrinks with increasing temperature and splits upon application of a magnetic field; hence it is identified as a cold magnetic transition. In contrast, p1 and p2 show some temperature dependence, but they do not respond to the magnetic field. Similar to **1**, they are attributed to vibrational excitations[16e] and, as expected for isostructural compounds, they appear at nearly identical energies for **1** and **2**. The INS spectra plotted in Figure 5a also show feature M1 at 12.9(3) cm^{-1}, and its temperature dependence is consistent with the THz-EPR data. Further, INS reveals the presence of two more peaks, m1 and x, at energies of 7.3(4) and 3.8(4) cm^{-1}, that appear at elevated temperatures and feature p3 at 14.6(4) cm^{-1}. The spectra plotted in Figure 5b contain another cold transition, M2, at 24.0(5) cm^{-1} and a small warm peak, p4, at 20.0(5) cm^{-1}. An inspection of the dependence of the peak heights on temperature and momentum transfer reveals that only M1, M2, and m1 are of magnetic origin.

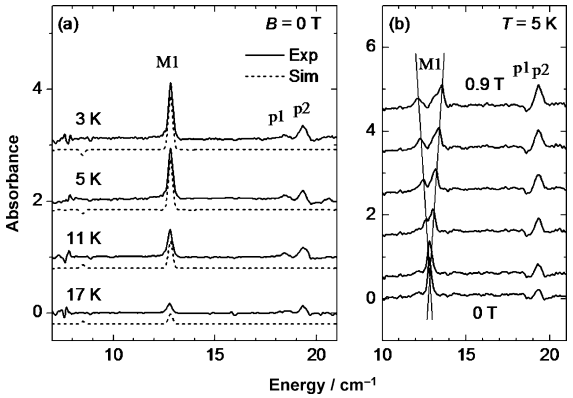

Figure 4. Absorbance spectra obtained by THz-EPR of a powder sample of **2** for different temperatures (a) and magnetic fields (b). The curves have been offset to improve visibility. The dashed lines are calculated curves obtained by using the best-fit parameters and model described in the text. Original data were first shown in ref. [15].

The temperature-dependent χT products of **1** and **2** are shown in Figure 6a and c, respectively. Upon cooling from room temperature, the χT product of **1** remains nearly constant down to approximately 100 K. Then, χT shows a slight increase up to a maximum of 8.1 $cm^3 K mol^{-1}$, which is reached at 16 K, and finally it steeply drops towards the lowest temperatures. The room-temperature value of 6.13 $cm^3 K mol^{-1}$ is consistent with the presence of two spins,

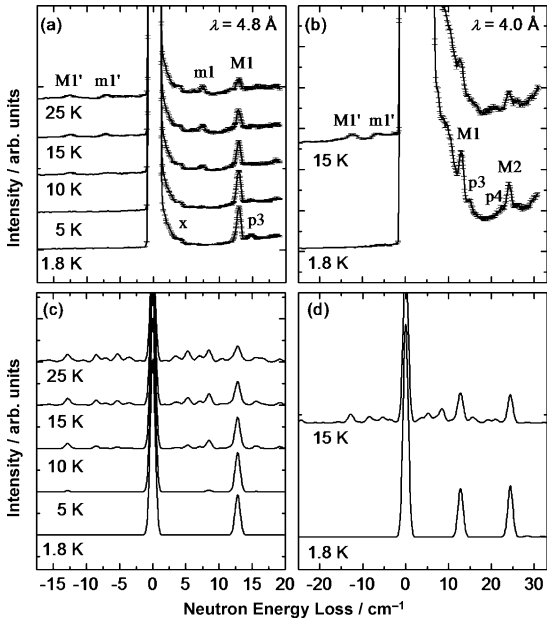

Figure 5. a) and b) INS spectra recorded on a powder sample of **2** for different temperatures and wavelengths. c) and d) Simulated INS spectra for the same experimental parameters as those used in parts a) and b) obtained by using the best-fit parameters and model described in the text. The curves have been offset for clarity.

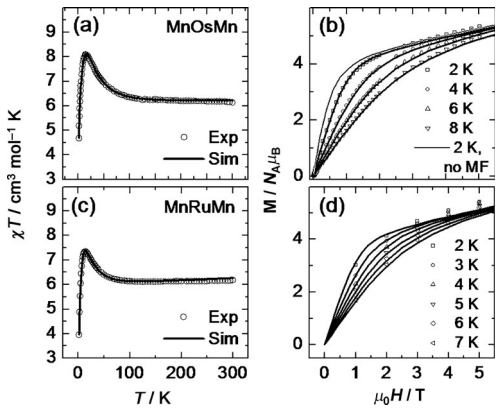

Figure 6. Open circles in parts a) and (c): Temperature dependence of the dc magnetic susceptibility, shown as the χT product. Full symbols in parts b) and d) represent measured $M(H)$. Solid lines in parts a)–d) are calculated curves obtained by using the best-fit parameters and model described in the text. The gray line is a calculated $M(H)$ curve for $T=2$ K with a mean-field strength λ set to zero. Original data given in parts c) and d) were first shown in ref. [15].

$S=2$ with $g=2.0$ and a spin $\tau=1/2$ with $g=1.8$, in the cluster. The qualitative behavior of the χT products of **2** is very similar to that of **1**. Here, χT reaches a maximum of 7.4 $cm^3 K mol^{-1}$ at 14 K. Its room-temperature value of 6.2 $cm^3 K mol^{-1}$ is close to the value expected for two spins, $S=2$ with $g=2.0$ and a spin $\tau=1/2$ with $g=1.9$, in the cluster. The g factors of 1.8 and 1.9 are explained later in the text. The χT product of **1** shown herein looks slightly different from that published in reference [14] because of an aging process discovered in the course of this study. This aging effect does not alter the finding of anisotropic exchange coupling. We found that the χT product of aged samples can be well reproduced by the identical spin-Hamiltonian parameters of **1** mentioned later in the text and manually increasing the intermolecular coupling strength, λ. This is in agreement with our hypothesis that aging occurs due to the loss of coordinated solvent, which leads to increased intermolecular coupling. Nevertheless, we have performed a thorough characterization of the aging process; this can be found in the Supporting Information. The $M(H)$ curves for both **1** and **2**, as shown in Figure 6b and d, reveal the absence of saturation, suggesting the presence of strong anisotropy and/or low-lying excited states.

We now turn to modeling of the spectroscopic and magnetic data of **1** and **2**. The ground state of the Os^{III} ion in an octahedral ligand field is an isotropic Kramers doublet associated with the irreducible representation Γ_7 of the double group O_h^*. The separation in energy, Δ, of the next-higher states is determined by spin-orbit coupling and amounts to $\Delta=3/2\zeta_{Os}=4500\ cm^{-1}$.[14,18] The analogous situation is encountered in the Ru^{III} ion, but with a smaller spin-orbit coupling constant of $\zeta_{Ru}=880\ cm^{-1}$.[15,19] For both Os^{III} and Ru^{III}, the g factor of the ground-state Kramers doublets can be estimated by $g_{eff}=(g_e+4\kappa)/3$ with the orbital reduction factor, κ,[20] yielding $g_{eff,Os}=1.8$ and $g_{eff,Ru}=1.9$.[14,15] In a previous study, the Hamiltonian found to give the best match with the dc susceptibility and INS data of **1** is given by Equation (1):[14]

$$\begin{aligned}\hat{H} = &\sum_{i=1,3}\left[D_{Mn}(\hat{S}_{i,z}^2 - \frac{1}{3}S_i(S_i+1)) + E_{Mn}(\hat{S}_{i,x}^2 - \hat{S}_{i,y}^2)\right]\\ &- J_{zz}\hat{\tau}_z(\hat{S}_{1,z}+\hat{S}_{3,z}) - J_{Mn-Mn}\hat{\mathbf{S}}_1\cdot\hat{\mathbf{S}}_3\\ &+\mu_B[g_{eff,Os}\hat{\boldsymbol{\tau}} + g_{Mn}(\hat{\mathbf{S}}_1+\hat{\mathbf{S}}_3)]\cdot\mathbf{B}\end{aligned} \quad (1)$$

in which $\hat{\boldsymbol{\tau}}$ and $\hat{\mathbf{S}}_i$ represent the angular momentum operators for the Os^{III} and Mn^{III} ions, respectively, with $\tau=1/2$ and $S_1=S_3=2$ and the ions are numbered according to their spatial position in the Mn(1)–Os(2)–Mn(3) cluster. The first term describes the uni- and biaxial magnetic anisotropies of the Mn^{III} ions, respectively. The second and third terms describe the magnetic interaction between Mn^{III} and Os^{III} ions, and between the two Mn^{III} ions. The last term accounts for the interaction with an applied magnetic field. Whereas the Mn–Os coupling is of Ising type in Equation (1), we expand our model to the more general description of exchange coupling by a matrix **J** and consider the case of a diagonal **J** with entries J_{xx}, J_{yy}, and J_{zz}. The augmented Hamiltonian is given by Equation (2):

$$\begin{aligned}\hat{H} = &\sum_{i=1,3}\hat{\mathbf{S}}_i\cdot\mathbf{D}_{Mn}\cdot\hat{\mathbf{S}}_i - \hat{\boldsymbol{\tau}}\cdot\mathbf{J}\cdot(\hat{\mathbf{S}}_1+\hat{\mathbf{S}}_3) +\\ &\mu_B\left[g_{eff}\hat{\boldsymbol{\tau}} + g_{Mn}(\hat{\mathbf{S}}_1+\hat{\mathbf{S}}_3)\right]\cdot\mathbf{B}\end{aligned} \quad (2)$$

In comparison to Hamiltonian Equation (1), the Ising coupling is replaced by a coupling matrix **J**. Also, the Mn^{III}–Mn^{III} coupling is removed for the sake of simplicity. A small intercluster magnetic coupling, which was reported in previous studies,[14,15,16de] was taken into account by using a mean-field approach.[21] Hence, the powder susceptibility was calculated according to Equation (3):

$$\chi_{MF} = \frac{1}{3}\sum_{a=x,y,z}\left[\frac{1}{\chi_{calcd,a}} - \lambda\right]^{-1} \quad (3)$$

in which $\chi_{calcd,\alpha}$ represents the susceptibility calculated by using Hamiltonian Equation (2) and λ is the molecular-field constant. Temperature-independent paramagnetism contributions of 1.85×10^{-4} and $7.94\times10^{-4}\,cm^3\,mol^{-1}$ for **1**[18a] and **2**,[19] respectively, were taken into account. We performed simultaneous least-squares fits on the χT data and on the INS and THz-EPR peak positions of **1** using Hamiltonian Equation (2). First, the isotropic g factors of the Mn^{III} and Os^{III} ions were fixed to $g_{Mn}=2.0$ and $g_{eff,Os}=1.8$. The $\mathbf{D}_{Mn}$ tensor was fixed to a uniaxial anisotropy with strength $D=-4.0\,cm^{-1}$ pointing at an angle $\theta=38°$ away from the z axis in the yz plane to account for the bent geometry of the Mn^{III}–Os^{III} unit. The angle was obtained from the crystal structure by assuming that the Jahn–Teller axis was parallel to the line through the nitrogen atom connecting the Mn^{III} and Os^{III} ions and the oxygen atom of the MeOH capping ligand. The fixed value of D is close to the one found ($D=-3.72(5)\,cm^{-1}$) for the isostructural Ir^{III} ($S=0$) compound $NEt_4[Mn^{III}_2(5\text{-Brsalen})_2(MeOH)_2Ir^{III}(CN)_6]$ by INS and high-field, high-frequency EPR spectroscopy.[22] The corresponding biaxial anisotropy (E term) was neglected here because of its smallness. Mathematically, $\mathbf{D}_{Mn}=\mathbf{R}^{-1}{}_x(\theta)\mathbf{D}'\mathbf{R}_x(\theta)$, in which $\mathbf{R}_x(\theta)$ is the rotation about the x axis by θ degrees and $\mathbf{D}'=\mathrm{diag}(-1/3D,\ -1/3D,\ 2/3D)$. A first fitting attempt by using an isotropic coupling $J_{iso}=J_{xx}=J_{yy}=J_{zz}$ could not reproduce the spectroscopic and magnetic data. Instead we found that agreement with the spectra and susceptibility data could only be achieved if exchange anisotropy was introduced. Independent nonzero longitudinal $J_{zz}=J_{||}$ and transverse couplings $J_{xx}=J_{yy}=J_{\perp}$ yielded tolerable results. Trying different starting values and different combinations of $J_{\alpha\alpha}$, we observed that the agreement became much better if the couplings were grouped as $J_{xx}=J_{zz}=J'$ and J_{yy} instead of $J_{||}$ and $J_{\perp}$. Leaving all three J_{xx}, J_{yy}, and J_{zz} to vary freely yielded excellent agreement with all data as well as reasonable fit values. If the Mn^{III} anisotropy $\mathbf{D}_{Mn}$ is not rotated ($\theta=0°$), the absolute values of J_{xx}, J_{yy}, and J_{zz} are smaller by a few cm^{-1}, but nothing is changed fundamentally regarding the **J** anisotropy. The best-fit parameters obtained for **1** with θ fixed to 38° are given by Equation (4):

$$\begin{aligned} J_{xx} &= -18(2)\,cm^{-1}\\ J_{yy} &= \ \ 35(2)\,cm^{-1}\\ J_{zz} &= -33(2)\,cm^{-1}\\ \lambda &= -0.118(4)\,mol\,cm^{-3}\\ g_{Mn} &= \ \ 1.98\ (fixed)\\ D &= -4.0\,cm^{-1}\ (fixed) \end{aligned} \quad (4)$$

The calculated curves obtained by using these parameters are plotted in Figures 2, 3, and 6, demonstrating excellent agreement with the data.

The fitting of the data obtained on **2** was performed in a similar way as that used for **1** and the same rotation of the $\mathbf{D}_{Mn}$ anisotropy tensor around the x axis was applied. Here, the Mn^{III} g factor was fixed to 1.96 and the strength of the Mn anisotropy D was allowed to vary freely. Identical observations regarding the **J** anisotropy were made to those in the case of **1**. Again, the best-fit result is obtained when leaving all $J_{\alpha\alpha}$ to vary freely. The best-fit parameters for **2** are given in Equation (5):

$$\begin{aligned} J_{xx} &= -20(3)\,cm^{-1}\\ J_{yy} &= \ \ 25(3)\,cm^{-1}\\ J_{zz} &= -26(3)\,cm^{-1}\\ \lambda &= -0.15(3)\,mol\,cm^{-3}\\ g_{Mn} &= \ \ 1.96\,(fixed)\\ D &= -3.9(3)\,cm^{-1} \end{aligned} \quad (5)$$

The calculated curves obtained by using our new model with the best-fit parameters are shown in Figures 4–6, demonstrating again excellent agreement with experimental observations.

Discussion

For both **1** and **2** realistic parameter sets are obtained. The Mn^{III} single-ion anisotropy parameters are in very good agreement with the values recently observed in references [14–16e,22], and also λ is well within the range expected from previous studies. When comparing the anisotropic exchange couplings in **1** and **2**, we find that indeed there is an increase of the average of their absolute values $J_{av}=(|J_{xx}|+|J_{yy}|+|J_{zz}|)/3$ by a factor of 1.2 when moving from Ru^{III} to Os^{III}. This is expected from the more diffuse character of the 5d orbitals with respect to the 4d ones, resulting in a larger overlap with the cyanide ligand bridges.

However, while in reference [14] an Ising-type exchange coupling was found for **1**, we obtained a strong three-axis **J** anisotropy for both **1** and **2**. It should be noted that in our previous studies exchange anisotropy in the form of $J_{||}\neq J_{\perp}$ was observed (**1**: $J_{||}=+30.6\,cm^{-1}$, $J_{\perp}=0$; **2**: $J_{||}=+24\,cm^{-1}$, $J_{\perp}=-20\,cm^{-1}$), with the apparent discrepancy of an Ising-

type anisotropy in **1** but not in **2**. The additional THz-EPR and INS data allow for more detailed fitting of all three $J_{\alpha\alpha}$ values and the observation of antiferromagnetic J_{xx} and J_{zz} and of ferromagnetic J_{yy} consistently in both **1** and **2**. Interestingly, for **2**, the previously determined values are similar to those found in this work [Eq. (5)] after performing a cyclic permutation $x \rightarrow y$, $y \rightarrow z$, $z \rightarrow x$. This indicates that the observation of **J** anisotropy in **2** has not changed fundamentally except for a few details (see below). This is in marked contrast to the case of **1**. To illustrate that the **J** anisotropy in **1** becomes clear from our spectroscopic data without ambiguity, we have simulated the positions of the observed peaks by using the two different models [Eqs. (1) and (2)] and parameter sets obtained in reference [14] and in this work. The results are shown in Figure 7a and b. Clearly, the INS transitions are located at the same energies for both

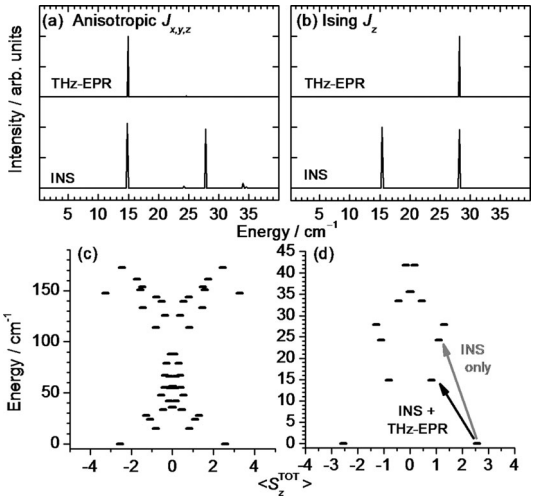

Figure 7. Positions of the THz-EPR and INS transitions of **1** for spin-Hamiltonian models [Eq. (2)] pinpointing the anisotropic exchange coupling. Calculations used best-fit parameters given in the text (a) and Equation (1) with parameters given in ref. [14] (b). c) Spectrum of Hamiltonian Equation (2) with best-fit parameters. d) Magnification of the spectrum shown in part c). The spectroscopic transitions are marked by arrows.

models with similar intensities. However, the intensities of the THz-EPR transitions at these energies are entirely different, such that the model of Equation (1) can be unequivocally ruled out.[23] Apart from the large peaks appearing in Figure 7a there are a few very small features. However, these are not seen in the experimental spectra, since their strength is well below the noise level. In the present study, both INS and THz-EPR are important because the decisive strength only arises from their combination. It should be noted that the spectroscopic measurements in addition to the dc magnetic susceptibility are crucial to pinpoint the presence of the anisotropic exchange, which would be less clear from magnetic data only. The same argument holds for compound **2**.

The reason why it is difficult to experimentally distinguish anisotropic exchange from other cases, such as an Ising-type coupling, is briefly outlined. When the Mn^{III} zero-field splitting energy is "switched off", the energy spectra of clusters **1** and **2** are invariant, as far as symmetry is concerned, with respect to permutations of the $\alpha = x, y, z$ spin coordinates in the **J** matrix. Therefore, the six possible permutations of the xyz indices result in six absolutely equivalent root mean square (rms) minima in the least squares fits and to identical energy spectra of clusters **1** or **2**. Switching on the Mn^{III} zero-field splitting changes this situation little, since the Os^{III}–Mn^{III} superexchange interaction dominates in energy over the Mn^{III} zero-field splitting. Hence, six least-squares minima with nearly identical rms values exist and it may be difficult to discriminate between them. Indeed, as noted before, for compound **2** the best-fit parameters obtained in reference [15] are remarkably similar to the improved minimum found in Equation (5), with a permutation of coordinate axes considered. For **1** the availability of additional spectroscopic data, however, altered the model drastically.

The full spectrum of Hamiltonian Equation (2) and a magnification of the low-energy portion are shown in Figure 7c and d, respectively, for compound **1**. Here, the expectation values of the total spin $M_z = <\hat{S}_z^{TOT}>$ operator serve as abscissa. Because of the presence of **J** anisotropy and rotation of the Mn^{III} **D** tensor, there is a strong admixture of the eigenstates of the $\hat{S}_z^{TOT}$ operator, making it hard to obtain an intuitive understanding of the energy spectrum. However, it becomes clear that the lowest-energy states have spin projections onto the z axis of $M_z \approx \pm 5/2$. There are no states exhibiting the maximum total spin projection of $M_z = \pm 9/2$, which would be expected for a ferromagnetic arrangement of all Mn^{III} and Os^{III} magnetic moments. Also, the low-energy spectrum does not resemble that of an anisotropy-split spin multiplet, which is typically seen in SMMs. These effects are a result of the choice of the z axis as the quantization axis in $M_z = <\hat{S}_z^{TOT}>$ together with the rotated Mn^{III} **D** tensor and **J** anisotropy. The THz-EPR and INS transitions are marked by arrows in Figure 7d. The first excited states are located at about 15 cm^{-1}, as observed from THz-EPR and INS. This energy is very close to the height of the effective barrier ($\Delta_{eff} = 14.2$ cm^{-1}) observed in the ac susceptibility measurements (cf. ref. [15] and the Supporting Information), suggesting that the relaxation of magnetization is due to tunneling through the first-excited states. While the exchange couplings are smaller in magnitude by about 1.2 times in **2** compared with **1**, the height of the energy barrier in **2** does not follow exactly (17 K for **2** versus 20 K for **1**). This can be explained by a joint contribution to the barrier that originates from anisotropic exchange coupling, but also from single-ion anisotropy of the Mn^{III} ions, which is only weakly affected by the choice of the central ion of the trinuclear unit.

To gain deeper insight into the mechanism responsible for the generation of the observed anisotropic exchange coupling, we investigated the exchange coupling theoretically in a hypothetical Os^{III}-CN-Mn^{III} dimer (Figure 8), in particular,

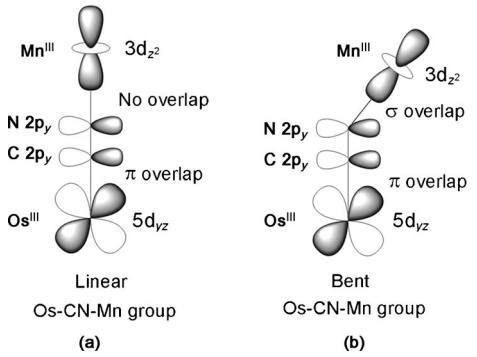

Figure 8. Os–Mn superexchange pathways in the linear (a) and bent (b) geometries. In the linear geometry, this pathway gives no contribution to exchange parameters due to orthogonality of the $5d_{yz}$(Os) and $3d_{z^2}$(Mn) magnetic orbitals, whereas in the bent geometry a new pathway of mixed $\sigma\pi$ type opens up, which becomes very efficient at large bending angles.

taking into account its dependence on the three orbital states of the Os^{III} ion (orbitally dependent exchange).[7] This will allow us to relate the exchange parameters J_{xx}, J_{yy}, and J_{zz} with (isotropic) orbital exchange parameters J_1, J_2, and J_3 associated with the exchange between the individual orbital components of the ground $^2T_{2g}(5d^5)$ orbital triplet of the octahedral $\{Os(CN)_6\}^{3-}$ moiety and the $S=2$ spin of the Mn^{III} center.

In the absence of spin-orbit coupling, the interaction can be described by the Hamiltonian given in Equation (6):

$$H = -\begin{pmatrix} J_1 & 0 & 0 \\ 0 & J_2 & 0 \\ 0 & 0 & J_3 \end{pmatrix} \hat{\mathbf{S}}_{Os} \cdot \hat{\mathbf{S}}_{Mn} \tag{6}$$

on the basis of the many-body wave functions $|zx\pm\rangle$, $|xy\pm\rangle$, and $|yz\pm\rangle$ of the $^2T_{2g}(5d^5)$ orbital triplet defined in Equation (S2) in the Supporting Information. $\hat{\mathbf{S}}_{Os}$ and $\hat{\mathbf{S}}_{Mn}$ are operators acting on the spin of the Os^{III} and Mn^{III} ions and J_k are orbital exchange parameters with the orbital J matrix acting on the orbital part only. More details can be found in the Supporting Information. With spin-orbit interactions, the $^2T_{2g}(5d^5)$ orbital triplet becomes split and the ground Kramers doublet Γ_7 can be mapped onto an effective spin of $\tau=1/2$. Its two $m=\pm1/2$ components $\Gamma_7(m)$ are expressed by Equation (7):

$$\begin{aligned} \Gamma_7(-1/2) &= \frac{1}{\sqrt{3}}(|zx-\rangle - |xy+\rangle - i|yz-\rangle) \\ \Gamma_7(+1/2) &= \frac{1}{\sqrt{3}}(|zx+\rangle - |xy-\rangle + i|yz+\rangle) \end{aligned} \tag{7}$$

The effective spin Hamiltonian $\hat{H}_{eff}$ describing the exchange interaction between the Γ_7 Kramers doublet and the Mn^{III} spin is obtained by projection of Hamiltonian Equation (6) onto the space of wave functions given in Equation (8):

$$|m, M_s\rangle = \Gamma_7(m) \otimes |S, M_s\rangle \tag{8}$$

in which M_s is the projection of the Mn^{III} spin S and $\otimes$ stands for the antisymmetrized product. The effective spin Hamiltonian $\hat{H}_{eff}$ is obtained in first-order perturbation theory by equating the matrix elements of $\hat{H}_{eff}$ and $\hat{H}$ in Equation (6) in the space of the wave functions $|m, M_s\rangle$. For the idealized structure of a bent Os^{III}-CN-Mn^{III} cyanide-bridged group, as shown in Figure 8b and Figure S1b in the Supporting Information, it is given by:

$$\hat{H}_{eff} = -J_{xx}\hat{\tau}_x\hat{S}_{Mn,x} - J_{yy}\hat{\tau}_y\hat{S}_{Mn,y} - J_{zz}\hat{\tau}_z\hat{S}_{Mn,z} \tag{10}$$

involving no off-diagonal spin terms $J_{\alpha\beta}\hat{\tau}_\alpha\hat{S}_{Mn,\beta}$. The exchange parameters J_{xx}, J_{yy}, and J_{zz} are expressed in terms of the orbital exchange parameters J_1, J_2, and J_3 in Equation (6) by Equation (11):

$$\begin{aligned} J_{xx} &= (-J_1 + J_2 + J_3)/3 \\ J_{yy} &= (J_1 + J_2 - J_3)/3 \\ J_{zz} &= (J_1 + J_2 + J_3)/3 \end{aligned} \tag{11}$$

Interestingly, these calculations indicate that the antisymmetric Dzyaloshinsky–Moriya exchange term $\boldsymbol{G}[\hat{\tau}_{Os}\times\hat{\boldsymbol{S}}_{Mn}]$ is always absent in the effective spin Hamiltonian [Eq. (10)], although it is formally allowed by the symmetry conditions for the assumed Os-CN-Mn group depicted in Figure 8b. This feature comes from a special orbital composition of the ground-state $\Gamma_7(m)$ wave functions [Eq. (7)] for strictly octahedral $\{Os^{III}(CN)_6\}^{3-}$, in which the three orbital components [Eq. (S2) in the Supporting Information] enter with equal weight. Off-diagonal exchange parameters in Equation (10) are absent due to the diagonal character of the orbital **J** matrix in Equation (6) for the assumed idealized structure.

With these equations we can now explain, in a natural way, the origin of the three-axis anisotropic Hamiltonian [Eq. (10)] and our model Equation (2), as well as the observation J_{xx}, $J_{zz}<0$ and $J_{yy}>0$. For a linear Os-CN-Mn group (Figure 8a), two equivalent antiferromagnetic orbital exchange parameters are predicted, $J_1=J_3<0$, which correspond to the antiferromagnetic superexchange pathways of the $5d_{zx}$(Os)–$3d_{zx}$(Mn) and $5d_{yz}$(Os)–$3d_{yz}$(Mn) orbitals through the CN group. The J_2 parameter is weakly ferromagnetic due to orthogonality of the $5d_{xy}$(Os) orbital with respect to all 3d(Mn) orbitals, $J_2>0$ and $|J_{1,3}| \gg |J_2|$. Thus, for a linear Os-CN-Mn group, the effective spin Hamiltonian [Eq. (10)] has a nearly antiferromagnetic Ising-like character with $J_{||}=(2J_1+J_2)/3<0$ and $J_\perp=J_2/3>0$, and $|J_{||}| \gg |J_\perp|$.

However, in a strongly bent Os-CN-Mn group, as in the case of **1** and **2** (with $\sphericalangle$C-N-Mn=142°), the antiferromagnetic J_3 parameter dominates over the J_1 and J_2 parameters ($|J_3| \gg |J_1|$, $|J_2|$) due to the opening of an efficient mixed $\sigma\pi$ superexchange pathway between the $5d_{yz}$(Os) and $3d_{z^2}$(Mn) orbitals (Figure 8b). According to Equation (11), the exchange parameters in the effective spin Hamiltonian

[Eq. (10)] are approximately given by $J_{xx} \approx J_{zz} \approx J_3/3 < 0$ and $J_{yy} \approx -J_3/3 > 0$. This finding is in excellent agreement with the experimentally obtained exchange parameters for compounds **1** [Eq. (4)] and **2** [Eq. (5)]. Using Equation (11) and the experimentally determined exchange values, we obtain values of $J_1 = -22.5\ cm^{-1}$, $J_2 = +25.5\ cm^{-1}$, and $J_3 = -102\ cm^{-1}$ for **1** and $J_1 = -9.0\ cm^{-1}$, $J_2 = +7.5\ cm^{-1}$, and $J_3 = -76.5\ cm^{-1}$ for **2**. Notably, the magnitude of the J_3 parameter indeed dominates over J_1 and J_2, which is consistent with expectations from the exchange pathways. These results also show the general trend that the exchange parameters are larger for compound **1**, as expected for the more diffuse 5d orbitals of Os^{III}, compared with the 4d orbitals of Ru^{III}. Finally, a pure ferromagnetic Ising-type exchange anisotropy, as reported previously in reference [14], is inconsistent with the basic orbital exchange model outlined herein because the J_3 parameter is always dominant and antiferromagnetic in a strongly bent M-CN-Mn group.

Conclusion

We have studied SMMs **1** and **2** using THz-EPR, INS, and SQUID magnetometry. The position of the magnetic ground-state THz-EPR excitation is incompatible with a ferromagnetic Ising-type exchange coupling between Mn^{III}–Os^{III} and Mn^{III}–Ru^{III} ions and requires the introduction of a three-axis anisotropic exchange coupling. Although these two models lead to essentially identical excitation energies in the low-energy range, experimentally they could be distinguished unambiguously by strikingly different intensity patterns, as revealed in the comparison of THz-EPR and INS spectra. Anisotropy is maximal in the sense that J_{xx} and J_{zz} are antiferromagnetic, while J_{yy} is ferromagnetic; this is different from previous findings. Furthermore, the average magnitude of the exchange coupling is found to be stronger in **1** than that of **2**; this is consistent with the more diffuse nature of the 5d orbitals with respect to 4d. Analytical calculations based on an orbitally dependent exchange model yield detailed theoretical insight, suggesting that the bent geometry encountered in both Mn-M-Mn title compounds is at the origin of the three-axis anisotropic exchange, whereas in a linear geometry the two-axis Ising-like exchange coupling would be expected. Furthermore, calculations strongly support the observed signs of the J_{xx}, J_{yy}, and J_{zz} exchange coupling values, providing a link between the molecular structure and magnetic properties of the 4d and 5d compounds studied.

Experimental Section

Synthesis: Compounds **1** and **2** were synthesized in the cold by using the procedure described for **2** in ref. [15]. $K_4Os(CN)_6$ was synthesized directly from OsO_4, as reported in ref. [24]. By this route to **1**, contamination with the isostructural Fe compound is circumvented.

Frequency-domain Fourier-transform THz-EPR: Measurements were performed on powder samples (mass ≈100 mg) at the THz beamline at the BESSY II storage ring, Berlin, Germany. Linearly polarized THz radiation was coupled out from the ring, passed through a FTIR spectrometer (Bruker IFS 125 HR, resolution set to $0.2\ cm^{-1}$), and sent through the pellet mounted in a cryostat (Oxford Spectromag 4000-11) equipped with a 11 T superconducting magnet. The transmitted intensity was detected by a liquid-helium-cooled bolometer. Absorbance, A, is calculated from $A(E) = -\log[I_T(E)/I_{ref}(E)]$, in which $I_T(E)$ refers to the spectrum taken at temperature T, whereas $I_{ref}(E)$ denotes the reference spectrum obtained at higher temperatures. The references were recorded at 50 and 25 K for compounds **1** and **2**, respectively. Details about the method can be found in reference [17].

INS: Spectra were collected on a time-of-flight spectrometer IN5 at the Institut Laue-Langevin, Grenoble, France. About 2 g of non-deuterated crystalline powder was loaded into a 10 mm diameter double-walled hollow aluminum cylinder. A standard ILL Orange cryostat and a cryofurnace were used for temperature control of **1** and **2**, respectively. The data were analyzed by using the LAMP program package.[25]

Magnetic measurements: Magnetic measurements were performed using a Quantum-Design MPMS-XL SQUID magnetometer. For dc susceptibility measurements, a field of 100 mT was applied. The polycrystalline samples directly obtained from the synthetic procedure were filtered off, washed with MeOH, and immediately transferred to a polycarbonate capsule and covered with 1-octadecene. The susceptibility was corrected for diamagnetic contributions by means of Pascal's constants.[26]

Numerical simulations: Numerical simulations and fits are based on exact diagonalization of the spin Hamiltonians given in the text by using home-written MATLAB and C codes. All fits are least-squares fits that minimize the sum of the squared deviations. If a weight function was used this is explicitly stated in the text.

Acknowledgements

This work was supported by the Deutsche Forschungsgemeinschaft and the German Ministry of Education and Research (BMBF) within the network project EPR-Solar (03SF0328). We thank Professor Robert Bittl (Freie Universität Berlin) for providing access to the FTIR spectrometer and the magnet. K.S.P. thanks the Danish Centre for the use of Synchrotron X-ray and Neutron facilities (DANSCATT) for financial support.

[1] a) A. Caneschi, D. Gatteschi, R. Sessoli, A. L. Barra, L. C. Brunel, M. Guillot, *J. Am. Chem. Soc.* **1991**, *113*, 5873–5874; b) R. Sessoli, D. Gatteschi, A. Caneschi, M. A. Novak, *Nature* **1993**, *365*, 141–143; c) L. Thomas, F. Lionti, R. Ballou, D. Gatteschi, R. Sessoli, B. Barbara, *Nature* **1996**, *383*, 145–147; d) G. Christou, D. Gatteschi, D. N. Hendrickson, R. Sessoli, *MRS Bull.* **2000**, *25*, 66–71; e) D. Gatteschi, R. Sessoli, *Angew. Chem.* **2003**, *115*, 278–309; *Angew. Chem. Int. Ed.* **2003**, *42*, 268–297; f) W. Wernsdorfer in *Classical and Quantum Magnetization Reversal Studied in Nanometer-Sized Particles and Clusters, Advances in Chemical Physics*, Vol. 118, John Wiley & Sons, **2007**.

[2] a) J. R. Long in *Chemistry of Nanostructured Materials*; P. Yang, Ed.; World Scientific, Hong Kong, **2003**, 291–315; b) G. Aromi, E. K. Brechin in *Single-Molecule Magnets and Related Phenomena*; R. E. P. Winpenny, Ed.; **2006**, Springer, Berlin; c) J.-N. Rebilly, T. Mallah in *Single-Molecule Magnets and Related Phenomena*; R. E. P. Winpenny, Ed.; **2006**, Springer, Berlin; d) T. Glaser, *Chem. Commun.* **2011**, *47*, 116–130.

[3] a) O. Waldmann, *Inorg. Chem.* **2007**, *46*, 10035–10037; b) E. Ruiz, J. Cirera, J. Cano, S. Alvarez, C. Loose, J. Kortus, *Chem. Commun.* **2008**, 52–54.

[4] a) N. Ishikawa, M. Sugita, T. Ishikawa, S.-y. Koshihara, Y. Kaizu, *J. Am. Chem. Soc.* **2003**, *125*, 8694–8695; b) N. Ishikawa, M. Sugita, N. Tanaka, T. Ishikawa, S.-y. Koshihara, Y. Kaizu, *Inorg. Chem.* **2004**, *43*, 5498–5500; c) M. A. AlDamen, J. M. Clemente-Juan, E. Corona-

do, C. Marti-Gastaldo, A. Gaita-Arino, *J. Am. Chem. Soc.* **2008**, *130*, 8874–8875; d) P.-H. Lin, T. Burchell, L. Ungur, L. Chibotaru, W. Wernsdorfer, M. Murugesu, *Angew. Chem.* **2009**, *121*, 9653–9656; *Angew. Chem. Int. Ed.* **2009**, *48*, 9489–9492; e) R. Sessoli, A. K. Powell, *Coord. Chem. Rev.* **2009**, *253*, 2328–2341; f) S.-D. Jiang, B.-W. Wang, H.-L. Sun, Z.-M. Wang, S. Gao, *J. Am. Chem. Soc.* **2011**, *133*, 4730–4733; g) R. J. Blagg, C. A. Muryn, E. J. L. McInnes, F. Tuna, R. E. P. Winpenny, *Angew. Chem.* **2011**, *123*, 6660–6663; *Angew. Chem. Int. Ed.* **2011**, *50*, 6530–6533; h) J. D. Rinehart, M. Fang, W. J. Evans, J. R. Long, *Nat. Chem.* **2011**, *3*, 538–542; i) L. Sorace, C. Benelli, D. Gatteschi, *Chem. Soc. Rev.* **2011**, *40*, 3092–3104; j) J. D. Rinehart, M. Fang, W. J. Evans, J. R. Long, *J. Am. Chem. Soc.* **2011**, *133*, 14236–14239.

[5] a) X.-Y. Wang, C. Avendano, K. R. Dunbar, *Chem. Soc. Rev.* **2011**, *40*, 3213–3238; b) E. Ruiz, A. Rodriguez-Fortea, S. Alvarez, M. Verdaguer, *Chem. Eur. J.* **2005**, *11*, 2135–2144.

[6] T. D. Harris, C. Coulon, R. Clérac, J. R. Long, *J. Am. Chem. Soc.* **2011**, *133*, 123–130.

[7] a) J. J. Borrás-Almenar, J. M. Clemente-Juan, E. Coronado, A. V. Palii, B. S. Tsukerblat, *J. Phys. Chem. A* **1998**, *102*, 200–213; b) V. S. Mironov, L. F. Chibotaru, A. Ceulemans, *J. Am. Chem. Soc.* **2003**, *125*, 9750–9760; c) V. S. Mironov, L. F. Chibotaru, A. Ceulemans, *Phys. Rev. B* **2003**, *67*, 014424; d) V. S. Mironov, *Dokl. Phys. Chem.* **2006**, *408*, 130–136; e) V. Mironov, *Dokl. Phys. Chem.* **2007**, *415*, 199–204; f) A. V. Palii, O. S. Reu, S. M. Ostrovsky, S. I. Klokishner, B. S. Tsukerblat, M. Hilfiger, M. Shatruk, A. Prosvirin, K. R. Dunbar, *J. Phys. Chem. A* **2009**, *113*, 6886–6890; g) A. Palii, B. Tsukerblat, J. M. Clemente-Juan, E. Coronado, *Int. Rev. Phys. Chem.* **2010**, *29*, 135–230; h) A. Palii, B. Tsukerblat, S. Klokishner, K. R. Dunbar, J. M. Clemente-Juan, E. Coronado, *Chem. Soc. Rev.* **2011**, *40*, 3130–3156.

[8] T. S. Venkatakrishnan, R. Rajamani, J.-P. Sutter, *Inorg. Chem.* **2007**, *46*, 9569–9574.

[9] a) J. J. Sokol, A. G. Hee, J. R. Long, *J. Am. Chem. Soc.* **2002**, *124*, 7656–7657; b) D. E. Freedman, D. M. Jenkins, J. R. Long, *Chem. Commun.* **2009**, 4829–4831; c) X.-Y. Wang, M. G. Hilfiger, A. Prosvirin, K. R. Dunbar, *Chem. Commun.* **2010**, *46*, 4484–4486; d) X.-Y. Wang, A. V. Prosvirin, K. R. Dunbar, *Angew. Chem.* **2010**, *122*, 5207–5210; *Angew. Chem. Int. Ed.* **2010**, *49*, 5081–5084.

[10] a) J. H. Yoon, J. H. Lim, H. C. Kim, C. S. Hong, *Inorg. Chem.* **2006**, *45*, 9613–9615; b) J.-P. Sutter, S. Dhers, R. Rajamani, S. Ramasesha, J.-P. Costes, C. Duhayon, L. Vendier, *Inorg. Chem.* **2009**, *48*, 5820–5828; c) M.-G. Alexandru, D. Visinescu, A. M. Madalan, F. Lloret, M. Julve, M. Andruh, *Inorg. Chem.* **2012**, *51*, 4906–4908.

[11] a) E. J. Schelter, A. V. Prosvirin, W. M. Reiff, K. R. Dunbar, *Angew. Chem.* **2004**, *116*, 5020–5023; *Angew. Chem. Int. Ed.* **2004**, *43*, 4912–4915; b) E. J. Schelter, A. V. Prosvirin, K. R. Dunbar, *J. Am. Chem. Soc.* **2004**, *126*, 15004–15005; c) E. J. Schelter, F. Karadas, C. Avendano, A. V. Prosvirin, W. Wernsdorfer, K. R. Dunbar, *J. Am. Chem. Soc.* **2007**, *129*, 8139–8149; d) D. E. Freedman, D. M. Jenkins, A. T. Iavarone, J. R. Long, *J. Am. Chem. Soc.* **2008**, *130*, 2884–2885; e) J. M. Zadrozny, D. E. Freedman, D. M. Jenkins, T. D. Harris, A. T. Iavarone, C. Mathonière, R. Clérac, J. R. Long, *Inorg. Chem.* **2010**, *49*, 8886–8896; f) T. D. Harris, H. S. Soo, C. J. Chang, J. R. Long, *Inorg. Chim. Acta* **2011**, *369*, 91–96.

[12] a) W. F. Yeung, P. H. Lau, T. C. Lau, H. Y. Wei, H. L. Sun, S. Gao, Z. D. Chen, W. T. Wong, *Inorg. Chem.* **2005**, *44*, 6579–6590.

[13] a) M. G. Hilfiger, M. Shatruk, A. Prosvirin, K. R. Dunbar, *Chem. Commun.* **2008**, 5752–5754; <*lit* b>M. G. Hilfiger, M. Chen, T. V. Brinzari, T. M. Nocera, M. Shatruk, D. T. Petasis, J. L. Musfeldt, C. Achim, K. R. Dunbar, *Angew. Chem.* **2010**, *122*, 1452–1455; *Angew. Chem. Int. Ed.* **2010**, *49*, 1410–1413.

[14] K. S. Pedersen, M. Schau-Magnussen, J. Bendix, H. Weihe, A. V. Palii, S. I. Klokishner, S. Ostrovsky, O. S. Reu, H. Mutka, P. L. W. Tregenna-Piggott, *Chem. Eur. J.* **2010**, *16*, 13458–13464.

[15] K. S. Pedersen, J. Dreiser, J. Nehrkorn, M. Gysler, M. Schau-Magnussen, A. Schnegg, K. Holldack, R. Bittl, S. Piligkos, H. Weihe, P. Tregenna-Piggott, O. Waldmann, J. Bendix, *Chem. Commun.* **2011**, *47*, 6918–6920.

[16] a) H. Miyasaka, N. Matsumoto, H. Okawa, N. Re, E. Gallo, C. Floriani, *J. Am. Chem. Soc.* **1996**, *118*, 981–994; b) H. J. Choi, J. J. Sokol, J. R. Long, *Inorg. Chem.* **2004**, *43*, 1606–1608; c) M. Ferbinteanu, H. Miyasaka, W. Wernsdorfer, K. Nakata, K.-i. Sugiura, M. M. Yamashita, C. Coulon, R. Clérac, *J. Am. Chem. Soc.* **2005**, *127*, 3090–3099; d) P. L. W. Tregenna-Piggott, D. Sheptyakov, L. Keller, S. I. Klokishner, S. M. Ostrovsky, A. V. Palii, O. S. Reu, J. Bendix, T. Brock-Nannestad, K. Pedersen, H. Weihe, H. Mutka, *Inorg. Chem.* **2009**, *48*, 128–137; e) J. Dreiser, A. Schnegg, K. Holldack, K. S. Pedersen, M. Schau-Magnussen, J. Nehrkorn, P. Tregenna-Piggott, H. Mutka, H. Weihe, J. Bendix, O. Waldmann, *Chem. Eur. J.* **2011**, *17*, 7492–7498.

[17] A. Schnegg, J. Behrends, K. Lips, R. Bittl, K. Holldack, *Phys. Chem. Chem. Phys.* **2009**, *11*, 6820–6825.

[18] a) P. Albores, L. D. Slep, L. M. Baraldo, R. Baggio, M. T. Garland, E. Rentschler, *Inorg. Chem.* **2006**, *45*, 2361–2363; b) W. Van den Heuvel, M. F. A. Hendrickx, A. Ceulemans, *Inorg. Chem.* **2007**, *46*, 8032–8037.

[19] J. Bendix, P. Steenberg, I. Søtofte, *Inorg. Chem.* **2003**, *42*, 4510–4512.

[20] a) J. S. Griffith in *The Theory of Transition-Metal Ions*, Cambridge, University Press, Cambridge, **1961**, p. 365; b) M. Gerloch, J. R. Miller, *Prog. Inorg. Chem.* **1968**, *10*, 1–47.

[21] N. W. Ashcroft, N. D. Mermin in *Solid State Physics*, Saunders College Publishing, Florida, **1976**, **p.** 718.

[22] K. S. Pedersen, M. Sigrist, H. Weihe, P. Tregenna-Piggott, M. Schau-Magnussen, J. Dreiser, H. Mutka, A. L. Barra, J. Bendix, *Inorg. Chem. Commun.* **2012**, *24*, 24–28.

[23] To rule out the scenario that feature M1 corresponds to a weakly allowed transition and there is a much stronger THz-EPR transition at the energy of M2, we have recorded THz-EPR spectra at lower resolution which do not show a strong transition M2, see Supporting Information.

[24] M. G. Hilfiger, PhD Thesis, Texas A&M University, **2010**.

[25] a) LAMP, the Large Array Manipulation Program. http://www.ill.fr/data_treat/lamp/lamp.html; b) D. Richard, M. Ferrand, G. J. Kearley, *J. Near Infrared Spectrosc.* **1996**, *4*, 33.

[26] G. A. Bain, J. F. Berry, *J. Chem. Educ.* **2008**, *85*, 532–536.

Received: October 23, 2012
Published online: February 5, 2013

IV:

Angular dependence of the exchange interaction in fluoride-bridged Gd-III-Cr-III complexes

S. K. Singh, K. S. Pedersen, M. Sigrist, C. A. Thuesen, M. Schau-Magnussen, H. Mutka, S. Piligkos, H. Weihe, G. Rajaraman, J. Bendix

Chemical Communications **49**, 5583-5585 (2013)

ChemComm

RSC Publishing

COMMUNICATION

View Article Online
View Journal | View Issue

Cite this: *Chem. Commun.*, 2013, **49**, 5583

Received 8th April 2013,
Accepted 1st May 2013

DOI: 10.1039/c3cc42552e

www.rsc.org/chemcomm

Angular dependence of the exchange interaction in fluoride-bridged Gd^{III}–Cr^{III} complexes†

Saurabh Kumar Singh,‡[a] Kasper S. Pedersen,‡[b] Marc Sigrist,[bc] Christian Aa. Thuesen,[b] Magnus Schau-Magnussen,[b] Hannu Mutka,[c] Stergios Piligkos,[b] Høgni Weihe,[b] Gopalan Rajaraman*[a] and Jesper Bendix*[b]

The observed angular variation of the magnetic exchange coupling parameter in a series of fluoride-bridged chromium(III)–gadolinium(III) complexes is explained by DFT calculations.

The relatively new research field of magnetic refrigeration, by means of adiabatic demagnetisation, in paramagnetic, molecular, polynuclear, complexes[1] and MOFs[2] has reinvigorated the study of magnetically isotropic, polynuclear d- and f-metal ion compounds.[3] As the magnetocaloric effect (MCE) delicately depends on the nature of the low-lying energy levels of such systems, it is necessary to develop methodologies for the prediction of the sign and magnitude of the magnetic exchange interactions between their constituent metal ions.[4] Gd^{III} has a well-isolated, orbitally non-degenerate $^8S_{7/2}$ ground term and can be considered magnetically isotropic.[5] Similarly, Cr^{III} has only weak magnetic anisotropy.[6] Thus, a combination of these two metal-ions for the development of new molecular refrigerants seems promising. We have recently reported a pentanuclear, trigonal bipyramidal $\{Gd_3Cr_2\}$ complex displaying good refrigeration properties.[7] We report here magneto-structural correlation studies on a simple dinuclear Cr^{III}–Gd^{III} model complex and three, previously described, polynuclear Gd^{III}–Cr^{III} complexes (Fig. 1).[8] Characteristically, only very small differences in the Cr^{III}–F and Gd^{III}–F bond lengths are observed in the series **1–4** suggesting that the differences in exchange interactions are essentially governed by the Gd^{III}–F–Cr^{III} angle. The synthetic approach to the series is based on the kinetic robustness of Cr^{III} which prevents the precipitation of highly insoluble GdF_3.[9] The intrinsic preference of the fluoride ion for linear bridging facilitates the prediction of the cluster topology, giving rods for *trans*-difluorido, squares for *cis*-difluorido and trigonal bipyramids for *fac*-trifluorido chromium(III) precursors.

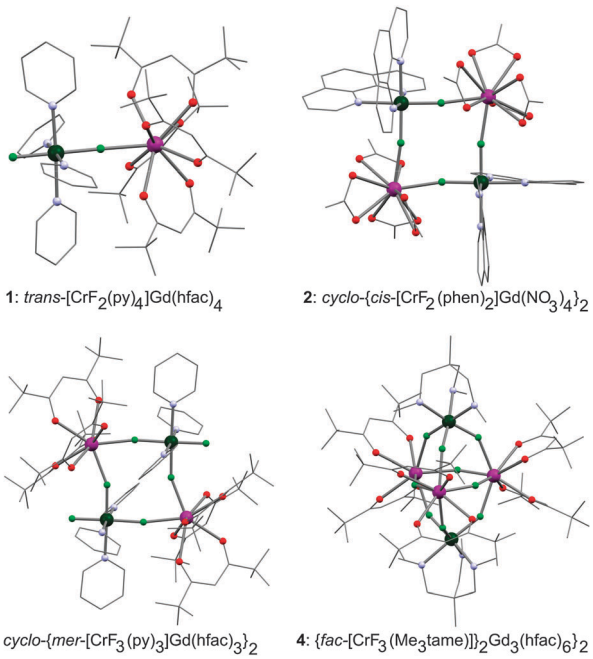

Fig. 1 Molecular structures of **1–4** (see also Scheme S1, ESI†). Gd, purple; Cr, dark green; F, light green; O, red; N, blue. The auxiliary ligand sphere is shown as a wireframe and hydrogens are omitted for clarity.

The χT products of **1–4** are shown in Fig. 2 of which the magnetic properties of **2–4** have already been reported.[7,8b] The high-temperature χT values are all in agreement with the values expected for the uncorrelated ions (S_{Gd} = 7/2, S_{Cr} = 3/2, g = 2.0 for both Cr^{III} and Gd^{III}). On cooling, all χT products decrease indicating the presence of intra-cluster antiferromagnetic interactions. All thermodynamic magnetometry data were fitted by use of the Levenberg–Marquardt algorithm[10] and by numerical diagonalisation of the isotropic spin-Hamiltonian (1):

$$\hat{H}_{iso} = \mu_B \boldsymbol{B} \sum_i g_i \hat{\boldsymbol{S}}_i + J_{ij} \sum_{i,j>i} \hat{\boldsymbol{S}}_i \hat{\boldsymbol{S}}_j \qquad (1)$$

[a] *Department of Chemistry, Indian Institute of Technology Bombay, Powai, Mumbai, 400076, India. E-mail: rajaraman@chem.iitb.ac.in; Fax: +91-22-2576-7152; Tel: +91-22-2576-7183*

[b] *Department of Chemistry, University of Copenhagen, Universitetsparken 5, DK-2100 Copenhagen, Denmark. E-mail: bendix@kiku.dk; Fax: +45 35320214; Tel: +45 3520111*

[c] *Institut Laue-Langevin, 38042 Grenoble Cedex 9, France*

† Electronic supplementary information (ESI) available: Synthetic procedures, crystallographic details, spectroscopic results, reduced magnetization data, computational details. CCDC 921006. For ESI and crystallographic data in CIF or other electronic format see DOI: 10.1039/c3cc42552e

‡ These authors contributed equally to the work.

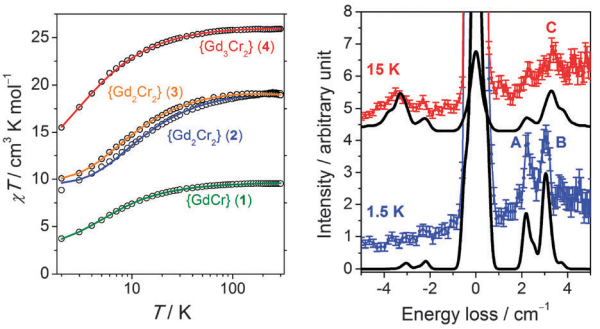

Fig. 2 (left) χT ($\chi = M/H$) data for **1–4** acquired with H_{dc} = 1000 Oe (circles) and best fits as described in the main text (solid lines). (right) INS spectra of **1** obtained with an incident neutron wavelength of λ_i = 6.5 Å at T = 1.5 K and 15 K. Solid black lines are simulations.

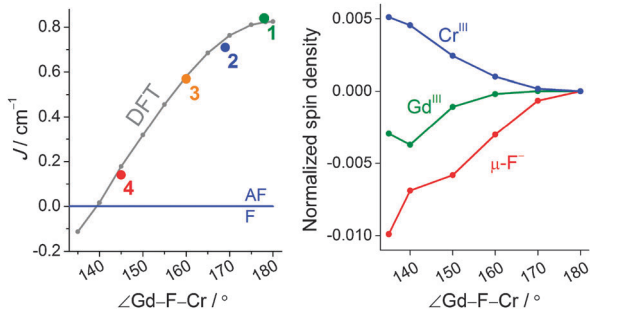

Fig. 3 (left) Angular dependence on the J parameters for **1–4** (coloured circles) and DFT results (grey circles). (right) Normalized spin density plot for an angular distortion of **1**.

where the indices i and j run through the constitutive single-ions of each compound, g is the single-ion g-factor, $\hat{\boldsymbol{S}}$ is a spin-operator and J is the isotropic exchange parameter. Note that a non-zero value for J_{Gd-Gd} is only employed in the case of **4**. Independently fitting the χT product and low temperature magnetization data (Fig. S2, ESI†) of **1** affords J = 0.84(4) cm^{-1} and J = 0.82(4) cm^{-1}, respectively, with the g factors fixed to g_{Cr} = 1.97 and g_{Gd} = 1.99. Determination of an isotropic exchange parameter of this small magnitude solely from magnetic measurements may be inaccurate as other small terms, such as zero-field splittings, may be non-negligible, especially at low temperatures. Inelastic neutron scattering (INS) is a well-suited method for the determination of the magnetic anisotropy and exchange parameters in paramagnetic complexes due to the selection rules $\Delta S = 0, \pm 1$ and $\Delta M_S = 0, \pm 1$. Despite the extremely large neutron absorption cross-section of ^{157}Gd (*ca.* 16% natural abundance), we managed to acquire INS spectra of **1** (Fig. 2 and Fig. S3, ESI†). Although noisy, the energy loss peaks A, at 2.2 cm^{-1}, and B, at 3.0 cm^{-1}, are clearly discernible in the spectrum at λ_i = 6.5 Å and assigned to magnetic excitations originating from the ground state, on the basis of their temperature dependence. Unfortunately, the poor quality of the observed Q-dependence, because of the presence of ^{157}Gd and large incoherent scattering from ^{1}H, does not allow affirming the magnetic nature of these excitations. The experimental spectra were interpreted by use of home-written software[11] invoking the anisotropic extension of spin-Hamiltonian (1) given in eqn (2):

$$\hat{H}_{aniso} = \hat{H}_{iso} + D_{Cr}\left(\hat{S}_{z,Cr}{}^2 - \frac{1}{3}S_{Cr}(S_{Cr}+1)\right) \qquad (2)$$

where D_{Gd} is neglected.[5] For comparison, the broader, but more intense, spectrum at λ_i = 4.8 Å is shown in Fig. S3 (ESI†). In the T = 15 K spectrum (Fig. 2, right), a hot peak (C) arises at 3.3 cm^{-1}. For D_{Cr} = 0, the S = 3, 4 and 5 spin manifolds are separated from the S = 2 ground state by 3J, 7J and 12J (Fig. S4, ESI†), respectively, and only one prominent INS peak would be observed at low temperature from the S = 2 to S = 3 excitation (Fig. S5, ESI†). Introduction of D_{Cr} breaks the degeneracy of the M_S levels, and an optimized value of D_{Cr} = 0.5 cm^{-1}, together with J = 0.87 cm^{-1}, results in good agreement with the experiment (*cf.* Fig. 2, right).

The obtained J parameters for **2–4**, for which the INS spectra were not acquired, are shown together with that for **1** in Fig. 3 as a function of the Gd–F–Cr angle. All the extracted couplings are antiferromagnetic and their strength seems to correlate with the Gd–F–Cr angle. Magnetic interactions in {3d–Gd} dinuclear complexes are in general ferromagnetic with some notable exceptions, such as a cyanide-bridged {CrGd} complex.[12,13] A {GdCr$_4$} hydroxide bridged complex is also reported to be antiferromagnetic in nature.[14] This fuelled our curiosity as to whether Cr^{III} in particular promotes antiferromagnetic interactions. Indeed, for **1–4**, the exchange interaction is antiferromagnetic. Moreover, there is a structural correlation to this antiferromagnetic interaction as shown in Fig. 3, which presents J as a function of the Gd–F–Cr angle. To shed light on this issue, as well as on the angular dependence of J, we performed DFT (B3LYP/TZV) calculations on **1**. All the calculations were performed with the Gaussian 09 program suite (*cf.* ESI† for computational details). The computed J value of 0.80 cm^{-1} for **1** is in excellent agreement with the values extracted from experiments (see Table S2 for DFT computed energies, ESI†). The reproduction of both the sign and the magnitude of J provides confidence in the computed J values.

Understanding the mechanism by which the coupling is operational in this {Cr–Gd} pair is important, as it is expected to provide clues about the nature of the exchange interaction and its angular dependence. The following generic mechanistic points emerge from our earlier studies.[15a–f] In a general {3d–4f} pair, the overlap between the 4f orbitals and the 3d orbitals only partly determines the nature of the magnetic exchange interaction. Orthogonality between the 3d and 4f orbitals results in ferromagnetic, J_F, contributions, whereas, non-vanishing overlap of the same orbitals results in antiferromagnetic, J_{AF}, contributions to the magnetic exchange. Additionally, charge transfer excitations from a 3d orbital to an empty 5d orbital of the lanthanide contribute to J_F. Since the 4f orbitals are contracted, contributions to J_{AF} are generally weak and therefore most of the {3d–4f} pairs exhibit ferromagnetic behaviour. In complex **1**, the unpaired electrons on Cr^{III} are located in the t_{2g} {d_{xy}, d_{xz}, d_{yz}} set of orbitals. Since these orbitals exhibit π character, an efficient σ-type charge transfer from 3d to 5d, observed for {Cu^{II}($t_{2g}^6e_g^3$)–Gd} and {Ni($t_{2g}^6e_g^2$)–Gd} complexes, is absent in **1** and thus, the J_F contribution is significantly reduced.[15a–c] To estimate the J_{AF} contributions, the overlap integrals (S_{ab}) between the magnetic orbitals of Cr^{III} and Gd^{III} have been computed and significant S_{ab} values have been detected indicating a relatively strong 3d–4f overlap (Fig. S6, ESI†). Previously, we have shown that the number

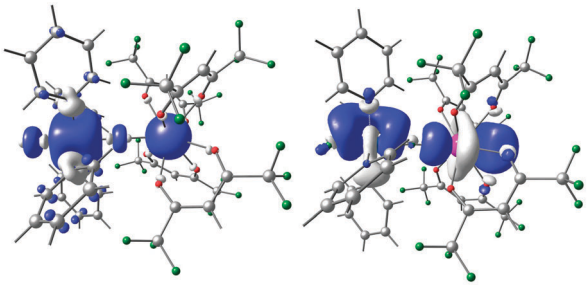

Fig. 4 (left) Spin density plot for the parent Cr–Gd complex. (right) Representation of charge transfer donor(Cr^{III} $3d_{z^2}$)–acceptor(Gd^{III} $5d_{z^2}$) NBO plot from second order perturbation theory analysis.

of bridges plays a vital role in the sign of magnetic coupling. In particular, when going from two alkoxo-bridges to one bridge in {3d–Gd} complexes, a strong antiferromagnetic interaction is predicted, essentially due to a larger direct 3d–4f orbital overlap and thus a large J_{AF} contribution.[15b] This correlates well with the single fluoride bridge and the antiferromagnetic interaction observed in this series. Additional insight into the mechanism of the exchange interaction is provided by DFT-calculated spin densities. Spin densities of 3.09 on Cr^{III} and 7.03 Gd^{III} indicate predominant spin polarisation (Fig. 4, left; Table S3, ESI†). All the coordinated nitrogen and oxygen atoms have negative spin densities, however the fluoride ions, both the bridging and the terminal, have positive spin densities in the high spin state (*cf.* Table S4, ESI†). The bridging fluoride has negative spin density values in the broken symmetry state and this essentially indicates that delocalization from Cr^{III} predominates over the Gd^{III}. Comparing the magnitude and the sign of the spin densities at the fluoride bridge, it is apparent that a mixture of spin delocalization and polarization is operational on these atoms and this diminishes the charge transfer component and thus reduces the J_F part. This is also supported by our NBO analysis where an extremely weak Cr^{III} $3d_{z^2}$–Gd^{III} $5d_{z^2}$ donor–acceptor interaction has been detected (Fig. 4, right). To gain insight into the angle dependency, the Cr–F–Gd angle was gradually varied from 135° to 180° in steps of 10°. The computed variation of J with the bridging angle is shown in Fig. 3 along with the experimental points.

As the angle increases the J becomes more antiferromagnetic, but shows a plateau at larger angles. On the other hand at an acute angle (at *ca.* 138°), a switch from antiferro- to ferromagnetic interaction is predicted. Mapping the experimental J's and structural parameters on the computed graph yields an excellent match. The plateau at higher angles and less antiferromagnetic J at lower angles was nicely reproduced. To analyse the factors behind the observed trend, we have computed the overlap integrals, which reveal that there is a significant decrease in the Cr–Gd orbital overlap as the angle decreases leading to a reduction in the J_{AF} contribution. (*cf.* Table S5, ESI†) This along with a moderate increase in the charge transfer (*cf.* 5d occupation in Table S6, ESI†) leads to a predicted ferromagnetic coupling at lower Cr–F–Gd angles. Our analysis reveals that at lower angles, the metal ion spin densities increase and, concomitantly, for μ-F^- the spin densities decrease proportionally indicating an increasing ferromagnetic contribution as evidenced from the computed J values (see Fig. 3, right; Table S4, ESI†).

In conclusion, the angular dependence of the exchange in a small family of fluoride-bridged $\{Gd^{III}_xCr^{III}_y\}$ complexes has been analysed. The observed variation and magnitude of J is reproduced and rationalised by DFT calculations in terms of geometric variation of 3d–4f overlap and charge transfer. This insight paves the way for preparative control of magnetic exchange interactions in systems with small magnetic anisotropy and thereby for the development of new molecular, magnetic coolers.

K.S.P. and S.P. thank the Danish Ministry of Science, Innovation and Higher Education for an EliteForsk travel scholarship and a Sapere Aude Fellowship (10-081659), respectively. GR thanks DST (SR/S1/IC-41/2010; SR/NM/NS-1119/2011) for financial support and SKS thanks IITB for SRF fellowship. GR and SKS acknowledge the HPC facility at IITB.

Notes and references

1 (*a*) M. Evangelisti and E. K. Brechin, *Dalton Trans.*, 2010, **39**, 4672–4676; (*b*) J. W. Sharples and D. Collison, *Polyhedron*, 2013, **54**, 91–103.
2 (*a*) G. Lorusso, M. A. Palacios, G. S. Nichol, E. K. Brechin, O. Roubeau and M. Evangelisti, *Chem. Commun.*, 2012, **48**, 7592–7594; (*b*) R. Sibille, T. Mazet, B. Malaman and M. François, *Chem.–Eur. J.*, 2012, **18**, 12970.
3 (*a*) R. E. P. Winpenny, *Chem. Soc. Rev.*, 1998, **27**, 447–452; (*b*) C. Benelli and D. Gatteschi, *Chem. Rev.*, 2002, **102**, 2369–2388; (*c*) M. Andruh, J.-P. Costes, C. Diaz and S. Gao, *Inorg. Chem.*, 2009, **48**, 3342–3359.
4 E. Cremades, S. Gómez-Coca, D. Aravena, S. Alvarez and E. Ruiz, *J. Am. Chem. Soc.*, 2012, **134**, 10532–10542.
5 O. Kahn, *Molecular Magnetism*, VCH, New York, 1993.
6 H. I. Karunadasa, K. D. Arquero, L. A. Berben and J. R. Long, *Inorg. Chem.*, 2010, **49**, 4738–4740.
7 T. Birk, K. S. Pedersen, C. Aa. Thuesen, T. Weyhermüller, M. Schau-Magnussen, S. Piligkos, H. Weihe, S. Mossin, M. Evangelisti and J. Bendix, *Inorg. Chem.*, 2012, **51**, 5435–5443.
8 (*a*) J. Dreiser, K. S. Pedersen, C. Piamonteze, S. Rusponi, Z. Salman, Md. E. Ali, M. Schau-Magnussen, C. Aa. Thuesen, S. Piligkos, H. Weihe, H. Mutka, O. Waldmann, P. Oppeneer, J. Bendix, F. Nolting and H. Brune, *Chem. Sci.*, 2012, **3**, 1024–1032; (*b*) C. Aa. Thuesen, K. S. Pedersen, M. Schau-Magnussen, M. Evangelisti, J. Vibenholt, S. Piligkos, H. Weihe and J. Bendix, *Dalton Trans.*, 2012, **41**, 11284–11292.
9 (*a*) A. McRobbie, A. R. Sarwar, S. Yeninas, H. Nowell, M. L. Baker, D. Allan, M. Luban, C. A. Muryn, R. G. Pritchard, R. Prozorov, G. Timco, F. Tuna, G. F. S. Whitehead and R. E. P. Winpenny, *Chem. Commun.*, 2011, **47**, 6251–6253; (*b*) J. Dreiser, K. S. Pedersen, T. Birk, M. Schau-Magnussen, C. Piamonteze, S. Rusponi, T. Weyhermüller, H. Brune, F. Nolting and J. Bendix, *J. Phys. Chem. A*, 2012, **116**, 7842–7847.
10 W. H. Press, S. A. Teukolsky, W. T. Vetterling and B. P. Flannery, *Numerical Recipes in C: The Art of Scientific Computing*, Cambridge University Press, Cambridge, MA, 2nd edn, 1992.
11 P. L. W. Tregenna-Piggott, D. Sheptyakov, L. Keller, S. I. Klokishner, S. M. Ostrovsky, A. V. Palii, O. S. Reu, J. Bendix, T. Brock-Nannestad, K. Pedersen, H. Weihe and H. Mutka, *Inorg. Chem.*, 2009, **48**, 128–137.
12 (*a*) N. Georgopoulou, R. Adam, C. P. Raptopoulou, V. Psycharis, R. Ballesteros, B. Abarca and A. K. Boudalis, *Dalton Trans.*, 2010, **39**, 5020–5027; (*b*) M. Ferbinteanu, F. Cimpoesu, M. A. Gîrțu, C. Enachescu and S. Tanase, *Inorg. Chem.*, 2012, **51**, 40–50.
13 H.-Z. Kou, S. Gao, C.-H. Li, D.-Z. Liao, B.-C. Zhou, R.-J. Wang and Y. Li, *Inorg. Chem.*, 2002, **41**, 4756–4762.
14 D. J. Hodgson, K. Michelsen and E. J. Pedersen, *J. Chem. Soc., Chem. Commun.*, 1988, 1558–1559.
15 (*a*) S. K. Singh, N. K. Tibrewal and G. Rajaraman, *Dalton Trans.*, 2011, **40**, 10897–10906; (*b*) S. K. Singh and G. Rajaraman, *Dalton Trans.*, 2013, **42**, 3623–3630; (*c*) G. Rajaraman, F. Totti, A. Bencini, A. Caneschi, R. Sessoli and D. Gatteschi, *Dalton Trans.*, 2009, 3153–3161; (*d*) J. Paulovic, F. Cimpoesu, M. Ferbinteanu and K. Hirao, *J. Am. Chem. Soc.*, 2004, **126**, 3321–3331; (*e*) T. Rajeshkumar and G. Rajaraman, *Chem. Commun.*, 2012, **48**, 7856–7858; (*f*) S. K. Singh, T. Rajeshkumar, V. Chandrasekhar and G. Rajaraman, *Polyhedron*, 2013, DOI: 10.1016/j.poly.2013.02.037.

V:

Mn-III zero-field splitting parameters and weak exchange interactions in a cyanide-bridged {Mn-III-Ir-III-Mn-III} cluster

K. S. Pedersen, M. Sigrist, H. Weihe, P. L. W. Tregenna-Piggott, M. Schau-Magnussen, J. Dreiser, H. Mutka, A. L. Barra, J. Bendix

Inorganic Chemistry Communications **24**, 24-28 (2012)

Inorganic Chemistry Communications 24 (2012) 24–28

Contents lists available at SciVerse ScienceDirect

Inorganic Chemistry Communications

journal homepage: www.elsevier.com/locate/inoche

Mn^{III} zero-field splitting parameters and weak exchange interactions in a cyanide-bridged {Mn^{III}–Ir^{III}–Mn^{III}} cluster

Kasper S. Pedersen [a,*], Marc Sigrist [a,b], Høgni Weihe [a,*], Philip L.W. Tregenna-Piggott [c,1], Magnus Schau-Magnussen [a], Jan Dreiser [d], Hannu Mutka [b], Anne-Laure Barra [e], Jesper Bendix [a,*]

[a] Department of Chemistry, University of Copenhagen, Universitetsparken 5, DK-2100 Copenhagen, Denmark
[b] Institut Laue-Langevin, 38042 Grenoble Cedex 9, France
[c] Laboratory for Neutron Scattering, Paul Scherrer Institut, CH-5232 Villigen PSI, Switzerland
[d] Swiss Light Source, Paul Scherrer Institut, CH-5232 Villigen PSI, Switzerland
[e] High Magnetic Field Laboratory, 38042 Grenoble Cedex 9, France

ARTICLE INFO

Article history:
Received 29 May 2012
Accepted 23 July 2012
Available online 29 July 2012

Keywords:
Magnetic anisotropy
Manganese
Iridium
Electron paramagnetic resonance
Inelastic neutron scattering

ABSTRACT

The reaction of [Mn^{III}(5-Brsalen)(MeOH)](ClO_4) (5-Brsalen^{2-} = *N*,*N*′-ethylenebis(5-bromosalicylidene-iminate)) with [$Ir^{III}(CN)_6]^{3-}$ yields a trinuclear, cyanide-bridged Mn^{III}–Ir^{III}–Mn^{III} cluster which is a member of an isostructural series of Mn^{III}–M^{III}–Mn^{III} clusters. The presence of the large, diamagnetic $[Ir^{III}(CN)_6]^{3-}$ bridging unit facilitates a precise determination of the Mn^{III} zero-field splitting (zfs) parameters by the combined use of inelastic neutron scattering, high-field, high-frequency EPR spectroscopy and magnetic measurements. The single-ion axial (*D*) and rhombic (*E*) zfs parameters are found to be $D = -3.72(5)$ cm^{-1} and $|E| = 0.21(1)$ cm^{-1}. The experimental data are consistent with a small, antiferromagnetic exchange interaction between the two Mn^{III} ions.

In the field of molecular magnetism, so-called single-molecule magnets (SMMs) have gained considerable interest as the intrinsic "magnet-like" behaviour of the isolated molecule renders SMMs interesting building blocks for future applications in e.g. quantum computing [1]. One element that has received the majority of research efforts is manganese and some of the most widely employed building blocks are Mn^{III} Schiff-base complexes [2]. Recently, we reported the synthesis, structure and magnetic properties of four Mn^{III}–M^{III}–Mn^{III} clusters [3] where M=Cr [4], Fe [5], Ru [6] or Os [5], all exhibiting SMM behaviour. The Ru and Os clusters are unique examples of the growing class of 4d and 5d-based SMMs [7]. The advantages of the heavier transition metals in molecule-based magnetic materials become manifest in stronger intra-molecular exchange interactions resulting from the diffuse character of the 4d and 5d orbitals over 3d and the possibly stronger magnetic anisotropy [8]. We now present a new member, $(NEt_4)[Mn^{III}_2$(5-Brsalen)$_2(MeOH)_2Ir^{III}(CN)_6]$ (**1**), of this family of Mn^{III}–M^{III}–Mn^{III} compounds by employing $[Ir^{III}(CN)_6]^{3-}$. **1** was synthesized analogously to the ruthenium and osmium analogues by using $(PPh_4)_3[Ir^{III}(CN)_6]$ as the starting material. $K_3[Ir^{III}(CN)_6]$ was prepared by a modified literature procedure [9] and $[Ir^{III}(CN)_6]^{3-}$ was isolated as the PPh_4^+ salt from aqueous solution. To a solution of $(PPh_4)_3[Ir^{III}(CN)_6]$ (0.50 g, 0.37 mmol) in methanol (40 mL) was added solid NEt_4ClO_4 (0.25 g, 1.1 mmol) and the mixture was stirred vigorously for 1 h. The mixture was filtered to remove PPh_4ClO_4 and the filtrate was added to a solution of $[Mn^{III}$(5-Brsalen)$(H_2O)]ClO_4$ [5] (0.24 g, 0.40 mmol) in methanol (50 mL) without stirring. The resulting solution was left standing for 2 days to yield dark brown crystals suitable for structure determination. Yield: 89% based on Mn^{III}; elemental analysis calcd (%) for $C_{48}H_{52}Br_4IrMn_2N_{11}O_6$: C 38.42, H 3.49, N 10.27; found: C 38.34, H 3.14, N 10.16. **1** constitutes, to the best of our knowledge, the first example of a polynuclear transition metal complex incorporating $[Ir^{III}(CN)_6]^{3-}$. The molecular structure (shown in Fig. 1, left) is very similar to that of the other members of the series [10].

The crystal packing including hydrogen bond interactions is shown in Fig. 1 (right). The anionic cluster in **1** is engaged in intermolecular hydrogen bond interactions via the Mn^{III} terminal methanol ligands. Crystallographic data for **1** are given in Table 1.

Recently, we have employed inelastic neutron scattering (INS) to gain detailed insight in the lower-lying energy levels in similar clusters [3d,4,5]. However, the complicating (eventually anisotropic) exchange interactions prevent a precise determination of the Mn^{III} single-ion zfs parameters. For that reason a spectroscopic investigation involving both INS and high-field, high-frequency EPR spectroscopy was undertaken. Notably, only few INS studies of magnetically isolated Mn^{III} (and isoelectronic Cr^{II}) are reported in the literature

* Corresponding authors.
E-mail addresses: ksp@kiku.dk (K.S. Pedersen), weihe@kiku.dk (H. Weihe), bendix@kiku.dk (J. Bendix).
[1] Deceased.

1387-7003/$ – see front matter © 2012 Elsevier B.V. All rights reserved.
http://dx.doi.org/10.1016/j.inoche.2012.07.045

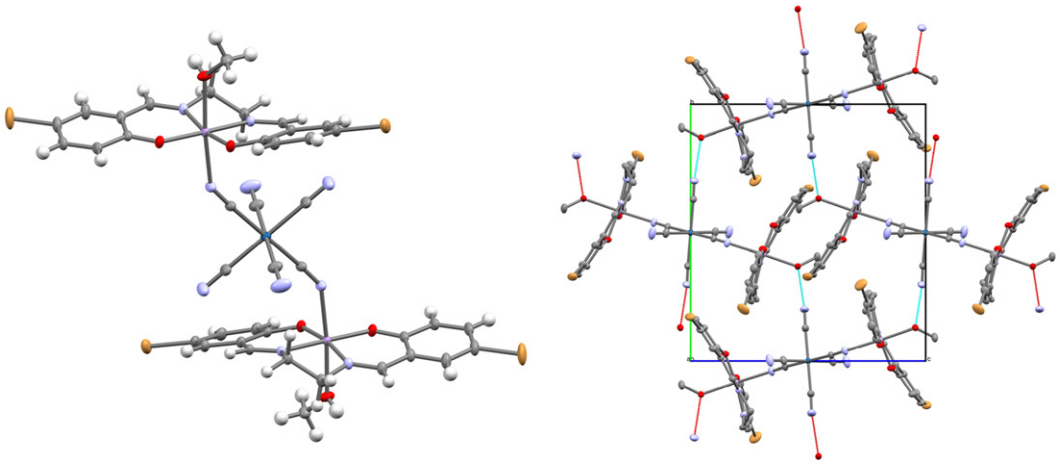

Fig. 1. Molecular structure of the anionic cluster in **1** (left) and unit cell contents along the *a* axis (right). Blue and red bonds indicate hydrogen bonds. Ellipsoids are drawn at 50% probability level. The tetraethylammonium counter-ion has been omitted for clarity. Colour code: Ir, navy; Mn, purple; Br, yellow; O, red; N, light blue; C, grey; H, white. Selected bond length (Å) and angles (°): Ir–C 2.012(2)–2.042(2); Mn–O_{eq} 1.8838(15), 1.8853(16); Mn–O_{ax} 2.2404(16); Mn–N_{eq} 1.9918(16), 2.0063(18); Mn–N_{ax} 2.2571(18); C–$N_{bridging\ cyanide}$ 1.159(3); C–$N_{terminal\ cyanide}$ 1.156(3), 1.154(3); C–Ir–C_{cis} 87.89(9)–92811(9); Mn–N–C 144.11(16). The hydrogen bonds are O – H···N 2.69 Å and the closest Mn–Mn intra- and inter-molecular distances are 6.3 Å and 10.3 Å, respectively.

[11]. All spectroscopic and magnetic data were modelled by means of the spin Hamiltonian

$$\hat{H} = \mu_B g\ B\cdot\sum_{1,2}\hat{\mathbf{S}}_i + D\sum_{1,2}\left(\hat{S}^2_{i,z} - \frac{1}{3}S_{\mathbf{Mn}}(S_{\mathbf{Mn}}+1)\right) + E\sum_{1,2}\left(\hat{S}^2_{i,x} - \hat{S}^2_{i,y}\right) + J\ \hat{\mathbf{S}}_1\cdot\hat{\mathbf{S}}_2 \quad (1)$$

where D and E are the Mn^{III} single-ion axial and rhombic zfs parameters, respectively. As a consequence of an inversion centre being located on the iridium site, the zfs tensors of Mn1 and Mn2 are identical and co-axial, therefore D and E for the two centres are identical. The last term in Eq. (1) takes into account the possible small magnetic exchange interaction between the two Mn^{III} through the diamagnetic $[Ir^{III}(CN)_6]^{3-}$ bridge. INS experiments on **1** were performed at the direct geometry time-of-flight spectrometer IN5 located at Institut Laue-Langevin (Grenoble, France). The time-of-flight to energy conversion and data reduction was performed using the LAMP package [12]. Around 2 g of non-deuterated **1** was loaded in a double-wall aluminium can and placed in a standard ILL orange cryostat. Spectra were collected at temperatures 1.5, 6 and 15 K with incident neutron wavelengths of 5 Å and 6.5 Å. The low-temperature (1.5 K) INS spectrum with incident neutron wavelength $\lambda_i = 5$ Å shows one doublet with peaks placed at 10.6 cm^{-1} (I) and 11.8 cm^{-1} (II) (Fig. 2 (a)). Upon heating till 15 K, the intensities of I and II decrease as expected for magnetic, ground-state (cold) excitations. Furthermore, a hot doublet (III and IV) emerges at 3.1 cm^{-1} (III) and 4.2 cm^{-1} (IV). All the transitions are also observed on the energy gain side and given primed labels. In the higher resolution spectra at 6.5 Å incident neutron wavelength, a hot transition is observed at 1.2 cm^{-1} (V′) on the energy gain side (see Fig. 2 (b)). On the energy loss side, this transition is partially hidden in the quasi-elastic line.

Table 1
X-ray structure and refinement data for **1**.

Chemical formula	$C_{48}H_{52}Br_4IrMn_2N_{11}O_6$
Formula mass	1500.73
Crystal system	Monoclinic
Space group	$P2_1/c$
a/Å	12.2954(11)
b/Å	15.5470(11)
c/Å	15.6440(13)
β/°	114.99(1)
Unit cell volume/Å^3	2710.5(4)
No. of formula units per unit cell, Z	2
Absorption coefficient, μ/mm^{-1}	5.91
No. of reflections measured	120,661
No. of independent reflections	16,865
R_{int}	0.051
Final R_1 values ($I > 2\sigma(I)$)[a]	0.033
Final $wR(F^2)$ values ($I > 2\sigma(I)$)[b]	0.072
Final R_1 values (all data)[a]	0.056
Final $wR(F^2)$ values (all data)[b]	0.084
Goodness of fit on F^2	1.16

[a] $R_1 = \Sigma||F_o| - |F_c||/\Sigma|F_o|$.
[b] $wR = [\Sigma w(F_o^2 - F_c^2)^2/\Sigma w(F_o^2)^2]^{1/2}$.

The axial elongation of the Mn^{III} coordination geometry in **1** resulting from the Jahn–Teller effect yields a $^5B_{1g}$ ground term in idealized D_{4h} symmetry. For $D<0$ (as normally observed for tetragonally elongated Mn^{III} [13]) and $E = 0$ the ground state is characterized by $|S, M_S\rangle = |2, \pm 2\rangle$ with a first excited state of $|2, \pm 1\rangle$ separated by $3D$. In the case of $E \neq 0$, the first order correction to the energy yields a splitting of $|2, \pm 1\rangle$ by an energy of $2\Delta = 6E$ whereas $|2, \pm 2\rangle$ is split to second order by only $2\delta = 3E^2/|D|$. Fig. 3 illustrates the energy level diagram pertinent to the ground state manifold. INS transitions I and II correspond to the excitations from a weakly split ~$|2, \pm 2\rangle$ state to the split ~$|2, \pm 1\rangle$ state. The hot bands III and IV are transitions from the split ~$|2, \pm 1\rangle$ to $|2, 0\rangle$. Transition V is a direct measure of the splitting of ~$|2, \pm 1\rangle$.

The experimental INS spectra are well reproduced by $D = -3.72(5)$ cm^{-1} and $|E| = 0.21(1)$ cm^{-1} obtained by least-squares fitting of the peak positions to Eq. (1) omitting the magnetic exchange term. The calculated spectra, *including* the exchange term with $J = 0.05$ cm^{-1} are shown in the lower traces of Fig. 2. The presence of the exchange term only leads to broadening of the left-most peaks in Fig. 2 (b). The splitting of ~$|2, \pm 1\rangle$ is directly visible from the splitting of INS peaks I and II whereas the splitting of ~$|2, \pm 2\rangle$ with the extracted parameter set is expected to be only 0.032 cm^{-1} which is far below the resolution of the INS experiments. To gain further confidence on the extracted parameters, high-field and high-frequency EPR measurements were performed [14]. HF-EPR spectra were obtained at 285 GHz at temperatures 5, 15 and 25 K and are shown in Fig. 4. Although the INS spectra are reproduced by only D and E, reasonable agreement of simulations of EPR spectra with experiments needed a small Mn–Mn exchange coupling parameter. The magnitude is limited upwards by the fact that no exchange splitting of the INS peaks is observed. The compromise reveals an exchange coupling constant of the order of J ~ 0.05 cm^{-1}. The small J mainly affects the low-field part of the EPR spectra and only leads to a

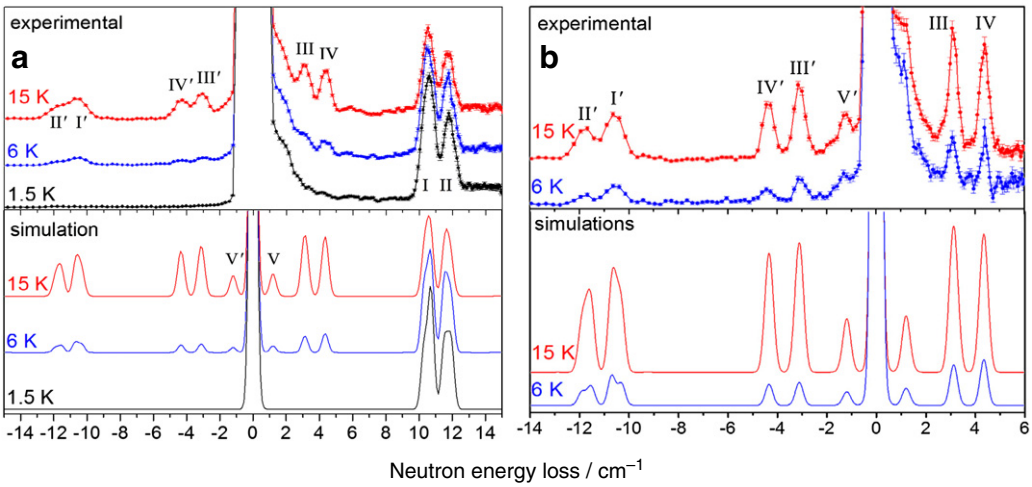

Fig. 2. Inelastic neutron scattering spectra of **1** (top) obtained with $\lambda_i = 5$ Å (a) and at $\lambda_i = 6.5$ Å (b) at selected temperatures. The data were summed over the detectors in the angular range 25–125° corresponding to a linear momentum transfer range at the elastic line position of $Q = 0.56$–2.2 Å^{-1} or 0.44–1.7 Å^{-1} for $\lambda_i = 5$ Å and 6.5 Å, respectively. The FWHM of the elastic line was 0.7 cm^{-1} ($\lambda_i = 5$ Å) or 0.3 cm^{-1} ($\lambda_i = 6.5$ Å). The lower traces are calculated spectra obtained as described in Ref. [3d] and with the parameters given in the body text. The calculated elastic peak is only the magnetic part and the energy transfer dependence of the resolution has not been included in the calculations but included in the uncertainties on the peak positions.

small broadening of the INS peaks. In order to further justify the small exchange interaction, the magnetic susceptibility was measured in the temperature range 1.8–300 K with a dc field of 1000 Oe and the data are shown in Fig. 5 as the χT product. The room temperature value of 6.1 cm^3 K mol^{-1} is close to the value expected for the two magnetically isolated Mn(III) ions. The χT stays roughly constant until ~15 K where a steep drop sets in due to the combined effect of zfs and possible intra- or inter-molecular antiferromagnetic interactions. The absolute sign of the exchange interaction is not known from the analysis of the EPR spectra but model calculations with the $D = -3.7$ cm^{-1} and $|E| = 0.20$ cm^{-1} and three different choices of J suggest antiferromagnetic Mn–Mn interactions (see Fig. 5). Introduction of higher order B_4^4 and B_0^4 terms did not affect the low-field region of the EPR spectra and led to worse agreement at higher fields and were for that reason completely excluded. As can be seen from the lowest traces in Fig. 4, the splitting of the low field line at approximately 1 T is reproduced by a small exchange coupling constant. The "rhombicity" $|E/D| = 0.054$ is close to the values reported for e.g. $[Mn^{III}(OD_2)_6]^{3+}$ [11a] and $[Mn^{III}(dbm)_3]$ (dbmH = dibenzoylmethane) [15] whereas the absolute value of E and D is smaller in **1**. Only one HF-EPR study of Mn^{III} salen-type complexes is found in the literature [16]. Interestingly, the magnitude of D in **1** is significantly larger than found for the similar "Jacobsen catalyst" in CH_2Cl_2/toluene frozen solution ($D = -2.47$ cm^{-1}) but has a similar value of $E = 0.17$ cm^{-1} [16]. On the contrary, **1** has a D value very similar to those determined for $[Mn^{III}X_3(terpy)]$ (X = F, N_3; terpy = 2,2′;6′2″-terpyridine) and $[Mn^{III}F_3(bpea)]$ (bpea = *N*,*N*-bis(2-pyridylmethyl)ethylamine) by HF-EPR [17]. In the isostructural $\{Mn^{III}$–Cr^{III}–$Mn^{III}\}$ cluster we found a similar value for D of $-3.63(4)$ cm^{-1} but a non-zero E was not evident from the available INS and Fourier-transform frequency-domain EPR data [4].

The INS spectra are considerably simpler than the spectra for the closely related $K[Mn^{III}_2(5\text{-Brsalen})_2(H_2O)_2Co^{III}(CN)_6]\cdot 2H_2O$ incorporating diamagnetic $[Co^{III}(CN)_6]^{3-}$ which can be attributed to the much weaker Mn–Mn couplings in **1**. Previously, it was argued that $[Co^{III}(CN)_6]^{3-}$ is mediating the Mn–Mn exchange interaction [3d], however, a hydrogen bond mediated mechanism seems now more probable. The main structural difference between $K[Mn^{III}_2(5\text{-Brsalen})_2(H_2O)_2Co^{III}(CN)_6]\cdot 2H_2O$ and **1** lies in the presence of only one hydrogen bond pathway of the terminal MeOH to the $\{Ir^{III}(CN)_6\}$ unit of a neighbouring

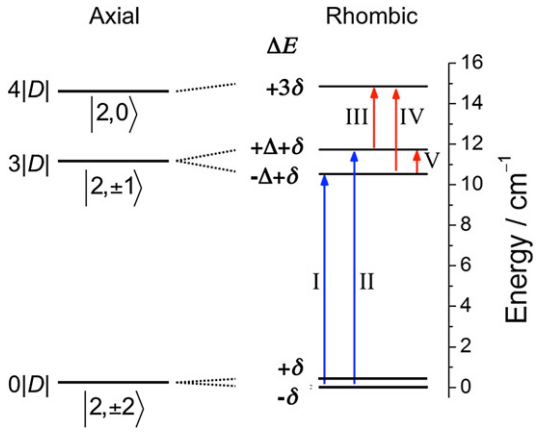

Fig. 3. Energy level diagram of a monomeric Mn^{III} with $D<0$ in axial symmetry (left) and rhombic symmetry (right) with $\Delta = 3E$ and $\delta = (3/2)|E^2/D|$. The energy splittings are calculated with the parameters $D = -3.7$ cm^{-1} and $E = 0.20$ cm^{-1}. The splitting of the ground state ~$|2,\pm2\rangle$ of only $2\delta = 3E^2/|D| = 0.032$ cm^{-1} is drawn out of scale. The labels pertain to the experimentally observed INS transitions. Application of $J = 0.05$ cm^{-1} in a dinuclear model splits in total the ~$|2,+2\rangle$ and ~$|2,-2\rangle$ low-lying states by 0.4 cm^{-1}.

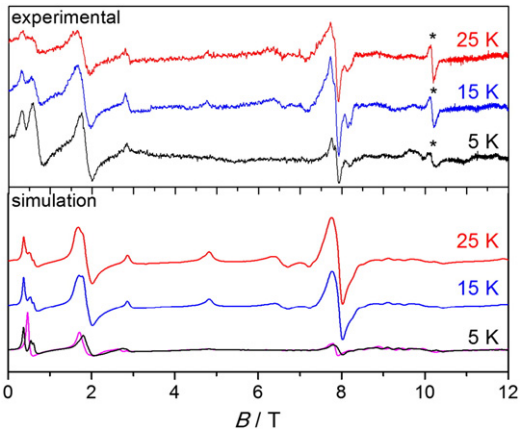

Fig. 4. HF-EPR spectra ($\nu = 285$ GHz) of **1** at temperatures 5 K, 15 K and 25 K (top) and simulations (bottom) obtained as described in the body text. The asterisk designates a $g = 2$ impurity. The purple spectrum at 5 K is calculated by omitting the exchange interaction term.

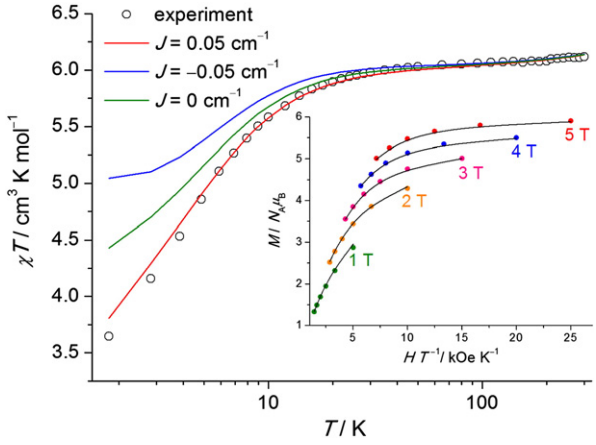

Fig. 5. Magnetic susceptibility (H_{dc} = 1000 Oe) data of **1** shown as χT ($\chi = M/H$). Data were corrected for diamagnetic contributions by means of Pascal constants. The curves represent calculated χT products using $D = -3.7$ cm^{-1}, $E = 0.20$ cm^{-1} and three different choices of J. Inset: reduced magnetization data and simulation obtained with $g = 1.98$, $D = -3.7$ cm^{-1}, $E = 0.20$ cm^{-1} and $J = 0.05$ cm^{-1}. The modelling has been performed with the MagProp programme [3d].

molecule (see Fig. 1, right). In $K[Mn^{III}_2(5\text{-Brsalen})_2(H_2O)_2Co^{III}(CN)_6]\cdot 2H_2O$, the Mn^{III} terminal water molecule in addition has a hydrogen bond to another neighbouring water molecule giving a short distance magnetic pathway which transmits a coupling of $J = 0.63$ cm^{-1}, which is similar to the value ($J = 0.70$ cm^{-1}) found in a hydrogen-bonded $[Mn^{III}(5\text{-TMAMsalen})(H_2O)_2]^{3+}$ (5-TMAMsalen^{2-} = *N,N′*-ethylenebis(5-trimethylammonio-methylsalicylideneiminate)) dimer [18]. The Mn^{III}–Mn^{III} magnetic exchange through $[Co^{III}(CN)_6]^{3-}$ has been estimated [19] to be around 0.05 cm^{-1} in a $\{Mn^{III}_6Co^{III}\}$ cluster in good agreement with our present finding for the Mn^{III}–Mn^{III} exchange coupling through $[Ir^{III}(CN)_6]^{3-}$. In the other members of the $\{Mn^{III}$–M^{III}–$Mn^{III}\}$ (M=Cr, Fe, Ru and Os) clusters, small inter-molecular exchange interactions were introduced in the frame of molecular field theory to fully reproduce magnetic data. This, however, does not apply to **1** as the only likely pathway for the inter-molecular coupling is through the hydrogen bonds connecting paramagnetic Mn^{III} with diamagnetic Ir^{III}.

In conclusion, the combined use of INS, HF-EPR and magnetic measurements has revealed the zfs parameters for axially elongated Mn^{III} in a salen-type ligand environment with *N*-cyanide and methanol co-ligands. *D* was found to be slightly larger than determined for mononuclear Mn^{III} salen-type complexes by magnetization measurements [20]. The Mn^{III}–Mn^{III} coupling in **1** of $J \sim 0.05$ cm^{-1} provides an upper limit for the strength of the interactions as the INS and EPR spectra exhibit no and small splittings, respectively, due to the exchange interaction.

Supplementary materials related to this article can be found online at doi:10.1016/j.inoche.2012.07.045.

Acknowledgements

K.S.P. and J.B. thank the Danish Neutron Scattering Society (DANSCATT) for financial support.

References

[1] (a) R. Sessoli, D. Gatteschi, A. Caneschi, M.A. Novak, Magnetic bistability in a metal-ion cluster, Nature 265 (1993) 141–143;
(b) D. Gatteschi, R. Sessoli, J. Villain, Molecular nanomagnets, Oxford University Press, 2006.;
(c) Single-molecule magnets and related phenomena, in: R.E.P. Winpenny (Ed.), Struc. Bonding, 122, Springer, Berlin, 2006;
(d) L. Bogani, W. Wernsdorfer, Molecular spintronics using single-molecule magnets, Nat. Mater. 7 (2008) 179–186.
[2] a) H. Miyasaka, A. Saitoh, S. Abe, Magnetic assemblies based on Mn(III) salen analogues, Coord. Chem. Rev. 251 (2007) 2622–2664 (and references cited therein);
b) H.J. Choi, J.J. Sokol, J.R. Long, High-spin metal-cyanide clusters: species incorporating $[Mn(salen)]^+$ complexes as a source of anisotropy, J. Phys. Chem. Solids 65 (2004) 839–844;
(c) T. Birk, K.S. Pedersen, S. Piligkos, C.Aa. Thuesen, H. Weihe, J. Bendix, Magnetic properties of a manganese(III) chain with monoatomic bridges: *catena*-MnF(salen), Inorg. Chem. 50 (2011) 5312–5314;
(d) T. Senapati, C. Pichon, R. Ababei, C. Mathonière, R. Clérac, Cyanido-bridged Fe(III)–Mn(III) heterobimetallic materials built from Mn(III) Schiff base complexes and di- or tri-cyanido Fe(III) precursors, Inorg. Chem. 51 (2012) 3796–3812.
[3] (a) H. Miyasaka, N. Matsumoto, H. Okawa, N. Re, E. Gallo, C. Floriani, Complexes derived from the reaction of manganese(III) Schiff base complexes and hexacyanoferrate(III): syntheses, multidimensional network structures, and magnetic properties, J. Am. Chem. Soc. 118 (1996) 981–994;
(b) H. Miyasaka, H. Ieda, N. Matsumoto, N. Re, R. Crescenzi, C. Floriani, Assembling bi-, tri- and penta-nuclear complexes into extended structures using a desolvation reaction: synthesis, structure and magnetic properties of manganese(III)-Schiff-base-hexacyanoferrate polymeric compounds and their derived extended structures, J. Am. Chem. Soc. 37 (1998) 255–263;
(c) M. Ferbinteanu, H. Miyasaka, W. Wernsdorfer, K. Nakata, K.-i. Sugiura, M. Yamashita, C. Coulon, R. Clérac, Single-chain magnet $(NEt_4)[Mn_2(5\text{-MeOsalen})_2Fe(CN)_6]$ made of Mn^{III}–Fe^{III}–Mn^{III} trinuclear single-molecule magnet with an $S_T = 9/2$ spin ground state, J. Am. Chem. Soc. 127 (2005) 3090–3099;
(d) P.L.W. Tregenna-Piggott, D. Sheptyakov, L. Keller, S.I. Klokishner, S.M. Ostrovsky, A.V. Palii, O.S. Reu, J. Bendix, T. Brock-Nannestad, K. Pedersen, H. Weihe, H. Mutka, Single-ion anisotropy and exchange interactions in the cyano-bridged trimers $Mn^{III}_2M^{III}(CN)_6$ (M^{III}=Co, Cr, Fe) species incorporating $[Mn(5\text{-Brsalen})]^+$ units: an inelastic neutron scattering and magnetic susceptibility study, Inorg. Chem. 48 (2009) 128–137.
[4] J. Dreiser, A. Schnegg, K. Holldack, K.S. Pedersen, M. Schau-Magnussen, J. Nehrkorn, P. Tregenna-Piggott, H. Mutka, H. Weihe, J. Bendix, O. Waldmann, Frequency-domain Fourier-transform terahertz spectroscopy of the single-molecule magnet $(NEt_4)[Mn_2(5\text{-Brsalen})_2(MeOH)_2Cr(CN)_6]$, Chem. Eur. J. 17 (2011) 7492–7498.
[5] K.S. Pedersen, M. Schau-Magnussen, J. Bendix, H. Weihe, A.V. Palii, S.I. Klokishner, S. Ostrovsky, O.S. Reu, H. Mutka, P.L.W. Tregenna-Piggott, Enhancing the blocking temperature in single-molecule magnets by incorporating 3d–5d exchange interactions, Chem. Eur. J. 16 (2010) 13458–13464.
[6] K.S. Pedersen, J. Dreiser, J. Nehrkorn, M. Gysler, M. Schau-Magnussen, A. Schnegg, K. Holldack, R. Bittl, S. Piligkos, H. Weihe, P. Tregenna-Piggott, O. Waldmann, J. Bendix, A linear single-molecule magnet based on $[Ru^{III}(CN)_6]^{3-}$, Chem. Commun. 47 (2011) 6918–6920.
[7] X.-Y. Wang, C. Avendaño, K.R. Dunbar, Molecular magnetic materials based on 4d and 5d transition metals, Chem. Soc. Rev. 40 (2011) 3213–3238 (and references cited therein).
[8] (a) T.D. Harris, C. Coulon, R. Clérac, J.R. Long, Record ferromagnetic exchange through cyanide and elucidation of the magnetic phase diagram for a $Cu^{II}Re^{IV}(CN)_2$ chain compound, J. Am. Chem. Soc. 133 (2011) 123–130;
(b) X. Feng, T.D. Harris, S. Hill, J.R. Long, Slow magnetic relaxation induced by a large transverse zero-field splitting in a $Mn^{II}Re^{IV}(CN)_2$ single-chain magnet, J. Am. Chem. Soc. 134 (2012) 7521–7529.
[9] G.W. Watt, E.P. Helvenston, L.E.J. Sharif, Ammines of iridium(0), Inorg. Nucl. Chem. 24 (1962) 1067–1072.
[10] Single-crystal X-ray diffraction data were collected at 122 K using a Nonius Kappa CCD area-detector diffractometer with Mo Kα radiation (λ = 0.71073 Å) equipped with an Oxford Cryostreams low-temperature device. The structures were solved using direct methods (SHELXS97) and refined using the SHELXL97 software package. (G. M. Sheldrick, Acta Crystallogr. Sect. A 64 (2008) 112–122.) All non-hydrogen atoms were refined anisotropically, whereas hydrogen atoms were fixed. CCDC-755223 contains the supplementary crystallographic data for this paper. These data can be obtained free of charge from The Cambridge Crystallographic Database via www.ccdc.cam.uk/data_request/cif.
[11] (a) R. Basler, P.L.W. Tregenna-Piggott, H. Andres, C. Dobe, H.-U. Güdel, S. Janssen, G.J. McIntyre, Magnetic excitations of $CsMn(SO_4)2\cdot 12D2O$, J. Am. Chem. Soc. 123 (2001) 3377–3378;
(b) C. Dobe, H.-P. Andres, P.L.W. Tregenna-Piggott, S. Mossin, H. Weihe, S. Janssen, Variable temperature inelastic neutron scattering study of chromium(II) Tutton salt: manifestation of the $^5E \otimes e$ Jahn–Teller effect, Chem. Phys. Lett. 362 (2002) 387–396;
(c) Q. Scheifele, C. Riplinger, F. Neese, H. Weihe, A.-L. Barra, F. Juranyi, A. Podlesnyak, P.L.W. Tregenna-Piggott, Spectroscopic and theoretical study of a mononuclear manganese(III) complex exhibiting a tetragonally compressed geometry, Inorg. Chem. 47 (2008) 439–447.
[12] D. Richard, M. Ferrand, G.J. Kearley, J. Neutron Res. 4 (1996) 33–39.
[13] S. Mossin, H. Weihe, A.-L. Barra, Is the axial zero-field splitting parameter of tetragonally elongated high-spin manganese(III) complexes always negative? J. Am. Chem. Soc. 142 (2002) 8764–8765.
[14] EPR data was acquired at the High Magnetic Field Laboratory (Grenoble, France). Detailed descriptions of the equipment can be found in a) Muller, F.; Hopkins, A.; Coron, N.; Grynberg, M.; Brunel, L.-C.; Martinez, G. Rev. Sci. Instrum. 60 (1989) 3681. b) A.-L. Barra, L.C. Brunel, J.B. Robert, Chem. Phys. Lett. 165 (1990) 107. The spectra were simulated using home-written software (J. Glerup, H. Weihe, Magnetic susceptibility and EPR spectra of (μ-hydroxo)bis[pentaamminechromium(III)] chloride monohydrate, Inorg. Chem. 36 (1997) 2816–2819).
[15] A.-L. Barra, D. Gatteschi, R. Sessoli, G.L. Abbati, A. Cornia, A.C. Fabretti, M.G. Uytterhoeven, Electronic structure of manganese(III) compounds from high-frequency EPR spectra, Angew. Chem. Int. Ed Engl. 36 (1997) 2329–2331.

[16] J. Krzystek, J. Telser, High frequency and field EPR spectroscopy of Mn(III) complexes in frozen solution, J. Magn. Reson. 162 (2003) 454–465.
[17] a) C. Mantel, A. Hassan, J. Pecaut, A. Deronzier, M.N. Collomb, C. Duboc-Toia, A high-frequency and high-field EPR study of new azide and fluoride mononuclear Mn(III) complexes, J. Am. Chem. Soc. 125 (2003) 12337–12344;
(b) J. Limburg, J.S. Vrettos, R.H. Crabtree, G.W. Brudvig, J.C. de Paula, A. Hassan, A.-L. Barra, C. Duboc-Toia, M.N. Collomb, High-frequency EPR study of a new mononuclear manganese(III) complex: [(terpy)Mn(N_3)$_3$] (terpy = 2,2′:6′,2″-terpyridine), Inorg. Chem. 40 (2001) 1698–1703.
[18] H. Miyasaka, T. Madanbashi, A. Saitoh, N. Motokawa, R. Ishikawa, M. Yamashita, S. Bahr, W. Wernsdorfer, R. Clérac, Cyano-bridged Mn^{III}–M^{III} single-chain magnets with M^{III} = Co^{III}, Fe^{III}, Mn^{III}, and Cr^{III}, Chem. Eur. J. 18 (2012) 3942–3954.
[19] E. Krickemeyer, V. Hoeke, A. Stammler, H. Bögge, J. Schnack, T. Glaser, Synthesis and characterization of the heptanuclear $[Mn_6^{III}Co^{III}]^{3+}$ triplesalen complex: evidence for exchange pathways involving low-spin Co^{III}, Z. Naturforsch. 65b (2010) 295–303.
[20] B.J. Kennedy, K.S. Murray, Magnetic properties and zero-field splitting in high-spin manganese(III) complexes. 1. Mononuclear and polynuclear Schiff-base chelates, Inorg. Chem. 24 (1985) 1552–1557.

Appendix C: structural information files

CIF for compound **2:**

```
data_shelxl

_audit_creation_method            SHELXL-97
_chemical_name_systematic
;
 ?
;
_chemical_name_common             [NEt4]3[Mn3Zn2(Et-sao)3O(N3)6Cl2]
_chemical_melting_point           ?
_chemical_formula_moiety          ?
_chemical_formula_sum
 'C21 H20 Cl1.60 Mn3 N8 O3 Zn2'
_chemical_formula_weight          784.73

loop_
 _atom_type_symbol
 _atom_type_description
 _atom_type_scat_dispersion_real
 _atom_type_scat_dispersion_imag
 _atom_type_scat_source
 'C'  'C'   0.0033   0.0016
 'International Tables Vol C Tables 4.2.6.8 and 6.1.1.4'
 'H'  'H'   0.0000   0.0000
 'International Tables Vol C Tables 4.2.6.8 and 6.1.1.4'
 'Mn'  'Mn'   0.3368   0.7283
 'International Tables Vol C Tables 4.2.6.8 and 6.1.1.4'
 'N'  'N'   0.0061   0.0033
 'International Tables Vol C Tables 4.2.6.8 and 6.1.1.4'
 'O'  'O'   0.0106   0.0060
 'International Tables Vol C Tables 4.2.6.8 and 6.1.1.4'
 'Zn'  'Zn'   0.2839   1.4301
 'International Tables Vol C Tables 4.2.6.8 and 6.1.1.4'
 'Cl'  'Cl'   0.1484   0.1585
 'International Tables Vol C Tables 4.2.6.8 and 6.1.1.4'

_symmetry_cell_setting            ?
_symmetry_space_group_name_H-M    ?

loop_
 _symmetry_equiv_pos_as_xyz
 'x, y, z'
 'x, -y, z+1/2'
 'x+1/2, y+1/2, z'
 'x+1/2, -y+1/2, z+1/2'

_cell_length_a                    23.1510(15)
_cell_length_b                    13.4470(17)
_cell_length_c                    22.3940(17)
_cell_angle_alpha                 90.000(8)
_cell_angle_beta                  101.193(9)
_cell_angle_gamma                 90.000(8)
_cell_volume                      6838.9(11)
_cell_formula_units_Z             10
_cell_measurement_temperature     293(2)
_exptl_crystal_density_meas       ?
_exptl_crystal_density_diffrn     1.905
_exptl_crystal_density_method     'not measured'
_exptl_crystal_F_000              3882
_exptl_absorpt_coefficient_mu     3.271
_exptl_absorpt_correction_type    ?
_exptl_absorpt_correction_T_min   ?
_exptl_absorpt_correction_T_max   ?
_exptl_absorpt_process_details    ?

_exptl_special_details
;
 ?
;

_diffrn_ambient_temperature       293(2)
_diffrn_radiation_wavelength      0.71073
_diffrn_radiation_type            MoK\a
_diffrn_radiation_source          'fine-focus sealed tube'
_diffrn_radiation_monochromator   graphite
_diffrn_measurement_device_type   ?
_diffrn_measurement_method        ?
_diffrn_detector_area_resol_mean  ?
_diffrn_standards_number          ?
_diffrn_standards_interval_count  ?
_diffrn_standards_interval_time   ?
_diffrn_standards_decay_%         ?
_diffrn_reflns_number             122359
_diffrn_reflns_av_R_equivalents   0.1905
_diffrn_reflns_av_sigmaI/netI     0.0794
_diffrn_reflns_limit_h_min        -33
_diffrn_reflns_limit_h_max        33
_diffrn_reflns_limit_k_min        -19
_diffrn_reflns_limit_k_max        19
_diffrn_reflns_limit_l_min        -32
_diffrn_reflns_limit_l_max        32
_diffrn_reflns_theta_min          1.76
_diffrn_reflns_theta_max          31.49
_reflns_number_total              20547
_reflns_number_gt                 16404
_reflns_threshold_expression      >2sigma(I)

_computing_data_collection        ?
_computing_cell_refinement        ?
_computing_data_reduction         ?
_computing_structure_solution     'SHELXS-97 (Sheldrick, 1990)'
_computing_structure_refinement   'SHELXL-97 (Sheldrick, 1997)'
_computing_molecular_graphics     ?
_computing_publication_material   ?

_refine_special_details
;
 Refinement of F^2^ against ALL reflections.  The weighted R-factor wR
and
 goodness of fit S are based on F^2^, conventional R-factors R are based
 on F, with F set to zero for negative F^2^. The threshold expression of
 F^2^ > 2sigma(F^2^) is used only for calculating R-factors(gt) etc. and is
 not relevant to the choice of reflections for refinement.  R-factors based
 on F^2^ are statistically about twice as large as those based on F, and R-
 factors based on ALL data will be even larger.
;

_refine_ls_structure_factor_coef  Fsqd
_refine_ls_matrix_type            full
_refine_ls_weighting_scheme       calc
_refine_ls_weighting_details
 'calc w=1/[\s^2^(Fo^2^)+(0.1023P)^2^+40.8915P] where
P=(Fo^2^+2Fc^2^)/3'
_atom_sites_solution_primary      direct
_atom_sites_solution_secondary    difmap
_atom_sites_solution_hydrogens    geom
_refine_ls_hydrogen_treatment     mixed
_refine_ls_extinction_method      none
_refine_ls_extinction_coef        ?
_refine_ls_abs_structure_details
 'Flack H D (1983), Acta Cryst. A39, 876-881'
_refine_ls_abs_structure_Flack    -0.009(13)
_refine_ls_number_reflns          20547
_refine_ls_number_parameters      874
_refine_ls_number_restraints      2
_refine_ls_R_factor_all           0.0962
_refine_ls_R_factor_gt            0.0744
_refine_ls_wR_factor_ref          0.2077
_refine_ls_wR_factor_gt           0.1868
_refine_ls_goodness_of_fit_ref    1.062
_refine_ls_restrained_S_all       1.062
_refine_ls_shift/su_max           0.452
_refine_ls_shift/su_mean          0.013

loop_
 _atom_site_label
 _atom_site_type_symbol
```

_atom_site_fract_x
_atom_site_fract_y
_atom_site_fract_z
_atom_site_U_iso_or_equiv
_atom_site_adp_type
_atom_site_occupancy
_atom_site_symmetry_multiplicity
_atom_site_calc_flag
_atom_site_refinement_flags
_atom_site_disorder_assembly
_atom_site_disorder_group

C82 C -0.2842(6) -0.0649(10) -0.1421(8) 0.043(3) Uani 0.50 1 d P A 1
H82A H -0.2623 -0.1237 -0.1261 0.052 Uiso 0.50 1 calc PR A 1
H82B H -0.2564 -0.0108 -0.1414 0.052 Uiso 0.50 1 calc PR A 1
C84 C -0.349(2) 0.0518(17) -0.1153(14) 0.107(14) Uani 0.50 1 d P A 1
H84A H -0.3646 0.0696 -0.0795 0.128 Uiso 0.50 1 calc PR A 1
H84B H -0.3837 0.0375 -0.1462 0.128 Uiso 0.50 1 calc PR A 1
C106 C -0.3331(17) 0.1405(13) -0.1334(12) 0.098(10) Uani 0.50 1 d P A 1
H10A H -0.3669 0.1834 -0.1420 0.147 Uiso 0.50 1 calc PR A 1
H10B H -0.3170 0.1326 -0.1695 0.147 Uiso 0.50 1 calc PR A 1
H10C H -0.3040 0.1693 -0.1018 0.147 Uiso 0.50 1 calc PR A 1
C102 C -0.2844(9) -0.0221(19) -0.0386(8) 0.059(4) Uani 0.50 1 d P A 1
H10D H -0.2650 -0.0848 -0.0262 0.071 Uiso 0.50 1 calc PR A 1
H10E H -0.2543 0.0250 -0.0448 0.071 Uiso 0.50 1 calc PR A 1
C103 C -0.3121(10) 0.0144(18) 0.0109(9) 0.068(6) Uani 0.50 1 d P A 1
H10F H -0.2827 0.0217 0.0473 0.102 Uiso 0.50 1 calc PR A 1
H10G H -0.3414 -0.0323 0.0180 0.102 Uiso 0.50 1 calc PR A 1
H10H H -0.3303 0.0776 -0.0003 0.102 Uiso 0.50 1 calc PR A 1
C94 C -0.3675(9) -0.1187(14) -0.0959(9) 0.058(5) Uani 0.50 1 d P A 1
H94A H -0.3975 -0.1192 -0.1328 0.069 Uiso 0.50 1 calc PR A 1
H94B H -0.3871 -0.1031 -0.0626 0.069 Uiso 0.50 1 calc PR A 1
C85 C -0.3439(10) -0.2233(15) -0.0860(12) 0.071(6) Uani 0.50 1 d P A 1
H85A H -0.3757 -0.2679 -0.0832 0.107 Uiso 0.50 1 calc PR A 1
H85B H -0.3150 -0.2260 -0.0490 0.107 Uiso 0.50 1 calc PR A 1
H85C H -0.3262 -0.2426 -0.1196 0.107 Uiso 0.50 1 calc PR A 1
C83 C -0.3161(7) -0.0851(14) -0.2101(9) 0.056(4) Uani 0.50 1 d P A 1
H83A H -0.2873 -0.1015 -0.2341 0.083 Uiso 0.50 1 calc PR A 1
H83B H -0.3372 -0.0266 -0.2264 0.083 Uiso 0.50 1 calc PR A 1
H83C H -0.3432 -0.1395 -0.2111 0.083 Uiso 0.50 1 calc PR A 1
C91 C -0.4079(8) -0.0270(19) -0.0349(8) 0.063(5) Uani 0.50 1 d P A 2
H91A H -0.4482 -0.0428 -0.0345 0.095 Uiso 0.50 1 calc PR A 2
H91B H -0.4022 0.0436 -0.0308 0.095 Uiso 0.50 1 calc PR A 2
H91C H -0.3828 -0.0601 -0.0017 0.095 Uiso 0.50 1 calc PR A 2
C90 C -0.3932(5) -0.0599(12) -0.0925(7) 0.038(3) Uani 0.50 1 d P A 2
H90A H -0.4202 -0.0283 -0.1256 0.046 Uiso 0.50 1 calc PR A 2
H90B H -0.3999 -0.1311 -0.0962 0.046 Uiso 0.50 1 calc PR A 2
C87 C -0.3250(9) -0.0849(15) -0.1623(7) 0.058(4) Uani 0.50 1 d P A 2
H87A H -0.3286 -0.1565 -0.1591 0.069 Uiso 0.50 1 calc PR A 2
H87B H -0.3579 -0.0616 -0.1926 0.069 Uiso 0.50 1 calc PR A 2
C100 C -0.2835(9) -0.0822(18) -0.0515(9) 0.060(5) Uani 0.50 1 d P A 2
H10I H -0.2456 -0.0544 -0.0551 0.072 Uiso 0.50 1 calc PR A 2
H10J H -0.2920 -0.0589 -0.0132 0.072 Uiso 0.50 1 calc PR A 2
C101 C -0.2762(12) -0.1925(18) -0.0468(11) 0.077(6) Uani 0.50 1 d P A 2
H10K H -0.2449 -0.2084 -0.0133 0.115 Uiso 0.50 1 calc PR A 2
H10L H -0.2668 -0.2179 -0.0839 0.115 Uiso 0.50 1 calc PR A 2
H10M H -0.3122 -0.2222 -0.0403 0.115 Uiso 0.50 1 calc PR A 2
C104 C -0.2697(8) -0.0621(15) -0.1832(8) 0.053(4) Uani 0.50 1 d P A 2
H10N H -0.2704 -0.0928 -0.2220 0.080 Uiso 0.50 1 calc PR A 2
H10O H -0.2368 -0.0872 -0.1542 0.080 Uiso 0.50 1 calc PR A 2
H10P H -0.2658 0.0086 -0.1869 0.080 Uiso 0.50 1 calc PR A 2
C107 C -0.3202(13) 0.076(2) -0.089(4) 0.32(6) Uani 0.50 1 d P A 2
H10Q H -0.3358 0.1000 -0.0545 0.381 Uiso 0.50 1 calc PR A 2
H10R H -0.2801 0.0994 -0.0871 0.381 Uiso 0.50 1 calc PR A 2
C105 C -0.3605(6) 0.095(5) -0.150(3) 0.27(4) Uani 0.50 1 d P A 2
H10S H -0.3640 0.1658 -0.1574 0.405 Uiso 0.50 1 calc PR A 2
H10T H -0.3987 0.0679 -0.1499 0.405 Uiso 0.50 1 calc PR A 2
H10U H -0.3443 0.0646 -0.1820 0.405 Uiso 0.50 1 calc PR A 2
Zn1 Zn -0.03763(3) -0.29653(5) -0.22666(3) 0.02462(13) Uani 1 1 d . . .
Zn2 Zn -0.13042(3) -0.16758(5) -0.48670(3) 0.02598(14) Uani 1 1 d . . .
Mn3 Mn -0.04342(3) -0.34323(6) -0.38440(3) 0.02203(15) Uani 1 1 d . . .
Mn4 Mn -0.04414(4) -0.11210(6) -0.34125(3) 0.02253(15) Uani 1 1 d . . .
Mn5 Mn -0.16062(4) -0.24916(6) -0.34442(4) 0.02403(16) Uani 1 1 d . . .
Cl6 Cl -0.16032(7) -0.11227(12) -0.58232(6) 0.0327(3) Uani 1 1 d . . .
Cl7 Cl -0.00095(9) -0.34210(13) -0.12995(7) 0.0423(4) Uani 1 1 d . . .
O42 O 0.02190(17) -0.1606(3) -0.37399(18) 0.0255(7) Uani 1 1 d . . .
O52 O -0.08184(18) -0.2363(3) -0.35405(18) 0.0234(7) Uani 1 1 d . . .
N49 N -0.1251(2) -0.2831(4) -0.2415(2) 0.0276(9) Uani 1 1 d . . .
O41 O -0.11473(17) -0.4175(3) -0.40018(18) 0.0280(8) Uani 1 1 d . . .
N39 N -0.1116(2) -0.0646(4) -0.3049(2) 0.0257(9) Uani 1 1 d . . .
N38 N -0.1550(2) -0.3943(4) -0.3655(2) 0.0264(9) Uani 1 1 d . . .
O33 O -0.00337(19) -0.4457(3) -0.41607(19) 0.0300(8) Uani 1 1 d . . .
O40 O -0.16436(17) -0.1110(3) -0.32487(19) 0.0277(8) Uani 1 1 d . . .
O32 O -0.0111(2) 0.0146(3) -0.33122(19) 0.0299(8) Uani 1 1 d . . .
N37 N 0.0306(2) -0.2627(3) -0.3719(2) 0.0244(8) Uani 1 1 d . . .
O31 O -0.23770(18) -0.2711(4) -0.3349(2) 0.0328(9) Uani 1 1 d . . .
N50 N -0.1512(2) -0.2573(4) -0.2035(2) 0.0305(10) Uani 1 1 d . . .
C26 C -0.1656(3) 0.0376(5) -0.2449(3) 0.0339(12) Uani 1 1 d . . .
H26A H -0.1937 -0.0156 -0.2535 0.041 Uiso 1 1 d R . .
H26B H -0.1560 0.0486 -0.2018 0.041 Uiso 1 1 d R . .
N43 N -0.0984(2) -0.0534(4) -0.4333(2) 0.0287(9) Uani 1 1 d . . .
N47 N 0.0089(2) -0.4707(4) -0.2662(2) 0.0276(9) Uani 1 1 d . . .
C19 C 0.0307(3) 0.1462(4) -0.2707(3) 0.0334(12) Uani 1 1 d . . .
H19 H 0.0597 0.1524 -0.2958 0.040 Uiso 1 1 d R . .
N44 N -0.1321(3) 0.0168(4) -0.4317(2) 0.0348(11) Uani 1 1 d . . .
N46 N -0.0190(3) -0.3994(4) -0.2851(2) 0.0314(10) Uani 1 1 d . . .
C29 C -0.1114(3) 0.0099(4) -0.2679(3) 0.0293(11) Uani 1 1 d . . .
C8 C -0.2337(3) -0.4487(5) -0.3188(3) 0.0322(12) Uani 1 1 d . . .
C15 C -0.0584(3) 0.0704(4) -0.2499(3) 0.0303(11) Uani 1 1 d . . .
C13 C -0.2589(3) -0.5307(6) -0.2939(3) 0.0366(14) Uani 1 1 d . . .
H13 H -0.2452 -0.5968 -0.2994 0.044 Uiso 1 1 d R . .
C23 C 0.0679(3) -0.5709(5) -0.3996(3) 0.0375(13) Uani 1 1 d . . .
H23 H 0.0388 -0.6185 -0.4178 0.045 Uiso 1 1 d R . .
C34 C 0.0848(2) -0.2940(5) -0.3657(3) 0.0293(11) Uani 1 1 d . . .
C30 C -0.1878(2) -0.4672(5) -0.3537(3) 0.0294(11) Uani 1 1 d . . .
C11 C -0.3235(3) -0.4247(7) -0.2522(3) 0.0435(17) Uani 1 1 d . . .
H11 H -0.3536 -0.4161 -0.2285 0.052 Uiso 1 1 d R . .
C12 C -0.3027(3) -0.5188(6) -0.2611(3) 0.0428(16) Uani 1 1 d . . .
H12 H -0.3192 -0.5753 -0.2442 0.051 Uiso 1 1 d R . .
C20 C 0.0518(3) -0.4697(4) -0.3947(3) 0.0297(11) Uani 1 1 d . . .
N51 N -0.1784(4) -0.2353(6) -0.1681(3) 0.0555(18) Uani 1 1 d . . .
C18 C 0.0328(3) 0.2097(5) -0.2222(3) 0.0419(15) Uani 1 1 d . . .
H18 H 0.0635 0.2585 -0.2127 0.050 Uiso 1 1 d R . .
C10 C -0.3012(3) -0.3432(6) -0.2772(3) 0.0394(15) Uani 1 1 d . . .
H10 H -0.3168 -0.2783 -0.2721 0.047 Uiso 1 1 d R . .
C14 C -0.0132(2) 0.0735(4) -0.2845(3) 0.0274(10) Uani 1 1 d . . .
C17 C -0.0084(4) 0.2025(5) -0.1848(3) 0.0447(16) Uani 1 1 d . . .
H17 H -0.0060 0.2465 -0.1506 0.054 Uiso 1 1 d R . .
C25 C -0.1939(4) 0.1316(8) -0.2755(4) 0.056(2) Uani 1 1 d . . .
H25A H -0.2287 0.1466 -0.2598 0.067 Uiso 1 1 d R . .
H25B H -0.2044 0.1216 -0.3187 0.067 Uiso 1 1 d R . .
H25C H -0.1667 0.1859 -0.2670 0.067 Uiso 1 1 d R . .
N48 N 0.0352(3) -0.5419(5) -0.2487(3) 0.0482(15) Uani 1 1 d . . .
C16 C -0.0540(3) 0.1351(5) -0.1993(3) 0.0353(12) Uani 1 1 d . . .
H16 H -0.0825 0.1318 -0.1735 0.042 Uiso 1 1 d R . .
C35 C 0.1338(3) -0.2204(6) -0.3576(4) 0.0396(14) Uani 1 1 d . . .
H35A H 0.1197 -0.1568 -0.3470 0.048 Uiso 1 1 d R . .
H35B H 0.1647 -0.2427 -0.3254 0.048 Uiso 1 1 d R . .
C21 C 0.0962(3) -0.4016(5) -0.3696(3) 0.0345(12) Uani 1 1 d . . .
C27 C -0.1749(3) -0.5712(5) -0.3750(4) 0.0441(17) Uani 1 1 d . . .
H27A H -0.2089 -0.6124 -0.3756 0.053 Uiso 1 1 d R . .
H27B H -0.1664 -0.5675 -0.4152 0.053 Uiso 1 1 d R . .
C24 C 0.1249(4) -0.6025(6) -0.3806(4) 0.054(2) Uani 1 1 d . . .
H24 H 0.1343 -0.6714 -0.3846 0.065 Uiso 1 1 d R . .
C36 C 0.1586(3) -0.2112(7) -0.4156(4) 0.052(2) Uani 1 1 d . . .
H36A H 0.1904 -0.1641 -0.4101 0.063 Uiso 1 1 d R . .
H36B H 0.1276 -0.1890 -0.4477 0.063 Uiso 1 1 d R . .
H36C H 0.1726 -0.2749 -0.4262 0.063 Uiso 1 1 d R . .
N45 N -0.1592(4) 0.0855(5) -0.4282(4) 0.0552(17) Uani 1 1 d . . .
C22 C 0.1539(3) -0.4378(7) -0.3502(5) 0.063(3) Uani 1 1 d . . .
H22 H 0.1853 -0.3931 -0.3338 0.075 Uiso 1 1 d R . .
C9 C -0.2556(2) -0.3527(5) -0.3107(2) 0.0301(11) Uani 1 1 d . . .
C28 C -0.1238(4) -0.6198(6) -0.3328(5) 0.063(2) Uani 1 1 d . . .
H28A H -0.1176 -0.6850 -0.3479 0.075 Uiso 1 1 d R . .
H28B H -0.1317 -0.6250 -0.2924 0.075 Uiso 1 1 d R . .
H28C H -0.0892 -0.5801 -0.3320 0.075 Uiso 1 1 d R . .
N54 N 0.0501(2) -0.1556(4) -0.2247(2) 0.0350(12) Uani 1 1 d . . .
N57 N -0.0235(3) -0.2510(4) -0.5053(2) 0.0321(10) Uani 1 1 d . . .
N56 N -0.0661(2) -0.2665(4) -0.4823(2) 0.0271(9) Uani 1 1 d . . .
N53 N -0.0011(2) -0.1680(4) -0.2447(2) 0.0274(9) Uani 1 1 d . . .
N61 N -0.4706(3) -0.5815(4) -0.0144(3) 0.0374(12) Uani 1 1 d . . .
N59 N -0.1941(2) -0.2245(4) -0.4489(2) 0.0300(10) Uani 1 1 d . . .
N60 N -0.2403(3) -0.2562(6) -0.4721(3) 0.0459(15) Uani 1 1 d . . .
C64 C -0.5262(3) -0.5334(5) -0.0479(3) 0.0334(12) Uani 1 1 d . . .
H64A H -0.5537 -0.5270 -0.0210 0.040 Uiso 1 1 d R . .
H64B H -0.5169 -0.4687 -0.0614 0.040 Uiso 1 1 d R . .
C65 C -0.5568(3) -0.5898(6) -0.1025(3) 0.0435(15) Uani 1 1 d . . .
H65A H -0.5917 -0.5550 -0.1217 0.052 Uiso 1 1 d R . .
H65B H -0.5674 -0.6547 -0.0902 0.052 Uiso 1 1 d R . .
H65C H -0.5306 -0.5963 -0.1306 0.052 Uiso 1 1 d R . .
C62 C -0.4825(4) -0.6846(5) 0.0088(3) 0.0404(15) Uani 1 1 d . . .
H62A H -0.4974 -0.7275 -0.0250 0.048 Uiso 1 1 d R . .
H62B H -0.4465 -0.7117 0.0316 0.048 Uiso 1 1 d R . .
C67 C -0.4456(3) -0.5146(6) 0.0396(3) 0.0425(15) Uani 1 1 d . . .
H67A H -0.4364 -0.4504 0.0251 0.051 Uiso 1 1 d R . .
H67B H -0.4743 -0.5075 0.0650 0.051 Uiso 1 1 d R . .
C63 C -0.5277(5) -0.6868(6) 0.0491(4) 0.051(2) Uani 1 1 d . . .
H63A H -0.5328 -0.7538 0.0620 0.062 Uiso 1 1 d R . .
H63B H -0.5648 -0.6617 0.0275 0.062 Uiso 1 1 d R . .
H63C H -0.5139 -0.6458 0.0840 0.062 Uiso 1 1 d R . .
N58 N 0.0175(3) -0.2399(6) -0.5256(3) 0.0494(16) Uani 1 1 d . . .
C66 C -0.4268(3) -0.5951(6) -0.0564(4) 0.0457(16) Uani 1 1 d . . .
H66A H -0.3907 -0.6226 -0.0340 0.055 Uiso 1 1 d R . .
H66B H -0.4430 -0.6390 -0.0891 0.055 Uiso 1 1 d R . .

N55 N 0.0986(3) -0.1423(7) -0.2054(4) 0.064(2) Uani 1 1 d . . .
N70 N -0.1622(4) -0.5249(5) -0.0949(3) 0.0554(18) Uani 1 1 d . . .
C74 C -0.1221(3) -0.5081(6) -0.0343(3) 0.0443(16) Uani 1 1 d . . .
H74A H -0.1416 -0.5288 -0.0023 0.053 Uiso 1 1 d R . .
H74B H -0.0867 -0.5463 -0.0324 0.053 Uiso 1 1 d R . .
C71 C -0.1018(4) -0.4039(6) -0.0197(3) 0.0458(16) Uani 1 1 d . . .
H71A H -0.0765 -0.4012 0.0197 0.055 Uiso 1 1 d R . .
H71B H -0.1357 -0.3629 -0.0199 0.055 Uiso 1 1 d R . .
H71C H -0.0808 -0.3803 -0.0499 0.055 Uiso 1 1 d R . .
C69 C -0.3911(5) -0.5516(8) 0.0797(4) 0.066(3) Uani 1 1 d . . .
H69A H -0.3788 -0.5054 0.1124 0.079 Uiso 1 1 d R . .
H69B H -0.3607 -0.5582 0.0563 0.079 Uiso 1 1 d R . .
H69C H -0.3986 -0.6152 0.0962 0.079 Uiso 1 1 d R . .
C75 C -0.1819(5) -0.6345(6) -0.0961(4) 0.060(2) Uani 1 1 d . . .
H75A H -0.1488 -0.6762 -0.0984 0.073 Uiso 1 1 d R . .
H75B H -0.1960 -0.6494 -0.0595 0.073 Uiso 1 1 d R . .
N79 N -0.2872(5) -0.2834(11) -0.4929(4) 0.096(4) Uani 1 1 d . . .
C68 C -0.4102(5) -0.4998(8) -0.0853(6) 0.075(3) Uani 1 1 d . . .
H68A H -0.3827 -0.5146 -0.1111 0.090 Uiso 1 1 d R . .
H68B H -0.3927 -0.4541 -0.0541 0.090 Uiso 1 1 d R . .
H68C H -0.4450 -0.4705 -0.1092 0.090 Uiso 1 1 d R . .
C78 C 0.1678(4) -0.5353(8) -0.3556(6) 0.077(4) Uani 1 1 d . . .
H78 H 0.2074 -0.5573 -0.3407 0.093 Uiso 1 1 d R . .
C72 C -0.1358(7) -0.5002(8) -0.1465(4) 0.084(4) Uani 1 1 d . . .
H72A H -0.1655 -0.5047 -0.1829 0.101 Uiso 1 1 d R . .
H72B H -0.1205 -0.4337 -0.1422 0.101 Uiso 1 1 d R . .
C77 C -0.2172(5) -0.4560(9) -0.0992(7) 0.087(4) Uani 1 1 d . . .
H77A H -0.2053 -0.3875 -0.0987 0.104 Uiso 1 1 d R . .
H77B H -0.2455 -0.4692 -0.1358 0.104 Uiso 1 1 d R . .
C76 C -0.2269(8) -0.6648(8) -0.1487(7) 0.104(6) Uani 1 1 d . . .
H76A H -0.2353 -0.7342 -0.1449 0.124 Uiso 1 1 d R . .
H76B H -0.2145 -0.6535 -0.1866 0.124 Uiso 1 1 d R . .
H76C H -0.2618 -0.6266 -0.1477 0.124 Uiso 1 1 d R . .
C73 C -0.0834(9) -0.5728(10) -0.1522(9) 0.130(8) Uani 1 1 d . . .
H73A H -0.0682 -0.5532 -0.1873 0.156 Uiso 1 1 d R . .
H73B H -0.0977 -0.6399 -0.1573 0.156 Uiso 1 1 d R . .
H73C H -0.0527 -0.5689 -0.1167 0.156 Uiso 1 1 d R . .
N80 N -0.3285(3) -0.0380(6) -0.1011(3) 0.0469(15) Uani 1 1 d . . .
C86 C -0.2493(6) -0.4687(14) -0.0461(12) 0.138(8) Uani 1 1 d . . .
H86A H -0.2827 -0.4226 -0.0520 0.165 Uiso 1 1 d R . .
H86B H -0.2230 -0.4543 -0.0072 0.165 Uiso 1 1 d R . .
H86C H -0.2637 -0.5372 -0.0458 0.165 Uiso 1 1 d R . .

loop_
 _atom_site_aniso_label
 _atom_site_aniso_U_11
 _atom_site_aniso_U_22
 _atom_site_aniso_U_33
 _atom_site_aniso_U_23
 _atom_site_aniso_U_13
 _atom_site_aniso_U_12
C82 0.023(6) 0.031(6) 0.077(11) 0.002(6) 0.014(7) -0.002(5)
C84 0.22(4) 0.044(11) 0.091(17) 0.016(11) 0.11(2) 0.043(17)
C106 0.19(3) 0.027(8) 0.088(16) 0.030(9) 0.054(19) 0.030(12)
C102 0.058(11) 0.075(13) 0.050(9) -0.001(9) 0.024(8) -0.015(10)
C103 0.071(13) 0.086(14) 0.049(9) -0.024(9) 0.021(9) -0.029(11)
C94 0.059(10) 0.064(11) 0.061(10) -0.002(8) 0.036(9) -0.028(9)
C85 0.059(11) 0.055(10) 0.106(17) 0.001(11) 0.032(12) 0.007(9)
C83 0.039(8) 0.062(10) 0.071(11) -0.015(8) 0.023(8) -0.003(7)
C91 0.045(9) 0.101(15) 0.050(9) -0.005(9) 0.025(8) 0.002(9)
C90 0.018(5) 0.052(8) 0.044(7) -0.005(6) 0.008(5) -0.002(5)
C87 0.064(11) 0.069(11) 0.038(7) 0.005(7) 0.005(7) -0.027(9)
C100 0.056(11) 0.068(12) 0.053(10) -0.009(9) 0.000(8) 0.005(10)
C101 0.089(16) 0.081(14) 0.067(12) 0.022(11) 0.031(12) -0.005(12)
C104 0.043(8) 0.068(10) 0.054(9) 0.000(8) 0.021(8) -0.006(7)
C107 0.064(17) 0.039(12) 0.89(17) -0.10(4) 0.19(5) -0.026(12)
C105 -0.014(4) 0.43(8) 0.37(7) -0.33(7) -0.020(12) -0.001(13)
Zn1 0.0244(3) 0.0274(3) 0.0225(3) -0.0009(2) 0.0057(2) -0.0050(2)
Zn2 0.0253(3) 0.0322(3) 0.0197(3) 0.0010(2) 0.0027(2) -0.0077(2)
Mn3 0.0198(3) 0.0260(3) 0.0207(3) -0.0028(3) 0.0051(3) -0.0091(3)
Mn4 0.0225(4) 0.0241(3) 0.0213(3) -0.0017(3) 0.0050(3) -0.0076(3)
Mn5 0.0193(3) 0.0314(4) 0.0219(3) -0.0004(3) 0.0051(3) -0.0081(3)
Cl6 0.0312(7) 0.0432(7) 0.0224(6) 0.0048(5) 0.0020(5) -0.0012(6)
Cl7 0.0591(10) 0.0437(8) 0.0229(6) 0.0004(5) 0.0049(6) 0.0173(7)
O42 0.0233(18) 0.0245(17) 0.0303(18) 0.0011(14) 0.0090(15) -0.0063(14)
O52 0.0226(17) 0.0239(15) 0.0252(16) -0.0018(13) 0.0085(14) -
0.0108(13)
N49 0.023(2) 0.037(2) 0.022(2) 0.0009(18) 0.0024(17) -0.0078(19)
O41 0.0202(17) 0.036(2) 0.0295(18) -0.0073(15) 0.0084(15) -0.0135(15)
N39 0.024(2) 0.030(2) 0.0220(19) -0.0018(16) 0.0010(16) -0.0059(17)
N38 0.024(2) 0.034(2) 0.0211(19) -0.0007(16) 0.0051(17) -0.0175(18)
O33 0.0254(19) 0.0299(18) 0.034(2) -0.0078(16) 0.0039(16) -0.0052(15)
O40 0.0169(17) 0.036(2) 0.0293(18) -0.0035(15) 0.0035(15) -0.0029(15)
O32 0.033(2) 0.0242(17) 0.033(2) -0.0029(15) 0.0088(17) -0.0111(15)
N37 0.020(2) 0.028(2) 0.024(2) -0.0026(16) 0.0012(17) -0.0074(16)
O31 0.0195(18) 0.045(2) 0.035(2) 0.0016(18) 0.0086(16) -0.0069(17)
N50 0.031(2) 0.038(3) 0.021(2) 0.0028(18) 0.0005(19) -0.002(2)
C26 0.027(3) 0.043(3) 0.032(3) -0.007(2) 0.006(2) -0.002(2)
N43 0.031(2) 0.030(2) 0.023(2) -0.0005(17) 0.0006(18) -0.0065(19)
N47 0.022(2) 0.034(2) 0.026(2) 0.0000(18) 0.0039(18) -0.0049(18)
C19 0.028(3) 0.026(2) 0.041(3) -0.004(2) -0.004(2) -0.003(2)
N44 0.035(3) 0.038(3) 0.029(2) 0.003(2) 0.001(2) -0.001(2)
N46 0.039(3) 0.034(2) 0.021(2) -0.0030(17) 0.009(2) -0.003(2)
C29 0.033(3) 0.031(3) 0.023(2) -0.0017(19) 0.004(2) -0.003(2)
C8 0.024(3) 0.047(3) 0.025(2) 0.000(2) 0.005(2) -0.017(2)
C15 0.031(3) 0.031(3) 0.026(2) -0.005(2) -0.004(2) 0.004(2)
C13 0.029(3) 0.053(4) 0.028(3) 0.002(2) 0.005(2) -0.023(3)
C23 0.036(3) 0.035(3) 0.041(3) -0.005(2) 0.004(3) 0.001(2)
C34 0.019(2) 0.037(3) 0.032(3) -0.006(2) 0.003(2) -0.003(2)
C30 0.017(2) 0.039(3) 0.032(3) -0.004(2) 0.004(2) -0.014(2)
C11 0.021(3) 0.084(5) 0.028(3) 0.008(3) 0.010(2) -0.011(3)
C12 0.025(3) 0.066(5) 0.038(3) 0.009(3) 0.007(3) -0.020(3)
C20 0.032(3) 0.031(3) 0.027(2) -0.005(2) 0.007(2) -0.003(2)
N51 0.058(4) 0.073(5) 0.039(3) -0.008(3) 0.020(3) 0.003(4)
C18 0.031(3) 0.040(3) 0.049(4) -0.013(3) -0.007(3) -0.010(3)
C10 0.020(2) 0.070(5) 0.030(3) 0.002(3) 0.008(2) -0.005(3)
C14 0.024(2) 0.025(2) 0.030(2) -0.0019(19) -0.004(2) -0.0032(19)
C17 0.050(4) 0.039(3) 0.042(3) -0.014(3) 0.001(3) -0.005(3)
C25 0.031(3) 0.069(5) 0.062(5) 0.000(4) -0.003(3) 0.013(3)
N48 0.058(4) 0.039(3) 0.047(3) 0.003(2) 0.008(3) 0.007(3)
C16 0.030(3) 0.042(3) 0.031(3) -0.009(2) -0.002(2) -0.004(2)
C35 0.020(3) 0.047(3) 0.054(4) -0.014(3) 0.011(3) -0.014(2)
C21 0.026(3) 0.035(3) 0.040(3) -0.009(2) 0.000(2) 0.000(2)
C27 0.045(4) 0.038(3) 0.055(4) -0.012(3) 0.022(3) -0.027(3)
C24 0.046(4) 0.041(4) 0.067(5) -0.012(3) -0.011(4) 0.010(3)
C36 0.026(3) 0.070(5) 0.063(5) -0.012(4) 0.016(3) -0.018(3)
N45 0.061(4) 0.045(3) 0.059(4) 0.004(3) 0.009(4) 0.009(3)
C22 0.023(3) 0.057(5) 0.097(7) -0.032(5) -0.016(4) 0.010(3)
C9 0.019(2) 0.049(3) 0.022(2) 0.003(2) 0.004(2) -0.012(2)
C28 0.058(5) 0.038(4) 0.093(7) 0.005(4) 0.016(5) -0.010(4)
N54 0.033(3) 0.049(3) 0.026(2) 0.004(2) 0.013(2) -0.018(2)
N57 0.034(3) 0.040(3) 0.022(2) 0.0000(18) 0.006(2) -0.010(2)
N56 0.021(2) 0.036(2) 0.023(2) 0.0033(17) 0.0009(17) -0.0035(18)
N53 0.026(2) 0.029(2) 0.027(2) 0.0021(17) 0.0024(18) -0.0097(18)
N61 0.035(3) 0.039(3) 0.034(3) -0.009(2) -0.003(2) 0.011(2)
N59 0.027(2) 0.040(3) 0.022(2) 0.0022(18) 0.0012(18) -0.012(2)
N60 0.042(3) 0.066(4) 0.027(2) -0.002(2) 0.002(2) -0.026(3)
C64 0.031(3) 0.035(3) 0.033(3) -0.002(2) 0.004(2) 0.014(2)
C65 0.042(4) 0.048(4) 0.037(3) -0.003(3) -0.003(3) 0.009(3)
C62 0.056(4) 0.031(3) 0.032(3) -0.001(2) 0.004(3) 0.021(3)
C67 0.036(3) 0.043(3) 0.046(4) -0.013(3) 0.000(3) 0.010(3)
C63 0.076(6) 0.037(3) 0.045(4) 0.001(3) 0.020(4) 0.015(4)
N58 0.041(3) 0.074(4) 0.038(3) 0.008(3) 0.020(3) -0.012(3)
C66 0.039(4) 0.047(4) 0.054(4) -0.010(3) 0.014(3) 0.013(3)
N55 0.035(3) 0.097(6) 0.059(4) 0.030(4) 0.004(3) -0.027(4)
N70 0.073(5) 0.043(3) 0.041(3) 0.016(3) -0.012(3) 0.000(3)
C74 0.038(3) 0.056(4) 0.035(3) 0.011(3) -0.003(3) -0.003(3)
C71 0.042(4) 0.060(4) 0.034(3) 0.001(3) 0.004(3) -0.005(3)
C69 0.062(5) 0.067(6) 0.054(5) -0.020(4) -0.028(4) 0.026(5)
C75 0.067(6) 0.040(4) 0.061(5) 0.018(3) -0.021(4) 0.000(4)
N79 0.066(6) 0.158(11) 0.057(5) -0.009(6) -0.005(4) -0.072(7)
C68 0.064(6) 0.065(6) 0.108(9) 0.004(6) 0.047(6) 0.003(5)
C78 0.037(4) 0.065(6) 0.110(8) -0.031(6) -0.035(5) 0.027(4)
C72 0.163(13) 0.057(5) 0.041(4) -0.003(4) 0.040(6) -0.026(7)
C77 0.047(5) 0.066(6) 0.126(10) 0.016(6) -0.037(6) 0.005(5)
C76 0.128(13) 0.050(6) 0.106(10) 0.024(6) -0.044(9) -0.007(6)
C73 0.180(17) 0.059(7) 0.191(18) -0.044(9) 0.138(16) -0.032(9)
N80 0.031(3) 0.061(4) 0.052(3) -0.005(3) 0.016(3) -0.010(3)
C86 0.046(6) 0.107(12) 0.26(3) 0.008(14) 0.037(11) 0.008(7)

_geom_special_details
;
 All esds (except the esd in the dihedral angle between two l.s. planes)
 are estimated using the full covariance matrix. The cell esds are taken
 into account individually in the estimation of esds in distances, angles
 and torsion angles; correlations between esds in cell parameters are only
 used when they are defined by crystal symmetry. An approximate (isotropic)
 treatment of cell esds is used for estimating esds involving l.s. planes.
;
 loop_
 _geom_bond_atom_site_label_1
 _geom_bond_atom_site_label_2
 _geom_bond_distance
 _geom_bond_site_symmetry_2
 _geom_bond_publ_flag
C82 N80 1.546(16) . ?
C82 C83 1.58(3) . ?
C82 H82A 0.9700 . ?
C82 H82B 0.9700 . ?
C84 N80 1.32(2) . ?
C84 C106 1.33(3) . ?
C84 H84A 0.9700 . ?
C84 H84B 0.9700 . ?
C106 H10A 0.9600 . ?
C106 H10B 0.9600 . ?
C106 H10C 0.9600 . ?
C102 C103 1.47(3) . ?
C102 N80 1.58(2) . ?
C102 H10D 0.9700 . ?
C102 H10E 0.9700 . ?
C103 H10F 0.9600 . ?
C103 H10G 0.9600 . ?
C103 H10H 0.9600 . ?
C94 N80 1.430(16) . ?
C94 C85 1.51(3) . ?
C94 H94A 0.9700 . ?
C94 H94B 0.9700 . ?
C85 H85A 0.9600 . ?
C85 H85B 0.9600 . ?
C85 H85C 0.9600 . ?
C83 H83A 0.9600 . ?
C83 H83B 0.9600 . ?
C83 H83C 0.9600 . ?
C91 C90 1.47(2) . ?
C91 H91A 0.9600 . ?
C91 H91B 0.9600 . ?
C91 H91C 0.9600 . ?
C90 N80 1.575(14) . ?
C90 H90A 0.9700 . ?
C90 H90B 0.9700 . ?
C87 C104 1.48(2) . ?
C87 N80 1.526(19) . ?
C87 H87A 0.9700 . ?
C87 H87B 0.9700 . ?
C100 C101 1.49(3) . ?
C100 N80 1.49(2) . ?
C100 H10I 0.9700 . ?
C100 H10J 0.9700 . ?
C101 H10K 0.9600 . ?
C101 H10L 0.9600 . ?
C101 H10M 0.9600 . ?
C104 H10N 0.9600 . ?
C104 H10O 0.9600 . ?
C104 H10P 0.9600 . ?
C107 C105 1.52(10) . ?
C107 N80 1.57(3) . ?
C107 H10Q 0.9700 . ?
C107 H10R 0.9700 . ?
C105 H10S 0.9600 . ?
C105 H10T 0.9600 . ?
C105 H10U 0.9600 . ?
Zn1 N53 1.999(4) . ?
Zn1 N49 1.996(5) . ?
Zn1 N46 2.009(5) . ?
Zn1 Cl7 2.2523(16) . ?
Zn2 N56 1.986(5) . ?
Zn2 N59 1.989(5) . ?
Zn2 N43 1.998(5) . ?
Zn2 Cl6 2.2456(15) . ?
Mn3 O33 1.875(4) . ?
Mn3 O52 1.885(4) . ?
Mn3 O41 1.903(4) . ?
Mn3 N37 2.000(4) . ?
Mn3 N46 2.312(5) . ?
Mn3 N56 2.386(5) . ?
Mn4 O32 1.863(4) . ?
Mn4 O52 1.881(4) . ?
Mn4 O42 1.933(4) . ?
Mn4 N39 2.002(5) . ?
Mn4 N53 2.324(5) . ?
Mn4 N43 2.334(5) . ?
Mn5 O31 1.861(4) . ?
Mn5 O52 1.886(4) . ?
Mn5 O40 1.915(4) . ?
Mn5 N38 2.019(5) . ?
Mn5 N49 2.337(5) . ?
Mn5 N59 2.341(5) . ?
O42 N37 1.386(6) . ?
N49 N50 1.187(7) . ?
O41 N38 1.361(6) . ?
N39 C29 1.299(7) . ?
N39 O40 1.367(6) . ?
N38 C30 1.298(7) . ?
O33 C20 1.314(7) . ?
O32 C14 1.321(7) . ?
N37 C34 1.306(7) . ?
O31 C9 1.326(7) . ?
N50 N51 1.145(8) . ?
C26 C29 1.493(9) . ?
C26 C25 1.524(11) . ?
C26 H26A 0.9600 . ?
C26 H26B 0.9598 . ?
N43 N44 1.230(8) . ?
N47 N48 1.162(8) . ?
N47 N46 1.186(7) . ?
C19 C18 1.374(9) . ?
C19 C14 1.401(8) . ?
C19 H19 0.9600 . ?
N44 N45 1.126(9) . ?
C29 C15 1.461(8) . ?
C8 C13 1.411(8) . ?
C8 C9 1.412(10) . ?
C8 C30 1.458(8) . ?
C15 C16 1.416(8) . ?
C15 C14 1.421(9) . ?
C13 C12 1.372(10) . ?
C13 H13 0.9600 . ?
C23 C24 1.374(11) . ?
C23 C20 1.421(9) . ?
C23 H23 0.9598 . ?
C34 C21 1.476(9) . ?
C34 C35 1.490(8) . ?
C30 C27 1.525(9) . ?
C11 C10 1.377(10) . ?
C11 C12 1.382(12) . ?
C11 H11 0.9600 . ?
C12 H12 0.9601 . ?
C20 C21 1.409(8) . ?
C18 C17 1.392(12) . ?
C18 H18 0.9599 . ?
C10 C9 1.414(8) . ?
C10 H10 0.9600 . ?
C17 C16 1.381(10) . ?
C17 H17 0.9601 . ?
C25 H25A 0.9600 . ?
C25 H25B 0.9602 . ?
C25 H25C 0.9599 . ?
C16 H16 0.9600 . ?
C35 C36 1.526(11) . ?
C35 H35A 0.9599 . ?
C35 H35B 0.9599 . ?
C21 C22 1.409(9) . ?
C27 C28 1.512(13) . ?
C27 H27A 0.9603 . ?
C27 H27B 0.9600 . ?
C24 C78 1.379(13) . ?
C24 H24 0.9599 . ?
C36 H36A 0.9601 . ?
C36 H36B 0.9600 . ?
C36 H36C 0.9600 . ?
C22 C78 1.362(12) . ?
C22 H22 0.9600 . ?
C28 H28A 0.9600 . ?
C28 H28B 0.9599 . ?
C28 H28C 0.9601 . ?
N54 N55 1.138(9) . ?
N54 N53 1.194(7) . ?
N57 N58 1.138(8) . ?
N57 N56 1.216(7) . ?
N61 C64 1.505(8) . ?
N61 C62 1.525(9) . ?
N61 C66 1.522(9) . ?
N61 C67 1.527(9) . ?
N59 N60 1.176(8) . ?
N60 N79 1.156(10) . ?
C64 C65 1.495(9) . ?
C64 H64A 0.9603 . ?
C64 H64B 0.9601 . ?
C65 H65A 0.9600 . ?
C65 H65B 0.9600 . ?
C65 H65C 0.9596 . ?
C62 C63 1.510(12) . ?
C62 H62A 0.9599 . ?
C62 H62B 0.9601 . ?
C67 C69 1.485(11) . ?
C67 H67A 0.9600 . ?
C67 H67B 0.9596 . ?
C63 H63A 0.9600 . ?
C63 H63B 0.9602 . ?
C63 H63C 0.9599 . ?
C66 C68 1.518(13) . ?
C66 H66A 0.9600 . ?
C66 H66B 0.9599 . ?
N70 C72 1.448(12) . ?
N70 C74 1.505(10) . ?
N70 C75 1.541(11) . ?
N70 C77 1.564(14) . ?
C74 C71 1.494(11) . ?
C74 H74A 0.9600 . ?
C74 H74B 0.9601 . ?
C71 H71A 0.9600 . ?
C71 H71B 0.9600 . ?
C71 H71C 0.9601 . ?
C69 H69A 0.9602 . ?
C69 H69B 0.9601 . ?
C69 H69C 0.9600 . ?
C75 C76 1.472(15) . ?
C75 H75A 0.9599 . ?
C75 H75B 0.9599 . ?
C68 H68A 0.9600 . ?
C68 H68B 0.9601 . ?
C68 H68C 0.9602 . ?
C78 H78 0.9599 . ?
C72 C73 1.58(2) . ?
C72 H72A 0.9600 . ?
C72 H72B 0.9602 . ?
C77 C86 1.53(3) . ?
C77 H77A 0.9600 . ?
C77 H77B 0.9598 . ?
C76 H76A 0.9600 . ?
C76 H76B 0.9601 . ?
C76 H76C 0.9601 . ?
C73 H73A 0.9599 . ?
C73 H73B 0.9599 . ?
C73 H73C 0.9599 . ?
C86 H86A 0.9801 . ?
C86 H86B 0.9800 . ?
C86 H86C 0.9801 . ?

loop_
 _geom_angle_atom_site_label_1
 _geom_angle_atom_site_label_2
 _geom_angle_atom_site_label_3
 _geom_angle
 _geom_angle_site_symmetry_1
 _geom_angle_site_symmetry_3
 _geom_angle_publ_flag
N80 C82 C83 111.9(11) . . ?
N80 C82 H82A 109.2 . . ?
C83 C82 H82A 109.2 . . ?
N80 C82 H82B 109.2 . . ?
C83 C82 H82B 109.2 . . ?
H82A C82 H82B 107.9 . . ?
N80 C84 C106 142(4) . . ?
N80 C84 H84A 102.0 . . ?
C106 C84 H84A 102.0 . . ?
N80 C84 H84B 101.1 . . ?
C106 C84 H84B 101.1 . . ?
H84A C84 H84B 104.8 . . ?
C84 C106 H10A 110.3 . . ?
C84 C106 H10B 109.5 . . ?
H10A C106 H10B 109.5 . . ?
C84 C106 H10C 108.6 . . ?
H10A C106 H10C 109.5 . . ?
H10B C106 H10C 109.5 . . ?

C103 C102 N80 114.3(17) . . ?
C103 C102 H10D 108.6 . . ?
N80 C102 H10D 108.7 . . ?
C103 C102 H10E 108.7 . . ?
N80 C102 H10E 108.7 . . ?
H10D C102 H10E 107.6 . . ?
C102 C103 H10F 109.5 . . ?
C102 C103 H10G 109.5 . . ?
H10F C103 H10G 109.5 . . ?
C102 C103 H10H 109.4 . . ?
H10F C103 H10H 109.5 . . ?
H10G C103 H10H 109.5 . . ?
N80 C94 C85 120.2(17) . . ?
N80 C94 H94A 107.3 . . ?
C85 C94 H94A 107.3 . . ?
N80 C94 H94B 107.3 . . ?
C85 C94 H94B 107.3 . . ?
H94A C94 H94B 106.9 . . ?
C94 C85 H85A 109.4 . . ?
C94 C85 H85B 109.5 . . ?
H85A C85 H85B 109.5 . . ?
C94 C85 H85C 109.5 . . ?
H85A C85 H85C 109.5 . . ?
H85B C85 H85C 109.5 . . ?
C82 C83 H83A 109.5 . . ?
C82 C83 H83B 109.5 . . ?
H83A C83 H83B 109.5 . . ?
C82 C83 H83C 109.5 . . ?
H83A C83 H83C 109.5 . . ?
H83B C83 H83C 109.5 . . ?
C90 C91 H91A 109.5 . . ?
C90 C91 H91B 109.5 . . ?
H91A C91 H91B 109.5 . . ?
C90 C91 H91C 109.5 . . ?
H91A C91 H91C 109.5 . . ?
H91B C91 H91C 109.5 . . ?
C91 C90 N80 116.1(12) . . ?
C91 C90 H90A 108.3 . . ?
N80 C90 H90A 108.3 . . ?
C91 C90 H90B 108.3 . . ?
N80 C90 H90B 108.3 . . ?
H90A C90 H90B 107.4 . . ?
C104 C87 N80 113.5(14) . . ?
C104 C87 H87A 108.9 . . ?
N80 C87 H87A 108.9 . . ?
C104 C87 H87B 108.9 . . ?
N80 C87 H87B 108.8 . . ?
H87A C87 H87B 107.7 . . ?
C101 C100 N80 120.0(18) . . ?
C101 C100 H10I 107.3 . . ?
N80 C100 H10I 107.3 . . ?
C101 C100 H10J 107.3 . . ?
N80 C100 H10J 107.3 . . ?
H10I C100 H10J 106.9 . . ?
C100 C101 H10K 109.5 . . ?
C100 C101 H10L 109.5 . . ?
H10K C101 H10L 109.5 . . ?
C100 C101 H10M 109.5 . . ?
H10K C101 H10M 109.5 . . ?
H10L C101 H10M 109.5 . . ?
C87 C104 H10N 109.5 . . ?
C87 C104 H10O 109.5 . . ?
H10N C104 H10O 109.5 . . ?
C87 C104 H10P 109.5 . . ?
H10N C104 H10P 109.5 . . ?
H10O C104 H10P 109.5 . . ?
C105 C107 N80 89(4) . . ?
C105 C107 H10Q 113.9 . . ?
N80 C107 H10Q 114.1 . . ?
C105 C107 H10R 114.0 . . ?
N80 C107 H10R 113.6 . . ?
H10Q C107 H10R 110.9 . . ?
C107 C105 H10S 108.8 . . ?
C107 C105 H10T 109.9 . . ?
H10S C105 H10T 109.5 . . ?
C107 C105 H10U 109.8 . . ?
H10S C105 H10U 109.5 . . ?
H10T C105 H10U 109.5 . . ?
N53 Zn1 N49 110.1(2) . . ?
N53 Zn1 N46 108.1(2) . . ?
N49 Zn1 N46 107.1(2) . . ?
N53 Zn1 Cl7 109.51(15) . . ?
N49 Zn1 Cl7 111.46(14) . . ?
N46 Zn1 Cl7 110.53(16) . . ?
N56 Zn2 N59 109.4(2) . . ?
N56 Zn2 N43 107.3(2) . . ?
N59 Zn2 N43 105.1(2) . . ?
N56 Zn2 Cl6 111.04(14) . . ?
N59 Zn2 Cl6 114.61(15) . . ?
N43 Zn2 Cl6 109.03(14) . . ?
O33 Mn3 O52 177.61(18) . . ?
O33 Mn3 O41 91.09(18) . . ?
O52 Mn3 O41 90.81(17) . . ?
O33 Mn3 N37 88.75(19) . . ?
O52 Mn3 N37 89.29(18) . . ?
O41 Mn3 N37 177.25(19) . . ?
O33 Mn3 N46 94.40(19) . . ?
O52 Mn3 N46 86.97(18) . . ?
O41 Mn3 N46 92.78(19) . . ?
N37 Mn3 N46 89.97(19) . . ?
O33 Mn3 N56 90.39(19) . . ?
O52 Mn3 N56 88.09(18) . . ?
O41 Mn3 N56 91.62(17) . . ?
N37 Mn3 N56 85.63(18) . . ?
N46 Mn3 N56 173.43(18) . . ?
O32 Mn4 O52 176.4(2) . . ?
O32 Mn4 O42 91.02(18) . . ?
O52 Mn4 O42 91.15(16) . . ?
O32 Mn4 N39 89.64(19) . . ?
O52 Mn4 N39 88.28(18) . . ?
O42 Mn4 N39 178.09(19) . . ?
O32 Mn4 N53 95.28(18) . . ?
O52 Mn4 N53 87.52(17) . . ?
O42 Mn4 N53 90.93(18) . . ?
N39 Mn4 N53 87.23(19) . . ?
O32 Mn4 N43 86.29(18) . . ?
O52 Mn4 N43 90.66(17) . . ?
O42 Mn4 N43 96.27(18) . . ?
N39 Mn4 N43 85.55(19) . . ?
N53 Mn4 N43 172.60(19) . . ?
O31 Mn5 O52 176.1(2) . . ?
O31 Mn5 O40 92.34(19) . . ?
O52 Mn5 O40 91.43(17) . . ?
O31 Mn5 N38 88.8(2) . . ?
O52 Mn5 N38 87.38(18) . . ?
O40 Mn5 N38 178.80(19) . . ?
O31 Mn5 N49 91.03(18) . . ?
O52 Mn5 N49 88.15(17) . . ?
O40 Mn5 N49 89.26(18) . . ?
N38 Mn5 N49 90.90(18) . . ?
O31 Mn5 N59 89.90(19) . . ?
O52 Mn5 N59 90.70(18) . . ?
O40 Mn5 N59 94.01(19) . . ?
N38 Mn5 N59 85.81(19) . . ?
N49 Mn5 N59 176.6(2) . . ?
N37 O42 Mn4 116.2(3) . . ?
Mn4 O52 Mn3 119.7(2) . . ?
Mn4 O52 Mn5 119.6(2) . . ?
Mn3 O52 Mn5 120.40(19) . . ?
N50 N49 Zn1 123.2(4) . . ?
N50 N49 Mn5 121.3(4) . . ?
Zn1 N49 Mn5 109.5(2) . . ?
N38 O41 Mn3 116.1(3) . . ?
C29 N39 O40 117.0(5) . . ?
C29 N39 Mn4 126.8(4) . . ?
O40 N39 Mn4 116.0(3) . . ?
C30 N38 O41 115.9(5) . . ?
C30 N38 Mn5 128.0(4) . . ?
O41 N38 Mn5 115.9(3) . . ?
C20 O33 Mn3 124.0(4) . . ?
N39 O40 Mn5 116.1(3) . . ?
C14 O32 Mn4 124.5(4) . . ?
C34 N37 O42 116.9(4) . . ?
C34 N37 Mn3 128.3(4) . . ?
O42 N37 Mn3 114.7(3) . . ?
C9 O31 Mn5 124.2(4) . . ?
N51 N50 N49 176.8(7) . . ?
C29 C26 C25 111.7(6) . . ?
C29 C26 H26A 109.1 . . ?
C25 C26 H26A 108.2 . . ?
C29 C26 H26B 109.7 . . ?
C25 C26 H26B 108.6 . . ?
H26A C26 H26B 109.5 . . ?
N44 N43 Zn2 116.3(4) . . ?
N44 N43 Mn4 118.1(4) . . ?
Zn2 N43 Mn4 110.0(2) . . ?
N48 N47 N46 178.3(7) . . ?
C18 C19 C14 121.4(6) . . ?
C18 C19 H19 119.2 . . ?
C14 C19 H19 119.4 . . ?
N45 N44 N43 174.4(7) . . ?
N47 N46 Zn1 119.6(4) . . ?
N47 N46 Mn3 128.5(4) . . ?
Zn1 N46 Mn3 111.0(2) . . ?
N39 C29 C15 120.3(5) . . ?
N39 C29 C26 120.8(5) . . ?
C15 C29 C26 118.9(5) . . ?
C13 C8 C9 118.5(6) . . ?
C13 C8 C30 118.6(6) . . ?
C9 C8 C30 122.8(5) . . ?
C16 C15 C14 118.2(6) . . ?
C16 C15 C29 119.3(6) . . ?
C14 C15 C29 122.3(5) . . ?
C12 C13 C8 121.6(7) . . ?
C12 C13 H13 118.3 . . ?
C8 C13 H13 120.1 . . ?
C24 C23 C20 121.5(7) . . ?
C24 C23 H23 118.5 . . ?
C20 C23 H23 120.0 . . ?
N37 C34 C21 119.3(5) . . ?
N37 C34 C35 119.4(6) . . ?
C21 C34 C35 121.2(5) . . ?
N38 C30 C8 119.8(6) . . ?
N38 C30 C27 118.1(5) . . ?
C8 C30 C27 122.1(5) . . ?
C10 C11 C12 120.0(6) . . ?
C10 C11 H11 119.9 . . ?
C12 C11 H11 120.1 . . ?
C13 C12 C11 120.0(6) . . ?
C13 C12 H12 120.7 . . ?
C11 C12 H12 119.4 . . ?
O33 C20 C21 124.6(5) . . ?
O33 C20 C23 117.2(5) . . ?
C21 C20 C23 118.2(6) . . ?
C19 C18 C17 120.6(6) . . ?
C19 C18 H18 120.8 . . ?
C17 C18 H18 118.5 . . ?
C11 C10 C9 121.5(7) . . ?
C11 C10 H10 119.7 . . ?
C9 C10 H10 118.8 . . ?
O32 C14 C19 117.2(5) . . ?
O32 C14 C15 124.0(5) . . ?
C19 C14 C15 118.7(5) . . ?
C16 C17 C18 119.1(6) . . ?
C16 C17 H17 121.1 . . ?
C18 C17 H17 119.8 . . ?
C26 C25 H25A 109.1 . . ?
C26 C25 H25B 109.8 . . ?
H25A C25 H25B 109.5 . . ?
C26 C25 H25C 109.4 . . ?
H25A C25 H25C 109.5 . . ?
H25B C25 H25C 109.5 . . ?
C17 C16 C15 121.7(6) . . ?
C17 C16 H16 118.2 . . ?
C15 C16 H16 120.1 . . ?
C34 C35 C36 110.7(6) . . ?
C34 C35 H35A 109.6 . . ?
C36 C35 H35A 109.9 . . ?
C34 C35 H35B 108.8 . . ?
C36 C35 H35B 108.3 . . ?
H35A C35 H35B 109.5 . . ?
C20 C21 C22 118.2(6) . . ?
C20 C21 C34 122.4(6) . . ?
C22 C21 C34 119.3(6) . . ?
C28 C27 C30 112.3(6) . . ?
C28 C27 H27A 107.5 . . ?
C30 C27 H27A 108.9 . . ?
C28 C27 H27B 109.2 . . ?
C30 C27 H27B 109.5 . . ?
H27A C27 H27B 109.5 . . ?
C23 C24 C78 119.8(7) . . ?
C23 C24 H24 119.4 . . ?
C78 C24 H24 120.8 . . ?
C35 C36 H36A 110.5 . . ?
C35 C36 H36B 108.1 . . ?
H36A C36 H36B 109.5 . . ?
C35 C36 H36C 109.8 . . ?
H36A C36 H36C 109.5 . . ?
H36B C36 H36C 109.5 . . ?
C78 C22 C21 122.1(7) . . ?
C78 C22 H22 117.6 . . ?
C21 C22 H22 120.2 . . ?
O31 C9 C10 117.9(6) . . ?
O31 C9 C8 123.7(5) . . ?
C10 C9 C8 118.3(6) . . ?
C27 C28 H28A 109.2 . . ?
C27 C28 H28B 110.5 . . ?
H28A C28 H28B 109.5 . . ?
C27 C28 H28C 108.7 . . ?
H28A C28 H28C 109.5 . . ?
H28B C28 H28C 109.5 . . ?
N55 N54 N53 178.8(9) . . ?
N58 N57 N56 177.0(7) . . ?
N57 N56 Zn2 121.7(4) . . ?

N57 N56 Mn3 114.4(4) . . ?
Zn2 N56 Mn3 111.4(2) . . ?
N54 N53 Zn1 118.2(4) . . ?
N54 N53 Mn4 121.2(4) . . ?
Zn1 N53 Mn4 110.3(2) . . ?
C64 N61 C62 111.5(6) . . ?
C64 N61 C66 110.6(5) . . ?
C62 N61 C66 106.7(5) . . ?
C64 N61 C67 107.4(5) . . ?
C62 N61 C67 109.3(5) . . ?
C66 N61 C67 111.4(6) . . ?
N60 N59 Zn2 129.7(4) . . ?
N60 N59 Mn5 119.1(4) . . ?
Zn2 N59 Mn5 110.6(2) . . ?
N79 N60 N59 176.0(11) . . ?
C65 C64 N61 114.4(5) . . ?
C65 C64 H64A 106.9 . . ?
N61 C64 H64A 109.4 . . ?
C65 C64 H64B 107.6 . . ?
N61 C64 H64B 108.8 . . ?
H64A C64 H64B 109.5 . . ?
C64 C65 H65A 110.0 . . ?
C64 C65 H65B 109.5 . . ?
H65A C65 H65B 109.5 . . ?
C64 C65 H65C 108.8 . . ?
H65A C65 H65C 109.5 . . ?
H65B C65 H65C 109.5 . . ?
C63 C62 N61 114.4(5) . . ?
C63 C62 H62A 105.9 . . ?
N61 C62 H62A 109.9 . . ?
C63 C62 H62B 107.8 . . ?
N61 C62 H62B 109.3 . . ?
H62A C62 H62B 109.5 . . ?
C69 C67 N61 115.4(6) . . ?
C69 C67 H67A 106.7 . . ?
N61 C67 H67A 109.7 . . ?
C69 C67 H67B 106.2 . . ?
N61 C67 H67B 109.2 . . ?
H67A C67 H67B 109.5 . . ?
C62 C63 H63A 109.7 . . ?
C62 C63 H63B 110.3 . . ?
H63A C63 H63B 109.5 . . ?
C62 C63 H63C 108.4 . . ?
H63A C63 H63C 109.5 . . ?
H63B C63 H63C 109.5 . . ?
N61 C66 C68 114.6(6) . . ?
N61 C66 H66A 109.9 . . ?
C68 C66 H66A 106.4 . . ?
N61 C66 H66B 109.6 . . ?
C68 C66 H66B 106.7 . . ?
H66A C66 H66B 109.5 . . ?
C72 N70 C74 113.8(9) . . ?
C72 N70 C75 112.1(8) . . ?
C74 N70 C75 106.7(6) . . ?
C72 N70 C77 106.2(9) . . ?
C74 N70 C77 108.6(8) . . ?
C75 N70 C77 109.3(8) . . ?
C71 C74 N70 116.8(6) . . ?
C71 C74 H74A 106.4 . . ?
N70 C74 H74A 109.3 . . ?
C71 C74 H74B 105.2 . . ?
N70 C74 H74B 109.4 . . ?
H74A C74 H74B 109.5 . . ?
C74 C71 H71A 110.2 . . ?
C74 C71 H71B 108.4 . . ?
H71A C71 H71B 109.5 . . ?
C74 C71 H71C 109.8 . . ?
H71A C71 H71C 109.5 . . ?
H71B C71 H71C 109.5 . . ?
C67 C69 H69A 109.7 . . ?
C67 C69 H69B 109.1 . . ?
H69A C69 H69B 109.5 . . ?
C67 C69 H69C 109.7 . . ?
H69A C69 H69C 109.5 . . ?
H69B C69 H69C 109.5 . . ?
C76 C75 N70 116.1(7) . . ?
C76 C75 H75A 104.1 . . ?
N70 C75 H75A 108.8 . . ?
C76 C75 H75B 108.7 . . ?
N70 C75 H75B 109.5 . . ?
H75A C75 H75B 109.5 . . ?
C66 C68 H68A 109.6 . . ?
C66 C68 H68B 109.6 . . ?
H68A C68 H68B 109.5 . . ?
C66 C68 H68C 109.3 . . ?
H68A C68 H68C 109.5 . . ?
H68B C68 H68C 109.5 . . ?
C22 C78 C24 120.2(7) . . ?
C22 C78 H78 119.5 . . ?
C24 C78 H78 120.3 . . ?
N70 C72 C73 111.8(10) . . ?
N70 C72 H72A 108.6 . . ?
C73 C72 H72A 109.1 . . ?
N70 C72 H72B 109.8 . . ?
C73 C72 H72B 108.0 . . ?
H72A C72 H72B 109.5 . . ?
C86 C77 N70 113.4(10) . . ?
C86 C77 H77A 106.3 . . ?
N70 C77 H77A 109.8 . . ?
C86 C77 H77B 106.8 . . ?
N70 C77 H77B 110.8 . . ?
H77A C77 H77B 109.5 . . ?
C75 C76 H76A 108.7 . . ?
C75 C76 H76B 112.1 . . ?
H76A C76 H76B 109.5 . . ?
C75 C76 H76C 107.5 . . ?
H76A C76 H76C 109.5 . . ?
H76B C76 H76C 109.5 . . ?
C72 C73 H73A 107.7 . . ?
C72 C73 H73B 109.8 . . ?
H73A C73 H73B 109.5 . . ?
C72 C73 H73C 110.9 . . ?
H73A C73 H73C 109.5 . . ?
H73B C73 H73C 109.5 . . ?
C84 N80 C94 121(2) . . ?
C84 N80 C100 136(2) . . ?
C94 N80 C100 89.9(14) . . ?
C84 N80 C87 104.0(15) . . ?
C94 N80 C87 84.5(11) . . ?
C100 N80 C87 110.7(13) . . ?
C84 N80 C107 34(3) . . ?
C94 N80 C107 142.1(17) . . ?
C100 N80 C107 103(3) . . ?
C87 N80 C107 122(3) . . ?
C84 N80 C82 108.8(13) . . ?
C94 N80 C82 111.8(10) . . ?
C100 N80 C82 84.3(11) . . ?
C87 N80 C82 38.0(9) . . ?
C107 N80 C82 105(2) . . ?
C84 N80 C102 103(2) . . ?
C94 N80 C102 110.0(12) . . ?
C100 N80 C102 32.4(11) . . ?
C87 N80 C102 135.6(12) . . ?
C107 N80 C102 71(3) . . ?
C82 N80 C102 99.7(10) . . ?
C84 N80 C90 84(2) . . ?
C94 N80 C90 38.6(10) . . ?
C100 N80 C90 112.3(11) . . ?
C87 N80 C90 104.5(10) . . ?
C107 N80 C90 104.5(12) . . ?
C82 N80 C90 141.7(9) . . ?
C102 N80 C90 112.6(9) . . ?
C77 C86 H86A 108.3 . . ?
C77 C86 H86B 110.9 . . ?
H86A C86 H86B 109.5 . . ?
C77 C86 H86C 109.3 . . ?
H86A C86 H86C 109.5 . . ?
H86B C86 H86C 109.5 . . ?

_diffrn_measured_fraction_theta_max
0.964
_diffrn_reflns_theta_full 31.49
_diffrn_measured_fraction_theta_full 0.964
_refine_diff_density_max 1.477
_refine_diff_density_min -1.124
_refine_diff_density_rms 0.144

CIF for compound **3:**

```
data_shelxl
_audit_creation_date              2014-04-06
_audit_creation_method
;
Olex2 1.2
(compiled 2013.12.10 svn.r2850 for OlexSys, GUI svn.r4736)
;
_publ_contact_author_address     ?
_publ_contact_author_email       ?
_publ_contact_author_name        ?
_publ_contact_author_phone       ?
_publ_section_references
;
Bourhis, L.J., Dolomanov, O.V., Gildea, R.J., Howard, J.A.K.,
Puschmann, H.
 (2013). in preparation

Bourhis, L.J., Dolomanov, O.V., Gildea, R.J., Howard, J.A.K.,
Puschmann, H.
 (2013). in preparation

Dolomanov, O.V., Bourhis, L.J., Gildea, R.J, Howard, J.A.K. &
Puschmann, H.
 (2009), J. Appl. Cryst. 42, 339-341.
;
_chemical_formula_moiety         'C42 H33 Cl2 Mn3 N21 O7 Zn2, 3(C8
H20 N)'
_chemical_formula_sum            'C66 H93 Cl2 Mn3 N24 O7 Zn2'
_chemical_formula_weight         1701.14
loop_
  _atom_type_symbol
  _atom_type_scat_dispersion_real
  _atom_type_scat_dispersion_imag
  _atom_type_scat_Cromer_Mann_a1
  _atom_type_scat_Cromer_Mann_a2
  _atom_type_scat_Cromer_Mann_a3
  _atom_type_scat_Cromer_Mann_a4
  _atom_type_scat_Cromer_Mann_b1
  _atom_type_scat_Cromer_Mann_b2
  _atom_type_scat_Cromer_Mann_b3
  _atom_type_scat_Cromer_Mann_b4
  _atom_type_scat_Cromer_Mann_c
  _atom_type_scat_source
  _atom_type_scat_dispersion_source
 C 0.00347 0.00161 2.31000 1.02000 1.58860 0.86500 20.84390
10.20750 0.56870
 51.65120 0.215599998832
 'International Tables Volume C Table 6.1.1.4 (pp. 500-502)'
 'Henke, Gullikson and Davis, At. Data and Nucl. Data Tables, 1993, 54,
2'
 Cl 0.14873 0.16029 11.46040 7.19640 6.25560 1.64550 0.01040 1.16620
18.51940
 47.77840 -9.55739974976
 'International Tables Volume C Table 6.1.1.4 (pp. 500-502)'
 'Henke, Gullikson and Davis, At. Data and Nucl. Data Tables, 1993, 54,
2'
 H 0.00000 0.00000 0.49300 0.32291 0.14019 0.04081 10.51090
26.12570 3.14236
 57.79970 0.0030380000826
 'International Tables Volume C Table 6.1.1.4 (pp. 500-502)'
 'Henke, Gullikson and Davis, At. Data and Nucl. Data Tables, 1993, 54,
2'
 Mn 0.34779 0.73263 11.28190 7.35730 3.01930 2.24410 5.34090
0.34320 17.86740
 83.75430 1.089599967
 'International Tables Volume C Table 6.1.1.4 (pp. 500-502)'
 'Henke, Gullikson and Davis, At. Data and Nucl. Data Tables, 1993, 54,
2'
 Zn 0.31207 1.46666 14.07430 7.03180 5.16520 2.41000 3.26550 0.23330
10.31630
 58.70970 1.30410003662
 'International Tables Volume C Table 6.1.1.4 (pp. 500-502)'
 'Henke, Gullikson and Davis, At. Data and Nucl. Data Tables, 1993, 54,
2'
 O 0.01158 0.00611 3.04850 2.28680 1.54630 0.86700 13.27710 5.70110
0.32390
 32.90890 0.250800013542
 'International Tables Volume C Table 6.1.1.4 (pp. 500-502)'
 'Henke, Gullikson and Davis, At. Data and Nucl. Data Tables, 1993, 54,
2'
 N 0.00653 0.00323 12.21260 3.13220 2.01250 1.16630 0.00570 9.89330
28.99750
 0.58260 -11.5290002823
 'International Tables Volume C Table 6.1.1.4 (pp. 500-502)'
 'Henke, Gullikson and Davis, At. Data and Nucl. Data Tables, 1993, 54,
2'

_space_group_crystal_system      'monoclinic'
_space_group_IT_number           14
_space_group_name_H-M_alt        'P 1 21/c 1'
_space_group_name_Hall           '-P 2ybc'
loop_
  _space_group_symop_id
  _space_group_symop_operation_xyz
 1 x,y,z
 2 -x,y+1/2,-z+1/2
 3 -x,-y,-z
 4 x,-y-1/2,z-1/2

_symmetry_Int_Tables_number      14
_cell_length_a                   22.4620(15)
_cell_length_b                   14.202(3)
_cell_length_c                   28.407(4)
_cell_angle_alpha                90.000(14)
_cell_angle_beta                 116.633(9)
_cell_angle_gamma                90.000(12)
_cell_volume                     8100(2)
_cell_formula_units_Z            4
_cell_measurement_temperature    122
_exptl_absorpt_coefficient_mu    1.168
_exptl_absorpt_correction_T_max  0.883
_exptl_absorpt_correction_T_min  0.704
_exptl_absorpt_correction_type   integration
_exptl_crystal_colour            'clear dark black'
_exptl_crystal_colour_lustre     clear
_exptl_crystal_colour_modifier   dark
_exptl_crystal_colour_primary    black
_exptl_crystal_density_diffrn    1.3948
_exptl_crystal_description       prism
_exptl_crystal_F_000             3536.8291
_exptl_crystal_preparation       ?
_exptl_crystal_size_max          0.301
_exptl_crystal_size_mid          0.197
_exptl_crystal_size_min          0.14
_diffrn_reflns_av_R_equivalents  0.1457
_diffrn_reflns_av_unetI/netI     0.0618
_diffrn_reflns_limit_h_max       26
_diffrn_reflns_limit_h_min       -26
_diffrn_reflns_limit_k_max       16
_diffrn_reflns_limit_k_min       -16
_diffrn_reflns_limit_l_max       33
_diffrn_reflns_limit_l_min       -33
_diffrn_reflns_number            121992
_diffrn_reflns_theta_full        25.0881
_diffrn_reflns_theta_max         25.09
_diffrn_reflns_theta_min         1.46
_diffrn_ambient_temperature      122
_diffrn_measured_fraction_theta_full 0.9950
_diffrn_measured_fraction_theta_max 0.9950
_diffrn_radiation_type           'Mo K\a'
_diffrn_radiation_wavelength     0.71073
_reflns_Friedel_coverage         0.0
_reflns_limit_h_max              23
_reflns_limit_h_min              -26
_reflns_limit_k_max              16
_reflns_limit_k_min              0
_reflns_limit_l_max              33
_reflns_limit_l_min              0
_reflns_number_gt                10726
_reflns_number_total             14327
_reflns_threshold_expression     I>=2u(I)
_computing_molecular_graphics    'Olex2 (Dolomanov et al., 2009)'
_computing_publication_material  'Olex2 (Dolomanov et al., 2009)'
_computing_structure_refinement  'olex2.refine (Bourhis et al., 2013)'
_computing_structure_solution    'olex2.solve (Bourhis et al., 2013)'
_refine_diff_density_max         2.0012
_refine_diff_density_min         -1.6468
_refine_diff_density_rms         0.3558
_refine_ls_d_res_high            0.8381
_refine_ls_d_res_low             13.9116
_refine_ls_goodness_of_fit_ref   1.2177
_refine_ls_hydrogen_treatment    mixed
_refine_ls_matrix_type           full
_refine_ls_number_constraints    162
_refine_ls_number_parameters     876
_refine_ls_number_reflns         14327
_refine_ls_number_restraints     0
_refine_ls_R_factor_all          0.1725
```

```
_refine_ls_R_factor_gt            0.1359
_refine_ls_restrained_S_all       1.2177
_refine_ls_shift/su_max           0.0400
_refine_ls_shift/su_mean          0.0020
_refine_ls_structure_factor_coef  Fsqd
_refine_ls_weighting_details
;
'w=1/[\s^2^(Fo^2^)+(0.0954P)^2^+303.1297P] where
P=(Fo^2^+2Fc^2^)/3'
_refine_ls_weighting_scheme       calc
_refine_ls_wR_factor_gt           0.3376
_refine_ls_wR_factor_ref          0.4123
_olex2_refinement_description
;

1. Fixed Uiso
 At 1.2 times of:
  All C(H) groups, All C(H,H) groups
 At 1.5 times of:
  All C(H,H,H) groups
2. Uiso/Uaniso restraints and constraints
Uanis(C16) = Uanis(C15) = Uanis(C22) = Uanis(C21) = Uanis(C17)
3. Others
 Sof(N26a)=Sof(N27a)=1-FVAR(1)
 Sof(N26)=Sof(N27)=FVAR(1)
 Sof(C59a)=Sof(H59c)=Sof(H59d)=Sof(C60a)=Sof(H60d)=Sof(H60e)=Sof(H60f)=1-FVAR(2)
 Sof(C59)=Sof(H59a)=Sof(H59b)=Sof(C60)=Sof(H60a)=Sof(H60b)=Sof(H60c)=FVAR(2)
 Sof(C63a)=Sof(H63c)=Sof(H63d)=Sof(C64a)=Sof(H64d)=Sof(H64e)=Sof(H64f)=1-FVAR(3)
 Sof(C64)=Sof(H64a)=Sof(H64b)=Sof(H64c)=Sof(C63)=Sof(H63a)=Sof(H63b)=FVAR(3)
4.a Secondary CH2 refined with riding coordinates:
 C47(H47a,H47b), C49(H49a,H49b), C43(H43a,H43b), C61(H61a,H61b), C53(H53a,
 H53b), C45(H45a,H45b), C55(H55a,H55b), C57(H57a,H57b), C51(H51a,H51b),
 C59(H59a,H59b), C63(H63a,H63b), C65(H65a,H65b), C59a(H59c,H59d), C63a(H63c,
 H63d)
4.b Aromatic/amide H refined with riding coordinates:
 C21(H21), C9(H9), C19(H19), C40(H40), C11(H11), C18(H18), C12(H12), C37(H37),
 C39(H39), C3(H3), C20(H20), C7(H7), C4(H4), C25(H25), C5(H5), C23(H23),
 C26(H26), C6(H6), C17(H17), C33(H33), C35(H35), C32(H32), C34(H34), C31(H31)
4.c Idealised Me refined as rotating group:
 C48(H48a,H48b,H48c), C14(H14a,H14b,H14c), C42(H42a,H42b,H42c), C50(H50a,H50b,
 H50c), C46(H46a,H46b,H46c), C44(H44a,H44b,H44c), C56(H56a,H56b,H56c), C28(H28a,
 H28b,H28c), C60(H60a,H60b,H60c), C58(H58a,H58b,H58c), C52(H52a,H52b,H52c),
 C62(H62a,H62b,H62c), C64(H64a,H64b,H64c), C66(H66a,H66b,H66c), C54(H54a,H54b,
 H54c), C60a(H60d,H60e,H60f), C64a(H64d,H64e,H64f)
;

_atom_sites_solution_primary      iterative
loop_
  _atom_site_label
  _atom_site_type_symbol
  _atom_site_fract_x
  _atom_site_fract_y
  _atom_site_fract_z
  _atom_site_U_iso_or_equiv
  _atom_site_adp_type
  _atom_site_occupancy
  _atom_site_refinement_flags_posn
  _atom_site_disorder_group
 Zn1 Zn 0.25761147(14) 0.52190469(14) 0.51618030(14) 0.03106(5)
Uani 1.000000
 . .
 Zn2 Zn 0.19070569(14) 0.87279488(14) 0.37065424(14) 0.04367(5)
Uani 1.000000
 . .
 Mn3 Mn 0.24013320(14) 0.62330087(14) 0.39596044(14) 0.03151(5)
Uani 1.000000
 . .
 Mn1 Mn 0.13939216(14) 0.70381812(14) 0.44095403(14) 0.02766(5)
Uani 1.000000
 . .
 Mn2 Mn 0.29604694(14) 0.76679804(14) 0.49663388(14) 0.03747(5)
Uani 1.000000
 . .
 Cl1 Cl 0.28776874(14) 0.39057088(14) 0.56522033(14) 0.04805(5) Uani
1.000000
 . .
 Cl2 Cl 0.18037140(14) 1.00151495(14) 0.32186706(14) 0.06006(5) Uani
1.000000
 . .
 O2 O 0.05270806(14) 0.70193378(14) 0.43424888(14) 0.03236(5) Uani
1.000000 . .
 O1 O 0.22588552(14) 0.70021296(14) 0.44424873(14) 0.02926(5) Uani
1.000000 . .
 O7 O 0.17184915(14) 0.76802479(14) 0.50711085(14) 0.03241(5) Uani
1.000000 . .
 N13 N 0.20093058(14) 0.75167684(14) 0.33457977(14) 0.03553(5) Uani
1.000000 .
 .
 N7 N 0.11927548(14) 0.84371255(14) 0.39357724(14) 0.03324(5) Uani
1.000000 . .
 C21 C 0.20863805(14) 0.88599903(14) 0.63094993(14) 0.03795(5) Uani
1.000000 .
 .
 H21 H 0.25118139(14) 0.86120786(14) 0.65381060(14) 0.04554(6) Uiso
1.000000 R
 .
 O4 O 0.25696608(14) 0.54814457(14) 0.34939202(14) 0.03736(5) Uani
1.000000 . .
 O3 O 0.15349527(14) 0.57010245(14) 0.37145152(14) 0.03227(5) Uani
1.000000 . .
 O5 O 0.35803425(14) 0.71592092(14) 0.47377504(14) 0.05192(5) Uani
1.000000 . .
 N5 N 0.11178683(14) 0.50434594(14) 0.46171722(14) 0.03045(5) Uani
1.000000 . .
 O6 O 0.36610781(14) 0.82811913(14) 0.55324203(14) 0.04641(5) Uani
1.000000 . .
 N8 N 0.08496559(14) 0.90112659(14) 0.40091045(14) 0.03274(5) Uani
1.000000 . .
 N14 N 0.17244254(14) 0.73835867(14) 0.29220176(14) 0.04475(5) Uani
1.000000 .
 .
 N19 N 0.16739448(14) -0.05527823(14) 0.13865413(14) 0.03619(5)
Uani 1.000000
 . .
 C13 C -0.00146076(14) 0.71144464(14) 0.38991451(14) 0.03234(5)
Uani 1.000000
 . .
 N20 N 0.14333965(14) 0.21426488(14) 0.42317217(14) 0.04949245(14)
Uiso
 1.000000 . .
 N4 N 0.16015615(14) 0.55205194(14) 0.48490878(14) 0.03175(5) Uani
1.000000 . .
 C9 C -0.07163095(14) 0.67342458(14) 0.29719442(14) 0.03210(5) Uani
1.000000 .
 .
 H9 H -0.07794683(14) 0.64045665(14) 0.26620147(14) 0.03852(6) Uiso
1.000000 R
 .
 N23 N 0.33118533(14) 0.67916667(14) 0.42234401(14) 0.04325(5) Uani
1.000000 .
 .
 C19 C 0.10212051(14) 0.94787429(14) 0.61799255(14) 0.04846(5) Uani
1.000000 .
 .
 H19 H 0.07237335(14) 0.96541032(14) 0.63193197(14) 0.05815(6) Uiso
1.000000 R
 .
 C40 C 0.28487345(14) 0.52219525(14) 0.27978536(14) 0.03408(5) Uani
1.000000 .
 .
 H40 H 0.25027019(14) 0.47665155(14) 0.26620089(14) 0.04090(6) Uiso
1.000000 R
 .
 C11 C -0.11254314(14) 0.77627526(14) 0.34195483(14) 0.03656(5)
Uani 1.000000
```

. .
H11 H -0.14648279(14) 0.81636325(14) 0.34180883(14) 0.04387(6)
Uiso 1.000000
R .
N9 N 0.04967302(14) 0.95197078(14) 0.40788173(14) 0.04886(5) Uani
1.000000 . .
N1 N 0.30557768(14) 0.63798511(14) 0.55459675(14) 0.03482(5) Uani
1.000000 . .
C8 C -0.01059643(14) 0.66410796(14) 0.34201913(14) 0.03109(5) Uani
1.000000 .
.
N6 N 0.06351149(14) 0.46034637(14) 0.43845698(14) 0.03450(5) Uani
1.000000 . .
N3 N 0.33375731(14) 0.68485738(14) 0.64206513(14) 0.05562(5) Uani
1.000000 . .
C18 C 0.08440069(14) 0.96240176(14) 0.56573815(14) 0.06013(5) Uani
1.000000 .
.
H18 H 0.04226178(14) 0.98894771(14) 0.54337634(14) 0.07215(6) Uiso
1.000000 R
.
C2 C 0.02890413(14) 0.53630637(14) 0.29858207(14) 0.03027(5) Uani
1.000000 . .
C16 C 0.19098082(14) 0.90089012(14) 0.57792732(14) 0.03795(5) Uani
1.000000 .
.
C12 C -0.05359189(14) 0.76665357(14) 0.38787343(14) 0.03499(5)
Uani 1.000000
. .
H12 H -0.04876104(14) 0.79869095(14) 0.41874387(14) 0.04199(6)
Uiso 1.000000
R .
C15 C 0.24202878(14) 0.88091548(14) 0.55889693(14) 0.03795(5) Uani
1.000000 .
.
C10 C -0.12313336(14) 0.72814639(14) 0.29576584(14) 0.04077(5)
Uani 1.000000
. .
N2 N 0.31854098(14) 0.66136265(14) 0.59834501(14) 0.03888(5) Uani
1.000000 . .
C37 C 0.38481031(14) 0.65577649(14) 0.31888066(14) 0.03604(5) Uani
1.000000 .
.
H37 H 0.41867640(14) 0.70247158(14) 0.33152584(14) 0.04324(6) Uiso
1.000000 R
.
C38 C 0.37288780(14) 0.60762574(14) 0.27219171(14) 0.04058(5) Uani
1.000000 .
.
C41 C 0.29604561(14) 0.57141398(14) 0.32662909(14) 0.03433(5) Uani
1.000000 .
.
C39 C 0.32299002(14) 0.53858720(14) 0.25319969(14) 0.04136(5) Uani
1.000000 .
.
H39 H 0.31529338(14) 0.50341940(14) 0.22254888(14) 0.04963(6) Uiso
1.000000 R
.
N22 N 0.10544872(14) 0.62627102(14) 0.37407190(14) 0.02928(5) Uani
1.000000 .
.
C3 C 0.06350792(14) 0.53498898(14) 0.26750325(14) 0.05386(5) Uani
1.000000 . .
H3 H 0.09526575(14) 0.58266758(14) 0.27195336(14) 0.06463(6) Uiso
1.000000 R .
C36 C 0.34829942(14) 0.63761691(14) 0.34811167(14) 0.04144(5) Uani
1.000000 .
.
C24 C 0.36248818(14) 1.07754772(14) 0.62984100(14) 0.05711(5) Uani
1.000000 .
.
N15 N 0.14402699(14) 0.72252053(14) 0.24488673(14) 0.06433(5) Uani
1.000000 .
.
N10 N 0.27216060(14) 0.89301475(14) 0.43964859(14) 0.05873(5) Uani
1.000000 .
.
C20 C 0.16226133(14) 0.90834358(14) 0.65030832(14) 0.03859(5) Uani
1.000000 .
.
H20 H 0.17298774(14) 0.89577890(14) 0.68607064(14) 0.04631(6) Uiso
1.000000 R
.
C27 C 0.36069656(14) 0.90937426(14) 0.57676700(14) 0.04305(5) Uani
1.000000 .
.
C7 C -0.01355582(14) 0.46491445(14) 0.29239322(14) 0.04532(5) Uani
1.000000 .
.
H7 H -0.03666552(14) 0.46380055(14) 0.31337836(14) 0.05439(6) Uiso
1.000000 R
.
C48 C 0.09271257(14) -0.19446277(14) 0.08781508(14) 0.06041(5)
Uani 1.000000
. .
H48a H 0.09192638(14) -0.24926945(14) 0.06658274(14) 0.09061(8)
Uiso 1.000000
GR .
H48b H 0.09120021(14) -0.21565228(14) 0.12009336(14) 0.09061(8)
Uiso 1.000000
GR .
H48c H 0.05404514(14) -0.15442438(14) 0.06759120(14) 0.09061(8)
Uiso 1.000000
GR .
C47 C 0.15623901(14) -0.13870259(14) 0.10204742(14) 0.04279(5)
Uani 1.000000
. .
H47a H 0.15589103(14) -0.11534771(14) 0.06908862(14) 0.05135(6)
Uiso 1.000000
R .
H47b H 0.19458545(14) -0.18206246(14) 0.11880330(14) 0.05135(6)
Uiso 1.000000
R .
C49 C 0.18030545(14) -0.08719162(14) 0.19405902(14) 0.04749(5)
Uani 1.000000
. .
C43 C 0.10578075(14) 0.00746348(14) 0.11910116(14) 0.03866(5) Uani
1.000000 .
.
H43a H 0.06880700(14) -0.02897093(14) 0.12013005(14) 0.04639(6)
Uiso 1.000000
R .
H43b H 0.11529583(14) 0.06126297(14) 0.14358990(14) 0.04639(6)
Uiso 1.000000
R .
C14 C -0.18865862(14) 0.74010748(14) 0.24786353(14) 0.05763(5)
Uani 1.000000
. .
H14a H -0.19118885(14) 0.80343572(14) 0.23338190(14) 0.08645(8)
Uiso 1.000000
GR .
H14b H -0.19255379(14) 0.69316233(14) 0.22134873(14) 0.08645(8)
Uiso 1.000000
GR .
H14c H -0.22503173(14) 0.73153689(14) 0.25757208(14) 0.08645(8)
Uiso 1.000000
GR .
C4 C 0.05119167(14) 0.46376124(14) 0.23020819(14) 0.06187(5) Uani
1.000000 . .
H4 H 0.07256429(14) 0.46558209(14) 0.20796180(14) 0.07425(6) Uiso
1.000000 R .
C61 C 0.14295024(14) 0.25388780(14) 0.47266386(14) 0.08716549(14)
Uiso
1.000000 . .
C25 C 0.41525446(14) 1.05078242(14) 0.62407598(14) 0.06607(5) Uani
1.000000 .
.
H25 H 0.45349537(14) 1.09016556(14) 0.63798787(14) 0.07929(6) Uiso
1.000000 R
.
C29 C 0.36889601(14) 0.68216450(14) 0.39802062(14) 0.04656(5) Uani
1.000000 .
.
C53 C 0.53494258(14) 0.37789219(14) 0.40421799(14) 0.10272054(14)
Uiso
1.000000 . 3
H53a H 0.54517794(14) 0.40010401(14) 0.44007810(14) 0.12326464(17)
Uiso
1.000000 R 3
H53b H 0.56894809(14) 0.33094786(14) 0.40699721(14) 0.12326464(17)
Uiso
1.000000 R 3
C42 C 0.41250187(14) 0.62956195(14) 0.24286312(14) 0.05428(5) Uani
1.000000 .
.
H42a H 0.39386177(14) 0.68535223(14) 0.22080967(14) 0.08142(8)
Uiso 1.000000
GR .
H42b H 0.45892092(14) 0.64178751(14) 0.26805143(14) 0.08142(8)
Uiso 1.000000
GR .
H42c H 0.41061804(14) 0.57588546(14) 0.22055659(14) 0.08142(8)
Uiso 1.000000
GR .
C5 C 0.00879692(14) 0.39188595(14) 0.22558886(14) 0.05260(5) Uani
1.000000 . .

H5 H 0.00229077(14) 0.34179093(14) 0.20160309(14) 0.06312(6) Uiso 1.000000 R .
C50 C 0.24417462(14) -0.13926695(14) 0.22311649(14) 0.06371(5) Uani 1.000000 . .
H50a H 0.24477857(14) -0.19440279(14) 0.20259081(14) 0.09556(8) Uiso 1.000000 GR .
H50b H 0.28158266(14) -0.09782784(14) 0.22851341(14) 0.09556(8) Uiso 1.000000 GR .
H50c H 0.24812625(14) -0.15978503(14) 0.25733672(14) 0.09556(8) Uiso 1.000000 GR .
C22 C 0.30290657(14) 0.93649668(14) 0.58030356(14) 0.03795(5) Uani 1.000000 . .
C23 C 0.30511192(14) 1.02101550(14) 0.60798884(14) 0.05018(5) Uani 1.000000 . .
H23 H 0.26686364(14) 1.03963387(14) 0.61177723(14) 0.06021(6) Uiso 1.000000 R .
C46 C 0.24795873(14) 0.08307463(14) 0.17618343(14) 0.05943(5) Uani 1.000000 . .
H46a H 0.21267539(14) 0.13073365(14) 0.16299294(14) 0.08915(8) Uiso 1.000000 GR .
H46b H 0.25649578(14) 0.06427847(14) 0.21185043(14) 0.08915(8) Uiso 1.000000 GR .
H46c H 0.28872540(14) 0.10931011(14) 0.17692887(14) 0.08915(8) Uiso 1.000000 GR .
N24 N 0.23071942(14) 0.81595410(14) 0.52305569(14) 0.03457(5) Uani 1.000000 . .
C45 C 0.22653678(14) -0.00111089(14) 0.14070226(14) 0.04832(5) Uani 1.000000 . .
H45a H 0.26478636(14) -0.04486903(14) 0.15201452(14) 0.05799(6) Uiso 1.000000 R .
H45b H 0.21582106(14) 0.01993398(14) 0.10455438(14) 0.05799(6) Uiso 1.000000 R .
C1 C 0.04433912(14) 0.61039529(14) 0.34002005(14) 0.03001(5) Uani 1.000000 . .
C26 C 0.41783062(14) 0.96786720(14) 0.59867922(14) 0.05622(5) Uani 1.000000 . .
H26 H 0.45719750(14) 0.95093555(14) 0.59612587(14) 0.06746(6) Uiso 1.000000 R .
C44 C 0.08298482(14) 0.04566680(14) 0.06344119(14) 0.04033(5) Uani 1.000000 . .
H44a H 0.08165876(14) -0.00574795(14) 0.03998113(14) 0.06049(8) Uiso 1.000000 GR .
H44b H 0.03843758(14) 0.07313364(14) 0.05083730(14) 0.06049(8) Uiso 1.000000 GR .
H44c H 0.11422487(14) 0.09413835(14) 0.06377566(14) 0.06049(8) Uiso 1.000000 GR .
C6 C -0.02459905(14) 0.39277539(14) 0.25621669(14) 0.05346(5) Uani 1.000000 . .
H6 H -0.05526277(14) 0.34394104(14) 0.25259831(14) 0.06416(6) Uiso 1.000000 R .
C17 C 0.12900731(14) 0.93776112(14) 0.54534563(14) 0.03795(5) Uani 1.000000 . .
H17 H 0.11645461(14) 0.94651915(14) 0.50895087(14) 0.04554(6) Uiso 1.000000 R .
N11 N 0.31166834(14) 0.95305394(14) 0.44520628(14) 0.06547(5) Uani 1.000000 . .
C55 C 0.43562335(14) 0.31460770(14) 0.32350357(14) 0.10579076(14) Uiso 1.000000 . 3
H55a H 0.39026855(14) 0.28832912(14) 0.31120287(14) 0.12694891(17) Uiso 1.000000 R 3
H55b H 0.43215897(14) 0.37403651(14) 0.30422548(14) 0.12694891(17) Uiso 1.000000 R 3
C33 C 0.55574057(14) 0.82447859(14) 0.46630183(14) 0.12449(5) Uani 1.000000 . .
H33 H 0.59766396(14) 0.85548410(14) 0.48135063(14) 0.14939(6) Uiso 1.000000 R .
C35 C 0.49402126(14) 0.68666197(14) 0.43467550(14) 0.08670(5) Uani 1.000000 . .
H35 H 0.49359651(14) 0.62123026(14) 0.42758182(14) 0.10405(6) Uiso 1.000000 R .
N21 N 0.46321931(14) 0.33240685(14) 0.37721649(14) 0.08121950(14) Uiso 1.000000 . 3
C56 C 0.47924146(14) 0.24497779(14) 0.31244637(14) 0.11180662(14) Uiso 1.000000 . 3
C28 C 0.35805672(14) 1.17107746(14) 0.65703604(14) 0.07771(5) Uani 1.000000 . .
H28a H 0.37771598(14) 1.16157637(14) 0.69522141(14) 0.11657(8) Uiso 1.000000 GR .
H28b H 0.38240599(14) 1.22083899(14) 0.64908306(14) 0.11657(8) Uiso 1.000000 GR .
H28c H 0.31126799(14) 1.18949508(14) 0.64386509(14) 0.11657(8) Uiso 1.000000 GR .
N12 N 0.35016262(14) 1.01149011(14) 0.44995999(14) 0.09068(5) Uani 1.000000 . .
C32 C 0.50034296(14) 0.87337317(14) 0.45659134(14) 0.12384(5) Uani 1.000000 . .
H32 H 0.50266696(14) 0.93928112(14) 0.46288909(14) 0.14861(6) Uiso 1.000000 R .
C30 C 0.43485454(14) 0.73217161(14) 0.42390626(14) 0.06453(5) Uani 1.000000 . .
C57 C 0.47426793(14) 0.25841832(14) 0.41552339(14) 0.10614738(14) Uiso 1.000000 . 3
H57a H 0.51159594(14) 0.21714971(14) 0.41912408(14) 0.12737686(17) Uiso 1.000000 R 3
H57b H 0.48413459(14) 0.28525387(14) 0.45042019(14) 0.12737686(17) Uiso 1.000000 R 3
C51 C 0.41510778(14) 0.40600022(14) 0.38370644(14) 0.10838435(14) Uiso 1.000000 . 3
H51a H 0.40670604(14) 0.45758838(14) 0.35805456(14) 0.13006122(17) Uiso 1.000000 R 3
H51b H 0.37195418(14) 0.37486779(14) 0.37488628(14) 0.13006122(17) Uiso 1.000000 R 3
C59 C 0.08573838(14) 0.16948991(14) 0.38295388(14) 0.06218954(14) Uiso 0.60902000(14) . 1
H59a H 0.09497363(14) 0.15728026(14) 0.35254224(14) 0.07462745(17) Uiso 0.60902000(14) R 1
H59b H 0.08046971(14) 0.10751960(14) 0.39660461(14) 0.07462745(17) Uiso 0.60902000(14) R 1
C60 C 0.02029308(14) 0.22008204(14) 0.36290670(14) 0.07818944(14) Uiso 0.60902000(14) . 1
H60a H 0.01548581(14) 0.26241657(14) 0.33417227(14) 0.1172842(2) Uiso 0.60902000(14) GR 1
H60b H -0.01608470(14) 0.17407717(14) 0.34991196(14) 0.1172842(2) Uiso 0.60902000(14) GR 1
H60c H 0.01873012(14) 0.25679848(14) 0.39154132(14) 0.1172842(2) Uiso 0.60902000(14) GR 1
C58 C 0.40427232(14) 0.20068572(14) 0.39125962(14) 0.13918720(14) Uiso 1.000000 . 3

H58a H 0.36906039(14) 0.24085996(14) 0.39171290(14) 0.2087808(2) Uiso
1.000000 GR 3
H58b H 0.39257972(14) 0.18215377(14) 0.35492803(14) 0.2087808(2) Uiso
1.000000 GR 3
H58c H 0.40902068(14) 0.14427288(14) 0.41252462(14) 0.2087808(2) Uiso
1.000000 GR 3
C34 C 0.55276006(14) 0.73422087(14) 0.45526208(14) 0.09057(5) Uani
1.000000 .
.
H34 H 0.59259706(14) 0.70144983(14) 0.46182524(14) 0.10868(6) Uiso
1.000000 R
.
C31 C 0.43869833(14) 0.82626401(14) 0.43698676(14) 0.08963(5) Uani
1.000000 .
.
H31 H 0.39982599(14) 0.85924459(14) 0.43277912(14) 0.10756(6) Uiso
1.000000 R
.
C52 C 0.44357664(14) 0.45223948(14) 0.44355102(14) 0.23086287(14)
Uiso
1.000000 . 3
C62 C 0.12549503(14) 0.18319923(14) 0.50260035(14) 0.22307558(14)
Uiso
1.000000 . .
H62a H 0.08206822(14) 0.15548262(14) 0.47972718(14) 0.3346134(2)
Uiso
1.000000 GR .
H62b H 0.15943657(14) 0.13362209(14) 0.51513636(14) 0.3346134(2)
Uiso
1.000000 GR .
H62c H 0.12340441(14) 0.21361396(14) 0.53279069(14) 0.3346134(2)
Uiso
1.000000 GR .
C64 C 0.16951417(14) 0.30616776(14) 0.35843251(14) 0.09506225(14)
Uiso
0.57021000(14) . 1
H64a H 0.12650932(14) 0.30878885(14) 0.32692656(14) 0.1425934(2)
Uiso
0.57021000(14) GR 1
H64b H 0.19739428(14) 0.35891531(14) 0.35800068(14) 0.1425934(2)
Uiso
0.57021000(14) GR 1
H64c H 0.19182766(14) 0.24664960(14) 0.35885924(14) 0.1425934(2)
Uiso
0.57021000(14) GR 1
C63 C 0.15874906(14) 0.31238165(14) 0.40561998(14) 0.06343766(14)
Uiso
0.57021000(14) . 1
H63a H 0.12111628(14) 0.35566266(14) 0.39851014(14) 0.07612519(17)
Uiso
0.57021000(14) R 1
H63b H 0.19899355(14) 0.33938723(14) 0.43482214(14) 0.07612519(17)
Uiso
0.57021000(14) R 1
C65 C 0.19262432(14) 0.12759537(14) 0.44302139(14) 0.18343480(14)
Uiso
1.000000 . .
H65a H 0.17678639(14) 0.08022407(14) 0.46039339(14) 0.22012177(17)
Uiso
1.000000 R .
H65b H 0.19702897(14) 0.09727668(14) 0.41335588(14) 0.22012177(17)
Uiso
1.000000 R .
C66 C 0.25784941(14) 0.16957462(14) 0.48160895(14) 0.25300204(14)
Uiso
1.000000 . .
H66a H 0.27148355(14) 0.21833831(14) 0.46401559(14) 0.3795031(2)
Uiso
1.000000 GR .
H66b H 0.25266317(14) 0.19755452(14) 0.51109210(14) 0.3795031(2)
Uiso
1.000000 GR .
H66c H 0.29188653(14) 0.12017463(14) 0.49485355(14) 0.3795031(2)
Uiso
1.000000 GR .
C54 C 0.53513969(14) 0.46877368(14) 0.36649660(14) 0.11053602(14)
Uiso
1.000000 . 3
H54a H 0.53579997(14) 0.44485756(14) 0.33437379(14) 0.1658040(2)
Uiso
1.000000 GR 3
H54b H 0.49501931(14) 0.50687282(14) 0.35708856(14) 0.1658040(2)
Uiso
1.000000 GR 3
H54c H 0.57471485(14) 0.50764248(14) 0.38600770(14) 0.1658040(2)
Uiso
1.000000 GR 3
N26 N 0.29467942(14) 0.44032359(14) 0.44511321(14) 0.04287(5) Uani
0.49444000(14) . 1
N27 N 0.30948896(14) 0.36431909(14) 0.43121777(14) 0.06667(5) Uani
0.49444000(14) . 1
N25 N 0.28449628(14) 0.50710299(14) 0.45776947(14) 0.03125(5) Uani
1.000000 .
.
N26a N 0.34214534(14) 0.47598662(14) 0.47074117(14) 0.03981(5)
Uani
0.50556000(14) . 2
N27a N 0.39797714(14) 0.45952505(14) 0.48362993(14) 0.09661(5)
Uani
0.50556000(14) . 2
C59a C 0.06191864(14) 0.20608251(14) 0.38958585(14) 0.04532903(14)
Uiso
0.39098000(14) . 2
H59c H 0.04461873(14) 0.16564842(14) 0.40907397(14) 0.05439483(17)
Uiso
0.39098000(14) R 2
H59d H 0.04195496(14) 0.26940237(14) 0.38615761(14) 0.05439483(17)
Uiso
0.39098000(14) R 2
C60a C 0.04103531(14) 0.16474520(14) 0.33465935(14) 0.04585384(14)
Uiso
0.39098000(14) . 2
H60d H 0.06145629(14) 0.20127097(14) 0.31643512(14) 0.0687808(2)
Uiso
0.39098000(14) GR 2
H60e H 0.05583824(14) 0.09911526(14) 0.33788658(14) 0.0687808(2)
Uiso
0.39098000(14) GR 2
H60f H -0.00755876(14) 0.16738389(14) 0.31449067(14) 0.0687808(2)
Uiso
0.39098000(14) GR 2
C63a C 0.16686867(14) 0.24865931(14) 0.38835675(14) 0.04790679(14)
Uiso
0.42979000(14) . 2
H63c H 0.21611341(14) 0.24525128(14) 0.40614761(14) 0.05748815(17)
Uiso
0.42979000(14) R 2
H63d H 0.15104447(14) 0.20602595(14) 0.35754542(14) 0.05748815(17)
Uiso
0.42979000(14) R 2
C64a C 0.14674819(14) 0.34945084(14) 0.36814217(14) 0.05308211(14)
Uiso
0.42979000(14) . 2
H64d H 0.09986142(14) 0.35040643(14) 0.34195081(14) 0.0796232(2)
Uiso
0.42979000(14) GR 2
H64e H 0.15295232(14) 0.39073468(14) 0.39763451(14) 0.0796232(2)
Uiso
0.42979000(14) GR 2
H64f H 0.17456913(14) 0.37164077(14) 0.35191936(14) 0.0796232(2)
Uiso
0.42979000(14) GR 2
H52a H 0.43764883(14) 0.40699808(14) 0.46715989(14) 0.3462943(2)
Uiso
1.000000 GR 3
H52b H 0.49100122(14) 0.46699374(14) 0.45688282(14) 0.3462943(2)
Uiso
1.000000 GR 3
H52c H 0.41888697(14) 0.51002478(14) 0.44194066(14) 0.3462943(2)
Uiso
1.000000 GR 3
H56a H 0.49331972(14) 0.19463686(14) 0.33883075(14) 0.1677099(2)
Uiso
1.000000 GR 3
H56b H 0.45393520(14) 0.21782832(14) 0.27728531(14) 0.1677099(2)
Uiso
1.000000 GR 3
H56c H 0.51857971(14) 0.27759430(14) 0.31409710(14) 0.1677099(2)
Uiso
1.000000 GR 3
H61a H 0.18757744(14) 0.27982078(14) 0.49565705(14) 0.10459858(17)
Uiso
1.000000 R .
H61b H 0.11057908(14) 0.30637420(14) 0.46276367(14) 0.10459858(17)
Uiso
1.000000 R .
H49a H 0.18058979(14) -0.03108991(14) 0.21484403(14) 0.05699(6)
Uiso 1.000000
R .
H49b H 0.14310900(14) -0.12813867(14) 0.19108488(14) 0.05699(6)
Uiso 1.000000
R .

```
loop_
  _atom_site_aniso_label
  _atom_site_aniso_U_11
  _atom_site_aniso_U_22
  _atom_site_aniso_U_33
  _atom_site_aniso_U_12
  _atom_site_aniso_U_13
  _atom_site_aniso_U_23
 Zn1 0.03896(6) 0.03346(3) 0.02378(9) -
0.00258(4) 0.01674(7) -0.00118(5)
 Zn2 0.07879(6) 0.03305(3) 0.02604(9) -
0.02365(4) 0.02961(7) -0.00874(5)
 Mn3 0.04120(6) 0.03785(3) 0.01812(9) -
0.01442(4) 0.01563(7) -0.00916(5)
 Mn1 0.04436(6) 0.02026(3) 0.02025(9) -
0.00792(4) 0.01616(7) -0.00433(5)
 Mn2 0.05245(6) 0.04376(3) 0.01966(9) -
0.02496(4) 0.01926(7) -0.01203(5)
 Cl1 0.06493(6) 0.04124(3) 0.04396(9)
0.00648(4) 0.02973(7) 0.00354(5)
 Cl2 0.10071(6) 0.04397(3) 0.04060(9) -
0.02018(4) 0.03622(7) -0.00317(5)
 O2 0.04409(6) 0.01498(3) 0.04359(9) -
0.00376(4) 0.02465(7) -0.00568(5)
 O1 0.04347(6) 0.02561(3) 0.02096(9) -
0.01267(4) 0.01647(7) -0.00742(5)
 O7 0.04363(6) 0.02803(3) 0.02714(9) -
0.01682(4) 0.01726(7) -0.01181(5)
 N13 0.05669(6) 0.03205(3) 0.02293(9) -
0.01832(4) 0.02237(7) -0.00960(5)
 N7 0.06667(6) 0.02676(3) 0.01409(9) -
0.00905(4) 0.02503(7) -0.00012(5)
 C21 0.06343(6) 0.02346(3) 0.01723(9) -
0.00087(4) 0.00940(7) -0.00023(5)
 O4 0.05425(6) 0.04567(3) 0.02147(9) -
0.01947(4) 0.02527(7) -0.01647(5)
 O3 0.03698(6) 0.03784(3) 0.02415(9) -
0.00301(4) 0.01563(7) -0.00787(5)
 O5 0.04796(6) 0.09381(3) 0.02261(9) -
0.03800(4) 0.02350(7) -0.02865(5)
 N5 0.05451(6) 0.02974(3) 0.01750(9)
0.00715(4) 0.02541(7) 0.00774(5)
 O6 0.06979(6) 0.05053(3) 0.02602(9) -
0.03434(4) 0.02782(7) -0.02181(5)
 N8 0.04654(6) 0.02112(3) 0.02370(9) -
0.00537(4) 0.00963(7) 0.00679(5)
 N14 0.06575(6) 0.03521(3) 0.05069(9) -
0.00523(4) 0.04160(7) 0.00823(5)
 N19 0.04397(6) 0.04090(3) 0.03172(9)
0.00123(4) 0.02410(7) 0.00071(5)
 C13 0.04863(6) 0.01336(3) 0.03164(9) -
0.01139(4) 0.01497(7) -0.00004(5)
 N4 0.04220(6) 0.03768(3) 0.01756(9) -
0.01099(4) 0.01536(7) -0.00137(5)
 C9 0.05377(6) 0.02138(3) 0.02806(9) -
0.00413(4) 0.02449(7) 0.00027(5)
 N23 0.04612(6) 0.06096(3) 0.03115(9) -
0.03432(4) 0.02488(7) -0.02013(5)
 C19 0.05502(6) 0.03690(3) 0.04328(9) -
0.00201(4) 0.01295(7) -0.01484(5)
 C40 0.03762(6) 0.04393(3) 0.01979(9)
0.00029(4) 0.01206(7) -0.00187(5)
 C11 0.04043(6) 0.03242(3) 0.03832(9) -
0.00484(4) 0.01896(7) -0.00520(5)
 N9 0.05455(6) 0.03535(3) 0.05026(9) -
0.00355(4) 0.01776(7) 0.00959(5)
 N1 0.04350(6) 0.03584(3) 0.01970(9) -
0.01170(4) 0.00934(7) -0.00590(5)
 C8 0.05457(6) 0.01472(3) 0.02962(9) -
0.01123(4) 0.02391(7) -0.00028(5)
 N6 0.03403(6) 0.03123(3) 0.04086(9) -
0.01141(4) 0.01913(7) -0.00423(5)
 N3 0.07964(6) 0.07152(3) 0.01769(9) -
0.02569(4) 0.02360(7) -0.01769(5)
 C18 0.06140(6) 0.04361(3) 0.04504(9)
0.02608(4) -0.00318(7) -0.01142(5)
 C2 0.04372(6) 0.03081(3) 0.00722(9) -
0.00066(4) 0.00335(7) -0.00513(5)
 C16 0.06343(6) 0.02346(3) 0.01723(9) -
0.00087(4) 0.00940(7) -0.00023(5)
 C12 0.04737(6) 0.02215(3) 0.04068(9) -
0.00630(4) 0.02440(7) -0.00707(5)
 C15 0.06343(6) 0.02346(3) 0.01723(9) -
0.00087(4) 0.00940(7) -0.00023(5)
 C10 0.05258(6) 0.01603(3) 0.05386(9)
0.00168(4) 0.02400(7) 0.00413(5)
 N2 0.05234(6) 0.03816(3) 0.03372(9) -
0.01580(4) 0.02606(7) -0.00362(5)
 C37 0.03603(6) 0.04472(3) 0.02611(9) -
0.00840(4) 0.01281(7) -0.00183(5)
 C38 0.03997(6) 0.05838(3) 0.03383(9)
0.00683(4) 0.02584(7) 0.00583(5)
 C41 0.03006(6) 0.04281(3) 0.03342(9) -
0.00219(4) 0.01718(7) -0.00162(5)
 C39 0.05443(6) 0.05315(3) 0.01508(9)
0.00108(4) 0.01432(7) -0.00052(5)
 N22 0.04364(6) 0.02321(3) 0.02703(9) -
0.00413(4) 0.02123(7) -0.00045(5)
 C3 0.06247(6) 0.07976(3) 0.02283(9) -
0.02375(4) 0.02221(7) -0.02389(5)
 C36 0.04446(6) 0.05228(3) 0.03670(9) -
0.00832(4) 0.02632(7) -0.00775(5)
 C24 0.09547(6) 0.04323(3) 0.02169(9) -
0.02212(4) 0.01652(7) -0.00148(5)
 N15 0.10558(6) 0.05301(3) 0.03827(9) -
0.01162(4) 0.03571(7) -0.01532(5)
 N10 0.09033(6) 0.06232(3) 0.02443(9) -
0.05348(4) 0.02652(7) -0.01856(5)
 C20 0.04952(6) 0.04454(3) 0.02272(9) -
0.00879(4) 0.01710(7) -0.01296(5)
 C27 0.05651(6) 0.04248(3) 0.02364(9) -
0.02313(4) 0.01216(7) -0.00193(5)
 C7 0.05379(6) 0.05043(3) 0.03424(9) -
0.02035(4) 0.02195(7) -0.00343(5)
 C48 0.06997(6) 0.03483(3) 0.06525(9) -
0.00330(4) 0.02035(7) -0.00489(5)
 C47 0.06192(6) 0.03699(3) 0.03768(9)
0.01000(4) 0.02965(7) -0.00379(5)
 C49 0.04905(6) 0.06692(3) 0.02813(9)
0.00432(4) 0.01875(7) 0.00563(5)
 C43 0.05680(6) 0.04014(3) 0.02704(9)
0.01088(4) 0.02594(7) 0.00139(5)
 C14 0.05639(6) 0.04583(3) 0.05918(9)
0.01715(4) 0.01566(7) 0.00674(5)
 C4 0.06339(6) 0.10308(3) 0.02619(9) -
0.01023(4) 0.02635(7) -0.01743(5)
 C25 0.09633(6) 0.05385(3) 0.02883(9) -
0.04338(4) 0.01093(7) -0.01253(5)
 C29 0.04782(6) 0.05443(3) 0.04540(9) -
0.02270(4) 0.02801(7) -0.00838(5)
 C42 0.06885(6) 0.07621(3) 0.03347(9) -
0.01979(4) 0.03692(7) -0.01463(5)
 C5 0.07107(6) 0.04331(3) 0.02529(9)
0.00808(4) 0.00544(7) -0.01038(5)
 C50 0.06427(6) 0.09431(3) 0.03925(9) -
0.00141(4) 0.02919(7) 0.00580(5)
 C22 0.06343(6) 0.02346(3) 0.01723(9) -
0.00087(4) 0.00940(7) -0.00023(5)
 C23 0.09846(6) 0.02658(3) 0.01569(9) -
0.02308(4) 0.01686(7) -0.00227(5)
 C46 0.08026(6) 0.04232(3) 0.07507(9) -
0.00965(4) 0.05205(7) -0.01165(5)
 N24 0.05788(6) 0.02820(3) 0.02009(9) -
0.01231(4) 0.01968(7) -0.00436(5)
 C45 0.05663(6) 0.04877(3) 0.04608(9) -
0.00426(4) 0.02882(7) -0.00595(5)
 C1 0.03865(6) 0.02009(3) 0.03703(9) -
0.01035(4) 0.02209(7) 0.00325(5)
 C26 0.06313(6) 0.04600(3) 0.03085(9) -
0.03390(4) -0.00449(7) -0.00965(5)
 C44 0.05602(6) 0.04060(3) 0.03414(9)
0.00951(4) 0.02893(7) 0.00390(5)
 C6 0.07979(6) 0.02816(3) 0.04433(9) -
0.01652(4) 0.02058(7) -0.02070(5)
 C17 0.06343(6) 0.02346(3) 0.01723(9) -
0.00087(4) 0.00940(7) -0.00023(5)
 N11 0.09733(6) 0.06915(3) 0.03823(9) -
0.04206(4) 0.03777(7) -0.01977(5)
 C33 0.12004(6) 0.22177(3) 0.04737(9) -
0.10800(4) 0.05152(7) -0.03856(5)
 C35 0.06719(6) 0.14392(3) 0.03306(9) -
0.04854(4) 0.00826(7) 0.00905(5)
 C28 0.12060(6) 0.03899(3) 0.04291(9) -
0.02776(4) 0.00935(7) -0.02751(5)
 N12 0.14319(6) 0.05916(3) 0.09924(9) -
0.06913(4) 0.08068(7) -0.04157(5)
 C32 0.16649(6) 0.15747(3) 0.10579(9) -
0.11222(4) 0.11292(7) -0.07786(5)
 C30 0.06378(6) 0.10654(3) 0.03255(9) -
0.05777(4) 0.02986(7) -0.03342(5)
 C34 0.06082(6) 0.17340(3) 0.02762(9) -
0.05307(4) 0.01104(7) 0.00579(5)
 C31 0.11106(6) 0.09980(3) 0.09792(9) -
0.06119(4) 0.08240(7) -0.03660(5)
 N26 0.02746(6) 0.06248(3) 0.03419(9)
0.00072(4) 0.00983(7) 0.02231(5)
 N27 0.10838(6) 0.02645(3) 0.06892(9)
0.01951(4) 0.04307(7) 0.00479(5)
 N25 0.03710(6) 0.03780(3) 0.02646(9) -
0.00207(4) 0.02104(7) -0.00993(5)
 N26a 0.03757(6) 0.06631(3) 0.02119(9) -
0.00075(4) 0.01818(7) 0.01532(5)
 N27a 0.04472(6) 0.17655(3) 0.08152(9)
0.05320(4) 0.03984(7) 0.07017(5)

loop_
  _geom_bond_atom_site_label_1
  _geom_bond_atom_site_label_2
  _geom_bond_distance
  _geom_bond_site_symmetry_2
 Zn1 Cl1 2.2433(5) .
 Zn1 N4 2.0052(2) .
 Zn1 N1 2.0038(4) .
 Zn1 N25 2.0150(2) .
 Zn2 Cl2 2.2423(4) .
 Zn2 N13 2.0671(4) .
 Zn2 N7 2.02624(16) .
 Zn2 N10 2.0140(3) .
 Mn3 Mn1 3.2642(3) .
 Mn3 Mn2 3.2694(6) .
 Mn3 O1 1.8896(3) .
 Mn3 N13 2.4007(5) .
 Mn3 O4 1.8657(3) .
 Mn3 O3 1.9047(2) .
 Mn3 N23 2.0000(3) .
 Mn3 N25 2.2870(5) .
 Mn1 Mn2 3.2701(4) .
 Mn1 O2 1.86968(13) .
 Mn1 O1 1.90339(13) .
 Mn1 O7 1.9148(3) .
 Mn1 N7 2.3276(5) .
 Mn1 N4 2.4290(5) .
 Mn1 N22 2.0261(4) .
 Mn2 O1 1.8681(3) .
 Mn2 O5 1.92172(19) .
 Mn2 O6 1.8847(3) .
 Mn2 N1 2.4058(5) .
 Mn2 N10 2.3115(5) .
 Mn2 N24 2.04728(19) .
 O2 C13 1.3080(2) .
 O7 N24 1.37117(19) .
 N13 N14 1.09719(18) .
 N7 N8 1.20255(18) .
 C21 C16 1.3911(2) .
 C21 C20 1.41487(12) .
 O4 C41 1.34416(12) .
 O3 N22 1.37063(18) .
 O5 N23 1.4074(2) .
 N5 N4 1.1966(2) .
 N5 N6 1.1664(2) .
 O6 C27 1.3660(3) .
 N8 N9 1.15318(16) .
 N14 N15 1.2229(2) .
 N19 C47 1.5213(3) .
 N19 C49 1.5354(2) .
 N19 C43 1.5260(2) .
 N19 C45 1.51350(19) .
 C13 C8 1.4474(2) .
 C13 C12 1.38868(18) .
 N20 C61 1.5180(2) .
 N20 C59 1.4347(2) .
 N20 C63 1.5700(3) .
 N20 C65 1.5808(3) .
 N20 C59a 1.64444(19) .
 N20 C63a 1.40167(16) .
 C9 C8 1.3976(2) .
 C9 C10 1.37907(18) .
 N23 C29 1.31205(11) .
 C19 C18 1.3692(2) .
 C19 C20 1.3678(2) .
 C40 C41 1.4223(2) .
 C40 C39 1.39187(13) .
 C11 C12 1.3874(2) .
 C11 C10 1.4020(2) .
 N1 N2 1.18955(18) .
 C8 C1 1.47330(18) .
 N3 N2 1.17900(18) .
 C18 C17 1.40795(12) .
 C2 C3 1.41392(13) .
```

C2 C7 1.3484(2) .
C2 C1 1.4990(3) .
C16 C15 1.49775(12) .
C16 C17 1.3833(2) .
C15 C22 1.4551(2) .
C15 N24 1.3116(2) .
C10 C14 1.5004(2) .
C37 C38 1.4071(2) .
C37 C36 1.42798(13) .
C38 C39 1.4023(3) .
C38 C42 1.49919(14) .
C41 C36 1.4113(3) .
N22 C1 1.29625(18) .
C3 C4 1.3998(3) .
C36 C29 1.4270(2) .
C24 C25 1.32292(11) .
C24 C23 1.4049(2) .
C24 C28 1.5621(3) .
N10 N11 1.1891(2) .
C27 C22 1.40014(12) .
C27 C26 1.4172(2) .
C7 C6 1.3924(3) .
C48 C47 1.5197(2) .
C49 C50 1.4916(2) .
C43 C44 1.5267(2) .
C4 C5 1.3616(2) .
C61 C62 1.4777(2) .
C25 C26 1.3957(3) .
C29 C30 1.5045(2) .
C53 N21 1.5790(2) .
C53 C54 1.6788(3) .
C5 C6 1.38021(13) .
C22 C23 1.4237(3) .
C46 C45 1.4974(3) .
N11 N12 1.16187(19) .
C55 N21 1.3886(2) .
C55 C56 1.5206(2) .
C33 C32 1.34124(18) .
C33 C34 1.3142(3) .
C35 C30 1.38314(18) .
C35 C34 1.3591(2) .
N21 C57 1.4518(3) .
N21 C51 1.5725(2) .
C32 C31 1.4084(2) .
C30 C31 1.3793(3) .
C57 C58 1.6272(2) .
C51 C52 1.6600(3) .
C59 C60 1.5003(2) .
C64 C63 1.46754(18) .
C65 C66 1.5045(2) .
N26 N27 1.2447(2) .
N26 N25 1.0746(2) .
N25 N26a 1.25701(14) .
N26a N27a 1.16181(11) .
C59a C60a 1.5307(3) .
C63a C64a 1.5331(3) .

loop_
_geom_angle_atom_site_label_1
_geom_angle_atom_site_label_2
_geom_angle_atom_site_label_3
_geom_angle
_geom_angle_site_symmetry_1
_geom_angle_site_symmetry_3
N4 Zn1 Cl1 114.7346(3) . .
N1 Zn1 Cl1 114.0090(3) . .
N1 Zn1 N4 106.2170(3) . .
N25 Zn1 Cl1 107.8232(3) . .
N25 Zn1 N4 109.1531(3) . .
N25 Zn1 N1 104.3492(3) . .
N13 Zn2 Cl2 112.0700(3) . .
N7 Zn2 Cl2 119.1641(2) . .
N7 Zn2 N13 105.6442(3) . .
N10 Zn2 Cl2 106.4037(3) . .
N10 Zn2 N13 110.2876(3) . .
N10 Zn2 N7 102.7749(3) . .
Mn2 Mn3 Mn1 60.06768(19) . .
O1 Mn3 Mn1 30.74290(15) . .
O1 Mn3 Mn2 29.35024(15) . .
N13 Mn3 Mn1 85.7213(3) . .
N13 Mn3 Mn2 91.9445(3) . .
N13 Mn3 O1 87.8167(3) . .
O4 Mn3 Mn1 150.98469(18) . .
O4 Mn3 Mn2 148.9114(2) . .
O4 Mn3 O1 178.2572(2) . .
O4 Mn3 N13 92.5467(3) . .
O3 Mn3 Mn1 60.5313(2) . .
O3 Mn3 Mn2 119.7291(3) . .
O3 Mn3 O1 90.9667(3) . .
O3 Mn3 N13 93.0812(3) . .
O3 Mn3 O4 90.7158(3) . .
N23 Mn3 Mn1 119.0948(3) . .
N23 Mn3 Mn2 59.8409(2) . .
N23 Mn3 O1 88.6340(3) . .
N23 Mn3 N13 87.2159(3) . .
N23 Mn3 O4 89.6810(3) . .
N23 Mn3 O3 179.4932(3) . .
N25 Mn3 Mn1 95.2855(3) . .
N25 Mn3 Mn2 85.0612(3) . .
N25 Mn3 O1 90.9790(3) . .
N25 Mn3 N13 175.81200(15) . .
N25 Mn3 O4 88.5387(3) . .
N25 Mn3 O3 90.9489(3) . .
N25 Mn3 N23 88.7459(3) . .
Mn2 Mn1 Mn3 60.0459(2) . .
O2 Mn1 Mn3 145.9124(2) . .
O2 Mn1 Mn2 154.0067(2) . .
O1 Mn1 Mn3 30.49720(17) . .
O1 Mn1 Mn2 29.57378(16) . .
O1 Mn1 O2 176.4091(2) . .
O7 Mn1 Mn3 121.6927(2) . .
O7 Mn1 Mn2 62.6972(2) . .
O7 Mn1 O2 91.5896(3) . .
O7 Mn1 O1 91.9136(3) . .
N7 Mn1 Mn3 93.5312(3) . .
N7 Mn1 Mn2 86.2212(3) . .
N7 Mn1 O2 91.7155(3) . .
N7 Mn1 O1 88.8942(3) . .
N7 Mn1 O7 92.9130(3) . .
N4 Mn1 Mn3 83.3015(2) . .
N4 Mn1 Mn2 94.4188(3) . .
N4 Mn1 O2 89.4779(3) . .
N4 Mn1 O1 89.6736(3) . .
N4 Mn1 O7 90.9833(3) . .
N4 Mn1 N7 175.8914(2) . .
N22 Mn1 Mn3 58.5281(2) . .
N22 Mn1 Mn2 118.2446(3) . .
N22 Mn1 O2 87.6931(3) . .
N22 Mn1 O1 88.7527(3) . .
N22 Mn1 O7 175.4528(2) . .
N22 Mn1 N7 91.5969(3) . .
N22 Mn1 N4 84.5215(3) . .
Mn1 Mn2 Mn3 59.8864(2) . .
O1 Mn2 Mn3 29.72264(19) . .
O1 Mn2 Mn1 30.18995(19) . .
O5 Mn2 Mn3 61.4759(2) . .
O5 Mn2 Mn1 121.2817(2) . .
O5 Mn2 O1 91.1916(3) . .
O6 Mn2 Mn3 151.7379(2) . .
O6 Mn2 Mn1 147.6675(3) . .
O6 Mn2 O1 175.6857(3) . .
O6 Mn2 O5 90.4414(3) . .
N1 Mn2 Mn3 90.3500(3) . .
N1 Mn2 Mn1 82.4941(3) . .
N1 Mn2 O1 86.8319(3) . .
N1 Mn2 O5 95.1459(3) . .
N1 Mn2 O6 89.0448(3) . .
N10 Mn2 Mn3 89.6133(3) . .
N10 Mn2 Mn1 90.6731(3) . .
N10 Mn2 O1 89.2322(3) . .
N10 Mn2 O5 91.7661(3) . .
N10 Mn2 O6 94.7091(3) . .
N10 Mn2 N1 172.1115(2) . .
N24 Mn2 Mn3 118.4129(2) . .
N24 Mn2 Mn1 58.5275(2) . .
N24 Mn2 O1 88.6987(3) . .
N24 Mn2 O5 177.4960(2) . .
N24 Mn2 O6 89.4954(3) . .
N24 Mn2 N1 82.3503(3) . .
N24 Mn2 N10 90.7338(3) . .
C13 O2 Mn1 124.9856(4) . .
Mn1 O1 Mn3 118.7599(3) . .
Mn2 O1 Mn3 120.9271(3) . .
Mn2 O1 Mn1 120.2363(3) . .
N24 O7 Mn1 116.5596(4) . .
Mn3 N13 Zn2 110.9777(3) . .
N14 N13 Zn2 123.2053(3) . .
N14 N13 Mn3 120.6383(3) . .
Mn1 N7 Zn2 112.5427(2) . .
N8 N7 Zn2 125.3615(3) . .
N8 N7 Mn1 116.8718(4) . .
C20 C21 C16 118.9800(3) . .
C41 O4 Mn3 125.7377(3) . .
N22 O3 Mn3 116.7199(3) . .
N23 O5 Mn2 116.8727(3) . .
N6 N5 N4 177.9001(3) . .
C27 O6 Mn2 125.7613(3) . .
N9 N8 N7 176.0293(3) . .
N15 N14 N13 176.3771(5) . .
C49 N19 C47 111.6137(3) . .
C43 N19 C47 111.1833(3) . .
C43 N19 C49 105.6176(4) . .
C45 N19 C47 107.1523(4) . .
C45 N19 C49 110.5750(3) . .
C45 N19 C43 110.7563(3) . .
C8 C13 O2 122.3998(4) . .
C12 C13 O2 120.1007(4) . .
C12 C13 C8 117.4797(3) . .
C63 N20 C59 112.8919(4) . .
C65 N20 C61 104.6049(3) . .
C63a N20 C59a 106.7565(3) . .
Mn1 N4 Zn1 109.7012(3) . .
N5 N4 Zn1 131.6432(3) . .
N5 N4 Mn1 107.5592(3) . .
C10 C9 C8 123.1945(4) . .
O5 N23 Mn3 115.2455(4) . .
C29 N23 Mn3 127.4948(3) . .
C29 N23 O5 117.2113(3) . .
C20 C19 C18 120.6048(4) . .
C39 C40 C41 122.1396(3) . .
C10 C11 C12 121.4588(4) . .
Mn2 N1 Zn1 113.0611(3) . .
N2 N1 Zn1 128.2160(4) . .
N2 N1 Mn2 114.0670(3) . .
C9 C8 C13 118.7038(4) . .
C1 C8 C13 120.5615(3) . .
C1 C8 C9 120.6878(4) . .
C17 C18 C19 119.6015(3) . .
C7 C2 C3 117.6011(3) . .
C1 C2 C3 120.0820(3) . .
C1 C2 C7 122.0916(4) . .
C15 C16 C21 117.9824(3) . .
C17 C16 C21 119.6676(4) . .
C17 C16 C15 122.2637(4) . .
C11 C12 C13 121.7619(4) . .
C22 C15 C16 118.3271(3) . .
N24 C15 C16 120.0120(3) . .
N24 C15 C22 121.6475(4) . .
C11 C10 C9 117.3256(3) . .
C14 C10 C9 124.0141(4) . .
C14 C10 C11 118.6529(3) . .
N3 N2 N1 177.5859(4) . .
C36 C37 C38 122.9613(3) . .
C39 C38 C37 118.9476(4) . .
C42 C38 C37 120.8788(3) . .
C42 C38 C39 120.1732(4) . .
C40 C41 O4 116.7352(3) . .
C36 C41 O4 123.4796(4) . .
C36 C41 C40 119.7155(4) . .
C38 C39 C40 119.2192(4) . .
O3 N22 Mn1 113.1289(3) . .
C1 N22 Mn1 128.4458(4) . .
C1 N22 O3 117.0276(4) . .
C4 C3 C2 120.3106(3) . .
C41 C36 C37 116.8699(4) . .
C29 C36 C37 118.8646(3) . .
C29 C36 C41 124.1491(4) . .
C23 C24 C25 118.4529(3) . .
C28 C24 C25 124.3890(3) . .
C28 C24 C23 117.0830(4) . .
Mn2 N10 Zn2 113.2882(3) . .
N11 N10 Zn2 121.9919(4) . .
N11 N10 Mn2 122.5476(3) . .
C19 C20 C21 120.5914(4) . .
C22 C27 O6 123.7935(3) . .
C26 C27 O6 116.6436(4) . .
C26 C27 C22 119.5623(3) . .
C6 C7 C2 122.0786(5) . .
C48 C47 N19 115.7845(4) . .
C50 C49 N19 113.9841(4) . .
C44 C43 N19 114.3867(4) . .
C5 C4 C3 120.4708(4) . .
C62 C61 N20 113.2232(3) . .
C26 C25 C24 123.6054(3) . .
C36 C29 N23 120.6986(3) . .
C30 C29 N23 118.9942(4) . .
C30 C29 C36 120.3011(4) . .
C54 C53 N21 107.3689(3) . .
C6 C5 C4 119.1201(3) . .
C27 C22 C15 123.2695(3) . .
C23 C22 C15 118.7973(4) . .
C23 C22 C27 117.8911(3) . .
C22 C23 C24 121.5866(4) . .
O7 N24 Mn2 116.9488(3) . .

C15 N24 Mn2 127.0984(3) . .
C15 N24 O7 115.3482(4) . .
C46 C45 N19 116.3210(4) . .
C2 C1 C8 119.3947(3) . .
N22 C1 C8 120.4115(4) . .
N22 C1 C2 120.1901(4) . .
C25 C26 C27 118.8423(4) . .
C5 C6 C7 120.3075(3) . .
C16 C17 C18 120.4707(4) . .
N12 N11 N10 179.0855(5) . .
C56 C55 N21 109.4975(3) . .
C34 C33 C32 120.8359(3) . .
C34 C35 C30 120.9392(3) . .
C55 N21 C53 117.6401(4) . .
C57 N21 C53 97.9108(3) . .
C57 N21 C55 122.2729(3) . .
C51 N21 C53 106.0385(3) . .
C51 N21 C55 104.9565(3) . .
C51 N21 C57 106.7820(4) . .
C31 C32 C33 119.4981(3) . .
C35 C30 C29 121.7077(3) . .
C31 C30 C29 121.1999(3) . .
C31 C30 C35 117.0801(3) . .
C58 C57 N21 103.8362(3) . .
C52 C51 N21 114.4253(3) . .
C35 C34 C33 121.5460(4) . .
C30 C31 C32 119.8981(4) . .
C66 C65 N20 104.4092(3) . .
Mn3 N25 Zn1 111.6311(3) . .

. .

CIF for compound **5:**

```
data_10ms001

_audit_creation_method           SHELXL-97
_chemical_name_systematic
;
 ?
;
_chemical_name_common            Mn3(Me-sao)3(2,4′-bipyridine)3ReO4
_chemical_melting_point          ?
_chemical_formula_moiety         ?
_chemical_formula_sum
'C55 H46.50 Mn3 N9.50 O11 Re'
_chemical_formula_weight         1367.54

loop_
 _atom_type_symbol
 _atom_type_description
 _atom_type_scat_dispersion_real
 _atom_type_scat_dispersion_imag
 _atom_type_scat_source
 'C'  'C'   0.0033   0.0016
 'International Tables Vol C Tables 4.2.6.8 and 6.1.1.4'
 'H'  'H'   0.0000   0.0000
 'International Tables Vol C Tables 4.2.6.8 and 6.1.1.4'
 'N'  'N'   0.0061   0.0033
 'International Tables Vol C Tables 4.2.6.8 and 6.1.1.4'
 'O'  'O'   0.0106   0.0060
 'International Tables Vol C Tables 4.2.6.8 and 6.1.1.4'
 'Mn'  'Mn'   0.3368   0.7283
 'International Tables Vol C Tables 4.2.6.8 and 6.1.1.4'
 'Re'  'Re'  -1.0185   7.2310
 'International Tables Vol C Tables 4.2.6.8 and 6.1.1.4'

_symmetry_cell_setting           ?
_symmetry_space_group_name_H-M    ?

loop_
 _symmetry_equiv_pos_as_xyz
 'x, y, z'
 '-y, x-y, z'
 '-x+y, -x, z'
 '-x, -y, -z'
 'y, -x+y, -z'
 'x-y, x, -z'

_cell_length_a                   12.8252(6)
_cell_length_b                   12.8252(6)
_cell_length_c                   18.5900(9)
_cell_angle_alpha                 90.00
_cell_angle_beta                  90.00
_cell_angle_gamma                 120.00
_cell_volume                     2648.1(2)
_cell_formula_units_Z            2
_cell_measurement_temperature     120(2)
_cell_measurement_reflns_used     ?
_cell_measurement_theta_min       ?
_cell_measurement_theta_max       ?

_exptl_crystal_description        ?
_exptl_crystal_colour             ?
_exptl_crystal_size_max           ?
_exptl_crystal_size_mid           ?
_exptl_crystal_size_min           ?
_exptl_crystal_density_meas       ?
_exptl_crystal_density_diffrn     1.715
_exptl_crystal_density_method     'not measured'
_exptl_crystal_F_000              1362
_exptl_absorpt_coefficient_mu     3.049
_exptl_absorpt_correction_type    ?
_exptl_absorpt_correction_T_min   ?
_exptl_absorpt_correction_T_max   ?
_exptl_absorpt_process_details    ?

_exptl_special_details
;
 ?
;

_diffrn_ambient_temperature       120(2)
_diffrn_radiation_wavelength      0.71073
_diffrn_radiation_type            MoK\a
_diffrn_radiation_source          'fine-focus sealed tube'
_diffrn_radiation_monochromator   graphite
_diffrn_measurement_device_type   ?
_diffrn_measurement_method        ?
_diffrn_detector_area_resol_mean  ?
_diffrn_standards_number          ?
_diffrn_standards_interval_count  ?
_diffrn_standards_interval_time   ?
_diffrn_standards_decay_%         ?
_diffrn_reflns_number             52012
_diffrn_reflns_av_R_equivalents   0.0295
_diffrn_reflns_av_sigmaI/netI     0.0179
_diffrn_reflns_limit_h_min        -18
_diffrn_reflns_limit_h_max        19
_diffrn_reflns_limit_k_min        -19
_diffrn_reflns_limit_k_max        19
_diffrn_reflns_limit_l_min        -27
_diffrn_reflns_limit_l_max        27
_diffrn_reflns_theta_min          1.83
_diffrn_reflns_theta_max          32.38
_reflns_number_total              6074
_reflns_number_gt                 5511
_reflns_threshold_expression      >2\s(I)

_computing_data_collection        ?
_computing_cell_refinement        ?
_computing_data_reduction         ?
_computing_structure_solution     ?
_computing_structure_refinement   'SHELXL-97 (Sheldrick, 2008)'
_computing_molecular_graphics     ?
_computing_publication_material   ?

_refine_special_details
;
 Refinement of F^2^ against ALL reflections.  The weighted R-factor wR
and
 goodness of fit S are based on F^2^, conventional R-factors R are based
 on F, with F set to zero for negative F^2^. The threshold expression of
 F^2^ > 2\s(F^2^) is used only for calculating R-factors(gt) etc. and is
 not relevant to the choice of reflections for refinement.  R-factors based
 on F^2^ are statistically about twice as large as those based on F, and R-
 factors based on ALL data will be even larger.
;

_refine_ls_structure_factor_coef  Fsqd
_refine_ls_matrix_type            full
_refine_ls_weighting_scheme       calc
_refine_ls_weighting_details
 'calc w=1/[\s^2^(Fo^2^)+(0.0292P)^2^+1.7079P] where
P=(Fo^2^+2Fc^2^)/3'
_atom_sites_solution_primary      direct
_atom_sites_solution_secondary    difmap
_atom_sites_solution_hydrogens    geom
_refine_ls_hydrogen_treatment     mixed
_refine_ls_extinction_method      none
_refine_ls_extinction_coef        ?
_refine_ls_number_reflns          6074
_refine_ls_number_parameters      283
_refine_ls_number_restraints      149
_refine_ls_R_factor_all           0.0267
_refine_ls_R_factor_gt            0.0208
_refine_ls_wR_factor_ref          0.0571
_refine_ls_wR_factor_gt           0.0537
_refine_ls_goodness_of_fit_ref    1.089
_refine_ls_restrained_S_all       1.089
_refine_ls_shift/su_max           0.001
_refine_ls_shift/su_mean          0.000

loop_
 _atom_site_label
 _atom_site_type_symbol
 _atom_site_fract_x
 _atom_site_fract_y
 _atom_site_fract_z
 _atom_site_U_iso_or_equiv
 _atom_site_adp_type
 _atom_site_occupancy
 _atom_site_symmetry_multiplicity
 _atom_site_calc_flag
 _atom_site_refinement_flags
 _atom_site_disorder_assembly
 _atom_site_disorder_group
Mn1 Mn 0.73150(2) 0.22840(2) 0.273820(14) 0.01733(5) Uani 1 1 d . . .
O1 O 0.6667 0.3333 0.26523(12) 0.0194(4) Uani 1 3 d S . .
Re1 Re 0.6667 0.3333 0.435153(6) 0.01543(3) Uani 1 3 d S . .
O3 O 0.6667 0.3333 0.52757(11) 0.0205(4) Uani 1 3 d S A .
O4 O 0.75241(11) 0.27271(11) 0.40350(7) 0.0199(2) Uani 1 1 d . A .
```

```
C1 C 0.62862(15) -0.00868(14) 0.37589(9) 0.0180(3) Uani 1 1 d . A .
C2 C 0.74515(15) 0.04043(14) 0.34499(9) 0.0181(3) Uani 1 1 d . . .
O2 O 0.78497(12) 0.11969(11) 0.29176(7) 0.0212(2) Uani 1 1 d . A .
C3 C 0.82208(16) -0.00039(16) 0.37004(10) 0.0234(3) Uani 1 1 d . A .
H3 H 0.8985 0.0285 0.3480 0.028 Uiso 1 1 calc R . .
C4 C 0.78879(17) -0.08163(17) 0.42606(11) 0.0259(4) Uani 1 1 d . . .
H4 H 0.8422 -0.1081 0.4419 0.031 Uiso 1 1 calc R A .
C5 C 0.67741(17) -0.12514(16) 0.45960(10) 0.0244(3) Uani 1 1 d . A .
H5 H 0.6560 -0.1781 0.4996 0.029 Uiso 1 1 calc R . .
C6 C 0.59858(16) -0.09001(15) 0.43371(10) 0.0215(3) Uani 1 1 d . . .
H6 H 0.5217 -0.1217 0.4556 0.026 Uiso 1 1 calc R A .
C7 C 0.53633(15) 0.01551(15) 0.34719(9) 0.0184(3) Uani 1 1 d . . .
C8 C 0.40937(16) -0.05361(17) 0.37456(11) 0.0251(3) Uani 1 1 d . A .
H8A H 0.3585 -0.0312 0.3469 0.038 Uiso 1 1 calc R . .
H8B H 0.4076 -0.0346 0.4255 0.038 Uiso 1 1 calc R . .
H8C H 0.3791 -0.1401 0.3692 0.038 Uiso 1 1 calc R . .
N7 N 0.56569(13) 0.09815(13) 0.29800(8) 0.0183(3) Uani 1 1 d . . .
O5 O 0.89080(11) 0.36527(11) 0.26647(7) 0.0208(2) Uani 1 1 d . A .
N11A N 0.7322(8) 0.1820(6) 0.1552(8) 0.0232(7) Uani 0.755(5) 1 d PDU
A 1
C12A C 0.8358(4) 0.2025(3) 0.12489(17) 0.0250(6) Uani 0.755(5) 1 d
PDU A 1
H12A H 0.9029 0.2219 0.1551 0.030 Uiso 0.755(5) 1 calc PR A 1
C13A C 0.8488(3) 0.1965(3) 0.05141(16) 0.0275(6) Uani 0.755(5) 1 d
PDU A 1
H13A H 0.9230 0.2101 0.0319 0.033 Uiso 0.755(5) 1 calc PR A 1
C14A C 0.7523(5) 0.1704(5) 0.0063(3) 0.0284(9) Uani 0.755(5) 1 d PDU
A 1
C15A C 0.6436(10) 0.1457(11) 0.0375(9) 0.0322(6) Uani 0.755(5) 1 d
PDU A 1
H15A H 0.5748 0.1250 0.0086 0.039 Uiso 0.755(5) 1 calc PR A 1
C16A C 0.6381(14) 0.1521(11) 0.1116(8) 0.0291(10) Uani 0.755(5) 1 d
PDU A 1
H16A H 0.5636 0.1344 0.1327 0.035 Uiso 0.755(5) 1 calc PR A 1
C17A C 0.7630(3) 0.1712(3) -0.0739(3) 0.0336(9) Uani 0.755(5) 1 d
PDU A 1
N18A N 0.6685(5) 0.1502(5) -0.1155(4) 0.0473(8) Uani 0.755(5) 1 d
PDU A 1
C19A C 0.6815(5) 0.1549(6) -0.1882(5) 0.0492(11) Uani 0.755(5) 1 d
PDU A 1
H19A H 0.6149 0.1395 -0.2178 0.059 Uiso 0.755(5) 1 calc PR A 1
C20A C 0.7892(4) 0.1817(4) -0.2198(2) 0.0489(12) Uani 0.755(5) 1 d
PDU A 1
H20A H 0.7982 0.1864 -0.2706 0.059 Uiso 0.755(5) 1 calc PR A 1
C21A C 0.8835(3) 0.2014(5) -0.17557(17) 0.0628(14) Uani 0.755(5) 1 d
PDU A 1
H21A H 0.9584 0.2192 -0.1962 0.075 Uiso 0.755(5) 1 calc PR A 1
C22A C 0.8710(3) 0.1958(4) -0.10230(16) 0.0466(9) Uani 0.755(5) 1 d
PDU A 1
H22A H 0.9360 0.2087 -0.0720 0.056 Uiso 0.755(5) 1 calc PR A 1
N11B N 0.730(3) 0.194(2) 0.156(3) 0.0232(7) Uani 0.245(5) 1 d PD A 2
C12B C 0.630(5) 0.150(4) 0.115(3) 0.0291(10) Uani 0.245(5) 1 d PD A 2
H12B H 0.5544 0.1213 0.1378 0.035 Uiso 0.245(5) 1 calc PR A 2
C13B C 0.636(3) 0.145(4) 0.041(3) 0.0322(6) Uani 0.245(5) 1 d PD A 2
H13B H 0.5633 0.1130 0.0145 0.039 Uiso 0.245(5) 1 calc PR A 2
C14B C 0.7428(16) 0.1857(18) 0.0037(9) 0.0284(9) Uani 0.245(5) 1 d PD
A 2
C15B C 0.8442(12) 0.2295(10) 0.0464(5) 0.0275(6) Uani 0.245(5) 1 d PD
A 2
H15B H 0.9211 0.2581 0.0250 0.033 Uiso 0.245(5) 1 calc PR A 2
C16B C 0.8339(14) 0.2317(11) 0.1203(6) 0.0250(6) Uani 0.245(5) 1 d PD
A 2
H16B H 0.9055 0.2622 0.1480 0.030 Uiso 0.245(5) 1 calc PR A 2
C17B C 0.7541(11) 0.1957(12) -0.0765(9) 0.0336(9) Uani 0.245(5) 1 d
PD A 2
N18B N 0.8638(9) 0.2552(10) -0.1057(4) 0.0466(9) Uani 0.245(5) 1 d PD
A 2
C19B C 0.8736(11) 0.2650(12) -0.1775(4) 0.0628(14) Uani 0.245(5) 1 d
PD A 2
H19B H 0.9517 0.3074 -0.1983 0.075 Uiso 0.245(5) 1 calc PR A 2
C20B C 0.7748(13) 0.2161(13) -0.2223(8) 0.0489(12) Uani 0.245(5) 1 d
PD A 2
H20B H 0.7838 0.2241 -0.2731 0.059 Uiso 0.245(5) 1 calc PR A 2
C21B C 0.6626(18) 0.1551(18) -0.1909(16) 0.0492(11) Uani 0.245(5) 1 d
PD A 2
H21B H 0.5929 0.1206 -0.2206 0.059 Uiso 0.245(5) 1 calc PR A 2
C22B C 0.650(2) 0.1434(19) -0.1169(15) 0.0473(8) Uani 0.245(5) 1 d PD
A 2
;

loop_
 _geom_bond_atom_site_label_1
 _geom_bond_atom_site_label_2
 _geom_bond_distance
 _geom_bond_site_symmetry_2
 _geom_bond_publ_flag
Mn1 O2 1.8658(13) . ?
Mn1 O1 1.9097(3) . ?
Mn1 O5 1.9203(13) . ?
Mn1 N7 1.9906(15) . ?
Mn1 N11B 2.24(5) . ?
Mn1 N11A 2.285(14) . ?
Mn1 O4 2.4604(13) . ?
O1 Mn1 1.9097(3) 2_655 ?
O1 Mn1 1.9097(3) 3_665 ?
Re1 O3 1.718(2) . ?
Re1 O4 1.7364(12) . ?
Re1 O4 1.7364(12) 3_665 ?
Re1 O4 1.7364(12) 2_655 ?
C1 C6 1.411(2) . ?
C1 C2 1.421(2) . ?
C1 C7 1.466(2) . ?
C2 O2 1.324(2) . ?
H22B H 0.5724 0.1013 -0.0949 0.057 Uiso 0.245(5) 1 calc PR A 2
C31A C 0.0000 0.0000 0.0744(8) 0.061(2) Uiso 0.335(8) 3 d SPD B 1
H31A H -0.0831 -0.0456 0.0568 0.091 Uiso 0.112(3) 1 calc PR B 1
H31B H 0.0456 -0.0375 0.0568 0.091 Uiso 0.112(3) 1 calc PR B 1
H31C H 0.0375 0.0831 0.0568 0.091 Uiso 0.112(3) 1 calc PR B 1
C32A C 0.0000 0.0000 0.1527(8) 0.061(2) Uiso 0.335(8) 3 d SPD B 1
N33A N 0.0000 0.0000 0.2145(7) 0.061(2) Uiso 0.335(8) 3 d SPD B 1
C31B C 0.0000 0.0000 0.1680(15) 0.061(2) Uiso 0.165(8) 3 d SPD B 2
H31D H -0.0830 -0.0364 0.1855 0.091 Uiso 0.055(3) 1 calc PR B 2
H31E H 0.0465 0.0830 0.1855 0.091 Uiso 0.055(3) 1 calc PR B 2
H31F H 0.0364 -0.0465 0.1855 0.091 Uiso 0.055(3) 1 calc PR B 2
C32B C 0.0000 0.0000 0.0901(13) 0.061(2) Uiso 0.165(8) 3 d SPD B 2
N33B N 0.0000 0.0000 0.0288(13) 0.061(2) Uiso 0.165(8) 3 d SPD . 2

loop_
 _atom_site_aniso_label
 _atom_site_aniso_U_11
 _atom_site_aniso_U_22
 _atom_site_aniso_U_33
 _atom_site_aniso_U_23
 _atom_site_aniso_U_13
 _atom_site_aniso_U_12
Mn1 0.01874(11) 0.01797(11) 0.01538(12) 0.00042(8) 0.00236(8)
0.00925(9)
O1 0.0197(6) 0.0197(6) 0.0187(10) 0.000 0.000 0.0098(3)
Re1 0.01661(4) 0.01661(4) 0.01307(5) 0.000 0.000 0.00830(2)
O3 0.0238(6) 0.0238(6) 0.0138(9) 0.000 0.000 0.0119(3)
O4 0.0208(5) 0.0217(6) 0.0194(6) -0.0006(4) 0.0001(4) 0.0122(5)
C1 0.0198(7) 0.0169(7) 0.0169(7) -0.0019(5) 0.0002(6) 0.0088(6)
C2 0.0206(7) 0.0168(7) 0.0170(7) -0.0028(5) 0.0014(6) 0.0094(6)
O2 0.0232(6) 0.0228(6) 0.0201(6) 0.0027(5) 0.0059(5) 0.0134(5)
C3 0.0225(8) 0.0240(8) 0.0260(9) 0.0001(7) 0.0024(6) 0.0134(7)
C4 0.0267(8) 0.0241(8) 0.0302(9) 0.0020(7) -0.0006(7) 0.0151(7)
C5 0.0278(8) 0.0200(7) 0.0245(9) 0.0024(6) -0.0009(7) 0.0114(7)
C6 0.0215(7) 0.0186(7) 0.0217(8) 0.0004(6) 0.0014(6) 0.0079(6)
C7 0.0187(7) 0.0183(7) 0.0169(7) -0.0027(5) 0.0009(5) 0.0083(6)
C8 0.0203(8) 0.0268(8) 0.0260(9) 0.0029(7) 0.0026(6) 0.0102(7)
N7 0.0190(6) 0.0196(6) 0.0175(6) -0.0021(5) -0.0009(5) 0.0105(5)
O5 0.0208(6) 0.0202(5) 0.0212(6) -0.0016(4) 0.0032(4) 0.0101(5)
N11A 0.0293(8) 0.0217(17) 0.0181(7) -0.0021(16) 0.0032(6) 0.0125(10)
C12A 0.0287(9) 0.0263(18) 0.0230(10) -0.0019(11) 0.0017(8) 0.0159(13)
C13A 0.0307(10) 0.0259(17) 0.0237(10) -0.0023(11) 0.0069(8)
0.0125(12)
C14A 0.0346(13) 0.0238(18) 0.0189(9) -0.0021(10) 0.0044(8) 0.0086(10)
C15A 0.0343(17) 0.0374(11) 0.0209(19) -0.0064(10) -0.0013(10)
0.0150(12)
C16A 0.027(2) 0.0340(11) 0.0226(18) -0.0057(10) 0.0026(15) 0.0121(13)
C17A 0.0414(13) 0.0247(18) 0.0198(10) -0.0019(13) 0.0062(9)
0.0053(11)
N18A 0.050(2) 0.0484(15) 0.0293(11) -0.0078(10) 0.0061(15) 0.0136(16)
C19A 0.049(2) 0.0520(15) 0.0310(14) -0.0106(11) -0.0030(19) 0.0139(16)
C20A 0.0500(18) 0.047(3) 0.0187(11) -0.0029(16) 0.0053(11) 0.0009(16)
C21A 0.0395(16) 0.084(3) 0.0312(14) -0.017(2) 0.0060(12) 0.005(2)
C22A 0.0398(14) 0.066(3) 0.0214(12) -0.0092(16) -0.0008(10) 0.0171(17)
N11B 0.0293(8) 0.0217(17) 0.0181(7) -0.0021(16) 0.0032(6) 0.0125(10)
C12B 0.027(2) 0.0340(11) 0.0226(18) -0.0057(10) 0.0026(15) 0.0121(13)
C13B 0.0343(17) 0.0374(11) 0.0209(19) -0.0064(10) -0.0013(10)
0.0150(12)
C14B 0.0346(13) 0.0238(18) 0.0189(9) -0.0021(10) 0.0044(8) 0.0086(10)
C15B 0.0307(10) 0.0259(17) 0.0237(10) -0.0023(11) 0.0069(8) 0.0125(12)
C16B 0.0287(9) 0.0263(18) 0.0230(10) -0.0019(11) 0.0017(8) 0.0159(13)
C17B 0.0414(13) 0.0247(18) 0.0198(10) -0.0019(13) 0.0062(9) 0.0053(11)
N18B 0.0398(14) 0.066(3) 0.0214(12) -0.0092(16) -0.0008(10) 0.0171(17)
C19B 0.0395(16) 0.084(3) 0.0312(14) -0.017(2) 0.0060(12) 0.005(2)
C20B 0.0500(18) 0.047(3) 0.0187(11) -0.0029(16) 0.0053(11) 0.0009(16)
C21B 0.049(2) 0.0520(15) 0.0310(14) -0.0106(11) -0.0030(19) 0.0139(16)
C22B 0.050(2) 0.0484(15) 0.0293(11) -0.0078(10) 0.0061(15) 0.0136(16)

_geom_special_details
;
 All s.u.'s (except the s.u. in the dihedral angle between two l.s. planes)
 are estimated using the full covariance matrix.  The cell s.u.'s are taken
 into account individually in the estimation of s.u.'s in distances, angles
 and torsion angles; correlations between s.u.'s in cell parameters are only
 used when they are defined by crystal symmetry.  An approximate
(isotropic)
 treatment of cell s.u.'s is used for estimating s.u.'s involving l.s. planes.
```

C2 C3 1.407(2) . ?
C3 C4 1.381(3) . ?
C3 H3 0.9500 . ?
C4 C5 1.394(3) . ?
C4 H4 0.9500 . ?
C5 C6 1.383(3) . ?
C5 H5 0.9500 . ?
C6 H6 0.9500 . ?
C7 N7 1.305(2) . ?
C7 C8 1.501(2) . ?
C8 H8A 0.9800 . ?
C8 H8B 0.9800 . ?
C8 H8C 0.9800 . ?
N7 O5 1.3777(18) 3_665 ?
O5 N7 1.3778(18) 2_655 ?
N11A C16A 1.341(3) . ?
N11A C12A 1.343(3) . ?
C12A C13A 1.383(3) . ?
C12A H12A 0.9500 . ?
C13A C14A 1.390(3) . ?
C13A H13A 0.9500 . ?
C14A C15A 1.393(4) . ?
C14A C17A 1.497(4) . ?
C15A C16A 1.384(3) . ?
C15A H15A 0.9500 . ?
C16A H16A 0.9500 . ?
C17A N18A 1.346(4) . ?
C17A C22A 1.364(4) . ?
N18A C19A 1.360(3) . ?
C19A C20A 1.378(4) . ?
C19A H19A 0.9500 . ?
C20A C21A 1.377(4) . ?
C20A H20A 0.9500 . ?
C21A C22A 1.369(3) . ?
C21A H21A 0.9500 . ?
C22A H22A 0.9500 . ?
N11B C16B 1.340(5) . ?
N11B C12B 1.341(5) . ?
C12B C13B 1.382(5) . ?
C12B H12B 0.9500 . ?
C13B C14B 1.384(5) . ?
C13B H13B 0.9500 . ?
C14B C15B 1.381(5) . ?
C14B C17B 1.496(10) . ?
C15B C16B 1.381(5) . ?
C15B H15B 0.9500 . ?
C16B H16B 0.9500 . ?
C17B N18B 1.335(5) . ?
C17B C22B 1.384(5) . ?
N18B C19B 1.341(5) . ?
C19B C20B 1.377(5) . ?
C19B H19B 0.9500 . ?
C20B C21B 1.378(5) . ?
C20B H20B 0.9500 . ?
C21B C22B 1.386(5) . ?
C21B H21B 0.9500 . ?
C22B H22B 0.9500 . ?
C31A C32A 1.455(15) . ?
C31A H31A 0.9800 . ?
C31A H31B 0.9800 . ?
C31A H31C 0.9800 . ?
C32A N33A 1.149(15) . ?
C31B C32B 1.447(19) . ?
C31B H31D 0.9800 . ?
C31B H31E 0.9800 . ?
C31B H31F 0.9800 . ?
C32B N33B 1.139(19) . ?
N33B N33B 1.07(5) 4 ?

loop_
 _geom_angle_atom_site_label_1
 _geom_angle_atom_site_label_2
 _geom_angle_atom_site_label_3
 _geom_angle
 _geom_angle_site_symmetry_1
 _geom_angle_site_symmetry_3
 _geom_angle_publ_flag
O2 Mn1 O1 173.57(7) . . ?
O2 Mn1 O5 94.31(6) . . ?
O1 Mn1 O5 89.37(4) . . ?
O2 Mn1 N7 88.29(6) . . ?
O1 Mn1 N7 87.21(4) . . ?
O5 Mn1 N7 170.08(6) . . ?
O2 Mn1 N11B 89.8(7) . . ?
O1 Mn1 N11B 95.4(7) . . ?
O5 Mn1 N11B 90.6(7) . . ?
N7 Mn1 N11B 99.0(7) . . ?
O2 Mn1 N11A 85.8(2) . . ?
O1 Mn1 N11A 99.3(2) . . ?
O5 Mn1 N11A 91.64(19) . . ?
N7 Mn1 N11A 98.1(2) . . ?
N11B Mn1 N11A 4.1(9) . . ?
O2 Mn1 O4 87.66(5) . . ?
O1 Mn1 O4 87.40(7) . . ?
O5 Mn1 O4 85.14(5) . . ?
N7 Mn1 O4 85.41(5) . . ?
N11B Mn1 O4 174.9(7) . . ?
N11A Mn1 O4 172.5(2) . . ?
Mn1 O1 Mn1 119.309(19) . 2_655 ?
Mn1 O1 Mn1 119.309(19) . 3_665 ?
Mn1 O1 Mn1 119.309(19) 2_655 3_665 ?
O3 Re1 O4 109.81(4) . . ?
O3 Re1 O4 109.81(4) . 3_665 ?
O4 Re1 O4 109.13(4) . 3_665 ?
O3 Re1 O4 109.81(4) . 2_655 ?
O4 Re1 O4 109.13(4) . 2_655 ?
O4 Re1 O4 109.13(4) 3_665 2_655 ?
Re1 O4 Mn1 114.53(6) . . ?
C6 C1 C2 118.28(15) . . ?
C6 C1 C7 118.87(15) . . ?
C2 C1 C7 122.72(15) . . ?
O2 C2 C3 117.37(15) . . ?
O2 C2 C1 123.97(15) . . ?
C3 C2 C1 118.61(16) . . ?
C2 O2 Mn1 124.22(11) . . ?
C4 C3 C2 121.36(17) . . ?
C4 C3 H3 119.3 . . ?
C2 C3 H3 119.3 . . ?
C3 C4 C5 120.50(17) . . ?
C3 C4 H4 119.8 . . ?
C5 C4 H4 119.8 . . ?
C6 C5 C4 118.92(17) . . ?
C6 C5 H5 120.5 . . ?
C4 C5 H5 120.5 . . ?
C5 C6 C1 122.16(16) . . ?
C5 C6 H6 118.9 . . ?
C1 C6 H6 118.9 . . ?
N7 C7 C1 119.44(15) . . ?
N7 C7 C8 120.31(16) . . ?
C1 C7 C8 120.26(15) . . ?
C7 C8 H8A 109.5 . . ?
C7 C8 H8B 109.5 . . ?
H8A C8 H8B 109.5 . . ?
C7 C8 H8C 109.5 . . ?
H8A C8 H8C 109.5 . . ?
H8B C8 H8C 109.5 . . ?
C7 N7 O5 117.82(14) . 3_665 ?
C7 N7 Mn1 126.39(12) . . ?
O5 N7 Mn1 115.05(10) 3_665 . ?
N7 O5 Mn1 113.33(9) 2_655 . ?
C16A N11A C12A 117.6(13) . . ?
C16A N11A Mn1 122.6(7) . . ?
C12A N11A Mn1 119.1(9) . . ?
N11A C12A C13A 122.6(8) . . ?
N11A C12A H12A 118.7 . . ?
C13A C12A H12A 118.7 . . ?
C12A C13A C14A 119.5(4) . . ?
C12A C13A H13A 120.3 . . ?
C14A C13A H13A 120.3 . . ?
C13A C14A C15A 118.3(9) . . ?
C13A C14A C17A 122.1(5) . . ?
C15A C14A C17A 119.6(8) . . ?
C16A C15A C14A 118.4(14) . . ?
C16A C15A H15A 120.8 . . ?
C14A C15A H15A 120.8 . . ?
N11A C16A C15A 123.7(15) . . ?
N11A C16A H16A 118.2 . . ?
C15A C16A H16A 118.2 . . ?
N18A C17A C22A 122.2(5) . . ?
N18A C17A C14A 120.0(5) . . ?
C22A C17A C14A 117.8(4) . . ?
C17A N18A C19A 119.0(7) . . ?
N18A C19A C20A 121.3(7) . . ?
N18A C19A H19A 119.3 . . ?
C20A C19A H19A 119.3 . . ?
C19A C20A C21A 118.1(5) . . ?
C19A C20A H20A 121.0 . . ?
C21A C20A H20A 121.0 . . ?
C22A C21A C20A 121.0(4) . . ?
C22A C21A H21A 119.5 . . ?
C20A C21A H21A 119.5 . . ?
C17A C22A C21A 118.4(4) . . ?
C17A C22A H22A 120.8 . . ?
C21A C22A H22A 120.8 . . ?
C16B N11B C12B 116(4) . . ?
C16B N11B Mn1 120(3) . . ?
C12B N11B Mn1 123(2) . . ?
N11B C12B C13B 121(5) . . ?
N11B C12B H12B 119.5 . . ?
C13B C12B H12B 119.5 . . ?
C12B C13B C14B 123(5) . . ?
C12B C13B H13B 118.3 . . ?
C14B C13B H13B 118.3 . . ?
C15B C14B C13B 115(3) . . ?
C15B C14B C17B 120.4(16) . . ?
C13B C14B C17B 125(3) . . ?
C14B C15B C16B 120.0(13) . . ?
C14B C15B H15B 120.0 . . ?
C16B C15B H15B 120.0 . . ?
N11B C16B C15B 125(3) . . ?
N11B C16B H16B 117.7 . . ?
C15B C16B H16B 117.7 . . ?
N18B C17B C22B 123.0(18) . . ?
N18B C17B C14B 118.9(16) . . ?
C22B C17B C14B 118.1(16) . . ?
C17B N18B C19B 118.8(11) . . ?
N18B C19B C20B 122.5(12) . . ?
N18B C19B H19B 118.8 . . ?
C20B C19B H19B 118.8 . . ?
C19B C20B C21B 117.7(17) . . ?
C19B C20B H20B 121.1 . . ?
C21B C20B H20B 121.1 . . ?
C20B C21B C22B 121(3) . . ?
C20B C21B H21B 119.4 . . ?
C22B C21B H21B 119.4 . . ?
C17B C22B C21B 117(3) . . ?
C17B C22B H22B 121.6 . . ?
C21B C22B H22B 121.6 . . ?
N33A C32A C31A 180.000(2) . . ?
C32B C31B H31D 109.5 . . ?
C32B C31B H31E 109.5 . . ?
H31D C31B H31E 109.5 . . ?
C32B C31B H31F 109.5 . . ?
H31D C31B H31F 109.5 . . ?
H31E C31B H31F 109.5 . . ?
N33B C32B C31B 180.000(2) . . ?
N33B N33B C32B 180.0 4 . ?

loop_
 _geom_torsion_atom_site_label_1
 _geom_torsion_atom_site_label_2
 _geom_torsion_atom_site_label_3
 _geom_torsion_atom_site_label_4
 _geom_torsion
 _geom_torsion_site_symmetry_1
 _geom_torsion_site_symmetry_2
 _geom_torsion_site_symmetry_3
 _geom_torsion_site_symmetry_4
 _geom_torsion_publ_flag
O2 Mn1 O1 Mn1 112.7(4) . . . 2_655 ?
O5 Mn1 O1 Mn1 -12.28(12) . . . 2_655 ?
N7 Mn1 O1 Mn1 158.41(12) . . . 2_655 ?
N11B Mn1 O1 Mn1 -102.9(7) . . . 2_655 ?
N11A Mn1 O1 Mn1 -103.8(2) . . . 2_655 ?
O4 Mn1 O1 Mn1 72.89(11) . . . 2_655 ?
O2 Mn1 O1 Mn1 -50.8(6) . . . 3_665 ?
O5 Mn1 O1 Mn1 -175.80(12) . . . 3_665 ?
N7 Mn1 O1 Mn1 -5.12(12) . . . 3_665 ?
N11B Mn1 O1 Mn1 93.6(7) . . . 3_665 ?
N11A Mn1 O1 Mn1 92.6(2) . . . 3_665 ?
O4 Mn1 O1 Mn1 -90.64(11) . . . 3_665 ?
O3 Re1 O4 Mn1 168.62(4) . . . . ?
O4 Re1 O4 Mn1 48.20(7) 3_665 . . . ?
O4 Re1 O4 Mn1 -70.97(5) 2_655 . . . ?
O2 Mn1 O4 Re1 -157.97(7) . . . . ?
O1 Mn1 O4 Re1 17.91(6) . . . . ?
O5 Mn1 O4 Re1 107.49(7) . . . . ?
N7 Mn1 O4 Re1 -69.50(7) . . . . ?
N11B Mn1 O4 Re1 142(7) . . . . ?
N11A Mn1 O4 Re1 172.3(13) . . . . ?
C6 C1 C2 O2 -178.31(15) . . . . ?
C7 C1 C2 O2 5.8(3) . . . . ?
C6 C1 C2 C3 4.3(2) . . . . ?
C7 C1 C2 C3 -171.58(16) . . . . ?
C3 C2 O2 Mn1 -155.17(13) . . . . ?
C1 C2 O2 Mn1 27.4(2) . . . . ?
O1 Mn1 O2 C2 6.0(6) . . . . ?
O5 Mn1 O2 C2 130.74(14) . . . . ?
N7 Mn1 O2 C2 -39.68(14) . . . . ?
N11B Mn1 O2 C2 -138.6(7) . . . . ?
N11A Mn1 O2 C2 -137.9(2) . . . . ?
O4 Mn1 O2 C2 45.80(13) . . . . ?
O2 C2 C3 C4 179.01(17) . . . . ?
C1 C2 C3 C4 -3.4(3) . . . . ?

C2 C3 C4 C5 -0.3(3) . . . . ?
C3 C4 C5 C6 3.0(3) . . . . ?
C4 C5 C6 C1 -2.0(3) . . . . ?
C2 C1 C6 C5 -1.7(3) . . . . ?
C7 C1 C6 C5 174.38(16) . . . . ?
C6 C1 C7 N7 174.10(15) . . . . ?
C2 C1 C7 N7 -10.0(2) . . . . ?
C6 C1 C7 C8 -5.5(2) . . . . ?
C2 C1 C7 C8 170.40(16) . . . . ?
C1 C7 N7 O5 172.84(14) . . . 3_665 ?
C8 C7 N7 O5 -7.6(2) . . . 3_665 ?
C1 C7 N7 Mn1 -17.5(2) . . . . ?
C8 C7 N7 Mn1 162.04(13) . . . . ?
O2 Mn1 N7 C7 36.12(14) . . . . ?
O1 Mn1 N7 C7 -139.28(15) . . . . ?
O5 Mn1 N7 C7 -69.3(4) . . . . ?
N11B Mn1 N7 C7 125.7(7) . . . . ?
N11A Mn1 N7 C7 121.7(3) . . . . ?
O4 Mn1 N7 C7 -51.66(14) . . . . ?
O2 Mn1 N7 O5 -153.99(11) . . . 3_665 ?
O1 Mn1 N7 O5 30.60(12) . . . 3_665 ?
O5 Mn1 N7 O5 100.6(3) . . . 3_665 ?
N11B Mn1 N7 O5 -64.4(7) . . . 3_665 ?
N11A Mn1 N7 O5 -68.4(2) . . . 3_665 ?
O4 Mn1 N7 O5 118.22(11) . . . 3_665 ?
O2 Mn1 O5 N7 -140.28(11) . . . 2_655 ?
O1 Mn1 O5 N7 34.45(12) . . . 2_655 ?
N7 Mn1 O5 N7 -35.4(4) . . . 2_655 ?
N11B Mn1 O5 N7 129.8(7) . . . 2_655 ?
N11A Mn1 O5 N7 133.8(2) . . . 2_655 ?
O4 Mn1 O5 N7 -53.00(10) . . . 2_655 ?
O2 Mn1 N11A C16A 130.7(4) . . . . ?
O1 Mn1 N11A C16A -45.5(4) . . . . ?
O5 Mn1 N11A C16A -135.1(4) . . . . ?
N7 Mn1 N11A C16A 43.0(4) . . . . ?
N11B Mn1 N11A C16A -59(13) . . . . ?
O4 Mn1 N11A C16A 160.5(14) . . . . ?
O2 Mn1 N11A C12A -59.6(4) . . . . ?
O1 Mn1 N11A C12A 124.2(4) . . . . ?
O5 Mn1 N11A C12A 34.6(4) . . . . ?
N7 Mn1 N11A C12A -147.3(4) . . . . ?
N11B Mn1 N11A C12A 110(13) . . . . ?
O4 Mn1 N11A C12A -29.8(16) . . . . ?
C16A N11A C12A C13A 1.5(2) . . . . ?
Mn1 N11A C12A C13A -168.7(3) . . . . ?
N11A C12A C13A C14A 1.2(2) . . . . ?
C12A C13A C14A C15A -2.9(4) . . . . ?
C12A C13A C14A C17A 175.5(3) . . . . ?
C13A C14A C15A C16A 2.0(5) . . . . ?
C17A C14A C15A C16A -176.4(4) . . . . ?
C12A N11A C16A C15A -2.4(4) . . . . ?
Mn1 N11A C16A C15A 167.4(4) . . . . ?
C14A C15A C16A N11A 0.7(5) . . . . ?
C13A C14A C17A N18A -177.3(3) . . . . ?
C15A C14A C17A N18A 1.1(5) . . . . ?
C13A C14A C17A C22A 1.6(6) . . . . ?
C15A C14A C17A C22A 180.0(5) . . . . ?
C22A C17A N18A C19A -0.8(2) . . . . ?
C14A C17A N18A C19A 178.1(3) . . . . ?
C17A N18A C19A C20A -0.5(2) . . . . ?
N18A C19A C20A C21A 1.2(5) . . . . ?
C19A C20A C21A C22A -0.6(6) . . . . ?
N18A C17A C22A C21A 1.3(5) . . . . ?
C14A C17A C22A C21A -177.5(4) . . . . ?
C20A C21A C22A C17A -0.6(6) . . . . ?
O2 Mn1 N11B C16B -69.0(15) . . . . ?
O1 Mn1 N11B C16B 114.7(15) . . . . ?
O5 Mn1 N11B C16B 25.3(15) . . . . ?
N7 Mn1 N11B C16B -157.2(14) . . . . ?
N11A Mn1 N11B C16B -79(13) . . . . ?
O4 Mn1 N11B C16B -9(8) . . . . ?
O2 Mn1 N11B C12B 119.9(9) . . . . ?
O1 Mn1 N11B C12B -56.4(9) . . . . ?
O5 Mn1 N11B C12B -145.8(9) . . . . ?
N7 Mn1 N11B C12B 31.6(9) . . . . ?
N11A Mn1 N11B C12B 110(13) . . . . ?
O4 Mn1 N11B C12B -180(34) . . . . ?
C16B N11B C12B C13B -0.4(3) . . . . ?
Mn1 N11B C12B C13B 171.0(12) . . . . ?
N11B C12B C13B C14B -0.5(3) . . . . ?
C12B C13B C14B C15B 1.1(6) . . . . ?
C12B C13B C14B C17B -172.4(14) . . . . ?
C13B C14B C15B C16B -0.7(8) . . . . ?
C17B C14B C15B C16B 173.1(13) . . . . ?
C12B N11B C16B C15B 0.8(7) . . . . ?
Mn1 N11B C16B C15B -170.9(11) . . . . ?
C14B C15B C16B N11B -0.2(9) . . . . ?
C15B C14B C17B N18B -5(2) . . . . ?
C13B C14B C17B N18B 168.3(13) . . . . ?
C15B C14B C17B C22B 175.8(12) . . . . ?
C13B C14B C17B C22B -11.1(14) . . . . ?
C22B C17B N18B C19B 0.1(3) . . . . ?
C14B C17B N18B C19B -179.3(13) . . . . ?
C17B N18B C19B C20B 0.0(3) . . . . ?
N18B C19B C20B C21B 0.0(7) . . . . ?
C19B C20B C21B C22B -0.1(9) . . . . ?
N18B C17B C22B C21B -0.1(7) . . . . ?
C14B C17B C22B C21B 179.2(13) . . . . ?
C20B C21B C22B C17B 0.1(9) . . . . ?
C31B C32B N33B N33B 0.0 . . . 4 ?

_diffrn_measured_fraction_theta_max
0.957
_diffrn_reflns_theta_full 31.00
_diffrn_measured_fraction_theta_full 0.998
_refine_diff_density_max 1.353
_refine_diff_density_min -0.588
_refine_diff_density_rms 0.096

CIF for compound **6**

```
data_shelxl
_audit_creation_date              2014-04-04
_audit_creation_method
;
Olex2 1.2
(compiled 2013.12.10 svn.r2850 for OlexSys, GUI svn.r4736)
;
_publ_contact_author_address     ?
_publ_contact_author_email       ?
_publ_contact_author_name        ?
_publ_contact_author_phone       ?
_publ_section_references
;
Bourhis, L.J., Dolomanov, O.V., Gildea, R.J., Howard, J.A.K.,
Puschmann, H.
 (2013). in preparation

Bourhis, L.J., Dolomanov, O.V., Gildea, R.J., Howard, J.A.K.,
Puschmann, H.
 (2013). in preparation

Dolomanov, O.V., Bourhis, L.J., Gildea, R.J, Howard, J.A.K. &
Puschmann, H.
 (2009), J. Appl. Cryst. 42, 339-341.
;
_chemical_name_systematic        ?
_chemical_formula_moiety
'4(C57 H51 Cl Mn3 N9 O11), C2 H3 N'
_chemical_formula_sum            'C230 H207 Cl4 Mn12 N37 O44'
_chemical_formula_weight         4994.50
_chemical_absolute_configuration  unk
loop_
  _atom_type_symbol
  _atom_type_scat_dispersion_real
  _atom_type_scat_dispersion_imag
  _atom_type_scat_Cromer_Mann_a1
  _atom_type_scat_Cromer_Mann_a2
  _atom_type_scat_Cromer_Mann_a3
  _atom_type_scat_Cromer_Mann_a4
  _atom_type_scat_Cromer_Mann_b1
  _atom_type_scat_Cromer_Mann_b2
  _atom_type_scat_Cromer_Mann_b3
  _atom_type_scat_Cromer_Mann_b4
  _atom_type_scat_Cromer_Mann_c
  _atom_type_scat_source
  _atom_type_scat_dispersion_source
 C 0.00347 0.00161 2.31000 1.02000 1.58860 0.86500 20.84390
10.20750 0.56870
 51.65120 0.215599998832
 'International Tables Volume C Table 6.1.1.4 (pp. 500-502)'
 'Henke, Gullikson and Davis, At. Data and Nucl. Data Tables, 1993, 54,
2'
 Cl 0.14873 0.16029 11.46040 7.19640 6.25560 1.64550 0.01040 1.16620
18.51940
 47.77840 -9.55739974976
 'International Tables Volume C Table 6.1.1.4 (pp. 500-502)'
 'Henke, Gullikson and Davis, At. Data and Nucl. Data Tables, 1993, 54,
2'
 H 0.00000 0.00000 0.49300 0.32291 0.14019 0.04081 10.51090
26.12570 3.14236
 57.79970 0.0030380000826
 'International Tables Volume C Table 6.1.1.4 (pp. 500-502)'
 'Henke, Gullikson and Davis, At. Data and Nucl. Data Tables, 1993, 54,
2'
 Mn 0.34779 0.73263 11.28190 7.35730 3.01930 2.24410 5.34090
0.34320 17.86740
 83.75430 1.089599967
 'International Tables Volume C Table 6.1.1.4 (pp. 500-502)'
 'Henke, Gullikson and Davis, At. Data and Nucl. Data Tables, 1993, 54,
2'
 O 0.01158 0.00611 3.04850 2.28680 1.54630 0.86700 13.27710 5.70110
0.32390
 32.90890 0.250800013542
 'International Tables Volume C Table 6.1.1.4 (pp. 500-502)'
 'Henke, Gullikson and Davis, At. Data and Nucl. Data Tables, 1993, 54,
2'
 N 0.00653 0.00323 12.21260 3.13220 2.01250 1.16630 0.00570 9.89330
28.99750
 0.58260 -11.5290002823
 'International Tables Volume C Table 6.1.1.4 (pp. 500-502)'
 'Henke, Gullikson and Davis, At. Data and Nucl. Data Tables, 1993, 54,
2'

_space_group_crystal_system      'hexagonal'
_space_group_IT_number           173
_space_group_name_H-M_alt        'P 63'
_space_group_name_Hall           'P 6c'
loop_
  _space_group_symop_id
  _space_group_symop_operation_xyz
 1 x,y,z
 2 x-y,x,z+1/2
 3 y,-x+y,z+1/2
 4 -y,x-y,z
 5 -x+y,-x,z
 6 -x,-y,z+1/2

_symmetry_Int_Tables_number      173
_cell_length_a                   13.056(3)
_cell_length_b                   13.056(2)
_cell_length_c                   37.265(7)
_cell_angle_alpha                90.000(15)
_cell_angle_beta                 90.000(17)
_cell_angle_gamma                120.000(9)
_cell_volume                     5501.1(18)
_cell_formula_units_Z            1
_cell_measurement_temperature    122
_exptl_absorpt_coefficient_mu    0.798
_exptl_absorpt_correction_T_max  0.910
_exptl_absorpt_correction_T_min  0.821
_exptl_absorpt_correction_type   integration
_exptl_crystal_colour            'clear dark black'
_exptl_crystal_colour_lustre     clear
_exptl_crystal_colour_modifier   dark
_exptl_crystal_colour_primary    black
_exptl_crystal_density_diffrn    1.5075
_exptl_crystal_description       prism
_exptl_crystal_F_000             2571.8257
_exptl_crystal_size_max          0.375
_exptl_crystal_size_mid          0.18
_exptl_crystal_size_min          0.17
_diffrn_reflns_av_R_equivalents  0.1072
_diffrn_reflns_av_unetI/netI     0.0570
_diffrn_reflns_limit_h_max       18
_diffrn_reflns_limit_h_min       -18
_diffrn_reflns_limit_k_max       18
_diffrn_reflns_limit_k_min       -18
_diffrn_reflns_limit_l_max       52
_diffrn_reflns_limit_l_min       -53
_diffrn_reflns_number            66481
_diffrn_reflns_theta_full        27.0972
_diffrn_reflns_theta_max         27.10
_diffrn_reflns_theta_min         1.09
_diffrn_ambient_temperature      122
_diffrn_measured_fraction_theta_full 0.9813
_diffrn_measured_fraction_theta_max 0.9813
_diffrn_measurement_device_type  'Bruker/Nonius Kappa CCD 4-circle'
_diffrn_radiation_type           'Mo K\a'
_diffrn_radiation_wavelength     0.71073
_reflns_Friedel_coverage         0.963
_reflns_limit_h_max              13
_reflns_limit_h_min              -13
_reflns_limit_k_max              14
_reflns_limit_k_min              -14
_reflns_limit_l_max              46
_reflns_limit_l_min              -47
_reflns_number_gt                7391
_reflns_number_total             7964
_reflns_threshold_expression     I>=2u(I)
_computing_molecular_graphics    'Olex2 (Dolomanov et al., 2009)'
_computing_publication_material  'Olex2 (Dolomanov et al., 2009)'
_computing_structure_refinement  'olex2.refine (Bourhis et al., 2013)'
_computing_structure_solution    'olex2.solve (Bourhis et al., 2013)'
_refine_diff_density_max         1.1098
_refine_diff_density_min         -0.8638
_refine_diff_density_rms         0.1848
_refine_ls_abs_structure_details
'Flack, H. D. (1983). Acta Cryst. A39, 876-881.'
_refine_ls_abs_structure_Flack   0.44(6)
_refine_ls_d_res_high            0.7802
_refine_ls_d_res_low             18.6325
_refine_ls_goodness_of_fit_ref   1.0171
_refine_ls_hydrogen_treatment    mixed
_refine_ls_matrix_type           full
_refine_ls_number_constraints    71
_refine_ls_number_parameters     408
_refine_ls_number_reflns         7964
_refine_ls_number_restraints     0
_refine_ls_R_factor_all          0.0868
_refine_ls_R_factor_gt           0.0799
```

```
_refine_ls_restrained_S_all      1.0171
_refine_ls_shift/su_max          0.0006
_refine_ls_shift/su_mean         0.0001
_refine_ls_structure_factor_coef  Fsqd
_refine_ls_weighting_details
'w=1/[\s^2^(Fo^2^)+(0.0788P)^2^+62.4885P] where
P=(Fo^2^+2Fc^2^)/3'
_refine_ls_weighting_scheme      calc
_refine_ls_wR_factor_gt          0.2123
_refine_ls_wR_factor_ref         0.2230
_olex2_refinement_description
;
1. Fixed Uiso
 At 1.2 times of:
  All C(H) groups, All C(H,H) groups
 At 1.5 times of:
  All C(H,H,H) groups
2. Uiso/Uaniso restraints and constraints
Uanis(C26) = Uanis(C32) = Uanis(C31)
Uanis(N6) = Uanis(C38) = Uanis(C37) = Uanis(C36) = Uanis(C35)
Uanis(N3) = Uanis(C19) = Uanis(C18) = Uanis(C17) = Uanis(C16)
Uanis(C30) = Uanis(C29) = Uanis(C28) = Uanis(C27)
Uanis(C4) = Uanis(C1) = Uanis(C9)
3. Others
 Fixed Sof: H8c(0.166667) H8a(0.166667) H8b(0.166667) C39(0.166667)
 C40(0.166667) H40a(0.16667) H40c(0.16667) H40b(0.16667)
N8(0.166667)
 H8c(0.166667) H8a(0.166667) H8b(0.166667) H42a(0.33333)
H42b(0.33333)
 H42c(0.33333) C41(0.166667) C42(0.166667) H42b(0.16667)
H42c(0.16667)
 H42a(0.16667) N9(0.166667)
4.a Secondary CH2 refined with riding coordinates:
 C2(H2a,H2b), C33(H33a,H33b)
4.b Aromatic/amide H refined with riding coordinates:
 C5(H5), C6(H6), C7(H7), C8(H8), C10(H10), C11(H11), C13(H13),
C14(H14),
 C16(H16), C17(H17), C18(H18), C19(H19), C20(H20), C21(H21),
C22(H22), C25(H25),
  C27(H27), C28(H28), C29(H29), C30(H30), C35(H35), C36(H36),
C37(H37), C38(H38)
4.c Idealised Me refined as rotating group:
 C3(H3a,H3b,H3c), C34(H34a,H34b,H34c), C42(H42b,H42c,H42a)
;
_atom_sites_solution_primary      iterative
loop_
  _atom_site_label
  _atom_site_type_symbol
  _atom_site_fract_x
  _atom_site_fract_y
  _atom_site_fract_z
  _atom_site_U_iso_or_equiv
  _atom_site_adp_type
  _atom_site_occupancy
  _atom_site_refinement_flags_posn
  _atom_site_refinement_flags_adp
  _atom_site_disorder_group
 Mn2 Mn 0.43449(9) 0.60318(9) 0.42346(4) 0.0170(2) Uani 1.000000 . . .
 Mn1 Mn 0.83658(9) 0.89670(9) 0.70302(4) 0.0171(2) Uani 1.000000 . . .
 Cl1 Cl 1.0 1.0 0.78239(8) 0.0166(6) Uani 1.000000 S T .
 Cl2 Cl 0.333333333333 0.666666666667 0.34421(8) 0.0165(6) Uani
1.000000 S T .
 O6 O 0.333333333333 0.666666666667 0.4312(2) 0.0161(19) Uani
1.000000 S T .
 O5 O 0.5377(5) 0.5497(5) 0.41140(16) 0.0237(12) Uani 1.000000 . . .
 O1 O 0.8797(5) 0.9505(5) 0.76901(15) 0.0206(11) Uani 1.000000 . . .
 N1 N 0.5630(5) 0.7640(5) 0.41069(18) 0.0175(12) Uani 1.000000 . . .
 O2 O 1.0 1.0 0.8209(3) 0.024(2) Uani 1.000000 S T .
 O3 O 0.3815(4) 0.5948(4) 0.35743(15) 0.0168(11) Uani 1.000000 . . .
 C8 C 0.6605(7) 0.5161(8) 0.3741(2) 0.0236(16) Uani 1.000000 . . .
 C9 C 0.6185(6) 0.5898(7) 0.3857(2) 0.0198(9) Uani 1.000000 . . .
 C1 C 0.6419(6) 0.7944(7) 0.3856(2) 0.0198(9) Uani 1.000000 . . .
 N2 N 0.4729(6) 0.5918(6) 0.4823(2) 0.0284(16) Uani 1.000000 . . .
 C5 C 0.7479(7) 0.7344(8) 0.3428(2) 0.0289(18) Uani 1.000000 . . .
 C2 C 0.7107(7) 0.9214(7) 0.3746(2) 0.0244(17) Uani 1.000000 . . .
 C4 C 0.6647(6) 0.7037(7) 0.3710(2) 0.0198(9) Uani 1.000000 . . .
 C3 C 0.8157(8) 0.9890(7) 0.3988(3) 0.035(2) Uani 1.000000 . . .
 O4 O 0.333333333333 0.666666666667 0.3072(3) 0.032(2) Uani
1.000000 S T .
 C7 C 0.7435(8) 0.5500(7) 0.3474(2) 0.0258(17) Uani 1.000000 . . .
 C12 C 0.4647(7) 0.5633(8) 0.5566(2) 0.0280(17) Uani 1.000000 . . .

loop_
  _atom_site_aniso_label
  _atom_site_aniso_U_11
  _atom_site_aniso_U_22
  _atom_site_aniso_U_33
  _atom_site_aniso_U_12
 C15 C 0.4507(8) 0.5435(8) 0.5962(2) 0.0309(18) Uani 1.000000 . . .
 N3 N 0.3916(8) 0.4314(8) 0.6071(2) 0.0431(10) Uani 1.000000 . . .
 C17 C 0.4764(10) 0.6168(10) 0.6558(3) 0.0431(10) Uani 1.000000 . . .
 C6 C 0.7857(8) 0.6597(8) 0.3309(2) 0.0310(19) Uani 1.000000 . . .
 C14 C 0.4414(9) 0.4868(8) 0.4972(2) 0.036(2) Uani 1.000000 . . .
 C13 C 0.4360(9) 0.4688(8) 0.5332(3) 0.035(2) Uani 1.000000 . . .
 C11 C 0.5039(8) 0.6727(8) 0.5406(3) 0.0318(19) Uani 1.000000 . . .
 C10 C 0.5070(8) 0.6820(7) 0.5044(3) 0.033(2) Uani 1.000000 . . .
 C16 C 0.4919(10) 0.6367(10) 0.6199(3) 0.0431(10) Uani 1.000000 . . .
 C18 C 0.4139(10) 0.5030(9) 0.6673(3) 0.0431(10) Uani 1.000000 . . .
 C19 C 0.3712(10) 0.4116(9) 0.6424(3) 0.0431(10) Uani 1.000000 . . .
 O10 O 0.9735(5) 0.7829(5) 0.69950(16) 0.0220(11) Uani 1.000000 . . .
 O7 O 0.5536(4) 0.8540(4) 0.42665(17) 0.0195(11) Uani 1.000000 . . .
 N5 N 0.8728(5) 0.7706(5) 0.71592(18) 0.0180(12) Uani 1.000000 . . .
 O9 O 1.0 1.0 0.6955(2) 0.022(2) Uani 1.000000 S T .
 N4 N 0.8019(6) 0.8340(5) 0.6451(2) 0.0220(14) Uani 1.000000 . . .
 C32 C 0.8213(7) 0.6889(7) 0.7399(2) 0.0193(9) Uani 1.000000 . . .
 C30 C 0.5251(7) 0.6704(7) 0.7523(2) 0.0240(8) Uani 1.000000 . . .
 C26 C 0.7060(7) 0.6604(7) 0.7548(2) 0.0193(9) Uani 1.000000 . . .
 C29 C 0.4769(7) 0.5869(7) 0.7795(2) 0.0240(8) Uani 1.000000 . . .
 C28 C 0.5427(7) 0.5445(7) 0.7954(2) 0.0240(8) Uani 1.000000 . . .
 C27 C 0.6562(7) 0.5811(7) 0.7831(2) 0.0240(8) Uani 1.000000 . . .
 C33 C 0.8785(7) 0.6167(7) 0.7499(2) 0.0254(17) Uani 1.000000 . . .
 C20 C 0.7803(7) 0.7254(8) 0.6361(3) 0.0316(19) Uani 1.000000 . . .
 C31 C 0.6402(7) 0.7111(6) 0.7402(2) 0.0193(9) Uani 1.000000 . . .
 C21 C 0.8169(8) 0.9041(8) 0.6172(3) 0.035(2) Uani 1.000000 . . .
 C22 C 0.8136(8) 0.8711(10) 0.5815(3) 0.040(2) Uani 1.000000 . . .
 C23 C 0.7971(8) 0.7640(10) 0.5734(3) 0.038(2) Uani 1.000000 . . .
 C24 C 0.7953(9) 0.7277(12) 0.5355(3) 0.048(3) Uani 1.000000 . . .
 O8 O 0.6794(5) 0.7911(5) 0.71457(15) 0.0230(12) Uani 1.000000 . . .
 C34 C 0.8334(9) 0.5101(8) 0.7254(3) 0.037(2) Uani 1.000000 . . .
 C25 C 0.7798(9) 0.6885(10) 0.6015(3) 0.041(2) Uani 1.000000 . . .
 N6 N 0.7621(14) 0.6087(16) 0.5298(3) 0.093(2) Uani 1.000000 . . .
 C35 C 0.8238(16) 0.803(2) 0.5094(4) 0.093(2) Uani 1.000000 . . .
 C38 C 0.7509(17) 0.570(2) 0.4950(4) 0.093(2) Uani 1.000000 . . .
 C37 C 0.7849(17) 0.651(2) 0.4678(4) 0.093(2) Uani 1.000000 . . .
 C36 C 0.8152(16) 0.761(2) 0.4734(4) 0.093(2) Uani 1.000000 . . .
 H34a H 0.849(6) 0.5366(9) 0.7003(3) 0.056(3) Uiso 1.000000 GR . .
 H34b H 0.874(5) 0.466(4) 0.7309(14) 0.056(3) Uiso 1.000000 GR . .
 H34c H 0.7481(15) 0.459(4) 0.7290(15) 0.056(3) Uiso 1.000000 GR . .
 H3a H 0.855(4) 1.0732(11) 0.3926(13) 0.052(3) Uiso 1.000000 GR . .
 H3b H 0.7893(11) 0.978(5) 0.4238(3) 0.052(3) Uiso 1.000000 GR . .
 H3c H 0.871(3) 0.960(4) 0.3957(14) 0.052(3) Uiso 1.000000 GR . .
 H33a H 0.9655(7) 0.6659(7) 0.7477(2) 0.031(2) Uiso 1.000000 R . .
 H33b H 0.8595(7) 0.5902(7) 0.7752(2) 0.031(2) Uiso 1.000000 R . .
 H2a H 0.7379(7) 0.9269(7) 0.3495(2) 0.029(2) Uiso 1.000000 R . .
 H2b H 0.6591(7) 0.9567(7) 0.3757(2) 0.029(2) Uiso 1.000000 R . .
 H14 H 0.4220(9) 0.4216(8) 0.4818(2) 0.043(2) Uiso 1.000000 R . .
 H13 H 0.4127(9) 0.3925(8) 0.5424(3) 0.042(2) Uiso 1.000000 R . .
 H10 H 0.5356(8) 0.7584(7) 0.4943(3) 0.040(2) Uiso 1.000000 R . .
 H11 H 0.5284(8) 0.7410(8) 0.5550(3) 0.038(2) Uiso 1.000000 R . .
 H19 H 0.3260(10) 0.3323(9) 0.6506(3) 0.0518(12) Uiso 1.000000 R . .
 H18 H 0.3995(10) 0.4861(9) 0.6921(3) 0.0518(12) Uiso 1.000000 R . .
 H17 H 0.5084(10) 0.6807(10) 0.6723(3) 0.0518(12) Uiso 1.000000 R . .
 H16 H 0.5314(10) 0.7155(10) 0.6110(3) 0.0518(12) Uiso 1.000000 R . .
 H30 H 0.4791(7) 0.7004(7) 0.7418(2) 0.0288(10) Uiso 1.000000 R . .
 H29 H 0.3979(7) 0.5590(7) 0.7871(2) 0.0288(10) Uiso 1.000000 R . .
 H28 H 0.5108(7) 0.4902(7) 0.8147(2) 0.0288(10) Uiso 1.000000 R . .
 H27 H 0.7011(7) 0.5511(7) 0.7944(2) 0.0288(10) Uiso 1.000000 R . .
 H21 H 0.8308(8) 0.9815(8) 0.6219(3) 0.042(3) Uiso 1.000000 R . .
 H22 H 0.8230(8) 0.9247(10) 0.5629(3) 0.048(3) Uiso 1.000000 R . .
 H25 H 0.7675(9) 0.6115(10) 0.5970(3) 0.049(3) Uiso 1.000000 R . .
 H20 H 0.7644(7) 0.6703(8) 0.6550(3) 0.038(2) Uiso 1.000000 R . .
 H35 H 0.8496(16) 0.884(2) 0.5141(4) 0.111(3) Uiso 1.000000 R . .
 H36 H 0.8316(16) 0.813(2) 0.4538(4) 0.111(3) Uiso 1.000000 R . .
 H37 H 0.7865(17) 0.626(2) 0.4439(4) 0.111(3) Uiso 1.000000 R . .
 H38 H 0.7202(17) 0.488(2) 0.4899(4) 0.111(3) Uiso 1.000000 R . .
 H5 H 0.7787(7) 0.8097(8) 0.3318(2) 0.035(2) Uiso 1.000000 R . .
 H6 H 0.8402(8) 0.6825(8) 0.3116(2) 0.037(2) Uiso 1.000000 R . .
 H7 H 0.7720(8) 0.4991(7) 0.3401(2) 0.031(2) Uiso 1.000000 R . .
 H8 H 0.6309(7) 0.4407(8) 0.3849(2) 0.0283(19) Uiso 1.000000 R . .
 N9 N 0.666666666667 0.333333333333 0.6348(12) 0.103(18) Uani
0.500000 S T .
 C42 C 0.666666666667 0.333333333333 0.5709(12) 0.074(14) Uani
0.500000 S T .
 C41 C 0.666666666667 0.333333333333 0.6080(14) 0.087(18) Uani
0.500000 S T .
 H42b H 0.66(3) 0.261(16) 0.5621(12) 0.11(2) Uiso 0.166670 GR . -1
 H42c H 0.597(18) 0.34(3) 0.5621(12) 0.11(2) Uiso 0.166670 GR . -1
 H42a H 0.739(16) 0.403(18) 0.5621(12) 0.11(2) Uiso 0.166670 GR . -1

  _atom_site_aniso_U_13
  _atom_site_aniso_U_23
 Mn2 0.0130(5) 0.0146(5) 0.0245(5) 0.0077(4) 0.0004(5) 0.0021(5)
 Mn1 0.0128(5) 0.0128(5) 0.0253(6) 0.0061(4) -0.0006(5) 0.0013(5)
 Cl1 0.0121(8) 0.0121(8) 0.0255(15) 0.0061(4) -0.000000 0.000000
 Cl2 0.0138(8) 0.0138(8) 0.0218(15) 0.0069(4) -0.000000 0.000000
 O6 0.007(2) 0.007(2) 0.034(6) 0.0037(12) -0.000000 0.000000
```

O5 0.020(3) 0.021(3) 0.035(3) 0.014(2) 0.006(2) 0.005(2)
O1 0.016(3) 0.015(3) 0.029(3) 0.006(2) -0.001(2) -0.002(2)
N1 0.006(3) 0.015(3) 0.027(3) 0.002(2) -0.001(2) -0.001(2)
O2 0.017(3) 0.017(3) 0.038(6) 0.0087(14) -0.000000 0.000000
O3 0.010(2) 0.009(2) 0.033(3) 0.0052(19) -0.002(2) 0.0003(19)
C8 0.017(4) 0.028(4) 0.032(4) 0.016(3) -0.002(3) 0.000(3)
C9 0.0100(19) 0.022(2) 0.027(2) 0.0075(17) -0.0034(17) 0.0005(18)
C1 0.0100(19) 0.022(2) 0.027(2) 0.0075(17) -0.0034(17) 0.0005(18)
N2 0.020(3) 0.021(3) 0.037(4) 0.005(3) -0.000(3) 0.010(3)
C5 0.018(4) 0.034(5) 0.026(4) 0.007(3) 0.000(3) 0.001(3)
C2 0.020(4) 0.018(4) 0.033(4) 0.008(3) 0.001(3) 0.002(3)
C4 0.0100(19) 0.022(2) 0.027(2) 0.0075(17) -0.0034(17) 0.0005(18)
C3 0.022(4) 0.012(4) 0.058(6) 0.000(3) -0.006(4) 0.000(4)
O4 0.033(3) 0.033(3) 0.031(7) 0.0166(17) -0.000000 0.000000
C7 0.026(4) 0.017(4) 0.037(5) 0.013(3) -0.002(3) -0.009(3)
C12 0.021(4) 0.032(4) 0.026(4) 0.009(3) -0.004(3) 0.001(3)
C15 0.030(4) 0.029(4) 0.030(4) 0.012(4) -0.005(3) 0.003(3)
N3 0.045(3) 0.038(2) 0.038(2) 0.015(2) -0.0036(19) 0.0038(18)
C17 0.045(3) 0.038(2) 0.038(2) 0.015(2) -0.0036(19) 0.0038(18)
C6 0.030(4) 0.032(5) 0.025(4) 0.012(4) 0.005(3) -0.006(3)
C14 0.050(6) 0.030(5) 0.032(5) 0.022(4) -0.008(4) -0.008(4)
C13 0.039(5) 0.024(4) 0.037(5) 0.012(4) -0.001(4) 0.004(4)
C11 0.026(4) 0.026(4) 0.039(5) 0.009(4) -0.005(4) 0.004(4)
C10 0.033(5) 0.015(4) 0.048(6) 0.009(3) -0.008(4) 0.003(4)
C16 0.045(3) 0.038(2) 0.038(2) 0.015(2) -0.0036(19) 0.0038(18)
C18 0.045(3) 0.038(2) 0.038(2) 0.015(2) -0.0036(19) 0.0038(18)
C19 0.045(3) 0.038(2) 0.038(2) 0.015(2) -0.0036(19) 0.0038(18)
O10 0.020(3) 0.021(3) 0.028(3) 0.013(2) -0.000(2) -0.002(2)
O7 0.011(2) 0.011(2) 0.036(3) 0.0043(19) -0.003(2) -0.005(2)
N5 0.013(3) 0.014(3) 0.030(3) 0.009(3) -0.002(2) -0.004(2)
O9 0.022(3) 0.022(3) 0.023(6) 0.0109(15) -0.000000 0.000000
N4 0.016(3) 0.009(3) 0.034(4) 0.001(2) -0.000(3) 0.006(3)
C32 0.017(2) 0.014(2) 0.025(2) 0.0068(17) -0.0052(18) -0.0033(17)
C30 0.0188(19) 0.0200(19) 0.031(2) 0.0081(16) 0.0024(16) 0.0010(16)
C26 0.017(2) 0.014(2) 0.025(2) 0.0068(17) -0.0052(18) -0.0033(17)
C29 0.0188(19) 0.0200(19) 0.031(2) 0.0081(16) 0.0024(16) 0.0010(16)
C28 0.0188(19) 0.0200(19) 0.031(2) 0.0081(16) 0.0024(16) 0.0010(16)
C27 0.0188(19) 0.0200(19) 0.031(2) 0.0081(16) 0.0024(16) 0.0010(16)
C33 0.021(4) 0.022(4) 0.037(5) 0.013(3) -0.003(3) 0.007(3)
C20 0.022(4) 0.034(5) 0.038(5) 0.013(4) -0.008(3) -0.003(4)
C31 0.017(2) 0.014(2) 0.025(2) 0.0068(17) -0.0052(18) -0.0033(17)
C21 0.022(4) 0.030(5) 0.045(5) 0.006(4) -0.006(4) 0.014(4)
C22 0.028(5) 0.053(6) 0.033(5) 0.016(5) 0.004(4) 0.015(4)
C23 0.017(4) 0.056(6) 0.035(5) 0.014(4) -0.003(3) -0.006(4)
C24 0.034(5) 0.080(9) 0.032(5) 0.029(6) -0.004(4) -0.014(5)
O8 0.019(3) 0.020(3) 0.026(3) 0.007(2) -0.000(2) 0.004(2)
C34 0.031(5) 0.015(4) 0.060(7) 0.008(4) -0.003(4) -0.003(4)
C25 0.033(5) 0.054(6) 0.034(5) 0.020(5) -0.004(4) -0.008(4)
N6 0.091(5) 0.133(7) 0.051(4) 0.054(5) 0.015(3) -0.004(4)
C35 0.091(5) 0.133(7) 0.051(4) 0.054(5) 0.015(3) -0.004(4)
C38 0.091(5) 0.133(7) 0.051(4) 0.054(5) 0.015(3) -0.004(4)
C37 0.091(5) 0.133(7) 0.051(4) 0.054(5) 0.015(3) -0.004(4)
C36 0.091(5) 0.133(7) 0.051(4) 0.054(5) 0.015(3) -0.004(4)
N9 0.12(3) 0.12(3) 0.08(4) 0.058(15) -0.000000 0.000000
C42 0.08(2) 0.08(2) 0.06(3) 0.041(11) -0.000000 0.000000
C41 0.10(3) 0.10(3) 0.05(3) 0.052(15) -0.000000 0.000000

loop_
 _geom_bond_atom_site_label_1
 _geom_bond_atom_site_label_2
 _geom_bond_distance
 _geom_bond_site_symmetry_2
Mn2 Mn2 3.2523(18) 4_665
Mn2 Mn2 3.2523(19) 5_565
Mn2 O6 1.8999(18) 4_665
Mn2 O5 1.857(5) .
Mn2 N1 1.982(6) .
Mn2 O3 2.543(6) .
Mn2 N2 2.271(8) .
Mn2 O7 1.919(5) 5_565
Mn1 Mn1 3.2374(19) 4_765
Mn1 Mn1 3.2374(19) 5_675
Mn1 O1 2.542(6) .
Mn1 O10 1.902(5) 5_675
Mn1 N5 1.986(6) .
Mn1 O9 1.8897(17) 5_675
Mn1 N4 2.273(7) .
Mn1 O8 1.862(6) .
Cl1 O1 1.455(5) 4_765
Cl1 O1 1.455(5) 5_675
Cl1 O1 1.455(5) .
Cl1 O2 1.434(11) .
Cl2 O3 1.453(5) .
Cl2 O3 1.453(5) 4_665
Cl2 O3 1.453(5) 5_565
Cl2 O4 1.379(12) .
O5 C9 1.322(10) .
N1 C1 1.299(10) .
N1 O7 1.375(8) .
C8 C9 1.393(11) .
C8 C7 1.373(12) .
C9 C4 1.407(11) .
C1 C2 1.494(11) .
C1 C4 1.462(11) .
N2 C14 1.339(12) .
N2 C10 1.319(12) .
C5 C4 1.417(11) .
C5 C6 1.368(13) .
C2 C3 1.505(12) .
C7 C6 1.394(13) .
C12 C15 1.493(12) .
C12 C13 1.401(13) .
C12 C11 1.389(12) .
C15 N3 1.331(12) .
C15 C16 1.375(14) .
N3 C19 1.340(13) .
C17 C16 1.358(15) .
C17 C18 1.358(15) .
C14 C13 1.358(13) .
C11 C10 1.353(14) .
C18 C19 1.390(15) .
O10 N5 1.384(8) .
N5 C32 1.293(10) .
N4 C20 1.342(11) .
N4 C21 1.335(11) .
C32 C26 1.468(11) .
C32 C33 1.513(11) .
C30 C29 1.387(12) .
C30 C31 1.395(11) .
C26 C27 1.390(11) .
C26 C31 1.429(10) .
C29 C28 1.367(12) .
C28 C27 1.387(11) .
C33 C34 1.517(13) .
C20 C25 1.376(14) .
C31 O8 1.316(9) .
C21 C22 1.390(15) .
C22 C23 1.339(16) .
C23 C24 1.489(14) .
C23 C25 1.377(15) .
C24 N6 1.40(2) .
C24 C35 1.30(2) .
N6 C38 1.38(2) .
C35 C36 1.43(2) .
C38 C37 1.37(3) .
C37 C36 1.30(3) .
N9 C41 1.00(6) .
C42 C41 1.38(7) .

loop_
 _geom_angle_atom_site_label_1
 _geom_angle_atom_site_label_2
 _geom_angle_atom_site_label_3
 _geom_angle
 _geom_angle_site_symmetry_1
 _geom_angle_site_symmetry_3
O6 Mn2 Mn2 31.14(7) 4_665 5_565
O5 Mn2 Mn2 149.70(19) . 5_565
O5 Mn2 O6 174.0(3) . 4_665
N1 Mn2 Mn2 115.72(18) . 5_565
N1 Mn2 O6 88.8(2) . 4_665
N1 Mn2 O5 87.2(3) . .
O3 Mn2 Mn2 75.35(11) . 5_565
O3 Mn2 O6 86.2(3) . 4_665
O3 Mn2 O5 89.0(2) . .
O3 Mn2 N1 83.2(2) . .
N2 Mn2 Mn2 104.10(19) . 5_565
N2 Mn2 O6 96.1(3) . 4_665
N2 Mn2 O5 89.1(3) . .
N2 Mn2 N1 101.7(3) . .
N2 Mn2 O3 174.6(2) . .
O7 Mn2 Mn2 60.22(15) 5_565 5_565
O7 Mn2 O6 89.62(15) 5_565 4_665
O7 Mn2 O5 93.5(2) 5_565 .
O7 Mn2 N1 169.2(3) 5_565 .
O7 Mn2 O3 86.0(2) 5_565 .
O7 Mn2 N2 89.1(3) 5_565 .
O1 Mn1 Mn1 83.18(12) . 4_765
O10 Mn1 Mn1 120.55(16) 5_675 4_765
O10 Mn1 O1 86.3(2) 5_675 .
N5 Mn1 Mn1 57.53(18) . 4_765
N5 Mn1 O1 83.3(2) . .
N5 Mn1 O10 169.5(3) . 5_675
O9 Mn1 Mn1 31.06(7) 5_675 4_765
O9 Mn1 O1 86.0(3) 5_675 .
O9 Mn1 O10 90.04(16) 5_675 5_675
O9 Mn1 N5 88.6(2) 5_675 .
N4 Mn1 Mn1 93.77(17) . 4_765
N4 Mn1 O1 174.3(2) . .
N4 Mn1 O10 99.4(3) . 5_675
N4 Mn1 N5 91.0(3) . .
N4 Mn1 O9 93.9(3) . 5_675
O8 Mn1 Mn1 145.09(18) . 4_765
O8 Mn1 O1 89.5(2) . .
O8 Mn1 O10 92.8(2) . 5_675
O8 Mn1 N5 87.8(3) . .
O8 Mn1 O9 174.5(3) . 5_675
O8 Mn1 N4 90.3(2) . .
O1 Cl1 O1 108.9(3) . 4_765
O1 Cl1 O1 108.9(3) 5_675 4_765
O1 Cl1 O1 108.9(3) 5_675 .
O2 Cl1 O1 110.0(2) . 4_765
O2 Cl1 O1 110.0(2) . .
O2 Cl1 O1 110.0(2) . 5_675
O3 Cl2 O3 109.1(3) 4_665 .
O3 Cl2 O3 109.1(2) 5_565 .
O3 Cl2 O3 109.1(3) 5_565 4_665
O4 Cl2 O3 109.8(2) . .
O4 Cl2 O3 109.8(2) . 4_665
O4 Cl2 O3 109.8(2) . 5_565
Mn2 O6 Mn2 117.73(14) . 5_565
Mn2 O6 Mn2 117.73(14) 4_665 5_565
Mn2 O6 Mn2 117.73(14) 4_665 .
C9 O5 Mn2 127.7(5) . .
Cl1 O1 Mn1 119.7(3) 5_675 .
C1 N1 Mn2 128.2(5) . .
O7 N1 Mn2 114.3(4) . .
O7 N1 C1 116.5(6) . .
Cl2 O3 Mn2 119.7(3) . .
C7 C8 C9 121.5(8) . .
C8 C9 O5 117.5(7) . .
C4 C9 O5 122.5(7) . .
C4 C9 C8 120.0(8) . .
C2 C1 N1 118.8(7) . .
C4 C1 N1 118.1(7) . .
C4 C1 C2 122.9(7) . .
C14 N2 Mn2 120.1(6) . .
C10 N2 Mn2 122.1(6) . .
C10 N2 C14 116.8(8) . .
C6 C5 C4 122.6(9) . .
C3 C2 C1 110.6(7) . .
C1 C4 C9 123.9(7) . .
C5 C4 C9 116.8(8) . .
C5 C4 C1 118.9(7) . .
C6 C7 C8 119.6(7) . .
C13 C12 C15 120.6(8) . .
C11 C12 C15 123.6(8) . .
C11 C12 C13 115.8(8) . .

N3 C15 C12 116.4(8) . .
C16 C15 C12 121.3(8) . .
C16 C15 N3 122.2(9) . .
C19 N3 C15 117.4(9) . .
C18 C17 C16 118.0(11) . .
C7 C6 C5 119.4(8) . .
C13 C14 N2 123.2(9) . .
C14 C13 C12 119.8(8) . .
C10 C11 C12 120.1(9) . .
C11 C10 N2 124.1(8) . .
C17 C16 C15 120.4(10) . .
C19 C18 C17 119.5(10) . .
C18 C19 N3 122.2(10) . .
N5 O10 Mn1 112.2(4) . 4_765
N1 O7 Mn2 112.6(4) . 4_665
O10 N5 Mn1 113.7(4) . .
C32 N5 Mn1 127.6(5) . .
C32 N5 O10 118.2(6) . .
Mn1 O9 Mn1 117.87(14) . 4_765
Mn1 O9 Mn1 117.87(14) 5_675 4_765
Mn1 O9 Mn1 117.87(14) 5_675 .
C20 N4 Mn1 121.0(6) . .
C21 N4 Mn1 124.0(6) . .
C21 N4 C20 114.4(8) . .
C26 C32 N5 121.0(7) . .
C33 C32 N5 118.1(7) . .
C33 C32 C26 120.8(7) . .
C31 C30 C29 121.0(8) . .
C27 C26 C32 121.0(7) . .
C31 C26 C32 121.1(7) . .
C31 C26 C27 117.9(7) . .
C28 C29 C30 120.3(8) . .
C27 C28 C29 119.8(8) . .
C28 C27 C26 121.8(8) . .
C34 C33 C32 109.6(7) . .
C25 C20 N4 124.3(9) . .
C26 C31 C30 118.8(7) . .
O8 C31 C30 117.1(7) . .
O8 C31 C26 124.0(7) . .
C22 C21 N4 124.1(9) . .
C23 C22 C21 120.2(9) . .
C24 C23 C22 121.1(10) . .
C25 C23 C22 117.4(9) . .
C25 C23 C24 121.6(11) . .
N6 C24 C23 116.2(11) . .
C35 C24 C23 121.1(14) . .
C35 C24 N6 122.6(13) . .
C31 O8 Mn1 127.1(5) . .
C23 C25 C20 119.4(10) . .
C38 N6 C24 117.9(16) . .
C36 C35 C24 118.1(19) . .
C37 C38 N6 119(2) . .
C36 C37 C38 122.4(17) . .
C37 C36 C35 119.8(19) . .
C42 C41 N9 180.0 . .

RES file for compound **9** at 295 K

```
TITL meohre VIVALDI 295K
CELL 0.71073 12.764 12.764 35.682 90 90 120
ZERR 18 0.000 0.000 0.000 0.00 0.00 0.00
LATT 3
SYMM -y,x-y,z
SYMM -x+y,-x,z
SFAC C 0 0 0 0 0 0 0 0 6.6484 0 0 0 0.77 12
SFAC H 0 0 0 0 0 0 0 0 -3.7409 0 0 0 0.32 1
SFAC N 0 0 0 0 0 0 0 0 9.36 0 0 0 .700 14
SFAC O 0 0 0 0 0 0 0 0 5.805 0 0 0 0.66 16
SFAC Mn 0 0 0 0 0 0 0 0 -3.75 0 0 0 0.80 50
SFAC Re 0 0 0 0 0 0 0 0 9.2 0 0 0 0.80 100
SFAC D 0 0 0 0 0 0 0 0 6.674 0 0 0 0.32 1
UNIT 162 198 18 84 18 6 4
TEMP -253
L.S. 4
ACTA
BOND $H
FMAP 2
PLAN 40
REM EXTI    0.000000
WGHT    0.020000
FVAR       0.11967
RE1   6    0.666667    0.333333    0.031478    10.33333    0.03033
0.03033 =
      0.03030    0.00000    0.00000    0.01516
MN1   5    0.502088    0.271526    0.114961    11.00000    0.02447
0.02430 =
      0.03702   -0.00045    0.00030    0.01192
O1    4    0.666667    0.333333    0.116109    10.33333    0.02424
0.02424 =
      0.04188    0.00000    0.00000    0.01212
O2    4    0.639386    0.523887    0.117791    11.00000    0.02849
0.02824 =
      0.04899   -0.00347   -0.00233    0.01517
O3    4    0.342240    0.223353    0.109502    11.00000    0.02582
0.03720 =
      0.04481    0.00793    0.00042    0.01479
O4    4    0.522853    0.254816    0.047372    11.00000    0.03113
0.04006 =
      0.04476   -0.00134   -0.00137    0.01472
O5    4    0.666667    0.333333   -0.016230    10.33333    0.05800
0.05800 =
      0.03330    0.00000    0.00000    0.02900
N1    3    0.537460    0.435226    0.103017    11.00000    0.02880
0.02677 =
      0.04201    0.00100    0.00009    0.01532
C1    1    0.301462    0.258558    0.081301    11.00000    0.02698
0.03377 =
      0.03999    0.00161    0.00043    0.01547
C2    1    0.190593    0.179201    0.066906    11.00000    0.03006
0.04298 =
      0.04845   -0.00015   -0.00425    0.01495
H2    2    0.143456    0.093527    0.079375    11.00000    0.04753
0.05734 =
      0.08130    0.01519   -0.00951    0.00806
C3    1    0.142107    0.209843    0.037709    11.00000    0.03809
0.05495 =
      0.04770   -0.00368   -0.01116    0.02152
H3    2    0.055865    0.146909    0.027086    11.00000    0.04931
0.07485 =
      0.07416   -0.00073   -0.01898    0.01801
C4    1    0.204296    0.321170    0.021759    11.00000    0.04866
0.05735 =
      0.05411    0.00269   -0.01542    0.02858
H4    2    0.167995    0.344878   -0.001784    11.00000    0.07249
0.08774 =
      0.08524    0.01108   -0.03335    0.03596
C5    1    0.313716    0.400911    0.036088    11.00000    0.04700
0.04539 =
      0.05869    0.00731   -0.01346    0.02327
H5    2    0.361107    0.488043    0.023535    11.00000    0.07955
0.05860 =
      0.11092    0.03106   -0.03161    0.02040
C6    1    0.364743    0.373549    0.065925    11.00000    0.03397
0.03324 =
      0.04758    0.00321   -0.00704    0.01698
C7    1    0.478343    0.464367    0.080723    11.00000    0.03530
0.02990 =
      0.05514    0.00392   -0.00710    0.01608
C8    1    0.530639    0.590752    0.069369    11.00000    0.06797
0.02873 =
      0.12162    0.01307   -0.03800    0.01726
H8A   2    0.469348    0.613516    0.061841    11.00000    0.12794
0.05959 =
      0.28426    0.02085   -0.08019    0.04847
H8B   2    0.579521    0.607137    0.048137    11.00000    0.24163
0.08887 =
      0.34625    0.12364    0.20233    0.09228
H8C   2    0.576602    0.643463    0.089895    11.00000    0.26422
0.04081 =
      0.29474   -0.00595   -0.19570    0.02192
O6    4    0.480516    0.282277    0.176014    11.00000    0.04639
0.04945 =
      0.03977    0.00467    0.00729    0.02277
D6    7    0.426291    0.213136    0.190121    0.69010    0.04835
0.05113 =
      0.04802    0.00996    0.00463    0.02051
C9    1    0.474396    0.380068    0.191028    11.00000    0.07943
0.04888 =
      0.05619   -0.00787    0.02224    0.01339
H9A   2    0.467959    0.373181    0.219908    11.00000    0.18412
0.13450 =
      0.06731   -0.01809    0.02057    0.08388
H9B   2    0.403049    0.378794    0.181969    11.00000    0.16849
0.13946 =
      0.15837   -0.03704   -0.00760    0.12096
H9C   2    0.548347    0.456744    0.182837    11.00000    0.12606
0.05642 =
      0.17784   -0.01480    0.07069    0.00286
C10   1    0.454590    0.743668    0.158835    0.19479    0.07592
0.24510 =
      0.23757    0.00347    0.02097    0.09644
REM D11   7    0.333333    0.666667    0.059512    0.30788    0.00001
D12   7    0.403372    0.697539    0.183027    0.20325    0.23523
REM AFIX   1
HKLF 4

REM  meohre VIVALDI 295K
REM R1 =  0.0736 for   2063 Fo > 4sig(Fo)  and  0.1311 for all   3285
data
REM    260 parameters refined using      0 restraints

END

WGHT      0.0690     42.1554
REM Highest difference peak  1.110,  deepest hole -0.959,  1-sigma level
0.151
Q1    1   0.5362  0.3610  0.1976  11.00000  0.05    1.11
Q2    1   0.7066  0.6479  0.0721  11.00000  0.05    0.60
Q3    1   0.7331  0.7270  0.0481  11.00000  0.05    0.59
Q4    1   0.2534  0.2861  0.0850  11.00000  0.05    0.57
Q5    1   0.5312  0.5487  0.0664  11.00000  0.05    0.56
Q6    1   0.5422  0.5194  0.0528  11.00000  0.05    0.54
Q7    1   0.1206  0.0771  0.0618  11.00000  0.05    0.53
Q8    1   0.4310  0.3098  0.2203  11.00000  0.05    0.52
Q9    1   0.1652  0.2788  0.0421  11.00000  0.05    0.51
Q10   1   0.6341  0.4760  0.1866  11.00000  0.05    0.51
Q11   1   0.5414  0.3354  0.1708  11.00000  0.05    0.51
Q12   1   0.5807  0.6268  0.1213  11.00000  0.05    0.51
Q13   1   0.4356  0.4477  0.2140  11.00000  0.05    0.51
Q14   1   0.5615  0.4977  0.1651  11.00000  0.05    0.51
Q15   1   0.6307  0.3366  0.1037  11.00000  0.05    0.50
Q16   1   0.6101  0.4885  0.1042  11.00000  0.05    0.49
Q17   1   0.6124  0.4086  0.1797  11.00000  0.05    0.48
Q18   1   0.6146  0.5811  0.2043  11.00000  0.05    0.47
Q19   1   0.1028  0.1421  0.0093  11.00000  0.05    0.47
Q20   1   0.3210  0.5199  0.0885  11.00000  0.05    0.47
Q21   1   0.5175  0.6719  0.0474  11.00000  0.05    0.47
Q22   1   0.4727  0.6533  0.1101  11.00000  0.05    0.47
Q23   1   0.2747  0.2229  0.0943  11.00000  0.05    0.47
Q24   1   0.5186  0.8772  0.1670  11.00000  0.05    0.47
Q25   1   0.2424  0.2162  0.0325  11.00000  0.05    0.46
Q26   1   0.3813  0.3367  0.0616  11.00000  0.05    0.46
Q27   1   0.0000  0.0000  0.0517  10.33333  0.05    0.46
Q28   1   0.5653  0.4429  0.2262  11.00000  0.05    0.46
Q29   1   0.5727  0.1564  0.0305  11.00000  0.05    0.46
Q30   1   0.7500  0.4605 -0.0327  11.00000  0.05    0.46
Q31   1   0.3903  0.4488  0.0639  11.00000  0.05    0.46
Q32   1   0.6619  0.7779  0.0655  11.00000  0.05    0.45
Q33   1   0.0942  0.3049  0.0060  11.00000  0.05    0.45
Q34   1   0.3903  0.3489  0.1386  11.00000  0.05    0.44
Q35   1   0.1018  0.0981  0.0816  11.00000  0.05    0.44
Q36   1   0.5588  0.8788  0.1268  11.00000  0.05    0.44
Q37   1   0.6312  0.4519  0.2165  11.00000  0.05    0.44
Q38   1   0.4491  0.2276  0.0414  11.00000  0.05    0.44
Q39   1   0.3984  0.2759  0.1942  11.00000  0.05    0.44
Q40   1   0.4973  0.6180  0.0331  11.00000  0.05    0.44
```

RES file for compound **9** at 2 K

```
TITL meohre VIVALDI 2K
CELL 0.71073 12.764 12.764 35.682 90 90 120
ZERR 18 0.000 0.000 0.000 0.00 0.00 0.00
LATT 3
SYMM -y,x-y,z
SYMM -x+y,-x,z
SFAC C 0 0 0 0 0 0 0 0 6.6484 0 0 0 0.77 12
SFAC H 0 0 0 0 0 0 0 0 -3.7409 0 0 0 0.32 1
SFAC N 0 0 0 0 0 0 0 0 9.36 0 0 0 .700 14
SFAC O 0 0 0 0 0 0 0 0 5.805 0 0 0 0.66 16
SFAC Mn 0 0 0 0 0 0 0 0 -3.75 0 0 0 0.80 50
SFAC Re 0 0 0 0 0 0 0 0 9.2 0 0 0 0.80 100
SFAC D 0 0 0 0 0 0 0 0 6.674 0 0 0 0.32 1
UNIT 162 198 18 84 18 6 4
TEMP -253
L.S. 4
ACTA
BOND $H
FMAP 2
PLAN 40
REM EXTI    0.000000
WGHT    0.020000
FVAR       0.38146
RE1   6    0.666667    0.333333    0.031949    10.33333    0.00241
0.00241 =
      0.00454    0.00000    0.00000    0.00121
MN1   5    0.500277    0.271205    0.115317    11.00000    0.00373
0.00443 =
      0.00708    0.00017   -0.00079    0.00246
O1    4    0.666667    0.333333    0.114493    10.33333    0.00394
0.00394 =
      0.01075    0.00000    0.00000    0.00197
O2    4    0.638897    0.526367    0.118168    11.00000    0.00506
0.00512 =
      0.01072   -0.00146   -0.00113    0.00236
O3    4    0.337652    0.223824    0.111242    11.00000    0.00509
0.00725 =
      0.01005    0.00074   -0.00060    0.00332
O4    4    0.520056    0.253633    0.047620    11.00000    0.00400
0.00653 =
      0.01002    0.00023    0.00014    0.00134
O5    4    0.666667    0.333333   -0.016718    10.33333    0.00938
0.00938 =
      0.00829    0.00000    0.00000    0.00469
N1    3    0.536103    0.436437    0.103141    11.00000    0.00479
0.00465 =
      0.01005   -0.00028   -0.00090    0.00257
C1    1    0.296629    0.258191    0.082051    11.00000    0.00467
0.00509 =
      0.00938   -0.00015   -0.00120    0.00204
C2    1    0.182879    0.177224    0.068092    11.00000    0.00501
0.00638 =
      0.01050    0.00035   -0.00138    0.00153
H2    2    0.133560    0.091232    0.082078    11.00000    0.01834
0.01614 =
      0.02916    0.00729   -0.00260    0.00247
C3    1    0.134242    0.206643    0.037855    11.00000    0.00597
0.00720 =
      0.01014   -0.00011   -0.00191    0.00216
H3    2    0.045485    0.143388    0.027710    11.00000    0.01520
0.01822 =
      0.02622    0.00209   -0.00582    0.00125
C4    1    0.198900    0.317166    0.020218    11.00000    0.00802
0.00849 =
      0.01198    0.00127   -0.00292    0.00357
H4    2    0.162908    0.340116   -0.004116    11.00000    0.02178
0.02458 =
      0.02690    0.00655   -0.00835    0.00936
C5    1    0.310062    0.398841    0.034406    11.00000    0.00713
0.00748 =
      0.01494    0.00267   -0.00378    0.00211
H5    2    0.358509    0.485209    0.021032    11.00000    0.02254
0.01608 =
      0.03548    0.00977   -0.00780    0.00177
C6    1    0.360994    0.372991    0.065549    11.00000    0.00611
0.00542 =
      0.01228    0.00123   -0.00269    0.00197
C7    1    0.475830    0.465529    0.080494    11.00000    0.00530
0.00394 =
      0.01546    0.00047   -0.00426    0.00105
C8    1    0.526316    0.593671    0.069880    11.00000    0.01457
0.00504 =
      0.04583    0.00628   -0.01493    0.00042
H8A   2    0.460667    0.613134    0.059774    11.00000    0.03540
0.02422 =
      0.07457    0.00536   -0.02397    0.01503
H8B   2    0.595124    0.620186    0.050766    11.00000    0.08782
0.05664 =
      0.21787    0.08660    0.09664    0.04988
H8C   2    0.562863    0.647159    0.094881    11.00000    0.13761
0.02077 =
      0.12406   -0.01771   -0.10225    0.02152
O6    4    0.486341    0.286903    0.176888    11.00000    0.00961
0.00921 =
      0.00932   -0.00009    0.00042    0.00358
D6    7    0.430964    0.215925    0.191068    0.72459    0.01656
0.01514 =
      0.01747    0.00334    0.00295    0.00598
C9    1    0.471867    0.382893    0.190725    11.00000    0.01138
0.00967 =
      0.01375   -0.00140    0.00216    0.00370
H9A   2    0.463598    0.377899    0.221303    11.00000    0.05233
0.03879 =
      0.01906   -0.00425    0.00268    0.02734
H9B   2    0.393233    0.378788    0.178658    11.00000    0.03171
0.04097 =
      0.04687   -0.01082   -0.00930    0.02684
H9C   2    0.550845    0.465649    0.182837    11.00000    0.03041
0.01427 =
      0.05109    0.00026    0.01618    0.00185
C10   1    0.463014    0.756380    0.139578    0.36398    0.01420
0.03032 =
      0.02171    0.00333    0.00245    0.01887
D11   7    0.333333    0.666667    0.123800    0.11425    0.02146
D12   7    0.455866    0.762498    0.178658    0.11840    0.00958
REM AFIX   1
HKLF 4

REM  meohre VIVALDI 2K
REM R1 =  0.0860 for   3968 Fo > 4sig(Fo)  and  0.1358 for all   5631
data
REM    263 parameters refined using      0 restraints

END

WGHT      0.0666    240.6878
REM Highest difference peak  2.471,  deepest hole -3.018,  1-sigma level
0.394
Q1    1   0.0000  0.0000  0.1097  10.33333  0.05    2.20
Q2    1   0.4782  0.5098  0.0703  11.00000  0.05    1.89
Q3    1   0.0712  0.0416  0.0792  11.00000  0.05    1.72
Q4    1   0.5010  0.6507  0.1124  11.00000  0.05    1.68
Q5    1   0.3925  0.4373  0.0360  11.00000  0.05    1.64
Q6    1   0.3343  0.4701  0.0635  11.00000  0.05    1.62
Q7    1   0.6461  0.4897  0.1277  11.00000  0.05    1.57
Q8    1   0.2424  0.3223  0.0076  11.00000  0.05    1.50
Q9    1   0.6291  0.3066  0.1037  11.00000  0.05    1.49
Q10   1   0.4730  0.4180  0.1776  11.00000  0.05    1.42
Q11   1   0.4367  0.4492  0.0470  11.00000  0.05    1.37
Q12   1   0.2967  0.3825 -0.0020  11.00000  0.05    1.36
Q13   1   0.1718  0.2507  0.0488  11.00000  0.05    1.35
Q14   1   0.5942  0.5187  0.1025  11.00000  0.05    1.34
Q15   1   0.6414  0.6524  0.0247  11.00000  0.05    1.33
Q16   1   0.0692  0.4320 -0.0064  11.00000  0.05    1.32
Q17   1   0.4773  0.3481  0.1470  11.00000  0.05    1.32
Q18   1   0.5410  0.4024  0.1142  11.00000  0.05    1.31
Q19   1   0.7166  0.3527 -0.0543  11.00000  0.05    1.31
Q20   1   0.2885  0.3065  0.0531  11.00000  0.05    1.31
Q21   1   0.5028  0.4410  0.1147  11.00000  0.05    1.30
Q22   1   0.2765  0.3879  0.0466  11.00000  0.05    1.30
Q23   1   0.3244  0.2466  0.0682  11.00000  0.05    1.29
Q24   1   0.2412  0.2385  0.1152  11.00000  0.05    1.28
Q25   1   0.1341  0.2937  0.0590  11.00000  0.05    1.28
Q26   1   0.5844  0.6469  0.1267  11.00000  0.05    1.27
Q27   1   0.4448  0.6269  0.0744  11.00000  0.05    1.25
Q28   1   0.6787  0.2992 -0.0051  11.00000  0.05    1.24
Q29   1   0.5781  0.2350  0.1674  11.00000  0.05    1.23
Q30   1  -0.0775  0.1637  0.0462  11.00000  0.05    1.22
Q31   1   0.4132  0.3055  0.0389  11.00000  0.05    1.21
Q32   1   0.5943  0.2829  0.1808  11.00000  0.05    1.21
Q33   1   0.4210  0.2546  0.1419  11.00000  0.05    1.21
Q34   1   0.4209  0.2014  0.1260  11.00000  0.05    1.21
Q35   1   0.1226  0.2383  0.0278  11.00000  0.05    1.20
Q36   1   0.5530  0.3800  0.2366  11.00000  0.05    1.20
Q37   1   0.3414  0.5244  0.0487  11.00000  0.05    1.20
Q38   1   0.4821  0.2094  0.0412  11.00000  0.05    1.19
Q39   1   0.5505  0.3964  0.1543  11.00000  0.05    1.19
Q40   1   0.3671  0.2858  0.2293  11.00000  0.05    1.19
```